Transactions of the ASME

Technical Editor, **L. B. FREUND**

APPLIED MECHANICS DIVISION

Chairman, **CHARLES R. STEELE**
Secretary, **J. D. ACHENBACH**
Associate Editors, **S. T. ARIARATNAM**
T. BELYTSCHKO
D. B. BOGY
M. M. CARROLL
R. J. CLIFTON
L. B. FREUND
MAURICE HOLT
W. D. IWAN
W. G. KNAUSS
A. S. KOBAYASHI
L. E. MALVERN
R. P. NORDGREN
R. H. PLAUT
R. T. SHIELD
C. T. SUN
J. S. WALKER
G. A. WEMPNER
S. E. WIDNALL

BOARD ON COMMUNICATIONS
Chairman and Vice-President
M. J. RABINS

Members-at-Large
W. BEGELL
W. G. GOTTENBERG
H. C. REEDER
D. KOENIG
M. KUTZ
F. LANDIS
J. W. LOCKE
J. E. ORTLOFF
C. PHILLIPS
K. REID

President, **FRANK M. SCOTT**
Exec. Dir.
PAUL ALLMENDINGER
Treasurer, **ROBERT A. BENNETT**

PUBLISHING STAFF
Mng. Dir., Pub., **J. J. FREY**
Dep. Mng. Dir., Pub.
JOS. SANSONE
Managing Editor,
CORNELIA MONAHAN
Production Editor, **SUZANNE MAGIDA**

The Journal of Applied Mechanics (ISSN 0021-8936) is published quarterly for $72 per year by The American Society of Mechanical Engineers, 345 East 47th Street, New York, NY 10017. Second class postage paid at New York, NY and additional mailing offices. POSTMASTER: Send address changes to The Journal of Applied Mechanics, c/o THE AMERICAN SOCIETY OF MECHANICAL ENGINEERS, P.O. Box 3199, Grand Central Station, New York, NY 10163. **CHANGES OF ADDRESS** must be received at Society headquarters seven weeks before they are to be effective. Please send old label and new address.

PRICES: To members, $36.00, annually; to nonmembers, $90.00. Single copies, $24.00 each. Add $6.00 for postage to countries outside the United States and Canada.

STATEMENT from By-Laws. The Society shall not be responsible for statements or opinions advanced in papers or . . . printed in its publications (B7.1, Par. 3).

COPYRIGHT © 1984 by the American Society of Mechanical Engineers. Reprints from this publication may be made on condition that full credit be given the TRANSACTIONS OF THE ASME, JOURNAL OF APPLIED MECHANICS, and the author, and date of publication be stated.

INDEXED by the Engineering Index, Inc.

Journal of Applied Mechanics

Published Quarterly by The American Society of Mechanical Engineers

VOLUME 51 • NUMBER 1 • MARCH 1984

TECHNICAL PAPERS

1 **Effects of Boundary Conditions on the Stability of Slender Viscous Fibers**
W. W. Schultz and S. H. Davis

6 **Steady Laminar Flows Between a Ball and a Spherical Cavity**
D. Bellet, D. P. Ly, and M. Milleret

13 **Liquid-Metal MHD Open-Channel Flows** (84-APM-2)
P. R. Hays and J. S. Walker

19 **Thin Airfoil Theory for Planar Inviscid Shear Flow**
W. C. Chin

27 **Boundary Layer Control by Means of Strong Injection**
R. -J. Yang and M. Holt

35 **Eigenvalues and Stable Time Steps for the Uniform Strain Hexahedron and Quadrilateral** (84-APM-5)
D. P. Flanagan and T. Belytschko

41 **A Theoretical Analysis of Transient Sound Radiation From a Clamped Circular Plate** (84-APM-1)
A. Akay, M. Tokunaga, and M. Latcha

48 **Fully Plastic Crack Problems Part 1: Solutions by a Penalty Method** (84-APM-9)
C. F. Shih and A. Needleman

57 **Fully Plastic Crack Problems Part 2: Application of Consistency Checks** (84-APM-10)
C. F. Shih and A. Needleman

65 **Resonance Effects for a Crack Near a Free Surface** (84-APM-7)
L. M. Keer, W. Lin, and J. D. Achenbach

71 **Transient Stress Intensity Factors of an Interfacial Crack Between Two Dissimilar Anisotropic Half-Spaces Part 1 Orhtotropic Materials**
A. Y. Kuo

77 **Surface Motion Excited by Acoustic Emission From a Buried Crack**
J. G. Harris and J. Pott

84 **Deformations and Stress Intensities Due to a Craze in an Extended Elastic Material** (84-APM-8)
J. R. Walton and Y. Weitsman

93 **Constitutive Restrictions for Idealized Elastic-Viscoplastic Materials**
P. M. Naghdi

102 **Impact Force of a Rigid-Plastic Missile** (84-APM-3)
M. P. White

107 **Constitutive Relations for Fiber-Reinforced Inelastic Laminated Plates**
J. Aboudi and Y. Benveniste

114 **Influence of the Yield Function Nonlinearity and Temperature in Dynamic Buckling of Viscoplastic Cylindrical Shells**
W. Wojewodzki and R. Bokowski

121 **Regularization and Inverse Problems in Viscoplasticity**
G. W. Hedstrom, L. Thigpen, B. P. Bonner, and P. H. Worley

125 **48 Hour Multiaxial Creep and Creep Recovery of 2618 Aluminum Alloy at 200°C** (84-APM-11)
J. -L. Ding and W. N. Findley

133 **Multiaxial Creep of 2618 Aluminum Under Proportional Loading Steps** (84-APM-12)
J. -L. Ding and W. N. Findley

141 **Nonlinear Bending and Collapse of Long, Thin, Open Section Beams and Corrugated Panels** (84-APM-4)
R. C. Benson

146 **A Nonlinear Theory for Elastic Plates With Application to Characterizing Paper Properties**
M. W. Johnson and T. J. Urbanik

153 **A Mutiple-Mode Approach to Large-Amplitude Vibration of Moderately Thick Elliptical Plates** (84-APM-6)
M. Sathyamoorthy and M. E. Prasad

159 **Parametric Instability of a Periodically Supported Pipe Without and With Vibration Absorbers**
A. K. Mallik, J. B. Kulkarni, and K. S. Ram

164 **Friction, Restitution, and Energy Loss in Planar Collisions**
R. M. Brach

171 **General Characteristics of the Motion of Multiple-Pode Joints**
T. W. Lee and E. Akbil

DESIGN DATA AND METHODS

179 **Vibration Frequencies of Tapered Bars With End Mass**
J. H. Lau

182 **Vibration Frequencies of Mode Shapes for a Constrained Cantilever**
J. H. Lau

(Contents continued on Inside Back Cover)

Downloaded 04 May 2010 to 171.66.16.49. Redistribution subject to ASME license or copyright; see http://www.asme.org/terms/Terms_Use.cfm

CONTENTS (CONTINUED)

BRIEF NOTES

Instability of Laminated Cylinders in Torsion — 188
D. Shaw and G. J. Simitses

Effect of Imperfections on the Vibrations of Loaded Structures — 191
I. Elishakoff, V. Birman, and J. Singer

On the Nature of Eigenvalues of General Nonconservative Systems — 193
M. Ahmadian and D. J. Inman

A Higher Order Theory for Free Vibration of Orthotropic, Homogeneous, and Laminated Rectangular Plates — 195
A. Bhimaraddi and L. K. Stevens

The Stability of Motion of a Rigid Body About a Fixed Point in the Case of Euler Within Damping Torque — 198
Z. -M. Ge and X. -X. Wu

Scattering of an Elastic Wave by a Subsurface Elastic Fiber — 199
R. L. Ryan and S. Mall

The Use of Manganin Stress Transducers in Impulsively Loaded Long Rod Experiments — 202
Z. Rosenberg, M. Mayseless, and Y. Partom

Local Nonsimilarity Solutions for Boundary Layers at Lubricated Walls — 204
H. I. Andersson

206 On the Torsion of the Slit Circular Cylindrical Shell
E. H. Mansfield

207 Large-Amplitude Vibrations of Clamped Circular Plate of Variable Thickness
S. K. Chaudhuri

210 A Note on the Incompressible Flow Past a Semi-Infinite Flat Plate in a Stream With Uniform Shear
J. Dey and G. Nath

211 Large-Amplitude Vibrations of Polygonal Plates – A New Approach
B. Banerjee

213 *On Transverse Membrane Vibration of Conical Shells*
C. H. Chang

214 Plane Thermostatic Problems for Inhomogeneous Anisotropic Materials
D. L. Clements and D. L. Hill

216 Effects of Geometric Imperfections on Large-Amplitude Vibrations of Rectangular Plated With Hysteresis Damping
David Hui

DISCUSSION

221-222 Discussion on previously published paper by **L. M. Keer, J. C. Lee,** and **T. Mura,** and **K. T. Chang** (No Closure)

BOOK REVIEWS

223 ***Mechanics of Solids – The Rodney Hill 60th Anniversary Issue*** edited by **H. G. Hopkins** and **M. J. Sewell** . . . Reviewed by **E. H. Lee**
Soil Mechanics – Transient and Cyclic Loads, Constitutive Relations and Numerical Treatment edited by **G. N. Pande** and **O. C. Zienkiewicz** . . . **Reviewed by S. C. Cowin**

224 ***Mechanics of Composite Materials: Recent Advances*** edited by **Z. Hashin** and **C. T. Herakovich** . . . Reviewed by **Y. Weitsman**

225 ***Ultrasonic Testing of Materials*** by **J. Krautkramer** and **H. Krautkramer** . . . Reviewed by **W. Sachse**

Contact Mechanics and Wear of Rail/Wheel Systems edited by **J. Kalousek, R. V. Dukkipati,** and **G. M. L. Gladwell** . . . Reviewed by **L. M. Keer**

226 ***Theory of Viscoelasticity, An Introduction, 2nd Edition*** by **R. M. Christensen** . . . Reviewed by **L. B. Freund**

ERRATA

227 Erratum on "A Treatment of Rigid Body Dynamics," by J. Casey and published in the December 1983 issue

---

18, 47, 56	Worldwide Mechanics Meeting List
12, 26, 113, 124,	Applied Mechanics Symposium Proceedings
132, 140, 145, 158	Applied Mechanics Symposium Proceedings
92	Change of Address Form
5	A Symposium on "Dislocations in Solids: Some Recent Advances"
222	A Symposium on Elastic Plastic Fracture
228	Postdoctoral Research Awards

Downloaded 04 May 2010 to 171.66.16.49. Redistribution subject to ASME license or copyright; see http://www.asme.org/terms/Terms_Use.cfm

W. W. Schultz[1]
Mem. ASME

S. H. Davis

Department of Engineering Science
and Applied Mathematics,
The Technological Institute,
Northwestern University,
Evanston, Ill. 60201

Effects of Boundary Conditions on the Stability of Slender Viscous Fibers

The one-dimensional isothermal flow of viscous-liquid fibers displays draw resonance instability when a constant-velocity winder condition is applied. This instability is removed when a constant-force condition occurs at the winder. The instability mechanism is examined and used to explain the stability trends when the effects of gravity, surface tension, inertia, and wind stress are included.

Introduction

For sufficiently large winder speeds, man-made textile processes are susceptible to a "draw resonance" instability. This instability causes time-periodic variations in the fiber diameter which lowers product performance and can disrupt the spinning process by causing fiber breakage.

Textile process instabilities are commonly studied by examining a simple fiber system composed of a constant-property Newtonian liquid entering a passive gaseous environment. Heat transfer and complex rheology have major qualitative influences, although the basic stability mechanism remains the same as the simplified system. Furthermore, the axisymmetric flow is usually replaced by a one-dimensional flow in which the axial velocity depends only on time t and the axial coordinate z. Such a model is expected to describe the steady basic flow and its stability as long as the axial velocity for both vary slowly along the fiber axis and (axisymmetric) end effects are confined to short regions near the orifice and winder. Consequently, the one-dimensional stability model we use well represents only disturbance wavelengths long compared to the fiber radius. This means that capillary instabilities, with wavelengths on the order of the fiber radius, will be suppressed. This is not a serious limitation for most textile processes.

In this work we will discuss the one-dimensional theory containing modified orifice and winder boundary conditions and their effects on fiber stability characteristics for a viscous-dominated fiber. These results give insight into the mechanism of draw resonance which is useful in predicting trends in more complicated systems.

Formulation of the Stability Problem

A liquid jet (fiber) emerges at an average axial velocity w_i from an orifice of radius r_i into a passive gaseous environment. At a distance L, the fiber is "wound up" at a given average axial velocity w_w. Gravity acts in the z direction. The fluid density ρ and viscosity μ are constant as well as the surface tension γ on the liquid-gas interface. Figure 1 shows a schematic of the fiber system.

The unsteady system of viscous-dominated fibers was first given in [1] and the full system is given in [2]. The steady system is derived systematically from the axisymmetric equations of motion in [3]. In nondimensional form the one-dimensional continuity and axial momentum equations are:

$$(WA)_z + A_t = 0 \tag{1a}$$

$$Re(W_t + WW_z) - G - 3W_{zz} - 3A^{-1}A_z W_z - (2Ca)^{-1}A_z A^{-3/2} = 0. \tag{1b}$$

The boundary conditions for the unsteady problem are

$$W(0,t) = 1, \quad W(1,t) = \mathrm{E} = e^{\alpha}, \quad A(0,t) = 1, \tag{1c,d,e}$$

where subscripts z and t denote partial differentiation. Here, the cross-sectional fiber area A and axial velocity W have been scaled by their values at the orifice, viz., πr_i^2 and w_i, respectively. The axial distance z and time t have been scaled on L and L/w_i, where L is the distance between the orifice and winder. The dimensionless groups are

$$Re = w_i L\rho/\mu \tag{1f}$$

$$G = \rho L^2/\mu w_i \tag{1g}$$

$$Ca = w_i \mu r_i/\gamma L \tag{1h}$$

$$\alpha = ln\ E = ln(w_w/w_i). \tag{1i}$$

The steady solution to system (1) is the basic state $A = A_s(z)$, $W = W_s(z)$ which, in general, must be obtained numerically [2].

We examine the stability of the basic state by superposing small disturbances, linearizing, and using normal modes in time. These disturbed variables have the form

$$W(z,t) = W_s(z)[1 + w(z)e^{\sigma t}] \tag{2a}$$

$$A(z,t) = A_s(z)[1 + a(z)e^{\sigma t}]. \tag{2b}$$

[1] Present Address: Department of Mechanical and Aerospace Engineering, College of Engineering, Rutgers University, Piscataway, N.J. 08854.

Contributed by the Applied Mechanics Division for publication in the JOURNAL OF APPLIED MECHANICS.

Discussion on this paper should be addressed to the Editorial Department, ASME, United Engineering Center, 345 East 47th Street, New York, N.Y. 10017, and will be accepted until two months after final publication of the paper itself in the JOURNAL OF APPLIED MECHANICS. Manuscript received by ASME Applied Mechanics Division, May, 1983.

Copyright © 1984 by ASME
Downloaded 02 May 2010 to 171.66.16.25. Redistribution subject to ASME license or copyright; see http://www.asme.org/terms/Terms_Use.cfm

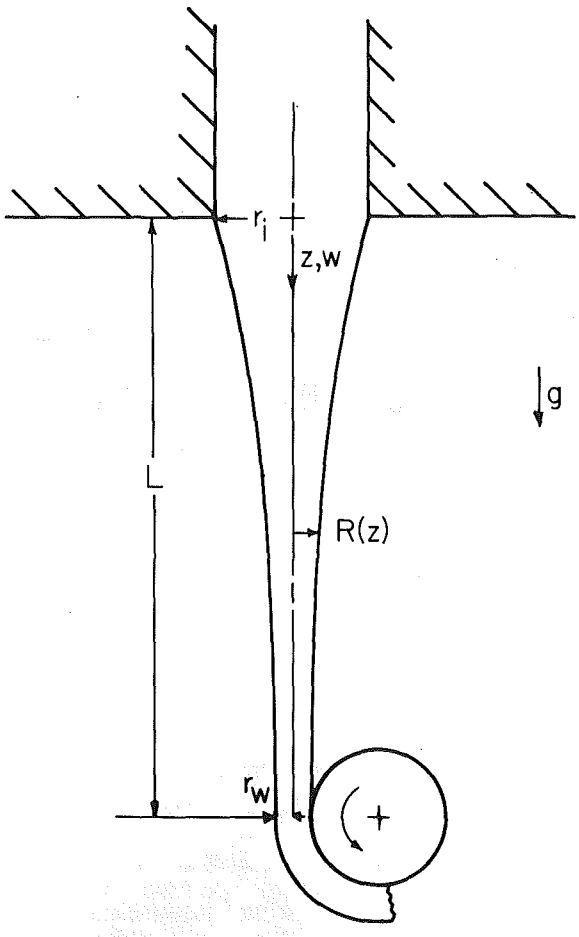

Fig. 1 Fiber coordinate system

where σ is the complex growth rate (eigenvalue) and a and w are complex-valued eigenfunctions. When $E=E_c$, the critical extension ratio, the real part of the growth rate is zero and the eigenvalue $\sigma=i\omega_c$, where ω_c is the frequency of oscillation at critical conditions. Factoring out the forms W_s and A_s (in effect scaling the disturbance quantities on the local basic-state values) simplifies the disturbance equations as compared to those obtained using $W=W_s+w$ and $A=A_s+a$.

The linearized disturbance equations become

$$a_z+w_z+A_s\sigma a=0 \tag{3a}$$

$$w_{zz}+(W_{s_z}A_sa_z)_z+A_sW_{s_z}a_z-Re[(\sigma+2W_{s_z})w + W_sw_z]/3+(6Ca)^{-1}W_s^{1/2}(A_sa_z-A_{s_z}a/2)=0. \tag{3b}$$

The disturbance boundary conditions from (1*c–e*) are

$$a(0)=0,\quad w(0)=0,\quad w(1)=0. \tag{3c,d,e}$$

The norm of the solution is set by

$$w_z(0)=1. \tag{3f}$$

The complex system (3) is broken into a set of six, first-order, real ordinary differential equations and integrated by a Gill-modified, Runge-Kutta shooting method.

The effect of individually varying gravity, surface tension, and inertia on α_c is shown in Fig. 2. The results of Fig. 2 are essentially those of Chang, Denn, and Geyling [4] who obtained more accurate values than the earlier results of Shah and Pearson [5]. Our independently obtained results are within 1 percent of those of [4]. Figure 2 shows that gravity and inertia stabilize the fiber while surface tension destabilizes the fiber. We will explain these trends after examining the instability mechanism for viscous-dominated fibers.

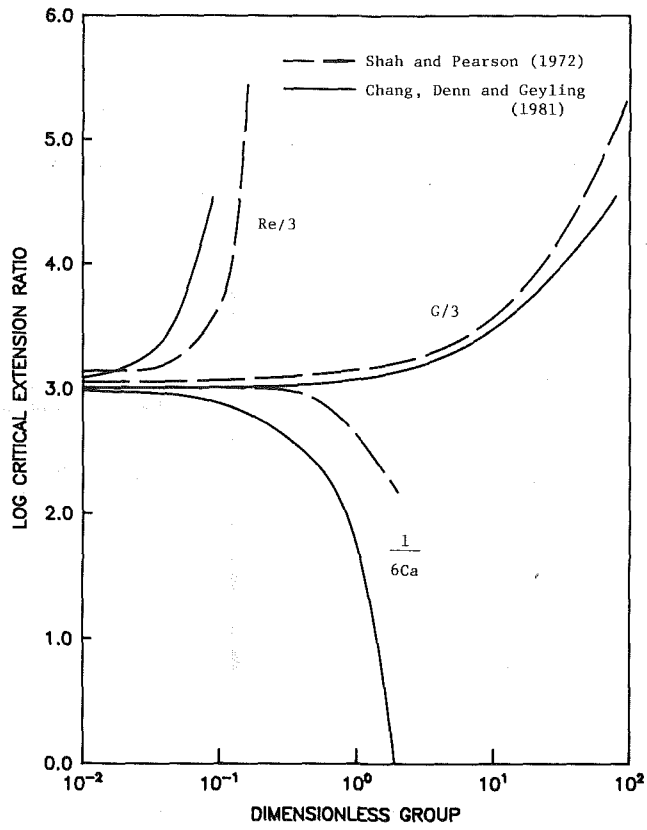

Fig. 2 Effect of gravity, surface tension, and inertia or fiber stability

Comparisons With Experiments

There are three sets of experiments on isothermal, Newtonian fibers [6–8]. These are in general agreement with the one-dimensional stability analysis as shown in [8] and summarized in Table 1. The experimental critical draw ratios are generally within 20 percent of the predicted values. Average draw ratios are about 15 percent less than the predictions while frequencies are roughly 30 percent less than that predicted. The trends of increasing gravity, surface tension, and inertia appear correct. Inexplicably, the data of [8] have a frequency one-sixth the predicted value.

There are some ambiguities in comparing experiments to the theory because the actual flow is two-dimensional near the fiber ends. Two-dimensional corrections for the steady jet radius in the region away from the ends (based on [3]) are less than one-half percent for the typical data of [7]. However, the two-dimensional regions at the fiber ends have an axial extent of approximately one diameter [9]. From the slenderness ratio ϵ (the orifice radius divided by jet length) shown in Table 2, we see that the boundary layer at the orifice is 2–14 percent of the fiber length. To bypass this region, Chang and Denn [8] move the origin of their coordinate system to the point of maximum die swell. Although radial variations of the axial velocity are small at this point, it is obvious that one-dimensional theory is still not valid there since dR/dz of the one-dimensional model cannot vanish in an accelerating jet. They also assume that the radius of the die swell region is fixed during unsteady flow. There is no reason to expect this.

There are also difficulties in evaluating the boundary condition at the winder. Chang and Denn [8] note that the peripheral winder speed is considerably higher than the average axial fiber velocity at the winder. This is indeed necessary if the winder is to apply a tension to an isothermal jet. Chang and Denn use the average jet velocity at the winder (calculated from fiber diameter measurements) in comparison

Downloaded 02 May 2010 to 171.66.16.25. Redistribution subject to ASME license or copyright; see http://www.asme.org/terms/Terms_Use.cfm

Table 1 Experimental stability comparisons

r_i	ρ	σ	μ	L	w_i	E_c	T
(cm)	(g/cm^3)	(d/cm)	(poise)	(cm)	(cm/s)		(s)
			Chang and Denn (1979)				
0.178	1.4	60.0	220	4	3.43	26.0	2.3
			Donnelly and Weinberger (1975)				
0.140	1.0	22.4	1000	2	1.04	17.0	1.2
0.140	1.0	22.4	1000	2	0.72	17.3	1.8
0.140	1.0	22.4	1000	2	0.50	17.2	1.4
0.140	1.0	22.4	1000	4	0.50	17.2	3.4
			D'Andrea and Weinberger (1976)				
0.120	1.0	22.4	1000	7.8	0.98	26.0	
0.120	1.0	22.4	1000	9.6	0.98	37.1	
0.120	1.0	22.4	1000	10.9	0.98	46.2	
0.093	1.0	22.4	1000	7.3	0.75	26.9	
0.120	1.0	22.4	1000	8.5	0.68	43.0	
0.120	1.0	22.4	1000	12.4	0.98	52.0	
0.075	1.0	22.4	1000	6.4	0.39	17.8	
0.120	1.0	22.4	1000	5.8	0.22	31.9	
0.075	1.0	22.4	1000	12.9	0.80	46.9	

Table 2 Analytical stability comparisons

$G/3$	$Re/3$	$Ca^{-1}/6$	ϵ	E_c	ω_c	T
			Chang and Denn (1979)			
9.7	0.02900	0.300	0.045	32.20	18.63	0.40
			Donnelly and Weinberger (1975)			
1.25	0.00069	0.051	0.070	20.78	14.67	0.82
1.81	0.00048	0.198	0.070	20.90	14.94	1.17
2.60	0.00033	0.285	0.070	21.05	15.32	1.64
10.4	0.00066	0.213	0.035	26.70	19.36	2.60
			D'Andrea and Weinberger (1976)			
20.2	0.0026	0.246	0.015	35.18	23.66	
30.6	0.0031	0.303	0.013	42.07	27.40	
39.4	0.0036	0.345	0.011	47.60	30.18	
23.2	0.0018	0.390	0.013	32.66	24.35	
34.8	0.0019	0.390	0.014	40.95	28.54	
51.1	0.0041	0.392	0.010	54.60	33.53	
34.0	0.0008	0.810	0.011	27.50	27.03	
49.2	0.0004	0.808	0.020	34.30	31.86	
68.1	0.0034	0.805	0.006	44.57	36.98	

of analysis to experiments but they still use the fixed jet speed winder boundary condition. Weinberger and coworkers use the winder speed in their calculations. Since there is slip between the wheel and fiber, a mixed boundary condition is more appropriate for the one-dimensional theory. These boundary conditions are analyzed further in the next section for the viscous-dominated case.

Winder Boundary Conditions

When gravity, surface tension, and inertia are neglected, the normal-mode disturbance equations and boundary conditions can be simplified to the following:

$$a_z + w_z + \sigma e^{-\alpha z} a = 0 \tag{4a}$$

$$w_{zz} + \alpha(a_z + w_z) = 0 \tag{4b}$$

$$a(0) = w(0) = w(1) = 0. \tag{4c,d,e}$$

The velocity can be eliminated to give the equivalent system:

$$a_{zz} + \sigma e^{-\alpha z} a_z = 0 \tag{5a}$$

$$a(0) = 0 \tag{5b}$$

$$a_z(1) - a_z(0) + (\sigma e^{-\alpha} - \alpha) a(1) = 0. \tag{5c}$$

Equation (5a) can be integrated directly to give

$$a = C_1 E_1\left(-\frac{\sigma}{\alpha} e^{-\alpha z}\right) + C_2, \tag{6}$$

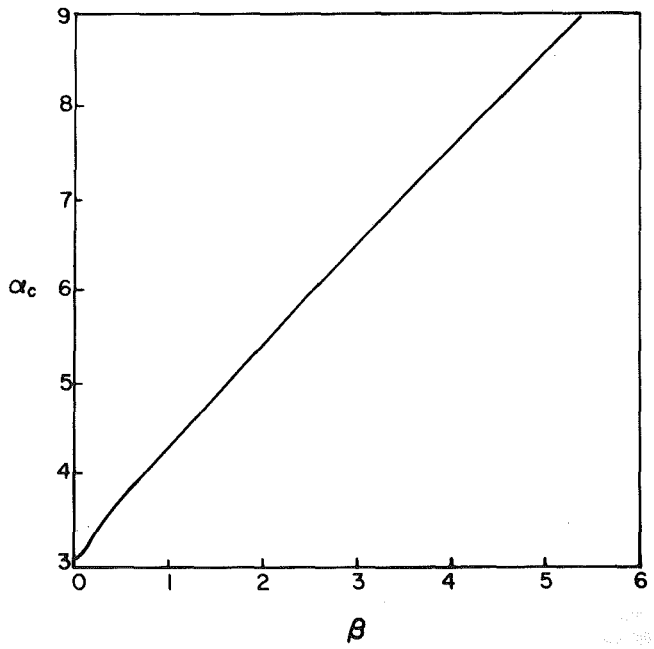

Fig. 3 Effect of winder slip on fiber stability

Downloaded 02 May 2010 to 171.66.16.25. Redistribution subject to ASME license or copyright; see http://www.asme.org/terms/Terms_Use.cfm

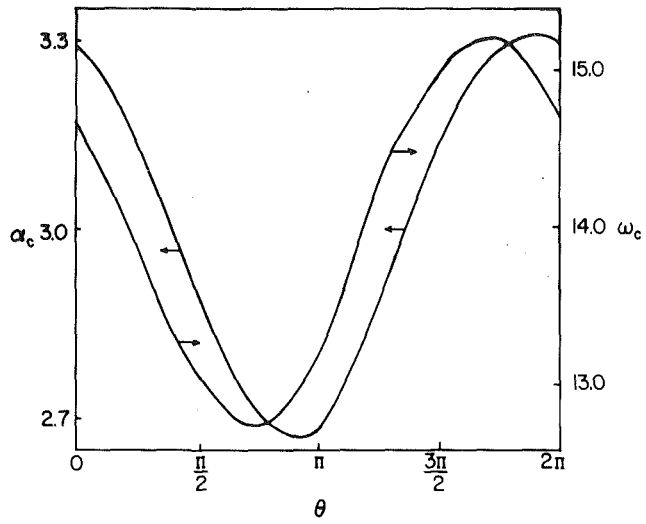

Fig. 4 Effect of winder boundary condition phase on critical α and ω

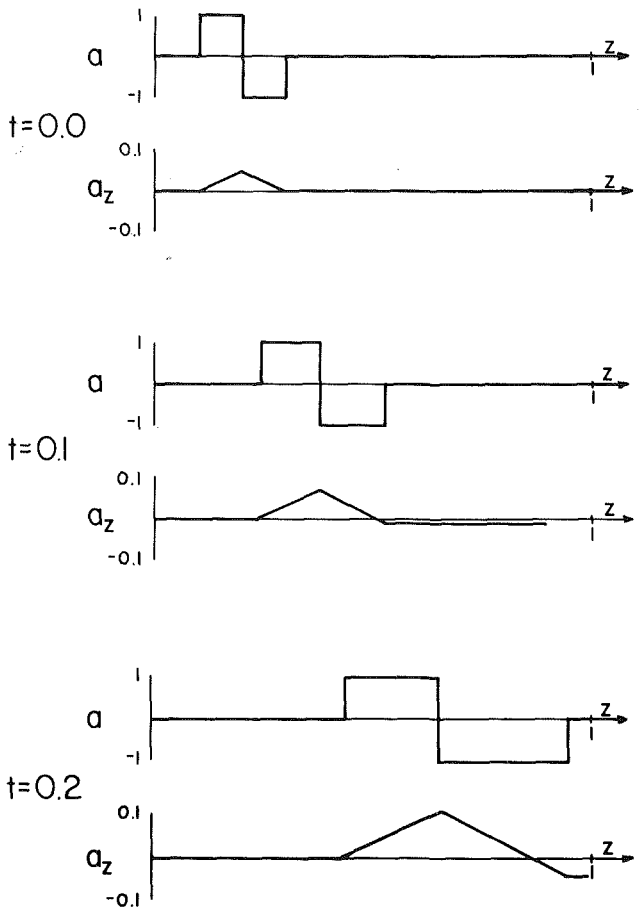

Fig. 5 Wave forms of disturbances for constant force winder

where E_1 is the exponential integral of the first kind and C_1 and C_2 are constants of integration. Application of boundary conditions gives the characteristic equation

$$e^{uv} - e^u + (uv-1)[E_1(-uv) - E_1(-u)] = 0, \tag{7}$$

where $u = \sigma/\alpha$ and $v = e^{-\alpha}$. This complex-valued equation can be solved by secant methods to find the now standard results [8, 10] very accurately:

$$\alpha_c = 3.006510\ (E_c = 20.21),\ \omega_c = 14.011.$$

As previously mentioned, a mixed (Robin) boundary condition would be more appropriate at the winder. This can be written as

$$w(1) + \beta f(1) = 0, \tag{8}$$

where f is the normal-mode amplitude of the force disturbance applied by the winder to the fiber. Now $\beta = 0$ represents the constant-velocity condition and $\beta = \infty$ represents the constant-force condition. Here, β might be a complex constant which could be determined experimentally. The value of β should depend on a number of factors but the real part should be positive since the fiber velocity at the winder should decrease as the resistance of the fiber to elongation increases. The force f is the integral of (4*b*),

$$f = w_z + \alpha(a + w). \tag{9}$$

If the orifice boundary condition remains as $a(0) = 0$, boundary condition (5*c*) is now replaced by

$$a_z(1) - (1+\beta)a_z(0) + (\sigma e^{-\alpha} - \alpha)a(1) = 0, \tag{10}$$

and the characteristic equation that replaces expression (7) is

$$e^{uv} - e^u + (uv-1)[E_1(-uv) - E_1(-u)] - \beta e^u = 0. \tag{11}$$

The critical α varies with β as shown in Fig. 3. The constant-velocity critical value is still $\alpha_c = 3.00657$ and the constant-force critical value approaches infinity so the jet appears to be *completely stabilized*. Kase and Denn [11] have mentioned without elaboration that the constant-force winder boundary condition stabilizes the fiber, and White and Ide [12] allude to this phenomenon. We note from (10) that as $\beta \to \infty$, the boundary value problem switches to an initial value problem. Thus, the eigenvalue character of the stability problem is lost.

Figure 3 indicates that fiber slippage at the winder increases the critical α and ω, which increases the disparity between predictions and experiments. If this disparity is due to slippage or the winder boundary condition in general, this could be caused by a phase difference between f and w. This phase would be a function of the winder motor characteristics, winder moment of inertia, etc. This phase lag θ is represented in equation (8) by a complex-valued β,

$$\beta = |\beta| e^{i\theta}. \tag{12}$$

As an example, Fig. 4 shows ω_c and α_c for $|\beta| = 0.2$ and $0 < \theta < 2\pi$. This shows that the predicted critical values can approach the experimental values when a phase θ is included in the model. Without further experimental information about the winder and an analysis near the orifice, we cannot proceed further.

The boundary conditions at the orifice could also be replaced by modified conditions at a new origin defined downstream of the point of maximum swell to avoid the two-dimensional region. With the added complexity of two boundary conditions at the orifice, this ad hoc approach seems unsatisfactory. Further study of unsteady flow near the orifice should examine the full axisymmetric equations.

The Instability Mechanism

The preceding analysis gives insight into the stability mechanism of draw resonance. When the winder boundary condition is that of constant force, the solution to the initial value problem can be solved by factoring the original disturbance equations (3) to show the hyperbolic character of the operator:

$$(\partial/\partial z + e^{-\alpha z}\partial/\partial t)\partial a/\partial z = 0, \tag{13a}$$

whose first integral is

$$a_z = G(t + e^{-\alpha z}/\alpha), \tag{13b}$$

where G is an arbitrary function. Equation (13*b*) can be further integrated to give the solution for a. These equations

Downloaded 02 May 2010 to 171.66.16.25. Redistribution subject to ASME license or copyright; see http://www.asme.org/terms/Terms_Use.cfm

first appeared in [2] and have been analyzed somewhat in [12]. The velocity of the wave of a_z from (13*a*) is seen to be the velocity of the basic state $e^{\alpha z}$, while the wave velocity of a is infinite. (This supports Denn's [13] criticism of the analysis by Hyun [14] who compared "wave residence time" with fluid residence time.)

The solution for the initial value problem for a specific extension ratio and initial disturbance is shown in Fig. 5. This shows that the a_z wave travels at the basic-state axial velocity W which increases exponentially downstream. Integrating this function shows that the disturbance near the orifice is immediately "felt" at the winder. If the Reynolds number had been nonzero, there would be a finite time required for the disturbance to travel to the winder.

When the winder boundary condition is that of constant force, the disturbances travel only downstream. When the boundary condition is other than that of constant force, the winder partially "reflects" the disturbance back upstream by changing the force in the entire fiber. Depending on the degree of reflection, the disturbance can grow or attenuate.

This interpretation of the mechanism can be used to explain the trends of gravity, surface tension, and inertia found in Fig. 2. Gravity decreases the role of the winder in accelerating the jet, so variations in the force there are not as severe. Hence, gravity stabilizes the fiber. Surface tension has the opposite effect. Increasing inertia is stabilizing because the winder force variations are damped by the inertia of the fiber near the winder. In addition, some unpublished results [15] show that the jet becomes more (less) stable when positive (negative) air drag is added to the fiber model.

Conclusions

We find that draw resonance can be interpreted as a wave phenomenon where the winder can cause wave reflection unless it applies a constant force to the fiber. This realization allows the prediction of trends in fiber-flow instabilities when new physical effects are included in the analysis.

Acknowledgment

The authors acknowledge the support of the Owens/Corning Fiberglass Corporation in funding this research.

References

1 Kase, S., and Matsuo, T., "Studies on Melt Spinning: II. Steady State and Transient Solutions of Fundamental Equations Compared With Experimental Results," *J. Appl. Polymer Sci.*, Vol. 11, 1967, pp. 251–287.

2 Pearson, J. R. A., and Matovich, M. A., "On Spinning a Molten Threadline: Stability," *Ind. Eng. Chem. Fund.*, Vol. 8, 1969, pp. 605–609.

3 Schultz, W. W., and Davis, S. H., "One-Dimensional Liquid Fibers," *J. Rheol.*, Vol. 26, 1982, pp. 331–345.

4 Chang, J. C., Denn, M. M., and Geyling, F. T., "Effects of Inertia, Surface Tension and Gravity on the Stability of Isothermal Drawing of Newtonian Fluids," *Ind. Eng. Chem. Fund.*, Vol. 20, 1981, pp. 147–149.

5 Shah, Y. T., and Pearson, J. R. A., "On the Stability of Nonisothermal Fiber Spinning: General Case," *Ind. Eng. Chem. Fund.*, Vol. 11, 1972, pp. 150–153.

6 Donnelly, G. J., and Weinberger, C. B., "Stability of Isothermal Fiber Spinning of a Newtonian Fluid," *Ind. Eng. Chem. Fund.*, Vol. 14, 1975, pp. 334–337.

7 D'Andrea, R. G., and Weinberger, C. B., "Effects of Surface Tension and Gravity Forces in Determining the Stability of Isothermal Fiber Spinning," *AIChE J.*, Vol. 22, 1976, pp. 923–925.

8 Chang, J. C., and Denn, M. M., "An Experimental Study of Isothermal Spinning of a Newtonian and a Viscoelastic Liquid," *J. Non-Newtonian Fluid Mech.*, Vol. 5, 1979, pp. 369–385.

9 Fisher, R. J., Denn, M. M., and Tanner, R. I., "Initial Profile Development in Melt Spinning," *Ind. Eng. Chem. Fund.*, Vol. 19, 1980, pp. 195–197.

10 Gelder, G., "The Stability of Fiber Drawing Processes," *Ind. Eng. Chem. Fund.*, Vol. 10, 1971, pp. 534–535.

11 Kase, S., and Denn, M. M., "Dynamics of the Melt Spinning Process," *Joint Automatic Control Conference*, Vol. 2, 1978, pp 71–84.

12 White, J. L., and Ide, Y., "Instabilities and Failure in Elongational Flow and Melt Spinning of Fibers," *J. App. Polymer Sci.*, Vol. 22, 1978, pp. 3057–3074.

13 Denn, M. M., "On an Analysis of Draw Resonance by Hyun," *AIChE J.*, Vol. 26, 1980, pp. 292–294.

14 Hyun, J. C., "Theory of Draw Resonance," *AIChE J.*, Vol. 24, 1978, pp. 418–426.

15 Lee, Y., Private Communication, 1983.

Downloaded 02 May 2010 to 171.66.16.25. Redistribution subject to ASME license or copyright; see http://www.asme.org/terms/Terms_Use.cfm

D. Bellet
Professor.

D. P. Ly
Master of Research,
C.N.R.S.

M. Milleret
Doctor in Mechanics.

Groupes de Transport Solide et de Rhéologie,
Institut de Mécanique des Fluides,
2, rue Camichel,
31071 Toulouse Cedex, France

Steady Laminar Flows Between a Ball and a Spherical Cavity

Steady laminar flows of a newtonian fluid in the vicinity of a spherical ball located inside a spherical cavity are studied. Two methods were employed: a method involving a finite element calculation and an experimental method based on measurements of local velocities by means of laser Doppler anemometry using the Bragg cell. The influences of the Reynolds numbers and of the ball positions in the cavity have been analyzed and compared.

1 Introduction

Experimental problems of determining the flow past fixed bodies have been investigated by many authors. In particular Cousins [1] has developed the Pitot tube to measure direction of flow as well as speed in flow past a sphere. One such instrument, the Warden tube, consists of an hemisphere mounted on a cylindrical shaft. Pressure readings can be taken from five holes located on the hemisphere; speed and direction of flow are then obtained either from experimental calibration or calculation. Cousins has determined the velocity distribution over the upstream part of the sphere by a numerical method using a Biot-Savart law. Such flow has been discussed also by Lighthill. This author has investigated how the addition of a parallel shear flow to a uniform stream affects the measurement of pressure [2].

When the flow is produced by a sphere located in a tube or a cavity, the Warden tube cannot be applied because its dimensions. Experimental studies are then performed by flow visualization [3, 4]. For instance, Doffin and Chagneau have photographed the motion of the particles in suspension in fluid which shows the trajectories of flow between a clot model and a stenosis. The flow visualization immediately gives the aspect of the streamlines associated with the steady streaming. With very few exceptions, however, the flow visualization does not allow accurate measurements.

This paper concerns the determination of velocity profiles in laminar steady flow of a newtonian fluid betweeen a sphere and a cavity by Laser Doppler anemometry. The model is composed of an obstacle of spherical shape held in different positions inside a spherical cavity.

According to experimental conditions, a numerical solution of the equations is performed by Finite-Element technique of the Galerkin type. This numerical process may be adapted to any axisymmetrical flow [6].

2 Mathematical Formulation

Basic Equations. Flows are assumed to be incompressible and newtonian. Owing to the boundary conditions imposed by the considered geometries, the velocity profiles are axisymmetric. By using a cylindrical coordinates reference centered at 0, the center of the spherical cavity as shown in Fig. 1, the components of V can be reduced to:

$$v_r = v(r,x); \quad v_\theta = 0; \quad v_z = u(r,x) \tag{1}$$

If body forces are neglected, the Navier Stokes equations are:

$$\frac{\partial p^*}{\partial x^*} - \frac{1}{R_e}\cdot\left(\frac{1}{r^*}\cdot\frac{\partial u^*}{\partial r^*} + \frac{\partial^2 u^*}{\partial x^{*2}} + \frac{\partial^2 u^*}{\partial r^{*2}}\right) + u^*\frac{\partial u^*}{\partial x^*} + v^*\frac{\partial u^*}{\partial r^*} = 0 \tag{2}$$

$$\frac{\partial p^*}{\partial r^*} - \frac{1}{R_e}\cdot\left(\frac{1}{r^*}\cdot\frac{\partial v^*}{\partial r^*} - \frac{v^*}{r^{*2}} + \frac{\partial^2 v^*}{\partial x^{*2}} + \frac{\partial^2 v^*}{\partial r^{*2}}\right) + u^*\frac{\partial v^*}{\partial x^*} + v^*\frac{\partial v^*}{\partial r^*} = 0 \tag{3}$$

$$\frac{v^*}{r^*} + \frac{\partial u^*}{\partial x^*} + \frac{\partial v^*}{\partial r^*} = 0 \tag{4}$$

where:

$$u^* = \frac{u}{V_0}\,;\ v^* = \frac{v}{V_0}\,;\ p^* = \frac{p}{\rho V_0^2}\,;\ x^* = \frac{x}{R}\,;\ r^* = \frac{r}{R}\,;\ R_e = \frac{\nu}{V_0 R}$$

where p is the static pressure, ρ is the fluid density and, η is the dynamic fluid viscosity.

V_0 is the upstream axial velocity at infinity; R is the radius of both the tube and the ball; ν is the kinematic fluid viscosity; and R_e is the Reynolds number.

Contributed by the Applied Mechanics Division for publication in the JOURNAL OF APPLIED MECHANICS.

Discussion on this paper should be addressed to the Editorial Department, ASME, United Engineering Center, 345 East 47th Street, New York, N.Y. 10017, and will be accepted until two months after final publication of the paper itself in the JOURNAL OF APPLIED MECHANICS. Manuscript received by ASME Applied Mechanics Division, April, 1982; final revision, May, 1983.

Copyright © 1984 by ASME
Downloaded 02 May 2010 to 171.66.16.25. Redistribution subject to ASME license or copyright; see http://www.asme.org/terms/Terms_Use.cfm

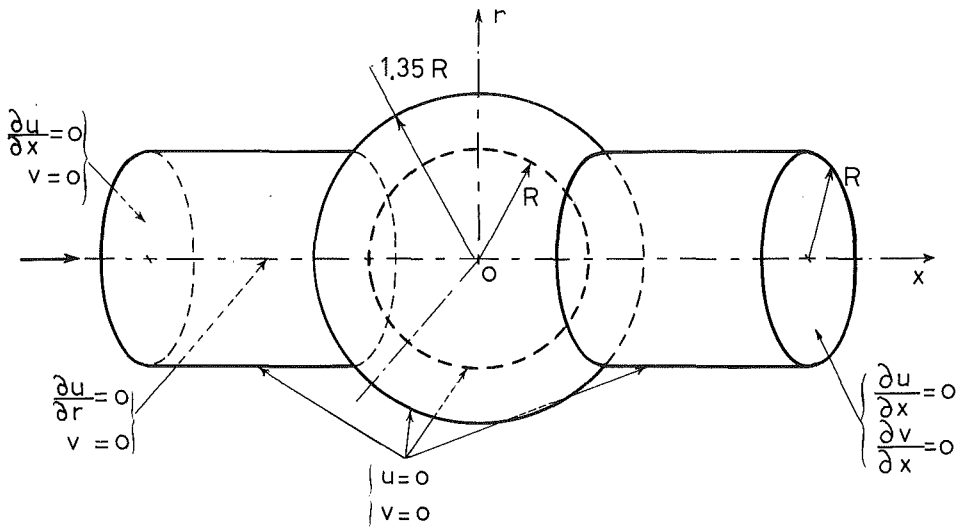

Fig. 1 Studied geometry in the case where the ball is centered in the spherical cavity center; work reference; boundary conditions of the flows

Since we will always, hereafter, consider the relations in nondimensional form, we will delete the * in order to simplify the writing.

Boundary Conditions. The boundary conditions relative to the problem are:

upstream boundary conditions:

$$\left.\frac{\partial u}{\partial x}\right|_{x\to-\infty}=0 \quad \left. v\right|_{x\to-\infty}=0 \tag{5}$$

downstream boundary conditions:

$$\left.\frac{\partial u}{\partial x}\right|_{x\to+\infty}=0 \quad \left.\frac{\partial v}{\partial x}\right|_{x\to+\infty}=0 \tag{6}$$

symmetry of the flow about the center line:

$$\left.\frac{\partial u}{\partial r}\right|_{r=0}=0 \quad \left. v\right|_{r=0}=0 \tag{7}$$

at the wall (no slip condition):

$$u=0; \quad v=0 \tag{8}$$

Figure 1 gives a synoptic representation of these boundary conditions.

3 Numerical Method

This method involves a finite element calculation based on the discretization of Galerkin. As the motion equations include the second partial derivatives of velocity with respect to x or r and the first derivatives of the pressure, therefore the approximations can be found for the velocity by using second-degree polynomials of x or r, and for pressure, by using a linear function.

The grid used in the solution consists of curvilinear quadrilaterals. The surface integrals of Galerkin formulation are calculated on each grid element by a nine-point Gauss method. Equations in finite difference forms are linearized by the Raphson-Newton's iterative method.

The calculation is started at the low Reynolds number ($R_e=1$) by choosing a distribution near upstream velocities. After having determined the velocity profiles for $R_e=1$, the case for a greater Reynolds number has been calculated by taking the last distribution of the previous case as the initial distribution for this one, and so on: for the succeeding values of R_e, the initial conditions have been taken as the found values for the previous R_e. The condition of obtaining the velocity is such that, at each point of the grid, the difference between two values calculated by two successive iterations is smaller than 10^{-3}. In this way, the convergence happens quickly.

4 Experimental Method

The experimental model has been constructed in such a way as to represent as faithfully as possible the system and the hypotheses previously considered, as much from the geometrical point of view as from the hydrodynamic point of view (Fig. 2).

The measurement unit is the main element of the model. It includes a circular cylindrical tube, radius $R=1.75\ 10^{-2}$ m issuing to a spherical cacity, radius $1.35\,R=2.36\ 10^{-2}$ m.

The whole set is machined in two transparent altuglas symmetrical parts. A spherical altuglas ball also transparent, radius, R, is maintained in position, centered on the unit axis by two thin metallic rods perpendicular to the flow. In addition to the central position ($Ex=0$) two upstream positions $Ex=-0.286\ R$ and $Ex=-0.572\ R$ and two downstream symmetrical positions $Ex=0.286\ R$ and $Ex=0.572\ R$ may be used in order to place the ball eccentrically with regard to the cavity (Fig. 1) through various rod fixation plugs. Two pressure tappings located at a distance of $2R$ from the system center are provided on the duct one upstream, the other downstream.

The velocity profiles have been determined by a counter-type Laser Doppler anemometer MARK II. This system does not disturb the flow. The spatial resolution is great, measurement volume is smaller than 0.25 mm^3. This technique leads to simultaneous measurements of the two components u and v of velocity V at each point. The "optical fringes setting" was adopted.

A Doppler frequency shift system with Bragg cells has been inserted between the laser source-optical unit set and the photomultiplier in order to detect the direction of flow in recirculation areas and to improve the precision of low velocity measurement.

Obtaining accurate positioning of the measurement points makes it necessary to avoid any refraction of the beams at the altuglas-fluid interface. To this end, a mixture of vaseline oil (60 percent) and tetraline oil (40 percent) (tetra)-hydronaphthalene) with a refraction index 1.493 equal to that of altuglas, was employed. This fluid has newtonian behavior.

Some hundred measurement points are explored for each

Downloaded 02 May 2010 to 171.66.16.25. Redistribution subject to ASME license or copyright; see http://www.asme.org/terms/Terms_Use.cfm

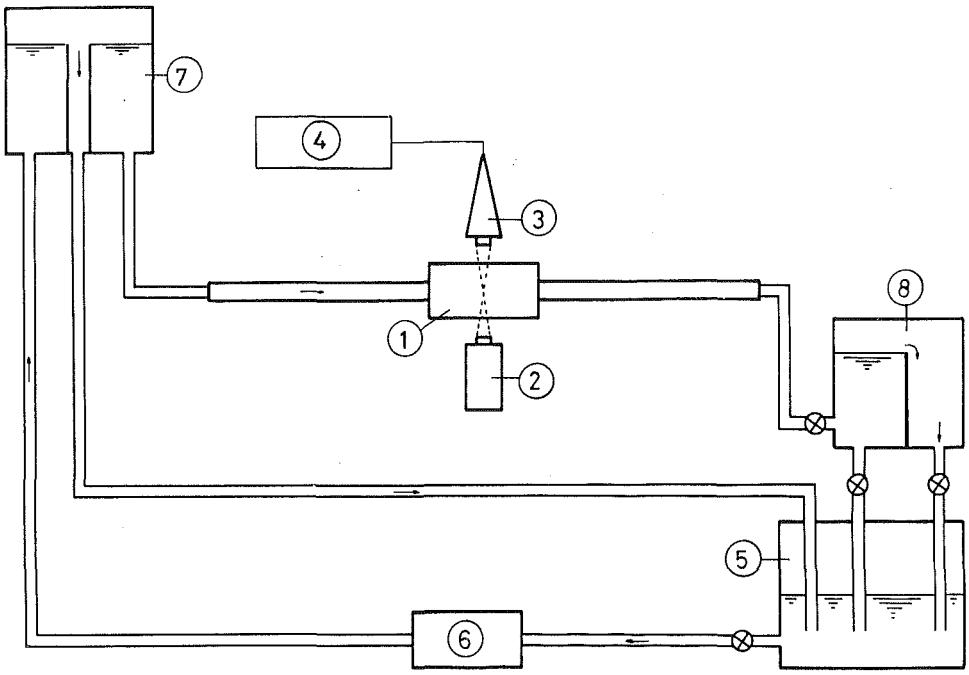

Fig 2 Diagram of the experimental set up: 1. Measurement unit of the test section. 2. Laser Doppler anemometer with Laser source. 3. Photomultiplier. 4. Processing unit. 5. Supply tank. 6. Pump. 7. Upstream tank with constant level and adjustable height. 8. Downstream tank with constant level.

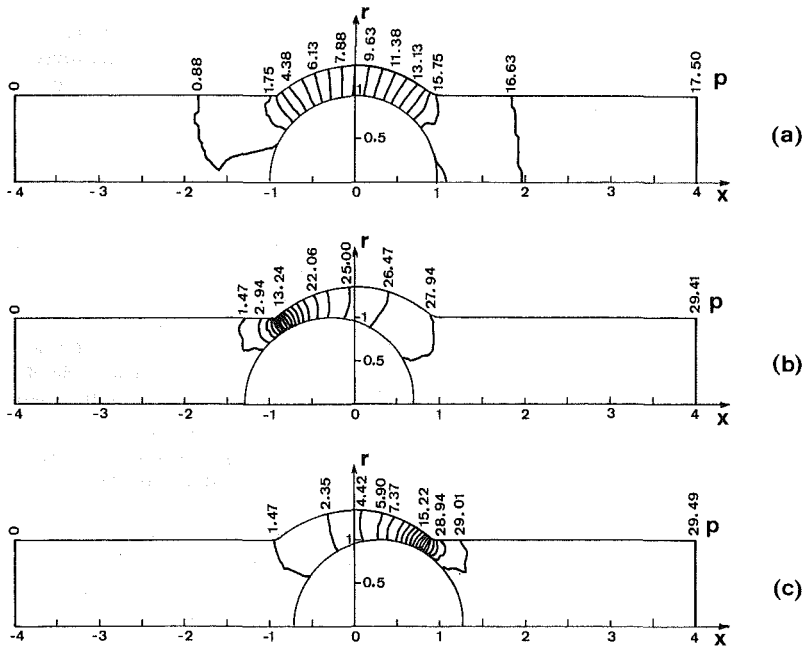

Fig. 3 Influence of ball eccentricity Ex on the reduced pressure distributions with fixed Reynolds number ($R_e = 10$). Case (a): $Ex = 0$.; case (b): $Ex = -0.286\ R$; case (c): $Ex = +0.286\ R$; graduations given in reduced pressures

case with various Reynolds numbers and different positions of the ball in the cavity.

5 Results

(A) Numerical Results

Isobar Curver. On each graph, isobars are regularly distributed from the reference pressure 0 to the outlet pressure. They are graduated in the reduced pressures $\Delta p/\rho V_0^2$. We can note that the pressure drop depends considerably on the eccentricity Ex of the ball in the cavity and increases along with the latter as it can be seen on Fig. 3. When the center of the ball coincides with the center of the cavity (Fig. 3(a)), the isobars in the entrance and the outlet of the gap are quite symmetrical. When the ball no longer coincides with the center of the cavity, isobars are close in the narrower passage between the ball and the cavity (Figs. 3(b) and (c)). Figure 4 shows the influence of Reynolds numbers

Downloaded 02 May 2010 to 171.66.16.25. Redistribution subject to ASME license or copyright; see http://www.asme.org/terms/Terms_Use.cfm

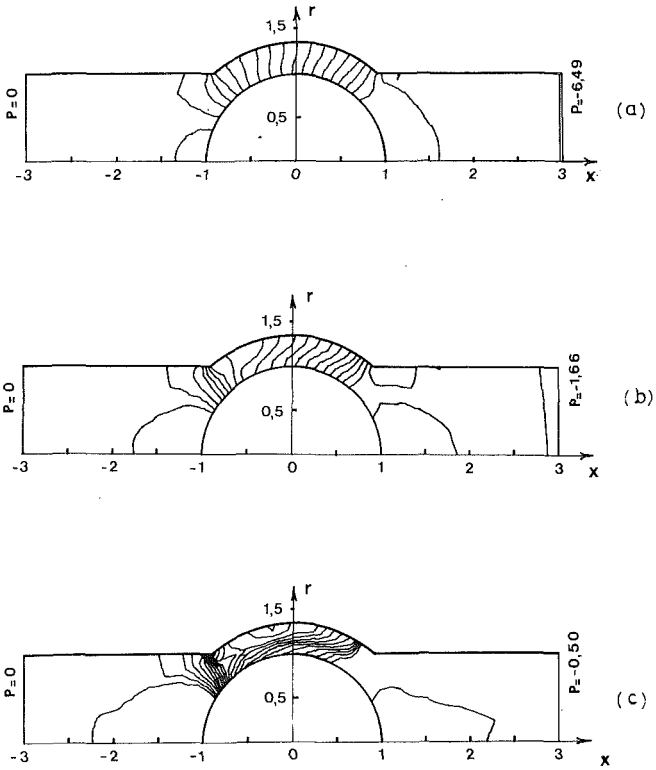

Fig. 4 Influence of Reynolds number on isobars, with fixed eccentricity: $Ex = 0$. Case (*a*): $R_e = 25$; case (*b*): $R_e = 100$; and case (*c*): $R_e = 400$.

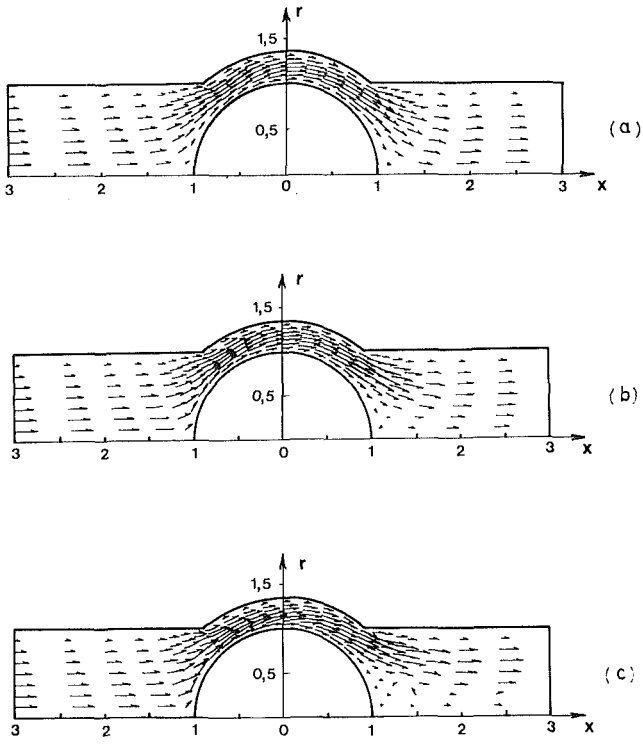

Fig. 5 Evolution of numerical velocity profiles along the model $Ex = 0$. Case (*a*): $R_e = 1$; case (*b*): $R_e = 100$; and case (*c*): $R_e = 600$

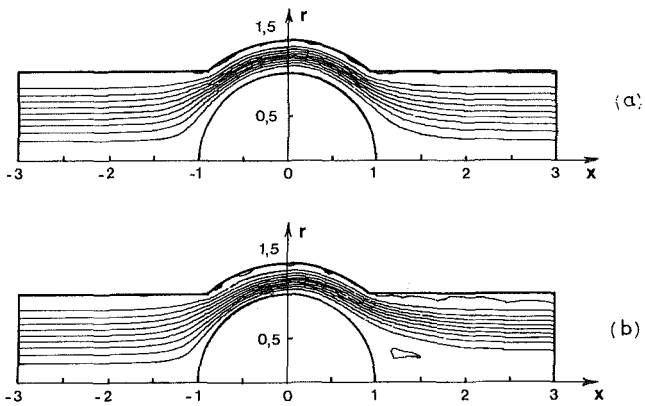

Fig. 6 Calculated streamlines. Case (*a*): $R_e = 25$; and case (*b*): $R_e = 600$

on the isobars for a fixed position of the ball ($Ex = 0$). For increased Reynolds numbers, isobars are very close at the entry of the feature and distorted at the outlet of the same one. For a large Reynolds number, $R_e = 400$, there is a stagnation area downstream the ball (Fig. 4(*c*)).

Velocity Profiles: In Fig. 5, in which the center of the ball coincides with the center of the cavity, the calculated velocity profiles are related to various sections of the feature, for three values of Reynolds number: $R_e = 1$; 100; 600. At $R_e = 1$, the velocity profiles of the entrance and outlet of the feature are similar, because the extremity effects are nearly the same at small Reynolds number. As R_e increased, the velocity profiles tend to hollow out toward the axis in the region just upstream of the obstacle. The same phenomenon is much more marked downstream. The distance required for the development of the parabolic profile increases. We can note a downstream eddy at $R_e = 600$. As R_e increases, the vortices are progressively stretched out downstream. The streamlines show the circulating eddy more distinctly (Fig. 6).

(*B*) Experimental Results

The velocity profiles are submitted to experimental investigation for various positions of the ball. Exploration meshes are of course looser than those for the numerical method: any two tested points are adequately remote to be able to separate them physically, so the measurement volume, assigned by the spatial resolution of the anemometer, are totally separate.

A precision check on the results for each section is carried out through a calculation of the reduced flow rate compared to that of the inlet section. Inside the cavity, the precision is affected by the small gap that necessitates very close measuring points. It is also in this area that parasitic refraction may occur because optical indices between fluid and solids are not exactly identical.

In Fig. 7, several positions of the ball are considered. For the center position $Ex = 0$, we may reach $R_e = 600$ and for small eccentricities ($E_x = \pm 0.286\ R$), $R_e = 100$ without causing turbulent flows which are excluded from this study. On the other hand, for bigger eccentricities such as $Ex = \pm 0.572\ R$, the values of R_e had to be restricted to 50 (Fig. 8)

To validate each of the two complementary methods employed, common cases are explored. Figure 9 shows three cases related to distinct values of R_e and Ex. We can notice a good agreement between numerical and experimental velocity profiles. It should be noted that the Finite-Element method allows a good approximation of phenomena; exploration of cases relating to larger Reynolds numbers require finer meshes and larger calculation times. The experimental method is comparatively less accurate.

6 One Application of Numerical Method

We propose another application of numerical method. This

Downloaded 02 May 2010 to 171.66.16.25. Redistribution subject to ASME license or copyright; see http://www.asme.org/terms/Terms_Use.cfm

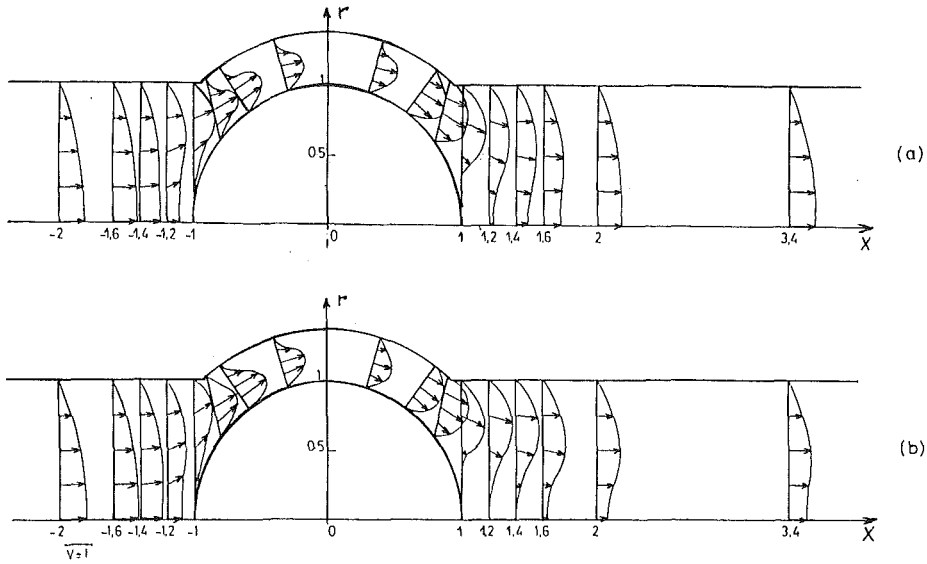

Fig. 7 Influence of Reynolds number on the shapes of the experimental velocity profiles for a centered ball ($Ex = 0$). Case (*a*): $R_e = 25$; and case (*b*): $R_e = 600$

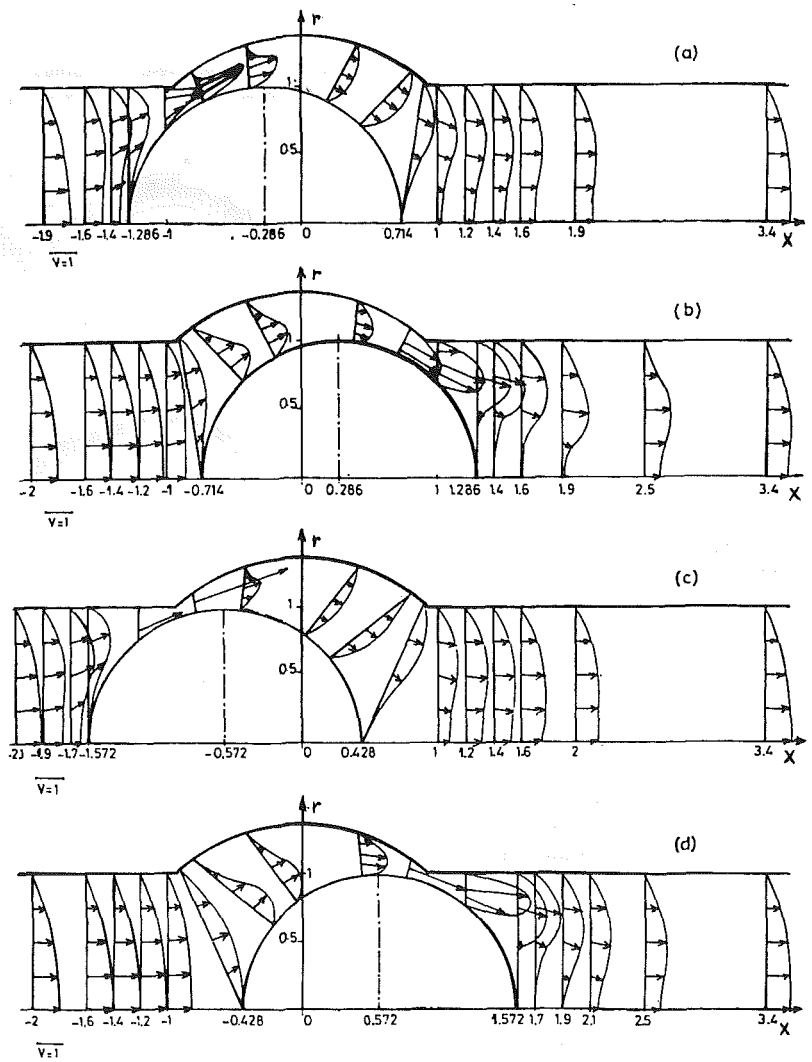

Fig. 8 Experimental velocity fields for different positions of the ball Ex and for various Reynolds number R_e. Case (*a*): $Ex = -0{,}286\ R$; $R_e = 100$; case (*b*): $Ex = +0.286\ R$; $R_e = 100$; case (c): $Ex = -0.572\ R$; $R_e = 50$; and case (*d*): $Ex = +0.572\ R$; $R_e = 50$

Downloaded 02 May 2010 to 171.66.16.25. Redistribution subject to ASME license or copyright; see http://www.asme.org/terms/Terms_Use.cfm

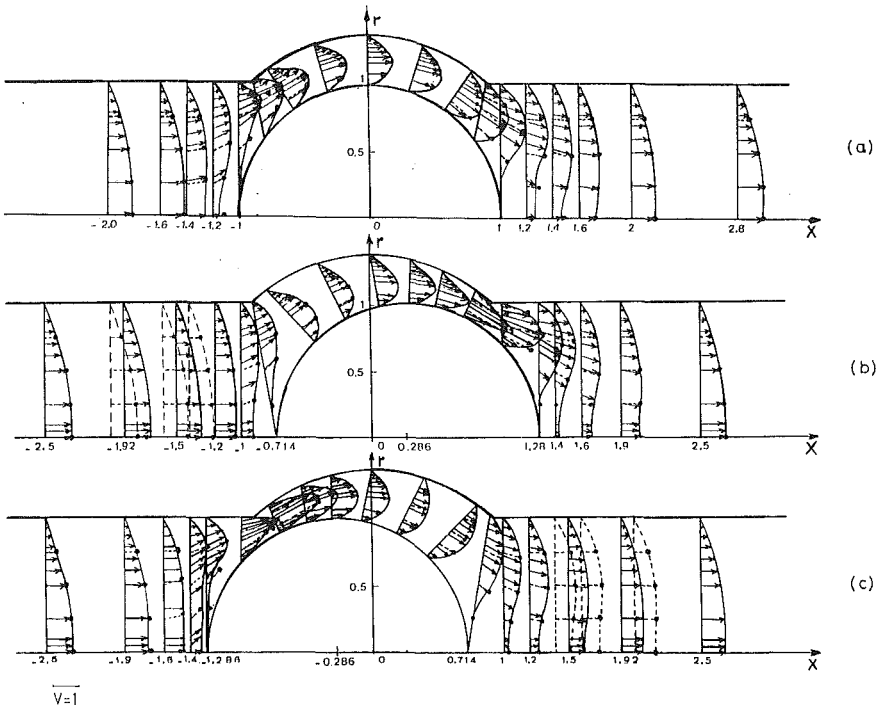

Fig. 9 Comparisons between numerical results (continuous arrowed lines) and experimental results (dotted pointed lines). Case (*a*): $Ex = 0$; $R_e = 20$; case (*b*): $Ex = +0.286\ R$; $R_e = 10$; and case (*c*): $Ex = -0.286\ R$; $R_e = 50$

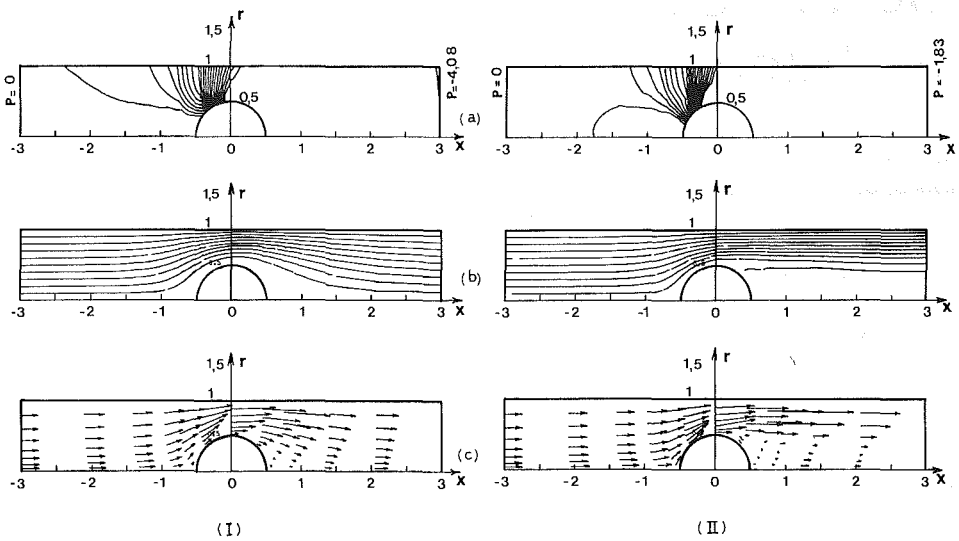

Fig. 10 Flows around series of parallel and circular cylinders, Case *I*: $R_e = 7$; Case *II*: $R_e = 100$. (*a*) : Pressure distributions, (*b*) : Streamlines, and (*c*) : velocity fields

application consists of plan flows around a series of parallel and circulars columns that are perpendicular to the flows. The previous flow characteristics can again be found here (Fig. 10). But there is one difference: the flow disturbance downstream of cylinders is important even at small R_e.

7 Conclusions

Both methods employed to carry out the study of incompressible laminar flows in the vicinity of a sphere located in a spherical cavity reveal the comparative influences of R_e variations and of the ball eccentricity E_x on the flows:

- When R_e increases, the intensity of the existing eddies rises and the velocity profiles tend to hollow out toward the axis both downstream and the upstream of the ball;
- Eccentricity of the ball Ex affects the velocity gradients.

Although each of these two methods is better suited for different Reynolds number ranges, they are complementary and provide results that are concordant. These results allow correlation to be established between the hydrodynamic properties of the flows and the geometric characteristics of such special features. Among others, these areas at low velocities or at high velocity gradients, are revealed.

Downloaded 02 May 2010 to 171.66.16.25. Redistribution subject to ASME license or copyright; see http://www.asme.org/terms/Terms_Use.cfm

For each of the methods used, certain simplifying hypotheses are chosen. The numerical process may be extended and adapted to any problem of the same type as far as the flow is axisymmetrical.

Provided that the equality of the refraction indices for both the fluid and altuglas is maintained, the experimental procedure may be applied to any type of geometry.

The next complementary stage of this task should consider unsteady flows. This study presents no experimental difficulty on account of the very short response time of the Laser Doppler anemometer using the Bragg cell. The numerical study is complicated since a different grid, adapted to the evolutionary position of the ball, must be continually employed.

This stage, into which we have already entered, should soon yield results.

References

1 Cousins, R. R., "A Note On Shear Flow Past a Sphere," *Journal of Fluid Mechanics*, Vol. 40, 1970, pp. 543–547.

2 Lighthill, M. J., "Contributions to the Theory of the Pitot-tube Displacement Effect," *Journal of Fluid Mechanic*, Vol. 2, 1957, pp. 493–512.

3 Gillani, N. V., and Swanson, W. M., "Time-Dependent Laminar Incompressible Flow Through a Spherical Cavity," *Journal of Fluid Mechanic*, Vol. 78, pp. 99–127.

4 Doffin, J., and Chagneau, F., "Study of Vortices Produced Past Wall Obstacles in Tube Flows," Euromech in Cardiovascular and Pulmonary Dynamics, Compiègne, France, 1979.

5 Wille, S. O., "Numerical Models of Arterial Blood Flow," Thèse, Oslo, 1979.

6 Zienkiewicz, O. C., *The Finite Element Method*, McGraw-Hill, 3rd Ed.,

Downloaded 02 May 2010 to 171.66.16.25. Redistribution subject to ASME license or copyright; see http://www.asme.org/terms/Terms_Use.cfm

Liquid-Metal MHD Open-Channel Flows

P. R. Hays
Research Associate,
Exploration and Production
Research Center,
Getty Oil Company,
Houston, Texas
Assoc. Mem. ASME

J. S. Walker
Professor,
Department of Theoretical and
Applied Mechanics,
University of Illinois,
Urbana, Ill. 61801
Mem. ASME

Many metallurgical applications of magnetohydrodynamics (MHD) involve open-channel liquid-metal flows with magnetic fields. This paper treats the three-dimensional, variable-depth flow in a rectangular open channel having an electrically insulating bottom and perfectly conducting sides. A steady, uniform magnetic field is applied perpendicular to the channel bottom. Induced magnetic fields and surface tension effects are neglected, while the applied magnetic field is sufficiently strong that inertial effects are negligible everywhere. Viscous effects are confined to boundary layers adjacent to the bottom, sides, and free surface. Solutions are presented for the inviscid core and the boundary layers. The locations of the free surface above the core and above the boundary layers adjacent to the sides are obtained. The side-layer variables are rescaled into universal profile functions which depend on the coordinates in the channel's cross section and on a parameter related to the local slopes of the bottom and the free surface. The solutions for the side layers in open channels are compared to the side-layer solutions for certain rectangular closed ducts in order to reveal the effects of the free surface. This comparison leads to a qualitative correspondence principle between open-channel and closed-duct side-layer solutions. The similarities and differences between corresponding open-channel and closed-duct side layers are discussed.

1 Introduction

While MHD flows in closed ducts have received considerable attention, the literature contains relatively few papers on open channel MHD flows with free surfaces. Walker [1] treats several fully developed flows with constant depths in straight, rectangular channels. Walker and Ludford [2] treat three-dimensional, variable-depth, inertialess, inviscid, MHD open-channel flows. The present paper extends the analysis of Walker and Ludford [2] to include viscous effects. The Hartmann number M is assumed to be sufficiently large that viscous effects are confined to Hartmann layers of $0(M^{-1})$ thickness, which are adjacent to the bottom and the free surface, and to side layers of $0(M^{-1/2})$ thickness, which are adjacent to the sides. The 0(1) and $0(M^{-1})$ core solutions are found. The inviscid solution presented by Walker and Ludford [2] is the 0(1) solution here and ignores all boundary layers. The Hartmann layer at the bottom has a well-known structure, but the Hartmann layer at the free surface must satisfy traction-free boundary conditions, instead of no-slip conditions, and has a higher-order structure than the familiar Hartmann layer. Solutions for the core, the Hartmann layers, and the location of the free surface above the core are presented in Section 2. The solutions for side layers and for the location of the free surface above the side layers are presented in Section 3.

Most of the experimental studies of open channel MHD flows involve channels with all insulating walls and with time-dependent, spatially variable, relatively weak magnetic fields [3]. There are some qualitative similarities between the experimental results [3] and the present flows with steady, uniform, strong magnetic fields, and these similarities are discussed by Walker and Ludford [2]. Further details of the numerical solution of the side-layer boundary value problem are presented in Hays' thesis [5].

2 Problem Formulation and Core Solution

This paper treats a liquid-metal flow in a straight, rectangular, open channel inclined at an angle α to the horizontal; see Fig. 1. A uniform magnetic field $B\hat{\mathbf{y}}$ is applied perpendicular to the electrically insulating bottom, and the perfectly conducting, vertical sides are at $z = \pm b$. Here B is the applied magnetic induction, and $\hat{\mathbf{y}}$ is a unit vector.

Two different flow situations are considered: for a pump, a DC voltage source is connected to the sides, and the electromagnetic (*EM*) body force drives the liquid metal up the channel in the minus x direction; for a flow control, the sides are connected to an external resistor, and the *EM* force retards the gravitationally driven flow down the channel. For both cases, the characteristic *EM* body force per unit mass, $\sigma U_c B^2/\rho$, is comparable to the gravitational body force per unit mass, $g\hat{\mathbf{g}}$ so that the appropriate characteristic velocity is

Contributed by the Applied Mechanics Division for presentation at the 1984 ASME Applied Mechanics, Bioengineering, and Fluids Engineering Conference, San Antonio, Texas, June 17-21, 1984 of THE AMERICAN SOCIETY OF MECHANICAL ENGINEERS.

Discussion on this paper should be addressed to the Editorial Department, ASME, United Engineering Center, 345 East 47th Street, New York, N.Y. 10017, and will be accepted until two months after final publication of the paper itself in the JOURNAL OF APPLIED MECHANICS. Manuscript received by ASME Applied Mechanics Division, February, 1983; final revision, June, 1983. Paper No. 84-APM-2.

Copies will be available until February, 1985.

Copyright © 1984 by ASME
Downloaded 02 May 2010 to 171.66.16.25. Redistribution subject to ASME license or copyright; see http://www.asme.org/terms/Terms_Use.cfm

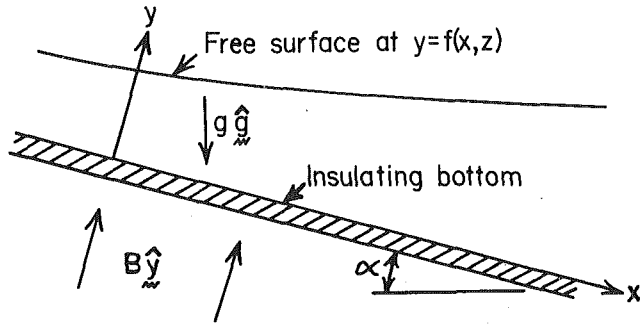

Fig. 1 Vertical section of the open channel

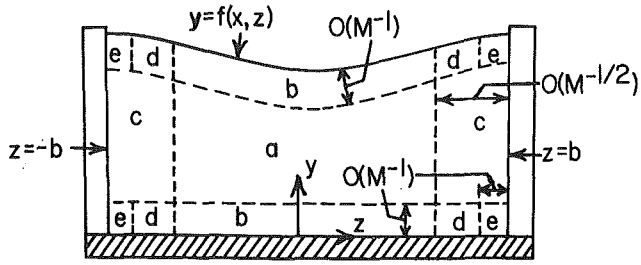

Fig. 2 Cross section of the channel showing subregions of the flow

$U_c = \rho g/\sigma B^2$, where ρ and σ are the liquid metal's density and electrical conductivity, respectively, and $\hat{\mathbf{g}}$ is a vertical unit vector.

We assume that the magnetic Reynolds number

$$R_m = \mu\,\sigma\,U_c L = \mu\,\rho\,g\,L/B^2 << 1,$$

so that the induced magnetic fields associated with the electric currents in the liquid metal are negligible. We also assume that the Hartmann number, $M = BL(\sigma/\eta)^{1/2} >> 1$, so that viscous effects are confined to thin boundary layers adjacent to the sides, bottom, and free surface. The interaction parameter is assumed to be much greater than the Hartmann number, i.e.,

$$N = \sigma\,B^2 L/\rho U_c = \sigma^2\,B^4 L/\rho^2 g >> M,$$

so that inertial effects are negligible everywhere. Here, μ and η are the liquid metal's magnetic permeability and viscosity, respectively, while L is the characteristic length, which is chosen as the normal depth, i.e., the depth for uniform, fully developed flow with constant depth [1]. The restriction on the interaction parameter for the inertialess approximation is derived by Walker, Ludford, and Hunt [4] for a closed, rectangular duct. For the present U_c, the inertialess restriction reduces to a condition for the magnetic induction in terms of the liquid metal's physical properties, namely, $B >> (\rho^4\,g^2/\sigma^3\eta)^{1/6}$.

For molten aluminum at its melting temperature, 660°C, $R_m = 0.03\,L/B^2$, $M = 54{,}500\,LB$, and $N = 302{,}000\,LB^4$, where the units of L and B are meters and tesla, respectively, and the inertialess restriction is $B >> 0.565\,T$. Some experiments [6] have indicated that the inertialess approximation gives surprisingly good results, and the present inertialess solution probably holds for molten aluminum, open channel flows with magnetic fields of one tesla or more.

With the present assumptions, the dimensionless governing equations are

$$\nabla\,p = \hat{\mathbf{g}} + \mathbf{j}\,x\,\hat{\mathbf{y}} + M^{-2}\nabla^2\,\mathbf{v}, \quad \nabla\cdot\mathbf{v} = 0, \tag{1a,b}$$

$$\mathbf{j} = -\nabla\,\phi + \mathbf{v}\,x\,\hat{\mathbf{y}}, \quad \nabla\cdot\mathbf{j} = 0 \tag{1c,d}$$

where p, $\mathbf{j}$, $\mathbf{v}$, and ϕ are the pressure, electric current density, velocity, and electric potential function, respectively, and these dimensionless variables have been normalized with ρgL, $\rho g/B$, $U_c = \rho g/\sigma B^2$, and $\rho gL/\sigma B$, respectively [2]. The boundary conditions at the insulating bottom and at the perfectly conducting sides are

$$\mathbf{v} = j_y = 0, \quad \text{at} \quad y = 0, \tag{2}$$

$$\mathbf{v} = 0, \quad \phi = \mp E_0 b, \quad \text{at} \quad z = \pm b, \tag{3a,b}$$

respectively, where the constant voltage difference, $2\,E_0 b$, is determined by the voltage source or resistance in the external electrical circuit. To define the boundary conditions at the free surface and to analyze the boundary layer in the fluid adjacent to the free surface, we introduce an orthogonal, curvilinear coordinate system (n, s, t), where s and t follow the free surface's lines of curvature, and the unit vector $\hat{\mathbf{n}}$ is normal to the free surface. If the atmosphere above the free surface is an electrical insulator, then the boundary conditions at the free surface are

$$\tau_{nn} = \tau_{ns} = \tau_{nt} = v_n = j_n = 0, \quad \text{at} \quad n = 0, \tag{4}$$

or at $y = f(x,z)$, where τ is the stress tensor, referred to ρgL. For this boundary value problem, the location of the free surface, f, is an unknown to be determined along with the fluid variables. The problem has a homogeneous solution, and the associated arbitrary constant is determined by the condition that f must approach one as the flow approaches uniform, fully developed flow, since the normal depth has been chosen as the characteristic length, L. In addition, the location of the origin along the infinite channel is arbitrary, so that the axial location of the free surface profiles must be fixed by specifying the dimensionless depth d (referred to normal depth) at $x = z = 0$.

The flow region may be divided into various subregions (see Fig. 2), and certain terms in the governing equations (1) may be neglected in each subregion. The subregions are: (*a*) the inviscid core, (*b*) the Hartmann layers adjacent to the core with $0(M^{-1})$ thickness, (*c*) the side layers with $0(M^{-1/2})$ thickness, (*d*) the Hartmann layers adjacent to the side layers, with $0(M^{-1})$ x $0(M^{-1/2})$ cross sections, and (*e*) the corner regions with $0(M^{-1})$ x $0(M^{-1})$ cross sections. The latter are needed to properly represent singularities in the side-layer solutions and need not be analyzed in detail for the determination of the leading term in each asymptotic expansion for the other subregions.

The Hartmann layer between the core and the bottom has a well-known, local, exponential structure. Its solution matches the core solution and satisfies the boundary conditions (2), provided the core solution satisfies the Hartmann conditions

$$v = M^{-1}(\partial u/\partial x + \partial w/\partial z),$$

$$j_y = M^{-1}(\partial u/\partial z - \partial w/\partial x), \quad \text{at} \quad y = 0, \tag{5}$$

where u, v, and w are the x, y, and z components of the velocity, respectively, and $0(M^{-2})$ terms are neglected [7].

For the Hartmann layer between the core and the free surface, the normal coordinate is stretched by substituting $\nu = Mn$, and each Hartmann-layer variable is replaced by an asymptotic expansion in powers of M^{-1}. For the 0(1) terms in these expansions, the boundary conditions (4) become

$$p = \partial v_s/\partial\nu = \partial v_t/\partial\nu = v_n = j_n = 0, \quad \text{at} \quad \nu = 0. \tag{6}$$

The solution of the rescaled equations (1) which satisfies the boundary conditions (6) indicates that all 0(1) Hartmann-layer variables are independent of ν, so that the 0(1) core variables must satisfy the boundary conditions

$$p = v_n = j_n = 0, \quad \text{at} \quad y = f. \tag{7a,b,c}$$

With the 0(1) $v_n = 0$ throughout the Hartmann layer, the boundary conditions (4) become the conditions (6) for the $0(M^{-1})$ Hartmann-layer variables as well. Matching the core solution indicates that, for the $0(M^{-1})$ variables $\partial v_s/\partial\nu$ and

Downloaded 02 May 2010 to 171.66.16.25. Redistribution subject to ASME license or copyright; see http://www.asme.org/terms/Terms_Use.cfm

$\partial v_t/\partial \nu$ do not approach zero as $\nu \to \infty$, so that v_s and v_t must vary exponentially with ν in order to accommodate the jump in these normal derivatives across the Hartmann layer. The $0(M^{-1})$ j_s and j_t have associated exponential solutions. However, the rescaled equations (1) also indicate that there are no jumps in the $0(M^{-1})$ p, ϕ, v_n, and j_n across the Hartmann layer, so that the $0(M^{-1})$ core variables must also satisfy the boundary conditions (7) at the free surface. The exponential variations of the $0(M^{-1})$ Hartmann-layer tangential velocity and electric current density, together with the rescaled continuity equations (1b,d), give nonzero values for the $0(M^{-2})$ core v_n and j_n at the free surface, but $0(M^{-2})$ terms are neglected in the present analysis.

The analysis for the side layers, which is presented in the next section, shows that the jump in ϕ across the side layers is no larger than $0(M^{-2})$. Therefore, the core ϕ must satisfy the boundary conditions (3b) to this order. In the core, all derivatives are 0(1), so that the viscous term in equation (1a) may be neglected. The core variables and f, the location of the free surface above the core, are replaced by asymptotic expansions, such as $f = f_0 + M^{-1} f_1$, where $0(M^{-2})$ terms are neglected.

The core variables which satisfy the equations (1) and the boundary conditions (3b), (5), and (7) are

$$u = k/f_0 - M^{-1} f_1' \cos\alpha, \quad w = j_x = j_y = 0,$$

$$v = k\, y\, f_0'/f_0^2 + M^{-1} \cos\alpha\ (y f_1'' - f_0''), \quad j_z = E_0 + u,$$

$$p = \cos\alpha\ (f_0 + M^{-1} f_1 - y), \quad \phi = -E_0 z, \tag{8}$$

where $0(M^{-2})$ terms are neglected, $k = \sin\alpha - E_0$, and the prime denotes differentiation with respect to x. The first two terms in the asymptotic expansion for the location of the free surface above the core are functions of x only and are given by

$$f_0 - d + \ln|(f_0 - 1)/(d-1)| = kx/\cos\alpha, \tag{9a}$$

$$f_1 = (1 - f_0^{-1}) \ln|(f_0 - 1)/(d-1)|. \tag{9b}$$

The conditions that $f_0 \to 1$ and $f_1 \to 0$, as $kx \to -\infty$, i.e., as the flow becomes uniform, fully developed flow, and the conditions that $f_0 = d$ and $f_1 = 0$, at $x = 0$, have been used to determine the four constants of integration that appear in the solutions of the two ordinary differential equations which result from the boundary condition (7b) and which govern f_0 and f_1. Since f is independent of z to this order, the free surface above the core is spanwise uniform.

For $k < 0$, i.e., for $E_0 > \sin\alpha$, the flow is up the channel, corresponding to a pump, while for $k > 0$, the flow is down the channel, corresponding to a flow regulator. Solutions for pumps and flow regulators are identical if $X = kx$ is used as the axial coordinate. Two free surface profiles are possible. For $d > 1$, f_0 increases from the normal depth of one far upstream, through the value d at $X = 0$, to infinite depth far downstream, while f_1 decreases and increases the depth for $X < 0$ and $X > 0$, respectively. For $d < 1$, f_0 decreases from the normal depth of one far upstream, through the value d at $X = 0$, to zero depth at $X \sec\alpha = -d - \ln(1 - d) > 0$, while f_1 increases and decreases the depth for $X < 0$ and $X > 0$, respectively.

3 Side Layers and Adjacent Free Surface

The flow is symmetric in z, so that we need only consider the side layer at $z = -b$. The substitutions,

$$y = f_0 Y, \quad z = -b + (f_0/M)^{1/2} Z, \tag{10a,b}$$

$$u = kU/f_0, \quad v = f_0' kV/f_0, \tag{10c,d}$$

$$w = f_0' kW/(Mf_0^3)^{1/2}, \quad j_x = f_0' k\, J_x/(Mf_0^3)^{1/2}, \tag{10e,f}$$

$$j_y = k\, J_y/(Mf_0^3)^{1/2}, \quad j_z = E_0 + k/f_0 + k\, J_z/Mf_0^2, \tag{10g,h}$$

$$p = \cos\alpha(f_0 - y) + f_0' k\, P/Mf_0, \tag{10i}$$

$$\phi = E_0 b - E_0 Z (f_0/M)^{1/2} + k\, \Phi/(Mf_0)^{1/2}, \tag{10j}$$

stretch the coordinate normal to the side and introduce rescaled side-layer coordinates and variables, which are denoted by capitals. Here, f_0 is the 0(1) term for the free surface location above the core, which is given by equation (9a), while the variables (10c–j) now denote the leading terms in the asymptotic expansions for the side layer. The expressions (10c,d) neglect $0(M^{-1/2})$ terms, the expressions (10e,f,g,j) neglect $0(M^{-1})$ terms, and the expressions (10h,i) neglect $0(M^{-3/2})$ terms.

With the substitutions (10), the leading terms in the equations (1) become

$$J_z = \partial^3\Phi/\partial Z^3 + (f_0')^2 S(P) - f_0 f_0'' P, \tag{11a}$$

$$\partial P/\partial Y = \partial^2 V/\partial Z^2, \quad J_x = \partial P/\partial Z, \tag{11b,c}$$

$$\partial V/\partial Y = 1 + \partial^2 P/\partial Z^2, \quad W = -\partial P/\partial Z + S(\Phi) - \Phi/2, \tag{11d,e}$$

$$J_y = -\partial\Phi/\partial Y, \quad U = 1 + \partial\Phi/\partial Z, \quad \partial^2\Phi/\partial Y^2 = \partial^4\Phi/\partial Z^4, \tag{11f,g,h}$$

$$S(P) = 0.5Z\ \partial P/\partial Z + Y\ \partial P/\partial Y - (f_0/f_0')\partial P/\partial x + P. \tag{11i}$$

The equations (11b,d,h) govern P, V, and Φ, and the expressions (11a,c,e,f,g) give the other five variables in terms of these three basic variables. The substitutions

$$V = Y + \partial\theta/\partial Z, \tag{12a}$$

$$P = \cos\alpha\, f_0 f_1/kf_0' - \int_Z^\infty \partial\theta/\partial Y\, dZ, \tag{12b}$$

satisfy the equation (11d), as well as the matching between the core and side-layer pressures. The number of basic variables is reduced to two, namely, Φ and θ, which are governed by equation (11h) and equation (11b), which now becomes

$$\partial^2\theta/\partial Y^2 = \partial^4\theta/\partial Z^4. \tag{13}$$

The core solution (8) and (9) is based on the fact that the jump in the electric potential across the side layers is, at most, $0(M^{-2})$, and this fact follows from the side-layer boundary conditions. The side-layer variables (10)–(12) match the core variables which satisfy the governing equations (1) and the Hartmann conditions (5) and (7), provided the side-layer Φ and θ approach functions of x only as $Z \to \infty$. The function for θ at infinity can be set equal to zero with no loss of generality, so that matching gives

$$\Phi \to q(x), \quad \theta \to 0, \quad \text{as} \quad Z \to \infty. \tag{14a,b}$$

The Hartmann layer between the side layer and the bottom has the well-known, local, exponential structure, which satisfies the boundary conditions (2) and matches the side-layer variables, provided the latter satisfy the Hartmann conditions

$$v = 0, \quad j_y = (Mf_0)^{-1/2} \partial u/\partial Z, \quad \text{at} \quad Y = 0,$$

neglecting $0(M^{-1})$ terms [7]. These conditions, together with the condition (14b), give

$$\partial\Phi/\partial Y + \partial^2\Phi/\partial Z^2 = \theta = 0, \quad \text{at} \quad Y = 0. \tag{15a,b}$$

The boundary conditions (3), together with the condition (15b) and the fact that θ is continuous at the corner $Y = Z = 0$, give

$$\Phi = \theta = \partial\Phi/\partial Z + 1 = \partial\theta/\partial Z + Y = 0, \quad \text{at} \quad Z = 0. \tag{16a,b,c,d}$$

The pressure is given by an essentially hydrostatic variation along magnetic field lines, and this is reflected by the expression for the pressure in the core solution (8). If the electromagnetic body force due to the axial electric current j_x produces a pressure variation with z, then the elevation of the free surface varies with z in order to maintain the hydrostatic pressure variation. In the core, $j_x = 0$, so that the free-surface elevation is independent of z, i.e., the free surface above the

Downloaded 02 May 2010 to 171.66.16.25. Redistribution subject to ASME license or copyright; see http://www.asme.org/terms/Terms_Use.cfm

core is spanwise uniform. In the side layers, the axial current is $0(M^{-1/2})$ and produces an $0(M^{-1})$ pressure variation across the side layers, so that we can expect an $0(M^{-1})$ variation of the free-surface elevation across the side layers. Therefore, the location of the free surface above the side layer at $z = -b$ is given by

$$y = f_0 + f_1/M + f_0' kF(x,Z)/\cos\alpha \; f_0 M.$$

The Hartmann layer betwwen the side layer and the free surface is analyzed using the orthogonal, curvilinear coordinates (n,s,t), where

$$\hat{\mathbf{n}} = [\hat{\mathbf{x}} \; f_0' - \hat{\mathbf{y}} + \hat{\mathbf{z}} \; f_0' k \sec\alpha (M f_0^3)^{-1/2} \partial F/\partial Z)/(1 + f_0'^2)^{1/2},$$

neglecting $0(M^{-1})$ terms. The 0(1) variables are all independent of the stretched normal $\nu = Mn$. The $0(M^{-1})$ tangential velocity and electric current density must vary exponentially with ν in order to satisfy the traction-free conditions, but the $0(M^{-1/2})j_n$, the $0(M^{-1})v_n$, and the $0(M^{-1})p$ are independent of ν. The exponential structure produces a nonzero $0(M^{-3/2})j_n$ and nonzero $0(M^{-2})v_n$ and p in the side layer at the free surface. Therefore, the side-layer variables at the free surface must satisfy the boundary conditions (7a,b), neglecting $0(M^{-2})$ terms, and the boundary condition (7c), neglecting $0(M^{-3/2})$ terms. The conditions (7), together with the conditions (16a,b) and the facts that Φ and θ are continuous at the corner $Y = 1$, $Z = 0$ give

$$F = -\int_Z^\infty \partial\theta/\partial Y \, dZ, \quad \Phi = \theta,$$

$$\partial\Phi/\partial Y + f_0' \tan\alpha \; \partial\theta/\partial Y = 0, \quad \text{at} \quad Y = 1. \qquad (17a,b,c)$$

The boundary conditions (14) and (17b) indicate that $q(x) = 0$, so that there is no jump in the $0(M^{-1/2})$ electric potential across the side layers. This conclusion required the fact that Φ and θ are continuous at the corners $Y = 0,1$, $Z = 0$, and this fact follows from the characteristics of the corner regions, which are subregions e in Fig. 2. A discontinuity in either function at either corner would imply a source or sink of fluid or electric current at that corner, and the corner regions cannot match such a source or sink. The expression (11g) and the boundary conditions (14a) and (16a), with $q = 0$, show that the volume flux deficiency for each side layer is zero. The side layers have a displacement thickness of zero and produce no $0(M^{-1/2})$ perturbation in the core. The first perturbation to the side-layer solution (10) must match the $0(M^{-1})$ core u and v, and must satisfy the no-slip condition at the side. The variables in this side-layer perturbation are $0(M^{-1})$ times the corresponding variables in the expressions (10), e.g., the perturbation Φ and P represent $0(M^{-3/2})$ and $0(M^{-2})$ terms, respectively. For the side-layer perturbation, the proof that there is no jump in the $0(M^{-3/2})$ electric potential across the side layers exactly parallels that for the $0(M^{-1/2})$ potential. The required continuity of the perturbation Φ and θ at the corners is proven by the application of the Principle of Minimum Singularity to the corresponding perturbation variables in the corner regions, so that the solution of the corner-region boundary value problems is again unnecessary [8]. Therefore, the jump in the electric potential function across the side layers is, at most, $0(M^{-2})$.

The boundary value problem (11h), (13)–(16), and (17b,c), with $q = 0$, can be solved independently in each x = constant cross section of the channel, and the solutions depend only on Y, Z and the parameter

$$\beta = (1 - f_0' \tan\alpha)/(1 + f_0' \tan\alpha).$$

Therefore the side-layer problem is reduced to the determination of a one-parameter family of solutions, $\Phi(Y,Z)$ and $\theta(Y,Z)$, for various values of the paramter β. Equations (11c,f,g) (12a), and (17a) indicate that the rescaled side-layer variables J_x, J_y, U, V, and F, respectively, are also universal profile functions which depend only on Y, Z, and β. Equations (11a,e) and (12b) indicate that J_z, W, and P, respectively, are each given by the sum of several universal profile functions multiplied by terms that are functions of x only and which involve f_0, f_0'', f_1, and f_1', as well as β.

The solution of the boundary value problem (11h), (13)–(16), and (17b,c), with $q = 0$, is similar to the solution of the side-layer boundary value problem for a closed rectangular duct with a uniform, applied magnetic field $B\hat{\mathbf{y}}$, with symmetrically diverging or converging, insulating top and bottom at $y = \pm f_c(x)$, and with parallel, perfectly conducting sides at $z = \pm 1$ [4]. Here we will summarize the method of solution with emphasis on the differences between the methods for open channels and for closed ducts. With a Fourier sine transform with respect to Z, the equations (11h) and (13) and the boundary conditions (15) and (17b,c) reduce to two ordinary differential equations in Y and a pair of boundary conditions at each of the points $Y = 0,1$, respectively. The Fourier sine transform incorporates the boundary conditions (14), and (16a,b), ignores the boundary conditions (16c,d), and gives each ordinary differential equation an inhomogeneous term involving an unknown function of Y. The two unknown functions are the values of $\partial^2\Phi/\partial Z^2$ and $\partial^2\theta/\partial Z^2$, evaluated at $Z = 0$, and represent the rescaled wall shear stresses τ_{xz} and τ_{yz} on the side. For the closed duct with symmetrically diverging or converging top and bottom, the two ordinary differential equations with two unknown functions could be combined into a single equation with a single unknown function, because of the symmetry in Y. No such simplification is possible for open channels.

The two ordinary differential equations are coupled through the transformed boundary conditions (17b,c). The transformed Φ and θ can be found in terms of the two unknown functions using either the method of variation of parameters or a Green's function approach. Indeed, solutions were found by both methods as a check. Analytical Fourier inversions are not possible, so that the solution for either Φ or θ is given by the sum of two intergrals with respect to an integration variable Y^*. The integrand of each integral consists of one of the unknown functions times a kernel that is a function of Y, Y^*, and Z, and which is given by a semi-infinite integral with respect to the Fourier transform variable.

When the solutions for Φ and θ are introduced into the previously ignored boundary conditions (16c,d), we obtain two integral equations governing the two unknown functions. Each integral equation holds for $0 \le Y \le 1$, has a known inhomogeneous term (1 or Y) and has an integral from $Y^* = 0$ to $Y^* = 1$ for each of the unknown functions. For each of the four integrals, the unknown function is multiplied by a kernel which is a function of Y and Y^*, and which is given by a semi-infinite integral with respect to the Fourier transform variable. For the closed duct, symmetry in Y again permitted reduction to a single integral equation with one unknown function, instead of two, and with one kernel, instead of four. No such simplification is possible for open channesl.

For each of the semi-infinite integrals defining one of the four kernels in the two coupled integral equations, the integrand is rewritten as the sum of several terms. Some terms can be integrated analytically with respect to the Fourier transform variable, while the remaining terms are exponentially small for large values of the transform variable. The remaining Fourier inversion integrals are evaluated numerically using a 24-point Gauss-Legendre quadrature for the range from zero to a fixed point and a 24-point Gauss-Laguerre quadrature for the range from this fixed point to infinity. Integration by parts, together with the boundary conditions (14) with $q = 0$, eliminates singularities in the integrands at zero. Various fixed points are used to check the accuracy of the numerical values for the kernels.

The four integrals with respect to Y^* are approximated by a

Downloaded 02 May 2010 to 171.66.16.25. Redistribution subject to ASME license or copyright; see http://www.asme.org/terms/Terms_Use.cfm

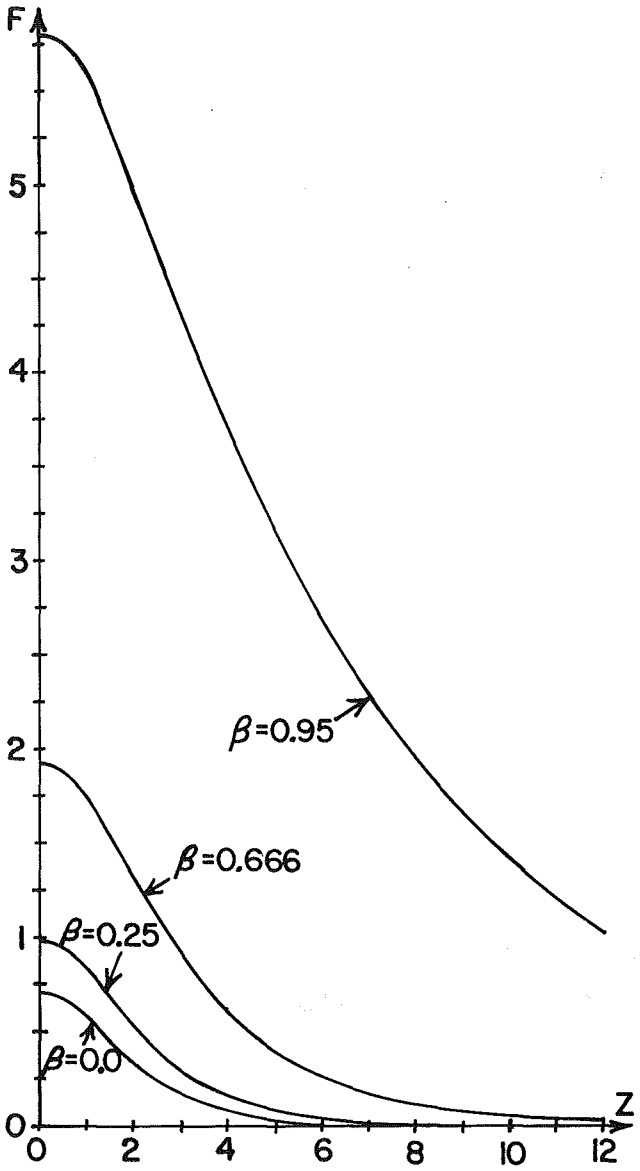

Fig. 3 The deviation of the elevation of the free surface above the side layer from that above the core

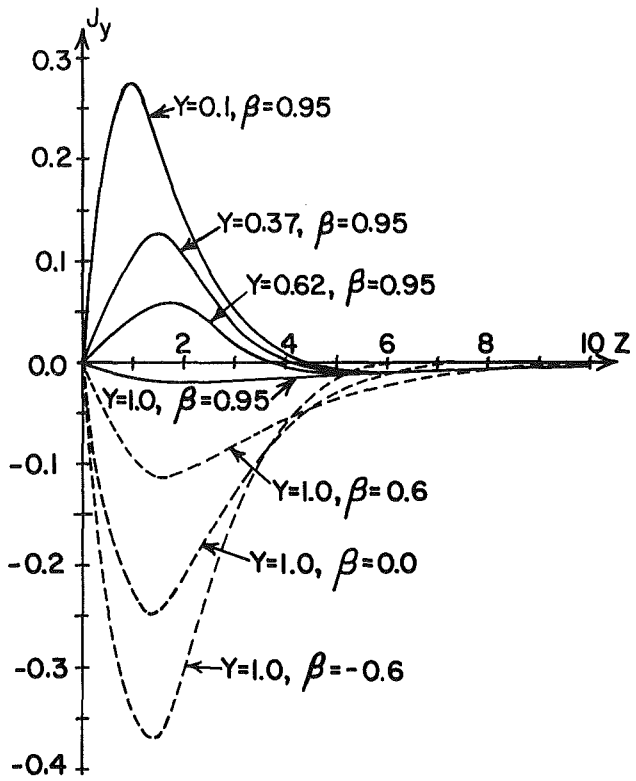

Fig. 4 Side-layer electric current J_y

24-point Gauss-Legendre quadrature. The integral equations are evaluated at the values of Y corresponding to the 24 Gauss-Legendre ordinates to properly represent the kernels along the diagonal $Y = Y^*$. This procedure yields 48 linear, algebraic equations, whose solution gives the 24 values of each of the two previously unknown functions at the values of Y corresponding to the 24 Gauss-Legendre ordinates.

In the solutions for Φ and θ, the integrals with respect to Y^* of the now determined rescaled wall shear stresses times kernels are evaluated with the same 24-point Gauss-Legendre quadrature. The semi-infinite integrals with respect to the Fourier transform variable which give the kernels are evaluated numerically in the same ways as the corresponding integrals in the integral equations. Therefore, the value of either Φ or θ at a point in the side layer is given by the sum of 48 terms. Each term is the product of one of the 48 wall shear stress values determined by the solution of the integral equations and a coefficient given by the numerical evaluation of semi-infinite Fourier inversion integral. Details of the numerical analysis are given in Hays' thesis [5].

The effects of the free surface on the side layers are revealed by comparing the side-layer velocity and electric current profiles for an open channel to the corresponding profiles for a closed rectangular duct [4]. For fully developed flow in a constant-area ($f_c' = 0$) closed duct which is sloping at an angle α to the horizontal and which has no axial pressure difference, the free-surface boundary conditions (6) are satisfied automatically at the plane of symmetry ($y = 0$) midway between the top and bottom, because of the symmetry in y. Therefore the uniform, fully developed flow in an open channel ($f_0 = 1$) is identical to that portion of the fully developed flow in a closed rectangular duct between the bottom and the plane of symmetry midway between the top and bottom [1]. In comparing corresponding three-dimensional flows in an open channel and a closed duct, it is also appropriate to compare results at the bottoms of both, to compare results at the free surface of the open channel and at the plane of symmetry midway between the closed duct's top and bottom, and to compare results at corresponding levels between the bottoms and the free surface or plane of symmetry. Corresponding three-dimensional flows in an open channel and a closed duct have equal values of the parameter β, where $\beta = (1 - f_c'^2)/(1 + f_c'^2)$ for the closed duct. This correspondence holds because x enters the side-layer problem for open channels through the $f_0' \tan \alpha$ in the boundary condition (17c), while x enters the side-layer problem for closed ducts through the factor $f_c'^2$ in the Hartmann conditions on the normal current at the top and bottom [4] in a parallel manner.

One obvious contrast between closed ducts and open channels is that the plane of symmetry in closed ducts remains plane for all values of β, while the elevation of the free surface above the side layer deviates from that above the core in open channels (see Fig. 3). The profiles of U, V, and J_x for open channels deviate by only a few percent from those for corresponding closed ducts.

The most dramatic effects of the free surface are revealed by the profiles of J_y (see Fig. 4). In a closed duct J_y is driven by the Hartmann currents at the top and bottom; J_y is positive

Downloaded 02 May 2010 to 171.66.16.25. Redistribution subject to ASME license or copyright; see http://www.asme.org/terms/Terms_Use.cfm

and maximum at the bottom and decreases to zero at the plane of symmetry. In the open channel J_y is driven by the Hartmann current at the bottom and by the deflection of the 0(1) transverse current j_z at the free surface, which slopes down from the side to the core. The free surface deflection produces a negative J_y at $Y = 1$, where the corresponding closed duct J_y is zero. For small f_0', the effect of the free surface deflection is small, and the solid lines in Fig. 4 are very similar to the corresponding closed duct profiles. As f_0' increases, the positive J_y driven by the Hartmann current near the bottom remains virtually identical for corresponding open channels and closed ducts. However, the negative J_y at the free surface driven by the deflection of j_z increases dramatically (see dashed lines in Fig. 4), while the corresponding closed duct $J_y = 0$. At a level between the bottom and the free surface, the two effects compete: the Hartmann current dominates near the side, so $J_y > 0$, and the surface deflection dominates near the core, so $J_y < 0$.

In both an open channel and a closed duct, the axial current produces a variation of pressure through the side layer. In the closed duct, the pressure cannot move the rigid boundaries, but in the open channel, the pressure variation through the side layer produces a deflection of the free surface above the side layer from its elevation above the core. The uniform, transverse current in the side layer of the open channel must follow the deflected free surface, and this produces a negative J_y at the free surface, while $J_y = 0$ at the corresponding plane of symmetry in the closed duct. This downward current at the free surface produces the only dramatic differences between the corresponding side-layer profiles for an open channel and a closed duct. While the differences between a few corresponding open-channel and closed-duct profiles are certainly important, the most significant result here is the principle of correspondence for the selection of a closed duct which has so many profiles that are very similar to the profiles in a given open channel.

Acknowledgment

This research was supported by the National Science Foundation under Grant CPE-8108952.

References

1 Walker, John S., "Uniform Open Channel Liquid Metal Flows With Transverse Magnetic Fields," *Developments in Mechanics*, Vol. 8, Proceedings of the 14th Midwestern Mechanics Conference, 1975, pp. 421–436.

2 Walker, J. S., and Ludford, G. S. S., "Liquid-Metal Flows in Open Channels," *MHD Flows and Turbulence*, Vol. II, Proceedings of the Second Bat Sheva Seminar, 1978, pp. 97–110.

3 Branover, H. H., Kirko, I. M., Lielausis, O. A., and Tsinober, A. B., "Open-Channel Upgrade Flow of a Liquid Metal Induced by a Traveling Magnetic Field," *Voprosy Magnitnaya Gidrodinamika*, Riga, 1963, pp. 65–76.

4 Walker, J. S., Ludford, G. S. S., and Hunt, J. C. R., "Three-Dimensional MHD Duct Flows With Strong Transverse Magnetic Fields. Part 2. Variable-Area Rectangular Ducts With Conducting Sides," *Journal of Fluid Mechanics*, Vol. 46, 1971, pp. 657–684.

5 Hays, Paul R., "Three-Dimensional Analysis of Boundary Layers in Magnetohydrodynamic Open Channel Flow," Ph.D. thesis, University of Illinois at Urbana-Champaign, 1980.

6 Hunt, J. C. R., "The Resistance of a Blunt Body in a Strong Transverse Magnetic Field," *Magnitnaya Gidrodinamika*, Vol. 6, 1970, pp. 35–38.

7 Walker, J. S., Ludford, G. S. S., and Hunt, J. C. R., "Three-Dimensional MHD Duct Flows With Strong Transverse Magnetic Fields. Part 3. Variable-Area Rectangular Ducts with Insulating Walls," *Journal of Fluid Mechanics*, Vol. 56, 1972, pp. 121–141.

8 Temperley, D. J., and Todd, L., "The Effects of Wall Conductivity in Magnetohydrodynamic Duct Flow at High Hartmann Number," *Proceedings of the Cambridge Philosophical Society*, Vol. 69, 1971, pp. 337–351.

Downloaded 02 May 2010 to 171.66.16.25. Redistribution subject to ASME license or copyright; see http://www.asme.org/terms/Terms_Use.cfm

Thin Airfoil Theory for Planar Inviscid Shear Flow

W. C. Chin
Applied AeroNalysis,
7703 Meadowbriar Lane,
Houston, Tex. 77063

Steady, inviscid, planar and constant density shear flows past thin airfoils have strongly coupled thickness and camber flowfields which can be simply analyzed using some invariant properties of Euler's equations. In this paper, both the nonlinear vorticity generation term in Poisson's disturbance stream-function equation and the Bernoulli constant (which varies from streamline to streamline) are explicitly evaluated in terms of the known plane parallel flow far upstream, recognizing that vorticity convects unstretched and unchanged along streamlines; this produces a governing differential equation with an explicitly available right side plus a Bernoulli integral with a true constant fixed throughout the entire flowfield. Using these results, the inverse problem, which solves for the shape that induces a prescribed pressure, is formulated as a nonlinear boundary value problem with mixed Dirichlet and Neumann surface conditions; here, trailing edge shape constraints are directly enforced by controlling jumps in the stream-function or its streamwise derivative through the downstream wake (analogies with potential flows past axisymmetric ringwings showing similar source and vortex interactions are also described). For flows with arbitrary profile curvature, we show that the linearized stream-function equation can be put in conservation form, thus leading to new and more general Cauchy-Riemann conditions which extend the notion of the velocity potential; the analysis problem, which determines the flow past a known shape subject to Kutta's condition, is shown to satisfy a simple boundary value problem for a "super-potential" identical to the irrotational planar formulation except for an axisymmetric-like change to the Cartesian form of Laplace's equation. For flows with uniformity vorticity, closed-form solutions are given which clearly illustrate the interaction between thickness and camber; also, for arbitrary thin airfoils, a particularly simple expression shows that the lift due to thickness varies directly as the product of vorticity and enclosed area. With more general shears, numerical approaches are especially convenient; these require only simple code changes to existing algorithms, for example, established potential function methods readily available for analysis problems, or "direct stream-function methods" for inverse problems recently developed by this author. Numerical methods and results that cross-check and extend derived analytical solutions are given for both analysis and design problems with vorticity. Also, extensions of the basic theory to three-dimensional constant density and planar compressible shear flows are given.

I Introduction

The analysis and design of airfoil sections in flows with vorticity is important in many practical engineering problems, for example, cascade design in turbomachinery flows, aerodynamic stability in wind shear, and flight in the boundary layer of large obstacles. Unlike irrotational motions where the basic features, essentially linear, satisfy Laplace's potential equation, flows with vorticity are inherently nonlinear: in the steady, planar, constant density and inviscid limit considered here, the vorticity generation term in the governing stream-function equation, unknown apriori, is a functional of the dependent variable, the same applying to Bernoulli's "constant" in the pressure integral, which generally varies from streamline to streamline. Thus, well-established potential function Neumann methods, which enforce Kutta's condition by zeroing the jump in streamwise disturbance potential derivative through the wake, do not apply. The obvious recourse appears to be a direct attack on Euler's equations; this, unfortunately, requires new and computationally expensive numerical methods, not to mention more precise ways to calculate pressure, since an explicit integral is unavailable. However, simplifying features

Contributed by the Applied Mechanics Division for publication in the JOURNAL OF APPLIED MECHANICS.

Discussion on this paper should be addressed to the Editorial Department, ASME, United Engineering Center, 345 East 47th Street, New York, N.Y. 10017, and will be accepted until two months after final publication of the paper itself in the JOURNAL OF APPLIED MECHANICS. Manuscript received by ASME Applied Mechanics Division, March, 1982; final revision May, 1983.

Copyright © 1984 by ASME
Downloaded 02 May 2010 to 171.66.16.25. Redistribution subject to ASME license or copyright; see http://www.asme.org/terms/Terms_Use.cfm

appear when the upstream velocity profile is a parallel shear flow: since the vorticity and Bernoulli's "constant" are invariant functionals of the stream-function, they should be expressible in terms of known conditions far upstream everywhere in the flowfield. This simple idea is pursued here. The vorticity term in the equation governing the disturbance stream-function ψ and Bernoulli's "constant" are written as power series in ψ with variable coefficients depending on the mean profile curvature; these results are used to formulate a "direct" nonlinear boundary value problem for "inverse" applications, where the shape is sought that induces a prescribed pressure, with the jump in ψ or its streamwise derivative used to specify trailing edge shape constraints. For flows with constant shear the curvature vanishes and analytical solutions can be obtained by expansion in powers of a nondimensional vorticity. Solutions illustrating the interaction between thickness and camber are presented; also given are closed-form results for the lift induced by thickness and exact analogies with potential flows past ringwings. For linearized flows with arbitrary curvature, the stream-function equation can be put in conservation form, leading to new and more general Cauchy-Riemann conditions that extend the notion of the velocity potential; it turns out the usual planar potential formulation again applies, provided an axisymmetric-like change to the planar equation is made to allow source and vortex coupling, and certain redefinitions are made. These results are important because existing potential function methods for analysis problems can be trivially modified to handle the effect of oncoming vorticity; "direct" stream-function approaches to inverse problems, recently developed by this author, are also easily modified, thus avoiding direct integration of Euler's equations.

The stream-function approach to aerodynamic inverse problems, first proposed by this author in 1979, is based on a particularly simple idea. For constant density, steady, planar, inviscid, and irrotational flows, "analysis" problems solve $\phi_{xx} + \phi_{yy} = 0$ with the surface slope ϕ_y/U_∞ specified on a mean chord and the jump $[\phi]$ chosen to satisfy Kutta's condition, ϕ being the disturbance potential; surface pressures are then evaluated from $C_p = -2\phi_x/U_\infty$. The harmonic conjugate to ϕ, namely the disturbance stream-function ψ, likewise satisfies Laplace's equation. But what does a mathematically similar boundary value problem solve? Interestingly, $\psi_y = \phi_x = -\frac{1}{2}U_\infty C_p$ is a pressure specification, while $[\psi]$ and $[\psi_x]$ control trailing edge closure and included angle, respectively (the required surface shape is evaluated from $dy^\pm(x)/dx = -\psi_x(x,0^\pm)/U_\infty$ or $y^\pm(x) = -\psi(x,0^\pm)/U_\infty$ + constant). Thus the stream-function formulation solves the inverse problem—and, as a practical matter, it uses exactly the same potential formulation "analysis" algorithm! References [1-4] developed this idea extensively, at times introducing "streamlike" functions, generalizing the basic approach to handle transonic supercritical flows, axisymmetric nacelles, three-dimensional wing design, inlet flows, cascades, and so on. These extensions were restricted to irrotational problems, however. The present research, thus, aimed at inverse formulations that include the effects of oncoming shear, the results of which are described in the Abstract. An important by-product of this work arose when, perhaps fortuitously, the linearized stream-function equation fell into conservation form (this possibility was motivated by some mathematical constructions in hydrodynamic stability). Obviously, extended Cauchy-Riemann conditions could then be introduced, from which the notion of the "superpotential," discussed here, would naturally appear. In this paper, a number of general results describing airfoil aerodynamics in the presence of shear are presented, and numerical results and applications are given.

When this work was first completed, the obvious extension of the method to axisymmetric problems was immediately sought; equivalent analysis and design formulations could be directed, for example, toward duct design in turbomachinery applications. Extensions of our planar results were, in fact, made. But a more challenging problem was tackled: the jet-engine external potential and internal rotational flow interaction obtained through an assumed actuator disk and through the trailing edge slipstream (here, a radial shear flow is prescribed at the downstream side of the actuator disk, simulating the radially varying work imparted by the turbomachinery, while the entire nacelle is immersed in a uniform irrotational flow). The complete flow pattern was numerically solved by a column relaxation method, using special derived matching operators applied at the actuator disk and crucial renormalizations of the governing dependent variables so that radial differencing through the slipstream, which separates regions characterized by distinctly different flow properties, was possible. The new approach, described in reference [5], expands on the author's earlier work on jet-engine power simulation methods, these being essentially flow models for problems characterized by more than one total pressure (see references [6-8]).

At any rate, the theory and results described in the present paper and in reference [5] point to a new, simple, and promising approach to solving "analysis" problems in flows with strong shear: the "superpotential" formulation. (This is not to be confused with the Clebsch potential, sometimes used to represent rotational flows, or Lighthill's well-known pressure function approach, which is restricted to weak shears.) For both planar and axisymmetric problems, the linearized disturbance stream-function equations derived here, of course, are not new; but now, they are complemented by exact Bernoulli pressure integrals with "true constants" fixed for the entire flow-field, thus permitting the construction of general "inverse" formulations designed along the lines of references [1-4]. In Section II, flows with constant vorticity or linearly varying oncoming velocity will be considered, and some general results are given; Section III discusses general shears, introduces the notion of the "superpotential" and, finally, numerical analysis and design results are reported in Section IV. Extensions of the planar model to handle compressibility and three-dimensionality separately are given in the Appendices.

II Planar Flows With Constant Vorticity

1 Planar Flows: Inverse Problems. Let U and V be x and y velocities, P be the static pressure, and ρ be the density. The continuity equation $U_x + V_y = 0$ leads to a stream-function Ψ satisfying $U = \Psi_y$ and $V = -\Psi_x$; together with $UU_x + VU_y = -P_x/\rho$ and $UV_x + VV_y = -P_y/\rho$, the constancy of $\omega = U_y - V_x$ implies that $\Psi_{xx} + \Psi_{yy} = \omega$ with $P/\rho + \frac{1}{2}(U^2 + V^2) - \omega\Psi$ constant throughout. Thus, disturbances to a uniform shear flow satisfy

$$\psi_{xx} + \psi_{yy} = 0 \tag{1}$$

$$C_p = \frac{P - P_\infty(y)}{\frac{1}{2}\rho U_\infty^2} = -2\left(1 + \frac{\omega y}{U_\infty}\right)\frac{\psi_y}{U_\infty} + \frac{2\omega\psi}{U_\infty^2} - \frac{\psi_x^2 + \psi_y^2}{U_\infty^2} \tag{2}$$

where $\Psi = U_\infty y + \frac{1}{2}\omega y^2 + \psi$, U_∞ is constant, and $P_\infty(y)$ is the pressure at infinity. For thin airfoils, the inverse problem solves equation (1) with

$$\frac{\psi_y(x,0^\pm)}{U_\infty} - \frac{\omega\psi(x,0^\pm)}{U_\infty^2} = -\frac{1}{2}C_p(x,0^\pm) \tag{3}$$

specified on $y = 0$; the mixed boundary conditions strongly couple the effects of thickness and camber. Trailing edge

Downloaded 02 May 2010 to 171.66.16.25. Redistribution subject to ASME license or copyright; see http://www.asme.org/terms/Terms_Use.cfm

constraints also apply; for example, the jump $[\psi]$ prescribed through the downstream "wake" controls ejected mass flow or closure while $[\psi_x]$ controls the included angle (both jumps can be prescribed if C_p is suitably modified). In addition, ψ vanishes at infinity. The required airfoil is obtained by integrating

$$\frac{dy^{\pm}(x)}{dx} = \frac{V}{U} = \frac{-\psi_x}{U_\infty + \omega y + \psi_y} \cong -\frac{\psi_x(x,0^{\pm})}{U_\infty} \tag{4}$$

to obtain

$$y^{\pm}(x) = -\frac{\psi(x,0^{\pm})}{U_\infty} + \text{constant} \tag{5}$$

2 Planar Flows: Direct Formulations. Here $(\Psi_x)_x + (\Psi_y - \omega y)_y = 0$ suggests a "potential" N satisfying $N_x = \Psi_y - \omega y$ and $N_y = -\Psi_x$. Equation (4) becomes $N_y(x,0^{\pm}) = U_\infty dy^{\pm}(x)/dx$; for closed trailing edges, ψ is single-valued, and Kutta's condition requires that $[N_x]$ vanish from equation (3). In terms of $\eta(x,y) = N - U_\infty x$, the complete streamline pattern is obtained by solving the irrotational problem

$$\begin{aligned} &\eta_{xx} + \eta_{yy} = 0 \\ &\eta_y(x,0^{\pm}) = U_\infty dy^{\pm}(x)/dx \text{ on the chord} \\ &[\eta_x] = 0 \text{ through the "wake"} \\ &\nabla\eta \to 0 \text{ at infinity} \end{aligned} \tag{6}$$

and then setting $\Psi_y = U_\infty + \omega y + \eta_x$ and $-\Psi_x = \eta_y$. Surface pressures are easily obtained. If $y^{\pm}(x) = 0$ at the leading edge $x = x_{LE}$, then $\psi(x,0^{\pm}) = \psi(x_{LE},0) - U_\infty y^{\pm}(x)$ from equation (5); substitution into equation (3) leads to

$$C_p(x,0^{\pm}) = -2\frac{\eta_x(x,0^{\pm})}{U_\infty} + \frac{2\omega\psi(x_{LE},0)}{U_\infty^2} - \frac{2\omega}{U_\infty} y^{\pm}(x) \tag{7}$$

The level $\psi(x_{LE},0)$ affects neither the pressure gradient nor the total lift; it can be determined by solving equation (1) with $\psi_y(x,0^{\pm}) = \eta_x(x,0^{\pm})$, which is known, along with vanishing ψ at infinity and appropriate edge constraints. Note that a symmetric airfoil, which has no lift in a uniform stream, has a shear induced lift

$$L_s = 2U_\infty \omega\rho \int_{\text{chord}} y^+(x)\,dx \tag{8}$$

which varies linearly with the vorticity ω and the enclosed area. For a pure camber line there is no additional induced lift; in this case, the net lift can be obtained irrotationally. Thus, equation (8) represents the only "additional" lift for a general airfoil with both thickness and camber: the effect of shear is, effectively, a change in the angle of zero lift relative to irrotational solutions.

3 Some Planar Analytical Solutions. The foregoing problems can be solved with slight modification to existing numerical methods, e.g., those outlined in the Introduction, but it is more instructive to study representative analytical solutions. First introduce the nondimensional variables $x^* = x/c$, $y^* = y/c$ and $\psi^*(x^*,y^*) = \psi/U_\infty c$ where $2c$ is the chord. If $\epsilon = \omega c/U_\infty$ is small, we expand $\psi^* = \psi_0^* + \epsilon\psi_1^* + \ldots$ to obtain

$$\begin{aligned} \psi_{0_{xx}} + \psi_{0_{yy}} &= 0 \\ \psi_{0_y}(x,0^{\pm}) &= -\tfrac{1}{2}C_p(x,0^{\pm}) \end{aligned} \tag{9}$$

$$\begin{aligned} \psi_{1_{xx}} + \psi_{1_{yy}} &= 0 \\ \psi_{1_y}(x,0^{\pm}) &= \psi_0(x,0^{\pm}) \end{aligned} \tag{10}$$

using $\psi_y(x,0^{\pm}) - \epsilon\,\psi(x,0^{\pm}) = -\tfrac{1}{2}C_p^{\pm}(x)$, where asterisks have been dropped. Two general observations are apparent. If $C_p^+ = C_p^-$, then $\psi_0^+ = -\psi_0^-$; then, the effect of weak shear, because the pressure ψ_{1_y} is antisymmetric, is an induced camber line. Alternatively, if $C_p^+ = -C_p^-$, then $\psi_0^+ = \psi_0^-$, which in turn induces a thickness distribution. Now we examine some specific solutions.

First assume $C_p^{\pm} = -2\tau$ with τ a small positive constant. The solution to equation (9) assuming closed edges is the classic ellipse $y_0^{\pm}(x) = \pm\tau(1-x^2)^{1/2}$ where $x = \mp 1$ are leading and trailing edges; from equation (5), $\psi_0(x,0^{\pm}) = \mp\tau(1-x^2)^{1/2}$ where the additive constant vanishes by the asymmetry in ψ_0. The assumption $\psi_1 = 1/4\pi\int_{-1}^{+1} h(s)\,\log((x-s)^2 + y^2)ds$ leads to $h(x) = -2\tau(1-x^2)^{1/2}$; thus, $dy_1/dx = -\psi_{1_x}(x,0) = \tau x$ and $y_1(x) = \tfrac{1}{2}\tau(x^2-1)$ is an upright parabola. The composite airfoil $y = y_0 + \epsilon y_1 = \pm\tau(1-x^2)^{1/2} + \tfrac{1}{2}\epsilon\tau(x^2-1)$ has negative camber if $\epsilon > 0$. This is expected: since a symmetrical airfoil experiences lift, the shape due to $C_p^+ = C_p^-$, with zero lift, must remove lift.

Next consider $C_p^{\pm} = \mp 2\alpha(1-x)^{1/2}/(1+x)^{1/2}$ which corresponds to the flat plate $y(x) = -\alpha(x+1)$ in irrotational flow. The assumption $\psi_0(x,y) = 1/4\,1/\pi\int_{-1}^{+1} 2\alpha(1-s)^{1/2}/(1+s)^{1/2}\log((x-s)^2+y^2)\,ds$ leads to $\psi_0(x,0^{\pm}) = \alpha(x - \log 2)$. Since $\psi_{1_y}(x,0^{\pm})$ is symmetric, the required thickness distribution having closed edges can be obtained from

$$\frac{dy^+(x)}{dx} = \frac{1}{\pi}\sqrt{\frac{1-x}{1+x}}\int_{-1}^{+1}\sqrt{\frac{1+s}{1-s}}\,\frac{\psi_{1_y}(s,0^{\pm})}{s-x}\,ds$$

$$-\frac{1}{\pi\sqrt{1-x^2}}\int_{-1}^{+1}\sqrt{\frac{1+s}{1-s}}\,\psi_{1_y}(s,0^{\pm})\,ds$$

If $y^+(-1) = 0$, $y^+(x) = \alpha(\tfrac{1}{2}x - \log 2)(1-x^2)^{1/2}$ contains both blunted leading and trailing edges. For positive $\alpha, y^+(x)$ is negative, thus reducing the "main" thickness; for negative $\alpha, y^+(x)$ is a "whale" with a large nose and an "almost sharp" tail swimming in the minus x direction, with a maximum thickness at $x \cong -0.4$.

4 Analogy To Ringwing Potential Flows. The planar inverse problem with shear is related to the potential flow past a given ringwing: in both cases the effects of sources and vorticity are coupled. For axisymmetric flows, the disturbance potential $\tilde{\phi}$ satisfies $\tilde{\phi}_{xx} + \tilde{\phi}_{rr} + \tilde{\phi}_r/r = 0$ where x and r are streamwise and radial coordinates. We assume the shape $r^{\pm}(x) = R + cF_{\pm}(\xi)$ where $2c$ and R are chord and mean radius and $\xi = x/c$; also, define $\rho = (r-R)/c$, $\tilde{\phi}(x,r) = U_\infty c\phi(\xi,\rho)$ and $\delta = c/R$. In the ringwing limit taking $\delta \ll 1$ and ρ being 0(1) the exact equation $\phi_{\xi\xi} + \phi_{\rho\rho} + \delta\phi_\rho/(1+\delta\rho) = 0$ becomes $\phi_{\xi\xi} + \phi_{\rho\rho} + \delta\phi_\rho = 0$ accounting for first-order curvature. Expansion in powers of δ leads to homogeneous solutions based on classic airfoil theory; however, even for simple shapes, it is not possible to evaluate a resulting particular integral, formally expressed in complex conjugate coordinates, much less resolve it in odd and even parts. An alternative exists: if $G = \phi\exp(\tfrac{1}{2}\delta\rho)$, $G_{\xi\xi} + G_{\rho\rho} = (\phi_{\xi\xi} + \phi_{\rho\rho} + \delta\phi_\rho + \tfrac{1}{4}\delta^2\phi)\exp(\tfrac{1}{2}\delta\rho) \cong 0$ by dropping the $O(\delta^2)$ term, and $\phi_\rho(\xi,0^{\pm}) = F'_{\pm}(\xi)$ becomes $G_\rho(\xi,0^{\pm}) - \tfrac{1}{2}\delta G(\xi,0^{\pm}) = F'_{\pm}(\xi)$ ($\phi_r = 0$ on the centerline transforms to a farfield regularity condition and $C_p = -2\phi_\xi = -2G_\xi\exp(-\tfrac{1}{2}\delta\rho)$ reduces to $-2G_\xi(\xi,0^{\pm})$ on the surface). But this is identical to $\psi_y(x,0^{\pm}) - \epsilon\psi(x,0^{\pm}) = -\tfrac{1}{2}C_p^{\pm}(x)$ if we identify F' with $-\tfrac{1}{2}C_p$ and $\tfrac{1}{2}\delta$ with ϵ! Obviously, the analogy is meaningful only for positive δ, and then, only for the edge constraint $[\psi_x] = 0$. One additional analogy exists. The stream-function defined from $\psi_\rho = (1+\delta\rho)\phi_\xi$ and $-\psi_\xi = (1+\delta\rho)\phi_\rho$ satisfies $\psi_{\xi\xi} + \psi_{\rho\rho} - \delta\psi_\rho/(1+\delta\rho) = 0$ which in the ringwing limit becomes $\psi_{\xi\xi} + \psi_{\rho\rho} - \delta\psi_\rho = 0$. Then the function $H = \psi\exp(-\tfrac{1}{2}\delta\rho)$ satisfies $H_{\xi\xi} + H_{\rho\rho} = 0$ to $O(\delta^2)$; since $\psi_\rho = -\tfrac{1}{2}(1+\delta\rho)C_p = -\tfrac{1}{2}C_p(\xi,0^{\pm})$ we find that $H_\rho(\xi,0^{\pm}) + \tfrac{1}{2}\delta H(\xi,0^{\pm}) = -\tfrac{1}{2}C_p(\xi,0^{\pm})$. Thus, the inverse problem for ringwings in irrotational flow and the same for airfoils in uniform shear are identical.

5 Source and Vortex Interactions for Ringwings.

Downloaded 02 May 2010 to 171.66.16.25. Redistribution subject to ASME license or copyright; see http://www.asme.org/terms/Terms_Use.cfm

Examples of ringwing potential flows are given to complement the airfoil design calculations in Section 3. Again, $r^{\pm}(x) = R + cF_{\pm}(\xi)$; assuming $\delta \ll 1$, we expand $G = G_0 + \frac{1}{2}\delta G_1 + \ldots$ to obtain

$$G_{0_{\xi\xi}} + G_{0_{\rho\rho}} = 0 \tag{11}$$

$$G_{0_\rho}(\xi, 0^{\pm}) = F'_{\pm}(\xi)$$

$$G_{1_{\xi\xi}} + G_{1_{\rho\rho}} = 0 \tag{12}$$

$$G_{1_\rho}(\xi, 0^{\pm}) = G_0(\xi, 0^{\pm})$$

Thus, a pure thickness distribution generates an $O(\delta)$ camberlike flow, while a pure camber distribution generates a thicknesslike flow. First consider the flow past the elliptical section $F_{\pm}(\xi) = \pm\tau(1-\xi^2)^{1/2}$; to leading order, the surface pressure is constant with $C_p = -2\tau$. Centerline "ground" effects induce a disturbance flow antisymmetric in ρ past an "effective" camber line "$d\rho/d\xi$" $= G_0(\xi, 0^{\pm}) = \tau\xi$ or $\rho(\xi) = \frac{1}{2}\tau(\xi^2 - 1)$, symmetric about $\xi = 0$; if the trailing edge pressure jump is zero, the local vortex strength must vanish, implying that $C_p(\xi, 0^{\pm}) = -2\tau \pm \delta\tau(1-\xi^2)^{1/2}$. This leads to a net force directed toward the centerline due to lower inner surface pressures caused by rapid internal accelerations. Finally consider the flat plate ringwing $F_{\pm}(\xi) = -\alpha(\xi + 1)$ at "angle of attack" α. The classic solution to equation (11) shows that $G_{0_\xi}(\xi, 0^{\pm}) = \pm\alpha(1-\xi)^{1/2}/(1+\xi)^{1/2}$ so that $G_{1_\rho}(\xi, 0^{\pm}) = \pm\alpha((1-\xi^2)^{1/2} + \text{arcsine } \xi)$ in equation (12). For positive α this is the slope of a fictitious "fishlike" thickness distribution "swimming" in the minus x direction with a small "head" of positive area and a large "tail" of negative area; this thickness distribution, whose opened trailing edge arises from surface cross-over, does not contribute to lift.

III Airfoils in General Parallel Shear Flow

Flows with arbitrary vorticity satisfy Euler's and not Laplace's equation; this, plus the lack of a simple Bernoulli integral, increases numerical difficulty. However, simplifications are possible assuming a parallel shear flow $U_m(y)$ far upstream with $d\psi_m(y)/dy = U_m(y)$. Then, disturbances ψ must obey $\psi_{xx} + \psi_{yy} = \omega(\psi_m + \psi) - \omega(\psi_m)$, noting that $\omega(\Psi)$ is constant along a streamline. Now we can approximate, for example,

$$\frac{\omega(\psi_m + \psi) - \omega(\psi_m)}{\psi}\psi \cong \psi \frac{d\omega(\Psi)}{d\Psi}\bigg|_{\psi_m} = \psi \frac{U''_m(y)}{U_m(y)}$$

using the chain rule with $\omega(\psi_m) = U'_m(y)$, but including higher order terms leads to

$$\frac{\partial^2\psi}{\partial x^2} + \frac{\partial^2\psi}{\partial y^2} = \frac{U''_m}{U_m}\psi + \frac{1}{2}\left(\frac{U'''_m}{U_m^2} - \frac{U''_m U'_m}{U_m^3}\right)\psi^2 \tag{13}$$

$$+ \frac{1}{6}\left(\frac{U''''_m}{U_m^3} - 3\frac{U'''_m U'_m}{U_m^4} + 3\frac{U''_m U'^2_m}{U_m^5} - \frac{U''^2_m}{U_m^4}\right)\psi^3 + \ldots$$

where the nonlinear right side, which depends on curvature, vanishes for linear velocity profiles (the leading U''_m/U_m coefficient appears in the linear Orr-Sommerfeld equation). For inverse problems, it is not necessary to formulate boundary conditions from a complete Bernoulli integral: the "horizontal" Euler equation $p_x/\rho + U_m(y)\psi_{yx} - \psi_x U'_m(y) = 0$ linearized about $U_m(y)$ integrates to $p/\rho + U_m\psi_y - U'_m\psi = g(y)$ where p is the disturbance pressure. But $g = 0$ since all disturbances vanish far upstream. Adding $P_\infty(y)/\rho$ to both sides leads to the obvious extension

$$P(x, 0^{\pm}) - P_\infty(0)$$

$$= \{-U_m(0)\psi_y(x, 0^{\pm}) + U'_m(0)\psi(x, 0^{\pm})\}\rho \tag{14}$$

of equation (3). For consistency, the linearized form of equation (13) is solved with equation (14) plus trailing edge-shape constraints. If the curvature $U''_m(y)$ is negligible our results for constant vorticity derived in Part II apply with ω replaced by $U'_m(0)$! Otherwise, numerical methods are generally necessary, unless U''_m/U_m is constant, so that analytic solutions in terms of Bessel functions are possible.

For flows with strong vorticity the nonlinear terms in equation (13) are important and corrections to equation (14) are similarly needed. We first derive a Bernoulli equation for arbitrary parallel flows. In the general case it is easy to verify that $(P/\rho + \frac{1}{2}(U^2 + V^2))_x - \omega(\Psi)\Psi_x = 0$ and $(P/\rho + \frac{1}{2}(U^2 + V^2))_y - \omega(\Psi)\Psi_y = 0$, so that $P/\rho + \frac{1}{2}(U^2 + V^2) - J(\Psi)$ is constant throughout, with $J'(\Psi) = \omega(\Psi)$. Thus, if $\omega(\Psi)$ is constant, as in Part II, $J = \omega\Psi$. The function J can be evaluated anywhere, but upstream conditions are simplest, since they are known; if $\psi_m = K(y)$, where K is given, we have

$$J(\Psi) = \int \omega(\Psi)\, d\Psi = \int U'_m(y)\, U_m(y)\, dy$$

$$= \frac{1}{2}U_m^2(y) + \text{constant}$$

with the inversion $y = K^{-1}(\Psi)$. This formula, not previously given, may be useful in other applications. For $y \cong 0$, $y \cong (\Psi - K(0))/K'(0)$ and $J(\Psi)$ is considerably simplified. In what follows we assume $U = U_m + u$, $V = v$, and $\Psi = \psi_m + \psi$ where u, v, and ψ are disturbances. Without approximation,

$$\frac{P}{\rho} + \frac{1}{2}\{U_m^2 + 2U_m u + u^2 + v^2\} - J(\psi_m + \psi)$$

$$= \frac{P_\infty(y)}{\rho} + \frac{1}{2}U_m^2 - J(\psi_m)$$

Dropping the $\frac{1}{2}(u^2 + v^2)$ leads to

$$C_p = \frac{P - P_\infty(y)}{\frac{1}{2}\rho U_{\text{ref}}^2} = -2\frac{U_m\psi_y}{U_{\text{ref}}^2} + \frac{2\psi}{U_{\text{ref}}^2}\frac{J(\psi_m + \psi) - J(\psi_m)}{\psi}$$

$$= -2\frac{U_m\psi_y}{U_{\text{ref}}^2} + \frac{2\psi}{U_{\text{ref}}^2}\left\{J'(\psi_m) + \frac{1}{2}J''(\psi_m)\psi + \frac{1}{6}J'''(\psi_m)\psi^2 + \ldots\right\} \tag{15}$$

$$= -2\frac{U_m\psi_y}{U_{\text{ref}}^2} + \frac{2\psi}{U_{\text{ref}}^2}\left\{U'_m(y) + \frac{1}{2}\frac{U''_m}{U_m}\psi + \frac{1}{6}\left(\frac{U'''_m}{U_m^2} - \frac{U''_m U'_m}{U_m^3}\right)\psi^2 + \ldots\right\}$$

extending equations (3) and (14).

We summarize our results as they relate to inverse problems: equation (13) is solved with $C_p(x, 0^{\pm})$ prescribed through combinations of ψ_y and ψ as shown in equation (15) and $[\psi]$ or $[\psi_x]$ specified through the downstream wake to control closure or included angle (both may be specified, following reference [4], if suitable changes to input surface pressures are allowed). Corresponding to equations (4) and (5) we have $dy^{\pm}(x)/dx = -\psi_x/(\psi'_m(y) + \psi_y) \cong -\psi_x(x, 0^{\pm})/\psi'_m(0)$ or $y^{\pm}(x) = -\psi(x, 0^{\pm})/\psi'_m(0) + \text{constant}$. The problem is nonlinear despite our neglect of $\frac{1}{2}(u^2 + v^2)$. Various modifications to the line relaxation methods of references [1-4] are possible, of course, but their numerical stability properties have not yet been investigated.

"Analysis" or "direct" problems solving the flow past prescribed shapes cannot be solved by stream-function methods. Prescribing shape fixes source density automatically and specifying $[\psi]$ or $[\psi_x]$ is redundant; Kutta's condition fixes an arbitrary vorticity level controlled by specifying a jump in potential. Also, the constant in "$\psi(x, 0^{\pm}) = -$

Downloaded 02 May 2010 to 171.66.16.25. Redistribution subject to ASME license or copyright; see http://www.asme.org/terms/Terms_Use.cfm

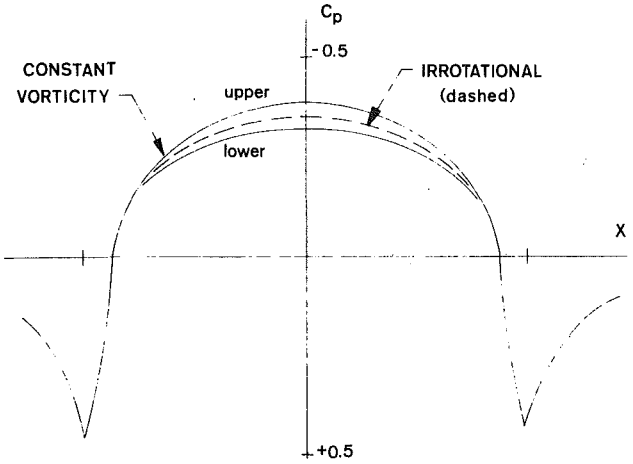

Fig. 1 Constant vorticity calculation

$\psi'_m(0)y^{\pm}(x)$ + constant," zero for pure thickness distributions, is indeterminate for camber lines; in this hypothetical Dirichlet formulation, nonzero surface pressures are identified with the unknown stream-function level. Thus "potentiallike" formulations using Neumann surface conditions specifying jumps in "potential" or its streamwise derivative are particularly desirable: they are natural to the physics and would require minor modification to existing potential flow difference methods. For simplicity consider linearized flows with arbitrary mean velocity curvature and drop the nonlinear terms in equation (13). Since $\psi_{xx} + \psi_{yy} - U''_m(y)\psi/U_m = 0$ can be put in the conservation form

$$\frac{\partial}{\partial x}\left\{+\frac{U_m(y)}{U_{\text{ref}}}\psi_x\right\}+\frac{\partial}{\partial y}\left\{\frac{U_m}{U_{\text{ref}}}\psi_y-\frac{U'_m}{U_{\text{ref}}}\psi\right\}=0$$

it is possible to introduce the "super-potential" $\phi^*(x,y)$ satisfying

$$\phi^*_y=-\frac{U_m}{U_{\text{ref}}}\psi_x \tag{16}$$

$$\phi^*_x=\frac{U_m}{U_{\text{ref}}}\psi_y-\frac{U'_m}{U_{\text{ref}}}\psi \tag{17}$$

These generalized Cauchy-Riemann conditions, which reduce to the irrotational ones when $U_m(y) = U_\infty$, imply the governing "potential equation"

$$\phi^*_{xx}+\phi^*_{yy}-2\frac{U'_m}{U_m}\phi^*_y=0 \tag{18}$$

For analysis problems, the corresponding tangency conditions are

$$\phi^*_y(x,0^{\pm})=-\frac{U_m(0)}{U_{\text{ref}}}\psi_x(x,0^{\pm})=\frac{U^2_m(0)}{U_{\text{ref}}}\frac{dy^{\pm}(x)}{dx} \tag{19}$$

Solving equation (17) for ψ_y and substituting in the linearized form of equation (15) gives the remarkably simple pressure formula

$$C_p=-2\frac{\phi^*_x}{U_{\text{ref}}} \tag{20}$$

Through the trailing edge wake, pressure is continuous, so that the jump in ϕ^* satisfies

$$[\phi^*_x]=0 \tag{21}$$

Thus, the mathematical formulation is exactly the same as in planar potential flow, except that the third "axisymmetriclike" term in equation (18) is needed to couple the effects of source and vorticity; hence, coding changes to existing finite difference algorithms, for example, solving $\phi^*_{xx} + \phi^*_{yy} = 0$ subject to equations (19) and (21), are extremely

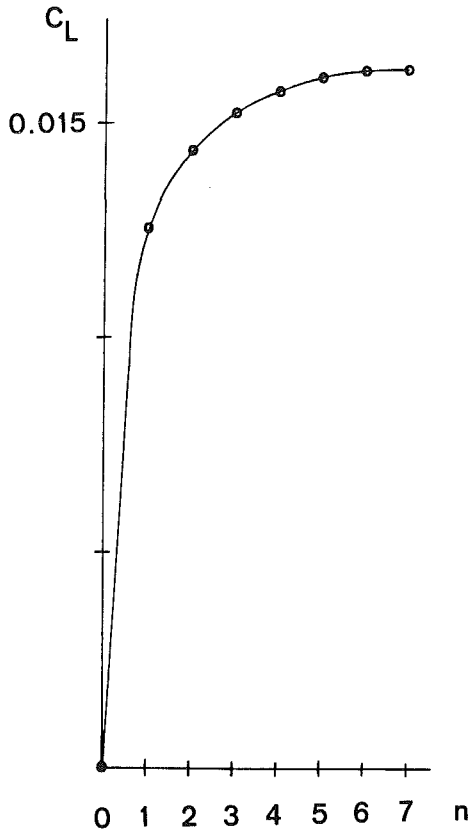

Fig. 2 Calculation with nonzero profile curvature

simple. For flows with constant vorticity, our earlier, simpler results can be used; we stress that ϕ^*_x is *not* the streamwise disturbance velocity, however, small disturbance streamline patterns can be obtained by integrating equation (16) with respect to x, since ϕ^*_y is proportional to the transverse speed.

IV Numerical Results

Both analysis and design numerical column relaxation algorithms have been devised to cross-check various analytical results previously derived; the computer methods, in addition, provide rapid means for the evaluation of flows containing strong shears with significant curvature, where closed-form solutions are not possible.

For analysis problems, the $-2U'_m\phi^*_y/U_m$ term in equation (18) was incorporated in a conventional finite-difference column relaxation potential flow code using central differences; also, the asymptotic formulas used in the irrotational code to update farfield computational box edge potentials were removed and replaced by the simpler conditions $\phi^*_x = \phi^*_y = 0$ (these represent the only required code modifications). The resulting code was first tested over several angles of attack for a 10 percent symmetric parabolic arc airfoil, in the irrotational limit, to ensure quantitative agreement with more exact pressures and with theoretical lift versus angle of attack results. We will take $U_{\text{ref}} = U_m(0)$, introduce the nondimensional superpotential $\bar{\phi}(\bar{x},\bar{y}) = \phi^*(x,y)/U_m(0)c$, again with $\bar{x} = x/c$ and $\bar{y} = y/c$ where c is the semichord, so that $\bar{\phi}_{\bar{y}}(\bar{x},0) = d\bar{y}/d\bar{x}$ and $C_p = -2\bar{\phi}_{\bar{x}}$ (only the ratio U'_m/U_m enters the calculation). We assume the prescribed shear flow $U_m(y) \sim 1+\alpha\bar{y}+\beta\bar{y}^2+n(\bar{y}+7.5)^{1/2}$ far upstream and solve for the disturbance shear flow induced by the symmetric parabolic arc airfoil $y^{\pm}(x)/c = \pm\tau(1-(x/c)^2)$ contained in $-1 \le \bar{x} \le +1$. Nondimensionalizations based on the semichord c lead to $C_L = [\bar{\phi}]_{TE}$, where TE denotes the trailing edge value, automatically available from

Downloaded 02 May 2010 to 171.66.16.25. Redistribution subject to ASME license or copyright; see http://www.asme.org/terms/Terms_Use.cfm

computed results without explicit pressure integration. For simplicity, the airfoil was centered in a computational box 3.4 × 7.5 chords in the streamwise and transverse directions, respectively, with 68 uniform horizontal meshes (20 over the chord) and 60 uniform vertical meshes. All irrotational and rotational computations were stably executed.

Specific calculations were performed to cross-check our analysis with the numerical algorithm. For airfoils in linear shear flows (i.e., straight-line velocity profiles having constant vorticity), equation (8) for the shear induced lift was inferred from the small-disturbance symmetry and antisymmetry properties of the quantities appearing in equation (7). The corresponding lift coefficient per unit span can be evaluated from

$$C_L = \frac{2\omega}{U_\infty c}\int_{\text{chord}} y^+(x)\,dx = \frac{8}{3}\left(\frac{\omega c}{U_\infty}\right)\tau$$

noting $U_\infty = U_m(0)$. With $\beta = n = 0$, $\alpha = 0.13$ and $\tau = 0.10$, theory gives $C_L = 0.0347$; numerical results, using the calibrated mesh, after 350 "sweeps" of the computational box (enough to guarantee less than 5 percent change in calculated surface C_p's per 100 sweeps), gave $C_L = [\phi]_{TE} = 0.0332$, a small 5 percent difference. The computed C_p distribution in Fig. 1, in agreement with theory, is symmetric with respect to midchord and properly "bisected" by the irrotational (dashed) solution shown. Additional calculations, not described here, also validate the linear dependence of lift on vorticity, as required in equation (8). A second set of calculations was performed where the oncoming mean profile curvature was nonvanishing. Here we took $\alpha = \beta = 0$ with $n = 0, 1, 2, \ldots 7$. The resulting surface pressures, somewhat uninteresting, qualitatively resemble the curves in Fig. 1; more interesting is the dependence of C_L on n which, unlike α, is definitely nonlinear, appearing to asymptote at $C_L = 0.016$ using Shank's extrapolation (See Fig. 2).

Finally, we describe several design mode calculations solving for the airfoil shape that induces a prescribed chordwise surface pressure. The stream-function algorithm used in the inverse procedures described in references [2–4], which enforce trailing edge closure by setting $[\psi] = 0$ through the downstream wake, was modified to handle mixed Dirichlet and Neumann pressure conditions as required in equation (3); numerical calculations were restricted to linear shears, for which analytical results have been derived, although algorithmic extensions to handle equations (13) and (15) for more general velocity profiles are not difficult. In classical thin airfoil theory for uniform oncoming freestreams, the closed airfoil inducing a constant C_p of -2τ on both surfaces is an ellipse of thickness ratio τ. In our calculations, $C_p^{\pm} = -0.2$ was fixed throughout and the values $\epsilon = 0.0, 0.25, 0.5, 0.75$, and 1.0 were chosen. Figures 3(a–e) corresponding, respectively, to our increasing ϵ's, verify the predicted

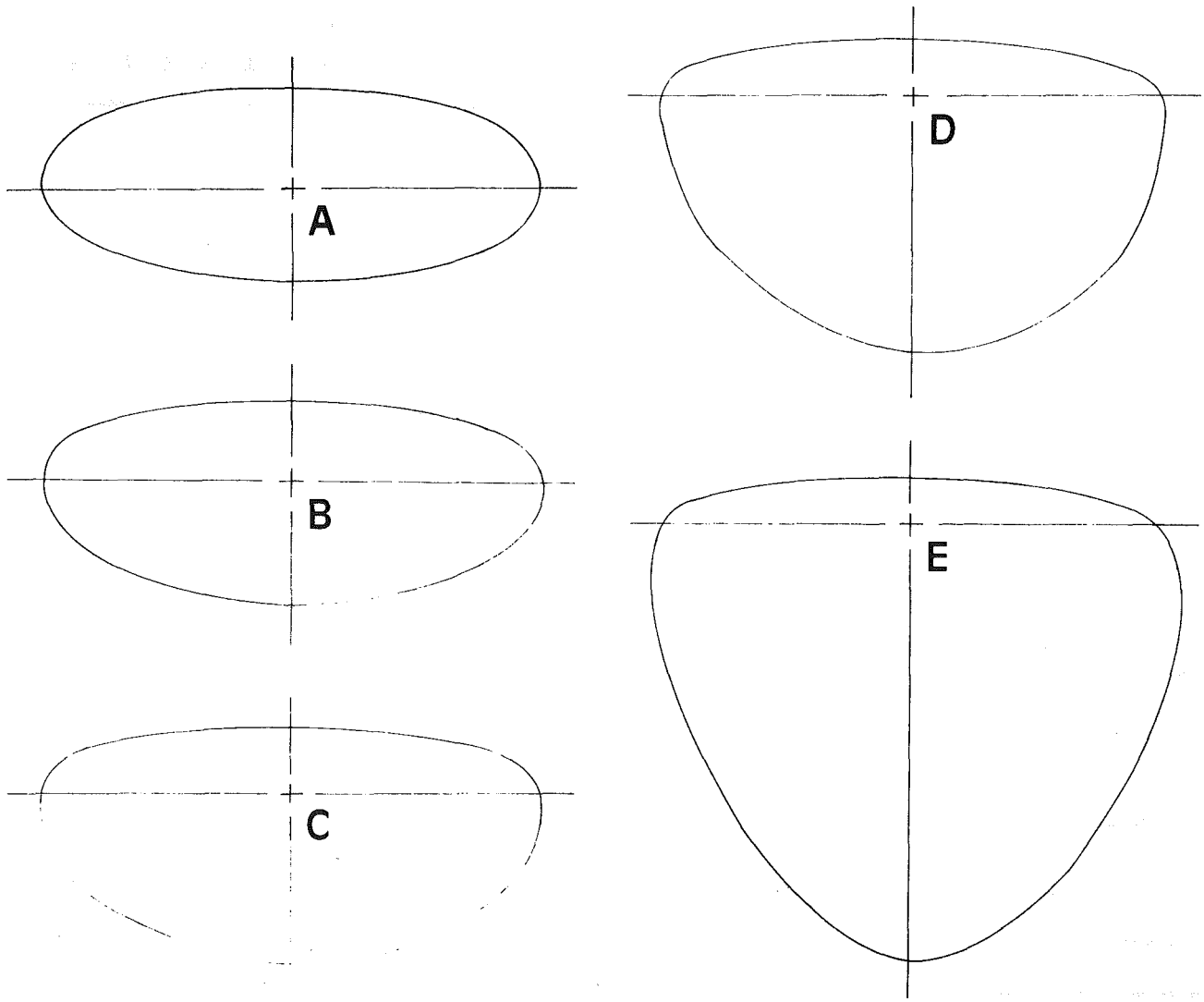

Fig. 3 Design calculations (vertical scale stretched four times)

Downloaded 02 May 2010 to 171.66.16.25. Redistribution subject to ASME license or copyright; see http://www.asme.org/terms/Terms_Use.cfm

negative camber for small ϵ's but the negative camber is found even for ϵ's not small. In conclusion, we have cross-checked both analytical and numerical analysis and design approaches, and validated the basic mathematical premises; the computer codes described in this paper, incidentally, are available from this author on request.

V Closing Remarks

We have presented a general mathematical description for flows past thin airfoils in the small disturbance limit. In the constant vorticity limit, analytical inverse and direct solutions for specific flow parameters were derived from general formulations, analogies to potential ringwing flows with similar source and vortex interaction were given, and closed-form results for the lift induced by shear were derived. The general theory for shear flows with arbitrary velocity profile curvature, in both analysis and design modes, was next presented, making use of several well-known properties of vorticity in planar inviscid flows. Various numerical algorithms and results illustrating thickness and camber coupling effects, applying the stream-function methodology to inverse applications and the "superpotential" idea to analysis problems, were next given which show results consistent with physical intuition. Finally, in Appendices I and II, extensions of the "scalar stream-function" approach to three-dimensional constant density shear flows, the three-dimensional "superpotential," and the planar compressible shear flow, are described, although numerical results will be deferred to a later paper. References to the classical literature on shear flow aerodynamics can be found in the book by Thwaites [9].

References

1 Chin, W. C., "On the Design of Thin Subsonic Airfoils," ASME JOURNAL OF APPLIED MECHANICS, Vol. 46, 1979, pp. 6-8.

2 Chin, W. C., and Rizzetta, D. P., "Airfoil Design in Subcritical and Supercritical Flows," ASME JOURNAL OF APPLIED MECHANICS, Vol. 46, 1979, pp. 761-766.

3 Chin, W. C., "Class of Shockfree Airfoils Producing the Same Surface Pressure," *Journal of Aircraft*, Apr. 1980, pp. 286-288.

4 Chin, W. C., "Direct Approach to Aerodynamic Design Problems," ASME JOURNAL OF APPLIED MECHANICS, Vol. 48, 1981, pp. 721-726.

5 Chin, W. C., "Superpotential Solution for Jet-Engine External Potential and Internal Rotational Flow Interaction," ASME JOURNAL OF APPLIED MECHANICS, Vol. 50, 1983, pp. 259-264.

6 Golden, D., Barber, T., and Chin, W. C., "An Axisymmetric Nacelle and Turboprop Inlet Analysis With Flow-Through and Power Simulation Capabilities," AIAA Paper No. 82-0256.

7 Golden, D., Barber, T., and Chin, W. C., "An Axisymmetric Nacelle and Turboprop Inlet Analysis Including Power Simulation," *Journal of Aircraft*, June, 1983, pp. 536-542.

8 Chin, W. C., "Engine Power Simulation for Transonic Flow-Through Nacelles," *AIAA Journal*, Oct. 1983, pp. 1471-1472.

9 Thwaites, B., *Incompressible Aerodynamics*, Oxford University Press, London, 1960.

10 Hafez, M., and Lovell, D., "Numerical Solution of Transonic Streamfunction Equation," Paper No. 81-1017, presented at the AIAA 5th Computational Fluid Dynamics Conference, Palo Alto, Calif., June 22-23, 1981.

APPENDIX I

Three-Dimensional Flows

Let z and W be spanwise coordinate and velocity. Then the continuity equation $U_x + V_y + W_z = 0$, rewritten in the form $(U + \int_{-\infty}^{x} W_z dx)_x + (V)_y = 0$, suggests the definitions $\Psi_y = U + \int_{-\infty}^{x} W_z dx$ and $\Psi_x = -V$. We assume a constant vorticity shear with $\omega = U_y - V_x$, $W_y = V_z$ and $W_x = U_z$. Thus,

$$\Psi_{xx} + \Psi_{yy} = \omega + \int_{-\infty}^{x} W_{yz} dx = \omega + \frac{\partial^2}{\partial z^2} \int_{-\infty}^{x} V\, dx$$

$$= \omega - \frac{\partial^2}{\partial z^2} \{ \Psi(x,y,z) - \Psi(-\infty,y,z) \}$$

$$\left\{ \frac{\partial^2}{\partial z^2} \Psi(-\infty,y,z) = 0 \right\} \tag{I.1}$$

or

$$\Psi_{xx} + \Psi_{yy} + \Psi_{zz} = \omega \tag{I.2}$$

which appears as a simple extension of the planar equation! The "horizontal" Euler equation linearized about the parallel flow $U_m(y)$ is simply $U_m(y)u_x + vU_m'(y) + p_x/\rho = 0$ where u, v, p are disturbances; since $v = -\psi_x$, integration gives $U_m(y)\psi_y - \omega\psi + p/\rho = g(y,z)$ where $\omega = U_m'(y)$ is constant. But $g = 0$ since all disturbance quantities vanish at infinity; for inverse problems, thus, equation (3) again applies.

If we now take $\Psi = U_\infty y + \frac{1}{2}\omega y^2 + \psi$ the disturbance stream-function satisfies $\psi_{xx} + \psi_{yy} + \psi_{zz} = 0$. The form $(\psi_x + \int_{-\infty}^{x} \psi_{zz} dx)_x + (\psi_y)_y = 0$ suggests the definitions $\phi_x = \psi_y$ and $\phi_y = -\psi_x - \int_{-\infty}^{x} \psi_{zz} dx$; then, differentiation of the first with respect to x and the second with respect to y shows, if $\phi_{zz}(-\infty,y,z)$ vanishes, that $\phi_{xx} + \phi_{yy} + \phi_{zz} = 0$! This equation is useful in analysis problems. For high aspect ratio wings, the integral term in the ϕ_y definition is small, leading to the usual Neumann condition $\phi_y(x,0^{\pm},z) = U_\infty dy^{\pm}(x,z)/dx$. Kutta's condition requires $[C_p] = 0$ at the trailing edge; from equation (3), $[\psi_y] = 0$ since ψ is single-valued for closed edges, thus implying $[\phi_x] = 0$. This is the usual irrotational formulation; because the boundary conditions are not mixed, thickness and camber do not interact and can be treated separately. For an unpitched wing with symmetric sections, the local shear-induced loading goes like $\omega[\psi]$ since $[\psi_y] = 0$; thus, equation (8) again applies per unit span. A "camber only" wing has no shear-induced lift; its lift can be obtained irrotationally.

APPENDIX II

Planar Compressible Shear Flow

In planar compressible isentropic shear flow, the total horizontal and vertical velocities U and V, the static pressure P, and the fluid density ρ satisfy $P = \bar{c}\rho^{\gamma}$, where γ is the ratio of specific heats, and $\bar{c}$ is a constant, and

$$UU_x + VU_y = -P_x/\rho \tag{II.1}$$

$$UV_x + VV_y = -P_y/\rho \tag{II.2}$$

$$(\rho U)_x + (\rho V)_y = 0 \tag{II.3}$$

Again we introduce the vorticity

$$\zeta = U_y - V_x \tag{II.4}$$

Equations (II.1)-(II.3) then imply that

$$U\zeta_x + V\zeta_y = -\zeta(U_x + V_y) \tag{II.5}$$

$$(U\rho_x + V\rho_y)/\rho = -(U_x + V_y) \tag{II.6}$$

Hence, in substantive derivative notation,

$$\frac{D}{Dt} \log \frac{\zeta}{\rho} = 0 \tag{II.7}$$

From this invariance, we will see that if $\zeta = U_m'(y)$ and $\rho = \rho_m(y)$ are known far upstream, the flow equations anywhere downstream can be written explicitly.

Let us now introduce a stream-function Ψ defined through

$$\Psi_y = \rho U \tag{II.8}$$

$$\Psi_x = -\rho V \tag{II.9}$$

Now, equation (II.7) indicates that ζ/ρ must be a function of

Downloaded 02 May 2010 to 171.66.16.25. Redistribution subject to ASME license or copyright; see http://www.asme.org/terms/Terms_Use.cfm

Ψ alone since it is constant along a streamline; thus, we can write

$$\zeta/\rho = g(\Psi) \tag{II.10}$$

Far upstream, the stream-function Ψ is known explicitly as a function of y, and hence, conversely; the right side in equation (*II*.10) can therefore be obtained by inserting this inversion for y into $U_m'(y)/\rho_m(y)$. For convenience, it is necessary to introduce the integral

$$G(\Psi) = \int^{\Psi} g(\xi)\, d\xi \tag{II.11}$$

defined to within an arbitrary constant. The definition $U_y - V_x = \zeta$, that is, $(\Psi_y/\rho)_y + (\Psi_x/\rho)_x = \rho g(\Psi)$, then leads to

$$\Psi_{xx} + \Psi_{yy} - \Psi_y \frac{\rho_y}{\rho} - \Psi_x \frac{\rho_x}{\rho} = \rho^2 g(\Psi) \tag{II.12}$$

However, as will be seen from Bernoulli's integral in the following, we have

$$\frac{\rho_x}{\rho} = \frac{\rho^2 g \Psi_x - \Psi_x \Psi_{xx} - \Psi_y \Psi_{xy}}{\tilde{c}\gamma\rho^{\gamma+1} - \Psi_x^2 - \Psi_y^2} \tag{II.13}$$

$$\frac{\rho_y}{\rho} = \frac{\rho^2 g \Psi_y - \Psi_y \Psi_{yy} - \Psi_x \Psi_{xy}}{\tilde{c}\gamma\rho^{\gamma+1} - \Psi_x^2 - \Psi_y^2} \tag{II.14}$$

showing that

$$\Psi_{xx} + \Psi_{yy} + \frac{2\Psi_x \Psi_y \Psi_{xy} + \Psi_x^2 \Psi_{xx} + \Psi_y^2 \Psi_{yy} - \rho^2 g(\Psi)(\Psi_x^2 + \Psi_y^2)}{\tilde{c}\gamma\rho^{\gamma+1} - \Psi_x^2 - \Psi_y^2}$$

$$= \rho^2 g(\Psi) \tag{II.15}$$

From equations (*II*.1) and (*II*.2), it is possible to show that the quantity $\frac{1}{2}(U^2 + V^2) + \tilde{c}\gamma\rho^{\gamma-1}/(\gamma-1) - G(\Psi)$ is a "true constant" fixed throughout the entire flowfield, C_0 say, so that

$$\frac{1}{2\rho^2}(\Psi_x^2 + \Psi_y^2) + \frac{\tilde{c}\gamma}{\gamma-1}\rho^{\gamma-1} - G(\Psi) = C_0 \tag{II.16}$$

Equations (*II*.15) and (*II*.16) provide the required explicit stream-function and Bernoulli equations applicable to planar compressible shear flows; equation (*II*.15) also takes the alternative form

$$\Psi_{xx} + \Psi_{yy} + \frac{2\Psi_x \Psi_y \Psi_{xy} + \Psi_x^2 \Psi_{xx} + \Psi_y^2 \Psi_{yy} - \rho^2 g(\Psi)(\Psi_x^2 + \Psi_y^2)}{(\gamma-1)\rho^2(G + C_0) - \frac{\gamma+1}{2}(\Psi_x^2 + \Psi_y^2)}$$

$$= \rho^2 g(\Psi) \tag{II.17}$$

Although our results apply subsonically and supersonically, application to mixed transonic flows is still tentative; presumably, an extension of Hafez's [10] numerical procedure solving the well-known root problem (corresponding to the existence of two velocities, one subsonic and the other supersonic, given a streamwise mass flux) would render equations (*II*.15)–(*II*.17) amenable to "direct inverse algorithms," as described in reference [4], and compressible superpotentials could be available numerically in principle for analysis problems.

Downloaded 02 May 2010 to 171.66.16.25. Redistribution subject to ASME license or copyright; see http://www.asme.org/terms/Terms_Use.cfm

R.-J. Yang

M. Holt

Department of Mechanical Engineering,
University of California,
Berkeley, Calif. 94720

Boundary Layer Control by Means of Strong Injection

The gas mixture produced by coal gasifier contains components that have serious corrosive effects on the walls of the pipe flow system. To reduce these, a non-corrosive gas is injected into the stream of the coal gas products, in a direction parallel to the pipe wall. The interaction between the injected stream and the original pipe flow is investigated analytically and is an example of the so-called Wall Jet Problem.

1 Introduction

The current interest in energy conversion technology has focused attention on the production of synthetic natural gas from coal. Gas mixtures, in a coal gasification process, contain hydrogen, carbon dioxide, carbon monoxide, steam, and hydrogen sulfide. Of these, hydrogen sulfide can cause very serious pipe corrosion. Furthermore, solid particles contained in the gas stream may be projected against a pipe wall causing erosion. To protect the pipe wall from attack by corrosive gas and damaging particles, an attempt is made to inject a noncorrosive fluid, at the pipe entry, to form a thin layer on the inner pipe wall. Thus the corrosive gas and solid particles can be "washed away" or "blown off" the wall for a time.

Mass injection into a turbulent boundary layer by tangential injection has been studied for many years. In the past decade, the practical applications of this technique include reduction of skin friction on an airfoil, prevention of boundary layer separation over a surface subject to adverse pressure gradient, and protection of surface exposed to high-temperature environment encountered in combustion chambers, gas turbines, rocket nozzles, and high-speed flight vehicles. Recent works on this subject can be found in LaRue and Libby [1], [2], Cary, Bushnell, and Hefner [3], and Brune [4]. The flow condition at the initial stage considered by those authors is the confluent turbulent boundary layer forming when a turbulent flow above a splitter plate mixes with a fully developed turbulent channel flow beneath it.

In this work, we choose a simplified model shown in Fig. 1. The first stream is assumed to be hydrogen sulfide, H_2S, the most corrosive component in the gas mixture from a coal gasifier. The second stream is the injected fluid, for example, steam. Both streams are assumed to be of uniform density and flow at constant low speeds. The flow is isothermal, two-dimensional, and the boundary layer effects on both sides of the splitter plate can be neglected. In other words, a model that is a two-dimensional incompressible turbulent free mixing layer in the presence of a wall is used in this analysis.

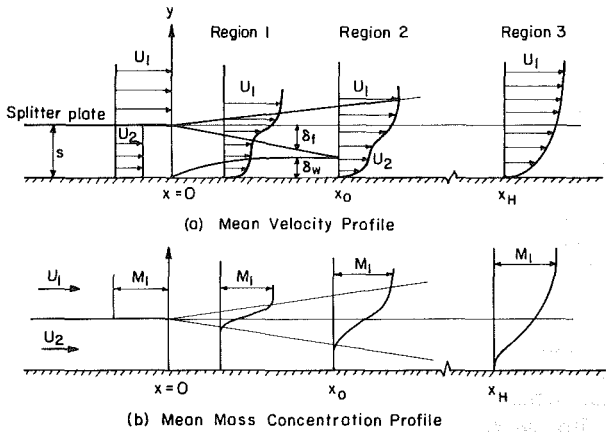

Fig. 1 Illustration of velocity and concentration profiles for a tangential injection flow field

A flow of this type involves the interaction of a free mixing layer and a wall boundary layer. Three zones can be physically perceived. First, at the end of the splitter plate the upper and lower streams begin to mix; in the meantime, a wall boundary layer is developing along the wall. Also, before the two layers merge, an embedded potential core exists in between. Recently, Pot [5] conducted an experiment to observe the phenomena of the interaction between a turbulent wake and a turbulent wall layer. He found that the wake and the wall layer develop independently before the two layers merge. Therefore, in the present work, we assume that the free mixing layer and the wall layer are not to be influenced by each other in the first region. Second, just downstream of the position where these two layers merge, there is a domain within which the two viscous regions interact. Thus the mixing layer gradually dissolves into a new boundary layer type flow. Third, far downstream from the origin of mixing, the stream mixing has been completed. In this zone the flow can be treated in terms of conventional turbulent boundary layer theory.

The purpose of this work is to find the location where the concentration of the first stream diffuses to the wall. The species equation is decoupled from the momentum equation as a result of the assumption made, in which both streams are regarded as incompressible fluids with the same density, and

Contributed by the Applied Mechanics Division for publication in the JOURNAL OF APPLIED MECHANICS.

Discussion on this paper should be addressed to the Editorial Department, ASME, United Engineering Center, 345 East 47th Street, New York, N.Y. 10017, and will be accepted until two months after final publication of the paper itself in the JOURNAL OF APPLIED MECHANICS. Manuscript received by ASME Applied Mechanics Division, October 1983; final revision, June, 1983.

Copyright © 1984 by ASME
Downloaded 02 May 2010 to 171.66.16.25. Redistribution subject to ASME license or copyright; see http://www.asme.org/terms/Terms_Use.cfm

are isothermal. Thus, the species equation can be solved separately after the momentum equation is solved.

The Method of Integral Relations (MIR), introduced by Dorodnitsyn [6] provides a simple and accurate means of solving laminar boundary layer flows. No approximations are made to the equations. Approximations are made in representing unknown integrands appearing in the basic integral relations. In two-dimensional boundary layer flows, the approximation is based on the representation of the streamwise velocity gradient in the transverse direction as a simple algebraic function of the streamwise velocity itself. Such a representation should reflect the physical character of the flow. If polynomials are used, the order of the approximation depends on the degree of the polynomials. In principle this can be as high as desired, but in practice the order of approximation is limited by the inversion of the resulting matrix, which becomes progressively more ill conditioned, and the amount of algebra required. However, these disadvantages have been largely overcome in the orthonormal version of MIR (Fletcher and Holt, [7]). This version has been applied to a number of internal flow problems connected with coal gasification, including control of laminar boundary layer pipe flow through strong injection, using both parallel and normal modes (Yeung and Holt [8]). Orthonormal MIR was extended to apply to turbulent boundary layers by Yeung and Yang [9] and tested successfully for a number of model flows. It is well suited to treat the highly inflected velocity profiles arising in such layers and is the method adopted in the present investigation.

Parallel injection was treated numerically by several earlier authors, notably by Miner and Lewis, using finite difference methods. The present investigation differs from those made earlier not only in terms of the method used but also in terms of the initial and boundary conditions imposed. In most earlier papers either the injectant entered the main stream as a fully developed pipe flow or the main stream flow was already an established turbulent boundary layer. In the present investigation both the main stream and injectant are initially parallel inviscid flows, simulating conditions at the entry of a heat exchange system.

This paper is divided into two main parts. The first discusses the numerical solution of the turbulent free mixing layer. Here MIR shows its advantage in that the approach yields a unique solution and this is independent of the third boundary condition (Ting [10]). Comparisons between the numerical results and experimental data are also made. The second part discusses the numerical solution of the interaction between the turbulent wall layer and the turbulent free mixing layer. The location where the mass concentration of H_2S diffuses to the wall surface is found and some interesting physical phenomena are cited.

2 Analysis of the Turbulent-Free Mixing Layer

2.1 Introduction. The characteristics of a turbulent mixing layer initiated by the confluence of two parallel streams has been of interest for many years because of its broad applications in technology. Early studies of this subject were made by Tollmein [11], Kuethe [12], and Görtler [13]. These classical solutions of the problem are based on the assumptions that the change of velocity from that of one stream to the other takes place in a mixing region of small thickness compared to the length of mixing in the streamwise direction and that the normal component of the velocity, v, is small compared to the component of velocity parallel to the main stream, u. Moreover, all of the solutions except that of Kuethe are based on an arbitrary third boundary condition (Ting, [10]).

Within the framework of boundary layer theory, the solution is unique for a flow over a plate by specifying three

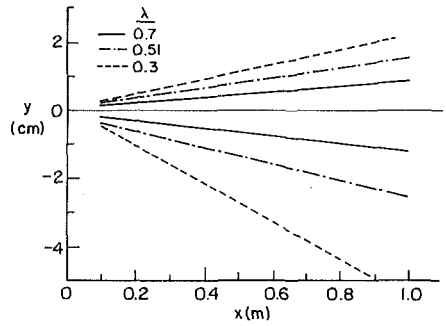

Fig. 2 Lines of constant velocity in the mixing region

conditions, namely at $y=0$ (i.e., on the plate surface) $u=v=0$, and at $y\to\infty$, $u\to u_\infty$ (∞ denotes free stream condition). However, the solution is nonunique for the mixing problem since only two conditions are available, namely $u\to U_1$ as $y\to\infty$, and $u\to U_2$ as $y\to-\infty$. The absence of a third boundary condition admits an infinite number of solutions to the mixing problem. Mathematically, if $g(y)$ is a solution satisfying the boundary conditions at $y=\pm\infty$, so is $g(y+c)$, where c is any constant. It is known that to compare this solution with experimental data, the theoretical distribution of axial velocity must be shifted in the transverse direction, so as to obtain a better agreement with experimental data.

Tollmien [11] obtained an analytical solution for the mean velocity profile of a mixing layer with the lower stream at rest (i.e., $U_2=0$) by applying Prandtl's mixing length hypothesis for the turbulent shear stress. He fixed his solution by making the transverse velocity v_1 vanish at the outer edge $y\to\infty$. Kuethe [12] extended Tollmien's approach to the case of two nonzero velocity streams, using von Karman's suggestion that the third boundary condition should correspond to no external forces acting on the total fluid system perpendicular to the main flow, i.e., $U_1v_1+U_2v_2=0$. However, the proof is not convincing. Later, Görtler [13] solved the same problem as Kuethe by using Prandtl's second hypothesis for the turbulent shear stress (i.e., the constant eddy viscosity hypothesis). He avoided the question of the third boundary condition. Instead, he fixed his solution by saying that the mean speed $(U_1+U_2)/2$ of the stream is along the line $y=0$. In addition, he introduced an empirical constant related to the rate of spread of the mixing layer and to the free-stream velocity ratio. Mills [14] noticed that the governing equations for the mixing problem, written in terms of Crocco variables, no longer contain the variable v, for which the boundary condition is not sufficient, and hence the problem has a unique solution. The unique solution is independent of the form of the third boundary condition.

The Method of Integral Relations (MIR) originally developed by Dorodnitsyn [6], and later modified by Fletcher and Holt [7], has been applied successfully by Yeung and Yang [9] to calculate the two-dimensional incompressible turbulent boundary layer. In this section, we discuss the application of MIR to the turbulent plane mixing problem. Similar to Mills' formulation, MIR renders the governing equations for mixing problems in a form containing no v by judiciously selecting a set of weighting functions. Thus, a unique solution exists and is independent of the third boundary condition. Unlike Mills' method which needs successive approximation, after using a transformation to weaken the singularity at the outer edges of the mixing layer, the present method overcomes the singularity by appropriate weighting functions.

2.2 Formation. It was observed by Brown and Roshko [15] that density effects on the spreading angle of turbulent plane mixing between two streams of different gases were relatively small; the strong effects were due to com-

Downloaded 02 May 2010 to 171.66.16.25. Redistribution subject to ASME license or copyright; see http://www.asme.org/terms/Terms_Use.cfm

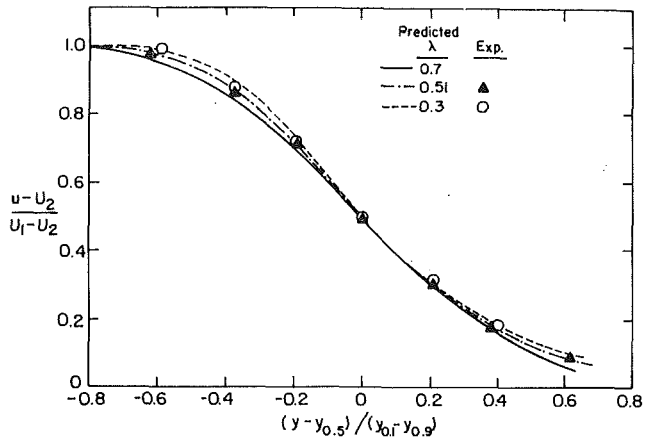

Fig. 3 Velocity distribution in the mixing region

pressibility. Thus a turbulent mixing of two semi-infinite streams of a homogeneous incompressible fluid, shed from a splitter plate, is assumed for the present study. It is well known that the contribution of molecular transport in all equations governing a fully developed free turbulent mixing of two streams at larger Reynolds number can be neglected. With this information the usual time-averaging techniques and assumptions associated with the boundary layer approximation of the mixing process lead, for two-dimensional, isobaric, steady flow, to the equations:

$$\frac{\partial u}{\partial x}+\frac{\partial v}{\partial y}=0, \tag{2.1}$$

$$u\frac{\partial u}{\partial x}+v\frac{\partial u}{\partial y}=\frac{\partial}{\partial y}\left(\nu_t\frac{\partial u}{\partial y}\right), \tag{2.2}$$

$$u\frac{\partial m}{\partial x}+v\frac{\partial m}{\partial y}=\frac{\partial}{\partial y}\left(D_t\frac{\partial m}{\partial y}\right), \tag{2.3}$$

where u and v are the mean velocity components in the x and y directions, respectively; the origin is taken as the point at which mixing begins; m is the mean mass concentration of the upper stream, and ν_t and D_t are defined, in analogy with molecular diffusion, as

$$-\overline{u'v'}=\nu_t\partial u/\partial y, \tag{2.4}$$

$$-\overline{m'v'}=D_t\partial m/\partial y, \tag{2.5}$$

where u', v', and m' are fluctuating quantities. The coefficients ν_t and D_t need empirical relations which will be discussed later. The boundary conditions for equations (2.1)-(2.3) are

$$y\to\infty,\ u\to U_1,\ m\to M_1,$$

$$y\to-\infty,\ u\to U_2,\ m\to 0.$$

It is convenient to work with the following nondimensional variables:

$$U=(u-U_2)/(U_1-U_2),\ \lambda=U_2/U_1,$$

$$V=(v-U_2)/(U_1-U_2),\ M=m/M_1. \tag{2.6}$$

Using (2.6), the governing equations (2.1)-(2.3) and the responding boundary conditions become

$$\frac{\partial U}{\partial x}+\frac{\partial V}{\partial y}=0, \tag{2.7}$$

$$\left(U+\frac{\lambda}{1-\lambda}\right)\frac{\partial U}{\partial x}+\left(V+\frac{\lambda}{1-\lambda}\right)\frac{\partial U}{\partial y}=\frac{1}{U_1-U_2}\frac{\partial}{\partial y}\left(\nu_t\frac{\partial U}{\partial y}\right), \tag{2.8}$$

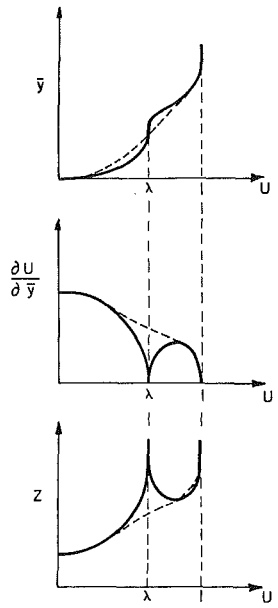

Fig. 4 Velocity and Z profiles at x_0

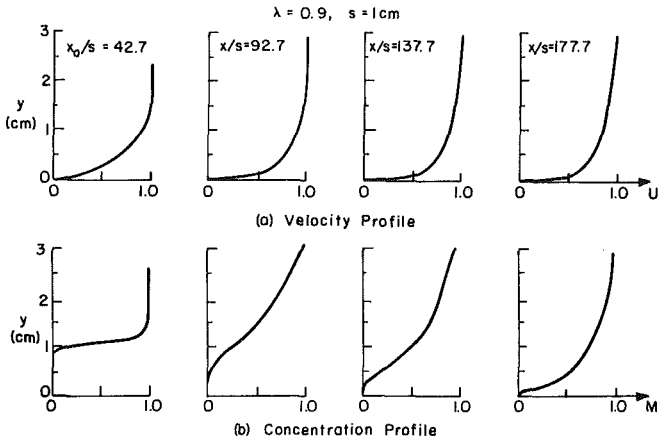

Fig. 5 The development of velocity profile and concentration profile in the streamwise direction

$$\left(U+\frac{\lambda}{1-\lambda}\right)\frac{\partial M}{\partial x}+\left(V+\frac{\lambda}{1-\lambda}\right)\frac{\partial M}{\partial y}=\frac{1}{U_1-U_2}\frac{\partial}{\partial y}\left(D_t\frac{\partial M}{\partial y}\right), \tag{2.9}$$

$$y\to\infty,\ U\to 1,\ M\to 1,$$

$$y\to-\infty,\ U\to 0,\ M\to 0. \tag{2.10}$$

Using the assumptions $\nu_t=D_t$ and M is a function of U only, one can easily show that $M=U$ from equations (2.8)-(2.10). Although the spread of species concentration is not the same as that of momentum in the turbulent mixing problem, the preceding assumptions are not bad for the short distance in which we are interested along the streamwise direction. This is because the boundary layer thickness grows linearly with respect to x, as is well known in the literature (see for example, Townsend, [16]). Therefore, once the velocity profile has been determined, the species concentration profile can also be obtained through $M=U$.

Let $\{f_i(U)\}$ be a set of linearly independent functions that satisfy $f_i(0)=f_i(1)=0$, where $i=1,2,\ldots,N$, and N denotes the order of approximation. Multiply equation (2.7) by f_i and equation (2.8) by f_i', defined as the first derivative of f_i with respect to U, add and integrate from $y\to-\infty$ to $y\to\infty$:

Downloaded 02 May 2010 to 171.66.16.25. Redistribution subject to ASME license or copyright; see http://www.asme.org/terms/Terms_Use.cfm

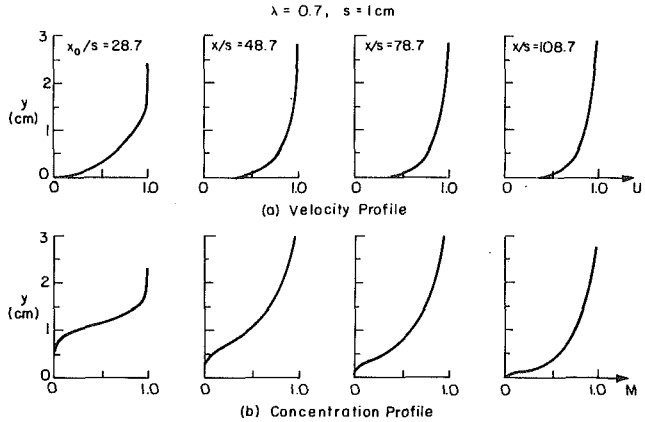

Fig. 6 The development of velocity profile and concentration profile in the streamwise direction

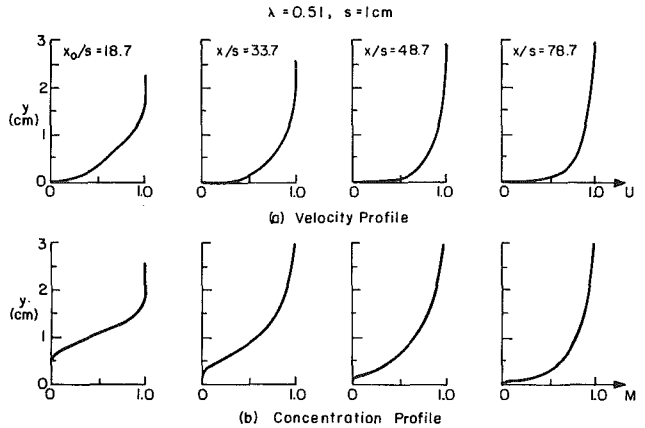

Fig. 7 The development of velocity profile and concentration profile in the streamwise direction

$$\frac{\partial}{\partial x}\int_{-\infty}^{\infty} f_i\left(U+\frac{\lambda}{1-\lambda}\right)dy = \frac{-1}{U_1-U_2}\int_{-\infty}^{\infty} \nu_t f_i''\left(\frac{\partial U}{\partial y}\right)^2 dy. \tag{2.11}$$

Change the variable of integration from y to U and define Z as

$$Z=\left(\frac{\partial U}{\partial y}\right)^{-1}.$$

Then, equation (2.11) can be written as

$$\frac{\partial}{\partial x}\int_0^1 f_i\left(U+\frac{\lambda}{1-\lambda}\right)ZdU = \frac{-1}{U_1-U_2}\int_0^1 \nu_t f_i''\frac{1}{Z}dU. \tag{2.12}$$

Notice the preceding equation is exact since we have not made any assumption for V at $y=\pm\infty$. V is cancelled through $f_i(0)=f_i(1)=0$. Since V no longer appears in the present formulation, the traditional third boundary condition for the mixing problem does not exist.

Z has a singularity of the following type:

$$Z\sim\frac{1}{U(1-U)}$$

due to the behavior of velocity profile at both edges of the mixing layer, i.e., $1/Z$ approaches zero as $U\to 0$ and $U\to 1$. To make the integral on the right-hand side of equation (2.12) finite, the functions f_i are chosen as $U^k(1-U)^k$ or the combination of $U^k(1-U)^k$, $k=1,2,\ldots$. This is consistent

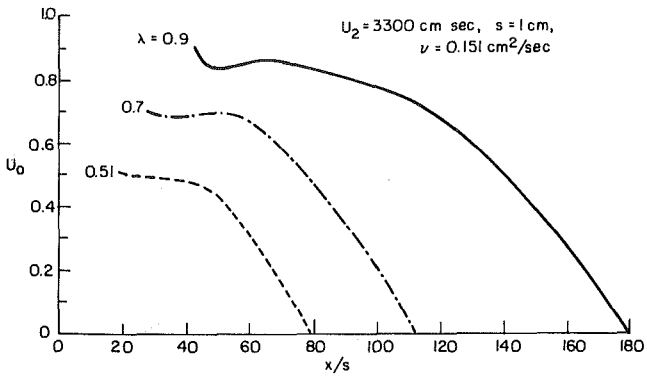

Fig. 8 Distribution of U_0

with the conditions that we imposed on f_i before, i.e., $f_i(0)=f_i(1)=0$.

To apply the orthonormal version of MIR, we represent

$$Z\left(U+\frac{\lambda}{1-\lambda}\right)=\frac{a_0+\sum_{j=1}^{N-1}a_j f_j}{U(1-U)}, \tag{2.13}$$

where $a_0,a_1,\ldots,a_{N-1}$ are unknown coefficients to be found, and $\{f_i\}$ is a set of orthonormal functions constructed from $U^k(1-U)^k$ by the Gram-Schmidt procedure (Isaacson and Keller, [17]). Hence:

$$f_i(U)=\sum_{k=1}^{i} d_{ik}U^k(1-U)^k$$

and

$$\int_0^1 f_i f_j\frac{dU}{U(1-U)}=\delta_{ij}. \tag{2.14}$$

with δ_{ij} being the Kronecker delta. Substituting equation (2.13) into equation (2.12) and invoking equation (2.14), we obtain an explicit set of ordinary differential equations in the coefficients $a_0,a_1,\ldots,a_{N-1}$:

$$\frac{da_0}{dx}\int_0^1\frac{f_i}{U(1-U)}dU+\frac{da_i}{dx}=\frac{-1}{U_1-U_2}\int_0^1\nu_t f_i''\frac{dU}{Z}, \quad i=1,2,\ldots,N-1 \tag{2.15}$$

and

$$\frac{da_0}{dx}\int_0^1\frac{f_N}{U(1-U)}dU=\frac{-1}{U_1-U_2}\int_0^1\nu_t f_N''\frac{dU}{Z}, \tag{2.16}$$

which can be integrated subject to appropriate initial conditions at some station $x=x_i$. We will discuss the initial conditions later.

2.2.1 Turbulence Modeling. Prandtl [18] proposed a model, equation (2.4), which is analogous to the Newtonian law of friction in laminar flow. He assumed that the coefficient of turbulent viscosity, ν_t, is constant over a cross section of the free mixing layer. He obtained

$$\nu_t=\kappa\delta(U_1-U_2), \tag{2.17}$$

where δ is the width of the mixing zone; κ is an empirical constant, which is equal to 0.0044. In terms of the present variables Z and U, equation (2.17) becomes

$$\nu_t=\kappa(U_1-U_2)\int_0^1 ZdU. \tag{2.18}$$

It is clear that ν_t is a function of x only.

2.2.2 Location of the Dividing Streamline. Using equations (2.1) and (2.2), and noting that the transverse velocity component v is zero while the tangential shear stress is continuous along the dividing streamline, one can obtain:

$$\int_0^{\infty}u(U_1-u)dy+\int_{-\infty}^{0}u(U_2-u)dy=0.$$

Downloaded 02 May 2010 to 171.66.16.25. Redistribution subject to ASME license or copyright; see http://www.asme.org/terms/Terms_Use.cfm

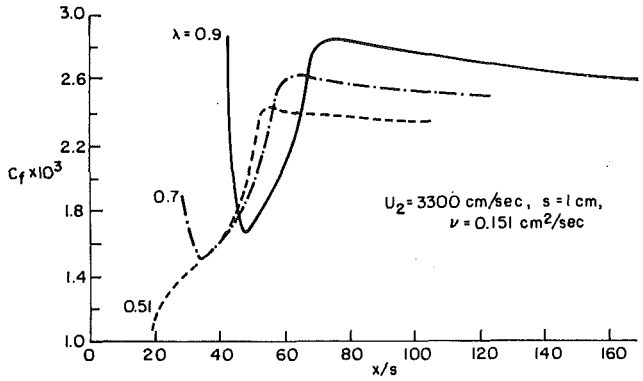

Fig. 9 Skin friction coefficient

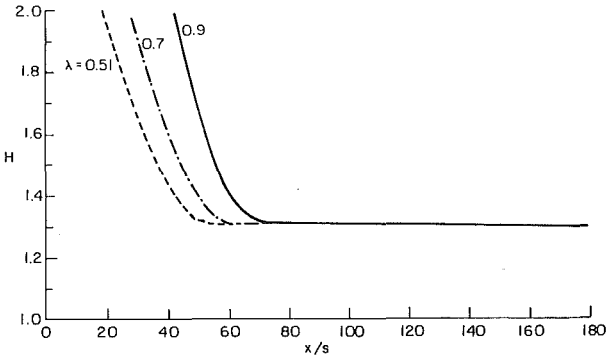

Fig. 10 Shape factor

Here the dividing streamline is chosen as the x-axis passing through the origin. Denote U_d as the dimensionless velocity component along the x-axis and use the present variables U and Z. Then the foregoing relation becomes:

$$\int_{U_d}^{1} UZdU + \frac{\lambda}{1-\lambda}\int_{U_d}^{1} ZdU = \int_{0}^{1} U^2 ZdU + \frac{\lambda}{1-\lambda}\int_{0}^{1} UZdU. \tag{2.19}$$

An iteration procedure has to be used to obtain U_d which is a function of x. Once U_d is found, the location y can be calculated from the following relation

$$y = \int_{U_d}^{U} ZdU. \tag{2.20}$$

2.2.3 Initial Conditions. Initial values of $\{a_0, a_1, \ldots, a_{N-1}\}$ at an initial station x_i, have to be specified in order to integrate the system of ordinary differential equations (2.15) and (2.16). It may be deduced from the momentum equation that a turbulent mixing layer between two constant velocity incompressible free streams can be self-preserving (see for example, Townsend, [16]). Thus, the initial condition can be selected fairly arbitrarily, say from experimental data or from the approximate analytical solutions, provided that they do not contradict boundary conditions at $y = \pm\infty$ when the self-preserving solution is of interest.

Görtler's solution gives a good approximation to the shape of the observed mean velocity profile, although it has to be shifted bodily in the transverse direction in order to fit the experimental data. However, this shift is independent of the slope, $\partial U/\partial y$, of the mean velocity profile for a given U value. Here Görtler's solution is illustrated to obtain the necessary conditions. Görtler's solution gives

$$U = \tfrac{1}{2}\left(1 + \frac{2}{\sqrt{\pi}}\int_0^{\xi} e^{-q^2} dq\right), \quad \xi = \sigma y/x, \tag{2.21}$$

where σ is a constant which has the following empirical relation (Birch and Eggers, [19]):

$$\sigma = \frac{\sigma_0(1+\lambda)}{1-\lambda}, \quad \sigma_0 = 11.$$

Thus, the slope of U gives

$$\frac{1}{Z} = \frac{\partial U}{\partial y} = \frac{1}{\sqrt{\pi}}\frac{\sigma}{x} e^{-\xi^2}. \tag{2.22}$$

Comparing equations (2.13) and (2.22), and invoking equation (2.21), we obtain N coupled algebraic equations in N unknowns, $a_0, a_1, \ldots, a_{N-1}$. Thus, solution for the N unknowns can be found, for example, by an iteration procedure.

2.3 Results and Discussion. With λ being a parameter, several cases were tested using the fourth approximation ($N=4$) and results are shown in Figs. 7 and 8. A recent review on the experimental data of turbulent plane mixing layer has been completed by Rodi [20]. Experimental data were marked on the same figures whenever appropriate. Figure 7 shows that the mixing layer penetrates more into the lower-speed stream than it does into the higher-speed stream. This is due to the continual deceleration of the fluid on the higher-speed side of the mixing layer and the acceleration of the fluid on the lower-speed side, which results in a slight deflection of the steramlines toward the lower-speed stream. In addition, lines of constant velocity ratio show the linear dependence on distance in the streamwise direction. This can also be seen from similarity analysis and is confirmed by all experimental data.

A comparison of the mean velocity distribution at the different longitudinal positions shows that the mixing layers have a region in which geometric similarity exists and in this region the mixing layer is self-preserving. Figure 8 shows the U profiles against $y^* = (y - y_{0.5})/(y_{0.1} - y_{0.9})$, where $y_{0.5}$ refers to the value of y at $U = 0.5$, others likewise. The agreement between the theoretical and experimental results is seen to be quite good. We observe that there is almost no change in the shape of the mean velocity profile with respect to the velocity ratio except at the edge of low U. This change in shape is also observed in experiments. In addition, it was shown from numerical experiments that U profiles against y^* do not depend on κ, the empirical constant for turbulent viscosity ν_t. Thus, the numerical values of κ can be selected arbitrarily if one wants to find the self-preserving solution of the problem.

3 Analysis of the Interaction Between the Free Mixing Layer and the Wall Layer

3.1 Formulation. The turbulent-free mixing layer merges with the turbulent wall layer at $x = x_0$ (see Fig. 1) and the interaction between these two layers then begins. The velocity distribution at, and the location of, station x_0 can be obtainbed from Section 2 by the assumption that the free mixing layer and the wall layer develop independently in the x-direction and the velocity distribution of the merged flow at x_0 is simply the linear superposition of the mean velocity profiles of the two layers. The justification for this assumption is presented in Pot [5]. We assume that the boundary layer approximations still apply to the merged flow. Therefore, the problem to be considered here may be formulated as follows: At a given station $x = x_0$, the velocity profile is known; determine the downstream development of the boundary layer with this initial profile.

The governing equations for the mean quantities of the merged flow, which is still assumed to be two-dimensional, isobaric, and incompressible, are:

$$\frac{\partial u}{\partial x} + \frac{\partial v}{\partial y} = 0, \tag{3.1}$$

Downloaded 02 May 2010 to 171.66.16.25. Redistribution subject to ASME license or copyright; see http://www.asme.org/terms/Terms_Use.cfm

$$u\frac{\partial u}{\partial x}+v\frac{\partial u}{\partial y}=\frac{\partial}{\partial y}\left[\left(\nu+\frac{\epsilon}{\rho}\right)\frac{\partial u}{\partial y}\right], \tag{3.2}$$

$$u\frac{\partial m}{\partial x}+v\frac{\partial m}{\partial y}=\frac{\partial}{\partial y}\left[(D+D_t)\frac{\partial m}{\partial y}\right], \tag{3.3}$$

where u and v are the mean velocity components in the x and y directions, respectively; m is the mean mass concentration of the upper stream; ρ is the density, ν is the kinematic viscosity, and D is the coefficient of mass diffusivity of merged fluid flow. The quantities ϵ/ρ and D_t are defined as

$$\nu_t=\epsilon/\rho=-\overline{u'v'}/\frac{\partial u}{\partial y}, \tag{3.4}$$

$$D_t=-\overline{m'v'}/\frac{\partial m}{\partial y}, \tag{3.5}$$

where u', v' and m' are fluctuating quantities. The modeling for ϵ/ρ and D_t will be discussed later. The boundary conditions are

$$y\to 0,\ u=0,\ v=0,\ \partial m/\partial y=0,$$
$$y\to\infty,\ u\to U_1,\ m\to M_1,$$

where the subscript 1 denotes the free stream condition which is constant. Introduce the following nondimensional variables:

$$U=\frac{u}{U_1},\ V=\frac{vRe^{1/2}}{U_1},\ \bar{x}=\frac{x}{L},$$
$$\bar{y}=\frac{yRe^{1/2}}{L},\ M=\frac{m}{M_1},\ Re=\frac{U_1L}{\nu}. \tag{3.6}$$

Here L is a reference length. Using equation (3.6), the governing equations and the corresponding boundary conditions become:

$$\frac{\partial U}{\partial\bar{x}}+\frac{\partial V}{\partial\bar{y}}=0, \tag{3.7}$$

$$U\frac{\partial U}{\partial\bar{x}}+V\frac{\partial U}{\partial\bar{y}}=\frac{\partial}{\partial\bar{y}}\left[\left(1+\frac{\epsilon}{\rho}\right)\frac{\partial U}{\partial\bar{y}}\right], \tag{3.8}$$

$$U\frac{\partial M}{\partial\bar{x}}+V\frac{\partial M}{\partial\bar{y}}=\frac{\partial}{\partial\bar{y}}\left[\left(\frac{D}{\nu}+\frac{D_t}{\nu_t}\frac{\epsilon}{\mu}\right)\frac{\partial M}{\partial\bar{y}}\right], \tag{3.9}$$

$$\bar{y}=0,\ U=V=0,\ \partial M/\partial\bar{y}=0,$$
$$\bar{y}\to\infty,\ U\to 1,\ M\to 1. \tag{3.10}$$

Notice that the species equation is decoupled from the momentum equation. Therefore, the species equation can be solved separately after the momentum equation. To solve the momentum equation by means of MIR, we have the following basic integral relation:

$$\frac{\partial}{\partial\bar{x}}\int_0^1 f_iUZdU=-\frac{f_i'(0)}{Z_0}-\int_0^1\left(1+\frac{\epsilon}{\mu}\right)\frac{f_i''}{Z}dU, \tag{3.11}$$

where the weighting functions

$$f_i(U)=\sum_{k=1}^{i}c_{ik}(1-U)^k \tag{3.12}$$

are orthonormal, satisfying the relations

$$\int_0^1 f_kf_j\frac{U}{1-U}dU=\delta_{kj} \tag{3.13}$$

where δ_{kj} is the Kronecker delta. In addition

$$Z=(\partial U/\partial\bar{y})^{-1}. \tag{3.14}$$

We also assume M is a function of U only. Multiplying equations (3.7)–(3.9) by f_iM, $f_i'M$, and f_i, respectively, adding, and then integrating the result across the boundary layer with respect to $\bar{y}$, and introducing the variable Z, we get the basic integral relation for the mass concentration which reads

$$\frac{\partial}{\partial\bar{x}}\int_0^1 f_iUMZdU=-\frac{M_0f_i'(0)}{Z_0}$$
$$-\int_0^1\left[1+\frac{D}{\nu}+\left(1+\frac{D_t}{\nu_t}\right)\frac{\epsilon}{\mu}\right]\frac{f_i'}{Z}\frac{dM}{dU}dU$$
$$-\int_0^1\left(1+\frac{\epsilon}{\mu}\right)M\frac{f_i''}{Z}dU. \tag{3.15}$$

Equation (3.15) can be further simplified by noting that for $U<U_0$, where U_0 is the streamwise velocity component at the lower edge of the concentration boundary layer, M is equal to zero. Thus, before the concentration of the first stream diffuses to the wall surface equation (3.15) is reduced to

$$\frac{\partial}{\partial\bar{x}}\int_{U_0}^1 f_iUMZdU=-\int_{U_0}^1\left[1+\frac{D}{\nu}+\left(1+\frac{D_t}{\nu_t}\right)\frac{\epsilon}{\mu}\right]$$
$$\frac{f_i'}{Z}\frac{dM}{dU}dU-\int_{U_0}^1\left(1+\frac{\epsilon}{\mu}\right)M\frac{f_i''}{Z}dU. \tag{3.16}$$

Notice that U_0 is a function of x, it is equal to U_2/U_1 at $x=x_0$ where the free mixing layer merges with the wall layer and equal to zero at the wall surface, where the concentration of the upper stream diffuses.

The interpolating function for Z is chosen as

$$Z=\frac{b_0+\sum_{j=1}^{N+1}b_jf_j(U)}{1-U}. \tag{3.17}$$

The interpolating function for M is chosen to satisfy its physical boundary conditions, namely at $U=1$, $M=1$; and at $U=U_0$, $\partial M/\partial\bar{y}=0$, $M=0$. To the first approximation,

$$M=\left(\frac{U-U_0}{1-U_0}\right)^2. \tag{3.18}$$

Substituting expressions of Z, f_i, and M in equations (3.11) and (3.16), we obtain a system of ordinary differential equations:

$$\frac{db_0}{d\bar{x}}\int_0^1\frac{f_iU}{1-U}dU+\frac{db_i}{d\bar{x}}=-\frac{f_i'(0)}{Z_0}-\int_0^1\left(1+\frac{\epsilon}{\mu}\right)\frac{f_i''}{Z}dU,$$
$$i=1,2,\ldots,N-1, \tag{3.19}$$

$$\frac{db_0}{d\bar{x}}\int_0^1\frac{f_NU}{1-U}dU=-\frac{f_N'(0)}{Z_0}-\int_0^1\left(1+\frac{\epsilon}{\mu}\right)\frac{f_N''}{Z}dU,$$

and

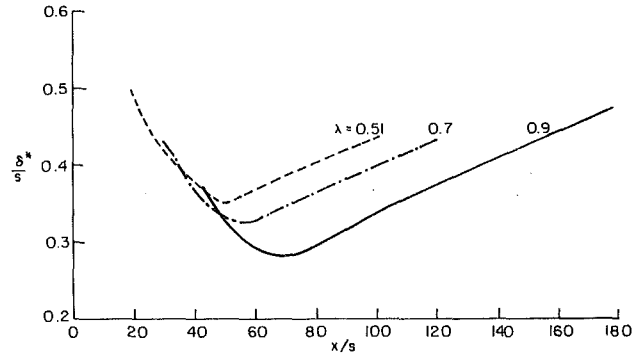

Fig. 11 Displacement thickness

Downloaded 02 May 2010 to 171.66.16.25. Redistribution subject to ASME license or copyright; see http://www.asme.org/terms/Terms_Use.cfm

$$A_1\frac{dU_0}{d\bar{x}}+A_2\frac{db_0}{d\bar{x}}+A_3\frac{db_1}{d\bar{x}}+\ldots+A_{N+1}\frac{db_{N-1}}{d\bar{x}}$$

$$=-\int_{U_0}^{1}\left[1+\frac{D}{\nu}+\left(1+\frac{D_t}{\nu_t}\right)\frac{\epsilon}{\mu}\right]\frac{f_i'}{Z}\frac{dM}{dU}\,dU, \qquad (3.20)$$

where $A_1, A_2, \ldots, A_{N+1}$ are certain coefficients varying with N. For example, if we choose $N=3$ then

$$\begin{aligned}A_1 &= -b_0(1+U_0)/6+(3U_0^2-U_0-2)(b_1c_{11}+b_2c_{21})/30\\ &\quad -b_2c_{22}(1-3U_0^2+2U_0^3)/30,\\ A_2 &= (3-2U_0-U_0^2)/12,\\ A_3 &= c_{11}(3-4U_0-U_0^2+2U_0^3)/60\\ A_4 &= c_{11}(3-4U_0-U_0^2+2U_0^3)/60\\ &\quad +c_{22}(1-2U_0+2U_0^3-U_0^4)/60.\end{aligned}$$

Initial conditions for the system of the ordinary differential equations (3.19) and (3.20) are discussed later.

3.1.1 Turbulence Modeling. Pot [5] conducted an experiment to investigate the behavior of the interaction between a wake and a wall layer. He found that the flow was not that of a normal equilibrium boundary layer during the interaction process. However, many problems have been solved in the literature by employing the traditional Prandtl's mixing length concept and Van Driest-Clauser eddy viscosity model to predict the same type of flow (Cary, Bushnell, and Hefner [3]; Miner and Lewis [21]; Dvorak [22]; Kacker, Pai, and Whitelaw [23]). Reasonable results, in comparison with experimental data, were obtained.

The turbulence structure of the interaction between the free mixing layer and the wall layer is complex and so far little understood. Seban and Back [24] correlated the experimental data for the mean velocity profile in turbulent boundary layers with tangential injection. They found that the mean velocity distribution was in good correspondence with the law of the wall and the law of the wake if the initial boundary layer effects on the splitter plate at the slot were small. Hence we can confidently employ the models adopted in Yeung and Yang [9].

The magnitude of the turbulent mass diffusivity, D_t, is always of the same order of magnitude as the turbulent eddy viscosity, ν_t (Bradshaw [25], p. 233). Experimental values of the turbulent Schmidt number $S_{ct}=\nu_t/D_t$, for the wake-wall boundary layer flow were found to be 0.5 ± 0.2 (Kacker, Pai, and Whitelaw [23]). Since there is little justification for using a particular value or functional variation for S_{ct}, we take $S_{ct}=0.7$ and $\nu/D=1$ in the present investigation. The last integral in equation (4.16) now can be evaluated as

$$\int_{U_0}^{1}(\ldots)dU=\begin{cases}\displaystyle\int_{U_0}^{U_m}(\ldots)dU+\int_{U_m}^{1}(\ldots)dU & \text{if } U_m\geq U_0\\ \displaystyle\int_{U_0}^{1}(\ldots)dU & \text{if } U_m<U_0\end{cases}$$

where $(\ldots)$ represents symbolically the integrand, U_m is the value where the wall region meets the wake region, and is determined in Yeung and Yang [9].

3.1.2 Initial Conditions. The location x_0 is determined by $s=\delta_w+\delta_f$ (see Fig. 1). Based on the nature of parabolic partial differential equations and the assumption for the mean velocity distribution at x_0, only the initial conditions and boundary conditions in the free stream and the wall are required and the mean velocity profile of the merged flow coincides with that of the superposition of both free mixing layer and wall boundary layer at x_0, the necessary initial values for $\{b_0, b_1, \ldots, b_{N-1}\}$ can be obtained by the following method. We consider the mean velocity and Z distributions at x_0 as shown in Fig. 9. The singularity of Z within $0<U<1$ only exists at $x=x_0$ because the interaction between the free mixing layer and the wall layer causes a momentum change that will smooth the velocity profile, and hence the Z profile after x_0. Presumably, we may extrapolate the U and Z profiles as shown in the dashed line on the same figure, and therefore use the new profiles as initial conditions. This is possible because the estimate of the locations of the edges of the wall boundary layer and the free mixing layer is rough, say at $U=0.98$ for the wall layer and $U=0.1$ (note the definition of U for the mixing layer is different from that of the wall layer) for the lower edge of the free mixing layer. The method of obtaining initial values for $\{b_0, b_1, \ldots, b_{N-1}\}$ based on the new profile is the same as that described in Yeung and Yang [9]. The initial value for U_0 in equation (3.20) is simply equal to λ at $x=x_0$.

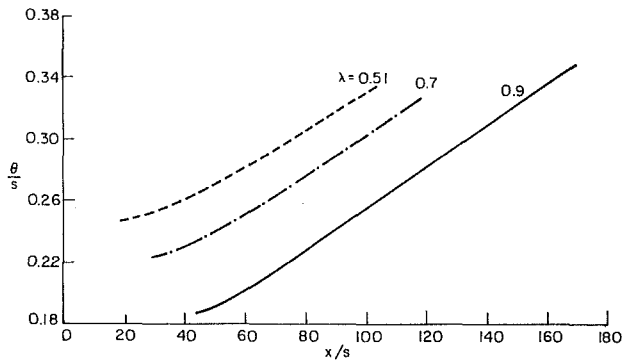

Fig. 12 Momentum thickness

3.2 Results and Discussion. In this section, theoretical predictions, based on the approximation $N=3$, for velocity profiles, skin friction coefficients, and concentration profiles are presented and discussed; representative integral properties are also presented. The calculations were carried out at three values of the velocity ratio U_2/U_1, namely 0.9, 0.7, and 0.51; and at one value of slot height, namely $s=1$ cm. The flow conditions of the injected mass are fixed and identical to those given by Wieghardt in Coles and Hirst [26] for the case ID 1400.

The shapes of the mean velocity profiles along the streamwise direction are shown in Figs. 5-7. It can be seen that there is a region in which the velocity gradient is increasing near the wall surface. This is due to the larger momentum of the upper stream which thins the sublayer of the wall boundary layer caused by the lower stream. Consequently, the local skin friction increases within this region. The corresponding concentration profiles of the upper stream are also shown in the same figures. The distribution of U_0, which is the parameter determining the concentration profile is shown in Fig. 8. It may be noted that the larger the value of the velocity ratio, the greater is the distance to the location where the mass concentration diffuses to the wall surface. As indicated in Section 2, a smaller velocity ratio results in a larger mixing region; thus the merging between the mixing layer and the wall layer occurs over a shorter distance. Physically, the larger velocity ratio produces greater momentum in the upper stream and the lower stream is unable to sustain the greater impingement within the same distance.

It is interesting to examine the local skin friction distribution in Fig. 9. For velocity ratio $U_2/U_1=0.9$ and $U_2/U_1=0.7$, the local skin friction distributions first decrease and then increase over a short distance, finally decreasing in the streamwise direction. The first decrease exists because the lower stream can sustain the impingement of the upper stream over a short distance. The increase, as mentioned earlier, is due to the sublayer of the wall layer and results from the lower

Downloaded 02 May 2010 to 171.66.16.25. Redistribution subject to ASME license or copyright; see http://www.asme.org/terms/Terms_Use.cfm

stream being thinned by the impingement of the upper stream. The final decrease is due to the development of the flow in the conventional turbulent boundary layer. For the velocity ratio $U_2/U_1 = 0.51$, unlike the other cases, the skin friction increases and then decreases, owing to the fact that the lower stream can not sustain the impingement of the upper stream under such a velocity ratio.

Figures 10–12 show the distributions of the integral properties, namely shape factor H, displacement thickness δ^*, and momentum thickness θ. During the interaction process of the free mixing layer and the wall layer, the shape factor decreases due to the decrease in displacement thickness (recall the sublayer next to the wall is thinned) and the increase in momentum thickness. Finally, the shape factor approaches a constant value which is equal to that for a conventional turbulent boundary layer over a flat plate with zero pressure gradient.

All arguments made in the foregoing are physically reasonable; however, the predictions should be compared with experimental data. Recently, an investigation of parallel jet injection on turbulent pipe flow using Laser Doppler Velocimetry has been carried out at Berkeley. In a sequel to this paper, the LDV results will be compared with other experimental work including that in the 1976 Ph.D. thesis of Konrad at California Institute of Technology, and with the present theoretical results.

4 Conclusion

A model for reducing the corrosive effects on a wall surface in a coal gasification process has been established. In this, a noncorrosive gas is injected beneath the main stream of the coal gas products in a direction parallel to the wall surface. The solution procedure consists of (1) solving the development of a turbulent wall boundary layer, (2) solving the development of a turbulent free mixing layer, and (3) solving the interaction between the wall layer and the mixing layer.

The application of the orthonormal version of the Method of Integral Relations (MIR) to the present investigation has been studied. As far as the development of the turbulent wall boundary layer is concerned, numerical results are shown to be in good agreement with experimental data. In addition, a means of determining the initial conditions from the experimental data at the initial station has been suggested and has proven to be effective. Regarding the development of the turbulent-free mixing layer, MIR eliminates the velocity component v from the governing equations. The traditional third boundary condition does not appear in the present formulation. Numerical results are also shown to be in good agreement with the available experimental data.

Numerical results of the analysis for the interaction between the wall layer and the mixing layer are plausible. A new boundary layer type flow is found within the distance of the interaction. In this, the skin friction coefficient may increase or decrease first, depending on the ratio of the main stream speed to the injected stream speed, then subsequently increases, and finally decreases along the streamwise direction. The interaction eventually leads to the formation of the conventional turbulent boundary layer.

Finally, the species equation is solved and the ratio of the distance protected from attack by the corrosive gas to the slot height is found to be of the order 0(100).

Acknowledgment

This work was supported by the Division of Material Sciences, Office of Basic Energy Sciences, U.S. Department of Energy, through Contract No. DE-AC03-76SF00098 with the Materials and Molecular Research Division, Lawrence Berkeley Laboratory, Dr. Alan V. Levy, Director.

References

1 LaRue, J. C., and Libby, P. A., "Measurements in the Turbulent Boundary Layer with Slot Injection of Helium," Phys. of Fluids, Vol. 20, 1977, pp. 192–202.

2 LaRue, J. C., and Libby, P. A., "Further Results Related to the Turbulent Boundary Layer With Slot Injection of Helium," *Phys. of Fluids*, Vol. 23, 1980, pp. 1111–1118.

3 Cary, A. M., Bushnell, D. M., and Hefner, J. N., "Predicted Effects of Tangential Slot Injection on Turbulent Boundary Layer Flow Over a Wide Speed Range," ASME *Journal of Heat Transfer*, Vol. 101, 1979, pp. 699–704.

4 Brune, G. W., "Theoretical Prediction of Confluent Boundary Layers," *Third Symp. on Turbulent Shear Flows*, University of California, Davis, 1981, pp. 1.21–1.27.

5 Pot, P. J., "A Wake Boundary Layer Mixing Experiment," *Second. Symp. on Turbulent Shear Flows*, Imperial College, 1979, pp. 6.6-6–6.11.

6 Dorodnitsyn, A. A., "General Method of Integral Relations and Its Application to Boundary Layer Theory," *Advances in Aero. Science*, Vol. 3, 1960, Pergamon Press, New York.

7 Fletcher, C. A. J., and Holt, M., "An Improvement of the Method of Integral Relations," *J. of Computational Physics*, Vol. 18, 1975, pp. 154–164.

8 Yeung, W. C.-C., and Holt, M., "Boundary Layer Control in Pipes Through Strong Injection," *ZAMM*, Vol. 62, 1982, pp. 391–399.

9 Yeung, W. S., and Yang, R. J., "Application of the Method of Integral Relations to the Calculation of Two-Dimensional Incompressible Turbulent Boundary Layer," ASME JOURNAL OF APPLIED MECHANICS, Vol. 48, 1981, pp. 701–706.

10 Ting, L., "On the Mixing of Two Parallel Streams," *J. of Math. and Phys.*, Vol. 38, 1959, pp. 153–165.

11 Tollmien, W., "Berechning turbulenter Ausbreitungsvorgange," *ZAMM*, Vol. 6, 1926, p. 6.

12 Kuethe, A. M., "Investigation of the Turbulent Mixing Regions Forced by Jets," ASME JOURNAL OF APPLIED MECHANICS, Vol. 2, 1935, pp. A87–95.

13 Görtler, H., "Berechnung von Aufgaben der freien Turbulenz auf Grund eines neuen Näherungsansatzes," *ZAMM*, Vol. 22, 1942.

14 Mills, R. D., "Numerical and Experimental Investigations of the Shear Layer Between Two Parallel Streams," *J. Fluid Mech.*, Vol. 33, 1968, pp. 591–616.

15 Brown, G. L., and Roshko, A., "On Density Effects and Large Structure in Turbulence Mixing Layers," *J. Fluid Mech.*, Vol. 64, 1974, pp. 775–816.

16 Townsend, A. A., *The Structure of Turbulent Shear Flow*, Cambridge University Press, 1976.

17 Isaacson, E., and Keller, H. B., *Analysis of Numerical Methods*, 1st Ed., Wiley, New York, 1966, p. 199.

18 Prandtl, L., "Bemerkunge zur Theorie der freien Turbulenz," *ZAMM*, Vol. 22, 1942, pp. 241–243.

19 Birch, S. F., and Eggers, J. M., "Critical Review of the Experimental Data for Developed Free Turbulent Shear Layers," *NASA Langley Working Conference on Free Turbulent Shear Flows*, 1972.

20 Rodi, W., "A Review of Experimental Data of Uniform Density Free Turbulent Boundary Layers," *Studies in Convection*, Vol. 1, Launder, B. E., ed., Academic Press, New York, 1975.

21 Miner, E. W., and Lewis, C. H., "Numerical Studies of Supersonic Turbulent Boundary-Layer Flows with Tangential Slot Injection," *Comp. Meth. in Appl. Mech. and Eng.*, Vol. 4, 1974, pp. 19–38.

22 Dvorak, F. A., "Calculation of Turbulent Boundary Layers and Wall Jets Over Curved Surfaces," *AIAA Journal*, Vol. 11, 1973, pp. 517–524.

23 Kacker, S. C., Pai, B. R., and Whitelaw, J. H., "The Prediction of Wall Jet Flows With Particular Reference to Film Cooling," *Progress in Heat and Mass Transfer*, Vol. 2, Pergamon Press, 1969, pp. 163–186.

24 Seban, R. A., and Back, L. H., "Velocity and Temperature Profiles in Turbulent Boundary Layers with Tangential Injection," ASME *Journal of Heat Transfer*, Vol. 84, 1962, pp. 45–54.

25 Bradshaw, P., Ed., *Topics in Applied Physics—Turbulence*, Vol. 12, Springer-Verlag, 1976 p. 233.

26 Coles, D., and Hirst, P., Eds., *Proceedings, Computation of Turbulent Boundary Layers - 1968 AFOSR-IPP Stanford Conference*, Vol. 2, Compiled Data, 1968.

Downloaded 02 May 2010 to 171.66.16.25. Redistribution subject to ASME license or copyright; see http://www.asme.org/terms/Terms_Use.cfm

Eigenvalues and Stable Time Steps for the Uniform Strain Hexahedron and Quadrilateral[1]

D. P. Flanagan
Sandia Laboratories,
Albuquerque, N. Mex.

T. Belytschko
Department of Civil Engineering,
Northwestern University,
Evanston, Ill. 60201
Mem. ASME

Simple formulas for bounding the maximum eigenvalues or computing them exactly are obtained for the uniform strain eight-node hexahedron and the four-node quadrilateral. The development is based on a novel technique that reduces the size of the eigenproblem to where it can be managed analytically. These formulas are useful for explicit time integration applications since they provide conserative estimates of stable time steps. The eigenvalue analysis is limited to linear, isotropic materials but the results are also useful in nonlinear problems since the linerized material properties may be used.

1 Introduction

Estimates of the maximum eigenvalues for a finite element are useful in two respects. First, they can be used to determine stable time steps for explicit time integration. Secondly, they aid in the selection of hourglass control parameters.

The eigenvalue analysis presented in this paper pertains to the four-node quadrilateral and eight-node hexadedron with one quadrature point [1]. These elements are commonly used in transient dynamic analysis using explicit time integration for two and three dimensions, yet precise bounds on the eigenvalues and hence conservative stable time step estimates were not available.

The development of the element eigenvalues is here based on a technique that reduces the size of the eigenvalue problem so that it can be treated easily either exactly or by Gershgorin bounds. Thus, the eigenvalue problem for the three-dimensional hexahedron, which originally involves a 24×24 matrix, is reduced to a 3×3 matrix. Similarly, the two-dimensional quadrilateral eigenproblem is reduced to a 2×2 matrix, which can be solved exactly or easily bounded.

Section 2 summarizes the eigenvalue problems for these two elements based on an isotropic, linear material. The reduced eigenvalue problem is then described in Section 3, and the fundamental modes of the hexahedron and its eigenvalues are obtained in Section 4. Section 5 summarizes the same procedure for the quadrilateral. Section 6 summarizes all of the bounds and compares them with exact eigenvalues and commonly used formulas based on element length.

[1] The results of this paper are partially based on a Ph.D. Thesis submitted to Northwestern University in 1981 by the first author.

Contributed by the Applied Mechanics Division for presentation at the 1984 PVP Conference and Exhibition, Joint with Applied Mechanics Division and Materials Division, San Antonio, Texas, June 17-21, 1984 of THE AMERICAN SOCIETY OF MECHANICAL ENGINEERS.

Discussion on this paper should be addresed to the Editorial Department, ASME, United Engineering Center, 345 East 47th Street, New York, N.Y. 10017, and will be accepted until two months after final publication of the paper itself in the JOURNAL OF APPLIED MECHANICS. Manuscript received by ASME Applied Mechanics Division, February, 1983; final revision, June, 1983. Paper No. 84-APM-5.

Copies will be available until February, 1985.

2 Linear Eigenvalue Problem

The eigenvalue problem for a single element is

$$\mathbf{K}\,\mathbf{u} = k\,\mathbf{u} \tag{1a}$$

where $\mathbf{K}$ is the element stiffness matrix, k are the eigenvalues (also called the modal stiffnesses) and $\mathbf{u}$ the eigenvectors, which are the nodal displacements of the element. This equation can be written in indicial form as

$$K_i I_j J\, u_{jJ} = k\, u_{iI} \tag{1b}$$

where lower case subscripts range over the spatial coordinates and upper case subscripts range over the element's nodes; repeated indices are summed.

A lumped mass matrix $\mathbf{M}$ which is a scalar multiple of the unit matrix is also considered; a common form for the hexahedron is

$$M_{iIjJ} = \frac{\rho V}{8}\,\delta_{ij}\,\delta_{IJ} \tag{2}$$

where δ_{ij} is the Kronecker delta (unit matrix) and ρ and V are the density and volume of the element. The eigenvalues k are then related to the natural frequencies of the element ω by

$$k = \frac{\rho V}{8}\,\omega^2 \tag{3}$$

Many of the results will be expressed in terms of the frequency ω.

In the uniform strain hexahedron, the displacement gradient is given by [1]

$$u_{i,j} = \frac{1}{V}\,u_{iI}\,B_{jI} \tag{4}$$

where commas designate a spatial derivative with the following variable and $\mathbf{B}$ is defined in Table 1. The matrix $\mathbf{B}$ and the nodal coordinates x_{iI} satisfy the identity

$$x_{iI}\,B_{jI} = V\,\delta_{ij} \tag{5}$$

The element nodal forces are given in terms of the Cauchy stress $\mathbf{T}$ by

Copyright © 1984 by ASME
Downloaded 02 May 2010 to 171.66.16.25. Redistribution subject to ASME license or copyright; see http://www.asme.org/terms/Terms_Use.cfm

$$f_{iI} = T_{ij}\, B_{jI} \tag{6a}$$

where the preceding represent discrete forms of the divergence of the Cauchy stress. For a linear material, the nodal forces are related to the nodal displacements by the stiffness matrix through

$$f_{iI} = K_{iIjJ}\, u_{jJ} \tag{6b}$$

Combining equations (6*a*) and (6*b*) yields

$$K_{iIjJ}\, u_{jJ} = T_{ij}\, B_{jI} \tag{7}$$

and comparing equation (7) with equation (1) shows that any eigenvector associated with nonzero eigenvalues can be written as a linear combination of the rows of **B**, that is, any eigenvector **u** can be written as

$$u_{jJ} = b_{jk}\, B_{kJ} \tag{8}$$

3 Transformation of Eigenproblem

Since many of the eigenvalues of **K** vanish, it is advantageous to work with a reduced matrix defined by

$$a_{ij} = B_{iI}\, B_{jI} \tag{9a}$$

The matrix **a** is symmetic, so it can be diagonalized. We denote the matrix **a** in its principal orientation by a superposed circumflex and note that the diagonal form then consists of the eigenvalues α_i, i.e.,

$$\hat{a}_{ij} = \begin{cases} \alpha_i & i=j \\ 0 & i\neq j \end{cases} \tag{9b}$$

The quadratic product of any vector with **a** is equivalent to the inner product of a vector with itself

$$v_i\, a_{ij}\, v_j = (v_i\, B_{iI})\ (v_j\, B_{jI}) \tag{10}$$

Therefore, the quadratic product is non-negative for any vector **v**. Furthermore, if the element volume does not vanish, it follows from equation (5) that

$$(v_j\, B_{jI})\, x_{iI} = V v_i = 0 \quad \text{if and only if} \quad v_i = 0 \tag{11}$$

Hence, **a** is positive-definite and its eigenvalues are positive. Without loss of generality, we may rank these eigenvalues as follows

$$\alpha_1 \geq \alpha_2 \geq \alpha_3 > 0 \tag{12}$$

The eigenvalues of **K** will now be related to those of **a**. The stress tensor for a linear isotropic material is given by

$$T_{ij} = \lambda\, u_{k,k}\, \delta_{ij} + \mu(u_{i,j} + u_{j,i}) \tag{13}$$

where λ and μ are the Lamé constants. By substituting equations (13) and (4) into the right-hand side of equation (7), we obtain

$$K_{iIjJ}\, u_{jJ} = \frac{1}{V}[\lambda\, B_{iI}\, B_{jJ} + \mu\,(\delta_{ij}\, B_{kI}\, B_{kJ} + B_{jI}\, B_{iJ})]\, u_{jJ} \tag{14}$$

Substituting equation (8) into equation (14) and using equation (9) then gives

$$K_{iIjJ}\, u_{jJ} = \frac{1}{V}[\lambda\, \delta_{ij}\, a_{km}\, b_{km} + \mu(a_{jk}\, b_{ik} + a_{ik}\, b_{jk})]\, B_{jI} \tag{15}$$

Since the left-hand side is equal to $k\mathbf{u}$, by using the linear independence of the rows of **B**, the eigenproblem (1) may be written as

$$k\, b_{ij} = \frac{1}{V}[\lambda\, \delta_{ij}\, a_{km} + \mu(\delta_{im}\, a_{jk} + \delta_{jm}\, a_{ik})]\, b_{km} \tag{16}$$

where k is the eigenvalue and **b** the eigenvector.

Table 1 Matrices for quadrilateral and hexahedron

Quadrilateral

$$B_{iI} = \frac{1}{2}\begin{bmatrix} y_{24} & y_{31} & y_{42} & y_{13} \\ x_{42} & x_{13} & x_{24} & x_{31} \end{bmatrix} \begin{matrix} i=1 \\ i=2 \end{matrix}$$

$$A = \frac{1}{2}(x_{31}y_{42} + x_{24}y_{31})$$

$$x_{IJ} = x_I - x_J \qquad y_{IJ} = y_I - y_J$$

Hexahedron

$$12\, B_{11} = y_2(z_{63} + z_{54}) + y_3 z_{24} + y_4(z_{38} + z_{25}) + y_5(z_{86} + z_{42}) + y_6 z_{52} + y_8 z_{45}$$

Other terms in the row of **B** are found by permuting the indices by the following table

T in B_{iI}	Indices on coordinates						
1	2	3	4	5	6	7	8
2	3	4	1	6	7	8	5
3	4	1	2	7	8	5	6
4	1	2	3	8	5	6	7
5	8	7	6	1	4	3	2
6	5	8	7	2	1	4	3
7	6	5	8	3	2	1	4
8	7	6	5	4	3	2	1

Other rows are found by interchanging the coordinates

i in B_{iI}	Coordinates	
1	y	z
2	z	x
3	x	y

$$V = \sum_{I=1}^{8} x_I\, B_{1I} = \sum_{I=1}^{8} y_I\, B_{2I} = \sum_{i=1}^{8} z_I\, B_{3I}$$

4 Eigenvalues of Hexahedron

When the eigenproblem is expressed in the principal system of **a**, equation (16) becomes

$$k\, \hat{b}_{ij} = \frac{1}{V}[\lambda\, \delta_{ij}\, \hat{a}_{km} + \mu(\delta_{im}\, \hat{a}_{jk} + \delta_{jm}\, \hat{a}_{ik})]\, \hat{b}_{km} \tag{17}$$

There are nine distinct modes: three zero-energy modes ($k = 0$), three shear-strain modes, and three normal-strain modes; the zero-energy modes are partially rotations. The size of the eigenproblem to be solved is now further reduced by identifying these modes and showing that the normal-strain modes always give the maximum eigenvalue. The eigenvalue problem associated with the normal-strain modes is of order 3.

The first zero-energy mode is given by

$$\hat{b}^0_{ij} = \begin{bmatrix} 0 & 0 & 0 \\ 0 & 0 & -\alpha_3 \\ 0 & \alpha_2 & 0 \end{bmatrix}; \quad k^0_1 = 0 \tag{18}$$

This can be verified by simply substituting equation (18) into (17). Two other zero-energy modes are defined similarly. In any case, k vanishes for the zero-energy modes, so

$$k^0_i = 0 \quad i = 1 \text{ to } 3 \tag{19}$$

Downloaded 02 May 2010 to 171.66.16.25. Redistribution subject to ASME license or copyright; see http://www.asme.org/terms/Terms_Use.cfm

A shear mode is given by

$$\hat{b}_{ij}^{\text{shear}} = \begin{bmatrix} 0 & 0 & 0 \\ 0 & 0 & 1 \\ 0 & 1 & 0 \end{bmatrix}; \quad k_1^{\text{shear}} = \frac{\mu}{V}(\alpha_2 + \alpha_3) \tag{20}$$

Similarly, two other shear modes may be defined. The eigenvalue of the shear modes may be expressed, in terms of the trace of **a**, as

$$k_i^{\text{shear}} = \frac{\mu}{V}(a_{kk} - \alpha_i) \quad i = 1 \text{ to } 3 \tag{21}$$

The normal-strain modes are defined by considering

$$\hat{b}_{ij}^{\text{normal}} = \begin{cases} b_i & i = j \\ 0 & i \neq j \end{cases} \tag{22}$$

By substituting the preceding equation into the eigenproblem (17), we obtain

$$k \begin{Bmatrix} b_1 \\ b_2 \\ b_3 \end{Bmatrix} = \frac{1}{V} \begin{bmatrix} (\lambda+2\mu)\alpha_1 & \lambda\alpha_2 & \lambda\alpha_3 \\ \lambda\alpha_1 & (\lambda+2\mu)\alpha_2 & \lambda\alpha_3 \\ \lambda\alpha_1 & \lambda\alpha_2 & (\lambda+2\mu)\alpha_3 \end{bmatrix} \begin{Bmatrix} b_1 \\ b_2 \\ b_3 \end{Bmatrix} \tag{23a}$$

The foregoing is not symmetric, but may be put into the following symmetric form as a generalized eigenvalue problem

$$k \begin{bmatrix} \alpha_1 & 0 & 0 \\ 0 & \alpha_2 & 0 \\ 0 & 0 & \alpha_3 \end{bmatrix} \begin{Bmatrix} b_1 \\ b_2 \\ b_3 \end{Bmatrix} = \frac{1}{V} \begin{bmatrix} (\lambda+2\mu)\alpha_1^2 & \lambda\alpha_1\alpha_2 & \lambda\alpha_1\alpha_3 \\ \lambda\alpha\alpha_2 & (\lambda+2\mu)\alpha_2^2 & \lambda\alpha_2\alpha_3 \\ \lambda\alpha_1\alpha_3 & \lambda\alpha_2\alpha_3 & (\lambda+2\mu)\alpha_3^2 \end{bmatrix} \begin{Bmatrix} b_1 \\ b_2 \\ b_3 \end{Bmatrix} \tag{23b}$$

Solutions to the foregoing can be obtained by solving cubic equations but this is not convenient in finite element computations. Therefore, we will develop several useful bounds for the eigenvalues associated with the normal strain modes. Rayleigh's quotient may be applied to the foregoing to obtain

$$k_{\max}^{\text{normal}} \geq \frac{\lambda(b_i\alpha_i)^2 + 2\mu\, b_i^2\alpha_i^2}{V\, b_i^2\, \alpha_i} \tag{24a}$$

It follows from the foregoing and equation (21) that

$$k_{\max}^{\text{normal}} \geq \frac{\lambda+2\mu}{V}\alpha_1 \geq \frac{\mu}{V}(\alpha_1+\alpha_2) = k_{\max}^{\text{shear}} \tag{24b}$$

so the maximum eigenvalue is always associated with normal-strain modes.

Next the maximum eigenvalue of the normal-strain modes is bounded by applying Gershgorin's theorem [3] to equation (23)

$$k_{\max} \leq \frac{1}{V}(\lambda a_{ii} + 2\mu\,\alpha_1) \tag{25}$$

A lower bound is obtained from Rayleigh's quotient (24*a*), in terms of invariants of **a**, as

$$k_{\max} \geq \frac{1}{V}\left(\lambda a_{ii} + 2\mu \frac{a_{ij}\, a_{ij}}{a_{kk}}\right) \tag{26}$$

Simpler bounds are developed in terms of the trace of equation (23) by using the positive-definiteness of **K** and **a**. We find that

$$\frac{\lambda+2\mu}{3V} a_{ii} \leq k_{\max} \leq \frac{\lambda+2\mu}{V} a_{ii} \tag{27}$$

Remark 1. For a cube or $\mu = 0$, the equality holds in equations (25) and (26) and the two equations are equivalent; (25) becomes an equality also for $\lambda = 0$. The left-hand side of equation (27) becomes an equality only for a cube with $\lambda = 0$, the right-hand side becomes an equality if $\mu = 0$.

Remark 2. The bounds in equations (26) and (27) depend only on invariants of **a**. The bounds of equation (27) are coarser than (25), but more rapidly computed. Equation (25) requires an estimate of the maximum eigenvalue of **a**, which is most efficiently estimated by Gershgorin envelope [3] of **a**.

Remark 3. The bounds given by equations (26) and (27) also apply to the constant strain tetrahedron if in the definition of **a**, equation (7), the **B** matrix for the tetrahedron is used, so that the summation over I ranges from 1 to 4.

5 Quadrilateral Element

The eigenvalue analysis of the uniform strain quadrilateral follows closely the procedure for the hexahedron. The eigenvalue is related to the modal frequency by the counterpart of equation (3)

$$k = \frac{\rho h A}{4}\omega^2 \tag{28}$$

where h and A are the element thickness and area, respectively. The counterparts of equations (7) and (4) are

$$K_{iIjJ}\, u_{jJ} = h\, T_{ij}\, B_{jI} \tag{29}$$

$$u_{i,j} = \frac{1}{A} u_{iI}\, B_{jI} \tag{30}$$

Throughout this section, lowercase subscripts have a range of 2 and uppercase subscripts have a range of 4.

The definition and properties of the principal axes for the quadrilateral parallel those of the hexahedron (equations (9)–(12)). The isotropic material law is identical to equation (12) for plane strain (only λ need be modified for plane stress [4]). The eigenproblem for the quadrilateral in the principal system of **a** is analogous to (17)

$$k\,\hat{b}_{ij} = \frac{h}{A}\left[\lambda\,\delta_{ij}\,\hat{a}_{km} + \mu(\delta_{im}\,\hat{a}_{jk} + \delta_{jm}\,\hat{a}_{ik})\right]\hat{b}_{km} \tag{31}$$

The rigid body rotation and shear-strain modes for the foregoing are given by

$$\hat{b}_{ij}^0 = \begin{bmatrix} 0 & -\alpha_2 \\ \alpha_1 & 0 \end{bmatrix}; \quad k^0 = 0 \tag{32}$$

$$\hat{b}_{ij}^{\text{shear}} = \begin{bmatrix} 0 & 1 \\ 1 & 0 \end{bmatrix}; \quad k^{\text{shear}} = \frac{\mu h}{A} a_{ii} \tag{33}$$

The normal-strain modes of equation (22) yield the following eigenproblem

$$k \begin{Bmatrix} b_1 \\ b_2 \end{Bmatrix} = \frac{h}{A} \begin{bmatrix} (\lambda+2\mu)\alpha_1 & \lambda\alpha_2 \\ \lambda\alpha_1 & (\lambda+2\mu)\alpha_2 \end{bmatrix} \begin{Bmatrix} b_1 \\ b_2 \end{Bmatrix} \tag{34}$$

Downloaded 02 May 2010 to 171.66.16.25. Redistribution subject to ASME license or copyright; see http://www.asme.org/terms/Terms_Use.cfm

Since the procedure for obtaining eigenvalue bounds for equation (34) is identical to that for the hexahedron, we will simply summarize the results

$$k_{\max}^{\text{normal}} \geq \frac{(\lambda+2\mu)}{A}\alpha_1 \geq \frac{\mu h}{A} a_{ii} = k^{\text{shear}} \tag{35}$$

$$k_{\max} \leq \frac{h}{A}(\lambda a_{ii} + 2\mu\alpha_1) \tag{36}$$

$$k_{\max} \geq \frac{h}{A}\left(\lambda a_{ii} + 2\mu\frac{a_{ij}a_{ij}}{a_{ii}}\right) \tag{37}$$

$$\frac{(\lambda+2\mu)h}{2A} a_{ii} \leq k_{\max} \leq \frac{(\lambda+2\mu)h}{A} a_{ii} \tag{38}$$

6 Summmary of Results of Comparisons

Upper and lower bounds for the maximum frequency of the uniform strain hexahedron are given by combining equations (3), (25), and (26).

$$\frac{8}{\rho V^2}\left(\lambda a_{ii} + 2\mu\frac{a_{ij}a_{ij}}{a_{kk}}\right) \leq \omega_{\max}^2 \leq \frac{8}{\rho V^2}(\lambda a_{ii} + 2\mu\alpha_1) \tag{39}$$

where α_1 is the maximum eigenvalue of **a**. The bounds given in the following, which are obtained from equation (27), are not as narrow as those in the foregoing, but are somewhat easier to compute.

$$\frac{8c^2}{3V^2} a_{ii} \leq \omega_{\max}^2 \leq \frac{8c^2}{V^2} a_{ii} \tag{40}$$

where c is the dilatational wave-speed [7] given by

$$c^2 = \frac{\lambda+2\mu}{\rho} \tag{41}$$

The bounds, analgous to the foregoing, for the uniform strain quadrilateral are

$$\frac{4}{\rho A^2}\left(\lambda a_{ii} + 2\mu\frac{a_{ij}a_{ij}}{a_{kk}}\right) \leq \omega_{\max}^2 \leq \frac{4}{\rho A^2}(\lambda a_{ii} + 2\mu\alpha_1) \tag{42}$$

$$\frac{2c^2}{A^2} a_{ii} \leq \omega_{\max}^2 \leq \frac{4c^2}{A^2} a_{ii} \tag{43}$$

Equations (40) and (43) may be combined as

$$\frac{n_N c^2}{n_D \Omega^2} a_{ii} \leq \omega_{\max}^2 \leq \frac{n_N c^2}{\Omega^2} a_{ii} \tag{44}$$

where n_D is the number of dimensions, n_N the number of nodes of the element, and Ω equals V or A for the hexahedron and quadrilateral, respectively.

The stability condition for the central difference operator without damping is [8]

$$\Delta t \leq \frac{2}{\omega_{\max}} \tag{45}$$

where $\omega_{\max}$ is the maximum frequency of the mesh. Since the maximum frequency among the elements is an upper bound on the maximum global frequency [6], a stable time step (45) may be determined from the maximum element frequency.

The stability limit for finite element schemes is often taken to be the traversal time of a dilatational wave across the minimum mesh dimension, l. This corresponds to the following estimate of the maximum frequency

$$\bar{\omega}_{\max} \leq \frac{2c}{l} \tag{46}$$

The notion of a minimum dimension l for a finite element is rather vague. Furthermore, it is not convenient to compute l while processing an element. One purpose for performing this eigenvalue analysis, consequently, was to derive a more precise stability criterion. In comparing these estimates with equation (46) for some special cases, it was found that equation (46) is not necessarily conservative.

Table 2 Maximum frequency versus estimates for hexahedron

Case	Maximum frequency, equation (A.6)		Frequency, based on l, equation (46)	Recommended estimate, equation (A.7)
(*I*) Cube	$\frac{2}{l}\sqrt{\frac{3\lambda+2\mu}{\rho}}$	$\geq$	$\frac{2}{l}\sqrt{\frac{\lambda+2\mu}{\rho}}$	$\frac{2}{l}\sqrt{\frac{3\lambda+6\mu}{\rho}}$
(*II*) Thin slab	$\frac{2}{l}\sqrt{\frac{\lambda+2\mu}{\rho}}$	$=$	$\frac{2}{l}\sqrt{\frac{\lambda+2\mu}{\rho}}$	$\frac{2}{l}\sqrt{\frac{\lambda+2\mu}{\rho}}$
(*III*) $\lambda=0$	$\frac{2}{l}\sqrt{\frac{2\mu}{\rho}}$	$=$	$\frac{2}{l}\sqrt{\frac{2\mu}{\rho}}$	$\frac{2}{l}\sqrt{\frac{2\mu}{\rho}\left(1+\frac{l^2}{s_2^2}+\frac{l^2}{s_3^2}\right)}$
(*IV*) $\mu=0$	$\frac{2}{l}\sqrt{\frac{\lambda}{\rho}\left(1+\frac{l^2}{s_2^2}+\frac{l^2}{s_3^2}\right)}$	$>$	$\frac{2}{l}\sqrt{\frac{\lambda}{\rho}}$	$\frac{2}{l}\sqrt{\frac{\lambda}{\rho}\left(1+\frac{l^2}{s_2^2}+\frac{l^2}{s_3^2}\right)}$

Table 3 Maximum frequency versus estimates for quadrilateral

Case	Maximum frequency, equation (B.8)		Frequency, based on l, equation (46)	Recommended estimate, equation (B.9)
(*I*) Square	$\frac{2}{l}\sqrt{\frac{2\lambda+2\mu}{\rho}}$	$\geq$	$\frac{2}{l}\sqrt{\frac{\lambda+2\mu}{\rho}}$	$\frac{2}{l}\sqrt{\frac{2\lambda+4\mu}{\rho}}$
(*II*) Bar	$\frac{2}{l}\sqrt{\frac{\lambda+2\mu}{\rho}}$	$=$	$\frac{2}{l}\sqrt{\frac{\lambda+2\mu}{\rho}}$	$\frac{2}{l}\sqrt{\frac{\lambda+2\mu}{\rho}}$
(*III*) $\lambda=0$	$\frac{2}{l}\sqrt{\frac{2\mu}{\rho}}$	$=$	$\frac{2}{l}\sqrt{\frac{2\mu}{\rho}}$	$\frac{2}{l}\sqrt{\frac{2\mu}{\rho}\left(1+\frac{l^2}{s_2^2}\right)}$
(*IV*) $\mu=0$	$\frac{2}{l}\sqrt{\frac{\lambda}{\rho}\left(1+\frac{l^2}{s_2^2}\right)}$	$>$	$\frac{2}{l}\sqrt{\frac{\lambda}{\rho}}$	$\frac{2}{l}\sqrt{\frac{\lambda}{\rho}\left(1+\frac{l^2}{s_2^2}\right)}$

Downloaded 02 May 2010 to 171.66.16.25. Redistribution subject to ASME license or copyright; see http://www.asme.org/terms/Terms_Use.cfm

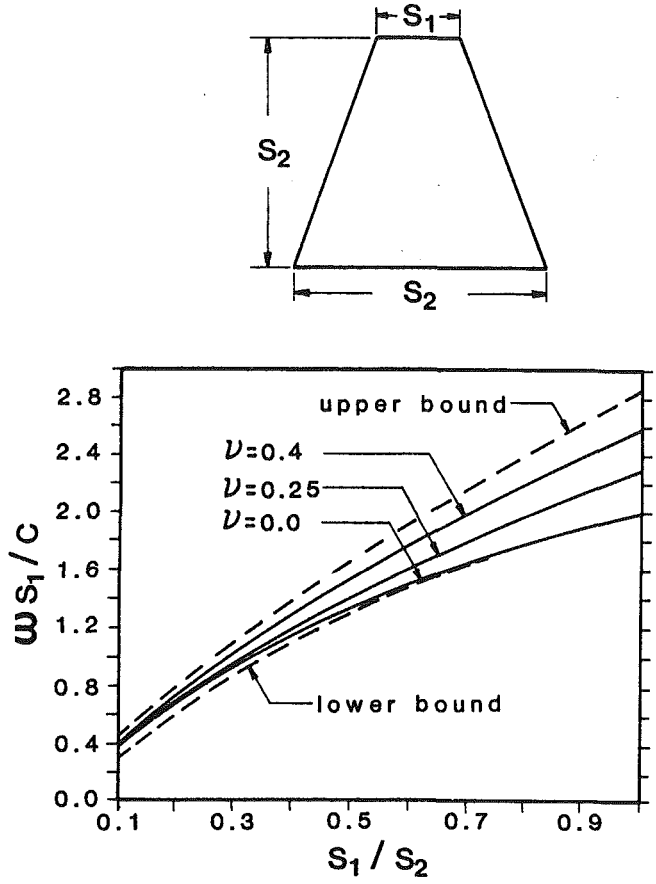

Fig. 1 Comparison of upper and lower bounds of equation (43) with exact maximum freqency for rectangular elements

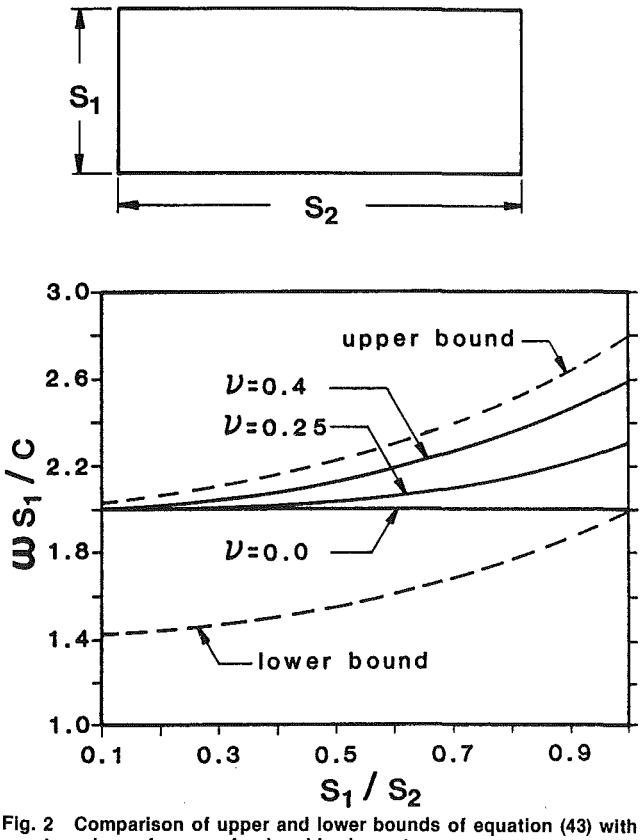

Fig. 2 Comparison of upper and lower bounds of equation (43) with exact maximum freqency for rhombic element

Tables 2 and 3 compare maximum frequency estimates with the actual maxima for several special cases. Details of how these frequencies were obtained are given in Appendices *A* and *B*. The "recommended" estimates in Tables 2 and 3 are the upper bounds of equations (40) and (43), respectively. Observe that in both Tables, for Cases 1 and 4, equation (46) underestimates the maximum frequency. In these cases, the time step (46) may not be satisfactory.

The upper and lower bounds on the frequency are compared to the exact maximum frequency as obtained in Appendix *B* for rectangles and certain rhombi in Figs. 1 and 2. As can be seen, the accuracy of the upper bound is better for larger values of Poisson's ratio, but for all of the parameters shown in Figs. 1 and 2, the upper bound is sufficiently close to the actual maximum frequency to provide an effective stable time step for explicit integration.

Conclusion

Upper and lower bounds have been developed for the maximum eigenvalues and frequencies of the uniform strain hexahedron and quadrilateral. A linear isotropic material was assumed. The estimates have been used successfully for nonlinear calculations by using the tangential material properties at each time step, but the theory for such applications is not yet available.

The eigenvalue bounds recommended are given by equation (27) for the hexahedron and equation (38) for the quadrilateral. Similarly, the recommended frequency bounds are given by equation (40) and (43), respectively. The recommended bounds are generally satisfactory and are the most readily computed.

The recommended maximum frequency estimates were compared with an estimate based on element dimensions, equation (44) and the actual frequency for several special cases. It was shown that the frequency based on a minimum element dimension l may not always be conservative. The frequency bounds obtained here are always conservative and are convenient for finite element computations.

Acknowledgment

The support for the second author, Ted Belytschko, of Grant F499620-82-K0013 of the Air Force Office of Scientific Research is gratefully acknowledged.

References

1 Flanagan, D. P., and Belytschko, T., "A Uniform Strain Hexahedron and Quadrilateral With Orthogonal Hourglass Control," *Int. Journal for Numerical Methods in Engineering*, Vol. 17, 1981, pp. 679–706.

2 Clough, R. W., and Penzien, J., *Dynamics of Structures*, McGraw Hill, New York, 1975.

3 Isaacson, E., and Keller, H. B., *Analysis of Nunerical Methods*, Wiley, New York, 1966.

4 Sokolnikoff, I. S., *Mathematical Theory of Elasticity*, McGraw-Hill, New York, 1956.

5 Ames, W. F., *Numerical Methods for Partial Differential Equations*, Academic Press, New York, 1977.

6 Flanagan, D. P., and Belytschko, T., "Simultaneous Relaxation in Structural Dynamics," *Journal of the Engineering Mechanics Division*, ASCE, Vol. 107, pp. 1039–1055.

7 Achenbach, J. D., *Wave Propagation in Elastic Solids*, North-Holland, 1973.

8 Belytschko, T., "Explicit Time Integration of Structure-Mechanical Systems," in *Advanced Structural Dynamics*, Donea, J., ed., Applied Science Publishers, Essex, England, 1980, pp. 97–122.

APPENDIX A

Special Cases for the Hexahedron

Assume that the hexahedron is a rectangular parallelepiped

Downloaded 02 May 2010 to 171.66.16.25. Redistribution subject to ASME license or copyright; see http://www.asme.org/terms/Terms_Use.cfm

with its sides parallel to the coordinates. The nodal coordinates and **B** are then expressed as

$$x_{iI} = \frac{1}{2} s_i \Lambda_{iI} \quad \text{(no sum)} \tag{A.1}$$

$$B_{iI} = \frac{1}{4} \frac{V}{s_i} \Lambda_{iI} \quad \text{(no sum)} \tag{A.2}$$

where $\mathbf{\Lambda}$ is given in Reference [1] and it is assumed that

$$s_3 \geq s_2 \geq s_1 = l \tag{A.3}$$

The volume V is given by

$$V = s_1 s_2 s_3 \tag{A.4}$$

and the eigenvalues α_i are

$$\alpha_i = \frac{1}{2} \left(\frac{V}{s_i} \right)^2 \tag{A.5}$$

For the cases considered, the equality of equation (25) holds. Combining equations (25) and (3) then yields

$$\omega_{\max}^2 = \frac{4}{\rho} \left(\lambda \left(\frac{1}{s_1^2} + \frac{1}{s_2^2} + \frac{1}{s_3^2} \right) + \frac{2\mu}{s_1^2} \right) \tag{A.6}$$

The frequency estimate $\hat{\omega}_{\max}$ from equation (40), which is denoted by $\hat{\omega}_{\max}$,

$$\hat{\omega}_{\max}^2 = \frac{4(\lambda + 2\mu)}{\rho} \left(\frac{1}{s_1^2} + \frac{1}{s_2^2} + \frac{1}{s_3^2} \right) \tag{A.7}$$

The eigenvalues in Table 1 are then obtained by simply applying equations (A.6) and (A.7) with s_i, λ, and μ specified as indicated. For the thin slab, s_2 and s_3 are considered to be much larger than s_1 and their reciprocals are neglected.

APPENDIX B

Formulas for Quadrilateral

For the quadrilateral. The exact maximum eigenvalues can easily be determined from equation (34) by a quadratic equation. If we define

$$\bar{k} = \frac{kA}{h} \tag{B.1}$$

then the eigenvalues are given by the solution of the equation

$$\bar{k}^2 - (\lambda + 2\mu)(\alpha_1 + \kappa_2)\bar{k} + 4\mu(\mu + \lambda)\alpha_1 \alpha_2 = 0 \tag{B.2}$$

which gives

$$2\bar{k} = (\lambda + 2\mu)\gamma_1 \pm [(\lambda + 2\mu)^2 \gamma_1^2 - 16\mu(\mu + \lambda)\gamma_2]^{1/2} \tag{B.3}$$

Note that α_1 and α_2 need not be determined explicitly since

$$\gamma_1 = \alpha_1 + \alpha_2 = \text{trace } \mathbf{a} = \frac{1}{2}(y_{24}^2 + y_{31}^2 + x_{42}^2 + x_{13}^2) \tag{B.4}$$

$$\gamma_2 = \alpha_1 \alpha_2 = \frac{1}{4}(y_{24}^2 + y_{31}^2)(x_{42}^2 + x_{13}^2) - \frac{1}{4}(y_{24}x_{42} + y_{31}x_{13})^2 \tag{B.5}$$

$$x_{IJ} = x_I - x_J$$

$$y_{IJ} = y_{IU} - y_J$$

where equation (B.5) results from the fact that the product of the roots is equal to the constant term in the canonical equation for α_i.

The maximum frequency is given by

$$\omega_{\max}^2 = \frac{2c^2}{A^2}(\gamma_1 + \sqrt{\gamma_1^2 - \bar{\nu}\gamma_2}) \tag{B.6}$$

where γ_i are defined in equations (B.4) and (B.5), c is the dilatational wave speed, equation (41) and

$$\bar{\nu} = \frac{4(1 - 2\nu)}{1 - \nu^2} \tag{B.7}$$

For the case where the element is rectangular with side s_1, s_2, $s_2 > s_1$, equations (3), (B.1), and (B.3)–(B.5) yield

$$\omega_{\max}^2 = \frac{4}{\rho} \left(\lambda \left(\frac{1}{s_1^2} + \frac{1}{s_2^2} \right) + \frac{2\mu}{s_1^2} \right) \tag{B.8}$$

The frequency estimate $\hat{\omega}_{\max}$ from equation (42) is equivalent to the following

$$\hat{\omega}_{\max}^2 = \frac{4(\lambda + 2\mu)}{\rho} \left(\frac{1}{s_1^2} + \frac{1}{s_2^2} \right) \tag{B.9}$$

The case for the square is obtained by letting $s_1 = s_2 = l$; the case for the bar is obtained by letting $s_2 >> s_1$ and neglecting the reciprocal of s_2.

Downloaded 02 May 2010 to 171.66.16.25. Redistribution subject to ASME license or copyright; see http://www.asme.org/terms/Terms_Use.cfm

A Theoretical Analysis of Transient Sound Radiation From a Clamped Circular Plate

A. Akay
Mem. ASME

M. Tokunaga[1]

M. Latcha
Assoc. Mem. ASME

Mechanical Engineering Department,
Wayne State University,
Detroit, Mich. 48202

A theoretical analysis of transient sound radiation from a clamped circular plate is given using a pressure impulse response method. The vibration response of the plate to a transient point force is obtained. The modal pressure impulse response functions for the plate are derived from the Rayleigh surface integral and numerically convoluted with the modal acceleration response of the plate. The impulse response functions are closely related to the mode shapes and the geometry of the problem. They relate the spatial domain to the temporal domain of the pressure waves. The pressure impulse response waveforms are given for a number of plate modes and the changes in the waveforms with distance from the plate are shown. Sound radiation due to forced and free vibrations of the plate are discussed.

Introduction

Acoustic radiation from planar elastic structures is a fundamental problem in acoustics. Transient radiation from vibrating surfaces represents an important subset of this problem in the analysis of a large number of diverse acoustics problems. Earlier work on this subject includes radiation from transient point-excitations of infinite plates [1-3], transient sound transmission through finite plates [4-8], and a large class of problems on transient radiation from a baffled planar piston. An extensive review of the latter subject is given in reference [9].

The specific problem of transient sound radiation from a finite plate excited by an impact has been the subject of a number of studies. However, most of these studies have been experimental in nature and have resulted in empirical relationships between various parameters [10]. A significant analytical study was reported by Strasberg [11] on radiation from a periodically struck diaphragm, where radiated acoustic power was obtained in the frequency domain.

Sound radiation from a vibrating plate in an infinite baffle can be obtained by solving the pressure wave equation with appropriate boundary and initial conditions. A number of mathematical techniques have been developed for the problem of sound radiation from a baffled piston. These can be grouped under four fundamental methods: (1) Rayleigh surface integral [12], (2) King integral [13], (3) Schoch solution [14], and (4) convolution integral [15, 16]. Among these methods only the King integral is limited to circular-shaped pistons. The other three methods are applicable to baffled planar pistons with arbitrary shapes.

The Rayleigh surface integral, which is a special case of the Helmholtz-Huygens Integral, was the first of these methods developed to treat the problem of radiation from baffled planar pistons. The other three methods are solutions of the wave equation; however, they can also be directly derived from the Rayleigh surface integral by appropriate change of coordinates. A detailed discussion of these methods and their interrelationships can be found in reference [9].

The problem of transient radiation from baffled planar radiators with nonuniform vibration amplitude was treated in a number of recent studies [17-20]. Greenspan [17] considered radiation from rigid, simply supported, clamped and Gaussian radiators, treating both steady-state and transient cases. Harris [18] developed a method for transient radiation from baffled planar pistons with arbitrary vibration amplitude. His method is an extension of the convolution method where a generalized spatial impulse response function is convolved with the piston vibration-time history. Harris's results compared the effects of point and finite size receivers. The problems of radiation from planar radiators with axisymmetric vibration distribution was treated by Stepanishen [19]. He developed a generalized Green's function which leads to representation of the acoustic field with a single integral. His results were further generalized for the case of radiators with arbitrary shape and nonuniform vibration distributions by Tjøtta and Tjøtta [20].

The present paper describes a theoretical analysis of transient acoustic radiation from an impact-excited clamped circular plate in an infinite baffle. The expression for the sound pressure is obtained using the spatial impulse response-convolution approach, where the pressure impulse response is

[1] Present Address: Daido-kiko Limited, 4-1-3 Hatchobori, Chuo-ku, Tokyo, Japan 104.

Contributed by the Applied Mechanics Division for presentation at the 1984 PVP Conference and Exhibition, Joint with Applied Mechanics Division and Materials Division, San Antonio, Texas, June 17-21, 1984 of THE AMERICAN SOCIETY OF MECHANICAL ENGINEERS.

Discussion on this paper should be addressed to the Editorial Department, ASME United Engineering Center, 345 East 47th Street, New York, N.Y. 10017, and will be accepted until two months after final publication of the paper itself in the JOURNAL OF APPLIED MECHANICS. Manuscript received by ASME Applied Mechanics Division, November, 1982; final revision, June 1983. Paper No. 84-APM-1.

Copies will be available until February, 1985.

Copyright © 1984 by ASME
Downloaded 02 May 2010 to 171.66.16.25. Redistribution subject to ASME license or copyright; see http://www.asme.org/terms/Terms_Use.cfm

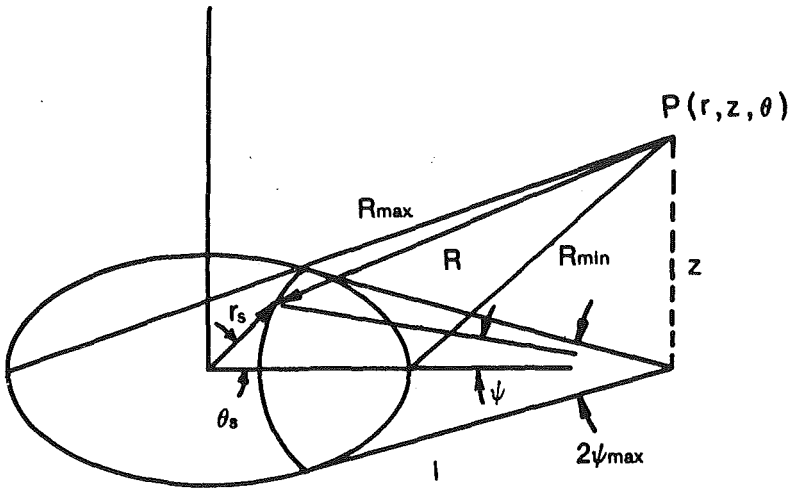

Fig. 1 Geometry of the problem

obtained as a line integral and convolved with the acceleration-time history of the plate to obtain the transient radiation. Several numerical results are given to illustrate the distinct differences in the sound pressure waveforms due to forced and free vibrations of a clamped plate in an infinite baffle excited by an impact force. The results are found to be the same as those obtained by direct numerical integration of the Rayleigh surface integral reported by the authors earlier [21].

Plate Vibrations

Radiation from a thin circular plate of radius **a** clamped at the outer edge and mounted in an infinite baffle is considered. An inviscid isotropic homogeneous fluid with a speed of sound c and a density ρ_0 much less than the density of the plate ρ is in contact with the plate. Geometry of the problem is shown in Fig. 1. The plate is assumed to be excited from rest with a transient point force. For mathematical convenience the Euler plate theory is used to determine the vibratory response of a thin plate. However, as pointed out in reference [3], for frequencies above which the wavelength in the plate is less than eight times its thickness, the Timoshenko-Mindlin plate theory should be used to prevent the slight error introduced into the group and phase velocities.

Using classical plate theory, the equation of motion for the transverse displacement, u, of a plate is given as:

$$D\nabla^4 u + C\partial u/\partial t + \rho h\partial^2 u/\partial t^2 = F(r_s,\theta_s,t) \qquad (1)$$

where h is the thickness of the plate and $D = Eh^3/12(1-\nu^2)$ is its flexural rigidity. E is Young's modulus, C is the damping coefficient, and ν is Poisson's ratio. $F(r_s,\theta_s,t)$ is the applied transverse force per unit surface area of the plate.

The general solution to equation (1) for a plate initially undeformed and at rest can be written as:

$$u(r_s,\theta_s,t) = (1/\rho h)\sum_{n=0}^{\infty}\sum_{m=0}^{\infty}[\phi_{nm}(r_s,\theta_s)/\omega^*_{nm}]$$
$$\int_0^t F_{nm}(\tau)e^{-\xi\omega_{nm}(t-\tau)}\sin\omega^*_{nm}(t-\tau)d\tau \qquad (2)$$

where $\omega^*_{nm} = \omega_{nm}\sqrt{1-\xi^2}$. ξ is the damping ratio and ω_{nm} are the natural frequencies of the plate, with the subscripts n and m denoting the radial and circular modes, respectively. ϕ_{nm} are the normal modes of the plate and are normalized using their orthogonality property as:

$$\int_0^{2\pi}\int_0^a \phi_{nm}(r_s,\theta_s)\phi_{pq}(r_s,\theta_s)r_s dr_s d\theta_s = \pi a^2\delta^{pq}_{nm} \qquad (3)$$

where

$$\delta^{pq}_{nm} = \begin{cases} 1 & n=p,\ m=q \\ 0 & n\neq p,\ m\neq q \end{cases}$$

The modal coefficients of the force $F_{nm}(t)$ are found as

$$F_{nm}(t) = \left[\int_0^{2\pi}\int_0^a F(r_s,\theta_s,t)\phi_{nm}(r_s,\theta_s)r_s dr_s d\theta_s\right]$$
$$\Big/\left[\int_0^{2\pi}\int_0^a \phi^2_{nm}(r_s,\theta_s)r_s dr_s d\theta_s\right]$$

A transient point force may be expressed as

$$F(r_s,\theta_s,t) = F_0\delta(r_s-r_0)\delta(\theta_s-\theta_0)f(t)/2\pi r_s \qquad (5)$$

where $f(t)$ is the arbitrary time dependence of the force and δ is the Dirac delta function. When the transient force is applied at the center of the plate, the force function takes the form

Nomenclature

- **a** = radius of plate
- c = wave speed in acoustic medium
- h = thickness of plate
- r,z,θ = cylindrical coordinates
- r_s,θ_s = polar coordinates on the plate surface
- u = transverse displacement of plate
- C = damping coefficient
- D = flexural rigidity of plate $= Eh^3/12(1-\nu^2)$
- E = Young's modulus
- F = applied load
- M = mass of plate
- $\delta(r)$ = Dirac delta function
- λ_n = freqency parameter
- ξ = damping ratio
- ν = Poisson's ratio for plate
- ρ = density of plate material
- ρ_0 = density of acoustic medium
- ϕ_n = eigenfunctions of plate nth mode
- ω_n = natural frequency of a clamped circular plate
- ω_0 = π/duration of transient force
- ω^*_n = $\omega_n\sqrt{1-\xi^2}$

Downloaded 02 May 2010 to 171.66.16.25. Redistribution subject to ASME license or copyright; see http://www.asme.org/terms/Terms_Use.cfm

$$F(r_s,t)=F_0\delta(r_s)f(t)/2\pi r_s \tag{6}$$

and the axisymmetric response of the plate is written as

$$u(r_s,t)=\frac{1}{\rho h}\sum_{n=0}^{\infty}\frac{\phi_n(r_s)}{\omega_n^*}\int_0^t F_n(\tau)\sin\omega_n^*(t-\tau)\,d\tau \tag{7}$$

where

$$F_n(t)=\int_0^{2\pi}\int_0^a F(r_s,t)\phi_n(r_s)r_s dr_s d\theta_s \Big/ \int_0^{2\pi}\int_0^a \phi_n^2(r_s)r_s dr_s d\theta_s \tag{8}$$

The mode shapes ϕ_n and the natural frequencies ω_n are determined by applying the boundary conditions to the homogeneous undamped equation of motion of the plate. For a circular plate with a clamped edge, the axisymmetric mode shapes and the natural frequencies are given by [22]:

$$\phi_n(r_s)=\frac{1}{\sqrt{2}}\left[\frac{J_0(\lambda_n r_s/a)}{J_0(\lambda_n)}-\frac{I_0(\lambda_n r_s/a)}{I_0(\lambda_n)}\right] \tag{9}$$

$$\omega_n=(\lambda_n/a)^2\sqrt{D/\rho h} \tag{10}$$

where λ_n are the roots of the frequency equation (11):

$$J_0(\lambda_n)I_1(\lambda_n)+J_1(\lambda_n)I_0(\lambda_n)=0. \tag{11}$$

J_0 and J_1 are Bessel functions of the first kind and I_0 and I_1 are modified Bessel functions of the first kind.

The transient force-time history is represented with a squared half-sine pulse in equation (6) to simulate elastic impact of a plate with a sphere [21]:

$$F(r_s,t)=\begin{cases} F_0\delta(r_s)\sin^2\omega_0 t/2\pi r_s, & 0\le t\le \pi/\omega_0 \\ 0, & \pi/\omega_0\le t \end{cases} \tag{12}$$

The axisymmetric displacement response in equation (7) to the forcing function in (12) becomes:

$$u(r_s,t)=\frac{F_0}{M}\sum_{n=0}^{\infty}\frac{\phi_n(0)\phi_n(r_s)}{(4\omega_0^2-\omega^2{}_n)\sin\Omega-4\xi\omega_n\omega_0\cos\Omega}$$

$$\begin{cases} \tfrac{1}{2}\sin(2\omega_0 t+\Omega)+X_1\exp(-\xi\omega_n t)\sin(\omega_n^* t_1+\Omega_1)+\mathrm{E}, \\ \qquad 0\leqq t\leqq \pi/\omega_0 \\ X_2\exp(-\xi\omega_n t_1)\sin(\omega_n^* t_1+\Omega_2), \quad t_1\geqq 0 \end{cases} \tag{13}$$

where

$$\begin{aligned}
\Omega &= \tan^{-1}[(\omega_n^2-4\omega^2)/4\xi\omega_0\omega_n], \\
\Omega_1 &= \tan^{-1}\{\omega_n^*(E+\tfrac{1}{2}\sin\Omega)/[\omega_0\cos\Omega+\xi\omega_n(E+\tfrac{1}{2}\sin\Omega)]\} \\
\Omega_2 &= \tan^{-1}[C_1\omega_n^*/(C_2+C_1\xi\omega_n)], \\
X_1 &= [\omega_0\cos\Omega/(\xi\omega_n\sin\Omega_1-\omega_n^*\cos\Omega_1)] \\
X_2 &= [C_2/(\omega_n^*\cos\Omega_2-\xi\omega_n\sin\Omega_2)], \\
C_1 &= \tfrac{1}{2}\sin\Omega+X_1\exp(-\xi\omega_n\pi/\omega_0)\sin[(\omega_n^*\pi/\omega_0)+\Omega_1]+E \\
C_2 &= \omega_0\cos\Omega+X_1\exp(-\xi\omega_n\pi/\omega_0)\{\omega_n^*\cos[(\omega_n^*\pi/\omega_0)+\Omega_1)]-\xi\omega_n\sin[(\omega_n^*\pi/\omega_0)+\Omega_1]\} \\
\mathrm{E} &= [(4\omega_0^2-\omega_n^2)\sin\Omega-4\xi\omega_0\omega_n\cos\Omega]/2\omega_n^2, \\
M &= \rho\pi a^2 h, t_1=t-\pi/\omega_0, \omega_n^*=\omega_n\sqrt{1-\xi^2}
\end{aligned}$$

Acoustic Radiation

The sound pressure radiated from a vibrating plate in a rigid infinite baffle ($z=0$ plane) can be obtained by evaluating the Rayleigh surface integral [12]. For an axisymmetric radiator the Rayleigh integral is written as:

$$p(r,z,t)=(\rho_0/2\pi)\int_S \ddot{u}[r_s(l,\psi),t-R/c]dS/R \tag{14}$$

where $\ddot{u}(r_s,t)$ is the acceleration-time history of plate vibrations and R is the distance from the receiver to any point on the plate surface. The elemental surface area is $dS = ldld\psi$ with the coordinates l,ψ shown in Fig. 1. Subscript s delineates the coordinates on the plate surface.

In the Rayleigh integral the delay in the arrival of the acoustic pressure waves emanating from points on the plate at different distances from the receiver point is taken into account by the delay-time (t-R/c) in the acceleration term. The integration is carried out over the plate surface.

The spatial impulse response or the convolution approach can be developed directly from the Rayleigh integral in equation (14) by first transforming the integration variables from the surface coordinates (r_s,θ_s) to receiver-oriented coordinates (R,ψ) and then performing one of the integrals. Referring to Fig. 1 and considering the relationship between the coordinates, $R^2 = z^2 + l^2$ and $RdR = ldl$, equation (14) can be written as

$$p(r,z,t)=\frac{\rho_0}{2\pi}\int_{R_{\min}}^{R_{\max}}\int_0^{2\psi_{\max}(R,z)}\ddot{u}[r_s(R,z,\psi),\,t-R/c]dRd\psi \tag{15}$$

where $R_{\min}$ and $R_{\max}$ are the closest and farthest distances from the receiver to the plate surface. $2\psi_{\max}$ is the largest angle ψ makes as shown in Fig. 1.

From equation (13) the axisymmetric acceleration response of an impact-excited clamped circular plate can be written as

$$\ddot{u}(r_s,t)=\sum_{n=1}^{\infty}\phi_n(r_s)\ddot{q}_n(t) \tag{16}$$

where

$$\ddot{q}_n(t)=\left(\frac{F_0}{M}\right)\frac{\phi_n(0)}{(4\omega_0^2-\omega_n^2)\sin\Omega-4\xi\omega_n\omega_0\cos\Omega}$$

$$X\begin{cases} -2\omega_0^2\sin(2\omega_0 t+\Omega)+X_1\exp(-\xi\omega_n t)[(\xi^2\omega_n^2-\omega_n^{*2}) \\ \qquad \sin(\omega_n^* t_1+\Omega_1)-2\xi\omega_n\omega_n^*\cos(\omega_n^* t+\Omega_1)], \\ \qquad 0\leqq t\leqq \pi/\omega_0 \\ X_2\exp(-\xi\omega_n t_1)[(\xi^2\omega_n^2-\omega_n^{*2})\sin(\omega_n^* t_1+\Omega_2) \\ \qquad -2\xi\omega_n\omega_n^*\cos(\omega_n^* t_1+\Omega_2)], \quad t_1\geqq 0 \end{cases}$$

$\phi_n(r)$ is given in equation (9).

Substitution of equation (16) in (15) gives:

$$p(r,z,t)=\frac{\rho_0}{2\pi}\int_{R_{\min}}^{R_{\max}}\int_0^{2\psi_{\max}(R,z)}\left\{\sum_{n=1}^{\infty}\phi_n[r_s(R,z,\psi)]\ddot{q}_n(t-R/c)\right\}dRd\psi \tag{17}$$

After changing the order of summation and integrations, and substituting $\tau = R/c$, equation (17) can be written as:

$$p(r,z,t)=\sum_{n=1}^{\infty}\int_{\tau_{\min}}^{\tau_{\max}}\ddot{q}_n(t-\tau)\left\{\frac{\rho_0 c}{\pi}\int_0^{\psi_{\max}(c\tau,z)}\phi_n[r_s(R,z,\psi)]_{R=c\tau}d\psi\right\}d\tau \tag{18}$$

Equation (18) shows the sound pressure at the receiver point to be a result of radiation at each mode, which can be written as:

Downloaded 02 May 2010 to 171.66.16.25. Redistribution subject to ASME license or copyright; see http://www.asme.org/terms/Terms_Use.cfm

$$p(r,z,t) = \sum_{n=1}^{\infty} [\ddot{q}_n(t) * p_{in}(r,z,t)]$$

$$R_{\min}/c \leqq t \leqq R_{\max}/c \tag{19}$$

where the modal impulse response function at the nth mode, p_{in}, is given as:

$$p_{in}(r,z,t) = \frac{\rho_0 c}{\pi} \int_0^{\psi_{\max}(R=ct,z)} \phi_n[r_s(R,z,\psi)]_{R=ct} d\psi \tag{20}$$

Equations (18) and (19) can be interpreted as convolution of plate acceleration-time history with the impulse response function, $p_{in}(t)$, at each mode. These results can be obtained using either the convolution integral method [9] or the impulse response approach developed using a Green's function solution [19].

Substituting equations (24) in equation (20) and performing the integration results in the following modal pressure impulse response expressions:

I. When $r > a$:

$$p_{in}(r,z,t) = \frac{\rho_0 c}{\pi\sqrt{2}} \left\{ \sum_{m=0}^{\infty} \epsilon_m J_m(\lambda_n r/a) J_m[\lambda_n (c^2t^2 - z^2)^{1/2}/a] \right.$$

$$\left. /J_0(\lambda_n) - \sum_{m=0}^{\infty} \epsilon_m (-1)^m I_m(\lambda_n r/a) I_m[\lambda_n (c^2t^2 - z^2)^{1/2}/a]/I_0(\lambda_n) \right\}$$

$$\frac{\sin m\psi}{m}, \quad R_{\min} \leqq ct \leqq R_{\max} \tag{25}$$

II. When $r \leqq a$:

$$p_{in}(r,z,t) = \begin{cases} \dfrac{\rho_0 c}{\sqrt{2}} \{ [J_0(\lambda_n r/a) J_0[\lambda_n (c^2t^2 - z^2)^{1/2}/a]/J_0(\lambda_n)] \\ - [I_0(\lambda_n r/a) I_0[\lambda_n (c^2t^2 - z^2)^{1/2}/a]/I_0(\lambda_n)] \}, \quad z \leqq ct \leqq R_{\min} \\ \text{same as equation (25)}, \quad R_{\min} \leqq ct \leqq R_{\max} \end{cases} \tag{26a}$$

It should be noted that the modal impulse response function, $p_{in}(t)$, relates the radiated acoustic pressure to the receiver-source geometry and to the mode shapes of the radiator. Further discussion on modal impulse response will be given later in this paper.

Evaluation of the Modal Impulse Response

The modal impulse response function, given in equation (20), is evaluated by first expressing the mode shape functions $\phi_n(r_s)$ in terms of the receiver coordinates as $\phi_n(R,\psi)$. Using the law of cosines and referring to Fig. 1:

$$r_s^2 = r^2 + R^2 - z^2 - 2r(R^2 - z^2)^{1/2} \cos\psi \tag{21}$$

The values of the angle ψ are defined as:

I. When $r > a$:

$$\psi(R,z) = \cos^{-1}[(R^2 - z^2 + r^2 - a^2)/2r(R^2 - z^2)^{1/2}],$$

$$R_{\min} \leqq ct \leqq R_{\max} \tag{22}$$

II. When $r \leqq a$:

$$\psi(R,z) = \begin{cases} \pi, & z < ct \leqq R_{\min} \\ \cos^{-1}[(R^2 - z^2 + r^2 - a^2)/2r(R^2 - z^2)^{1/2}], \\ R_{\min} \leqq ct \leqq R_{\max} \end{cases} \tag{23}$$

where $R_{\min} = [z^2 + (r-a)^2]^{1/2}$ and $R_{\max} = [z^2 + (r+a)^2]^{1/2}$.

The integration of the Bessel functions with respect to ψ can be simplified by using Neumann's addition theorem [23,24]:

$$J_0(\lambda_n r_s/a) = J_0(\lambda_n r/a) J_0[\lambda_n (R^2 - z^2)^{1/2}/a]$$

$$+ 2 \sum_{m=1}^{\infty} J_m(\lambda_n r/a) J_m[\lambda_n (R^2 - z^2)^{1/2}/a] \cos m\psi \tag{24a}$$

A similar relationship can be obtained for the modified Bessel functions as:

$$I_0(\lambda_n r_s/a) = I_0(\lambda_n r/a) I_0[\lambda_n (R^2 - z^2)^{1/2}/a]$$

$$+ 2 \sum_{m=1}^{\infty} (-1)^m I_m(\lambda_n r/a) I_m[\lambda_n (R^2 - z^2)^{1/2}/a] \cos m\psi \tag{24b}$$

where $\epsilon_0 = 1$ and $\epsilon_m = 2$ for $m \geqq 1$.

The first part of equation (26*a*) is similar to the result for a membrane given in [19]. Since the clamped plate cannot have rigid body motion, the result for a rigid piston, obtained by substituting $\lambda_n = 0$ in equation (26*a*), indicates zero sound pressure.

The acoustic radiation from a clamped plate excited by a transient force such as that given in equation (12) can be found by substituting equations (25) and (26) in the convolution integral given in equation (19).

Results

The transient sound pressure radiated from a clamped plate is obtained by evaluating the convolution for each mode and summing the results numerically. For the numerical examples, the case of radiation from a 0.50 m diameter steel plate of 1.59 mm thickness was used. The magnitude of the excitation force in 134 N with the force-time history given in equation (12).

The plate acceleration response at its midpoint, the pressure impulse response at $z = 0.10$ m on the axis of symmetry, and the resulting modal sound pressure at the same location are shown in Fig. 2 for a number of modes. The total plate acceleration response and sound pressure waveforms are obtained by summing the modal acceleration and sound pressure waveforms for 50 modes, as shown in Fig. 3. The sound pressure waveform in Fig. 3 shows a distinct pressure pulse before the resonant radiation or "ringing" starts. The initial pressure pulse is due to the forced deformation of the plate where the pressure waveform duplicates the plate velocity waveform at the excitation point. There is no sound radiation until the plate bending waves reflect from the plate edge back to the plate center. Since bending waves above the critical frequency radiate toward the direction of propagation, on the axis of symmetry sound pressure from the plate resonant vibrations is realized only after the bending waves reflect from the edge of the plate [21].

The pressure impulse response function is shown in Fig. 4 for the tenth mode at various distances from the center of the plate on its axis of symmetry. It is seen that as the receiver point moves away from the plate surface, the pressure waveform is compressed in time. This time compression is

Downloaded 02 May 2010 to 171.66.16.25. Redistribution subject to ASME license or copyright; see http://www.asme.org/terms/Terms_Use.cfm

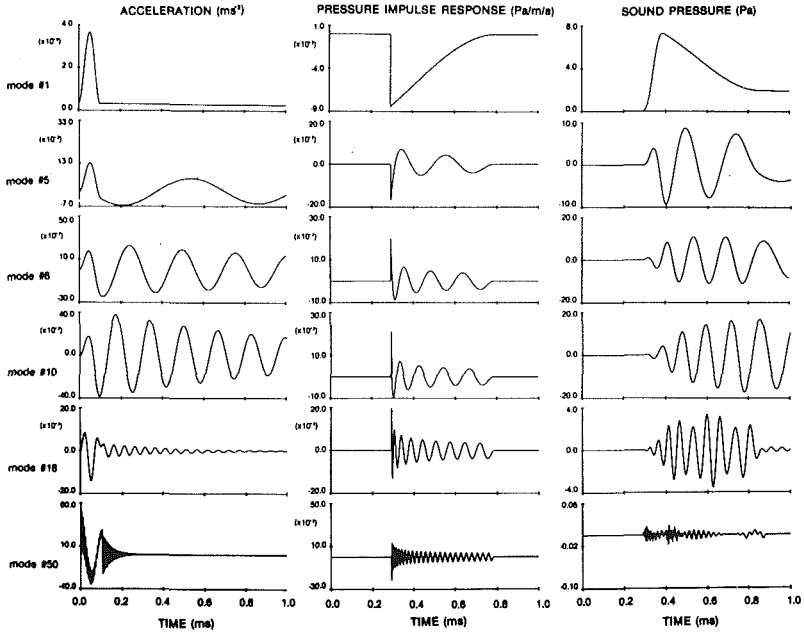

Fig. 2 The modal acceleration response, pressure impulse respone, and corresponding sound pressure radiation for various modes of the plate. $z = 0.10$ m, $\xi = 0.025$.

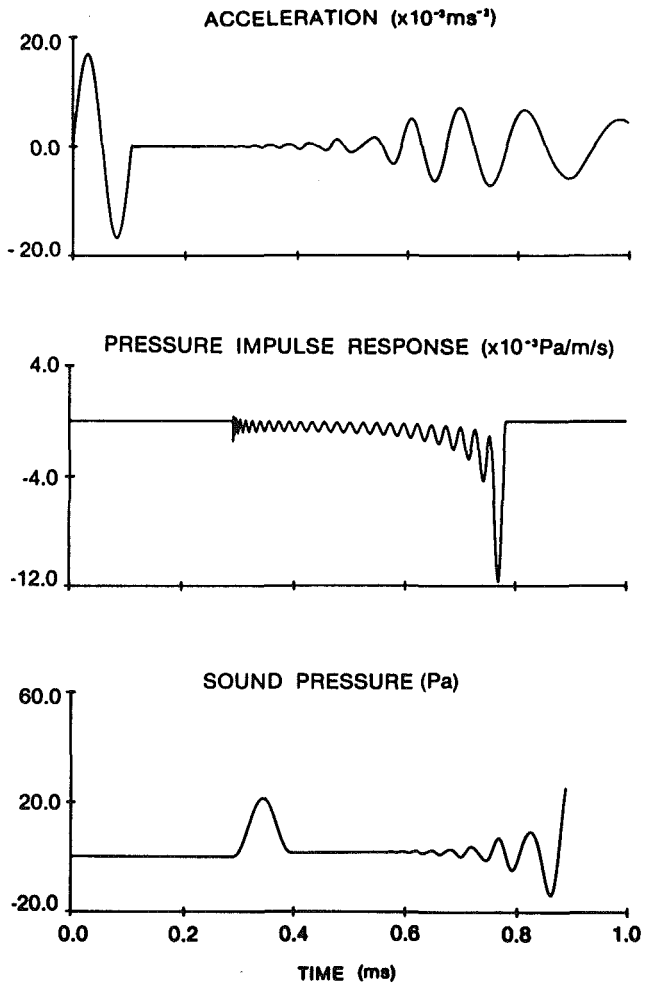

Fig. 3 The plate acceleration, pressure impulse response, and sound pressure obtained using the first 50 modes of the plate. $z = 0.10$ m, $\xi = 0.025$.

pronounced at the start of the waveform. This, of course, is due to the decrease in the difference between the time of arrival of sound waves from various points on the plate surface. Mathematically, it can be seen in the pressure impulse response equations (25) and (26), where the form of the argument, $(c^2 t^2 - z^2)^{1/2}$, leads to the time compression of the waveform. Another implication of this time compression is the inherent change of the frequency content of the pressure impulse response with distance. The sound pressure spectrum is shifted into higher frequencies as the distance from the plate is increased. The transition in the spectrum continues until $z \cong R_{\min}$ in equation (26*a*). When the approximation $z \cong R_{\min}$ is true, the receiver point is said to be in the acoustic far field of the plate. In the far field the spectral content is stable. However, when the receiver point is near the plate, where $z \cong R_{\min}$ is no longer true, lower frequency sound field is apparent in the pressure impulse response waveforms as shown in Fig. 4.

It should be noted that the changes in the pressure impulse waveform and its spectrum with distance are strictly due to the mode shapes and the geometry of the problem. The physical reasoning behind these changes is the interference of the pressure waves from different parts of the plate leading to cancellation at each mode. The results of the convolutions are modified accordingly. Although not shown here, similar time compression effects are also seen in the total sound pressure waveforms.

Summary and Conclusions

A sound pressure impulse response function is developed from the Rayleigh integral for radiation from a clamped plate in an infinite baffle. The time-dependent sound radiation from transient excitation of the plate is then found by a convolution of the plate acceleration waveform with the pressure impulse response. The results of this method are the same as those obtained by direct integration of the Rayleigh integral and experimental results reported earlier [21]. The time-dependent boundary conditions that are necessary for transient radiation when using the Rayleigh integral are in the

Downloaded 02 May 2010 to 171.66.16.25. Redistribution subject to ASME license or copyright; see http://www.asme.org/terms/Terms_Use.cfm

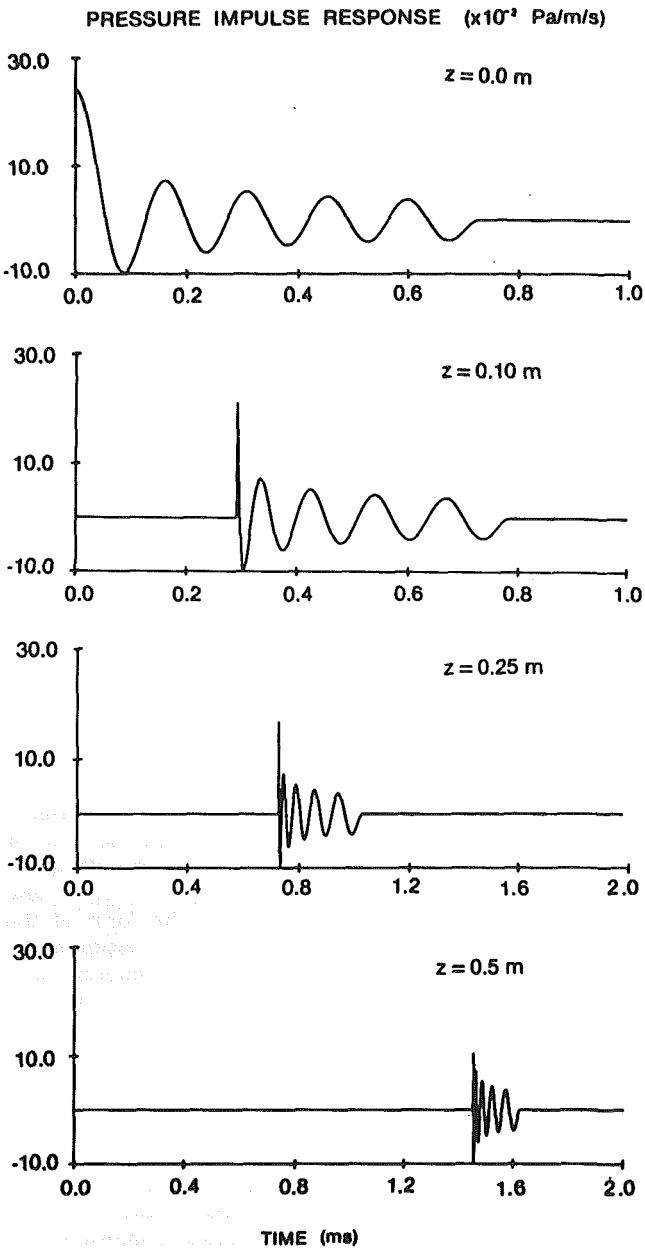

Fig. 4 The tenth modal pressure impulse response at various distances from the plate surface. $\xi = 0.025$.

form of time-dependent integrand and upper integration limit of the convolution integral in the present method.

An examination of the pressure impulse response in equations (25) and (26) reveals its close relationship to the vibration mode shapes and hence to the geometry and the boundary conditions of the plate. Hence, the pressure impulse response function developed here is a spatial phenomenon affecting the temporal domain. The resulting sound pressure radiation is also directly related to the acceleration response of the plate vibrations. The decay in the time history of the plate vibrations and the resulting radiation is a result of the damping of the plate material. In addition to the rate of decay, the damping of the plate material determines the pressure amplitude, particularly if the plate is excited at one of its resonances.

In the present problem formulation the plate vibration is uncoupled from the acoustic radiation, neglecting the fluid-loading effects on the plate. In general, the influence of fluid loading on plate vibrations is to shift the resonant frequencies and alter the mode shapes. The magnitude of the change depends on the frequency and on the nondimensional parameter $\beta = \rho_0 a/\rho h$, where a,h are the plate radius and thickness and ρ_0, ρ are the density of the fluid and the plate material respectively. For values of $\beta < 1$, the effect of fluid loading on the plate due to acoustic radiation is negligible, which is the case for radiation into air from metal plates [25].

The time history of the excitation force applied in the present problem is a smooth pulse without any discontinuities in its slope leading to a smooth acceleration response of the plate. A simple analysis of equation (16) shows that as the duration of the pulse, π/ω_0, is increased, the amplitude of the plate acceleration and therefore the radiation pressure amplitude decreases while shifting the spectrum into low frequencies. For the limiting case of an infinitely long pulse duration ($\omega_0 \to 0$), acoustic pressure amplitude vanishes. On the other hand, as the duration of the excitation force decreases, the radiation spectrum shifts into higher frequencies by virtue of the resonance.

The acoustic radiation from the plate shows characteristics similar to that from a rigid piston; however, in the case of a transiently excited large plate, radiation from the center of the plate reaches the receiver before the waves from the edge arrive. In addition, the amplitude of the vibrations near the restrained edge is usually small compared to the center of the plate where excitation takes place. Therefore, during the initial part of the transient radiation from a point-excited plate, the pressure on the axis of symmetry is dominated by the sound waves induced by the forced vibration of the plate, duplicating the plate velocity response. It is then followed by the resonant radiation from the plate.

The method developed here is applicable to axisymmetric vibrations of circular plates, membranes, and annular rings with various boundary conditions.

Acknowledgment

This work was partly supported by the Wayne State University Development Fund and by the National Science Foundation.

References

1 Magrab, E. B., and Reader, W. T., "Farfield Radiation From an Infinite Elastic Plate Excited by a Transient Point Loading," *Journal of the Acoustical Society of America*, Vol. 44, 1968, pp. 1623–1627.

2 Stuart, A. D., "Acoustic Radiation From a Point Excited Infinite Elastic Plate," Ph.D. Dissertation, The Pennsylvania State University, 1972.

3 Mackertich, S. S., and Hayek, S. I., "Acoustic Radiation From an Impulsively Excited Elastic Plate," *Journal of the Acoustical Society of America*, Vol. 69, 1981, pp. 1021–1028.

4 Nakayama, I., et al., "Insulation Characteristics of a Circular Plate for a Single Sound Pulse," *Japanese Journal of Applied Physics*, Vol. 16, 1977, p. 2285.

5 Nakayama, I., et al., "Transmission Characteristics of a Sound Pulse Through a Circular Plate," *Acustica*, Vol. 40, 1978, p. 40.

6 Nakayama, I., et al., "Transient Radiation Field From an Elastic Circular Plate Excited by a Sound Pulse," *Acustica*, Vol. 46, 1980, pp. 276–282.

7 Nakayama, I., "Sound Insulation of a Circular Plate for a Single Sound Pulse," *Acustica*, Vol. 46, 1980, pp. 330–340.

8 Nakayama, I., and Nakamura, A., "Mechanism of Transient Sound Radiation from a Circular Plate for Impulsive Sound Wave," *Journal of the Acoustical Society of Japan*, Vol. (E)2, 1981, pp. 151–159.

9 Harris, G. R., "Review of Transient Field Theory for a Baffled Planar Piston," *Journal of the Acoustical Society of America*, Vol. 70, 1981, pp. 10–20.

10 Akay, A., "A Review of Impact Noise," *Journal of the Acoustical Society of America*, Vol. 64, 1978, pp. 977–987.

11 Strasberg, M., "Radiation From a Diaphragm Struck Periodically by a Light Mass," *Journal of the Acoustical Society of America*, Vol. 20, 1948, pp. 683–690.

12 Lord Rayleigh, *Theory of Sound*, Vol. II, Section 278, Dover, New York, 1945.

13 King, L. V., "Acoustic Radiation Field of Piezoelectric Oscillation and Effect of Viscosity on Transmission," *Canadian Journal of Research*, Vol. 11, 1934, pp. 135–155.

14 Schoch, A., "Remarks on the Sound Field of a Stiff Diaphragm Moving Like a Piston," *Akust Z.* (in German) Vol. 6, 1941, pp. 318–326.

15 Rutgers, A. J., "Spatial Impulse Response of an Acoustic Line

Downloaded 02 May 2010 to 171.66.16.25. Redistribution subject to ASME license or copyright; see http://www.asme.org/terms/Terms_Use.cfm

Radiator—A Study of Boundary-Diffraction-Wave Phenomena and Their Experimental Detection," Ph.D. Dissertation, 1977, Catholic University of America, Washington, D.C.

16 Stepanishen, P. R., "Transient Radiation From Pistons in an Infinite Planar Baffle," *Journal of the Acoustical Society of America*, Vol. 49, 1971, pp. 1629–1638.

17 Greenspan, M., "Piston Radiator: Some Extensions of the Theory," *Journal of the Acoustical Society of America*, Vol. 65, 1979, pp. 608–621.

18 Harris, G. R., "Transient Field of a Baffled Planar Piston Having Arbitrary Vibration Amplitude Distribution," *Journal of the Acoustical Society of America*, Vol. 70, 1981, pp. 186–204.

19 Stephanishen, P. R., "Acoustic Transients From Planar Axisymmetric Vibrators Using the Impulse Response Approach," *Journal of the Acoustical Society of America*, Vol. 70, 1981, pp. 1176–1181.

20 Tjøtta, J. N., and Tjøtta, S., "Nearfield and Farfield of Pulsed Acoustic Radiators," *Journal of the Acoustical Society of America*, Vol. 71, 1982, pp. 824–834.

21 Akay, A., and Latcha, M., "Sound Radiation from an Impact-Excited Clamped Circular Plate in an Infinite Baffle," *Journal of the Acoustical Society of America*, Vol. 74, 1983 pp. 640–648.

22 Leissa, W. A., "Vibration of Plates," NASA-SP-160, 1969.

23 Gradshteyn, I. S., and Ryzhik, I. M., *Table of Integrals Series and Products*, Academic Press, New York, 1965.

24 Watson, G. N., *A Treatise on the Theory of Bessel Functions*, Cambridge University Press, Cambridge, England, 1944.

25 Lax, M., "The Effect of Radiation on the Vibrations of a Circular Diaphragm," *Journal of the Acoustical Society of America*, Vol. 16, 1944, pp. 5–13.

Downloaded 02 May 2010 to 171.66.16.25. Redistribution subject to ASME license or copyright; see http://www.asme.org/terms/Terms_Use.cfm

C. F. Shih
Mem. ASME

A. Needleman
Mem. ASME

Division of Engineering,
Brown University,
Providence, R.I. 02912

Fully Plastic Crack Problems

Part 1: Solutions by a Penalty Method

We formulate a finite-element reduced integration penalty method applicable to plane-strain problems with incompressible material behavior. This numerical method is employed to generate crack solutions for pure power-hardening solids. For two configurations of interest in applications, an edge cracked panel subject to remote tension and an edge-cracked panel subject to remote bending, we obtain solutions for a wide range of crack lengths and strain-hardening behaviors.

1 Introduction

Recent progress in elastic-plastic fracture mechanics has made possible the development of simplified engineering procedures for assessing the integrity of structrual components from a fracture viewpont [1]. In this paper we continue work within the framework developed in [2–7] which employs an estimation scheme, Shih and Hutchinson [5], to produce relatively accurate formulas for quantities of interest in fracture analysis over the range from small-scale yielding to fully yielded conditions. This estimation procedure requires the availability of elastic and fully plastic solutions to the crack configuration under consideration.

The elastic solutions for a wide variety of crack configurations are tabulated in several handbooks, e.g., Tada, Paris, and Irwin [17]. The required fully plastic solutions have been obtained by finite-element-based methods. However, the conventional displacement finite-element method cannot handle the incompressible deformation associated with the plane strain, axisymmetric, or three-dimensional fully plastic formulation. The first plane-strain fully plastic crack solutions were obtained by Goldman and Hutchinson [4] using a finite-element method for a slightly compressible solid and extrapolating to the incompressible limit. However, this method was not considered to be entirely satisfactory [4]. Subsequently Needleman and Shih [6] developed a finite-element method that could handle fully plastic incompressible plane-strain and axisymmetric problems economically and accurately. This method is based on satisfying the plane-strain incompressibility constraint pointwise by directly eliminating nodal degrees of freedom. The finite-element procedure developed in [6] has been employed in fully plastic crack analyses by Hutchinson, Needleman, and Shih [7], Kumar, German, and Shih [2, 3], and He and Hutchinson [8]. A fairly extensive tabulation of fully plastic solutions is now available in handbook format [2]. We also note that fully plastic solutions are of interest in their own right for application to a class of rate-dependent solids including power-law creeping solids [12, 13].

The numerical procedure developed in [6] is specifically designed for two-dimensional problems and cannot be generalized readily to three dimensions. There are important technical problems which are inherently three-dimensional, for example, surface flaws in plates and shells. It may be possible to utilize fully plastic solutions in conjunction with an estimation scheme for these problems and we therefore seek an alternative numerical method applicable to three-dimensional situations.

Candidate methods include the use of Lagrange multipliers and reduced integration penalty methods (RIP methods), Hughes [18], Malkus [19], and Malkus and Hughes [20], and Song, Oden, and Kikuchi [21]. Each of these has been employed in the analysis of plane-strain fully plastic crack problems with limited success, Parks [9], Yagawa, Aizawa, and Ando [10]. Of these alternatives a RIP method appears particularly attractive in that it permits the use of a standard displacement finite-element code, with only slight modification, and it can be employed as easily in three-dimensional problems as in two-dimensional ones. However, the RIP based methods are marginally stable numerically, Song et al. [21]. Here we develop a RIP method which gives accurate solutions to fully plastic crack problems for a wide range of strain-hardening behaviors.

We confine attention to two-dimensional problems and focus in particular on the problem of an edge-cracked panel subject to either tension or bending. These particular configurations are also of interest in connection with surface flaw problems since Rodin and Parks, [14] have extended the line spring model proposed by Rice [15] to analyze elastic-plastic surface flaw problems. A key component of the elastic-plastic line spring model is the fully plastic solution for a plane-strain, edge-cracked panel subject to combined tension and bending moment. In this regard we note that the solutions for the edge-cracked panel subject to tension and to bending, tabulated in [2, 11], do not possess the smoothness required to pass the consistency check developed by Parks, Kumar, and Shih [16]. Although this alone does not serve to show that the

Contributed by the Applied Mechanics Division for presentation at the 1984 PVP Conference and Exhibition, Joint with the Applied Mechanics Division and Materials Division, San Antonio, Texas, June 17–21, 1984 of THE AMERICAN SOCIETY OF MECHANICAL ENGINEERS.

Discussion on this paper should be addressed to the Editorial Department, ASME, United Engineering Center, 345 East 47th Street, New York, N.Y. 10017, and will be accepted until two months after final publication of the paper itself in the JOURNAL OF APPLIED MECHANICS. Manuscript received by ASME Applied Mechanics Division, May, 1983. Paper no. 84-APM-9

Copies will be available until February, 1985.

Copyright © 1984 by ASME
Downloaded 02 May 2010 to 171.66.16.25. Redistribution subject to ASME license or copyright; see http://www.asme.org/terms/Terms_Use.cfm

tabulated solutions are inaccurate, alternative solutions for these configurations appear worthwhile. The consistency checks of [16] are applied to the present solutions in Part 2.

2 Governing Equations

We employ a small displacement gradient formulation with the strain-displacement relation given by

$$\epsilon_{ij} = \frac{1}{2}\left(\frac{\partial u_i}{\partial x_j} + \frac{\partial u_j}{\partial x_i}\right) \tag{2.1}$$

The strain deviator e_{ij} and stress deviator s_{ij} are introduced via

$$e_{ij} = \epsilon_{ij} - \frac{1}{3}\epsilon_{kk}\delta_{ij} \quad s_{ij} = \sigma_{ij} - \frac{1}{3}\sigma_{kk}\delta_{ij} \tag{2.2}$$

Then with body forces absent the principle of virtual work is written as

$$\int_V \left[s_{ij}\delta e_{ij} + \frac{1}{3}\sigma_{kk}\delta\epsilon_{ll}\right]dV = \int_S T_i \delta u_i dS \tag{2.3}$$

where $T_i = \sigma_{ij}n_j$.

Since the numerical method we employ requires the use of a constitutive relation with some compressibility, a J_2 deformation theory formulation for a compressible elastic-plastic solid will be employed [27]. The incompressible limit will be approached numerically.

The strain is written as the sum of an elastic part, ϵ_{ij}^e, and a volume-preserving plastic part, e_{ij}^p,

$$\epsilon_{ij}^e = \frac{1+\nu}{E}s_{ij} + \frac{1-2\nu}{3E}\sigma_{kk}\delta_{ij} \tag{2.4}$$

$$e_{ij}^p = \frac{3}{2}\left(\frac{1}{E_s} - \frac{1}{E}\right)s_{ij} \tag{2.5}$$

where E is Young's modulus, ν is Poisson's ratio, and E_s is the ratio of stress to strain in uniaxial tension.

Combining (2.4) and (2.5) gives

$$s_{ij} = \frac{E_s}{1+\nu_s}e_{ij} \tag{2.6}$$

$$\sigma_{kk} = \frac{E}{1-2\nu}\epsilon_{kk} \tag{2.7}$$

Here, the effective Poisson's ratio ν_s is given by

$$\nu_s = \frac{1}{2} + \frac{E_s}{E}\left(\nu - \frac{1}{2}\right) \tag{2.8}$$

Since the problems considered here are strongly nonlinear we employ an iterative method. A modified Newton-Raphson method is employed which is based on an expansion of the principle of virtual work (2.3) about a known state. This expansion gives

$$\int_V \left[\dot{s}_{ij}\delta e_{ij} + \frac{1}{3}\dot{\sigma}_{kk}\delta\epsilon_{ll}\right]dV = \int_S \dot{T}_i \delta u_i \, dS$$

$$-\left\{\int_V \left[s_{ij}\delta e_{ij} + \frac{1}{3}\sigma_{kk}\delta\epsilon_{ll}\right]dV - \int_S T_i\delta u_i dS\right\} \tag{2.9}$$

where $\dot{(\ )}$ denotes the deviation from the known state. Equation (2.9) is solved repeatedly for the displacement deviations until a converged solution is obtained. To implement this scheme, the relation between the perturbation deviatoric quantities $\dot{s}$ and $\dot{e}$ is needed. From (2.6) we obtain

$$\dot{s}_{ij} = \frac{E_s}{1+\nu_s}\left[\dot{e}_{ij} - \frac{2}{3}\frac{[1-E_t/E_s]}{[1-(1-2\nu_s)E_t/3E_s]}\frac{e_{ij}e_{kl}}{\bar{\epsilon}^2}\dot{e}_{kl}\right] \tag{2.10}$$

where E_t is the slope of the uniaxial stress-strain curve and

$$\bar{\epsilon}^2 = \frac{2}{3}e_{ij}e_{ij} \tag{2.11}$$

The constitutive relation is completed by specifying the uniaxial stress-strain response. For a piecewise power-hardening relation

$$\frac{\epsilon}{\epsilon_0} = \begin{cases} \dfrac{\sigma}{\sigma_0} & \epsilon < \epsilon_0 \\ \left(\dfrac{\sigma}{\sigma_0}\right)^n & \epsilon \geq \epsilon_0 \end{cases} \tag{2.12}$$

where n is the strain-hardening exponent, ϵ_0 is a given constant, and we make the identification $\sigma_0 = E\epsilon_0$. From (2.12) with $\epsilon \geq \epsilon_0$

$$E_s = E\left(\frac{\epsilon}{\epsilon_0}\right)^{1/n-1} = E\left(\frac{\sigma}{\sigma_0}\right)^{1-n} \tag{2.13}$$

$$E_t = \frac{1}{n}E\left(\frac{\epsilon}{\epsilon_0}\right)^{1/n-1} = \frac{1}{n}E\left(\frac{\sigma}{\sigma_0}\right)^{1-n} \tag{2.14}$$

The constitutive relation described here is a consistent implementation of elastic-plastic J_2 deformation theory. However, to exploit the scaling properties of fully plastic solutions, our focus is on the pure power-hardening incompressible limit. The incompressible limit is approached by employing a value of Poisson's ratio near 0.5, we have used $\nu = 0.499$ in the calculations we will report on here. We then use the reduced/selective integration method described in the following section. To obtain pure power-hardening behavior with $n > 1$ it is necessary to ensure that all strains are greater than ϵ_0. In typical crack problems, negligible or vanishing strains occur near the crack flank so that some material points have strains less than ϵ_0. Even though the deformations in this zone have little or no effect on quantities of interest, the discontinuous tangent modulus at ϵ_0 has an adverse effect on the convergence of the Newton-Raphson iterative scheme.

For $n > 1$ we employ the modified uniaxial stress-strain relation

$$\frac{\epsilon}{\epsilon_0} = \frac{n}{n-1} - \left[\frac{1+n^2}{(n-1)^2} - \left(\frac{\sigma}{\sigma_0} + \frac{1}{n-1}\right)^2\right]^{1/2}, \quad \epsilon < \epsilon_0 \tag{2.15}$$

which gives a continuous stress, secant modulus, E_s, and tangent modulus, E_t, at ϵ_0. This function is also well behaved at $\epsilon = 0$. The relation (2.15) in conjunction with pure power hardening for $\epsilon > \epsilon_0$ satisfies the continuity conditions governing uniform quadratic convergence of the Newton-Raphson method [23].

Within the context of deformation theory plasticity, Rice [24] introduced the path-independent line integral defined by

$$J = \int_\Gamma (Wn_1 - \sigma_{ij}n_j u_{i,1})ds \tag{2.16}$$

where Γ is any counterclockwise contour surrounding the crack tip, n_i is the outward unit normal to Γ, ds is the arc length along Γ, and W is the strain energy density given by

$$W(\epsilon_{kl}) = \int_0^{\epsilon_{kl}} \sigma_{ij}d\epsilon_{ij} \tag{2.17}$$

An alternate and equivalent definition of J is the energy release rate per unit advance of the crack in its plane (per unit thickness). Hutchinson [25] and Rice and Rosengren [26] also showed that J is the amplitude of what is now called the HRR singularity field. These key papers led to the development of

Downloaded 02 May 2010 to 171.66.16.25. Redistribution subject to ASME license or copyright; see http://www.asme.org/terms/Terms_Use.cfm

nonlinear fracture mechanics [27], where J is the parameter of primary interest. We will employ the line-integral expression of J (2.16) and the energy release rate definition in subsequent analyses.

3 Numerical Implementation

Finite-Element Formulation. We confine attention to plane-strain deformations and employ quadratic isoparametric elements. The full Lagrangian shape functions are necessary for approaching the incompressible limit, Malkus and Hughes [20]. In isoparametric (η_1, η_2) $(-1 \leq \eta_i \leq 1, i = 1, 2)$ space the shape functions are constructed from the three basic functions

$$f_1 = -\frac{1}{2}\eta(1-\eta), \quad f_2 = (1-\eta)(1+\eta), \quad f_3 = \frac{1}{2}\eta(1+\eta) \tag{3.1}$$

via

$$N_{3J+I-3} = f_I(\eta_1) f_J(\eta_2) \quad I,J = 1,2,3 \tag{3.2}$$

Then the coordinates (x_1, x_2) in the physical space and the displacements (u_1, u_2) are written as

$$x_1 = \sum_{K=1}^{9} N_K X_{2K-1}, \quad x_2 = \sum_{K=1}^{9} N_K X_{2K} \tag{3.3}$$

$$u_1 = \sum_{K=1}^{9} N_K U_{2K-1}, \quad u_2 = \sum_{K=1}^{9} N_K U_{2K} \tag{3.4}$$

where $\mathbf{X}$ is the vector of nodal coordinates and $\mathbf{U}$ is the vector of nodal displacements.

The deviatoric and volumetric terms in the volume integrals (area integrals in plane strain) in (2.9) are evaluated separately; 3×3 Gaussian integration is employed for the deviatoric terms. For a particular element the deviatoric term on the left-hand side of (2.9) is written as

$$\int_{\text{elem}} \dot{s}_{ij}\delta e_{ij} dA$$

$$= \dot{\mathbf{U}}^{\mathbf{T}}\left[\sum_{\alpha=1}^{9} \{\mathbf{B}^T(\mathbf{J}^{-1})^T\mathbf{L}\mathbf{J}^{-1}\mathbf{B} \det(\mathbf{J})\}_\alpha w_\alpha\right]\delta\mathbf{U} \tag{3.5}$$

where $\mathbf{J}$ is the Jacobian matrix of the transformation (3.3), $\mathbf{B}$ is the strain-displacement matrix for the deviatoric strains calculated from (3.4), the moduli $\mathbf{L}$ are constructed from (2.10), w_α are the Gauss weights, and det(J) denotes the determinant of $\mathbf{J}$.

The volumetric terms are evaluated using 2×2 Gaussian integration giving

$$\int_{\text{elem}} \frac{1}{3}\dot{\sigma}_{kk}\delta\epsilon_{ll} dA$$

$$= \dot{\mathbf{U}}^T\left[\sum_{\alpha=1}^{4} \left\{\mathbf{b}(\mathbf{J}^{-1})^T \frac{E}{3(1-2\nu)} \mathbf{J}^{-1}\mathbf{b} \det(\mathbf{J})\right\}_\alpha w_\alpha\right]\delta\mathbf{U} \tag{3.6}$$

Here, $\mathbf{b}$ denotes the volumetric strain-displacement matrix.

Following standard procedures, Zienkiewicz [22], the element stiffness matrix, and load vector are evaluated. The linear algebraic equations resulting from (2.9) are then solved for the displacement perturbations. Once a converged solution is obtained the deviatoric stresses can readily be computed at the 3×3 Gauss points. The hydrostatic stress is most accurately computed at the 2×2 Gauss points. However, for subsequent calculations, e.g., calculation of the J-integral [24], the hydrostatic stress and deviatoric stresses are required at the same points. A direct calculation of the hydrostatic stress at the 3×3 Gauss points gives strongly oscillating values. We use Lagrangian bilinear shape functions in conjunction with the values of hydrostatic stress at the four 2×2 Gauss points to determine the hydrostatic stress throughout the element. This gives a reasonably smooth representation of the hydrostatic stresses.

Parameter Tracking. The Newton-Raphson method converges quadratically if the initial estimate of the solution is sufficiently close to the actual solution [23]. A systematic method for generating sufficiently close initial estimates is by parameter tracking. The nonlinearity of the equations (2.9) is governed by the strain-hardening exponent n; the degree of nonlinearity increases as n increases. The procedure begins with solving the equations (2.9) for $n = 1$, i.e., the linear elastic problem. An appropriately scaled elastic solution is then chosen as the initial estimate of the solution for $n = 2$. The converged solution for $n = 2$ is scaled and then used to start the iterations for the $n = 3$ problem and so forth. This procedure produces close enough estimates of the actual solution so that the Newton-Raphson method converges in five to seven iterations. Generally it requires three to four iterations to bring the normalized error down to about 10^{-2}. At this point, the convergence becomes quadratic and a Euclidean error norm of about 10^{-6} is reached in about two or three more iterations. Convergent solutions for n values of up to 20 have been obtained using this procedure. Without the tracking procedure, we were unable to obtain convergent solutions beyond $n = 3$.

***J*-integral Evaluation.** We employ the line-integral expression (2.16) to calculate the value of J. The integration paths are taken to be along either the η_1 axis or the η_2 axis. Consider a single element and let P_1 and P_2 denote the mapping functions for an elemental length $d\eta_1$ along the η_1 axis $(\eta_2 = 0)$ defined by

$$dx_1 = P_1 d\eta_1, \quad dx_2 = P_2 d\eta_1 \tag{3.7}$$

From (3.3) and (3.7)

$$P_1 = \sum_{K=1}^{9} \frac{\partial N_K(\eta_1, \eta_2 = 0)}{\partial \eta_1} X_{2K-1},$$

$$P_2 = \sum_{K=1}^{9} \frac{N_K(\eta_1, \eta_2 = 0)}{\partial \eta_1} X_{2K} \tag{3.8}$$

Similarly let R_1 and R_2 be the mapping functions along η_2 axis $(\eta_1 = 0)$ defined by

$$dx_1 = R_1 d\eta_2, \quad dx_2 = R_2 d\eta_2 \tag{3.9}$$

Then,

$$R_1 = \sum_{K=1}^{9} \frac{\partial N_K(\eta_1 = 0, \eta_2)}{\partial \eta_2} X_{2K-1},$$

$$R_2 = \sum_{K=1}^{9} \frac{\partial N_K(\eta_1 = 0, \eta_2)}{\partial \eta_2} X_{2K} \tag{3.10}$$

The contribution to J from integrating along the η_1 axis $(\eta_2 = 0)$ is given by

$$\Delta J = \sum_{i=1}^{3} w_i \left\{\left(W - \sigma_{11}\frac{\partial u_1}{\partial x_1} - \sigma_{21}\frac{\partial u_2}{\partial x_1}\right)P_2 + \left(\sigma_{12}\frac{\partial u_1}{\partial x_1} + \sigma_{22}\frac{\partial u_2}{\partial x_1}\right)P_1\right\}_i \tag{3.11}$$

Here, w_i are the appropriate Gauss weights and the quantities within $\{\ \}_i$ are evaluated at the respective Gauss points. The summation ranges from one to three since a path traversing

Downloaded 02 May 2010 to 171.66.16.25. Redistribution subject to ASME license or copyright; see http://www.asme.org/terms/Terms_Use.cfm

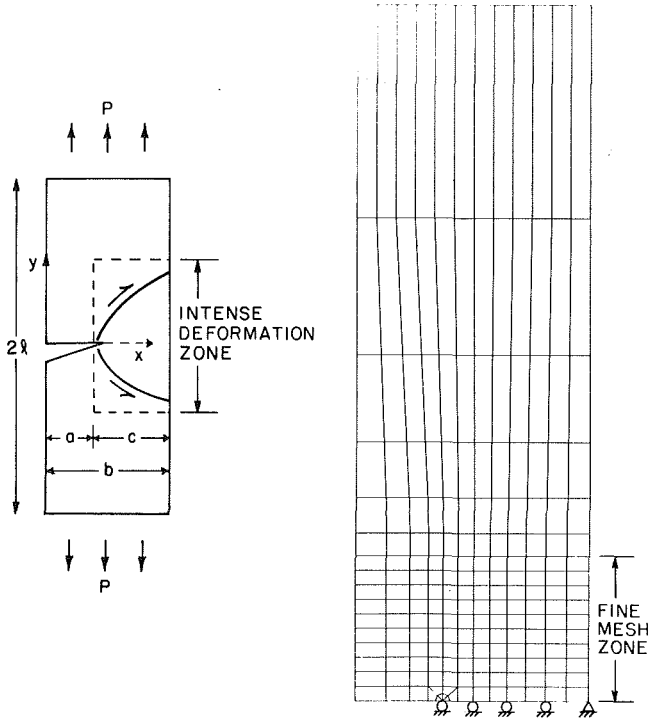

Fig. 1 Sketch of the edge-cracked panel subject to remote tension illustrating the slip-line field [15] and the finite-element mesh for the upper half of the panel

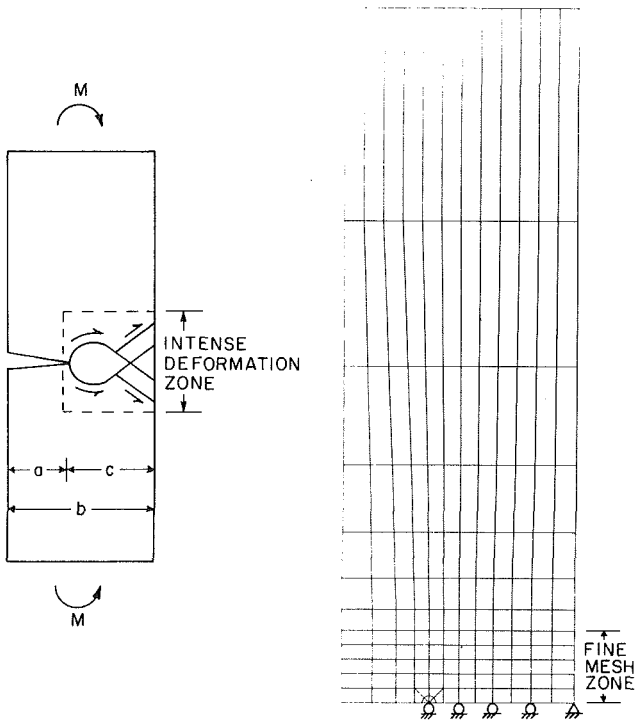

Fig. 2 Sketch of the edge-cracked panel subject to remote moment illustrating the slip-line field [28] and the finite-element mesh for the upper half of the panel

through an element passes through three Gauss points. When the integration path is taken along the η_2 axis then P_1 and P_2 in (3.11) are replaced by R_1 and R_2, respectively.

At certain positions along the integration path, it may become necessary to make a 90 deg turn at the center Gauss point ($i = 2$) by switching over to the other axis. In this case the lengths dx_1 and dx_2 associated with the second Gauss point are approximated by

$$dx_1 = \frac{1}{2}(P_1 d\eta_1 + R_1 d\eta_2), \quad dx_2 = \frac{1}{2}(P_2 d\eta_1 + R_2 d\eta_2) \quad (3.12)$$

The usual weights w_i are still applicable at all three Gauss points. By summing the contributions from all the Gauss points on an integration path, the value of J is obtained.

Mesh Design. We have previously mentioned the relevance of the edge-cracked panel (ECP) configuration to surface flaw analyses. The ECP configuration is also an important geometry in two-dimensional crack analyses. This configuration or a slight modification of it is frequently employed for fracture toughness measurements. We carried out several preliminary calculations for the edge-cracked panel subject to remote tension (this configuration will be designated as ECPT) and for the same panel subject to remote moment (ECPM). For the nonlinear cases ($n > 1$) it became obvious that a single mesh design was not appropriate for both configurations.

Large strain gradients develop in the vicinity of the crack tip and in the vicinity of the relevant slip-line fields which are shown schematically in Figs. 1 and 2. These large strain gradients can be accommodated by mesh refinement in the indicated zones. It is important to note that the size of the intense deformation zone is configuration-dependent. Hence it is essential that the mesh design be guided by the relevant slip-line fields.

The mesh generator we employ generates three distinct zones, namely, the near-tip zone, the ligament zone, and the remote zone. The near-tip zone consists of several layers of circular rings of elements which are centered about the crack-tip. The elements in the first ring are wedge-shaped, i.e., one edge of the element is shrunk to a point that coincides with the crack-tip location. Consequently, each element has three nodes at the crack-tip location. In an elastic analysis ($n = 1$), the nodes at the crack tip are tied together, and therefore they displace as a single node, while the midside nodes along the radial edges and the center node are placed at the respective quarter-positions. In a nonlinear analysis ($n > 1$), the nodes at the crack tip are free to displace independently and the midside nodes and the center node are left at their usual midpositions. These element-nodal arrangements yield displacement gradients containing $1/\sqrt{r}$ and $1/r$ terms, respectively, [29, 30]. In this regard, the latter displacement gradients are only appropriate for perfectly plastic bodies. Nevertheless, crack-tip fields obtained from strain-hardening analyses based on the latter element-node arrangement agreed favorably with the HRR singularity fields [31].

The extent of the refined mesh or ligament zone is determined by the relevant slip-line field. Elements in this zone have aspect ratios close to unity and the angles of the four corners are usually right angles. The typical element size is 1/15 of the ligament or crack length. In the remote zone, elements may have aspect ratios of up to 10. These features are reflected in the meshes shown in Figs. 1 and 2. The fully plastic results presented in this paper are obtained from meshes similar to these; however there are about four times as many elements in the near-tip zone and ligament zone.

Guided by the preceding factors, meshes were generated for the ECPT and ECPM configurations for crack length to width ratios, a/b, of 1/8, 1/4, 3/8, 1/2, 5/8, 3/4, and 7/8. The finite-element elastic solutions for J, the crack-opening displacement at the edge of the panel, δ, and the remote displacement (due to the crack), Δ_c, for all geometries are within 1 percent of the respective values given in [17]. Thus our meshes were more than adequate for elastic analyses.

Next, we carried out an evaluation of the 1/8, 3/8, and 3/4 geometries for $n > 1$ by systematically adjusting the mesh refinement and element aspect ratio. As the aspect ratio of the

Downloaded 02 May 2010 to 171.66.16.25. Redistribution subject to ASME license or copyright; see http://www.asme.org/terms/Terms_Use.cfm

elements in the ligament zone is allowed to deviate more and more from unity, the values of J (3.11) associated with paths passing through the affected elements become increasingly path-dependent. The path dependence increases in severity as the problem becomes more nonlinear. This path dependence of J is due to mesh inadequacies since the plasticity formulation employed in this paper requires that J be path-independent [24]. We employed the path-independent property of J as a criterion to evaluate and improve our meshes.

4 Fully Plastic Solutions

The configurations considered here are depicted in Fig. 1, the edge-cracked panel subject to tension (ECPT), and in Fig. 2, the edge-cracked panel subject to a bending moment (ECPM). For both geometries, a, b, and c are the crack length, width, and ligament length, respectively. The total length of the specimens is $2l$. The finite-element calculations are carried out with $l/b = 3$, since previous numerical analyses [1–10] have shown that this is sufficient to eliminate any dependence of quantities of interest on l. Hence the numerical results are regarded as those pertaining to the infinite panel limit.

In each case the relevant load quantity (traction or moment) is taken to be prescribed. The boundary value problem is solved by the finite-element method described previously. The numerical results are then used to calculate values for the J-integral, the work conjugate (generalized) displacement to the applied load, and certain crack-opening displacements. In particular, for the two configurations considered here the crack-opening displacement at the edge of the panel, defined by

$$\delta = u_y(0,0^+) - u_y(0,0^-) \tag{4.1}$$

is calculated. With this choice of axes the crack tip is at $x = a$.

Also it is convenient to identify the contribution, arising from the presence of a crack, to various displacement quantities. For a given configuration we presume the displacement of the uncracked body, q_{nc}, is known. The numerical results give the total displacement, q. Then the displacement arising from the presence of the crack, q_c, is defined by

$$q_c = q - q_{nc} \tag{4.2}$$

Solutions for the ECPT Configuration. Uniform traction σ_{yy} is imposed on the ends so that the load per unit thickness carried by the panel is

$$P = b\sigma_{yy}(x, \pm l) \tag{4.3}$$

The load-point displacement Δ is defined by

$$\Delta(l) = \frac{1}{b}\int_0^b [u_y(x,l) - u_y(x,-l)]dx \tag{4.4}$$

where u_y is the displacement in the y direction.

In the absence of a crack, the load point displacement is

$$\Delta_{nc}(l) = \sqrt{3}\alpha\epsilon_0 l\left[\frac{\sqrt{3}P}{2b\sigma_0}\right]^n \tag{4.5}$$

where α is a material constant to be defined shortly. The load-point displacement due to the presence of the crack Δ_c is calculated using (4.2).

The panel undergoes a relative rotation at its ends given by

$$\theta(l) = \frac{2}{b}\int_0^b [u_y(x,l) - \Delta(l)/2]/(b/2 - x)\,dx \tag{4.6}$$

Since $\theta_{nc}(l)$ is always zero for this configuration, $\theta_c = \theta$.

Following [2], we define the reference load per unit thickness as

$$P_0 = \left(\frac{2}{\sqrt{3}}\right)1.26\eta\, c\sigma_0 \tag{4.7}$$

where $c = b - a$ and η is given by

$$\eta = \sqrt{1 + (a/c)^2} - a/c \tag{4.8}$$

For the rigid-perfectly plastic panel ($n \to \infty$), P_0 is the limit load provided that 1.26η is the correct plastic crack constraint factor. Using the normalization introduced in [2, 4, ,5, 7], we write

$$J = \alpha\sigma_0\epsilon_0 c(a/b)h_1(a/b,n)\,(P/P_0)^{n+1} \tag{4.9}$$

$$\delta = \alpha\epsilon_0 a\, h_2(a/b,n)\,(P/P_0)^n \tag{4.10}$$

$$\Delta_c = \alpha\epsilon_0 a\, h_3(a/b,n)\,(P/P_0)^n \tag{4.11}$$

$$\theta_c = \alpha\epsilon_0\, h_5(a/b,n)\,(P/P_0)^n \tag{4.12}$$

Here h_1, h_2, h_3, and h_5 are dimensionless functions of a/b and n. The parameter α arises from using the relation $\epsilon/\epsilon_0 = \alpha(\sigma/\sigma_0)^n$ as the representation of the uniaxial pure power law. Fully plastic crack solutions for this stress-strain representation are employed in the estimation procedures [2, 3, 5].

With a mesh having 338 elements and 1431 nodes the time per iteration is about 10 CPU min on a VAX-11/780 computer. All the results presented in this paper are obtained with this refined mesh. For purposes of comparison several calculations using the finite-element program developed in [6] were carried out. Using the same mesh, i.e., identical nodal points (and not one of the meshes shown in Figs. 1 and 2), both programs gave nearly identical results and required comparable CPU times, with the precise comparison of CPU times depending on details of the implementation. For example, the higher-order element method benefits more from a skyline matrix solver than does the low-order element based approach of [6].

For all the geometries considered, the elastic ($n = 1$) values of the h_i calculated by the present finite-element method are within 1 percent of the values given in [17]. For $n > 1$, direct checks of the accuracy of the solutions are not possible. However consistency checks [16] are applied to these solutions in Part 2. Here we note that values of the J-integral computed using paths that traverse within the crack-tip zone, ligament zone, and remote zone exhibit no more than 2 percent variations except for the path nearest the crack tip where larger variations occur. Typically, two paths are taken within the crack-tip zone, ten paths traverse primarily within the ligament zone and five paths traverse the remote zone; h_1 is given by the average of the values from all the paths.

Calculated values of the h_i are given in Table 1 where the $n = 1$ values are our actual calculated results. In the range $1 \le n \le 10$ these values differ by as much as 100 percent from those in [2]. For $n > 10$, the differences are as great as 500 percent. These disagreements are substantial and therefore we defer discussion to Part 2 where the consistency check will be applied to both sets of results. The data points for h_1 and h_3 plotted against $1/n$ for $a/b = 1/8$, $1/4$, $3/8$, $1/2$, and $3/4$ are shown in Fig. 3; the solid lines are obtained by cubic spline interpolation of the tabulated values [23]. In Fig. 4, h_1 is shown as a function of relative crack length for several values of n. Calculations related to the stability of crack growth involve evaluating the rate of change of J with respect to crack length [1–3].

The aim of the normalization is to obtain slowly varying functions with respect to a/b and n, and therefore to permit accurate interpolation and extrapolation with respect to the tabulated values. It is clear from Fig. 4 that the normalization (4.9)–(4.12) is only partially successful. The ratio of the largest to the smallest values of the h_i is about 10^3. In the range $1/8 \le a/b \le 3/8$, the functions vary rather rapidly;

Downloaded 02 May 2010 to 171.66.16.25. Redistribution subject to ASME license or copyright; see http://www.asme.org/terms/Terms_Use.cfm

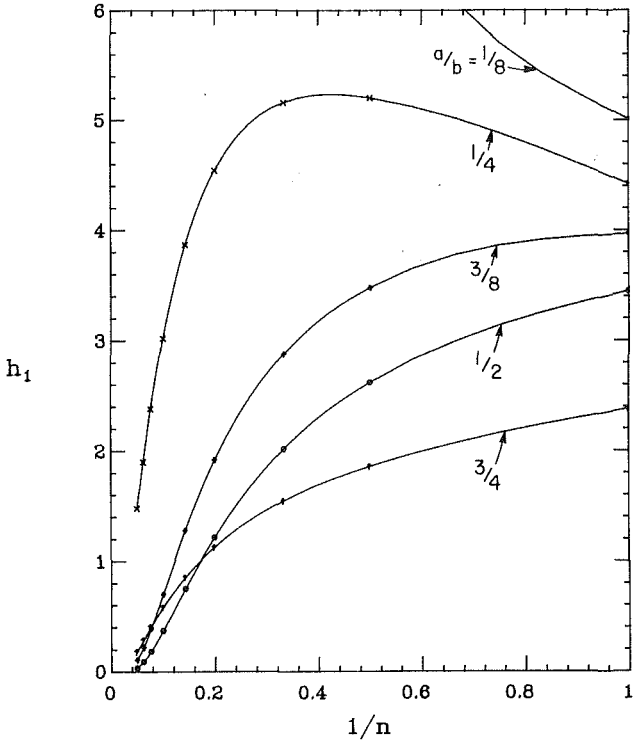

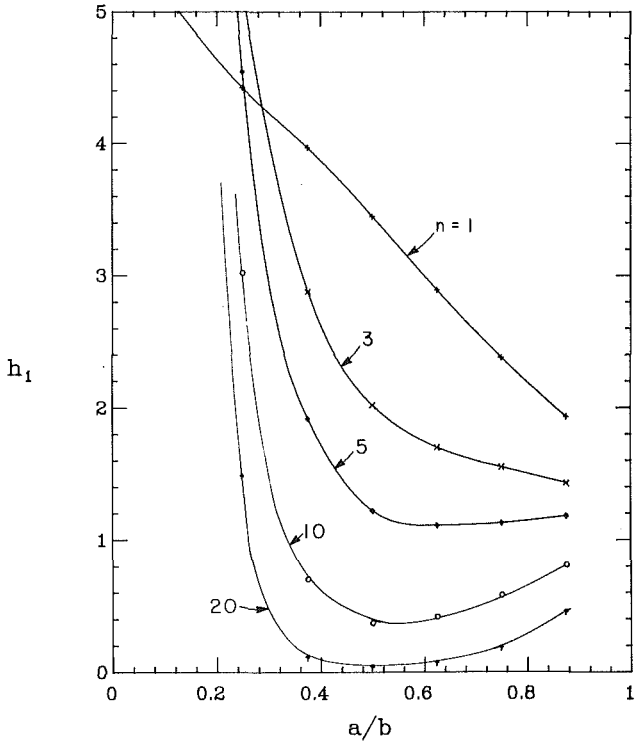

Fig. 4 Normalized *J*-integral as a function of *a*/*b* for various values of strain-hardening exponent *n* for the edge-cracked panel in tension

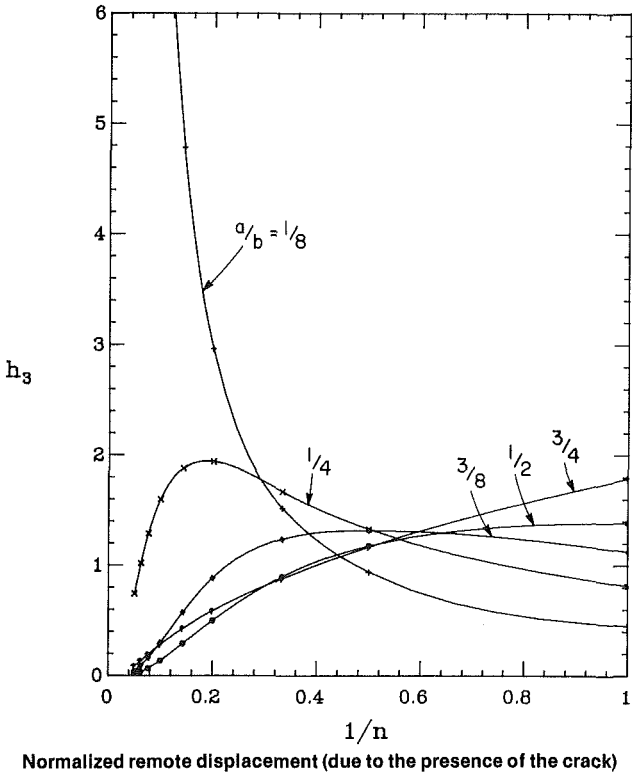

Fig. 3 Fully plastic solutions for the edge-cracked panel subject to remote tension

consequently interpolation or extrapolation based on these values may not be quite accurate.

Solutions for ECPM Configuration. These stress distribution associated with pure bending of the uncracked panel is imposed on the ends $y = \pm l$. The resultant moment of the stresses per unit thickness is

$$M = -\int_0^b \sigma_{yy}(x,l)\, x\, dx \tag{4.13}$$

Let the load-point rotation $\theta(l)$ be the work conjugate to M. Then

$$M\theta(l) = 2\int_0^b \sigma_{yy}(x,l)\, u_y(x,l)\, dx \tag{4.14}$$

where u_y is the displacement in the y direction. In the absence of the crack, the rotation at the ends is given by

$$\theta_{nc}(l) = \frac{2\sqrt{3}\alpha\epsilon_0 l}{b}\left[\left(\frac{2n+1}{n}\right)\frac{\sqrt{3}M}{\sigma_0 b^2}\right]^n \tag{4.15}$$

The rotation due to the presence of the crack θ_c is evaluated via (4.2).

For short cracks, i.e., $a/b \leq 1/4$, θ and θ_{nc} are comparable in magnitude. Since θ_c via (4.2) is given by the difference of two approximately equal quantities, small errors in θ are magnified in θ_c for short crack geometries. The discrete mesh is the principal source of this error. To minimize this mesh effect, fully plastic calculations for the uncracked panel were carried out employing meshes similar to those used for the short crack geometries. From the uncracked panel solutions, the rotation θ_{nc} is defined by

$$M\theta_{nc}(l) = 2\int_0^b \sigma_{yy}(x,l) u_y(x,l) dx \tag{4.16}$$

We apply the principle of virtual work, where the integration is performed over the entire geometry, to obtain values for both θ (4.14) and for θ_{nc}. Using (4.16), θ_c, calculated via (4.2), involves quantities that contain comparable discretization errors.

We define the reference moment per unit thickness by

$$M_0 = 0.364\sigma_0 c^2 \tag{4.17}$$

This is the limit moment of a perfectly plastic panel as long as

Downloaded 02 May 2010 to 171.66.16.25. Redistribution subject to ASME license or copyright; see http://www.asme.org/terms/Terms_Use.cfm

Table 1 *h* functions for edge-cracked panel subject to tension

		$n=1$	$n=2$	$n=3$	$n=5$	$n=7$	$n=10$	$n=13$	$n=16$	$n=20$
$a/b=0.125$	h_1	5.01	7.17	9.09	12.7	16.3	21.7	27.3	34.1	45.2
	h_2	5.34	6.72	8.02	10.6	13.2	17.2	21.3	26.3	33.3
	h_3	0.453	0.943	1.52	2.96	4.78	8.16	12.3	17.3	23.5
	h_5	0.307	0.573	0.847	1.39	1.89	2.45	2.78	3.08	3.42
$a/b=0.250$	h_1	4.42	5.20	5.16	4.54	3.87	3.02	2.38	1.90	1.48
	h_2	4.88	5.10	4.86	4.07	3.35	2.51	1.92	1.50	1.11
	h_3	0.816	1.33	1.67	1.94	1.88	1.60	1.29	1.02	0.744
	h_5	0.978	1.27	1.27	1.05	0.828	0.579	0.412	0.301	0.207
$a/b=0.375$	h_1	3.97	3.48	2.88	1.92	1.28	0.704	0.396	0.225	0.111
	h_2	4.64	3.70	2.88	1.78	1.12	0.591	0.325	0.182	0.0857
	h_3	1.13	1.32	1.24	0.886	0.576	0.301	0.165	0.0927	0.0438
	h_5	1.78	1.49	1.17	0.715	0.442	0.226	0.122	0.0677	0.0317
$a/b=0.500$	h_1	3.45	2.62	2.02	1.22	0.754	0.373	0.188	0.0952	0.0391
	h_2	4.48	2.99	2.13	1.18	0.691	0.331	0.164	0.0821	0.0334
	h_3	1.39	1.18	0.900	0.499	0.292	0.138	0.0682	0.0340	0.0138
	h_5	2.55	1.72	1.23	0.683	0.402	0.193	0.0962	0.0482	0.0196
$a/b=0.625$	h_1	2.89	2.16	1.70	1.11	0.744	0.420	0.243	0.142	0.0710
	h_2	4.39	2.76	1.99	1.19	0.764	0.419	0.238	0.138	0.0681
	h_3	1.61	1.12	0.808	0.478	0.305	0.166	0.0942	0.0544	0.0268
	h_5	3.20	2.03	1.47	0.886	0.573	0.316	0.180	0.104	0.0517
$a/b=0.750$	h_1	2.38	1.86	1.55	1.13	0.858	0.585	0.409	0.290	0.186
	h_2	4.31	2.74	2.07	1.39	1.01	0.670	0.459	0.322	0.205
	h_3	1.79	1.17	0.881	0.589	0.428	0.283	0.194	0.136	0.0861
	h_5	3.69	2.35	1.79	1.20	0.878	0.581	0.399	0.280	0.178
$a/b=0.875$	h_1	1.93	1.62	1.43	1.18	1.00	0.812	0.672	0.563	0.452
	h_2	4.30	2.82	2.24	1.68	1.37	1.07	0.867	0.717	0.568
	h_3	1.97	1.30	1.03	0.772	0.629	0.491	0.398	0.329	0.261
	h_5	4.06	2.67	2.12	1.59	1.29	1.01	0.820	0.678	0.538

Table 2 *h* functions for edge-cracked panel subject to moment

		$n=1$	$n=2$	$n=3$	$n=5$	$n=7$	$n=10$	$n=13$	$n=16$	$n=20$
$a/b=0.125$	h_1	1.03	1.15	1.28	1.56	1.87	2.42	3.11	3.97	5.48
	h_2	7.46	8.41	9.33	11.2	13.2	16.8	21.3	26.8	36.5
	h_3	0.417	0.692	1.02	1.85	2.89	4.95	7.69	11.2	17.6
$a/b=0.250$	h_1	1.40	1.37	1.36	1.34	1.32	1.29	1.26	1.23	1.21
	h_2	6.35	5.91	5.64	5.24	4.95	4.63	4.40	4.23	4.07
	h_3	1.23	1.59	1.87	2.19	2.32	2.33	2.27	2.19	2.10
$a/b=0.375$	h_1	1.54	1.42	1.34	1.22	1.13	1.02	0.942	0.882	0.821
	h_2	5.68	4.66	4.06	3.33	2.90	2.49	2.23	2.05	1.88
	h_3	2.10	2.25	2.25	2.06	1.82	1.57	1.40	1.28	1.17
$a/b=0.500$	h_1	1.59	1.43	1.33	1.18	1.09	0.992	0.923	0.869	0.813
	h_2	5.23	3.95	3.30	2.65	2.32	2.03	1.85	1.72	1.58
	h_3	2.89	2.63	2.36	1.94	1.70	1.49	1.36	1.26	1.16
$a/b=0.625$	h_1	1.59	1.42	1.31	1.17	1.08	0.988	0.919	0.866	0.810
	h_2	4.93	3.52	2.91	2.35	2.07	1.81	1.65	1.53	1.41
	h_3	3.53	2.81	2.38	1.93	1.70	1.49	1.36	1.26	1.16
$a/b=0.750$	h_1	1.58	1.41	1.30	1.17	1.08	0.984	0.915	0.862	0.805
	h_2	4.69	3.24	2.68	2.16	1.90	1.67	1.52	1.41	1.30
	h_3	3.99	2.88	2.39	1.93	1.70	1.49	1.36	1.26	1.16
$a/b=0.875$	h_1	1.58	1.40	1.30	1.16	1.07	0.973	0.902	0.847	0.788
	h_2	4.49	3.04	2.50	2.02	1.77	1.55	1.41	1.30	1.20
	h_3	4.25	2.89	2.38	1.92	1.69	1.47	1.34	1.24	1.14

a/b is sufficiently large [28]. Adopting the normalizations in [5, 7], we have

$$J = \alpha\sigma_0\epsilon_0 c\, h_1(a/b,n)\,(M/M_0)^{n+1} \tag{4.18}$$

$$\delta = \alpha\epsilon_0 a\, h_2(a/b,n)\,(M/M_0)^n \tag{4.19}$$

$$\theta_c = \alpha\epsilon_0\, h_3(a/b,n)\,(M/M_0)^n \tag{4.20}$$

Values of h_1, h_2, and h_3 are given in Table 2. The elastic ($n = 1$) values are within 1 percent of the values given in [17].

For $a/b = 1/8$ the values of h_i are rather large. This stems from the fact that the Green and Hundy limit load [28], from which the reference moment (4.17) is defined, is applicable for relative crack sizes, a/b, greater than about 1/4. Thus (4.17) is a poor choice for $a/b < 1/4$ and this is reflected in the tabulated values. A reference load that is valid for all relative crack sizes would be very useful for normalizing the solutions. In any case, the present choice of M_0 is adequate for $a/b \geq 1/4$. In this range the values of the h functions are of order unity. Furthermore for fixed values of n, the h_i vary slowly with a/b for $a/b \geq 0.5$ and $n \geq 3$. This suggests that the deeply cracked limit is already attained at $a/b = 0.5$ and for $n > 3$. An independent check of this assertion is given in Part 2. The results clearly demonstrate that the normalization introduced in [5, 7] works well for $a/b > 0.25$. Plots of h_1 and h_3 against $1/n$ are shown in Fig. 5 where the data points are interpolated by cubic spline functions. A plot of h_1 as a function of relative crack size is shown in Fig. 6. In this case, the normalization employed does lead to a slowly varying dependence on a/b.

In [7], values are presented for $a/b = 1/4$, 1/2, and 3/4 and

Downloaded 02 May 2010 to 171.66.16.25. Redistribution subject to ASME license or copyright; see http://www.asme.org/terms/Terms_Use.cfm

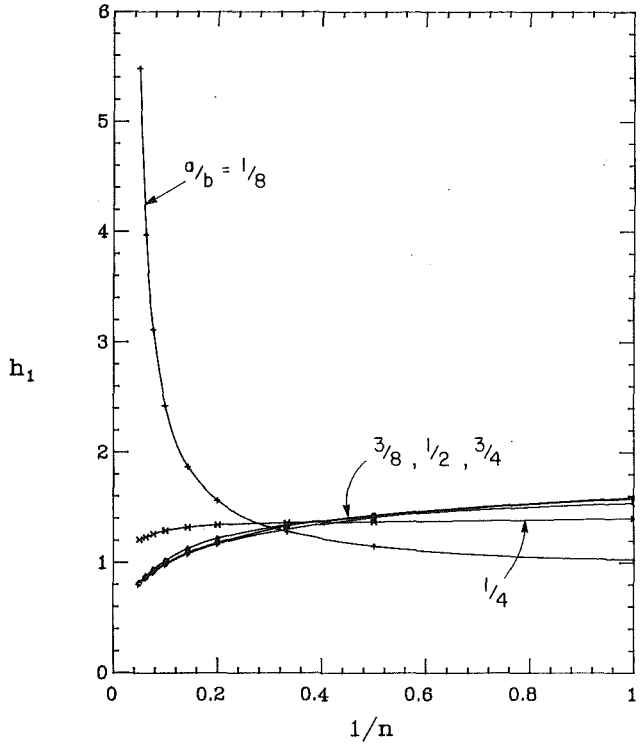

Normalized J-integral

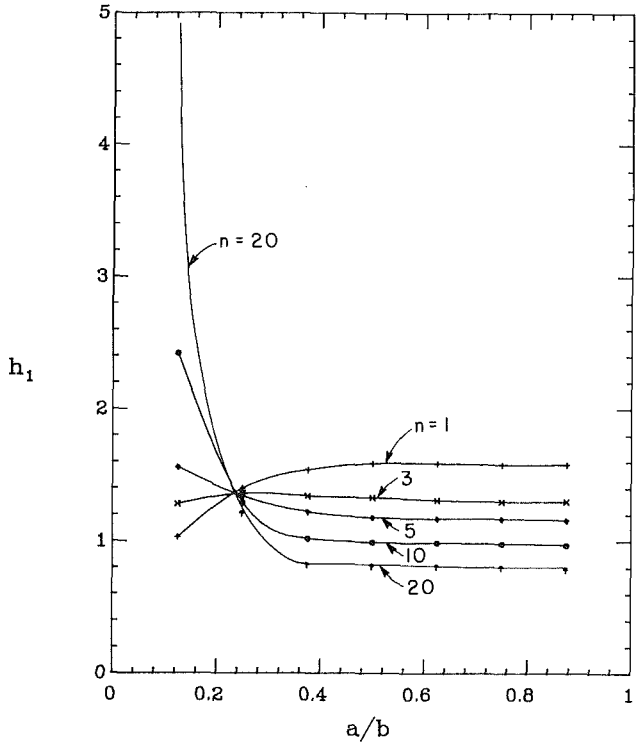

Fig. 6 Normalized J-integal as a function of a/b for various values of strain-hardening exponent n for the edge-cracked panel in bending

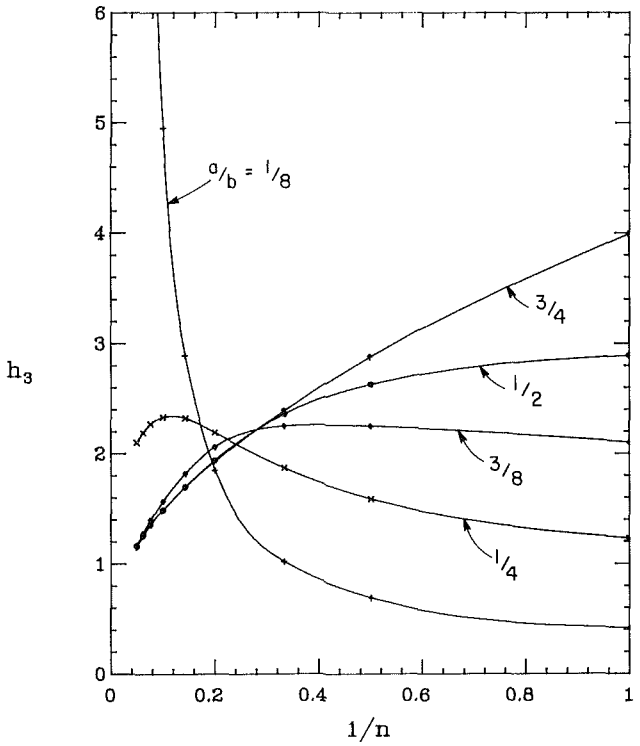

Normalized remote displacement (due to the presence of the crack)

Fig. 5 Fully plastic solutions for the edge-cracked panel subject to remote moment

for n values in the range $1 < n < 10$. We find differences of up to 30 percent between the present results and those in [7]. Our results also do not agree with those reported in [11, 16]. We will comment on the accuracy of these solutions in the context of the consistency check in Part 2.

Acknowledgment

The support of the Department of Energy Grant DE-AC02-80-ER10556 is gratefully acknowledged. The computations reported on here were carried out on the Brown University, Division of Engineering, VAX-11/780 computer. The acquisition of this computer was made possible by grants from the U.S. National Science Foundation (Grant ENG78-19378), the General Electric Foundation and the Digital Equipment Corporation.

References

1 Anon., "EPRI Ductile Fracture Research Review Document," Norris, D. M., et al., eds., NP-80-10-LD Special Study Project WS 80-912, Workshop Report, Electric Power Research Institute, Palo Alto, Calif., Dec. 1980.

2 Kumar, V., German, M. D., and Shih, C. F., "An Engineering Approach for Elastic-Plastic Fracture Analysis," EPRI Topical Report NP-1931, Electric Power Research Institute, Palo Alto, Calif., July, 1981.

3 Shih, C. F., German, M. D., and Kumar, V., "An Engineering Approach for Examining Crack Growth and Stability in Flawed Structures," *International Journal of Pressure Vessel and Piping*, Vol. 9, 1981, pp. 159–196.

4 Goldman, N. L., and Hutchinson, J. W., "Fully Plastic Crack Problems: The Center-Cracked Strip Under Plane Strain," *International Journal of Solids and Structures*, Vol. 11, 1975, pp. 575–591.

5 Shih, C. F., and Hutchinson, J. W., "Fully Plastic Solutions and Large Scale Yielding Estimates for Plane Stress Crack Problems," ASME *Journal of Engineering Materials and Technology*, Vol. 98, 1976, pp. 289–295.

6 Needleman, A., and Shih, C. F., "Finite Element Method for Plane Strain Deformations of Incompressible Solids," *Computer Methods in Applied Mechanics and Engineering*, Vol. 15, 1978, pp. 223–240.

7 Hutchinson, J. W., Needleman, A., and Shih, C. F., "Fully Plastic Crack Problems in Bending and Tension," in *Fracture Mechanics*, Perrone, N., et al., eds., University Press of Virginia, Charlottesville, 1978, pp. 515–528.

8 He, M. Y., and Hutchinson, J. W., "The Penny-Shaped Crack in a Round Bar of Power-Law Hardening Material," Harvard University Report Mech-23, Dec. 1981, to appear in *Elastic-Plastic Fracture: Vol. I—Inelastic Crack Analysis, ASTM STP 803*, Shih, C. F., and Gudas, J. P., eds., American Society for Testing and Materials, Philadelphia, 1983.

9 Parks, D. M., "Virtual Crack Extension: A General Finite Element

Downloaded 02 May 2010 to 171.66.16.25. Redistribution subject to ASME license or copyright; see http://www.asme.org/terms/Terms_Use.cfm

Technique for J-Integral Evaluation," in *Numerical Methods in Fracture Mechanics*, Luxmoore, A. R., and Owen, D. R. J., University College of Wales, Swansea, 1978, pp. 464–478.

10 Yagawa, G., Aizawa, T., and Ando, Y., "Linear and Nonlinear Elastic Analysis of Cracked Plate: Application of a Penalty Function and Superposition Method," *International Journal for Numerical Methods in Engineering*, Vol. 17, 1981, pp. 719–733.

11 Sauter, W., and Kumar, V., Estimation Technique for the Prediction of Elastic-Plastic Fracture of Structural Components of Nuclear Systems," Section 3.2 of Combined Fifth and Sixth Semiannual Report to EPRI, General Electric Company, Schenectady, N.Y., General Electric Report SRD-82-048, Mar., 1982.

12 Hult, J., "On the Stationarity of Stress and Strain Distributions in Creep," in *Proceedings of the International Symposium on Second-Order Effects in Elasticity, Plasticity and Fluid Dynamics*, Haifa, Pergamon Press, 1962, pp. 352–361.

13 Riedel H., "Creep Deformation at Crack Tips in Elastic-Viscoplastic Solids," *Journal of Mechanics and Physics of Solids*, Vol. 29, 1981, pp. 35–49.

14 Rodin, G. J., and Parks, D. M., "Calibration and Consistency Check for the Power Law Line Spring," paper in preparation. Also see Rodin, G. J., "The Line Spring Model for *J*-Analysis of Surface-Crack Plates and Shells: Calibration of the Power Law Spring M.Sc. Thesis, MIT, Cambridge, Mass., 1983.

15 Rice, J. R., "The Line-Spring Model for Surface Flaws," in *Surface Crack: Physical Problems and Computational Solutions*, Swedlow, J. L., ed., ASME, New York, 1972.

16 Parks, D. M., Kumar, V., and Shih, C. F., "Consistency Checks for Power Law Calibration Functions," to appear in *Elastic-Plastic Fracture: Vol. I—Inelastic Crack Analysis, ASTM STP 803*, Shih, C. F., and Gudas, J. P., eds., American Society for Testing and Materials, Philadelphia, 1983.

17 Tada, H., Paris, P. C., and Irwin, G. R., *The Stress Analysis of Cracks Handbook*, Del Research Corporation, Hellertown, Pa. 1973.

18 Hughes, T. J. R., "Equivalence of Finite Elements for Nearly-Incompressible Elasticity," ASME JOURNAL OF APPLIED MECHANICS, Vol. 44, 1977, pp. 181–183.

19 Malkus, D. S., "A Finite Element Displacement Model Valid for any Value of the Compressibility," *International Journal of Solids and Structures*, Vol. 12, 1976, pp. 731–738.

20 Malkus, D. S., and Hughes, T. J. R., "Mixed Finite Element Methods-Reduced and Selective Integration Techniques: A Unification of Concepts," *Computer Methods in Applied Mechanics and Engineering*, Vol. 15, 1978, pp. 63–81.

21 Song, Y. J., Oden, J. T., and Kikuchi, N., "Discrete LBB-Conditions for RIP-Finite Element Methods," Texas Institute for Computational Mechanics, Report 80-7, Aug. 1980.

22 Zienkiewicz, O. C., *The Finite Element Method*, McGraw-Hill, Maidenhead, England, 1977.

23 Young, D. M., and Gregory, R. T., *A Survey of Numerical Mathematics Vols. I and II*, Addison-Wesley, Reading, Mass. 1972.

24 Rice, J. R., "A Path-Independent Integral and the Approximate Analysis of Strain Concentration by Notches and Cracks," ASME JOURNAL OF APPLIED MECHANICS, Vol. 35, 1968, pp. 379–386.

25 Hutchinson, J. W., "Singular Behavior at the End of a Tensile Crack in Hardening Material," *Journal of the Mechanics and Physics of Solids*, Vol. 16, 1968, pp. 13–31.

26 Rice, J. R., and Rosengren, G. F., "Plane Strain Deformation Near a Crack Tip in a Power-Law Hardening Material," *Journal of the Mechanics and Physics of Solids*, Vol. 16, 1968, pp. 1–12.

27 Hutchinson, J. W., *Nonlinear Fracture Mechanics*, Department of Solid Mechanics, The Technical University of Denmark, Denmark, 1979.

28 Green, A. P., and Hundy, B. B., "Initial Plastic Yielding in Notch Bend Tests," *Journal of the Mechanics and Physics of Solids*, Vol. 4, 1956, pp. 128–144.

29 Barsoum, R. S., "Triangular Quarter-Point Elements as Elastic and Perfectly-Plastic Crack Tip Elements," *International Journal for Numerical Methods in Engineering*, Vol. 11, 1977, pp. 85–98.

30 Hussain, M. A., Shih, C. F., and German, M. D., "Lagrangian Elements as Singularity Elements in Crack Analysis," Generral Electric Company, Technical Information Series Report No. 80CRD291, Dec. 1980.

31 Shih, C. F., and German, M. D., "Requirements for a One-Parameter Characterization of Crack Tip Fields by the HRR Singularity," *International Journal of Fracture*, Vol. 17, 1981, pp. 27–43.

Downloaded 02 May 2010 to 171.66.16.25. Redistribution subject to ASME license or copyright; see http://www.asme.org/terms/Terms_Use.cfm

C. F. Shih
Mem. ASME

A. Needleman
Mem. ASME

Division of Engineering,
Brown University,
Providence, R.I. 02912

Fully Plastic Crack Problems

Part 2: Application of Consistency Checks

Consistency checks, including short and deep crack limiting relations, are applied to the solutions obtained in Part 1. An error measure is introduced to quantify the consistency check. The accuracy of the solutions of Part 1 is discussed in light of these consistency checks and comparison is made with previous solutions. Consistency checks appear useful in ascertaining the accuracy of existing fully plastic crack solutions and of proposed new solutions.

1 Introduction

Consistency checks for fully plastic crack problems have been formulated by Parks, Kumar, and Shih [3]. This consistency check has been applied to solutions for several configurations tabulated in handbook form in [4]. Some of these solutions were regarded as satisfying the consistency condition in [3]. However, as noted in Part 1, [1], the solutions in [4] for the edge-cracked panel subject to tension and to bending do not satisfy the consistency condition [3]. In this paper, we apply consistency checks to the solutions obtained in Part 1. The application of the consistency checks in [3] was qualitative. Here, we introduce an error measure in an attempt to quantify the degree of satisfaction of the consistency check. Similar consistency checks may be applied to fully plastic crack solutions obtained by other approaches [11–13]. Since various solutions are not always in agreement, such checks can be helpful in ascertaining the accuracy of solutions.

2 Consistency Relations for Cracked Bodies

In Part 1, the disagreements between the current results [1] and those reported in [4, 8, 10] were touched on. The solutions given in [4, 5, 8–10] were obtained by the method developed in [2]. Differences between the solutions obtained by several investigators using different numerical methods [6, 11–13] have also been noted and discussed in [3, 8, 11]. In some instances, the disagreements were substantial. For certain deeply cracked geometries, consistency relations between h_1 and h_3 were introduced in [7, 8] for purposes of evaluating the accuracy of the numerical results. More recently Parks, Kumar, and Shih [3] introduced a general consistency relation for cracked bodies. This relation is determined from the equivalence of J and energy differences with respect to crack length. We summarize the derivation of this relation which has been explained in detail in [3].

Consider a planar body subject to a generalized force Q per unit thickness with crack length a and ligament c as shown in Fig. 1. The width of the body, b, is fixed. Let q be the generalized displacement work-conjugate to Q. Similar to the discussion in Part 1, q can be viewed as the sum of a displacement "due to the presence of a crack," q_c, and a displacement "in the absence of a crack," q_{nc},

$$q_c = q - q_{nc}. \tag{2.1}$$

We next consider the energy difference between two bodies containing cracks of slightly different crack lengths a and $a + \Delta a$ (see Fig. 1). To within first-order terms, the area between the two generalized load-displacement curves is $J\Delta a$, i.e.,

$$J = \int_0^Q \left.\frac{\partial q}{\partial a}\right|_Q dQ. \tag{2.2}$$

Using (2.1) and (2.2) and noting that q_{nc} is independent of a, there results

$$J = \int_0^Q \left.\frac{\partial q_c}{\partial a}\right|_Q dQ. \tag{2.3}$$

Equation (2.3) is an alternate and equivalent definition of J [15, 3].

Next the functional form of the "fully plastic" q_c (see equations (4.11) and (4.20) of Part 1) is examined in conjunction with the right-hand side of (2.3). It is clear that only terms that are linear in h_3 and $\partial h_3/\partial a$ and homogeneous of degree $(n+1)$ in Q will appear here. Now the left-hand side of (2.3) is the "fully plastic" J which is independently given by (4.9) and (4.18) of Part 1. Since J is linear in h_1 and is also of degree $(n+1)$ in Q, a linear relation between h_1, h_3, and $\partial h_3/\partial a$, which is independent of Q, is obtained. This relation can serve as a stringent test of the "quality" of fully plastic solutions [3].

Consistency Checks of Solutions for the ECPT Configuration. Substituting (4.9) and (4.11) of Part 1 into (2.3) and rearranging, the following linear relation between h_1, h_3, and $\partial h_3/\partial \xi$ emerges [3],

Contributed by the Applied Mechanics Division for presentation at the 1984 PVP Conference and Exhibition, Joint with Applied Mechanics Division and Materials Division, San Antonio, Texas, June 17–21, 1984 of THE AMERICAN SOCIETY OF MECHANICAL ENGINEERS.

Discussion on this paper should be addressed to the Editorial Department, ASME, United Engineering Center, 345 East 47th Street, New York, N.Y. 10017, and will be accepted until two months after final publication of the paper itself in the JOURNAL OF APPLIED MECHANICS. Manuscript received by ASME Applied Mechanics Division, May, 1983. Paper No. 84-APM-10.

Copies will be available until February, 1985.

Copyright © 1984 by ASME
Downloaded 02 May 2010 to 171.66.16.25. Redistribution subject to ASME license or copyright; see http://www.asme.org/terms/Terms_Use.cfm

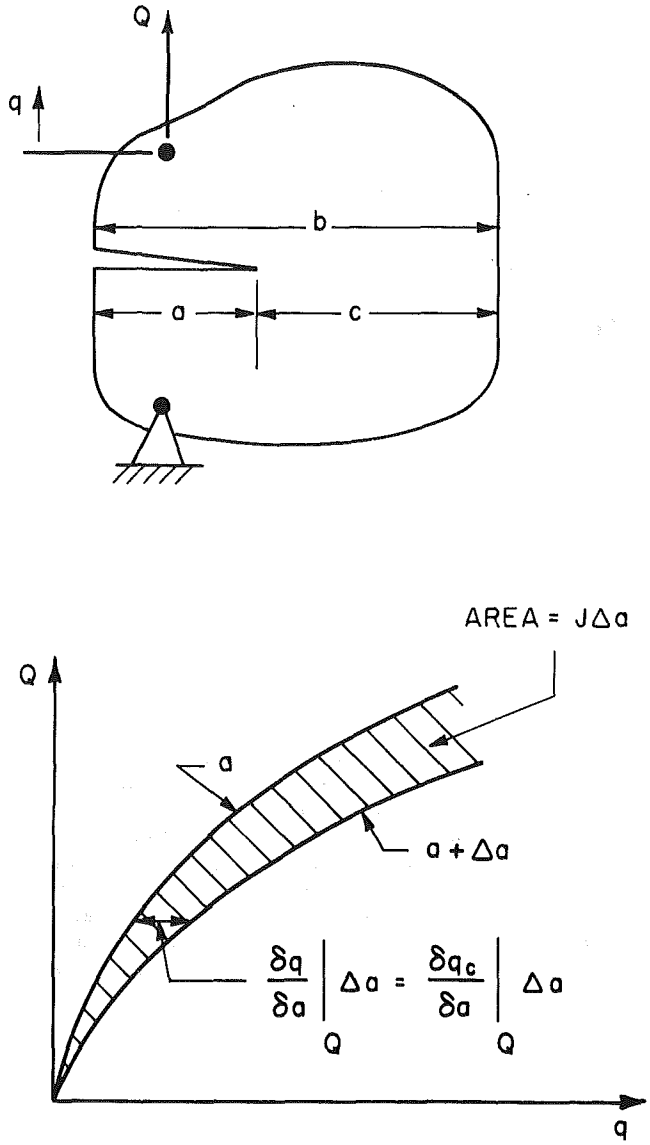

Fig. 1 Sketch of a planar cracked body subject to a generalized force Q per unit thickness, with work-conjugate displacement q. The generalized load-displacement curves for two such bodies containing cracks of slightly different lengths a and a + Δa are illustrated.

$$\frac{\partial h_3}{\partial \xi} = \left[\frac{n+1}{1.455\eta}\right] h_1 - \left[\frac{1}{\xi} + \frac{n\psi}{\xi\sqrt{1+\psi^2}}\{\eta + 2\psi + 1\}\right] h_3. \quad (2.4)$$

Here $\xi = a/b$, $\psi = a/c = \xi/(1-\xi)$, and η is defined by (4.8) of Part 1. The distinct variables ξ and ψ are used to facilitate the derivation of short and deep crack relations to be discussed subsequently.

The consistency test is applied in the following way. First we plot h_3 at the grid points $\xi = 1/8, 1/4, \ldots, 7/8$, for a fixed value of n, using the tabulated values in Table 1 of Part 1. Then we pass a smooth curve through the data points using cubic spline interpolation (second and lower order derivatives of the spline interpolation function are continuous everywhere) [17]. We employ the natural cubic spline which in a sense is the smoothest function that interpolates the data. Next we consider two neighboring grid points ξ_1 and ξ_2. The derivative $\partial h_3/\partial \xi$ can be calculated using (2.4) and the tabulated values of h_1 and h_3 [1]. Since h_3 and $\partial h_3/\partial \xi$ are known at ξ_1 and ξ_2, the data points can be connected by a cubic Hermitian interpolation polynomial in the subinterval $\xi_1 \le \xi \le \xi_2$ [17]. Proceeding in a similar manner, the data points in the interval $1/8 \le \xi \le 7/8$ are connected by six piecewise cubic polynomials. The proximity of the piecewise Hermite segments to the cubic spline curve is a measure of the consistency of the tabulated values for h_1 and h_3.

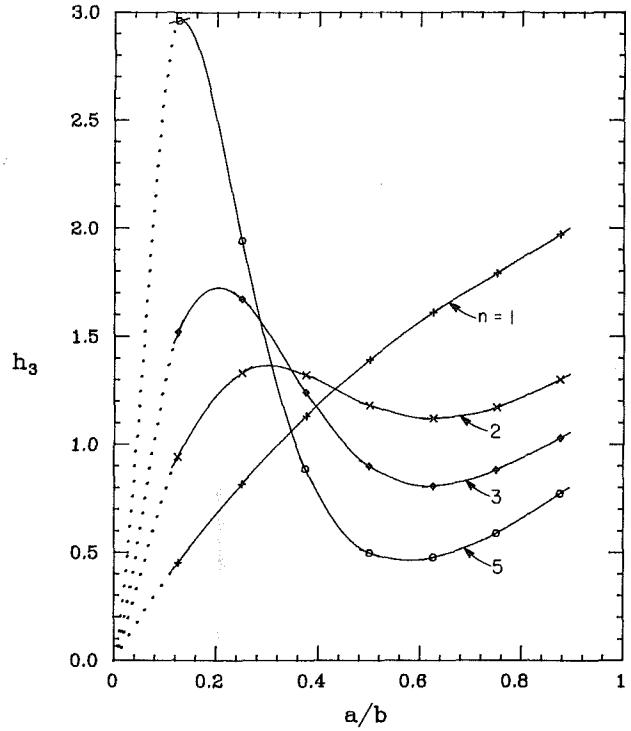

Data points, tangents, and fitted curves for n = 1, 2, 3, and 5

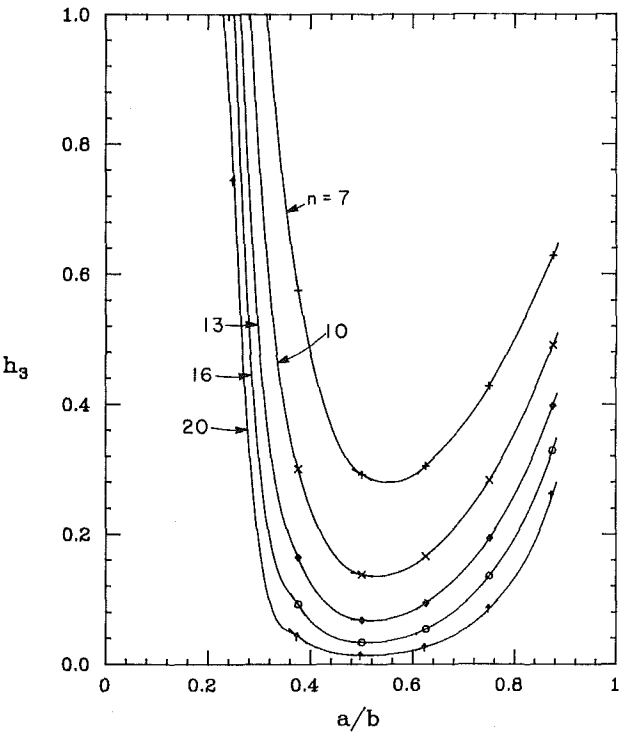

Data points, tangents, and fitted curves for n = 7, 10, 13, 16, and 20

Fig. 2 Normalized remote displacement due to the presence of a crack, Δ_c, versus a/b for the edge-cracked panel subject to tension. Two consecutive values of h_3 are connected by a cubic Hermite interpolation polynomial.

Downloaded 02 May 2010 to 171.66.16.25. Redistribution subject to ASME license or copyright; see http://www.asme.org/terms/Terms_Use.cfm

Table 1 Error analysis for h functions for edge-cracked panel subject to tension

Subinterval	Error measure computed from equation (2.6)								
a/b	$n=1$	$n=2$	$n=3$	$n=5$	$n=7$	$n=10$	$n=13$	$n=16$	$n=20$
0.125-0.250	0.0023	0.0023	0.0111	0.0417	0.0468	0.0061	0.0972	0.2016	0.2926
0.250-0.375	0.0007	0.0013	0.0047	0.0212	0.0191	0.0575	0.2857	0.7544	1.7934
0.375-0.500	0.0003	0.0014	0.0021	0.0117	0.0218	0.0664	0.5332	1.9453	6.8871
0.500-0.625	0.0002	0.0015	0.0020	0.0023	0.0062	0.0262	0.2008	0.7399	2.6077
0.625-0.750	0.0009	0.0008	0.0016	0.0022	0.0042	0.0017	0.0255	0.0874	0.2536
0.750-0.875	0.0009	0.0023	0.0017	0.0005	0.0071	0.0015	0.0026	0.0053	0.0133
	0.0009	0.0016	0.0039	0.0133	0.0175	0.0266	0.1908	0.6223	1.9746
0.250-0.375	0.0011	0.0072	0.0119	0.0016	0.0316	0.1004	0.1725	0.2379	0.2900
0.375-0.500	0.0003	0.0028	0.0053	0.0034	0.0313	0.1168	0.2331	0.3907	0.7507
0.500-0.625	0.0002	0.0018	0.0032	0.0049	0.0099	0.0450	0.0955	0.1615	0.3097
0.625-0.750	0.0009	0.0008	0.0016	0.0013	0.0050	0.0155	0.0222	0.0322	0.0461
0.750-0.875	0.0009	0.0024	0.0019	0.0006	0.0068	0.0055	0.0129	0.0245	0.0409
	0.0007	0.0030	0.0048	0.0024	0.0169	0.0566	0.1072	0.1694	0.2875

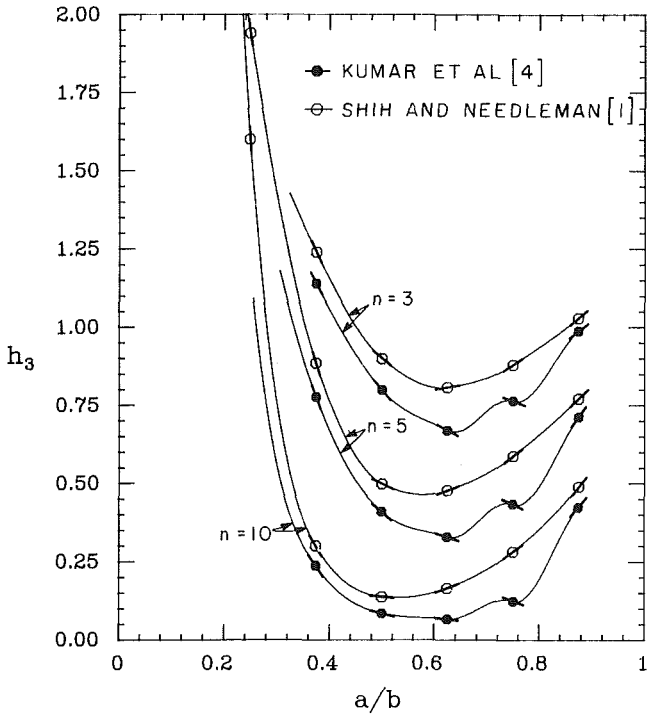

Fig. 3 Comparison of h_3 data, tangents, and fitted cubic Hermite curves for the edge-cracked panel in tension [1, 4]

Using the tabulated values in Table 1 of Part 1, the segments obtained by piecewise Hermitian interpolation in the interval $1/8 \le \xi \le 7/8$ are shown by solid lines in Fig. 2. The tangents computed from (2.4) are drawn through each data point. Since it is known that $h_3 \to 0$ as $\xi \to 0$, the dotted curves are included in Fig. 2(*a*) to suggest the possible behavior as $\xi \to 0$.

In Section 4 of Part 1, we noted that there are considerable differences between the values in Table 1 [1] and the corresponding values in [4]. The results in [4] are similar to results we have obtained from crude meshes. In Fig. 3, for comparison purposes, we plot the Hermitian segments obtained from the data in [4] and from the results in Part 1 for $n = 3$, 5, and 10, with the tangent from (2.4) indicated by the heavier lines. Note that the difference between the corresponding curves is greatest in the range $1/2 < \xi < 3/4$ and that this is where there are noticeable oscillations in the curves based on the data from [4].

As discussed in [3], the oscillations observed in the data from [4] can be reduced by incorporating additional geometric factors into the normalization of Δ_c. In light of the present results, however, it appears that the inconsistency in the tabulated values for the ECPT configuration in [4] is real and arises from the mesh employed. We also note that checks carried out in [3] for the center-cracked panel and for the compact tension specimen show that the tabulated values in [4] for these configurations appear to satisfy the consistency check.

It is worth noting that the consistency check is a rather stringent test of the accuracy of the fully plastic solutions. In (2.4), the coefficients of h_1 and h_3 are anywhere from one order to three orders of magnitude larger than the values of h_1 and h_3. Thus small errors in h_1 and/or h_3 introduce large errors in $\partial h_3/\partial \xi$ via (2.4).

To provide a quantitative measure of satisfaction (or lack of satisfaction) of this consistency check we have defined an error measure in the following way. First we let $S(\xi)$ denote the spline fit to the h_3 values and $H(\xi)$ denote the corresponding Hermite fit. Then in each subinterval $\xi_1 \le \xi \le \xi_2$ we define

$$f(\xi) = |S(\xi) - H(\xi)| \tag{2.5}$$

By construction $f(\xi_1) = f(\xi_2) = 0$. The error measure associated with the subinterval $[\xi_1, \xi_2]$ is taken as

$$e(\xi_1,\xi_2) = \frac{\left(\frac{1}{\xi_2 - \xi_1}\right)\int_{\xi_1}^{\xi_2} f(\xi)\,d\xi}{\frac{1}{2}[h_3(\xi_1) + h_3(\xi_2)]} \tag{2.6}$$

Table 1 displays the value of $e(\xi_1,\xi_2)$ associated with the ECPT solutions of Part 1. The upper values in Table 1 are based on using a spline fit to all data points ($1/8 \le a/b \le 7/8$). The lower error values shown are obtained when the spline fit is restricted to the range $1/4 \le a/b \le 7/8$. Also shown in this table is the average error that is simply the sum of $e(\xi_1,\xi_2)$ for all subintervals $[\xi_1,\xi_2]$ divided by the number of subintervals.

The tabulated normalized errors as defined by (2.6) are small for all subintervals with n equal to or less than 7. With $n > 10$, substantially larger error values can occur. A major factor contributing to the increased error for large n is the inability of the cubic spline curve to fit the rapidly varying h functions in the short crack range. As can be seen in Fig. 2(*b*) the fit Hermitian curves are rather smooth, except for the kink in the $n = 20$ curve, even though for $n > 10$ the h_1 and h_3 values range over two orders of magnitude. When the data points for $a/b = 1/8$ are excluded from the error analysis, the error measure for the higher values of n is generally lessened, as shown in the second row of values in Table 1. The error measure (2.6) is a relative error measure so that a constant difference between the spline and Hermitian curves shows up as a larger error where h_3 is small. In this context it is important to note that the cubic spline function fit does depend on which range of a/b is considered. On the other hand, the

Downloaded 02 May 2010 to 171.66.16.25. Redistribution subject to ASME license or copyright; see http://www.asme.org/terms/Terms_Use.cfm

Table 2 Effect of an additional data point on the error analysis for the ECPT with $n = 10$

From Table 1		With additional point		From Table 1		With additional point	
Subinterval	Error	Subinterval	Error	Subinterval	Error	Subinterval	Error
a/b		a/b		a/b		a/b	
0.1250–0.2500	0.0061	0.1250–0.2500	0.0070				
0.2500–0.3750	0.0575	0.2500–0.3125	0.0108	0.2500–0.3750	0.1004	0.2500–0.3125	0.0169
0.3750–0.5000	0.0664	0.3125–0.3750	0.0075	0.3750–0.5000	0.1168	0.3125–0.3750	0.0116
0.5000–0.6250	0.0262	0.3750–0.5000	0.0331	0.5000–0.6250	0.0450	0.3750–0.5000	0.0069
0.6250–0.7500	0.0017	0.5000–0.6250	0.0124	0.6250–0.7500	0.0155	0.5000–0.6250	0.0047
0.7500–0.8750	0.0015	0.6250–0.7500	0.0092	0.7500–0.8750	0.0055	0.6250–0.7500	0.0071
		0.7500–0.8750	0.0037			0.7500–0.8750	0.0031
	0.0266		0.0119		0.0566		0.0084

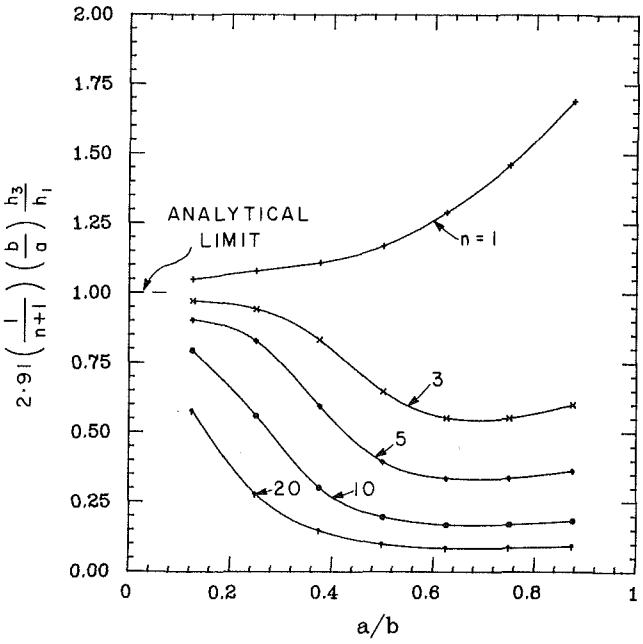

Short crack consistency check

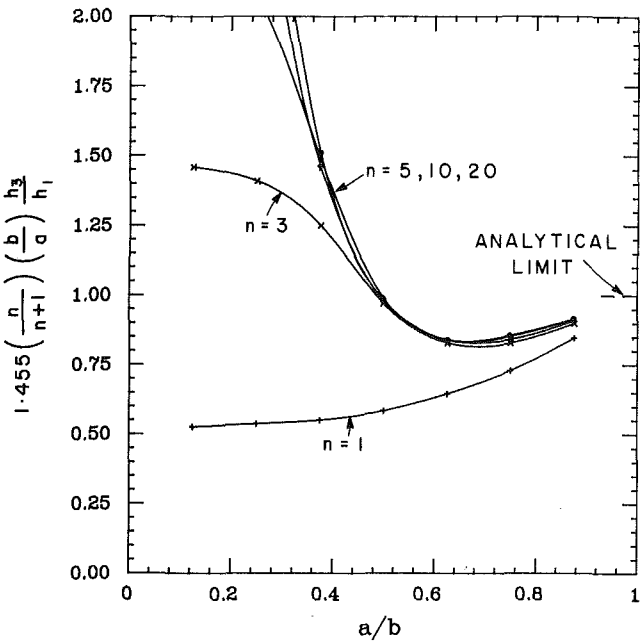

Deep crack consistency check

Fig. 4 Edge-cracked panel subject to tension

Hermitian interpolation for a subinterval depends only on the h function values associated with that particular subinterval.

The preceding discussion suggests that obtaining additional data points where the variation of the h functions is rapid should considerably reduce the error value. To explore this, solutions were obtained for $a/b = 5/16$ with n up to 10. For all values of n the additional data point tended to reduce the error value, with the greatest effect occurring with $n = 10$. The effect of the additional data point on the error values with $n = 10$ is shown in Table 2. For comparison purposes the values from Table 1 are repeated here. What is significant is that the values of h_1 and h_3 for $a/b = 5/16$ virtually fall on the Hermitian interpolation segment based on the values of the h functions at $a/b = 1/4$ and $a/b = 3/8$. This is consistent with the contention that much of the error in Table 1 at the high n values is attributable to the rapid variation in the h functions. It is important to note that when the h functions vary rapidly, slopes obtained from these h function values may not be accurate enough for crack growth stability analyses even if the tabulated values are accurate. More accurate slope values can be obtained from solutions tabulated at closer a/b values in regions where the h functions vary rapidly. Another possible remedy is to renormalize the solutions in a manner that reduces the variation.

We have also examined some of the ECPT solutions in [4] (with the corrected h_3 function values noted in [3]) using the error measure (2.6). The average errors associated with these solutions are 0.0218 with $n = 5$ and 0.100 with $n = 10$. These values should be compared with the lower set of values in Table 1 since the corrected h_3 values in [3] are given for $a/b \geq 1/4$. It is worth noting that with $n = 10$ the error values for the subintervals 0.250–0.375 and 0.375–0.500 are nearly the same as those in Table 1. For higher a/b values there is a substantial difference. For example, in the subinterval 0.625–0.750 the solutions in [4] give an error value of 0.199 as compared with 0.0155 from Table 1. It appears that the effect of the rapid variation in the h functions dominates the error measure for the smaller a/b values.

Short and Deep Crack Consistency Checks for the ECPT Configuration. In the short crack limit, $a/b \to 0$, (2.4) reduces to

$$2.91\left(\frac{1}{n+1}\right)\left(\frac{b}{a}\right)\frac{h_3}{h_1} = 1 \tag{2.7}$$

The derivation of (2.7) is given in the Appendix. Using the values from Table 1 of Part 1, we calculate the left-hand side of (2.7) at $a/b = 1/8, 1/4, \ldots$. This ratio of h_3 to h_1 is plotted against a/b in Fig. 4(a). For $1 \leq n \leq 3$ the ratio is within 7 percent of unity for $a/b \leq 0.25$. The analytical limit for $a/b \to 0$ is indicated in Fig. 4(a). The values for $a/b \leq 0.25$ and $1 \leq n \leq 3$ appear to satisfy the short crack relation (2.7). The behavior of the curves for larger values of n suggests that as n increases, the relative crack size for short

Downloaded 02 May 2010 to 171.66.16.25. Redistribution subject to ASME license or copyright; see http://www.asme.org/terms/Terms_Use.cfm

Table 3 Error analysis for h functions for edge-cracked panel subject to moment

Subinterval	Error measure computed from equation (2.6)								
a/b	$n=1$	$n=2$	$n=3$	$n=5$	$n=7$	$n=10$	$n=13$	$n=16$	$n=20$
0.125-0.250	0.0095	0.0063	0.0012	0.0169	0.0205	0.0067	0.0707	0.1573	0.2951
0.250-0.375	0.0006	0.0010	0.0010	0.0040	0.0073	0.0083	0.0428	0.1061	0.2501
0.375-0.500	0.0005	0.0013	0.0018	0.0025	0.0068	0.0050	0.0057	0.0303	0.0892
0.500-0.625	0.0004	0.0011	0.0018	0.0033	0.0038	0.0018	0.0050	0.0107	0.0258
0.625-0.750	0.0004	0.0009	0.0020	0.0005	0.0010	0.0023	0.0037	0.0016	0.0026
0.750-0.875	0.0007	0.0006	0.0021	0.0027	0.0051	0.0034	0.0049	0.0057	0.0133
	0.0020	0.0019	0.0016	0.0050	0.0074	0.0046	0.0221	0.0520	0.1127
0.250-0.375	0.0022	0.0009	0.0027	0.0045	0.0044	0.0136	0.0312	0.0495	0.0670
0.375-0.500	0.0003	0.0012	0.0021	0.0022	0.0050	0.0114	0.0207	0.0267	0.0301
0.500-0.625	0.0003	0.0011	0.0019	0.0040	0.0044	0.0009	0.0022	0.0047	0.0071
0.625-0.750	0.0004	0.0009	0.0020	0.0006	0.0010	0.0029	0.0057	0.0061	0.0081
0.750-0.875	0.0007	0.0006	0.0020	0.0028	0.0052	0.0037	0.0046	0.0040	0.0086
	0.0008	0.0009	0.0021	0.0028	0.0040	0.0065	0.0129	0.0182	0.0242

crack behavior decreases. This is not unexpected since it is known that in the fully yielded state, a crack in a perfectly plastic body must sense the remote boundary.

He and Hutchinson [14] obtained upper and lower bounds for J for $a/b \to 0$ and $1 \le n \le 7$. They normalized J by

$$J = \alpha\sigma_0\epsilon_0 a\, H_1(n) \left(\frac{\sqrt{3}}{2}\frac{\sigma^\infty}{\sigma_0}\right)^{n+1} \tag{2.8}$$

where H_1 is a function of n only.

For comparison purposes, we rewrite (4.9) of Part 1 as

$$J = \alpha\sigma_0\epsilon_0 a(c/b)\left(\frac{1}{1.26\eta}\right)^{n+1} h_1(a/b,n)\left(\frac{\sqrt{3}b}{2c}\frac{\sigma^\infty}{\sigma_0}\right)^{n+1} \tag{2.9}$$

where 1.26η is the plastic constraint factor. A straightforward extrapolation of (2.9) to $a/b \to 0$ is

$$J = \alpha\sigma_0\epsilon_0 a\left(\frac{1}{1.26\eta}\right)^{n+1} h_1(1/8,n)\left(\frac{\sqrt{3}}{2}\frac{\sigma^\infty}{\sigma_0}\right)^{n+1} \tag{2.10}$$

where η in (4.8) of Part 1 is evaluated at $a/b = 1/8$ and we have made use of the result $\partial h_1/\partial\xi \to 0$ as $\xi \to 0$ ($\xi = a/b$). Values of J calculated by (2.10) are within several percent of the average of the upper and lower bounds in [14] for $1 \le n \le 3$. For $n = 5$ and 7 our values differ from this average by 7 and 15 percent, respectively. Several solutions for $a/b = 0.05$ were obtained using meshes and boundary conditions specifically for the short crack limit. These solutions fall between the bounds given in [14] and will be reported in a separate paper.

As shown in the Appendix, in the deep crack limit, $a/b \to 1$, (2.4) reduces to

$$1.455\left(\frac{n}{n+1}\right)\left(\frac{b}{a}\right)\frac{h_3}{h_1} = 1 \tag{2.11}$$

An alternate derivation of (2.11) is instructive. Since the remaining ligament of the deeply cracked panel is subject primarily to bending, we can use a formula for J due to Rice et al. [15]. When the remaining ligament c is sufficiently small so that J depends only on c, the deep crack relation is

$$J_{dc} = \frac{2}{c}\int_0^{\Delta_c} P\, d\Delta_c \tag{2.12}$$

Using (4.11) of Part 1 in (2.12) we get

$$J_{dc} = 1.455\left(\frac{n}{n+1}\right)\alpha\sigma_0\epsilon_0 c\, h_3(a/b,n)\,(P/P_0)^{n+1}. \tag{2.13}$$

At the same value of P, the ratio of J_{dc} to J given by (4.9) of Part 1 is

$$\frac{J_{dc}}{J} = 1.455\left(\frac{n}{n+1}\right)\left(\frac{b}{a}\right)\frac{h_3}{h_1}. \tag{2.14}$$

Comparing (2.11) and (2.14), it is clear that the left-hand side of (2.11) is the ratio of J_{dc} to J.

We calculate the left-hand side of (2.11) using the values in Table 2 of Part 1 and plot the ratio against a/b in Fig. 4(b). The solid curves clearly extrapolate to the analytical limit of unity as $a/b \to 1$. The rather gradual approach to the deep crack limit is due to the choice of the reference load P (see (4.7) of Part 1) for normalizing h_1 and h_3. With cracks that are sufficiently deep, the ligament of the panel is essentially in bending. In this case, the Green and Hundy limit load [16] is the appropriate reference load. The present reference load given by (4.7) of Part 1 underestimates the Green and Hundy limit load for $a/b = 0.625$, 0.75, and 0.875 by 22, 11, and 5 percent, respectively. With J and Δ_c normalized by the Green and Hundy limit load, the left-hand side of (2.11) (based on the renormalized h_1 and h_3) is within 5 percent of unity for $a/b \ge 0.7$ and $n \ge 3$.

Consistency Checks of Solutions for the ECPM Configuration. Using (4.18) and (4.20) of Part 1 in (2.3) yields the relation [3],

$$\frac{\partial h_3}{\partial\xi} = \left(\frac{1}{1-\xi}\right)\left(\frac{n+1}{0.364}\right)h_1 - \left(\frac{2n}{1-\xi}\right)h_3 \tag{2.15}$$

where $\xi = a/b$. Using the procedure described in the section on the ECPT configuration and the tabulated values in Table 2 of Part 1, h_3 and its tangents computed from (2.15) are plotted in Fig. 5 at the grid points $\xi = 1/8, 1/4, \ldots, 7/8$. For each value of n, the data points in the interval $1/8 \le \xi \le 7/8$ are connected by six piecewise cubic Hermite polynomials. The dotted lines are included to suggest the behavior as $\xi \to 0$. The consistency error measures from (2.6) for the ECPM results are shown in Table 3. The errors associated with each subinterval are rather small except for large n and small a/b where the h functions vary rapidly. In Fig. 6, Hermite segments based on the present results and on tabulated values from Hutchinson et al. [8] and Sauter and Kumar [10] are shown for $n = 3$ and 10.

Hutchinson et al. [8] carried out a consistency check of their solutions for the deep crack limit and concluded that their deep crack values of h_1 and/or h_3 could be in error by about 10 percent. The differences between those values and the present values are indeed of the order of 10–20 percent. Since the solutions in [8] were obtained from meshes that are similar to crude meshes we have employed, the lack of consistency in the earlier solutions may be attributed to the use of a cruder mesh than the present one. Note that in the short crack range, the solutions in [10] differ by more than 100 percent from the present solutions. We also note that small errors in h_1 and/or h_3 can generate large oscillations particularly for a/b close to unity and/or large values of n. For these cases the coefficients

Downloaded 02 May 2010 to 171.66.16.25. Redistribution subject to ASME license or copyright; see http://www.asme.org/terms/Terms_Use.cfm

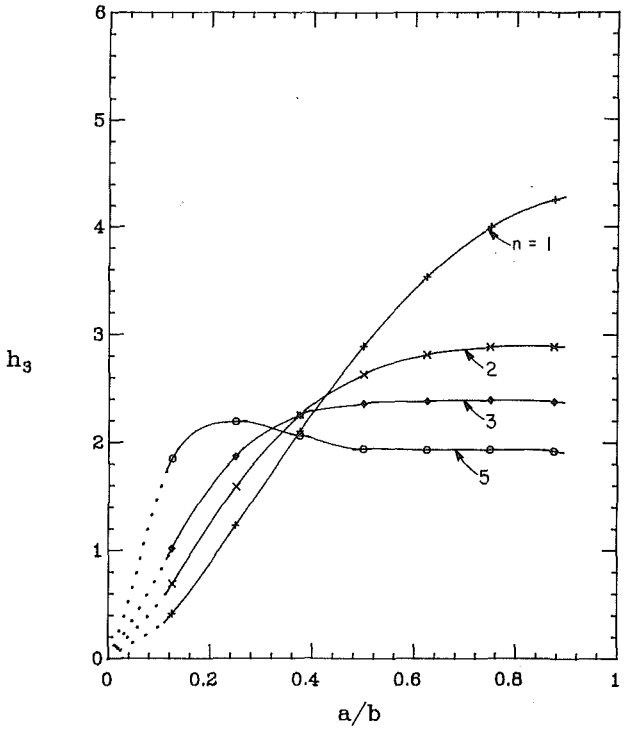

Data points, tangents, and fitted curves for $n = 1, 2, 3$, and 5

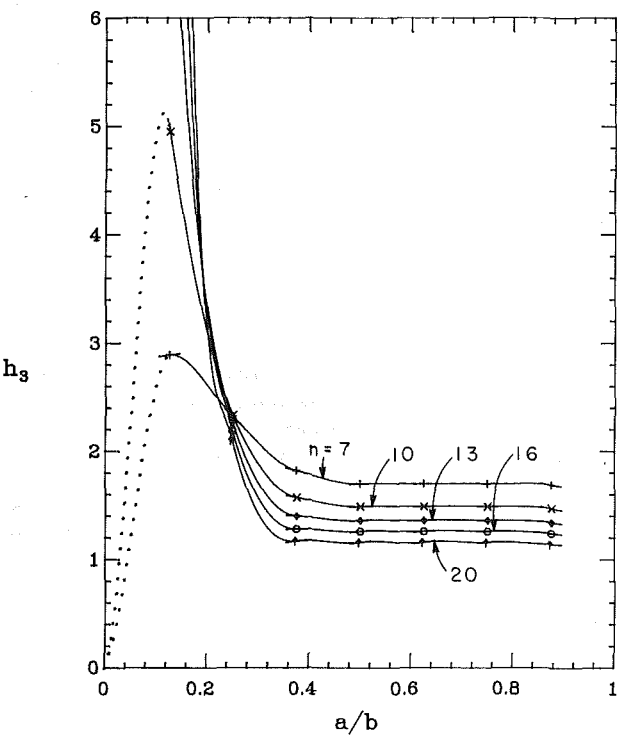

Data points, tangents, and fitted curves for $n = 7, 10, 13, 16$, and 20

Fig. 5 Normalized remote rotation due to the presence of a crack, θ_c, versus a/b for the edge-cracked panel subject to moment. Two consecutive values of h_3 are connected by a cubic Hermite interpolation polynomial.

of h_1 and h_3 in (2.15) are two to three orders of magnitude larger than h_1 and h_3.

Short and Deep Crack Consistency Checks for the ECPM Configuration. In the short crack limit, $a/b \to 0$, (2.15) reduces to

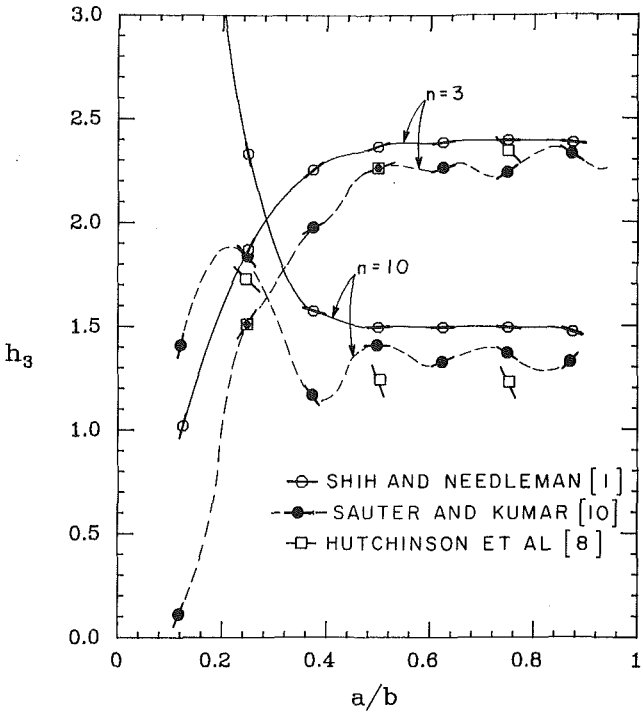

Fig. 6 Comparison of h_3 data, tangents, and fitted cubic Hermite curves for the edge-cracked panel in bending [1, 8, 10]

$$0.728\left(\frac{n}{n+1}\right)\left(\frac{b}{a}-1\right)\frac{h_3}{h_1}=1 \tag{2.16}$$

The derivation of (2.16) is given in the Appendix. The plot of the left-hand side of (2.16) against a/b in Fig. 7(*a*) is obtained from values of h_1 and h_3 in Table 2 of Part 1; the analytical limit as $a/b \to 0$ is indicated in Fig. 7(*a*). The ratio is approximately unity for $a/b \leq 0.125$ and $n \leq 10$. At larger values of n, the short crack limit is approached for vanishingly small relative crack size.

In the deep crack limit, $a/b \to 1$, equation (2.15) reduces to (see the Appendix for derivation)

$$0.728\left(\frac{1}{n+1}\right)\frac{h_3}{h_1}=1 \tag{2.17}$$

For this configuration a deep crack formula for J [15] is

$$J_{dc}=\frac{2}{c}\int_0^{\theta_c} M d\theta_c \tag{2.18}$$

Using (4.20) of Part 1 in (2.18) leads to [8],

$$J_{dc}=0.728\left(\frac{n}{n+1}\right)\alpha\sigma_0\epsilon_0 c h_3(a/b,n)\,(M/M_0)^{n+1} \tag{2.19}$$

Now J is also independently given by (4.18) of Part 1. Hence the ratio of J_{dc} to J is

$$\frac{J_{dc}}{J}=0.728\left(\frac{n}{n+1}\right)\frac{h_3}{h_1} \tag{2.20}$$

Thus the left-hand side of (2.17) is the ratio of J_{dc} to J. Using the values of h_1 and h_3 in Table 2 of Part 1, this ratio is found to be within 1 percent of unity for $a/b \geq 0.5$ and $n \geq 5$. The ratio is shown against a/b in Fig. 7(*b*) with the analytical limit indicated. It is apparent that the deep crack limit is already attained at $a/b = 0.5$ for $n \geq 3$.

Another check on the fully plastic results can be obtained from the relation between δ and θ_c [8]. For a rigid-perfectly plastic panel, $n \to \infty$, the center of rotation of the slip-line field is located at a distance $0.369c$ from the crack tip so that

Downloaded 02 May 2010 to 171.66.16.25. Redistribution subject to ASME license or copyright; see http://www.asme.org/terms/Terms_Use.cfm

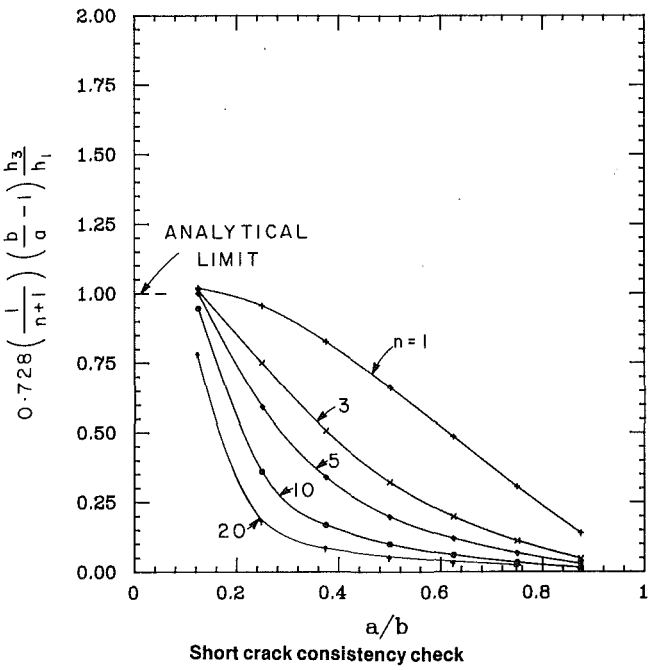

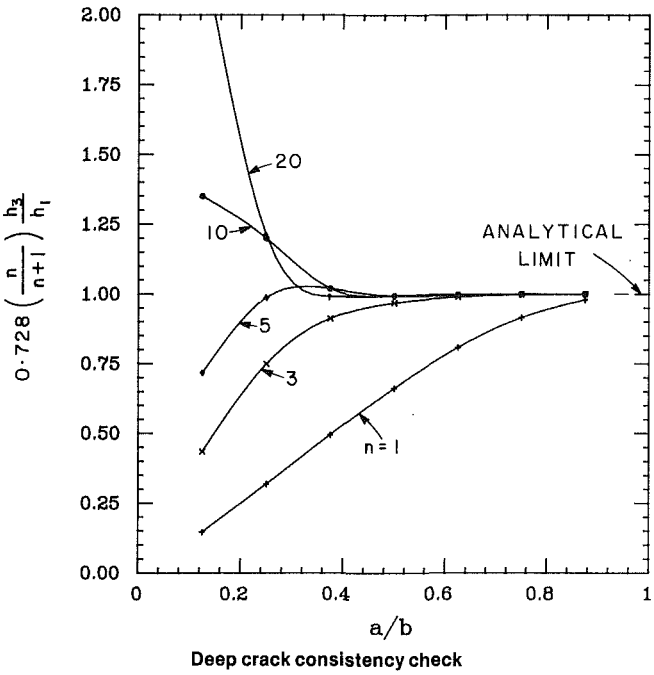

Fig. 7 Edge-cracked panel subject to moment

$$\frac{\delta}{a\theta_c} = 1 + 0.369\,\frac{c}{a} \tag{2.21}$$

Alternately the ratio of the "fully plastic" δ and θ_c (defined by (4.19) and (4.20) of Part 1) is given by

$$\frac{\delta}{a\theta_c} = \frac{h_2}{h_3} \tag{2.22}$$

Using the values in Table 2 of Part 1, we found that the latter ratio is within 1 percent of the limiting value (2.21) for $a/b \geq 0.5$ and $n \geq 5$.

3 Concluding Remarks

A reduced integration penalty (RIP) method has been used to obtain solutions to fully plastic plane-strain crack problems for a range of crack geometries and strain-hardening behaviors. For the solutions tabulated in Tables 1 and 2 of Part 1, we have introduced a quantitative measure that indicates how closely the consistency check of Parks et al. [3] is satisfied. The solutions of Part 1 satisfy the consistency checks rather closely except where the h functions vary rapidly with crack length. In this range interpolation between solutions for various crack lengths is difficult. This is reflected in the difficulties in obtaining a satisfactory spline interpolation for the quantitative consistency check. A satisfactory interpolation scheme is essential if the present results are to be employed for crack growth stability analyses [4, 5]. Such stability analyses employ the derivative of the h functions with respect to crack length and these slopes may not be accurately obtainable in regions of rapid variation even if the tabulated values are accurate. Hence, for short cracks, where the h functions vary rapidly, tabulation of the h functions at more closely spaced crack lengths (or an improved normalization) is necessary for accurate interpolation.

For nonlinear problems ($n > 1$), our studies on various mesh designs show that mesh refinement in the vicinity of the relevant slip-line field is essential for accurate solutions. Accuracy is also improved if the elements in the highly strained regions have aspect ratios close to unity. A key feature of an appropriately designed mesh is its ability to resolve a deformation pattern similar to the fully plastic slip-line field. Thus the adequacy of a mesh for fully plastic problems cannot be established by elastic calculations alone.

In Section 4 of Part 1 and in the present paper we noted that the fully plastic solutions obtained by various investigators are not always in agreement. In some cases, the differences are substantial. The studies carried out in [3] and in this paper indicate that consistency checks are a useful tool in ascertaining the accuracy of various solutions. The error measure we employ appears helpful in such a comparison although, as noted in the foregoing, when the h function values vary rapidly with crack length this error measure can be dominated by the effects of the rapid variation. Further steps in quantifying consistency checks seem worthwhile. In any case, in comparing solutions it is necessary that the solutions employ the same normalization and are carried out for the same range of crack lengths. In the short and deep crack limits additional limiting relations that serve as consistency checks are available. Consistency relations for other two-dimensional planar and axisymmetric configurations can be obtained along the lines described in [3] and in this paper.

Acknowledgment

The support of the Department of Energy Grant DE-AC02-80-ER10556 is gratefully acknowledged. We are pleased to acknowledge helpful discussions with Professor L. B. Freund. The computations reported on here were carried out on the Brown University, Division of Engineering, VAX-11/780 computer. The acquisition of this computer was made possible by grants from the U.S. National Science Foundation (Grant ENG78-19378), the General Electric Foundation and the Digital Equipment Corporation.

References

1 Shih, C. F., and Needleman, A., "Fully Plastic Crack Problems: Part 1: Solutions by a Penalty Method," ASME Journal of Applied Mechanics, Vol. 51, 1984, pp. 48–56.

2 Needleman, A., and Shih, C. F., "Finite Element Method for Plane Strain Deformations of Incompressible Solids," *Computer Methods in Applied Mechanics and Engineering*, Vol. 15, 1978, pp. 223–40.

3 Parks, D. M., Kumar, V., and Shih, C. F., "Consistency Checks for Power Law Calibration Functions," to appear in *Elastic-Plastic Fracture: Vol. I - Inelastic Crack Analysis, ASTM STP 803*, Shih, C. F., and Gudas, J. P., eds., American Society for Testing and Materials, Philadelphia, 1983.

Downloaded 02 May 2010 to 171.66.16.25. Redistribution subject to ASME license or copyright; see http://www.asme.org/terms/Terms_Use.cfm

4 Kumar, V., German, M. D., and Shih, C. F., "An Engineering Approach for Elastic-Plastic Fracture Analysis," EPRI Topical Report NP-1931, Electric Power Research Institute, Palo Alto, Calif., July, 1981.

5 Shih, C. F., German, M. D., and Kumar, V., "An Engineering Approach for Examining Crack Growth and Stability in Flawed Structures," *International Journal of Pressure Vessel and Piping*, Vol. 9, 1981, pp. 159–196.

6 Goldman, N. L., and Hutchinson, J. W., "Fully Plastic Crack Problems: The Center-Cracked Strip Under Plane Strain," *International Journal of Solids and Structures*, Vol. 11, 1975, pp. 575–591.

7 Shih, C. F., and Hutchinson, J. W., "Fully Plastic Solutions and Large Scale Yielding Estimates for Plane Stress Crack Problems," ASME *Journal of Engineering Materials and Technology*, Vol. 98, 1976, pp. 289–295.

8 Hutchinson, J. W., Needleman, A., and Shih, C. F., "Fully Plastic Crack Problems in Bending and Tension," in *Fracture Mechanics*, Perrone, N., et al., eds., University Press of Virginia, Charlottesville, 1978, pp. 515–528.

9 He, M. Y., and Hutchinson, J. W., "The Penny-Shaped Crack in a Round Bar of Power-Law Hardening Material," Harvard University Report Mech-23, Dec. 1981, to appear in *Elastic-Plastic Fracture: Vol. I - Inelastic Crack Analysis, ASTM STP 803*, Shih, C. F., and Gudas, J. P., eds., American Society for Testing and Materials, Philadelphia, 1983.

10 Sauter, W., and Kumar, V., "Estimation Technique for the Prediction of Elastic-Plastic Fracture of Structural Components of Nuclear Systems," Section 3.2 of Combined Fifth and Sixth Semiannual Report to EPRI, General Electric Company, Schenectady, N.Y., General Electric Report SRD-82-048, Mar. 1982.

11 Parks, D. M., "Virtual Crack Extension: A General Finite Element Technique for *J*-Integral Evaluation," in *Numerical Methods in Fracture Mechanics*, Luxmoore, A. R., and Owen, D. R. J., eds., University College of Wales, Swansea, 1978, pp. 464–478.

12 Yagawa, G., Aizawa, T., and Ando, Y., "Linear and Nonlinear Elastic Analysis of Cracked Plate: Application of a Penalty Function and Superposition Method," *International Journal for Numerical Methods in Engineering*, Vol. 17, 1981, pp. 719–733.

13 Ranaweera, M. P., and Leckie, F. A., "Solution of Nonlinear Elastic Fracture Problems by Direct Optimization," in *Numerical Methods in Fracture Mechanics*, Luxmoore, A. R., and Owen, D. R. J., eds., University College of Wales, Swansea, 1978, pp. 450–463.

14 He, M. Y., and Hutchinson, J. W., "Bounds for Fully Plastic Crack Problems for Infinite Bodies," Harvard University Report MECH-22, October, 1981, to appear in *Elastic-Plastic Fracture: Vol. I - Inelastic Crack Analysis, ASTM STP 803*, Shih, C. F., and Gudas, J. P., eds., American Society for Testing and Materials, Philadelphia, 1983.

15 Rice, J. R., Paris, P. C., and Merkle, J. G., "Some Further Results of *J*-Integral Analysis and Estimates," in *Progress in Flaw Growth and Fracture Toughness Testing, ASTM STP 536*, American Society for Testing and Materials, Philadelphia, 1973, pp. 231–245.

16 Green, A. P., and Hundy, B. B., "Initial Plastic Yielding in Notch Bend Tests," *Journal of the Mechanics and Physics of Solids*, Vol. 4, 1956, pp. 128–144.

17 Young, D. M., and Gregory, R. T., *A Survey of Numerical Mathematics Vols. I and II*, Addison-Wesley, Reading, Mass., 1972.

APPENDIX

Short Crack Consistency Relation for the ECPT Configuration

Equation (2.4) may be rewritten as

$$\left\{\frac{(n+1)h_1}{1.455\eta}-\frac{\partial h_3}{\partial\xi}\right\}\xi-\left\{1+\frac{n\psi}{\sqrt{1+\psi^2}}(\eta+2\psi+1)\right\}h_3=0 \quad (A.1)$$

Here $\psi = a/c$ and $\eta = \sqrt{1+\psi^2}-\psi$. In the short crack limit ($\xi \to 0$), $\psi \to 0$, and $\eta \to 1$. It can be shown from dimensional considerations and the short crack solutions given in [14, 7] that h_1 and $\partial h_3/\partial\xi$ are bounded as $\xi \to 0$. Since the first term, $\{\quad\}\xi$, in ($A.1$) vanishes as $\xi \to 0$, h_3 must also vanish in that limit. We use these results and ($A.1$) to get

$$\frac{(n+1)h_1}{1.455}=\frac{\partial h_3}{\partial\xi}+\frac{h_3}{\xi} \quad (A.2)$$

The right-hand side of ($A.2$) is finite and bounded since the left-hand side is finite and bounded. Expanding h_3 in a Taylor series about $\xi = 0$, for fixed finite values of n, and setting $h_3(0,n) = 0$ gives

$$\frac{\partial h_3}{\partial\xi}=\frac{h_3}{\xi}, \quad \xi\to 0 \quad (A.3)$$

Using ($A.3$) in ($A.2$), we arrive at the short crack relation

$$\frac{h_3}{h_1}\left(\frac{2.91}{n+1}\right)\frac{1}{\xi}=1 \quad (A.4)$$

Deep Crack Consistency Relation for the ECPT Configuration

We rearrange ($A.1$) as follows,

$$\frac{\xi(n+1)h_1}{1.455}-\left\{\eta+\frac{n\psi}{\sqrt{1+\psi^2}}(\eta^2+2\eta\psi+\eta)\right\}h_3=\xi\eta\frac{\partial h_3}{\partial\xi} \quad (A.5)$$

In the deep crack limit ($\xi \to 1$), $\psi \to \infty$, $\eta \to 0$, and $\psi\eta \to 1/2$. From dimensional considerations J depends linearly on the ligament c as $\xi \to 1$. These results and similar dimensional observations require that $\xi\eta\partial h_3/\partial\xi$ vanish in the deep crack limit. Equation ($A.5$) then reduces to

$$\xi\frac{(n+1)}{1.455}h_1-nh_3=0$$

or

$$\frac{h_3}{h_1}\left(\frac{1.455n}{n+1}\right)\frac{1}{\xi}=1 \quad (A.6)$$

Short Crack Consistency Relation for the ECPM Configuration

We rewrite (2.15) as

$$(1-\xi)\frac{\partial h_3}{\partial\xi}+2nh_3=\left(\frac{n+1}{0.364}\right)h_1 \quad (A.7)$$

In the short crack limit ($\xi \to 0$) it is obvious that $h_3 \to 0$. We rearrange ($A.7$) as follows,

$$\left(\frac{0.364}{n+1}\right)(1-\xi)\frac{\partial h_3}{\partial\xi}\frac{1}{h_1}=1 \quad (A.8)$$

Since J depends linearly on a as $\xi \to 0$, h_1 as defined by (4.18) of Part 1 must vanish, and therefore $\partial h_3/\partial\xi$ must vanish in order that the left-hand side of ($A.8$) remains bounded. To evaluate the left-hand side of ($A.8$) as $\xi \to 0$, we expand $\partial h_3/\partial\xi$ and h_1 in a Taylor series about $\xi = 0$, and apply l'Hôpital's rule to get the short crack relation

$$\frac{h_3}{h_1}\left(\frac{0.728}{n+1}\right)\left(\frac{1-\xi}{\xi}\right)=1 \quad (A.9)$$

Deep Crack Consistency Relation for the ECPM Configuration

It can be inferred from dimensional considerations that $\partial h_3/\partial\xi$ is bounded in the deep crack limit. Hence $(1-\xi)\partial h_3/\partial\xi$ must vanish as $\xi \to 1$. Using this result in ($A.7$) we get the deep crack relation,

$$\frac{h_3}{h_1}\left(\frac{0.728n}{n+1}\right)=1 \quad (A.10)$$

Downloaded 02 May 2010 to 171.66.16.25. Redistribution subject to ASME license or copyright; see http://www.asme.org/terms/Terms_Use.cfm

L. M. Keer
Mem. ASME

W. Lin

J. D. Achenbach
Fellow ASME

Department of Civil Engineering,
Northwestern University,
Evanston, Ill. 60201

Resonance Effects for a Crack Near a Free Surface

Stress intensity factors are computed for a horizontal subsurface crack that is subjected to time harmonic excitation. The problem is analyzed by determining displacement potentials that satisfy reduced wave equations and specified boundary conditions. The formulation of the problem leads to a system of coupled integral equations for the dislocation densities. The numerical solution of the integral equations leads directly to the stress intensity factors. Curves are presented for the ratios of the elastodynamic and the corresponding elastostatic Mode-I and Mode-II stress intensity factors. At specific values of the frequency, a resonance effect is observed and a correlation with the natural frequencies calculated by a Timoshenko plate theory for the layer between the crack and the free surface is noted.

1 Introduction

When rapidly varying loads are applied to a body that contains a crack, an accurate computation of the fields near the crack tips requires that inertia effects be taken into account. For example, computations of stress intensity factors for cracks in unbounded solids subjected to time-harmonic disturbances, show that the ratio of the elastodynamic stress-intensity factor to the corresponding elastostatic one has a very distinct dependence on the frequency, see e.g., references [1-3]. As the frequency increases, this ratio departs from unity to show a pattern of local maxima and minima. This behavior is a consequence of dynamic interactions due to the finite crack length, as discussed in reference [4].

The proximity of a boundary introduces another characteristic length, and hence the possibility of additional dynamic interactions. This is quite apparent for the case considered in this paper of a subsurface crack of length a which is parallel to a free surface at depth d. For small values of d/a, time-harmonic excitations of the body may induce quite strong resonance vibrations of the layer between the crack and the free surface. Such resonance vibrations give rise to substantial increases in both the Mode-*I* and Mode-*II* stress intensity factors. Similar effects have previously been noted in papers by Mal [5] for antiplane shear and Rokhlin [6] for a crack in a layer.

In this paper we consider a two-dimensional geometry and plane-strain deformations. A system of coupled singular integral equations for the Mode-*I* and Mode-*II* dislocation densities has been derived. These equations have been solved numerically for the cases of time-harmonic uniform tension and uniform shear. The ratios of elastodynamic to elastostatic stress intensity factors have been computed. For small values of d/a, the frequencies of the first maxima correlate reasonably well with the resonant frequencies of simply supported and clamped plates of length a and thickness d.

Related studies for surface-breaking cracks have been reported in references [7-9]. Elastodynamic stress-intensity factors for subsurface cracks normal to a free surface have been analyzed in [10] and [11].

2 Statement of the Problem

A homogeneous, isotropic, linearly elastic solid which occupies the half plane $y > 0$, contains a subsurface crack parallel to the free surface. The crack, whose length is a and whose faces are free of tractions, is located at a depth d beneath the free surface. The two-dimensional geometry is shown in Fig. 1. The formulation given in this section is valid for any system of plane-strain excitation.

The total fields generated by interaction of the externally excited field and the crack can be expressed as

$$u_i^t = u_i^{in} + u_i, \quad \sigma_{ij}^t = \sigma_{ij}^{in} + \sigma_{ij}, \qquad (2.1a,b)$$

where u_i^{in} and σ_{ij}^{in} are the displacement and stress components for the incident field which satisfy the appropriate conditions at the free surface of the half space, while u_i and σ_{ij} correspond to the scattered field. The time-harmonic factor $\exp(-i\omega t)$ has been suppressed. By virtue of linear superposition the scattered field is equivalent to the field generated in the cracked half plane by the application of tractions on the crack faces which are equal in magnitude but opposite in sign to the corresponding tractions due to the externally applied field in the uncracked half plane.

In the usual manner, the components of $\mathbf{u}(x,y)$ can be expressed in terms of displacement potentials $\phi(x,y)$ and $\psi(x,y)$ by the relations

$$u_x = \partial\phi/\partial x + \partial\psi/\partial y, \quad u_y = \partial\phi/\partial y - \partial\psi/\partial x. \qquad (2.2a,b)$$

Contributed by the Applied Mechanics Division for presentation at the 1984 PVP Conference and Exhibition, Joint with Applied Mechanics Division and Materials Division, San Antonio, Texas, June 17-21, 1984 of THE AMERICAN SOCIETY OF MECHANICAL ENGINEERS.

Discussion on this paper should be addressed to the Editorial Department, ASME, United Engineering Center, 345 East 47th Street, New York, N.Y. 10017, and will be accepted until two months after final publication of the paper itself in the JOURNAL OF APPLIED MECHANICS. Manuscript received by ASME Applied Mechanics Division, January, 1983; final revision, June, 1983. Paper No. 84-APM-7.

Copies will be available until February, 1985.

Copyright © 1984 by ASME
Downloaded 02 May 2010 to 171.66.16.25. Redistribution subject to ASME license or copyright; see http://www.asme.org/terms/Terms_Use.cfm

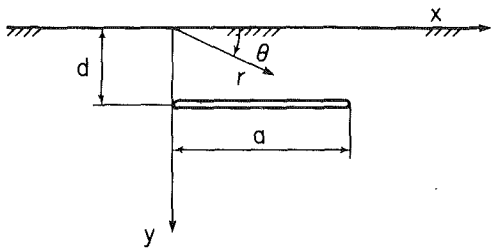

Fig. 1 Geometrical configuration of subsurface crack

The boundary-value problem can now be stated as that of finding potentials ϕ and ψ, which satisfy the following conditions:

(*i*) In the half plane ϕ and ψ satisfy the equations

$$(\nabla^2 + k_L^2)\phi = 0, \quad (\nabla^2 + k_T^2)\psi = 0, \tag{2.3a,b}$$

where ∇^2 is the two-dimensional Laplacian, and k_L and k_T are the wave numbers of longitudinal and transverse waves, respectively,

$$k_L = \omega/c_L, \quad c_L^2 = (\lambda + 2\mu)/\rho, \tag{2.4a,b}$$

$$k_T = \omega/c_T, \quad c_T^2 = (\mu/\rho). \tag{2.5a,b}$$

Here λ and μ are the Lame elastic constants and ρ is the mass density.

(*ii*) The surface tractions vanish on $y = 0$, and they take prescribed values on the faces of the crack:

$$\sigma_{xy} = \sigma_{yy} = 0, \quad -\infty < x < \infty, \quad y = 0, \tag{2.6}$$

$$\sigma_{xy} + \sigma_{xy}^{in} = 0, \quad y = d, \quad 0 < x < a \tag{2.7}$$

$$\sigma_{yy} + \sigma_{yy}^{in} = 0, \quad y = d, \quad 0 < x < a. \tag{2.8}$$

The components of the stress tensor are related to the potentials by equations (2.3*a*,*b*) and the constitutive relation

$$\sigma_{ij} = \lambda\delta_{ij}\partial u_k/\partial x_k + \mu(\partial u_i/\partial x_j + \partial u_j/\partial x_i). \tag{2.9}$$

(*iii*) At points where the unit vector normal to the crack surface suffers a step discontinuity, e.g., at the crack tip,

$$\sigma_{ij} = o(1/r_e), \quad u_i = 0(1), \quad \text{as} \quad r_e \to 0, \tag{2.10}$$

where $r_e = [(x-e)^2 + (y-d)^2]^{1/2}$ and $e = 0$ or a. This is an edge condition which states that the displacement and stress tensor are not so singular as to correspond to line sources of radiated energy.

(*iv*) The scattered field must also satisfy a radiation condition to the effect that at infinity it consists of outgoing surface waves and outgoing longitudinal and transverse body waves

$$\phi = A_\pm e^{\pm ik_R x - (k_R^2 - k_L^2)^{1/2} y} + A(\theta)(k_L r)^{-1/2} e^{ik_L r} + o((k_L r)^{-1/2}), \tag{2.11}$$

$$\psi = B_\pm e^{\pm ik_R x - (k_R^2 - k_T^2)^{1/2} y} + B(\theta)(k_T r)^{-1/2} e^{ik_T r} + o((k_T r)^{-1/2}), \tag{2.12}$$

as $r \to \infty$, where the polar coordinates (r,θ) are displayed in Fig. 1. The $\pm$ signs refer to the regions $x \gtrless 0$ and the constants $A_\pm, B_\pm$ satisfy the equation

$$A_+/B_+ = -A_-/B_- = (2k_R^2 - k_T^2)/2ik_R(k_R^2 - k_L^2)^{1/2}, \tag{2.13}$$

where $k_R = \omega/c_R$ is the wave number of a Reyleigh wave: i.e., the positive real root of $R(z) = 0$, where $R(z)$ is the Rayleigh determinant,

$$R(z) = (2z^2 - k_T^2)^2 - 4z^2(z^2 - k_L^2)^{1/2}(z^2 - k_T^2)^{1/2}. \tag{2.14}$$

3 Integral Representation for the Field

The fundamental singular solutions to the equations of time-harmonic plane strain motion in an elastic half space can be expressed in terms of the fundamental potential pairs (Φ^L, Ψ^L) and (Φ^T, Ψ^T), which in a different connection were first introduced by Lapwood [12]. They correspond to line sources in a half space of longitudinal and transverse body waves, respectively, and they can be calculated as combinations of Hankel functions and Fourier integrals. Explicit expressions can be found in reference [10].

Analogously to the development in reference [10], the displacement potentials for the half space containing the crack can be obtained in the form

$$\Phi(\mathbf{r}') = -\frac{1}{\mu k_T^2}\int_0^a [u_i](x)\,\sigma_{iy}^L(x,d;x',y')\,dx \tag{3.1}$$

$$\psi(\mathbf{r}') = -\frac{1}{\mu k_T^2}\int_0^a [u_i](x)\,\sigma_{iy}^T(x,d;x',y')\,dx, \tag{3.2}$$

where σ_{iy}^L and σ_{iy}^T are stress components derived via equations (2.2) and (2.9) from the fundamental potential pairs (Φ^L, Ψ^L) and (Φ^T, Ψ^T). Also

$$[u_i](x) = u_i(x,d^+) - u_i(x,d^-). \tag{3.3}$$

If these expressions are integrated by parts, they produce representations for the elastodynamic field in the interior of the solid in terms of the functions $d_i(x)$,

$$\phi(\mathbf{r}') = \frac{1}{\mu k_T^2}\int_0^a d_i(x)\,\tau_{iy}^L(x,d;x',y')\,dx \tag{3.4}$$

$$\psi(\mathbf{r}') = \frac{1}{\mu k_T^2}\int_0^a d_i(x)\,\tau_{iy}^T(x,d;x',y')\,dx, \tag{3.5}$$

where $d_i(x)$ is the dislocation density:

$$d_i(x) = \partial[u_i]/\partial x, \tag{3.6}$$

and τ_{iy}^L and τ_{iy}^T are any functions satisfying

$$\tau_{iy}^\beta = \int \sigma_{iy}^\beta dx + f^\beta(y), \quad i = x,y, \ \beta = L \ \text{ or } \ T. \tag{3.7}$$

An additional condition that is required to ensure that the crack is closed at its tips is

$$\int_0^a d_i(x)\,dx = 0. \tag{3.8}$$

This condition enables us to choose $f^\beta(y) \equiv 0$ in (3.7).

The components of the stress tensor in the scattered field are obtained by appropriate differentiations of (3.4) and (3.5). The following integral equations are obtained:

$$\sigma_{yy}(x',d) = -\sigma_{yy}^{in}(x',d) = \frac{\mu}{k_T^2}\int_0^a (d_y A_{11} - d_x A_{12})dx \tag{3.9}$$

$$\sigma_{xy}(x',d) = -\sigma_{xy}^{in}(x',d) = -\frac{\mu}{k_T^2}\int_0^a (d_y A_{21} - d_x A_{22})dx, \tag{3.10}$$

where A_{11}, A_{12}, A_{21}, and A_{22} are as follows:

$$A_{11} = -\int_\Gamma \frac{[(2\xi^2 - k_T^2)^2 e^{-\alpha_L d} - 4\xi^2\alpha_L\alpha_T e^{-\alpha_T d}]^2}{2\pi i R(\xi)\alpha_L\xi} e^{i\xi(x'-x)}d\xi + \frac{\text{sign}}{\pi}\int_\Gamma (e^{i\xi 2d} + 1)\left[\frac{(k_T^2 + 2\alpha_L^2)^2}{4\alpha_L^2} e^{-\alpha_L|x'-x|} - \xi^2 e^{-\alpha_T|x'-x|}\right]d\xi \tag{3.11}$$

$$A_{22} = -\int_\Gamma \frac{[4\xi^2\alpha_L\alpha_T e^{-\alpha_L d} - (2\xi^2 - k_T^2)^2 e^{-\alpha_T d}]^2}{2\pi i R(\xi)\alpha_T\xi} e^{i\xi(x'-x)}d\xi + \frac{\text{sign}}{\pi}\int_\Gamma (e^{i\xi 2d} + 1)\left[-\xi^2 e^{-\alpha_L|x'-x|}\right.$$

Downloaded 02 May 2010 to 171.66.16.25. Redistribution subject to ASME license or copyright; see http://www.asme.org/terms/Terms_Use.cfm

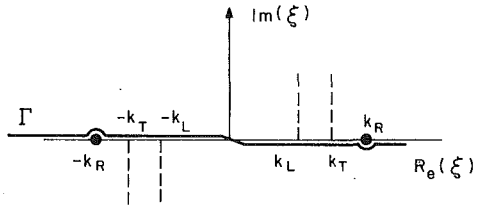

Fig. 2 Contour Γ used for evaluation of Green's functions

$$+\frac{(k_T^2+2\alpha_T^2)^2}{4\alpha_T^2}e^{-\alpha_T|x'-x|}\Big]d\xi \tag{3.12}$$

$$A_{12}=\int_\Gamma \frac{(2\xi^2-k_T^2)}{\pi R(\xi)}(e^{-\alpha_L d}-e^{-\alpha_T d})[(2\xi^2-k_T^2)^2 e^{-\alpha_L d} -4\xi^2\alpha_L\alpha_T e^{-\alpha_T d}]e^{i\xi(x'-x)}d\xi + \frac{i}{2\pi}\int_\Gamma e^{i\xi 2d}\Big[\frac{-\xi(k_T^2+2\alpha_L^2)}{\alpha_L}e^{-\alpha_L|x'-x|} + \frac{\xi(k_T^2+2\alpha_T^2)}{\alpha_T}e^{-\alpha_T|x'-x|}\Big]d\xi \tag{3.13}$$

$$A_{21}=\int_\Gamma \frac{-(2\xi^2-k_T^2)}{\pi R(\xi)}(e^{-\alpha_L d}-e^{-\alpha_T d})[4\xi^2\alpha_L\alpha_T e^{-\alpha_L d} -(2\xi^2-k_T^2)^2 e^{-\alpha_T d}]e^{i\xi(x'-x)}d\xi + \frac{i}{2\pi}\int_\Gamma e^{i\xi 2d}\Big[\frac{-\xi(k_T^2+2\alpha_L^2)}{\alpha_L}e^{-\alpha_L|x'-x|} + \frac{\xi(k_T^2+2\alpha_T^2)}{\alpha_T}e^{-\alpha_T|x'-x|}\Big]d\xi \tag{3.14}$$

Here

$$\text{sign}=(x-x')/|x-x'|. \tag{3.15}$$

and

$$\alpha_\beta^2=\xi^2-k_\beta^2 \tag{3.16}$$

where $Re(\alpha_\beta)\geq 0$ and $Im(\alpha_\beta)\leq 0$. The integrations in equations (3.11)–(3.14) are along the contour Γ depicted in Fig. 2.

The second integrals in A_{ij} are intergrable. They can be written as sums of four integrals:

$$I_1=\frac{\text{sign}}{\pi}\int_\Gamma (k_T^2+\alpha_\beta^2)e^{i\xi\bar{y}-\alpha_\beta\bar{x}}d\xi \tag{3.17a}$$

$$I_2=\frac{\text{sign}}{\pi}\int_\Gamma \frac{k_T^4}{4\alpha_\beta^2}e^{i\xi\bar{y}-\alpha_\beta\bar{x}}d\xi \tag{3.17b}$$

$$I_3=\frac{i}{2\pi}\int_\Gamma \frac{\xi(2\alpha_\beta^2+k_T^2)}{\alpha_\beta}e^{i\xi\bar{y}-\alpha_\beta\bar{x}}d\xi \tag{3.17c}$$

$$I_4=\frac{\text{sign}}{\pi}\int_\Gamma (-\xi^2)e^{i\xi\bar{y}-\alpha_\beta\bar{x}}d\xi \tag{3.17d}$$

where sign is defined by (3.15), $\bar{y}=0$ or $2d$, and $\bar{x}=|x'-x|$. By the change of variables $\xi=-k_\beta\cosh t$, we have $\alpha_\beta=-k_\beta\sinh t$ and the contour Γ changes to a contour C. By the use of, see [10],

$$H_n^1(k_\beta\bar{r})e^{in\bar{\theta}}=\frac{1}{\pi i}\int_c e^{-ik_\beta\bar{y}\cosh t+k_\beta\bar{x}\sinh t-n\pm u}dt, \tag{3.18a}$$

where $\bar{r}^2=(\bar{x}^2+\bar{y}^2)$ and $e^{i\bar{\theta}}=\bar{x}/\bar{r}-i\,\bar{y}/\bar{r}$, we obtain

$$I_1=\frac{i(\text{sign})k_\beta^3}{4}\Big[H_3^1(k_\beta\bar{r})\cos 3\bar{\theta} +\Big(\frac{4k_T^2}{k_\beta^2}-3\Big)H_1^1(k_\beta\bar{r})\cos\bar{\theta}\Big] \tag{3.18b}$$

$$I_3=\frac{ik_\beta^3}{4}\Big[H_3^1(k_\beta\bar{r})\sin 3\bar{\theta}+\Big(\frac{2k_T^2}{k_\beta^2}-1\Big)H_1^1(k_\beta\bar{r})\sin\bar{\theta}\Big] \tag{3.18c}$$

$$I_4=\frac{-i(\text{sign})k_\beta^3}{4}[H_3^1(k_\beta\bar{r})\cos 3\bar{\theta}+H_1^1(k_\beta\bar{r})\cos\bar{\theta}] \tag{3.18d}$$

$$I_2=\frac{-ik_T^4}{4k_\beta}J, \tag{3.18e}$$

Here

$J=\int^x k_\beta H_0^1[k_\beta(\bar{y}^2+(\eta-x')^2)^{1/2}]d\eta$ or equivalently

$J=\int^{x-x'} H_0^1[k_\beta(\bar{y}^2+z^2)^{1/2}]k_\beta dz$. When $\bar{y}=0$, we have

$$+\frac{2i}{\pi}\Big[e-S(k)+ln\frac{k_\beta\bar{r}}{2}\Big]+\frac{2i(-1)^l}{\pi}\Big]q\tan^{-1}\Big(\frac{p}{q}\Big) -p\sum_{m=0}^{l}\frac{(-1)^m}{2m+1}\Big(\frac{p}{q}\Big)^{2m}\Big]\Big\} \tag{3.19b}$$

For $\bar{y}=2d$, we have

$$J=\sum_{k=0}^{\infty}\frac{(-q^2/4)^k}{k!}\sum_{l=0}^{k}\frac{1}{l!\,(k-l)!\,(2l+1)}\Big\{p\Big(\frac{p}{q}\Big)^{2l}\Big[1 +\frac{2i}{\pi}\Big[e-S(k)+ln\frac{k_\beta\bar{r}}{2}\Big]+\frac{2i(-1)^l}{\pi}\Big[q\tan^{-1}\Big(\frac{p}{q}\Big) -p\sum_{m=0}^{n}\frac{(-1)^m}{2m+1}\Big(\frac{p}{q}\Big)^{2m}\Big]\Big\} \tag{3.19b}$$

where $p=k_\beta(x-x')$, $q=k_\beta\bar{y}$, e is the Euler number, and $S(k)=1+1/2+1/3+\ldots+1/k$, $S(0)=1$.

Equations (3.9) and (3.10) give coupled integral equations for the dislocation densities. The equations relate the stresses over the crack length and the corresponding dislocation densities.

The method can be applied to any arbitrary stress distribution on the crack faces, thus representing a general field.

4 Far-Field Response

The integral representations (3.4) and (3.5) are of the forms considered by Gregory [13], who showed by the method of steepest descents that they possess a far field of the form of equations (2.11) and (2.12). An explicit formula for the coefficient of the Rayleigh wave in the scattered field is

$$A_\pm=\frac{(2k_R^2-k_T^2)^2k_R}{2k_T^2S_1}\int_0^a[-d_x(x)P_\pm(x)+id_y(x)Q_\pm(x)]dx \tag{4.1}$$

where

$$P_\pm(x)=2i(k_R^2-k_L^2)^{1/2}(k_R^2-k_T^2)^{1/2}[e^{-(k_R^2-k_L^2)^{1/2}d} -e^{-(k_R^2-k_T^2)^{1/2}d}]e^{\mp ik_Rx} \tag{4.2}$$

$$Q_\pm(x)=\frac{\pm i(2k_R^2-k_T^2)(k_R^2-k_T^2)^{1/2}}{k_R}[e^{-(k_R^2-k_L^2)^{1/2}d} -e^{-(k_R^2-k_T^2)^{1/2}d}]e^{\mp ik_Rx} \tag{4.3}$$

$$S_1=(4k_R^4-k_T^4)(k_R^2-k_L^2)^{1/2}(k_R^2-k_T^2)^{1/2}-2k_R^4)(2k_R^2-k_L^2-k_T^2) \tag{4.4}$$

The corresponding expressions for $B_\pm$ follow from equation (2.13).

Downloaded 02 May 2010 to 171.66.16.25. Redistribution subject to ASME license or copyright; see http://www.asme.org/terms/Terms_Use.cfm

Similarly, the coefficients of the body waves are obtained as

$$A(\theta)=\frac{(2\pi)^{1/2}e^{i\pi/4}}{k_T^2}\int_0^a [d_y(x)H_1(\theta;\bar{r},\bar{\theta}) - d_x(x)H_2(\theta;\bar{r},\bar{\theta})]dx \tag{4.5}$$

$$B(\theta)=\frac{(2\pi)^{1/2}e^{i\pi/4}}{k_T^2}\int_0^a [d_y(x)H_3(\theta;\bar{r},\bar{\theta}) - d_x(x)H_4(\theta;\bar{r},\bar{\theta})]dx \tag{4.6}$$

where

$$\bar{\theta}=\tan^{-1}\left(\frac{d}{x}\right),\quad \bar{r}=(x^2+d^2)^{1/2} \tag{4.7a,b}$$

and

$$H_1(\theta;\bar{r},\bar{\theta})=(E_1-E_2)\left(\frac{-ik_T^2}{k_L\cos\theta}+2ik_L\cos\theta\right)+2E_3\Delta_1 \tag{4.8}$$

$$H_2(\theta;\bar{r},\bar{\theta})=(E_1-E_2)2k_L i\sin\theta - iE_3(k_L\cos\theta+\Delta_1^2/k_L\cos\theta) \tag{4.9}$$

$$E_1=\frac{-1}{4\pi}\exp[-ik_L\bar{r}\cos(\theta-\bar{\theta})] \tag{4.10}$$

$$E_2=\left[\frac{-2ik_L^3\Delta_1\cos^2\theta\sin\theta}{\pi R(k_L\cos\theta)}+\frac{1}{4\pi}\right]\exp[-ik_L\bar{r}\cos(\theta+\bar{\theta})] \tag{4.11}$$

$$E_3=\frac{-k_L^2\cos\theta\sin\theta(2k_L^2\cos^2\theta-k_T^2)}{\pi R(k_L\cos\theta)}e^{-ik_Lx\cos\theta-\Delta_1 d} \tag{4.12}$$

$$\Delta_1=-i(k_T^2-k_L^2\cos^2\theta)^{1/2} \tag{4.13}$$

$$H_3=(E_4-E_5)2k_T i\sin\theta+E_6\left(\frac{-ik_T}{\cos\theta}+2ik_T\cos\theta\right) \tag{4.14}$$

$$H_4=-i(E_4+E_5)\left(k_T\cos\theta-\frac{k_T\sin^2\theta}{\cos\theta}\right)+2E_6\Delta_2 \tag{4.15}$$

$$E_4=\frac{-1}{4\pi}\exp[-ik_T\bar{r}\cos(\theta-\bar{\theta})] \tag{4.16}$$

$$E_5=\left[\frac{-2ik_T^3\Delta_2\cos^2\theta\sin\theta}{\pi R(k_T\cos\theta)}+\frac{1}{4\pi}\right]\exp[-ik_T\bar{r}\cos(\bar{\theta}+\theta)] \tag{4.17}$$

$$E_6=\frac{k_T^4\cos\theta sin\theta(2\cos^2\theta-1)}{\pi R(k_T\cos\theta)}e^{-ik_Tx\cos\theta-\Delta_2 d} \tag{4.18}$$

where

$$\Delta_2=\begin{cases}(k_T^2\cos^2\theta-k_L^2)^{1/2} & \text{for } k_T^2\cos^2\theta>k_L^2 \quad (4.19a)\\ -i(k_L^2-k_T^2\cos^2\theta)^{1/2} & \text{for } k_L^2>k_T^2\cos^2\theta \quad (4.19b)\end{cases}$$

The far-field surface waves generated by the dislocation densities can be evaluated by using equations (2.2*a*,*b*), (2.11)–(2.13), and (4.1)–(4.4) while the far-field body waves can be calculated by applying equations (2.2*a*,*b*), (2.11), (2.12), and (4.5)–(4.19). Although the calculation of the body waves is costly, it is essential to the calculation of the balance of rates of energy in the next section.

5 Energy Considerations

For a steady-state time-harmonic system, the time-averaged input power should be equal to the time-averaged output power. For a crack of area A loaded by surface tractions, the time-averaged input power may be written as

$$<P_I>=\frac{1}{2}Re\int_a T_i v_i^* dA \tag{5.1}$$

where T_i are the traction components and v_i are the components of the particle velocity, while (*) denotes the complex conjugate. By using $T_i=\sigma_{ij}n_j$ and $v_i=-i\omega u_i$, we find for the present geometry

$$<P_I>=\frac{\omega}{2}Im\int_0^a \sigma_{iy}[u_i^*]dx \tag{5.2}$$

which can also be written as

$$<P_I>=-\frac{\omega}{2}Im\int_0^a \tau_{ij}d_i^* dx \tag{5.3}$$

where τ_{iy} and d_i^* are defined by (3.7) and (3.6), respectively.

By considering a half circular surface S far away from the crack, we find for the output power due to body waves [13]

$$\frac{2}{\omega\mu}<P_B>=\frac{1}{\mu}Im\int_s \sigma_{ij}n_j u_i^* dS=k_T^2\int_0^\pi \{|A^2(\theta)| + |B^2(\theta)|\}d\theta \tag{5.4}$$

For the surface wave, we find [13]

$$\frac{2}{\omega\mu}<P_R>=\frac{k_R}{2(k_R^2-k_L^2)^{1/2}}(4k_R^2-4k_L^2+k_T^2)|A_-|^2 + [2(k_R^2-k_L^2)^{1/2}(k_R^2-k_T^2)^{1/2}+2k_R^2+k_T^2]Im(A_-^* B_-) + \frac{k_R}{2(k_R^2-k_T^2)^{1/2}}(4k_R^2-3k_T^2)|B_-|^2 \tag{5.5}$$

Since (5.3), (5.4), and (5.5) should balance, a measure of the error in the numerical computations may be expressed as

$$\text{Error}=1-\frac{<P_I>}{<P_B>+2<P_R>} \tag{5.6}$$

Equation (5.6) has been used to check the accuracy of the numerical results.

6 Numerical Solution to the Integral Equation

The coupled integral equations for the dislocation densities are singular integrals of the Cauchy type. The numerical scheme used here is the Gauss-Chebyshev quadrature formula [14]. Equations (3.9) and (3.10) are written as

$$\sigma_{yy}(x_{oj})=\frac{\mu}{k_T^2}\frac{a}{2}\frac{\pi}{m}\sum_{i=1}^m(\bar{d}_y A_{11}-\bar{d}_x A_{12}) \tag{6.1a}$$

$$\sigma_{xy}(x_{oj})=\frac{-\mu}{k_T^2}\frac{a}{2}\frac{\pi}{m}\sum_{i=1}^m(\bar{d}_y A_{21}-\bar{d}_x A_{22}) \tag{6.1b}$$

where $\bar{d}_x(x_i)$, $\bar{d}_y(x_i)$, $A_{kl}(x_i,x_{oj})$, (k,l = 1,2) are defined as

$$z_i=\cos\frac{(i-0.5)\pi}{m}\quad (i=1,2,\ldots,m) \tag{6.2a}$$

$$x_i=(z_i+1)a/2 \tag{6.2b}$$

$$x_{oj}=(\cos j\pi/m+1)a/2\quad (j=1,2,\ldots,m-1) \tag{6.2c}$$

$$\frac{\bar{d}_x(x_i)}{d_x(x_i)}=\frac{\bar{d}_y(x_i)}{d_y(x_i)}=(1-z_i^2)^{1/2} \tag{6.2d}$$

The crack closure condition is

$$\sum_{i=1}^m \bar{d}_x(x_i)=\sum_{i=1}^m \bar{d}_y(x_i)=0 \tag{6.3}$$

By combining equations (6.1) and (6.3), we can solve for $\mu\bar{d}_x$ and $\mu\bar{d}_y$.

The stress intensity factors at the crack tips are defined as

Downloaded 02 May 2010 to 171.66.16.25. Redistribution subject to ASME license or copyright; see http://www.asme.org/terms/Terms_Use.cfm

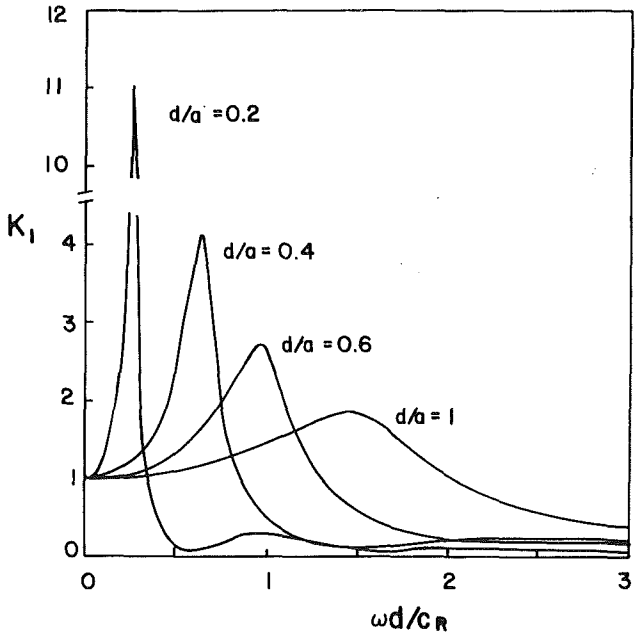

Fig. 3 Ratios of elastodynamic and elastostatic Mode-*I* stress intensity factors for uniform tension as functions of the frequency. Here, K_I (static) = 1.163, 1.385, 1.714, 2.906 for d/a = 1.0, 0.6, 0.4, 0.2.

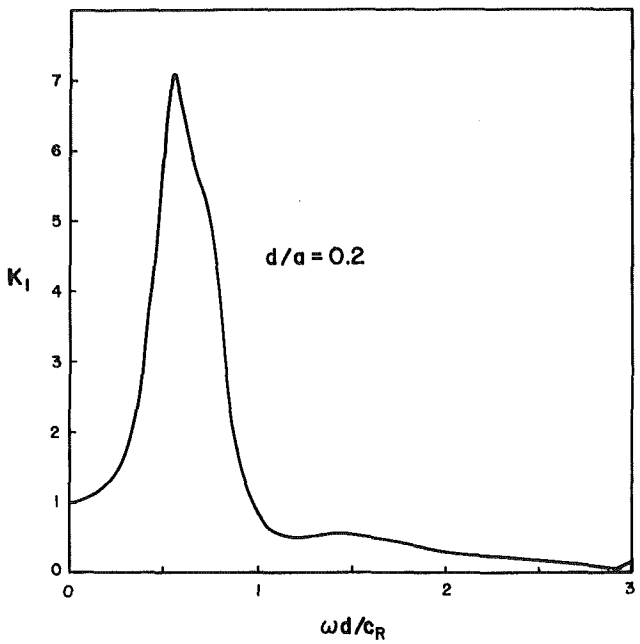

Fig. 5 Ratio of elastodynamic and elastostatic Mode-*I* stress intensity factor for uniform shear as a function of the frequency. Here, K_I (static) = 0.388 for d/a = 0.2.

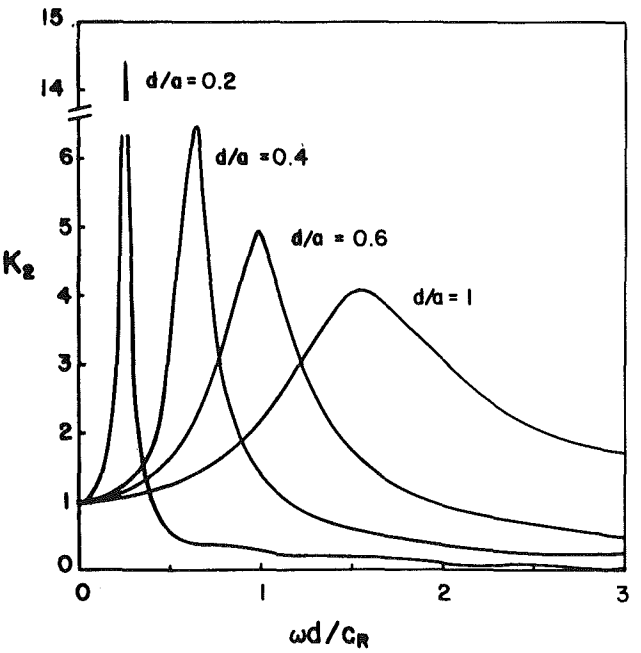

Fig. 4 Ratios of elastodynamic and elastostatic Mode-*II* stress intensity factors for uniform tension as functions of the frequency. Here, K_{II} (static) = 0.037, 0.125, 0.289, 0.994 for d/a = 1.0, 0.6, 0.4, 0.2.

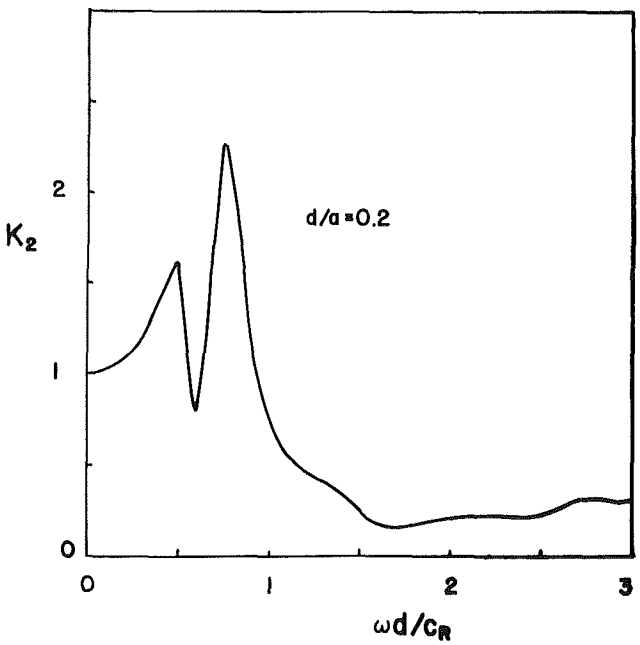

Fig. 6 Ratio of elastodynamic and elastostatic Mode-*II* stress intensity factor for uniform shear as a function of the frequency. Here, K_{II} (static) = 1.133 for d/a = 0.2.

$$\begin{Bmatrix} K_I \\ K_{II} \end{Bmatrix} = \lim_{x \to a} \; [2(x-a)]^{1/2} \begin{Bmatrix} |\sigma_{yy}(x,d)| \\ |\sigma_{xy}(x,d)| \end{Bmatrix}$$

$$= \frac{\mu(k_T^2 - k_L^2)}{k_T^2} \left(\frac{a}{2} \right)^{1/2} \begin{Bmatrix} |\tilde{d}_y(1)| \\ |\tilde{d}_x(1)| \end{Bmatrix} \tag{6.4}$$

where the argument of $\tilde{d}_x$, $\tilde{d}_y$ in equation (6.4) correspond to $z = 1$. The stress intensity factors, which depend on $\tilde{d}_i(\pm 1)$, may be determined from the extrapolation formula [16]

$$\tilde{d}_i\left(\begin{smallmatrix} +1 \\ -1 \end{smallmatrix}\right) = \frac{1}{m} \sum_{k=1}^{m} \frac{\sin\left[\dfrac{(2m-1)}{4m}(2k-1)\pi\right]}{\sin\left[\dfrac{(2k-1)\pi}{m}\right]} d_i\left(\begin{smallmatrix} x_k \\ x_{m+1-k} \end{smallmatrix}\right)$$

7 Results

Two specific cases have been studied; they are incident fields of uniform tension and uniform shear applied on $y = 0$,

Downloaded 02 May 2010 to 171.66.16.25. Redistribution subject to ASME license or copyright; see http://www.asme.org/terms/Terms_Use.cfm

Table 1 Natural frequencies of Timoshenko plate and freuqencies at maximum values of stress-intensity factors

$d/a=0.2$	$k_R d$				
mode	1	2	3	4	5
S	0.194	0.668	1.268	1.913	2.572
C	0.436	1.027	1.714	2.426	3.174
peak =	0.265(T)	0.54(S1)	1.0(T1)	---	---
	$k_R d$ (first mode only)				
d/a	0.2	0.4	0.6	1.0	
S	0.194	0.668	1.268	2.572	
C	0.436	1.518	3.124	---	
peak =	0.265(T)	0.64(T)	0.96(T)	1.5(T)	

(S): Simply supported plate
(C): Clamped plate
(T): Uniform tension (both K_1 an K_2)
($S1$): Uniform shear (K_1)
($T1$): Uniform tension (K_1)

which results on uniform tension and shear on the crack faces. In the numerical calculation Poisson's ratio has been taken as 0.3. The desired field quantities calculated in this paper are K_1 (Mode-*I*), and K_2 (Mode-*II*), which are the magnitudes of the ratios of dynamic and static stress intensity factors at the crack tips.

Uniform Tension. $\sigma_{yy}(x,d,t) = -\exp(ik_L d)\exp(-i\omega t)$: The results, which show the variations of K_1, K_2 with the dimensional parameters d/a and k_Rd, are given in Figs. 3 and 4. It is observed that K_1 and K_2 have local maxima (resonances), which deserve special attention; for small d/a they seem to correspond to plate resonances as will be discussed later. The limiting values of K_1 and K_2 as $k_R d \to 0$ correspond to the static case, and they agree with those calculated by Chen, et al. [15].

Uniform Shear. $\sigma_{xy}(x,d,t) = \exp(ik_T d)\exp(-i\omega t)$: Results showing the variation of K_1, K_2 for $d/a = 0.2$ are given in Figs. 5 and 6. It is again observed that K_1 and K_2 exhibit local maxima.

A comparison between the frequencies at maximum values of K_1 and K_2 both in tension and in shear and the natural frequencies of a Timoshenko plate (plane-strain case) shows a strong correlation (Table 1). For values of d/a small (~ 0.2) the clamped plate and the simply supported plate appear to provide an upper and lower bound, respectively, of the frequency at the first maximum. It is expected that a lower value of d/a will produce a stronger resonance effect (Figs. 3 and 4). For d/a relatively large, say greater than 0.4, the Timoshenko plate theory will no longer be valid; however, the natural frequencies calculated from this theory still provide information useful for the understanding of the peak points in Figs. 3 and 4.

In the vicinity of the first natural frequency it is difficult to determine the peak response by a numerical search. However, if the variations of K_1 and K_2 are assumed to correspond to the response of a damped single-degree-of-freedom system,

$$K_i = k_{oi}\{[1-(\omega/\omega_i)^2]^2 + (2p_i\omega/\omega_i)^2\}^{-1/2} \tag{7.1}$$

where $i = 1,2$, and w_i, k_{oi}, and p_i are constants, relating to the natural frequency, scaled amplitude, and damping coefficient, respectively, then equation (7.1) will approximately represent the behavior at the maxima, provided that the constants are suitably chosen. The constants can be easily determined from values of K_1 and K_2 calculated near the first natural frequency. For example, when $d/a = 0.2$ and $0.24 \le k_R d \le 0.28$ in the case of uniform tension, the approximate formulae are given by:

$$\begin{Bmatrix} K_1 \\ K_2 \end{Bmatrix} = \begin{Bmatrix} 2.4379 \\ 1.0838 \end{Bmatrix} \left\{ \left[1 - \left(\frac{k_R d}{0.26554}\right)^2\right]^2 + (0.286\, k_R d)^2 \right\}^{-1/2} \tag{7.2}$$

Similar formulas also exist for $d/a = 0.4$, 0.6, and 1.0. When d/a is smaller, the damping ratio is also smaller and the resonance effect is stronger.

Acknowledgment

The results reported in this paper were obtained in the course of research sponsored by the Air Force Office of Scientific Research under Grant AFOSR-78-3589-E.

References

1 Mal, A. K., "Interaction of Elastic Waves With a Griffith Crack," *Int. J. Eng. Sci.*, Vol. 8, 1970, pp. 763–776.

2 Loeber, J. F., and Sih, G. C., "Diffraction of Antiplane Shear Waves by a Finite Crack," *J. Acoust. Soc. Am.*, Vol. 44, 1968, pp. 90–98.

3 Luong, W. C., Keer, L. M., and Achenbach, J. D., "Elastodynamic Stress Intensity Factors of a Crack Near an Interface," *Int. J. Solids Structures*, Vol. 11, 1975, pp. 919–925.

4 Achenbach, J. D., and Gautesen, A. K., "A Ray Theory for Elastodynamic Stress Intensity Factors," ASME JOURNAL OF APPLIED MECHANICS, Vol. 45, 1978, pp. 123–129.

5 Mal, A. K., "Diffraction of *SH* Waves by a Near-Surface Crack," in *Review of Progress in Quantitative Nondestructive Evaluation*, Thompson, D. O., and Chimenti, D. E., eds., Volume 1, Plenum Press, New York, 1981, pp. 499–509.

6 Rokhlin, S., "Diffraction of Lamb Waves by a Finite Crack in an Elastic Layer," *J. Acoust. Soc. Am.*, Vol. 67, 1980, pp. 1157–1165.

7 Mendelson, D. A., Achenbach, J. D., and Keer, L. M., "Scattering of Elastic Waves by a Surface-Breaking Crack, *WAVE MOTION*, Vol. 2, 1980, pp. 277–292.

8 Mal, A. K., "Diffraction of Antiplane Shear Waves by an Edge Crack," ASME JOURNAL OF APPLIED MECHANICS, Vol. 47, 1980, pp. 359–362.

9 Datta, S. K., "Diffraction of SH-Waves by an Edge Crack," ASME JOURNAL OF APPLIED MECHANICS, Vol. 46, 1979, pp. 101–106.

10 Achenbach, J. D., and Brind, R. J., "Scattering of Surface Waves by a Sub-Surface Crack," *J. of Sound and Vibrations*, Vol. 76, 1981, pp. 43–56.

11 Achenbach, J. D., and Brind, R. J., "Elastodynamic Stress-Intensity Factors for a Crack Near a Free Surface," ASME JOURNAL OF APPLIED MECHANICS, Vol. 48, 1981, pp. 539–542.

12 Lapwood, E. R., "The Disturbance Due to a Line Source in a Semi-Infinite Elastic Medium," *Phil. Trans. Roy. Soc.*, Series *A*, Vol. 242, 1949, pp. 63–100.

13 Gregory, R. D., "The Non-Existence of Standing Modes in Certain Problems of Linear Elasticity," *Math. Proc. Camb. Phil. Soc.*, Vol. 77, 1974, pp. 385–404.

14 Erdogan, F., and Gupta, G. D., "On the Numerical Solution of Singular Integral Equations," *Quart. Appl. Math.*, Vol. 30, 1972, pp. 525–534.

15 Chen, S. H., Keer, L. M., and Achenbach, J. D., "Steady Motion of a Crack Parallel to a Bond-Plane," *Int. J. Eng. Sci.*, Vol. 18, 1980, pp. 225–238.

16 Krenk, S., "On the Use of the Interpolation Polynomial for Functions of Singular Integral Equations," *Quart. Appl. Math.*, Vol. 33, 1975, pp. 479–484.

Downloaded 02 May 2010 to 171.66.16.25. Redistribution subject to ASME license or copyright; see http://www.asme.org/terms/Terms_Use.cfm

Transient Stress Intensity Factors of an Interfacial Crack Between Two Dissimilar Anisotropic Half-Spaces

Part 1 Orthotropic Materials

A.-Y. Kuo
Applied Mechanics Group,
NUTECH Engineers, Inc.,
San Jose, Calif. 95119
Assoc. Mem. ASME

Transient response of an interfacial crack between two dissimilar elastic, orthotropic solids is investigated. The interfacial crack is excited by tractions suddenly applied on the crack surfaces. Governing equations, boundary conditions, and continuity conditions along the interface are reduced to a singular integral equation. Solution of the singular integral equation is obtained by the use of Jacobi polynomials. Expressions for stress intensity factors at the crack tip are given. As a sample problem, an interfacial crack in a 0 deg/90 deg fiber-reinforced composite solid excited by a suddenly applied uniform pressure on the crack surfaces is studied.

1 Introduction

Interfacial crack is one of the most commonly observed failure modes in fiber-reinforced composite laminates. The interfacial imperfection usually forms the nucleous of the fracture initiation and propagation in the medium. Composite laminates are highly anisotropic materials. Thus, the study of interfacial cracks between anisotropic media is of great importance in fracture analysis of composites.

The transient response of a finite dimensional crack in an isotropic solid has been presented analytically by Flitman [1], Kostrov [2], Tau and Lu, [3, 4], Sih and Loeber [5], and Sih, et al. [6]. Kuo [7] has formulated hybrid stress crack-tip elements for interfacial cracks between dissimilar anisotropic materials. Numerical solutions by using a finite element method with crack-tip elements have been presented for both static and dynamic problems in [7]. Some investigations have been carried out by Srivastava, et al. [8, 9] for the dynamic analysis of an interfacial crack between two dissimilar isotropic half-spaces. In [8, 9], the crack was assumed to be excited by a normally incident plane wave with a constant circular frequency. That is, solutions of [8, 9] are presented in the frequency domain. However, to the author's knowledge, no analytical solution has been presented for the problem of interfacial cracks between dissimilar anisotropic, elastic solids under dynamic loading.

This paper studies the dynamic stress intensity factors of a Griffith crack located at the interface of two orthotropic half-spaces with different elastic properties. Solutions of interfacial cracks between two fully anisotropic media will be reported in the second part of this paper. The crack is assumed to be excited by prescribed tractions on crack surfaces. Governing equations of the problem are reduced to a pair of singular integral equations. Solutions of the singular integral equations are expressed in terms of the Jacobi polynomials.

2 Formulation

Consider a crack of two unit length lying at the interface of two dissimilar orthotropic solids as shown in Fig. 1. A Cartesian coordinate system is chosen in such a way that x-axis is along the interface and the origin locates at the middle of the crack. Constitutive equations of the materials can be written in the contracted notation as

$$\sigma_k^{(\alpha)} = C_{kj}^{(\alpha)} \epsilon_j^{(\alpha)} \quad (k, j = 1,2,6;\ \alpha = 1,2) \tag{1}$$

where the repeated subscript indicates summation, C_{kj} is the stiffness tensor, and the superscripts 1 and 2 designate the upper and lower half-spaces, respectively. In the rest of this paper, the superscript will be dropped unless it is necessary to distinguish the upper and lower half-spaces. For orthotropic materials, C_{16}, C_{26}, C_{61}, and C_{62} are equal to zero. The engineering strains, ϵ_j, in equation (1) are defined by

$$\epsilon_1 = u_{,x},\ \epsilon_2 = v_{,y},\ \epsilon_6 = \gamma_{xy} = u_{,y} + v_{,x} \tag{2}$$

where u and v are displacement components. The stresses, σ_k,

Contributed by the Applied Mechanics Division for publication in the JOURNAL OF APPLIED MECHANICS.
Discussion on this paper should be addressed to the Editorial Department, ASME, United Engineering Center, 345 East 47th Street, New York, N.Y. 10017, and will be accepted until two months after final publication of the paper itself in the JOURNAL OF APPLIED MECHANICS. Manuscript received by ASME Applied Mechanics Division, April, 1983.

Copyright © 1984 by ASME
Downloaded 02 May 2010 to 171.66.16.25. Redistribution subject to ASME license or copyright; see http://www.asme.org/terms/Terms_Use.cfm

are defined in an analogous manner in the Cartesian coordinate system. Equations of motion of the problem are

$$C_{11}\ u_{,xx}+C_{66}\ u_{,yy}+(C_{12}+C_{66})\ v_{,xy}=\rho u_{,tt} \tag{3a}$$

$$(C_{12}+C_{66})\ u_{,xy}+C_{66}\ v_{,xx}+C_{22}\ v_{,yy}=\rho v_{,tt} \tag{3b}$$

where ρ is the density of the elastic material. Initial conditions of the problem are

$$u(x,y,0)=v(x,y,0)=0 \tag{4a}$$

$$u_{,t}(x,y,0)=v_{,t}(x,y,0)=0 \tag{4b}$$

The crack is excited by prescribed tractions suddenly applied at time $t=0$ on the crack surfaces. Thus, boundary conditions can be written as

$$\tau_{xy}(x,0,t)=-f_1(x)\ H(t) \qquad |x|\le 1 \tag{5a}$$

$$\sigma_y(x,0,t)=-f_2(x)\ H(t) \tag{5b}$$

where $H(t)$ is a Heaviside step function.

Continuity conditions along the interface of the dissimilar half-spaces are

$$\tau_{xy}^{(1)}(x,0,t)-\tau_{xy}^{(2)}(x,0,t)=0 \qquad \text{all } x \tag{6a}$$

$$\sigma_y^{(1)}(x,0,t)-\sigma_y^{(2)}(x,0,t)=0 \tag{6b}$$

and

$$u^{(1)}(x,0,t)-u^{(2)}(x,0,t)=0 \qquad |x|\ge 1 \tag{6c}$$

$$v^{(1)}(x,0,t)-v^{(2)}(x,0,t)=0 \tag{6d}$$

To further simplify the problem, the applied tractions are assumed to be symmetric to the y-axis, i.e., $f_1(-x)=-f_1(x)$ and $f_2(-x)=f_2(x)$. However, solutions to the asymmetric cases can be easily obtained by the same procedure described in this paper, and solutions of a general problem can always be expressed as the superposition of solutions of both cases. Such symmetric loads on crack surfaces lead to the following relations:

$$u(x,0,t)=-u(-x,0,t) \tag{7a}$$

$$v(x,0,t)=v(-x,0,t) \tag{7b}$$

3 Singular Integral Equations

To solve the problem, all equations are transformed into a frequency domain by applying the Laplace transform. Let s be the Laplace transform parameter and a tilde over a variable, e.g., $\tilde{u}$, represents the transformed function in the frequency domain. In the s-domain, transformed equations of equations (3a, 3b) are satisfied by taking

$$\tilde{u}^{(\alpha)}(x,y,s)=\frac{1}{(2\pi)^{1/2}}\int_{-\infty}^{\infty}A_j^{(\alpha)}\,e^{[i\xi x+(-1)^{\alpha}p_j^{(\alpha)}y]}d\xi \qquad (j=1,2) \tag{8a}$$

$$\tilde{v}^{(\alpha)}(x,y,s)=\frac{1}{(2\pi)^{1/2}}\int_{-\infty}^{\infty}A_j^{(\alpha)}\,\omega_j^{(\alpha)}\,e^{[i\xi x+(-1)^{\alpha}p_j^{(\alpha)}y]}d\xi \tag{8b}$$

where p_j is the jth root with positive real part of the equation

$$C_{22}C_{66}p^4-[(C_{11}C_{22}-C_{12}^2-2C_{12}C_{66})\xi^2+\rho s^2(C_{12}+C_{66})]p^2+(C_{11}\xi^2+\rho s^2)(C_{66}\xi^2+\rho s^2)=0 \tag{9}$$

A_j are unknown functions of ξ and s to be determined by boundary and continuity conditions, and

$$\omega_j=\frac{C_{66}p_j^2-C_{11}\xi^2-\rho s^2}{ip_j\xi(C_{12}+C_{66})} \quad \text{(no summation on } j) \tag{10}$$

Let

$$\tilde{u}^{(1)}(x,0,s)-\tilde{u}^{(2)}(x,0,s)=\frac{1}{(2\pi)^{1/2}}\int_{-\infty}^{\infty}\frac{1}{\xi}G_1(\xi,s)e^{i\xi x}\,d\xi \tag{11a}$$

$$\tilde{v}^{(1)}(x,0,s)-\tilde{v}^{(2)}(x,0,s)=\frac{1}{(2\pi)^{1/2}}\int_{-\infty}^{\infty}\frac{1}{\xi}G_2(\xi,s)e^{i\xi x}\,d\xi \tag{11b}$$

By using the symmetry conditions, equations (7a, b), G_1 and G_2 can be shown to be even and odd functions of ξ, respectively. Substituting equations (8a, b) into equations (6a,b) and equations (11a, b), we can write $A_j^{(\alpha)}$ in terms of G_1 and G_2 as

$$A_j^{(\alpha)}(\xi,s)=a_{(j+2\alpha-2)k}G_k(\xi,s)/\xi \qquad (j,k=1,2;\ \alpha=1,2) \tag{12}$$

where a_{jk} is an element of the inverse matrix of matrix $[D]$. Matrix $[D]$ is a four-by-four nonsingular matrix with the following elements:

$$\begin{aligned}
&D_{1j}=1,\ D_{1(j+2)}=-1,\ D_{2j}=\omega_j^{(1)},\ D_{2(j+2)}=\omega_j^{(2)}\\
&D_{3j}=C_{66}^{(1)}(i\omega_j^{(1)}\xi-p_j^{(1)})\\
&D_{3(j+2)}=C_{66}^{(2)}(i\omega_j^{(2)}\xi-p_j^{(2)}) \quad (j=1,2)\\
&D_{4j}=C_{12}^{(1)}i\xi-C_{22}^{(1)}\omega_j^{(1)}p_j^{(1)}\\
&D_{4(j+2)}=-C_{12}^{(2)}i\xi+C_{22}^{(2)}\omega_j^{(2)}p_j^{(2)}
\end{aligned} \tag{13}$$

Substituting equations (8a, b) into equations (5a, b) and eliminating A_j by equation (12), we obtain the following coupled integral equations:

$$\int_{-\infty}^{\infty}B_{jk}(\xi,s)G_k(\xi,s)\frac{1}{\xi}e^{i\xi x}d\xi=-f_j(x)/s, \quad |x|\le 1 \qquad (j,k=1,2) \tag{14}$$

where

$$B_{1k}(\xi,s)=C_{66}^{(1)}(i\omega_j^{(1)}\xi-p_j^{(1)})a_{jk} \qquad (j,k=1,2) \tag{15a}$$

$$B_{2k}(\xi,s)=(C_{12}^{(1)}i\xi-C_{22}^{(1)}\omega_j^{(1)}p_j^{(1)})a_{jk} \tag{15b}$$

If it is found that $B_{jk}(\xi,s)$ is an even function of ξ when j and k are equal and is an odd function of ξ when j and k are different. It is also observed that

$$B_{jk}(\xi,s)=B_{kj}(-\xi,s) \tag{16}$$

Equation (16) can also be proven by using Betti's reciprocal theorem. Assume

$$G_1(\xi,s)=\left(\frac{2}{\pi}\right)^{1/2}\int_0^1 r_1'(x,s)\cos\xi x\,dx \tag{17a}$$

$$G_2(\xi,s)=i\left(\frac{2}{\pi}\right)^{1/2}\int_0^1 r_2'(x,s)\sin\xi x\,dx \tag{17b}$$

where r_1' and $r_2'(x,s)$ are functions to be determined. Substituting equations (17a,b) into equation (14) yields

$$[M_1]\begin{bmatrix} r_2(x,s)\\ ir_1(x,s)\end{bmatrix}+\frac{1}{\pi i}[M_2]\int_{-1}^{1}\begin{bmatrix} r_2(\eta,s)\\ ir_1(\eta,s)\end{bmatrix}\frac{d\eta}{\eta-x}+\int_{-1}^{1}[H]\begin{bmatrix} r_2(\eta,s)\\ ir_1(\eta,s)\end{bmatrix}d\eta=\begin{bmatrix} if_1(x)/s\\ f_2(x)/s\end{bmatrix} \tag{18}$$

where

$$[M_1]=\begin{bmatrix} m_0 & 0\\ 0 & m_0\end{bmatrix},\quad [M_2]=\begin{bmatrix} 0 & n_1\\ n_2 & 0\end{bmatrix},$$

Downloaded 02 May 2010 to 171.66.16.25. Redistribution subject to ASME license or copyright; see http://www.asme.org/terms/Terms_Use.cfm

$$[H]=\begin{bmatrix} H_4 & iH_3 \\ -iH_2 & H_1 \end{bmatrix} \tag{19}$$

m_0, n_1, n_2, and H_1–H_4 are defined in Appendix 1, and $r_1(x,s)$, $r_2(x,s)$ are, respectively, even and odd extensions of $r_1'(x,s)$ and $r_2'(x,s)$ in $[-1,1]$.

Following the solution scheme suggested by Erdogan [10], the coupled singular integral equations, equation (18), can be transformed into an equivalent but simpler form as

$$\begin{bmatrix} \phi_1(x,s) \\ \phi_2(x,s) \end{bmatrix} + \frac{1}{\pi i}\int_{-1}^{1} \begin{bmatrix} (n_1n_2)^{1/2}/m_0 & 0 \\ 0 & -(n_1n_2)^{1/2}/m_0 \end{bmatrix} \begin{bmatrix} \phi_1(\eta,s) \\ \phi_2(\eta,s) \end{bmatrix} \frac{d\eta}{\eta-x} + \int_{-1}^{1} [L(\mu,x,s)] \begin{bmatrix} \phi_1(\eta,s) \\ \phi_2(\eta,s) \end{bmatrix} d\eta = [R]^{-1}[M_1]^{-1} \begin{bmatrix} if_1(x)/s \\ f_2(x)/s \end{bmatrix} \tag{20}$$

where

$$[R]=\begin{bmatrix} 1 & 1 \\ (n_2/n_1)^{1/2} & -(n_2/n_1)^{1/2} \end{bmatrix} \tag{21a}$$

$$\begin{bmatrix} r_1(x,s) \\ ir_2(x,s) \end{bmatrix} = [R] \begin{bmatrix} \phi_1(x,s) \\ \phi_2(x,s) \end{bmatrix} \tag{21b}$$

$$[L]=[R]^{-1}[M_1]^{-1}[H][R] = \begin{bmatrix} L_1(\eta,x,s) & L_2(\eta,x,s) \\ L_3(\eta,x,s) & L_4(\eta,x,s) \end{bmatrix} \tag{21c}$$

It can be shown that L_1 and L_4 are complex conjugate of each other, and so are L_2 and L_3. Since $\phi_2=-\bar{\phi}_1$, the two equations of equation (20) are negative complex conjugate of each other. Besides equation (20), the continuity conditions, equations (6c,d), lead to two additional equations to be satisfied:

$$\int_{-1}^{1} \begin{bmatrix} \phi_1(x,s) \\ \phi_2(x,s) \end{bmatrix} dx = 0 \tag{22}$$

Nevertheless, there exist only two independent equations out of equations (20) and (22). Thus, the governing equations as well as boundary conditions have been reduced to two equations:

$$\frac{m_0}{(n_1n_2)^{1/2}}\phi_1(x,s)+\frac{1}{\pi i}\int_{-1}^{1}\frac{\phi_1(\eta,s)}{\eta-x}d\eta + \int_{-1}^{1}[N_1(\eta,x,s)\phi_1(\eta,x,s) + N_2(\eta,x,s)\overline{\phi_1(\eta,x,s)}]d\eta = \frac{0.5}{s(n_1n_2)^{1/2}}\left[if_1(x)+\left(\frac{n_1}{n_2}\right)^{1/2}f_2(x)\right] \tag{23a}$$

$$\int_{-1}^{1}\phi_1(x,s)\,dx=0 \tag{23b}$$

where

$$N_1(\eta,x,s)=\frac{1}{2(n_1n_2)^{1/2}}\left[H_1(\eta,x,s)+H_4(\eta,x,s) -i\left(\frac{n_1}{n_2}\right)^{1/2}H_2(\eta,x,s)+i\left(\frac{n_2}{n_1}\right)^{1/2}H_3(\eta,x,s)\right] \tag{24a}$$

$$N_2(\eta,x,s)=\frac{1}{2(n_1n_2)^{1/2}}\left[H_1(\eta,x,s)-H_4(\eta,x,s) +i\left(\frac{n_1}{n_2}\right)^{1/2}H_2(\eta,x,s)+i\left(\frac{n_2}{n_1}\right)^{1/2}H_3(\eta,x,s)\right] \tag{24b}$$

4 Solution to a Singular Integral Equation

The singular integral equation, equation (23a), can be solved by employing Jacobi polynomial expansion [10–12]. As suggested by Srivastava, et al. [8, 9], the solution to equation (23a) can be written as an infinite series of Jacobi polynomials:

$$\phi_1(x,s)=C_n(s)\ W(x)\ P_n^{(a,\hat{a})}(x) \qquad (n=0,1,2,\ldots,\infty) \tag{25}$$

where C_n are unknown complex constants, $P_n^{(a,\hat{a})}$ is a Jacobi polynomial and

$$W(x)=(1-x)^a(1+x)^{\hat{a}} \tag{26}$$

is the weight function of $P_n^{(a,\hat{a})}$. In equation (25), a is a complex number defined by

$$a=-1/2-i\gamma \tag{27a}$$

where

$$\gamma=\frac{1}{2\pi}Ln\left[\frac{1-m_0/(n_1n_2)^{1/2}}{1+m_0/(n_1n_2)^{1/2}}\right] \tag{27b}$$

Thus, the order of stress singularity of dynamic response to the crack tip is $(-1/2\pm i\gamma)$ where γ is determined by equation (27b). Like elastostatic problems [13–15], the existence of an imaginary part of the stress singularity causes an inadmissible oscillation in both the stresses and displacements around the crack tip. Such oscillatory stresses and displacements lead to physically unrealistic overlapping of crack surfaces near the crack tip. However, this discrepancy may be neglected if the zones where overlapping occurs are very small, e.g., 10^{-4} of the crack length. It is found that the expression of γ in equation (27b) is identical to that derived by the Weiner-Hopf technique [7]. As expected, the stress singularity orders are the same for both dynamic and static problem [7]. By the relationship,

$$\phi_1(-x,s)=\overline{\phi_1(x,s)} \tag{28a}$$

$$W(-x)=\overline{W(x)} \tag{28b}$$

it can be shown that, in equation (25),

$$C_{2m}''=C_{2m+1}'=0 \quad (m=0,1,2,\ldots) \tag{29a}$$

where

$$C_n=C_n'+iC_n'' \tag{29b}$$

Substituting equation (25) into equations (23a, b) and using the orthogonal properties of Jacobi polynomials listed in Appendix 2 [16], we obtain a system of infinite linear algebra equations of C_n. Approximating ϕ_1 by the first $N+1$ terms, i.e.,

$$\phi_1(x,s)=C_n(s)\ W(s)\ P_n^{(a,\hat{a})}(x) \qquad (n=0,1,2,\ldots,N) \tag{30}$$

we obtain the following system:

$$-0.5ia_nC_{n+1}+b_{nj}C_j+d_{nj}\bar{C}_j=g_n \tag{31a}$$

$$(j,n=0,1,2,\ldots,N-1)$$

$$e_nC_n=0 \tag{31b}$$

where a_n, b_{nj}, d_{nj}, g_n, and e_n are defined in Appendix 3. The

Downloaded 02 May 2010 to 171.66.16.25. Redistribution subject to ASME license or copyright; see http://www.asme.org/terms/Terms_Use.cfm

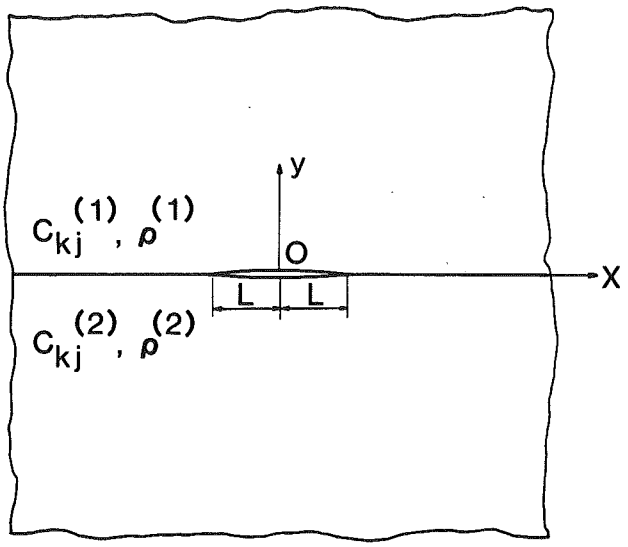

Fig. 1 Geometry of the problem

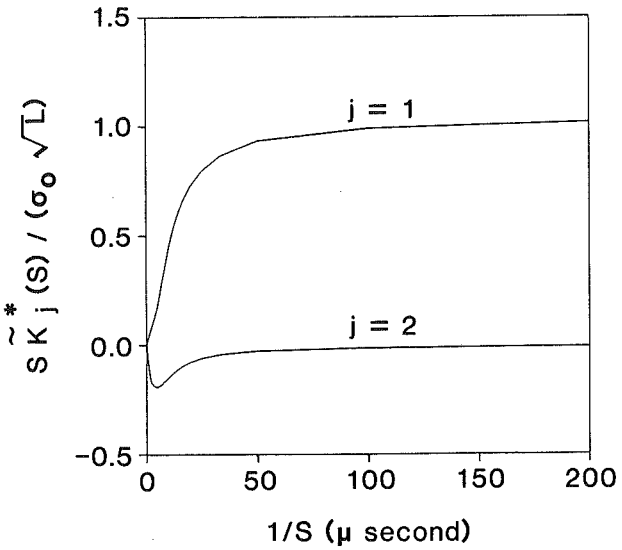

Fig. 2 Variation of $\tilde{K}_j^*$ in frequency domain ($f_1(x)=0, f_2(x)=\sigma_0$)

N + 1 equations of equations (31*a*, *b*) are used to determine the $N+1$ unknows, C_n.

5 Stress Intensity Factors

Some authors [8, 9, 17] have defined the stress intensity factors as

$$K_1^*(t) - iK_2^*(t) = \lim_{|x|\to 1} (x-1)^{-a}(x+1)^{-\bar{a}}[\sigma_y(x,0,t) - \tau_{xy}(x,0,t)] \tag{32}$$

For $|x|>1$, it can be shown that

$$(n_1 n_2)^{-1/2}\left[\left(\frac{n_1}{n_2}\right)^{1/2}\tilde{\sigma}_y(x,0,s) - i\tilde{\tau}_{xy}(x,0,s)\right] = -\frac{2}{\pi i}\int_{-1}^{1}\frac{\phi_1(z,s)W(z)}{z-x}dz - 2\int_{-1}^{1}[N_1(z,x,s)\phi_1(z,s) + N_2(z,x,s)\overline{\phi_1(z,s)}]dz \tag{33}$$

The first integration in equation (33) can be evaluated by using the relation:

$$\frac{1}{\pi i}\int_{-1}^{1} P_n^{(a,b)}(z)\,W(z)\,\frac{dz}{z-x} = \frac{-2}{1+e^{-2\pi\gamma}}[-W(x)P_n^{(a,b)}(x) + G_n(x)] \tag{34}$$

where $G_n(x)$ is the principal part of $W(x)P_n^{(a,b)}(x)$ at infinity. Thus, $\tilde{K}_1^*$ and $\tilde{K}_2^*$ can be written as summation of a series:

$$\frac{\tilde{K}_1^*(s)}{|n_2|} - \frac{i\tilde{K}_2^*(s)}{(n_1 n_2)^{1/2}} = \frac{-2i}{\cosh(\pi\gamma)}C_n(s)P_n^{(a,\bar{a})}(1) \qquad (n=0,1,\ldots,N) \tag{35}$$

Alternatively, stress intensity factors can be defined by

$$\lim_{x\to 1^+}[2\pi(x-1)]^{1/2}[\sigma_x(x,0,t) - i\tau_{xy}(x,0,t)] = K(t)e^{-i[Ln(x-1)-\beta(t)]} \tag{36}$$

K_1^*, K_2^* in equation (35) and K, β in equation (36) are related by

$$K(t) = \pi^{1/2}[K_1^{*2}(t) + K_2^{*2}(t)]^{1/2} \tag{37a}$$

$$\beta(t) = \tan^{-1}\left[\frac{K_1^*(t)\sin(\gamma Ln2) - K_2^*(t)\cos(\gamma Ln2)}{K_1^*(t)\cos(\gamma Ln2) + K_2^*(t)\sin(\gamma Ln2)}\right] \tag{37b}$$

Definition given by equation (36) will be used in this paper. However, K_1^* and K_2^* will be calculated first and transformed into K and β since equation (35) is more convenient for numerical computation.

The series solutions discussed so far are in the frequency domain of the Laplace transform. The next task is to perform the inverse Laplace transform. Many numerical schemes have been presented in the literature [18, 19] for the inverse Laplace transform. The inverse transform by using Jacobi polynomials suggested by Miller and Guy [19] is adopted in this paper.

6 Numerical Results and Discussions

Consider a composite solid made of two dissimilar unidirectional fiber-reinforced materials. As shown in Fig. 1, the fiber directions of the upper and lower media are out of paper and parallel to the x-axis, respectively. The following material properties of graphite fiber-epoxy composites are used:

$$\begin{aligned} &C_{11}^{(1)} = C_{22}^{(1)} = 15136.64\ \text{MPa}, C_{12}^{(1)} = 3178.36\ \text{MPa}\\ &C_{66}^{(1)} = 5856.5\ \text{MPa},\ \rho^{(1)} = 7.44\ \text{g/cm}^3\\ &C_{11}^{(2)} = 138440.77\ \text{MPa},\ C_{22}^{(2)} = 14536.52\ \text{MPa}\\ &C_{12}^{(2)} = 3052.96\ \text{MPa},\ C_{66}^{(2)} = 5856.5\ \text{MPa}\\ &\rho^{(2)} = 7.44\ \text{g/cm}^3 \end{aligned} \tag{38}$$

$f_1(x)$ and $f_2(x)$ in equations (5*a*, *b*) are, respectively, assumed to be equal to zero and σ_0 where σ_0 is a positive constant. The integrations of H_1–H_4 in Appendix 1 is carried out by using six point Gauss-Laguerre quadrature [16]. The double integrals of b_{nj}, d_{nj}, and e_n are evaluated by five-point Gauss-Hermite quadrature [16]. Nine-point Gaussian quadrature [16] is used to calculate g_n. The coefficients, C_n, in equation (30) are found to be covergent very fast. Eight terms have been used for the Jacobi polynomial expansion in equation (30) and 10 Jacobi polynomials, $P_n^{(0,0)}(t)$, have been included in the inverse Laplace transform.

The imaginary part of the stress singularity, γ, is found to be equal to 0.05024. The corresponding width of overlapping zone is in the order of 10^{-4} of crack length. The steady state solution that is obtained by taking the densities, ρ, to be zero is

$$\frac{K(\infty)}{\sigma_0(\pi L)^{1/2}} = 1.000,\ \beta(\infty) = -2.857\ \text{deg} \tag{39}$$

where L is the half crack length, i.e., one unit length in this example. The variation of $sK_1^*(s)$ and $sK_2^*(s)$ are exhibited in Fig. 2. The stress intensity factor, $K(t)$, and the phase angle,

Downloaded 02 May 2010 to 171.66.16.25. Redistribution subject to ASME license or copyright; see http://www.asme.org/terms/Terms_Use.cfm

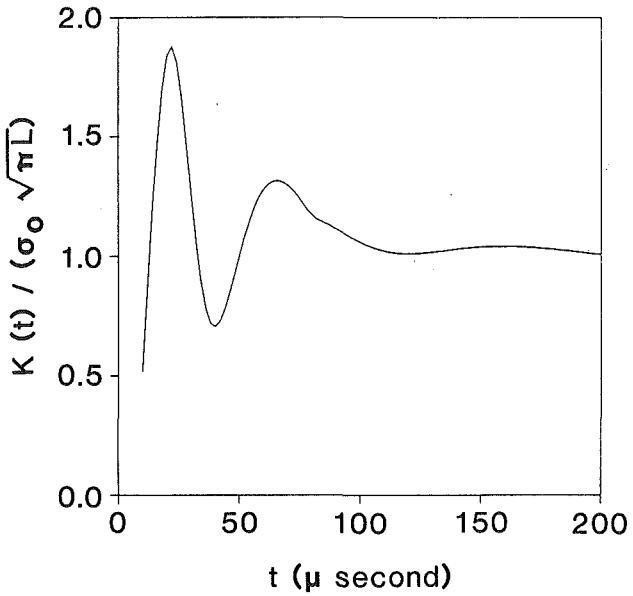

Fig. 3 Transient stress intensity factor $K(t)$ ($f_1(x) = 0, f_2(x) = \sigma_0$)

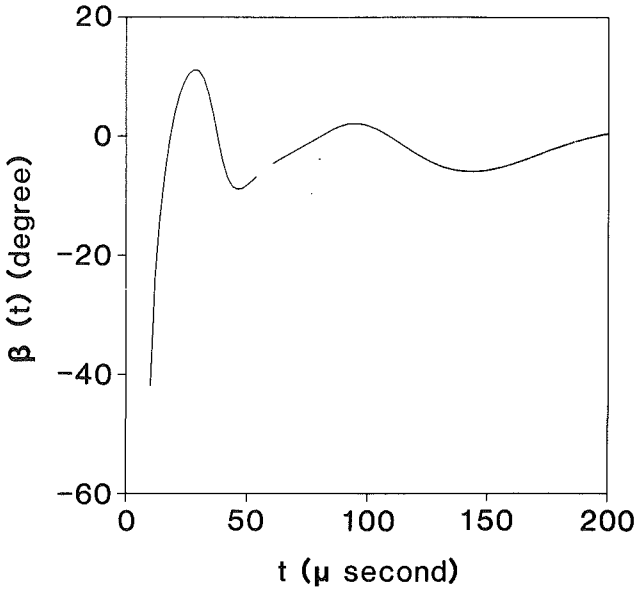

Fig. 4 Transient phase angle $\beta(t)$ ($f_1(x) = 0, f_2(x) = \sigma_0$)

$\beta(t)$, have been plotted in Figs. 3 and 4, respectively. It is observed that after two to three oscillations the dynamic solutions converge to the steady state solutions. As a result of the jump properties of the Heaviside function at $t = 0$, the numerical scheme of [19] cannot perform the inverse Laplace transform properly in the first 8μ seconds. As t approaches to zero, a nonzero $K(0)$, although very small, and an oscillating $\beta(t)$ were obtained numerically. By examining Fig. 2 and equations (37*a*, *b*), the correct values of $K(0)$ and $\beta(0)$ were estimated to be 0 and approximately 65 deg, respectively. The numerical solutions for the first 10μ seconds are not shown in Figs. 3 and 4; however, they can be obtained by drawing a monotonic curve from $t = 0$, $K(0) = 0$ in Fig. 3 and $t = 0$, $\beta(0) = 65$ deg in Fig. 4 to the first point of the numerical curve.

References

1 Flitman, L. M., "On the Motion of a Rigid Strip-Mass Lying on an Elastic Half-Space and Excited by a Seismic Wave," *Journal of Applied Mathematics and Mechanics*, Vol. 28, 1964, pp. 1582–1604.

2 Kostrov, B. V., "Motion of a Rigid Strip-Mass Soldered Into an Elastic Medium Excited by a Plane Wave," *Journal of Applied Mathematics and Mechanics*, Vol. 28, 1964, pp. 113–126.

3 Tau, S. A., and Lu, T., "Diffraction of Transient Horizontal Shear Waves by a Finite Rigid Ribbon," *International Journal of Engineering Science*, Vol. 7, 1971, pp. 857–874.

4 Tau, S. A., and Lu, T., "Transient Stress Intensity Factor for a Finite Crack in an Elastic Solid Caused by a Dilatational Wave," *International Journal of Solids and Structures*, Vol. 8, 1971, pp. 113–126.

5 Sih, G. C., and Loeber, J. F., "Wave Propagation in an Elastic Solid With a Line of Discontinuity or Finite Crack," *Quarterly of Applied Mathematics*, Vol. 27, 1969, pp. 193–213.

6 Sih, G. C., Embly, G. T., and Ravera, R. S., "Impact Response of a Finite Crack in Plane Extension," *International Journal of Solids and Structures*, Vol. 8, 1972, pp. 977–993.

7 Kuo, An-Yu, *Dynamic Analysis of Interfacial Cracks in Composite Laminates*, Ph.D. dissertation, Department of Theoretical and Applied Mechanics, University of Illinois at Urbana-Champaign, 1982.

8 Srivastava, K. N., Gupta, O. P., and Palaiya, R. M., "Interaction of Elastic Waves in Two Dissimilar Elastic Half-Planes Having Griffith Crack at Interface–I," *International Journal of Fracture*, Vol. 14, 1978, pp. 145–154.

9 Srivastava, K. N., Palaiya, R. M., and Gupta, O. P., "Interaction of Longitudinal Wave with a Penny-Shaped Crack at the Interface of Two Bonded Dissimilar Elastic Solids–II," *International Journal of Fracture*, Vol. 15, 1979, pp. 591–599.

10 Erdogan, F., "Approximate Solutions of Systems of Singular Integral Equations," *SIAM Journal of Applied Mathematics*, Vol. 17, 1969, pp. 1041–1059.

11 Erdogan, F., and Gupta, G. D., "On the Numerical Solution of Singular Integral Equations," *Quarterly of Applied Mathematics*, Vol. 30, 1972, pp. 525–534.

12 Krenk, Steen, "Polynomial Solutions to Singular Integral Equations with Application to Elasticity Theory," Risø National Laboratory, Denmark, 1981.

13 Williams, M. L., "The Stress Around a Fault or Crack in Dissimilar Media," *Bulletin of the Seismological Society of America*, Vol. 49, 1959, pp. 199–204.

14 England, A. H., "A Crack Between Dissimilar Media," ASME JOURNAL OF APPLIED MECHANICS, Vol. 32, 1965, pp. 400–402.

15 Erdogan, F., "Stress Distribution in Bonded Dissimilar Materials With Cracks," ASME JOURNAL OF APPLIED MECHANICS, Vol. 32, 1965, pp. 403–410.

16 Abramowitz, M., and Stegun, I., *Handbook of Mathematical Functions*, Dover, New York, 1965.

17 Erdogan, F., and Gupta, G. D., "Layer Composites with an Interface Flaw," *International Journal of Solids and Structures*, Vol. 7, 1971, pp. 1089–1107.

18 Papoulis, Athanasios, "A New Method of Inversion of the Laplace Transforms," *Quarterly of Applied Mathematics*, Vol. 14, 1957, pp. 405–414.

19 Miller, M. K., and Guy, W. T., Jr., "Numerical Inversion of the Laplace Transform by Use of Jacobi Polynomials," *SIAM Journal of Numerical Analysis*, Vol. 3, 1966, pp. 624–635.

APPENDIX 1

$$m_0 = \lim_{\xi \to \infty} \frac{B_{12}(\xi,s)}{i\xi} = -m_1 \{ [(C_{11}^{(1)} C_{22}^{(1)})^{1/2} - C_{12}^{(1)}][C_{11}^{(2)} C_{22}^{(2)} - C_{12}^{(2)^2}] - [(C_{11}^{(2)} C_{22}^{(2)})^{1/2} - C_{12}^{(2)}][C_{11}^{(1)} C_{22}^{(1)} - C_{12}^{(1)^2}] \}$$

$$n_1 = \lim_{\xi \to \infty} \frac{B_{11}(\xi,s)}{|\xi|} = m_1 \Bigg\{ (C_{11}^{(2)} C_{22}^{(2)} - C_{12}^{(2)^2})(C_{11}^{(1)} C_{22}^{(1)})^2 \cdot \left[\frac{C_{11}^{(1)} C_{22}^{(1)} - C_{12}^{(1)^2} - 2C_{12}^{(1)} C_{66}^{(1)}}{C_{22}^{(1)} C_{66}^{(1)}} + 2\left(\frac{C_{11}^{(1)}}{C_{22}^{(1)}} \right)^{1/2} \right]^{1/2} + (C_{11}^{(1)} C_{22}^{(1)} - C_{12}^{(1)^2}) \cdot (C_{11}^{(2)} C_{22}^{(2)})^{1/2} \left[\frac{C_{11}^{(2)} C_{22}^{(2)} - C_{12}^{(2)} - 2C_{12}^{(2)} C_{66}^{(2)}}{C_{22}^{(2)} C_{66}^{(2)}} + 2\left(\frac{C_{11}^{(2)}}{C_{22}^{(2)}} \right)^{1/2} \right]^{1/2} \Bigg\}$$

Downloaded 02 May 2010 to 171.66.16.25. Redistribution subject to ASME license or copyright; see http://www.asme.org/terms/Terms_Use.cfm

$$n_2 = \lim_{\xi\to\infty} \frac{B_{12}(\xi,s)}{|\xi|} = m_1\Big\{(C_{11}^{(2)}C_{22}^{(2)} - C_{12}^{(12)^2})C_{22}^{(1)}$$

$$\Big[\frac{C_{11}^{(1)}C_{22}^{(1)} - C_{12}^{(1)^2} - 2C_{12}^{(1)}C_{66}^{(1)}}{C_{11}^{(1)}C_{66}^{(1)}} + 2\Big(\frac{C_{11}^{(1)}}{C_{22}^{(1)}}\Big)^{1/2}\Big]^{1/2}$$

$$+ (C_{11}^{(1)}C_{22}^{(1)} - C_{12}^{(1)^2})C_{22}^{(2)}$$

$$\Big[\frac{C_{11}^{(2)}C_{22}^{(2)} - C_{12}^{(2)^2} - 2C_{12}^{(2)}C_{66}^{(2)}}{C_{22}^{(2)}C_{66}^{(2)}} + 2\Big(\frac{C_{11}^{(2)}}{C_{22}^{(2)}}\Big)^{1/2}\Big]^{1/2}\Big\}$$

$$m_1 = \lim_{\xi\to\infty} \frac{C_{66}^{(1)}C_{66}^{(2)}(p_1^{(1)} - p_1^{(1)})(p_1^{(2)} - p_2^{(2)})}{\Delta(C_{12}^{(1)} + C_{66}^{(1)})(C_{12}^{(2)} + C_{66}^{(2)})}$$

Δ = determinant of $[D]$ defined by equation (13)

$$H_1(\eta,x,s) = \frac{1}{\pi}\int_0^\infty B'_{12}(\xi,s)\cos(\xi\eta)\cos(\xi\eta)\,d\xi$$

$$H_2(\eta,x,s) = \frac{1}{\pi}\int_0^\infty B'_{22}(\xi,s)\sin(\xi\eta)\cos(\xi x)\,d\xi$$

$$H_3(\eta,x,s) = \frac{1}{\pi}\int_0^\infty B'_{11}(\xi,s)\cos(\xi\eta)\sin(\xi x)\,d\xi$$

$$H_4(\eta,x,s) = \frac{1}{\pi}\int_0^\infty B'_{12}(\xi,s)\sin(\xi\eta)\sin(\xi x)\,d\xi$$

$$B'_{11}(\xi,s) = [B_{11}(\xi,s) - n_1|\xi|]/\xi$$
$$B'_{22}(\xi,s) = [B_{22}(\xi,s) - n_2|\xi|]/\xi$$
$$B'_{12}(\xi,s) = -iB_{12}(\xi,s)/\xi - m_0$$

APPENDIX 2

$$\overline{p_n^{(a,\tilde{a})}(x)} = p_n^{(\tilde{a},a)}(x), p_n^{(a,\tilde{a})}(-x) = (-1)^n\overline{p_n^{(a,\tilde{a})}(x)}$$

$$\int_{-1}^{1} p_n^{(a,b)}(x)\,p_m^{(a,b)}(x)\,W(x)\,dx$$

$$= \begin{cases} \dfrac{2^{a+b+1}\Gamma(n+a+1)\Gamma(n+b+1)}{n!(2n+a+b+1)\Gamma(n+a+b+1)} & m\neq n \\ 0 & m=n \end{cases}$$

$$\lambda W(x)p_n^{(a,b)}(x) + \frac{1}{\pi i}\int_{-1}^{1} p_n^{(a,b)}(z)\,W(z)\,\frac{dz}{z-x}$$

$$= \begin{cases} \dfrac{(1-\lambda^2)^{1/2}}{2i}\; p_{n-1}^{(-a,-b)}(x) & n\geq 1 \\ 0 & n=0 \end{cases}$$

APPENDIX 3

$$a_n = -\pi i\Big(1 - \frac{m_0^2}{n_1n_2}\Big)^{1/2}\frac{|n+1/2+i\gamma|^2\ \ldots\ |1/2+i\gamma|^2}{[(n+1)!]^2\cosh(\pi\gamma)}$$

$$b_{nj} = \int_{-1}^{1}\int_{-1}^{1} N_1(\eta,x,s)W(\eta)[W(x)]^{-1}p_n^{(-a,-\tilde{a})}(x)$$
$$p_j^{(a,\tilde{a})}(\eta)\,d\eta\,dx$$
$$= \int_{-\infty}^{\infty}\int_{-\infty}^{\infty} R_1(\theta,\phi,s)e^{-2i\gamma(\phi-\theta)}\operatorname{sech}^3\phi\,\operatorname{sech}\theta\,d\theta\,d\phi$$

$$d_{nj} = \int_{-1}^{1}\int_{-1}^{1} N_2(\eta,x,s)\overline{W(\eta)}[W(x)]^{-1}p_n^{(-a,-\tilde{a})}(x)$$
$$\overline{p_j^{(a,\tilde{a})}(\eta)}\,d\eta\,dx$$
$$= \int_{-\infty}^{\infty}\int_{-\infty}^{\infty} R_2(\theta,\phi,s)\,e^{-2i\gamma(\phi+\theta)}\operatorname{sech}^3\phi\,\operatorname{sech}\theta\,d\theta\,d\phi$$

$$g_n = (n_1n_2)^{-1/2}\int_{-1}^{1} p_n^{(-a,-\tilde{a})}(x)\,[W(x)]^{-1}$$
$$\Big[if_1(x) + \Big(\frac{n_1}{n_2}\Big)^{1/2}f_2(x)\Big]\,dx$$

$$e_n = \int_{-1}^{1} W(x)p_n^{(a,\tilde{a})}(x)\,dx = \int_{-\infty}^{\infty} e^{2i\gamma\theta}\operatorname{sech}\theta$$
$$p_n^{(a,\tilde{a})}(\tanh\theta)\,d\theta$$

$$R_1(\theta,\phi,s) = N_1(\tanh\theta,\tanh\phi,s)p_n^{(-a,-\tilde{a})}(\tanh\phi)$$
$$p_j^{(a,\tilde{a})}(\tanh\theta)$$
$$R_2(\theta,\phi,s) = N_2(\tanh\theta,\tanh\phi,s)p_n^{(-a,\tilde{a})}(\tanh\phi)$$
$$p_j^{(a,\tilde{a})}(\tanh\theta)$$

Downloaded 02 May 2010 to 171.66.16.25. Redistribution subject to ASME license or copyright; see http://www.asme.org/terms/Terms_Use.cfm

Surface Motion Excited by Acoustic Emission From a Buried Crack

J. G. Harris
Assistant Professor,
Assoc. Mem. ASME.

J. Pott
Graduate Student.

Department of Theoretical and Applied Mechancis,
University of Illinois,
Urbana, Ill. 61801

The surface motions excited by acoustic emissions produced by fracture processes at the edge of a buried, penny-shaped crack are investigated. Firstly, wave-front approximations to the emissions generated by the sudden growth of a tensile crack in an unbounded elastic solid are reviewed. Then these approximations are Fourier transformed to give the high-frequency portion of their spectra. Secondly, time and frequency-domain approximations to the surface motions excited by this growing crack, when it is buried in a half-space, are calculated. These results are then scrutinized to elucidate what parts of the signals measured at the surface carry information about the crack's size, its orientation, and the fracture processes near the crack tip.

Introduction

One important source of acoustic emissions, at least in metals, is a tensile crack that suddenly starts to grow. By monitoring these emissions it may be possible to study the fracture processes near the edges of such cracks [1] and to assess the severity of these defects in important engineering structures such as pressure vessels [2]. In an attempt to relate the fracture processes to the form of the acoustic emissions, Rose [3] and Achenbach and Harris [4] carried out asymptotic analyses of the waves radiated from models, derived from fracture mechanics, of sudden tensile fractures in unbounded (homogeneous, isotropic, linearly elastic) media. When the cracks are embedded in an engineering structure, the form of the emissions is also greatly influenced by interaction with the structure's boundaries. To study this Hsu and Hardy [5] measured the response of a plate at a point opposite that at which an excitation, such as the breaking of a glass capillary, was applied and extracted the source time behavior from the overall response by using a transfer function for the plate. Pao [6] has also calculated the response of a plate to various nuclei of strain, which can be used to model sources of acoustic emission. To investigate the combined influence of propagation path and fracture processes, Rose [7], using the body force equivalent to an elementary tensile crack and to an elementary shear crack, calculated the reflection of compressional and shear emissions at a traction-free surface near the epicenter. The purpose of this paper is also to investigate the combined effects of the propagation path and fracture process. To do so we will place the model of the growing tensile crack used in [4] in an elastic half-space and calculate the interaction of the acoustic emissions with the free surface both near (near field) and far (far field) from the epicenter.

We start by reexamining the asymptotic analysis of acoustic emission begun in [4]. We then use these results to calculate the surface motion excited by the acoustic emissions from a buried, penny-shaped, tensile crack. The crack is assumed to have its plane sufficiently close to the vertical that it can grow toward the surface. We will be concerned, in the main, with that portion of the measured acoustic emission that arrives first and is strongest. In the near-field, we will calculate the surface motion excited by the incident compressional emission from the point on the crack edge closest to the surface. We will also calculate that excited by the incident shear emission, although this signal arrives later. In the far-field the strongest signal is the Rayleigh wave which, though it does not arrive first, constitutes an easily recognized coda. Thus we will calculate the surface motion in the far-field near the arrival time of the Rayleigh wave that is excited by the point on the crack edge closest to the surface. This later calculation is done using the same method as that used by Harris, Achenbach, and Norris [8] to calculate the Rayleigh waves excited by the starting and stopping phases of a faulting event. Throughout this paper we consider both the time and frequency-domain results.

Acoustic Emissions From a Growing Tensile Crack

Figure 1 shows a two-dimensional, semi-infinite, tensile crack that is imagined, at $t = 0$, to suddenly start to propagate in its own plane with a constant crack-tip speed c_F. Following reference [4], where this crack-propagation model is discussed at greater length, for small times, and hence for small distances ahead of the original crack tip, the displacement at the surface of the newly cracked material takes the functional form $F(t - s_F x)$ where

Contributed by the Applied Mechanics Division for publication in the JOURNAL OF APPLIED MECHANICS.

Discussion on this paper should be addressed to the Editorial Department, ASME, United Engineering Center, 345 East 47th Street, New York, N.Y. 10017, and will be accepted until two months after final publication of the paper itself in the JOURNAL OF APPLIED MECHANICS. Manuscript received by ASME Applied Mechanics Division, May, 1983; final revision, September, 1983.

Copyright © 1984 by ASME
Downloaded 02 May 2010 to 171.66.16.25. Redistribution subject to ASME license or copyright; see http://www.asme.org/terms/Terms_Use.cfm

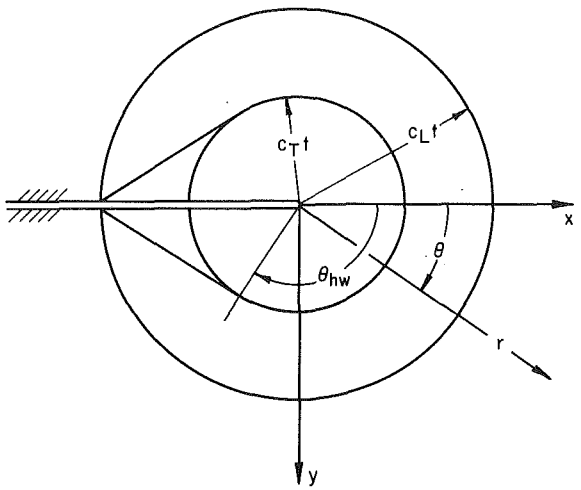

Fig. 1 Acoustic emission from a tensile crack that suddenly starts to grow with speed c_F

$$F(t) = H(t)\, U t^{\nu/2} \tag{1}$$

and $s_F = 1/c_F$. The parameter $\nu = 1$ for brittle fracture, otherwise $\nu > 1$; U is a constant that must be ascertained from a detailed study of the fracture processes. Achenbach and Harris [4] calculated wave-front approximations to the acoustic emissions from this crack model. We have repeated their calculations getting the same results, but we have given a different interpretation to the form of the shear emissions in the headwave region of the crack. The results of both these investigations are summarized in the following. The compressional emission $u_r(r,\theta,t)$ near its arrival time $s_L r$ and the shear emission $u_\theta(r,\theta,t)$ near its arrival time $s_T r$ are given by the following equations:

$$u_r(r,\theta,t) = r^{-1/2} E_L(s_F,\theta) e_L(t - s_L r) \tag{2}$$

$$u_\theta(r,\theta,t) = r^{-1/2}[E_{T1}(s_F,\theta) e_T(t - s_T r) - E_{T2}(s_F,\theta) f_T(t, s_T r, \theta)] \tag{3}$$

where

$$E_\alpha(s_F,\theta) = S(s_F)\, \Theta_\alpha(\theta), \quad \alpha = L,T \tag{4}$$

$$S(s_F) = \frac{K_-(-s_F)(1 + s_R/s_F)}{(1 + s_F/s_L)^{1/2}} \tag{5}$$

$$\Theta_L(\theta) = \frac{(1 + \cos\theta)^{1/2}[1 - 2(s_L/s_T)^2 \cos^2\theta]}{[1 - (s_L/s_F)\cos\theta][1 + (s_L/s_R)\cos\theta] K_-(-s_L \cos\theta)} \tag{6}$$

$$\Theta_T(\theta) = \frac{[1 + (s_T/s_L)\cos\theta]^{1/2} \sin 2\theta}{[1 - (s_T/s_F)\cos\theta][1 + (s_T/s_R)\cos\theta] K_-(-s_T \cos\theta)} \tag{7}$$

$$E_{T1}(s_F,\theta) = Re[E_T(s_F,\theta)]; \quad E_{T2}(s_F,\theta) = Im[E_T(s_F,\theta)] \tag{8a,b}$$

$$e_\alpha(t - s_\alpha r) = \frac{1}{\pi} \frac{s_\alpha}{s_R} \frac{1}{(2s_\alpha)^{1/2}} \int_{s_\alpha r}^{t} F(t-\tau) \times (\tau - s_\alpha r)^{-1/2} d\tau, \quad \alpha = L,T \tag{9}$$

$$f_T(t, s_T r, \theta) = \frac{1}{\pi} \frac{s_T}{s_R} \frac{1}{(2s_T)^{1/2}} \int_{t_{hw}}^{m} F(t-\tau) \times (s_T r - \tau)^{-1/2} d\tau. \tag{10}$$

The function $K_-(\eta)$ is given by equation (19) of reference [4]. The constant $s_L = 1/c_L$, $s_T = 1/c_T$, and $s_R = 1/c_R$ where c_L, c_T, and c_R are the compressional, shear, and Rayleigh wavespeeds.

To completely define the emission coefficients $E_\alpha(s_F,\theta)$ the radicals need to be specified for complex $\cos\theta$ (note that only $\cos\theta$ appears in equations (6) and (7)). The real part of each radical is taken as positive for all $\cos\theta$, and the imaginary part is taken as positive for $Im(\cos\theta)$ positive and as negative for $Im(\cos\theta)$ negative. Further, $E_{T2}(s_F,\theta)$, equation (8*b*), is evaluated by letting $Im(\cos\theta)$ go to zero through positive values. Note that the definition of the emission coefficient $E_T(s_F,\theta)$ differs from that given by equation (38) of [4]. There are a number of square roots here and elsewhere in the paper: the principal value of these roots is always to be taken unless otherwise specified.

Equations (2) and (3) represent the compressional and shear cylindrical waves shown in Fig. 1. Also present in the region $\theta_{hw} < |\theta| < \pi$, where $\theta_{hw} = \cos^{-1}(-s_L/s_T)$, is a headwave whose arrival time is $t_{hw} = s_L r \cos(|\theta| - \theta_{hw})$ and whose "end" time is $m = \min(t, s_T r)$. An approximation to the headwave near its arrival time is given by equations (41), (45), and (46) of reference [4]. The second term in equation (3), which is not present in the corresponding expression equation (37) of [4], is an approximation to the headwave near $t = s_T r$. Because of the square-root singularity at that point, the "end" of the headwave makes a more important contribution to the shear emission than does its wave front. Therefore, we have combined the former with the shear cylindrical wave, equation (3), and omitted the latter. Near $|\theta| = \theta_{hw}$ equation (3) is not an accurate description of the wave field because of the confluence of the headwave and cylindrical-shear wave fronts. A uniform approximation in this region is given by equations (37), (47), and (48) of [4].

As pointed out in [4] the wave field caused by the sudden stopping, at $t = 0$, of a crack that has been growing at speed c_F is given by the negative of equations (2) and (3).

To extend our results from two dimensions to three we will make the assumption that, at $t = 0$, all points on the crack edge start to grow normal to the original crack edge. Note, however, that this does not imply that c_F is the same at each point on the crack edge. For this case reference [9] shows that the two-dimensional results can be extended to three-dimensional ones by multiplying the former by $(1 + r/\bar{\rho})^{-1/2}$. This is a first-order correction for the curvature of the crack edge. The term $\bar{\rho}$ is given by $\bar{\rho} = \rho/\cos\theta$, where ρ is the radius of curvature of the crack edge. When considering a finite crack there is an additional complication to be noted. The sudden extension of the crack also excites surface waves on the crack faces which are subsequently diffracted by the crack edge producing emissions as strong as those first emitted. These emissions can be calculated using the techniques described by Achenbach, Gautesen, and McMaken [10]. However, because we are interested in first arrivals we have chosen not to include them here. All these considerations also apply to the frequency-domain results of the next section.

Spectra of the Acoustic Emissions

Wave-front approximations, or more precisely approximations near algebraic singularities, in the time domain correspond to high-frequency approximations in the frequency domain [11]. Therefore, when calculating the spectra of the transient acoustic emissions given in the preceding section, the Fourier transforms can be approximated for large ω, where ω is the angular frequency. The transform pair used here is

$$f(\omega) = \int_{-\infty}^{\infty} e^{i\omega t} f(t)\, dt; \quad f(t) = \frac{Re}{\pi} \int_0^{\infty} e^{-i\omega t} f(\omega)\, d\omega. \tag{11a,b}$$

Downloaded 02 May 2010 to 171.66.16.25. Redistribution subject to ASME license or copyright; see http://www.asme.org/terms/Terms_Use.cfm

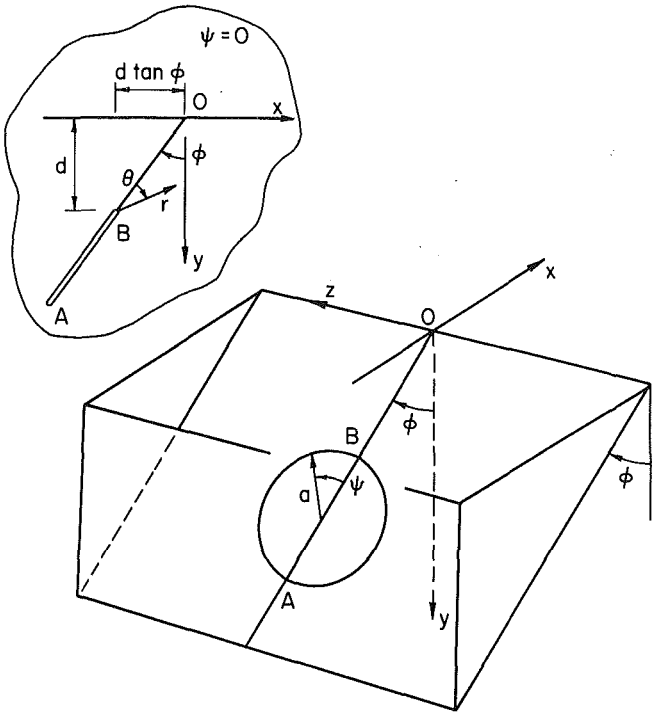

Fig. 2 A penny-shaped tensile crack growing in a plane which makes an angle ϕ with the vertical. At the instant shown, point *B*, which lies in the symmetry plane $\psi = 0$, is a distance *d* below the surface and is moving toward the origin O.

If $f(t)$ is real then $\bar{f}(\omega) = f(-\omega)$, where the overbar indicates the complex conjugate, and the inverse transform giving $f(t)$ can be expressed as equation (11*b*). The asymptotic approximation to the Fourier transform of the compressional-wave displacement $u_r(r,\theta,\omega)$ is

$$u_r(r,\theta,\omega) = (s_L/s_R)(2\pi s_L r)^{-1/2} E_L(s_F,\theta) \times F(\omega)(-i\omega)^{-1/2} e^{i\omega s_L r} \tag{12}$$

where $F(\omega)$ is the Fourier transform of $F(t)$. The asymptotic approximation to the Fourier transform of the shear-wave displacement $u_\theta(r,\theta,\omega)$ is

$$u_\theta(r,\theta,\omega) = (s_T/s_R)(2\pi s_T r)^{-1/2}[E_{T1}(s_F,\theta)(-i\omega)^{-1/2} + E_{T2}(s_F,\theta) b(\omega)] F(\omega) e^{i\omega s_T r} \tag{13}$$

where

$$b(\omega) = -\frac{1}{\pi^{1/2}} \int_0^c t^{-1/2} e^{-i\omega t} dt. \tag{14}$$

The function $b(\omega)$ arises from Fourier transforming $f_T(t,s_T r,\theta)$, equation (10), and noting that it is a convolution integral. The term $c = (s_T r - t_{hw})$. The function $b(\omega)$ may be approximated [12] as

$$b(\omega) = i(\omega/|\omega|)[(-i\omega)^{-1/2} - e^{-i\omega c}(\pi c)^{-1/2}(\omega)^{-1}]. \tag{15}$$

By retaining only the dominant term in equation (15), equation (13) becomes

$$u_\theta(r,\theta,\omega) = (s_T/s_R)(2\pi s_T r)^{-1/2}[E_{T1}(s_F,\theta) + i(\omega/|\omega|) E_{T2}(s_F,\theta)] F(\omega)(-i\omega)^{-1/2} e^{i\omega s_T r}. \tag{16}$$

Equation (16) can be written in a more informative way if we adopt the following convention: For ω positive, we evaluate the radical in $E_T(s_F,\theta)$ by letting $Im(\cos\theta)$ go to zero through positive values and for ω negative, we evaluate the radical by letting $Im(\cos\theta)$ go to zero through negative values. Thus, equation (16) can be written as

$$u_\theta(r,\theta,\omega) = (s_T/s_r)(2\pi s_T r)^{-1/2} E_T(s_F,\theta) \times F(\omega)(-i\omega)^{-1/2} e^{i\omega s_T r} \tag{17}$$

where $E_T(s_F,\theta)$ has an implicit dependence on the sign of ω. Equation (1) expresses $F(t)$ for small t; therefore, $F(\omega)$ for large ω is given by

$$F(\omega) = U\Gamma(\nu/2+1)(-i\omega)^{-(\nu+2)/2}. \tag{18}$$

Note that becasue we have not introduced any characteristic time or length scale, we cannot assign a frequency above which equation (18) is a good approximation. To do so would require a more detailed analysis of the fracture processes than has been given here.

Noting that both $u_r(r,\theta,\omega)$ and $u_\theta(r,\theta,\omega)$ satisfy the criteria $\bar{f}(\omega) = f(-\omega)$, equation (11*b*) can be used to invert equation (12) or equation (17) to recover the time-domain wavefront approximations to the compressional and shear emissions given previously. However, for $|\theta| > \theta_{hw}$ a problem arises. By approximating $b(\omega)$ by only the first term of equation (15), we have, in essence, let $t_{hw} \to -\infty$. Thus inverting equation (17) in the headwave region leads to equation (10) for $f_T(t,s_T r,\theta)$ with t_{hw} replaced by $(-\infty)$. But this is a divergent integral (recall that $F(t)$ is known only for small values of t). Therefore equation (17) cannot be inverted in the headwave region.

Model of a Buried Acoustic Emission Source

In the remaining sections of this paper we will consider the surface motion excited by the acoustic emissions from a growing tensile crack. The overall geometry is shown in Fig. 2. At $t = 0$ the crack is penny-shaped with radius a. At that instant the crack suddenly begins to grow outwards, normal to the initial crack edge, with a crack-tip speed that varies along the edge of the crack. The plane of the crack makes an angle ϕ with the normal to the surface. Because we are interested in cracks that grow toward the surface $|\phi|$ is imagined to be small and the crack is assumed not to be growing at point A. The crack is described by a toroidal coordinate system (r,θ,ψ). The angle ψ defines a point on the crack edge and, in each plane ψ = constant, (r,θ) form a polar coordinate system whose origin lies at that point. The inset to Fig. 2 shows this for the plane $\psi = 0$. The plane $\psi = 0$ is, moreover, a plane of reflection symmetry. The point B lies in it and is a depth d below the surface. A second coordinate system (x,y,z) is located with its origin at the intersection of the crack plane, the symmetry plane, and the surface of the half-space. The two coordinate systems are related as follows:

$$x = -d\tan\phi + (a + r\cos\theta)\cos\psi\sin\phi + r\sin\theta\cos\phi - a\sin\phi \tag{19}$$

$$y = d - (a + r\cos\theta)\cos\psi\cos\phi + r\sin\theta\sin\phi + a\cos\phi \tag{20}$$

$$z = (a + r\cos\theta)\sin\psi. \tag{21}$$

Note that these coordinate systems are consistent with that used in the previous sections. Though in some cases it is possible to calculate the surface motion out of the plane of symmetry (this point is discussed in Appendix *B* of reference [8]), this is in general difficult so that we eschew it here and confine ourselves to calculations in the symmetry plane. Therefore, the first arrivals will come from point B, where the crack is growing outward at a speed c_F.

Near-Field Surface Motion

The near-field surface motion will be dominated by reflection at the traction-free surface. Because we are in-

Downloaded 02 May 2010 to 171.66.16.25. Redistribution subject to ASME license or copyright; see http://www.asme.org/terms/Terms_Use.cfm

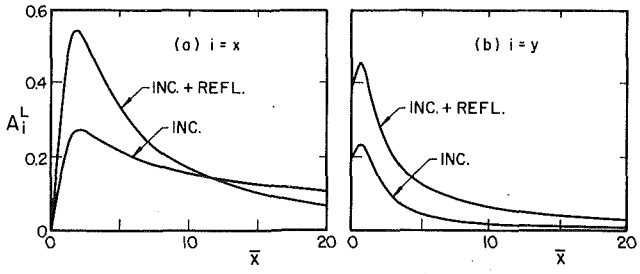

Fig. 3 The amplitudes of (a) the horizontal A_x^L and (b) the vertical A_y^L surface motion are plotted against $\bar{x}$. The angle $\phi = 0$, $\bar{d} = 2$, Poisson's ratio = 0.25, and $s_T/s_F = 0.5$.

terested only in high-frequency or wave-front approximations, the reflected waves may be calculated either by using ray theory [13] or by the integral-representation approach of the next section. These reflected waves are then added to the incident ones to give the net surface motion. The details are omitted.

The net particle displacement at the surface caused by the incident compressional emission is given by

$$\mathbf{u}^L(R,\theta) = [R_x^L(\theta)\mathbf{i} + R_y^L(\theta)\mathbf{j}](1 + R\cos\theta/a)^{-1/2} u_r(R,\theta) \tag{22}$$

where

$$R_x^L(\theta) = \frac{2\kappa \sin[2(\theta+\phi)]\sin\delta}{\kappa^2\cos^2(2\delta) - \sin(2\delta)\sin[2(\theta+\phi)]} \tag{23}$$

$$R_y^L(\theta) = \frac{2\kappa^2\cos(2\delta)\cos(\theta+\phi)}{\kappa^2\cos^2(2\delta) - \sin(2\delta)\sin[2(\theta+\phi)]} \tag{24}$$

$$R = d/\cos(\theta+\phi) \tag{25}$$

and $u_r(R,\theta) = u_r(R,\theta,t)$ (equation (2)) or $u_r(R,\theta,\omega)$ (equation (12)) for the time-domain or frequency-domain results, respectively. The angle δ is given by $s_T\cos\delta = -s_L\sin(\theta+\phi)$ and $\kappa = s_T/s_L$. The net particle displacement at the surface caused by the incident shear emissions, for values of $(\theta+\phi)$ such that $s_T|\sin(\theta+\phi)| < s_L$, is given by

$$\mathbf{u}^T(R,\theta) = [R_x^T(\theta)\mathbf{i} + R_y^T(\theta)\mathbf{j}](1 + R\cos\theta/a)^{-1/2} u_\theta(R,\theta) \tag{26}$$

where

$$R_x^T(\theta) = \frac{2\kappa^2\cos(\theta+\phi)\cos[2(\theta+\phi)]}{\kappa^2\cos^2[2(\theta+\phi)] - \sin(2\gamma)\sin[2(\theta+\phi)]} \tag{27}$$

$$R_y^T(\theta) = \frac{-2\sin(2\gamma)\cos(\theta+\phi)}{\kappa^2\cos^2[2(\theta+\phi)] - \sin(2\gamma)\sin[2(\theta+\phi)]} \tag{28}$$

and $u_\theta(R,\theta) = u_\theta(R,\theta,t)$ (equation (3)) or $u_\theta(R,\theta,\omega)$ (equation (17)) for the time-domain or frequency-domain results, respectively. The distance R is given by equation (25) and the angle γ by

$$s_L\cos\gamma = -s_T\sin(\theta+\phi). \tag{29}$$

Note that for values of $(\theta+\phi)$ such that

$$s_T|\sin(\theta+\phi)| > s_L \tag{30}$$

γ becomes imaginary and both $R_x^T(\theta)$ and $R_y^T(\theta)$ become complex. This is caused by the incident shear wave exciting a critically reflected compressional wave at the surface. In this case $\sin\gamma$ must be defined as

$$\sin\gamma = i(\omega/|\omega|)(\cos^2\gamma - 1)^{1/2} \tag{31}$$

to ensure that the critically reflected wave, in the frequency domain, decays into the interior (this is not directly apparent from equation (26) because it is evaluated at the surface).

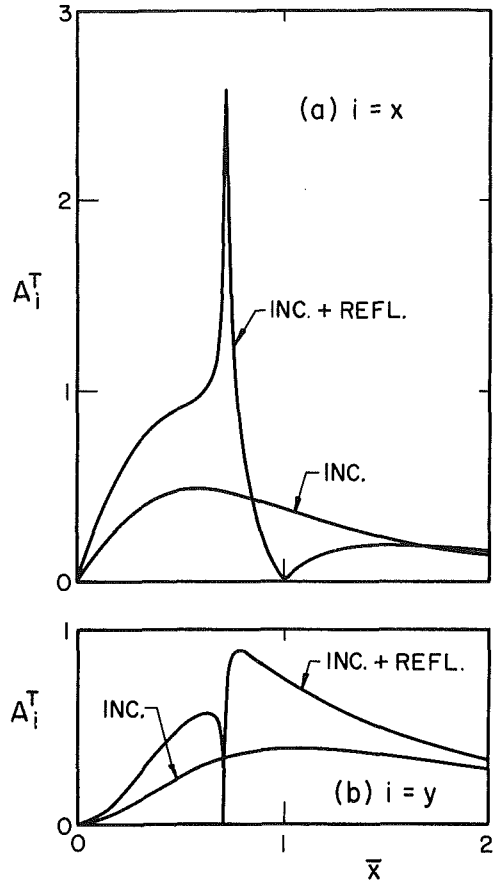

Fig. 4 The amplitudes of (a) the horizontal A_x^T and (b) the vertical A_y^T surface motion are plotted against $\bar{x}$. The angle $\phi = 0$, $\bar{d} = 2$, Poisson's ratio = 0.25, and $s_T/s_F = 0.5$.

Thus in the regions defined by equation (30), in the frequency domain, $R_x^T(\theta)$ and $R_y^T(\theta)$ assume one complex value for ω positive and the conjugate value for ω negative; that is, they have a structure identical to that of $E_T(s_F,\theta)$. Moreover, the overall structure, in the frequency domain, of equation (26) becomes identical to that of equation (17). Therefore, though equation (11*b*) can be applied to equation (26), the resulting integrals may not be convergent. Therefore, for values of $(\theta+\phi)$ satisfying equation (30), the previous expression, equation (26), is valid in the frequency domain but not in the time domain. Further, near points such that equation (30) becomes an equality, uniform approximations are needed to understand the surface motion completely, just as in the case of the crack a uniform approximation is needed near θ_{hw}. Further discussion of these points is given by Harris and Achenbach [14].

To illustrate these results consider the special case $\phi = 0$. The normalized horizontal $(i = x)$ and vertical $(i = y)$ amplitudes of the net surface motion are

$$A_i^\alpha = |(s_\alpha/s_L)^{1/2} R_i^\alpha(\theta)[(R/d)(1 + R\cos\theta/a)]^{-1/2} E_\alpha(s_F,\theta)|$$

where $\alpha = L$ when the incident emission is compressional and $\alpha = T$ when it is shear. In Fig. 3 we have plotted the A_i^L against $\bar{x} = x/d$ for $\bar{d} = 2$, Poisson's ratio = 0.25 and $s_T/s_F = 0.5$. The parameter $\bar{d} = d/a$. Also plotted are the corresponding horizontal and vertical amplitudes of the incident compressional emission. As expected, reflection amplifies the incident disturbance. Moreover, the figure shows that for $\bar{x} = 20$ the surface motion due to reflection has decayed to less than 20 percent of its maximum. Thus, for the

Downloaded 02 May 2010 to 171.66.16.25. Redistribution subject to ASME license or copyright; see http://www.asme.org/terms/Terms_Use.cfm

values of the parameters used here, we can estimate that the near field ends near that point. In Fig. 4 we have plotted the A_I^T against $\bar{x}$ using the same parameter values, as well as the corresponding components of the incident shear emission. The large spike in Fig. 4(*a*) and the zero in Fig. 4(*b*) indicate the point at which $s_T \sin\theta = s_L$. As indicated in the foregoing, the present calculation is not accurate near this point; however, it is possible to conclude that the surface motion varies rapidly near this point. Comparison of Figs. 3 and 4 (note that these two figures have quite different scales) shows that, except in a localized region directly above the crack tip, the compressional emission is the more important. In the time domain this motion will also be the first excited.

More generally, note that in the frequency domain the surface displacement, whether it be that given by equation (22) or equation (26), is directly proportional to $F(\omega)$ $(-i\omega)^{-1/2}\exp(i\omega s_\alpha R)$. The particle displacement at the surface would thus decay at high frequencies as $\omega^{-(\nu+3)/2}$. A measurement of this decay, by assigning a value to ν, would give some indication of the fracture processes at the crack tip.

Far-Field Surface Motion

The far-field surface motion will be dominated by the presence of a Rayleigh wave. We will begin by considering this wave in the frequency domain and then use equation (11*b*) to extend our results to the time domain. The method of calculation employed here is identical to that used in reference [8] to calculate the Rayleigh wave excited by a faulting event. There it was shown that the Fourier components of the displacement of the first-arriving Rayleigh wave $\mathbf{u}^R(\mathbf{x},\omega)$ could be expressed as

$$u_k^R(\mathbf{x},\omega) = \int_{S_i} [u_{i;k}^{GR}(\mathbf{x}',\mathbf{x},\omega)\ \tau_{ij}^I(\mathbf{x}',\omega) - u_i^I(\mathbf{x}',\omega)\ \tau_{ij;k}^{GR}(\mathbf{x}',\mathbf{x},\omega)]n_j dS(\mathbf{x}') \tag{32}$$

where S_i is a surface enclosing the crack edge and $\mathbf{n}$ is a unit normal pointing inward. The terms $u_{i;k}^{GR}$ and $\tau_{ij;k}^{GR}$ are the Rayleigh-wave components of the Green's displacement and stress tensors for the elastic half-space [15]. The terms $u_i^I(\mathbf{x},\omega)$ and $\tau_{ij}^I(\mathbf{x},\omega)$ consist of the sum of the compressional and shear waves emitted by the crack as it starts to grow. We are interested in high-frequency results; therefore, we can approximate $u_i^I(\mathbf{x},\omega)$ by an appropriate sum of the displacements given by equations (12) and (17). Further we need only the high-frequency approximations to $u_{i;k}^{GR}$ and $\tau_{ij;k}^{GR}$. The surface integral, equation (32), now consists of a compressional-wave part and a shear-wave part. The former is evaluated by selecting S_i to be the wave front of the compressional part of $U_i^I(\mathbf{x},\omega)$ and then approximating the integral asymptotically; the latter is similarly evaluated using the shear-wave wavefront.

As a result of the calculations described in the foregoing, the frequency-domain expressions for the Rayleigh-wave displacement in the plane of symmetry are

$$\mathbf{u}^R(x,y,0,\omega) = 4(1/\kappa_R)[g_L E_L(s_F,\theta)\exp(-i\omega s_L \tilde{\mathbf{p}}^L \cdot \mathbf{x}_B) - g_T \cot(2\theta_T)\ E_T(s_F,\theta)\exp(-i\omega s_T \tilde{\mathbf{p}}^T \cdot \mathbf{x}_B)] \times \mathbf{U}(\mathbf{x},\omega)\ D_0^{-1}\ F(\omega) e^{i\pi/2} \tag{33}$$

where θ takes the specific values $\theta = \pi/2 - \phi - \theta_L$ in $E_L(s_F, \theta)$ and $\theta = \pi/2 - \phi - \theta_T$ in $E_T(s_F,\theta)$. The cosines and sines of θ_α are given by

$$\cos\theta_\alpha = s_R/s_\alpha\ ;\ \sin\theta_\alpha = i(\omega/|\omega|)(\cos^2\theta_\alpha - 1)^{1/2} \tag{34a,b}$$

where the sign of $\sin\theta_\alpha$ is determined by the requirement that equation (33) decay with depth (compare this with equation (31)). The major terms $\mathbf{U}(\mathbf{x},\omega)$, g_α, E_α (s_F, θ), and $F(\omega)$ are given by

$$\mathbf{U}(\mathbf{x},\omega) = (2\kappa_R/\kappa^2)[\mathbf{d}^L \exp(i\omega s_L\ \mathbf{p}^L \cdot \mathbf{x}) + \kappa\cot(2\theta_T)\,\mathbf{d}^T \exp(i\omega s_T\ \mathbf{p}^T \cdot \mathbf{x})] \tag{35}$$

$$g_\alpha = \left[1 + \frac{d}{a}\left(\frac{x}{d} + \tan\phi\right)\frac{\sin(\phi+\theta_\alpha)}{\cos\theta_\alpha}\right]^{-1/2} \tag{36}$$

equation (4) and equation (18), respectively. The various ancillary expressions are as follows:

$$\mathbf{p}^\alpha = \cos\theta_\alpha\,\mathbf{i} + \sin\theta_\alpha\,\mathbf{j} \tag{37}$$

$$\mathbf{d}^L = \mathbf{p}^L\ ;\ \mathbf{d}^T = \mathbf{k}\times\mathbf{p}^T \tag{38a,b}$$

$$\mathbf{x} = x\,\mathbf{i} + y\,\mathbf{j}\ ;\ \mathbf{x}_B = -d\tan\phi\,\mathbf{i} + d\,\mathbf{j} \tag{39}$$

$$D_0 = [\kappa_R\kappa^2(\kappa_R^2 - \kappa^2)^{1/2}]^{-1}\frac{d}{dt}[4t^2(t^2-\kappa^2)^{1/2}(t^2-1)^{1/2} - (\kappa^2 - 2t^2)^2] \tag{40}$$

where $\kappa = s_T/s_L$, $\kappa_R = s_R/s_L$ and, in equation (40), $t = \kappa_R$. For Poisson's ratio = 0.25, $D_0 = 6.2$. The subscript or superscript α in each of the preceding is either L or T, the L indicating the compressional term and the T the shear term.

An examination of the various terms in equations (33)–(38*a*,*b*) shows that θ_α per se is not needed; rather only cos θ_α and sin θ_α are used. In particular note that $\cos(\pi/2 - \phi - \theta_\alpha) = (\sin\phi\cos\theta_\alpha + \cos\phi\sin\theta_\alpha)$. Therefore, in each of the emission coefficients, $Im(\cos\theta)$ is positive for ω positive and $Im(\cos\theta)$ is negative for ω negative causing the emission coefficients to assume conjugate values depending on the sign of ω. Moreover, each of the other terms contained in equation (33) also has this property. The time-domain results can therefore be obtained from the foregoing expressions by using equation (11*b*). Near the Rayleigh-wave arrival time the particle velocities are given by

$$\dot{\mathbf{u}}^R(x,y,0,t) = (2\kappa_R U/\kappa^2 D_0)(s_R d)^{(\nu-2)/2}[v_1(x,y,t)\,\mathbf{i} + v_2(x,y,t)\,\mathbf{j}] \tag{41}$$

where

$$v_i(x,y,t) = \frac{4}{\pi}\Gamma\left(\frac{\nu+2}{2}\right)\Gamma\left(\frac{2-\nu}{2}\right)\sum_{\alpha,\beta=L,T} v_i^{\alpha\beta}(x,y,t) \tag{42}$$

$$v_i^{\alpha\beta}(x,y,t) = \frac{A_i^{\alpha\beta}\cos\{[(2-\nu)/2]\tan^{-1}(B^{\alpha\beta}) - \theta_i^{\alpha\beta} - (\nu\pi/4)\}}{(C^{\alpha\beta})^{(2-\nu)/2}[1+(B^{\alpha\beta})^2]^{(2-\nu)/4}} \tag{43}$$

$$A_i^{\alpha\beta}\exp(i\theta_i^{\alpha\beta}) = d_i^\alpha\, S^{\alpha\beta}\, g_\beta\, E_\beta(s_F, \pi/2 - \phi - \theta_\beta) \times (s_\beta/s_R)\, e^{i\pi/2} \tag{44}$$

$$B^{\alpha\beta} = [(t/s_R d) - (x/d + \tan\phi)]/C^{\alpha\beta} \tag{45}$$

$$C^{\alpha\beta} = [1 - (s_\alpha/s_R)^2]^{1/2}(y/d) + [1 - (s_\beta/s_R)^2]^{1/2}. \tag{46}$$

In equations (42)–(46), $i = 1, 2$ and $\alpha, \beta = L, T$. The terms $S^{\alpha\beta}$ are given by

$$S^{LL} = 1;\quad S^{TL} = (s_T/s_L)\cot(2\theta_T) \tag{47a,b}$$

$$S^{LT} = -(s_L/s_T)\cot(2\theta_T);\quad S^{TT} = -\cot^2(2\theta_T). \tag{47c,d}$$

The parameter ν must satisfy the inequalities $1 \le \nu < 2$, where $\nu \ge 1$ for physical reasons (equation (1)), while $\nu < 2$ in order that the particular transform inversion used to calculate equations (41)–(46) remain valid. This range of ν includes the important case of brittle fracture ($\nu = 1$).

Note that in using equation (11*b*) to calculate the time-domain results for the Rayleigh-wave particle velocity, in contrast to our previous experience in attempting to invert

Downloaded 02 May 2010 to 171.66.16.25. Redistribution subject to ASME license or copyright; see http://www.asme.org/terms/Terms_Use.cfm

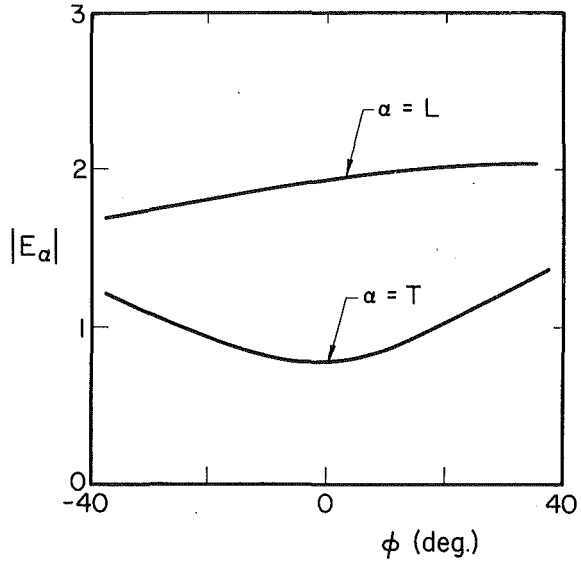

Fig. 5 The magnitudes of the emission coefficient $|E_\alpha(s_F, \theta)|$ evaluated at $\theta = \pi/2 - \phi - \theta_\alpha$, $\alpha = L, T$, are plotted against ϕ. Poisson's ratio = 0.25 and $s_T/s_F = 0.5$.

equation (17) in the headwave region, we were not led to divergent integrals. This can be explained as follows: The time-domain results can be expressed as the convolution of $F(t)$ with a propagation term. In all cases we can recover the propagation term in a form that is accurate near its arrival time. However, in the case of equation (17), when we convolve this result with $F(t)$, the propagation term is not singular enough to concentrate the overall time-domain response near the cylindrical shear-wave arrival time unless, as explained earlier, we can avoid integrating from $(-\infty)$ by retaining t_{hw}. In the case of the Rayleigh-wave particle velocity the propagation term is singular enough to concentrate the overall time-domain response near its arrival time so that the anomalous behavior of $F(t)$ for large t does not lead to any divergent integrals.

For the foregoing results we have adopted the following sign convention: The angle ϕ can take positive or negative values, but $(x + d\tan\phi)$ is always assumed to be positive. This, however, means that θ is positive in a downward sense for ϕ positive, but is positive in an upward sense for ϕ negative. The horizontal distance from the crack tip, in the plane of symmetry, is $(x + d\tan\phi)$ so that when ϕ is varied this distance changes even though x is fixed.

The arrival time, which follows from $B^{\alpha\beta} = 0$ (equations (43) and (45)), suggests that the Rayleigh wave is emitted from a point directly above the crack tip. However, no Rayleigh wave can exist at the surface unless the incident waves properly couple to the surface [16]. As a consequence a position at the surface where a Rayleigh wave is observed must satisfy one of the inequalities

$$(\bar{x} + \tan\phi) > [(s_R/s_\alpha)^2 - 1]^{-1/2} \tag{48}$$

where $\alpha = L$, or T and $\bar{x} = x/d$. Taking the more stringent of the two, and setting Poisson's ratio = 0.25, gives $(\bar{x} + \tan\phi) > 2.3$. However, as we discussed earlier, we are interested in regions where $\bar{x} = O(20)$ for $\phi = 0$, so that these inequalities are satisfied.

In the frequency domain the orientation of the crack influences the Rayleigh wave through the emission coefficients $E_\alpha(s_F, \pi/2 - \phi - \theta_\alpha)$ and through the geometrical spreading factors g_α. Figure 5 plots the magnitudes of the emission coefficients versus ϕ, for Poisson's ratio = 0.25 and $s_T/s_F = 0.5$. Recall that θ_α is complex so that these coefficients are being evaluated at complex angles. This figure should be compared with Figs. 3 and 4 of reference [4] where the emission coefficients $E_L(s_F, \theta)$ and $E_{T1}(s_F, \theta)$ are plotted for real θ. In the case of the shear emission coefficient, the negative values of ϕ mean that it is being evaluated in the headwave region. Thus even though the crack is orientated so that any emissions from the headwave region of point B would not strike the surface, knowledge of the emission coefficient in that region is essential if the Rayleigh waves are to be calculated. Note also, that, whereas for real angles the shear emission coefficient goes to zero at $|\theta| = \theta_{hw}$, for complex angles its behavior is more regular near θ_{hw}.

The magnitudes of the spreading factors have maxima for certain values of the triad $(\bar{x}, \bar{d}, \phi)$, where $\bar{x} = x/d$ and $\bar{d} = d/a$. However, for values of $\bar{d} = O(1)$ and $|\phi| = O(\pi/4)$ or less, and Poisson's ratio = 0.25, the maxima occur for values of $\bar{x}$ that do not satisfy the inequalities expressed by equation (48). Thus for the values of $\bar{x}$ considered here the spreading factors fall off approximately as $(\bar{x})^{-1/2}$, the geometrical decay for a Rayleigh wave excited by a point source. This situation should be compared with that of reference [8], where, for $\bar{d} = 0.5$ and $\phi = -30$ deg, the spreading factors do have maxima for values of $\bar{x}$ that also satisfy equation (48).

Comparison of equation (33) with equations (22) and (26) shows the interesting fact that, whereas the reflected waves carry the spectral term $F(\omega)(-i\omega)^{-1/2}\exp(i\omega s_\alpha R)$, the Rayleigh-wave displacement, at the surface, carries $F(\omega)$ multiplied by terms containing $\exp\{-\omega[(s_\alpha/s_R)^2 - 1]^{1/2}d\}$ times $\exp[i\omega s_R(x + d\tan\phi)]$. Thus the high-frequency spectrum of the Rayleigh wave will fall off exponentially rather than algebraically, with the falloff determined by ωd.

The influence of the depth d can also be seen in the time domain. The depth dependence of the Rayleigh-wave particle velocity manifests itself through the normalizing term $(s_R d)^{(\nu-2)/2}$ in equation (41) and through the term $(C^{\alpha\beta})^{(2-\nu)/2}$ in equation (43). Note that for $\nu = 1$ (brittle fracture) the decay with depth is greatest.

When examining the overall signal in the time domain, the Rayleigh-wave coda can often be recognized because of its distinctive form. To show this we have plotted, in Fig. 6, the normalized components of the particle velocities $v_i(x, y, t)$ $(i = 1, 2)$ evaluated at $y = 0$ against $\tau = \bar{t} - \bar{x}$, where $\bar{t} = t/(s_R d)$. The parameters in this figure are $\phi = 0$, $\bar{x} = 20$, $\bar{d} = 2$, $\nu = 1$, Poisson's ratio = 0.25, and $s_T/s_F = 0.5$.

More generally, note that in the time domain the geometry of the problem and the time dependence of the problem are mixed together by the presence of the angle $\theta_i^{\alpha\beta}$ in the cosine term in equation (43). Equation (44) shows that $\theta_i^{\alpha\beta}$ comes from the geometrical factors g_α and $E_\alpha(s_F, \pi/2 - \phi - \theta_\alpha)$ evaluated at the complex angle θ_α. This should be contrasted with the incident emissions, equations (2) and (3), for which the geometry and the time dependence, for $|\theta| < \theta_{hw}$, can be separated near their wave fronts.

Conclusions

The results of this paper lead to the following conclusions:

1. In the headwave region of the crack, the dominant contribution to the shear-wave emission comes from the region near $t = s_T r$ for both $t > s_T r$ and $t < s_T r$. As a consequence we were led to redefine the shear-wave emission coefficient $E_T(s_F, \theta)$ (equations (4), (5), and (7)). In the time domain it assumes the form shown in equation (3) and in the frequency domain it assumes that shown in either equation (16) or equation (17). Of particular note is the argument leading to equation (17) were $E_T(s_F, \theta)$ was assigned a value, for $|\theta| > \theta_{hw}$, for both positive and negative ω, thus permitting its correct evaluation for complex $\cos\theta$ in equation (33).

2. Our study of the near-field surface motion has shown that, in addition to being the first to arrive, the surface

Downloaded 02 May 2010 to 171.66.16.25. Redistribution subject to ASME license or copyright; see http://www.asme.org/terms/Terms_Use.cfm

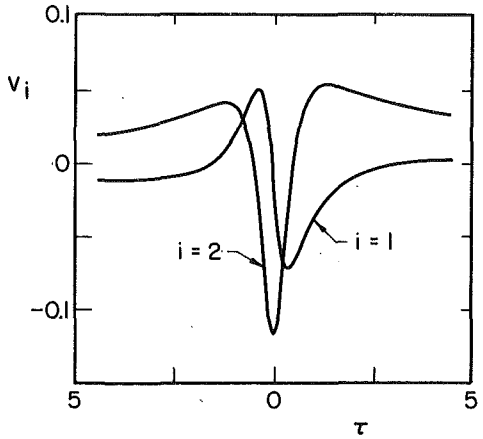

Fig. 6 The normalized components of the Rayleigh-wave particle velocity v_i, i = 1, 2, at the surface are plotted against $\tau = \bar{t} - \bar{x}$. The parameter values are $\phi = 0$, $\bar{x} = 20$, $\bar{d} = 2$, $\nu = 1$, Poissons' ratio = 0.25, and $s_T/s_F = 0.5$.

motion caused by the incident compressional emission dominates that caused by the incident shear emission except in a localized region directly above the crack-tip. In the far field the Rayleigh wave, though it is a later arrival, becomes, because of its slower geometrical decay rate, the dominant disturbance. Figure 6 indicates its distinctive form.

3. A measurement of acoustic emission should, in principle, give information about the crack's size, its orientation, and the fracture processes near the crack tip. Certainly size and orientation affect the emission as we have tried to show by our study of the parameters θ, ϕ, $\bar{d}$ in Figs. 3-6. But perhaps the most interesting result is our determination of how the spectral function $F(\omega)$, which is directly determined by the fracture processes at the crack tip, is modified by the propagation effects in the near and far field.

Acknowledgment

The work reported here was carried out in the course of research sponsored by the Solid Mechanics Program of the Division of Mechanical Engineering and Applied Mechancis, National Science Foundation, NSF Grant MEA 81-04738. Moreover, we wish to thank Richard L. Weaver and the reviewers for their helpful comments.

References

1 Wadley, H. N. G., and Scruby, C. B., "A Study of Deformation and Fracture Processes in a Low-Alloy Steel by Acoustic Emission Transient Analysis," *Acta Metallurgica*, Vol. 27, 1979, pp. 613-625.

2 Spanner, J. D., "Acoustic Emission, Applications and Trends," *Elastic Waves and Non-Destructive Testing of Materials*, Pao, Y.-H., ed., AMD Vol. 29, ASME, New York, pp. 71-84.

3 Rose, L. R. F., "The Stress-Wave Radiation from Growing Cracks," *International Journal of Fracture*, Vol. 17, 1981, pp. 45-60.

4 Achenbach, J. D., and Harris, J. G., "Acoustic Emission From a Brief Crack Propagation Event," ASME JOURNAL OF APPLIED MECHANICS, Vol. 46, 1979, pp. 107-112.

5 Hsu, N. N., and Hardy, S. C., "Experiments in Acoustic Emission Waveform Analysis for Characterization of A. E. Sources, Sensors and Structures," *Elastic Waves and Non-Destructive Testing of Materials*, Pao, Y.-H., ed., AMD Vol. 29, ASME, New York, pp. 85-106.

6 Pao, Y.-H., "Theory of Acoustic Emission," *Elastic Waves and Non-Destructive Testing of Materials*, Pao, Y.-H., ed., AMD Vol. 29, ASME, New York, pp. 107-128.

7 Rose, L. R. F., "On the Acoustic Emission Due to the Fracture of Brittle Inclusions," *Journal of Nondestructive Evaluation*, Vol. 1, 1980, pp. 149-155.

8 Harris, J. G., Achenbach, J. D., and Norris, A. N., "Rayleigh Waves Excited by the Discontinuous Advance of a Rupture Front," *Journal of Geophysical Research*, Vol. 88, 1983, pp. 2223-2239.

9 Ahluwalia, D. S., Keller, J. B., and Jarvis, R., "Elastic Waves Produced by Surface Displacements," *SIAM Journal of Applied Mathematics*, Vol. 26, 1974, pp. 108-119.

10 Achenbach, J. D., Gautesen, A. K., and McMaken, H., *Ray Methods for Waves in Elastic Solids*, Pitman, Boston, 1982, pp. 133-138.

11 Lighthill, M. J., *Fourier Analysis and Generalized Functions*, Cambridge University Press, Cambridge, 1958, pp. 46-58.

12 Carrier, G. F., Krook, M., and Pearson, C. E., *Functions of a Complex Variable*, McGraw-Hill, New York, 1966, pp. 253-257.

13 Achenbach, J. D., Gautesen, A. K., and McMaken, H., *Ray Methods for Waves in Elastic Solids*, Pitman, Boston, 1982, pp. 89-108.

14 Harris, J. G., and Achenbach, J. D., "Near-Field Surface Motions Excited by Radiation From a Slip Zone of Arbitrary Shape," *Journal of Geophysical Research*, Vol. 86, 1981, pp. 9352-9356.

15 Achenbach, J. D., Gautesen, A. K., and McMaken, H., *Ray Methods for Waves in Elastic Solids*, Pitman, Boston, 1982, pp. 63-73.

16 Ewing, W. M., Jardetzky, W. S., and Press, F., *Elastic Waves in Layered Media*, McGraw-Hill, New York, 1957, pp. 63-66.

Downloaded 02 May 2010 to 171.66.16.25. Redistribution subject to ASME license or copyright; see http://www.asme.org/terms/Terms_Use.cfm

Deformations and Stress Intensities Due to a Craze in an Extended Elastic Material

J. R. Walton
Associate Professor,
Department of Mathematics.

Y. Weitsman
Professor,
Department of Civil Engineering.
Mem. ASME

Texas A&M University,
College Station, Texas 77843

This paper presents an analytical solution, accompanied by a numerical scheme, to determine the displacement and stress fields in an extended elastic medium due to a thin craze of finite length directed transversely to the load at infinity. Crazes are thin elongated defects containing fine fibrils that connect their opposite interfaces. These fibrils are modeled as a distributed spring, leading to a formulation in terms of a singular integrodifferential equation. The paper also contains a treatment of central cracks within the craze and time-dependent craze response, and includes a discussion of "tip zone" correction.

Introduction

Crazes are thin, elongated defects that develop in glassy polymers. Although resembling cracks in their geometric configuration, crazes consist of interconnected voids transversed by thin fibrils which span the gap between the interfaces of the bulk polymer, and are therefore capable of transmitting forces [1-10]. A typical micrograph of the central portion of a "mature" craze is shown in Fig. 1.[1]

Crazes nucleate from impurities in the bulk polymeric material and grow transversely to the direction of principal tension. Alternately, crazes may emanate from the interfaces between the bulk material and dispersed rubber particles in filled polymers. The length of "mature" crazes is typically two to three orders of magnitude larger than their thickness. A schematic drawing of a craze is shown in Fig. 2[2] and a typical "craze opening profile" is sketched in Fig. 3. In Fig. 3, $h/a \sim 10^{-2} - 10^{-3}$ and the length α of the "tip zone" is of a magnitude $\alpha/a \sim 10^{-3}$ [2-6]. Note also that the tip zone is shaped like a "cusp," as occurs in brittle fracture.

The tip zone, called also a "mackeral region" [9] or a "craze formation region" [11], is the place where bulk polymeric material is transformed into a craze by a process of fibrillation. This zone resembles "fingers" of voids penetrating the bulk polymer, as shown in Fig. 4[3] and sketched in Fig. 5.

Crazes are the precursors of cracking and failure in many polymers, with cracks usually developing at the center of the crazes and growing toward their tips.

A distinction is made between "air crazes," which develop in dry polymers, and crazes in vapor or liquid environments. The latter exhibit a pronounced viscoelastic response, although time-dependent behavior was also observed in various other circumstances [11-19].

It is not our intention to review here the analytical approaches attempted thus far to model the mechanical response of a region containing long, thin crazes. It suffices to say that, in the absence of an appropriate solution, several investigators employed the classical, two-dimensional results for a crack, which they then proceeded to modify intuitively to account for the fact that crazes transmit stresses while the faces of cracks are traction-free. Other investigators circumvented the problem of a craze surrounded by a bulk polymer by considering the case of a craze associated with a crack. They subsequently attributed all fracture and growth mechanisms to the crack and analyzed the craze in the context of Barenblatt or Dugdale type "damage zones." A detailed analysis of the latter kind appeared recently [20], where the effects of viscoelastic craze response were emphasized and illuminated.

More recently, an analytical solution was obtained for a craze that was modeled as an elastic, transversely isotropic, elliptic inclusion [21]. This solution is clearly much more realistic than results derived from the plane crack case.

Finally, we should mention that the fact that the solution to thin crazes should yield results that are qualitatively similar to, and only quantitatively different from, the effects of cracks was intuitively recognized some time ago [19]. In this paper we will provide the details.

Viewing the craze as a collection of thin, parallel fibrils separated by voids we will model its response by a distributed, one-dimensional spring. The spring modulus need not be constant. In fact, we will consider it to vary with position, and subsequently also with time. In view of the extremely high

[1] We wish to acknowledge, with thanks, that this figure was given to us by Professor E. J. Kramer of Cornell University.

[2] Courtesy of Marcel Dekker Journals and Professor E. J. Kramer.

[3] Courtesy of Taylor & Francis, Inc., and Professor E. J. Kramer.

Contributed by the Applied Mechanics Division for presentation at the 1984 PVP Conference and Exhibition, Joint with Applied Mechanics Division and Materials Division, San Antonio, Texas, June 17-21, 1984 of THE AMERICAN SOCIETY OF MECHANICAL ENGINEERS.

Discussion on this paper should be addressed to the Editorial Department, ASME, United Engineering Center, 345 East 47th Street, New York, N.Y. 10017, and will be accepted until two months after final publication of the paper itself in the JOURNAL OF APPLIED MECHANICS. Manuscript received by ASME Applied Mechanics Division, January, 1983; final revision, June, 1983. Paper No. 84-APM-8.

Copies will be available until February, 1985.

Copyright © 1984 by ASME
Downloaded 02 May 2010 to 171.66.16.25. Redistribution subject to ASME license or copyright; see http://www.asme.org/terms/Terms_Use.cfm

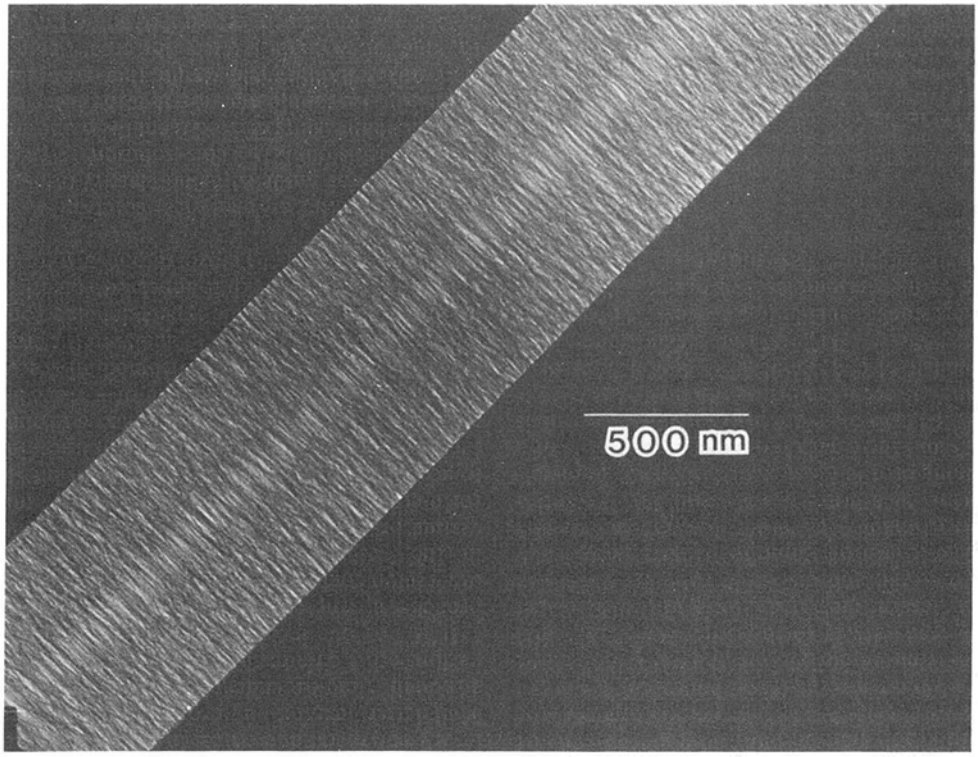

Fig. 1 The central portion of a "mature" craze

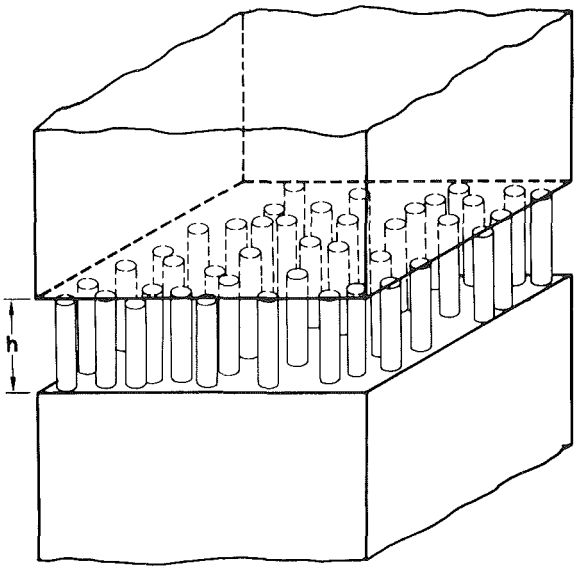

Fig. 2 A schematic drawing of a craze, with fibrils connecting the opposite faces of a bulk polymer

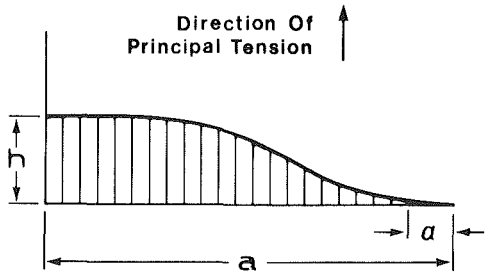

Fig. 3 A sketch of the craze opening displacement profile

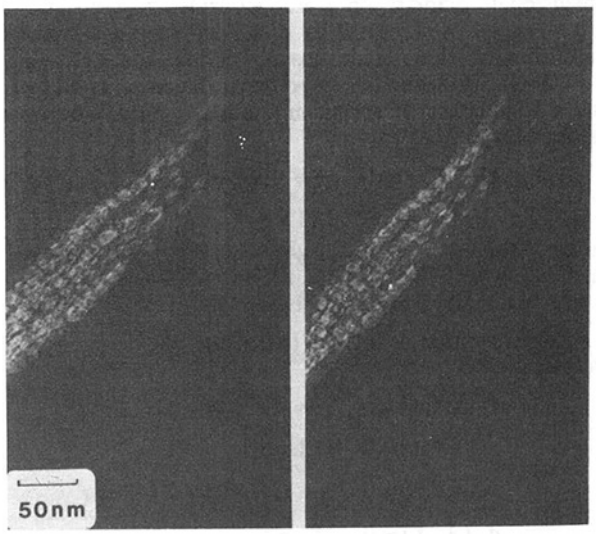

Fig. 4 A "Stereo pair" showing the details of the craze tip zone

ratio of length to thickness of the craze, we will consider the case of a vanishingly small thickness. The fact that the length of the tip zone is also much smaller than the craze length will enable us to employ an asymptotic analysis for the "tip zone correction" which will then provide a predicted tip profile that is cusplike.

Some data [1, 7] indicate that the stresses in crazes depend nonlinearly on the opening displacement V, namely $\sigma = F(V)$ instead of the linear relation $\sigma = KV$ employed in this work. This nonlinear model is the subject of a forthcoming paper. The present analysis is to be regarded as a first-order approximation to the nonlinear case.

It is worthwhile noting that a solution for an analogous problem was derived in cylindrical coordinates [22]. The results for cylindrical coordinates are not directly applicable to the rectangular coordinates case considered here. Although that work dealt with a nonlinear stress-displacement

Downloaded 02 May 2010 to 171.66.16.25. Redistribution subject to ASME license or copyright; see http://www.asme.org/terms/Terms_Use.cfm

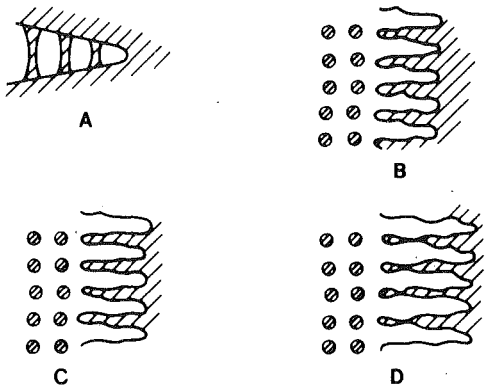

Fig. 5 A schematic drawing of the craze tip zone and its growth process

relationship it did not seem motivated by any particular physical circumstance. Consequently, many specific details relevant for application to crazes were not considered in that work.

Finally, it should be emphasized that the elasticity solution detailed in the early sections of this paper fails near the tip region. Just as in any elastic fracture analysis, this solution predicts singular stresses and an opening displacement with a vertical slope at the tip – both of which are obviously erroneous for real materials. The elastic solution is nevertheless useful here, as in fracture mechanics, because the stress intensity factor can be correlated to meaningful, physical material properties and because it provides a key to a corrective analysis which results in removing the singularity. That analysis provides the desired cusp-shaped displacements in the tip region. The details of such appropriate analysis are also given in this work.

Analysis

Consider an infinite, isotropic, homogeneous, linearly elastic region $-\infty<X,\ Y<\infty$ with G, ν denoting the shear modulus and Poisson's ratio, respectively. Let σ_X, σ_Y, τ_{XY}, U, and V designate stresses and displacements in a two-dimensional, plane-strain state. Consider further that the infinite region is subjected to $\sigma_Y=T$ as $Y\to\pm\infty$ and let a diminishingly thin craze extend along the X axis at $-a<X<a$. Modeling the response of the craze as that of an elastic foundation of spring modulus $K=K(X)$, we obtain the boundary value problem

$$\begin{aligned} &\tau^{\circ}_{XY}(X,0)=0 \quad -\infty<X<\infty\\ &V^{\circ}(X,0)=0 \quad |X|>a\\ &\sigma^{\circ}_{Y}(X,0)=K(X)\,V^{\circ}(X,0) \quad |X|<a\\ &\sigma^{\circ}_{Y}(X,Y)=T \quad |Y|\to\infty \end{aligned} \tag{1}$$

By superposition, it suffices to consider the boundary value problem

$$\begin{aligned} &\tau_{XY}(X,0)=0 \quad -\infty<X<\infty\\ &V(X,0)=0 \quad |X|>a\\ &\sigma_{Y}(X,0)=-T+K(X)\,V(X) \quad |X|<a\\ &\sigma_{Y}(X,Y)\to 0 \quad |Y|\to\infty \end{aligned} \tag{2}$$

It can be shown [23] that if $(2)_1$ holds we have

$$\sigma_Y(X,0)=\frac{G}{1-\nu}\,\frac{1}{\pi}\int_{-\infty}^{\infty}\frac{\partial V(\xi,0)}{\partial\xi}\,\frac{d\xi}{\xi-X} \tag{3}$$

In particular, when $V(X,0)$ vanishes for $|X|>a$ we have

$$\sigma_Y(X,0)=\frac{G}{1-\nu}\,\frac{1}{\pi}\int_{-a}^{a}\frac{\partial V(\xi,0)}{\partial\xi}\,\frac{d\xi}{\xi-X} \tag{4}$$

Inserting (4) in the third of equation (2) we obtain the singular integrodifferential equation

$$T=K(X)\,V(X,0)-\frac{G}{1-\nu}\,\frac{1}{\pi}\int_{-a}^{a}\frac{\partial V(\xi,0)}{\partial\xi}\,\frac{d\xi}{\xi-X} \tag{5}$$

Note that $V(\pm a,0)=0$.

From the properties of the Hilbert transform [24], we can rewrite (5) as follows

$$T=K(X)\,V(X,0)-\frac{G}{1-\nu}\,\frac{1}{\pi}\,\frac{d}{dX}\int_{-a}^{a}\frac{V(\xi,0)}{\xi-X}\,d\xi \tag{6}$$

Introduce the nondimensional quantities $x=X/a$, $v(x)=V(X,0)/\delta$, $k(x)=K(X)\delta/T$, $\tau=\xi/a$, and $\lambda=G\delta/[(1-\nu)aT]$, then (6) can be written as

$$1=k(x)v(x)-\lambda\,\frac{1}{\pi}\,\frac{d}{dx}\int_{-1}^{1}\frac{v(\tau)}{\tau-x}\,d\tau \tag{7}$$

Integration of (7), noting that v and k are even in their argument, yields

$$x=\int_0^x k(\tau)v(\tau)\,d\tau-\lambda\,\frac{1}{\pi}\int_{-1}^{1}\frac{v(\tau)}{\tau-x}\,d\tau \tag{8}$$

In general, the solution to the singular integral equation (8) will be singular as $x\to-1^+$ and $x\to1^-$ unless $v(x)=\sqrt{1-x^2}\,\chi(x)$ with χ regular over $[-1,1]$ [23, 25, 26], as it should be in the present case.

By comparison, the solution to the classical Griffith crack is $v(x)=(1-x^2)^{1/2}$ and as $x\to1^+$ $(\sigma_y/T)\sim(x^2-1)^{-1/2}$. In addition, the scaling was selected in such a manner to yield $\lambda=1$. Consequently, $\chi(1)$ relates the stress intensity factor in the present problem to that for a crack.

A convenient transformation of (8) is achieved by application of the operator $(\sqrt{1-x^2}/\pi)\int_{-1}^{1}(1/\sqrt{1-z^2})\,dz/(z-x)$.

Noting that $(1/\pi)\int_{-1}^{1}(z/\sqrt{1-z^2})\,dz/(z-x)=1$, equation (8) transforms to

$$1-\lambda\,\frac{v(x)}{\sqrt{1-x^2}}=\frac{1}{\pi}\int_{-1}^{1}(1-z^2)^{-1/2}\,\frac{dz}{z-x}\int_0^z k(\tau)v(\tau)\,d\tau \tag{9}$$

Considering the right-hand side of (9), we get

$$\begin{aligned} &\frac{1}{\pi}\int_{-1}^{1}(1-z^2)^{-1/2}\,\frac{dz}{z-x}\int_0^z k(\tau)v(\tau)\,d\tau\\ &=\frac{1}{\pi}\int_0^1(1-z^2)^{-1/2}\left(\frac{1}{z+x}+\frac{1}{z-x}\right)dz\int_0^z k(\tau)v(\tau)\,d\tau\\ &=\frac{1}{\pi}\int_0^1 k(\tau)v(\tau)\,d\tau\int_\tau^1(1-z^2)^{-1/2}\left(\frac{1}{z+x}+\frac{1}{z-x}\right)dz\\ &=\frac{1}{\pi}\int_0^1 k(\tau)v(\tau)\,d\tau\int_{\tau^2}^1(1-s)^{-1/2}\,\frac{ds}{s-x^2}\\ &=\frac{1}{\pi}\int_0^1 k(\tau)v(\tau)R_0(\tau^2,x^2)\,d\tau \end{aligned} \tag{10}$$

where

$$R_0(\tau^2,x^2)=\int_{\tau^2}^1(1-s)^{-1/2}\,\frac{ds}{s-x^2} \tag{11}$$

In deriving (10) we employed the eveness of k and v in x. The integral (11) can be further reduced [27], since

Downloaded 02 May 2010 to 171.66.16.25. Redistribution subject to ASME license or copyright; see http://www.asme.org/terms/Terms_Use.cfm

$$R_0(p,q)=\int_p^1 (1-s)^{-1/2}\frac{ds}{s-q}$$

$$=\begin{cases}\dfrac{(1-p)^{1/2}}{1-q}B\left(\dfrac{1}{2},1\right){}_2F_1\left(1,\dfrac{1}{2},\dfrac{3}{2};\dfrac{1-p}{1-q}\right) & 0<q<p\\[2ex] -(1-p)^{-1/2}B\left(-\dfrac{1}{2},1\right){}_2F_1\left(\dfrac{1}{2},1,\dfrac{3}{2};\dfrac{1-q}{1-p}\right) & p<q<1\end{cases}$$

where $B(1/2, 1) = -B(-1/2, 1) = 2$ and it can be shown that ${}_2F_1(1, 1/2, 3/2; \theta)$

$$={}_2F_1(1/2, 1, 3/2; \theta)=\frac{1}{2}\theta^{-1/2}ln\left(\frac{1+\theta^{1/2}}{1-\theta^{1/2}}\right)$$

Furthermore,

$$ln\left(\frac{1+\theta^{1/2}}{1-\theta^{1/2}}\right)=ln\left[\frac{(1+\theta^{1/2})^2}{1-\theta}\right]=-ln(1-\theta)+2ln(1+\theta^{1/2})$$

Consequently,

$$R_0(p, q)=(1-q)^{-1/2}R_1(p, q) \tag{12}$$

where

$$R_1(p,q)=\begin{cases}ln\left(\dfrac{1-q}{p-q}\right)+R_2(p,q) & 0<q<p<1\\[2ex] ln\left(\dfrac{1-p}{q-p}\right)+R_2(q,p) & 0<p<q<1\end{cases} \tag{13}$$

with

$$R_2(p,q)=\begin{cases}2ln\left[1+\left(\dfrac{1-p}{1-q}\right)^{1/2}\right] & 0<q<p<1\\[2ex] 2ln\left[1+\left(\dfrac{1-q}{1-p}\right)^{1/2}\right] & 0<p<q<1\end{cases} \tag{14}$$

Note that R_1 and R_2 are symmetric in p and q and that R_2 is bounded on $0 \le p, q \le 1$ and continuous except at $p=q=1$.

Substitution of equations (12)-(14) in (11) with $p=\tau^2$, $q=x^2$ reduces the governing equation (9) to a Fredholm integral equation of the second kind with a logarithmic singularity. Altogether, we obtain in place of (9)

$$\lambda\chi(x)+\frac{1}{\pi}\int_0^1 R(x^2, s^2)k(s)\chi(s)ds=1 \tag{15}$$

where

$$\sqrt{\frac{1-x^2}{1-s^2}}R(x^2,s^2)$$

$$=\begin{cases}-ln(x^2-s^2)+ln(1-s^2)+2ln\left[1+\sqrt{\dfrac{1-x^2}{1-s^2}}\right] & 0<s<x\\[2ex] -ln(s^2-x^2)+ln(1-x^2)+2ln\left[1+\sqrt{\dfrac{1-s^2}{1-x^2}}\right] & x<s<1\end{cases} \tag{16}$$

Note that $R(x^2, s^2)=(1-s^2)^{1/2}R_0(x^2,s^2)$.

Recall that

$$\chi(x)=(1-x^2)^{-1/2}v(x) \tag{17}$$

In particular, when $x\to 1^-$ we obtain

$$\lim_{x\to 1^-}R(x^2,s^2)=\lim_{x\to 1^-}2\frac{ln\left[1+\sqrt{\dfrac{1-x^2}{1-s^2}}\right]}{\sqrt{\dfrac{1-x^2}{1-s^2}}}=2 \tag{18}$$

whereby (15) reduces to

$$\lambda\chi(1)+\frac{2}{\pi}\int_0^1 k(s)\chi(s)ds=1 \tag{19}$$

Equations (15) and (19) must be solved numerically, by reducing them further to a system of linear algebraic equations for discrete values of $\chi(x)$. The numerical solution is outlined in the Appendix.

There are two special forms of $k(x)$, namely $k(x) = \sqrt{1-x^2}$ and $k(x)=1/\sqrt{1-x^2}$, which simplify the solution to equation (9), and do not require a reduction to the Fredholm equation (15). We will consider a combination of those forms, namely

$$k(x)=k_1(1-x^2)^{1/2}+(1-k_1)(1-x^2)^{-1/2} \tag{20}$$

Again, let $v(x) = (1-x^2)^{1/2}\chi(x)$ and consider

$$\chi(x)=\sum_{n=0}^{\infty}\beta_n x^{2n} \tag{21}$$

Substitution of (20) and (21) in (9) gives:

$$\lambda\sum_{n=0}^{\infty}\beta_n x^{2n}+\frac{1}{\pi}\int_{-1}^{1}(1-z^2)^{-1/2}\frac{dz}{z-x}\int_0^z \times(1-k_1\tau^2)\sum_{n=0}^{\infty}\beta_n\tau^{2n}d\tau=1 \tag{22}$$

Interchanging the order of summation and integration, and recalling that [28]

$$\frac{1}{\pi}\int_{-1}^{1}\frac{y^{2n+1}}{\sqrt{1-y^2}}\frac{dy}{y-x}=\sum_{i=0}^{n}x^{2i}T_{2(n-i)}$$

where $T_0 = 1$ and $T_{2m} = ((2m-1)/2m)\ T_{2(m-1)}$, we obtain from (22)

$$1=\lambda\beta_0+\sum_{j=0}^{\infty}\frac{T_{2j}}{2j+1}\beta_j-k_1\sum_{j=0}^{\infty}\frac{T_{2(j+1)}}{2j+3}\beta_j$$

$$0=\lambda\beta_n+\sum_{j=n}^{\infty}\frac{T_{2(j-n)}}{2j+1}\beta_j-k_1\sum_{j=n-1}^{\infty}\frac{T_{2(j+1-n)}}{2j+3}\beta_j \quad n\ge 1 \tag{23}$$

Equations (23) are an infinite, "upper triangular," system of algebraic equations in the unknown β_j. However, since $\beta_{N+1}\sim\beta_N/N!$ the system converges very rapidly and can be truncated after, say, 10 terms.

The stress intensity factor, as given by $\chi(1)$, is now obtained from

$$\sum_{j=0}^{N}\beta_j.$$

This provides an independent check on the numerical solution to (15).

Examples

Typical data for polystyrene [2] indicate that $G\sim 600$ MPa and $\nu = 0.4$, in which case a typical opening displacement for

Downloaded 02 May 2010 to 171.66.16.25. Redistribution subject to ASME license or copyright; see http://www.asme.org/terms/Terms_Use.cfm

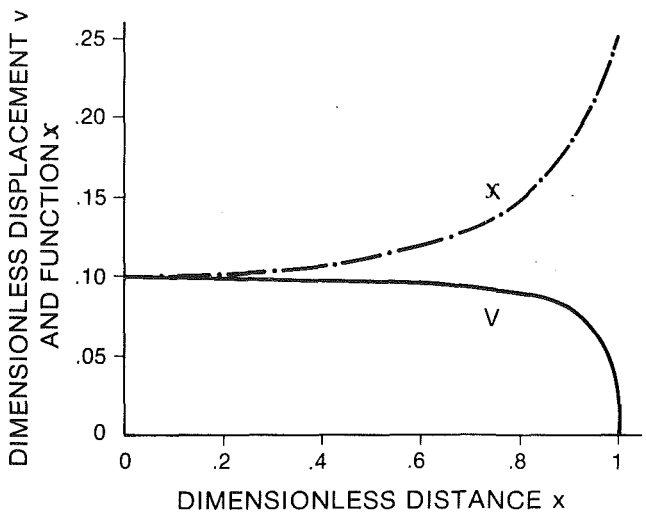

Fig. 6 The nondimensional displacement v (solid line) and function χ(dashed line) versus the nondimensional distance x for a craze with $\lambda = 0.93344$ and $k = 9.3344$

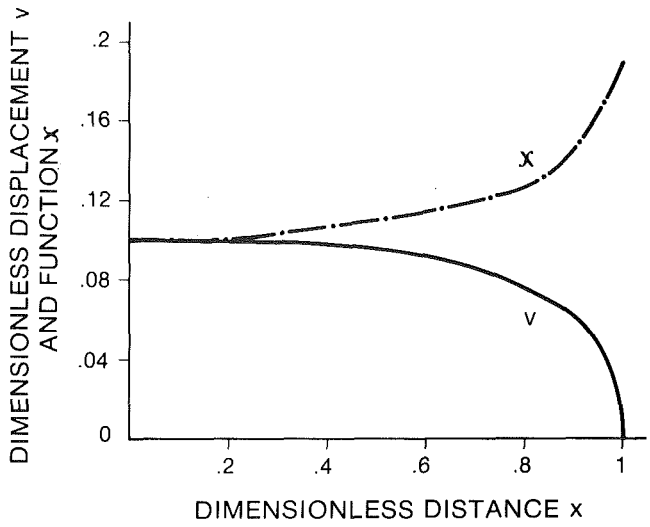

Fig. 8 The nondimensional displacement v (solid line) and function χ (dashed line) versus the nondimensional distance x for a craze with $\lambda = 0.92785$ and springs of varying stiffness. $k = 9.2785(1+x^6)$.

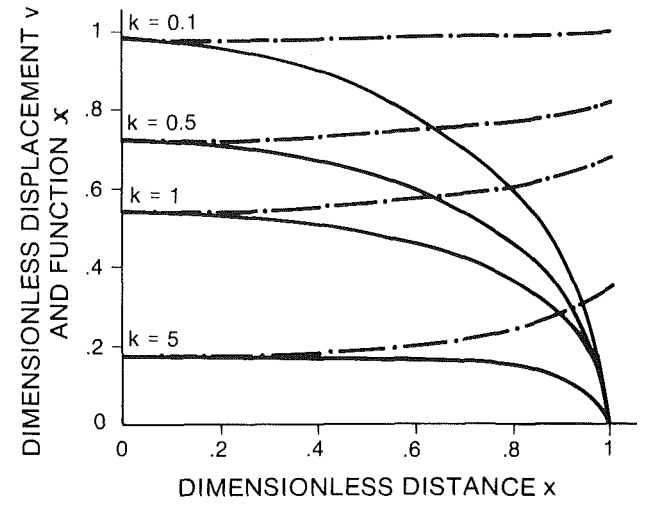

Fig. 7 The nondimensional displacement v (solid lines) and function χ (dashed lines) versus the nondimensional distance x for a craze with $\lambda = 0.93344$ and springs of decreasing stiffness. $k = 5, 1, 0.5, 0.1$.

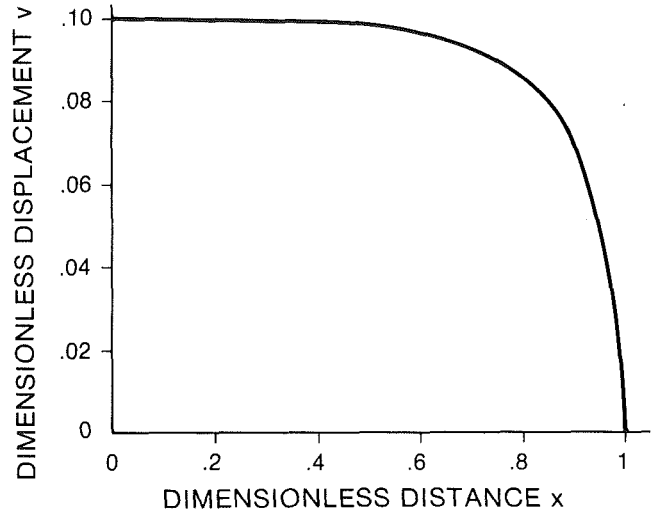

Fig. 9 The nondimensional displacement v versus the nondimensional distance x for a craze with $\lambda = 0.995$ and $k = 9.95\,[0.6(1-x^2)^{1/2} + 0.4(1-x^2)^{-1/2}]$

a craze of length $a = 10^{-4}$m under a load $T = 30$ MPa was measured to be $\delta_{CRAZE} \sim 0.3 \times 10^{-6}$m. This contrasts with a crack opening displacement $\delta_{CRACK} = 3 \times 10^{-6}$m. Thus, the craze inhibits the opening displacement to one-tenth of the magnitude it would attain for a crack of equal length.

In the absence of detailed a priori information on the functional form of $K(X)$ we assume at first that $K(X) = K_0$ (constant). To assess the value of K_0, consider an infinitely long craze, in which case the measured value of $V(0) = 0.3 \times 10^{-6}$m under $T = 30$ MPa yields $K_0 = 10^8$ MPa/m, whereby we get $k = 10$.

Preliminary computations with $\lambda = 1$ and $k = 10$ result in $v(0) = 0.093344$ instead of the desired value of $v(0) = \delta_{CRAZE}/\delta_{CRACK} = 0.1$. Due to the linearity of the problem we obtain the desired value of $v(0) = 0.1$ by rescaling λ and k to $\lambda = 0.93344$ and $k = 9.3344$. The resulting values of $\chi(x)$ and $v(x)$ are shown in Fig. 6. Note that the stress intensity factor is $\chi(1) = 0.25237$, in contrast with $\chi(1) = 1$ for a crack. Additional results are shown in Fig. 7 for $\lambda = 0.93344$ and $k = 5$, 1, 0.5, and 0.1. Note that as k diminishes $\chi(x)$ increases toward to value of $\chi(x) = 1$ which corresponds to a crack. Figure 8 exhibits results for $\lambda = 0.92785$ and a nonuniform $k(x) = 9.2785(1+x^6)$. The values of λ and k were scaled to give $v(0) = 0.1$ as in Fig. 6. Similarly, Fig. 9 shows the displacement profile $v(x)$ for $\lambda = 0.995$ and $k(x) = 9.95[0.6(1-x^2)^{1/2} + 0.4(1-x^2)^{-1/2}]$. Note that $v(x)$ in Figs. 8 and 9 decreases very slowly over $0 < x < 0.6$, resembling profiles observed in actual crazes.

As mentioned in the Introduction, the displacement profiles in Figs. 6, 8, 9 (as well as Fig. 10) do not exhibit the cusp shap shown in Fig. 3. This expected deficiency of elastic solution is corrected in a subsequent section.

A Central Crack Within the Craze

The case of a central, symmetric crack within the craze can be evaluated without difficulty. For a crack of nondimensional length $2c$ we simply let $k(x) = 0$ for $0 \le x \le c$ and employ the same numerical scheme given in the Appendix. Calculations were performed for $\lambda = 0.93344$ and $k = 9.3344$ with $c = 0.1, 0.2, \ldots, 0.9$ with 40 equal subdivisions of the interval [0, 1].

The displacement profiles $v(x)$ are illustrated in Fig. 10 for various crack lengths c, while the variation of the stress intensity factor $\chi(1, c)$ is shown in Fig. 11 in relation to c.

Time-Dependent Craze Response

In many circumstances, especially for liquid saturated

Downloaded 02 May 2010 to 171.66.16.25. Redistribution subject to ASME license or copyright; see http://www.asme.org/terms/Terms_Use.cfm

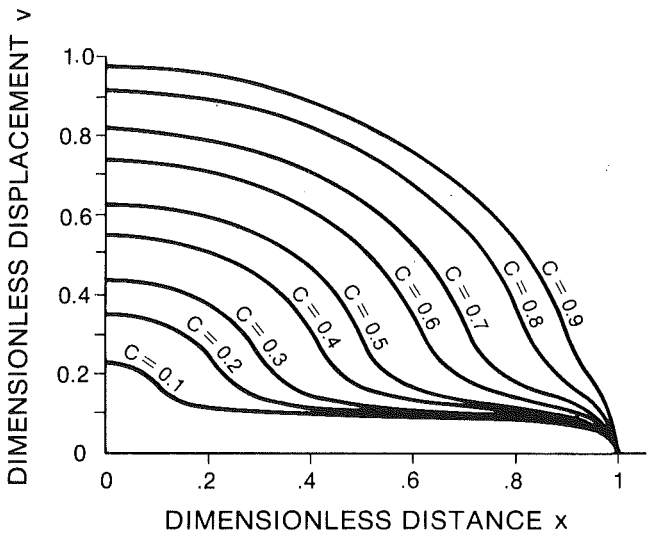

Fig. 10 Profiles of the nondimensional displacement v versus the nondimensional distance x for a craze with $\lambda = 0.93344$ and $k = 9.3344$, with central cracks of various relative half-lengths c

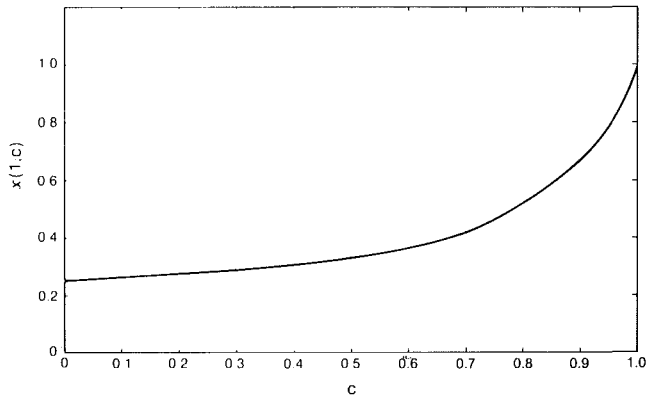

Fig. 11 The normalized stress intensity factor $\chi(1;c)$, versus the relative length c of cracks within a craze (details same as in Fig. 10)

crazes, it was found that the response of crazes is time-dependent [13-20].

Turning to equations (1-6), this implies that $K = \hat{K}(X, t)$, where t denotes time. Due to paucity in detailed information, as well as for simplicity, let us assume that

$$\hat{K}(X, t) = K(X)E(t) \tag{24}$$

In (24), $E(t)$ designates a dimensionless relaxation function which decreases with time.

Nondimensionalizing as before we get, in analogy with (7)

$$D(t) = k(x)v(x) - \frac{1}{\pi}\lambda D(t)\frac{d}{dx}\int_{-1}^{1}\frac{v(\tau)}{\tau - x}d\tau \tag{25}$$

where $D(t) = 1/E(t)$ represents compliance.

If we write (15), symbolically, as

$$(\lambda + \mathbf{K})\chi = 1 \tag{26}$$

then (25) can be converted to

$$(\lambda D + \mathbf{K})\chi = D \tag{27}$$

or, equivalently

$$(\lambda + E\mathbf{K})\chi = 1 \tag{27a}$$

In (26) and (27) $\mathbf{K}$ symbolizes the integral operator in (15) and $D = D(t)$, $E = E(t)$.

It is thus noted that the computational scheme given in the Appendix can be applied to the present circumstance with

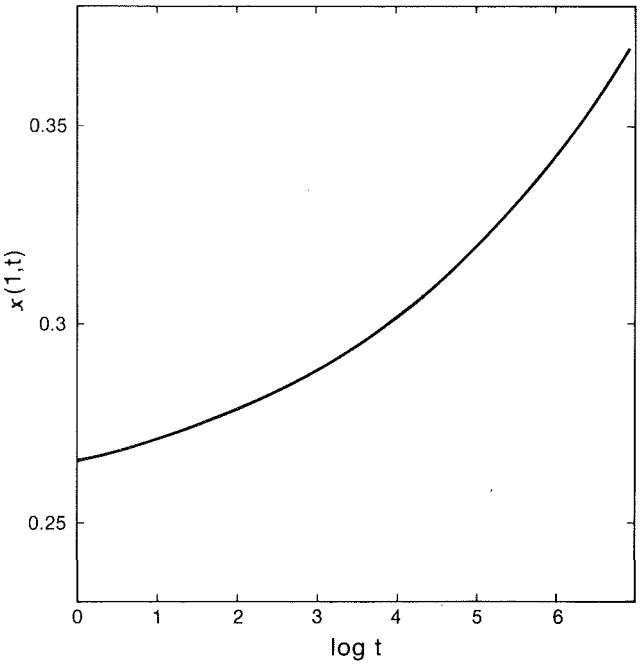

Fig. 12 Variation of the normalized stress intensity factor $\chi(1;t)$ of a craze with time t, for an assumed "power law" creep behavior of the craze material

trivial modifications and employed to relate the time dependence of the solution through the dependence on $D(t)$.

To express $\dot{\chi}(x, t) = (\partial/\partial t)\chi(x, t)$, we note that by differentiation of (27) we have, formally

$$(\lambda D(t) + \mathbf{K})\dot{\chi} = (1 - \lambda\chi)\dot{D} \tag{28}$$

By physical reasoning we have that $0 < \chi, \lambda < 1$, and $\dot{D}(t) > 0$, therefore, the right side of (28) is positive. Although we cannot make a general statement about $\dot{\chi}$ it was found in the subsequent calculation that $\dot{\chi}(1, t) > 0$ showing that the stress intensity factor increases as the craze relaxes – a result that is to be expected intuitively.

Calculations were performed for a "power law" creep compliance of the form $D(t) = 1 + Bt^q$ with $B = 0.1$ and $q = 0.15$. Since for all known creep data $0 < q < 1$ we note that $\dot{D}(0^+) \to \infty$, implying an abrupt initial change in χ at $t = 0^+$. This feature must be viewed as an artifact of the power-law form. Considering, in addition, $\lambda = 0.93344$ and $k = 9.3344$ as in Fig. 6 we obtained the varition of $\chi(1, t)$ with time by solving equation (27). Results are shown in Fig. 12.

Tip-Zone Correction

As shown in Figs. 4 and 5 there exists a highly localized zone of poorly defined structure at the tips of crazes. This zone is analogous to the localized plastic region at the tips of cracks. It was suggested, quite plausibly [11], that in the case of crazes there exists an additional plastic region within the bulk polymeric material, which extends a small distance ahead of the craze formation zone.

Since the length of the tip zone is about two to three orders of magnitude smaller than the length of the craze itself (see Fig. 3), it is possible to analyze its effect on blunting the mathematical singularity at $x = 1$ in a manner similar to Barenblatt's, [29] employing an asymptotic analysis.

Let the unknown stresses in the tip region $-\sigma_\epsilon(X)$ (pressure) act on the segments $a - \alpha < X < a$. Introducing the nondimensional quantities $-\sigma_\epsilon(X)/T = -p_\epsilon(x)$ and $\epsilon = \alpha/a$ we obtain, by analogy with equation (15)

$$\lambda\chi_\epsilon(x) + \frac{1}{\pi}\int_0^1 R(x^2, s^2)k(s)\chi_\epsilon(s)\,ds$$

Downloaded 02 May 2010 to 171.66.16.25. Redistribution subject to ASME license or copyright; see http://www.asme.org/terms/Terms_Use.cfm

$$= -\frac{1}{\pi}\int_{1-\epsilon}^{1} \frac{R/x^2,s^2)}{\sqrt{1-s^2}} p_\epsilon(s)\,ds \tag{29}$$

In (29) $\chi_\epsilon(x) = (1-x^2)^{-1/2} v_\epsilon(x)$, where $v_\epsilon(x)$ is the nondimensional displacement due to $-p_\epsilon(x)$.

Letting $x \to 1^-$ in (29) we obtain, in view of (18)

$$\lambda\chi_\epsilon(1) + \frac{2}{\pi}\int_0^1 k(s)\chi_\epsilon(s)\,ds = -\frac{2}{\pi}\int_{1-\epsilon}^{1} \frac{p_\epsilon(s)}{\sqrt{1-s^2}}\,ds \tag{30}$$

Consider now the asymptotic limit of $\chi_\epsilon(x)$ when $x < 1-\epsilon$ (fixed) while $\epsilon \to 0$, denoted by $\chi_0(x)$. In view of (29) we have

$$\lambda\chi_0(x) + \frac{1}{\pi}\int_0^1 R(x^2, s^2)k(s)\chi_0(s)\,ds$$

$$= -\frac{1}{\pi}\lim_{\epsilon\to 0}\int_{1-\epsilon}^{1} \frac{R(x^2,s^2)}{\sqrt{1-s^2}} p_\epsilon(s)\,ds \tag{31}$$

In the present case we consider x fixed, but the limiting process indicates that $s \to 1^-$ on the right-hand side of (31). Employing $(16)_2$ we now get $\lim_{s\to 1^-}(1-s^2)^{-1/2}R(x^2, s^2) = 0$. Consequently, $\chi_0(x)$ vanishes.

This result is not surprising, since it is well known that for crack problems the Barenblatt correction due to the tip zone effects does not change the displacement field outside that zone. We can therefore replace (30) by

$$\lambda\chi_\epsilon(1) \cong -\frac{2}{\pi}\int_{1-\epsilon}^{1} p_\epsilon(s)\frac{ds}{\sqrt{1-s^2}} = -C_\epsilon \tag{32}$$

The equations for $\chi_c(x) = \chi(x) + \chi_\epsilon(x)$, due to a remote load of normalized magnitude unity and the stress p_ϵ are

$$\chi_c(x) = \chi(x) \quad 0 < x < 1-\epsilon \tag{33}$$

while, in place of (19) we have

$$\lambda\chi_c(1) + \frac{2}{\pi}\int_0^1 k(s)\chi(s)\,ds = 1 - C_\epsilon \tag{34}$$

Obviously, for an "equilibrium craze," the amplitude of $p_\epsilon(x)$ in (30) must correspond to a value of C_ϵ which yields $\chi_c(1) = 0$.

Consider the existence of some critical value of C_ϵ in equation (34), denoted by C_ϵ^{CR}, assumed to be a material constant. Recall that $\lambda = (G\delta/1-\nu)\,(1/aT)$, while $k = K\delta\cdot(1/T)$. Therefore, by (15), $\chi = \chi(x; a, T)$. Consequently, equation (34) with C_ϵ^{CR} substituted for C_ϵ provides a relation between critical craze lengths $a = a^{CR}$ and levels of load T.

If, as a first approximation, we consider $p_\epsilon = \text{const.}$, equation (32) yields $C_\epsilon = \sqrt{2\epsilon}p_\epsilon$. Consequently, to obtain $\chi_c(1) = 0$ in (34) we have,

$$p_\epsilon = (2\epsilon)^{-1/2}\,[1 - (2/\pi)\textstyle\int_0^1 k(s)\chi(s)\,ds].$$

If we employ, for instance, the results shown in Fig. 6 then $C_\epsilon = 0.2614$ which corresponds to $p_\epsilon = 5.845$ for $\epsilon = 0.001$ and to $p_\rho = 4.133$ for $\epsilon = 0.002$. Specific evaluation of p_ϵ must await further experimental data.

It should be remarked that the smoothness of the solution $\chi_c(x)$ on $[-1, 1]$, together with $\chi_c(\pm 1) = 0$, assures a cusp-shaped displacement profile in the tip regions.

Concluding Remarks

In this paper a solution was presented for a single craze in an extended region, where the craze was modeled as a distributed linear spring. The major contribution provided in this work is that it disengaged the analysis of crazes from the confines of fracture analysis, to which it was artificially appended until now.

This paper is only a first step toward a better understanding of the mechanics of crazes. Important features, like craze thickening through drawing, nonlinear craze response, and interactions between adjacent crazes remain to be studied. We intend to investigate those aspects in the near future.

Acknowledgments

This work was performed under Contract N00014-82-K-0562 from the Office of Naval Research (ONR).

We are grateful to Professor E. J. Kramer of Cornell University for an illuminating discussion with one of the authors (Y.W.) and for providing us with most useful information.

References

1 Kambour, R. P., and Kopp, R. W., "Cyclic Stress-Strain Behavior of the Dry Polycarbonate Craze," *J. Polymer Science*, *A*-2, Vol. 7, 1969, pp. 183-200.

2 Lauterwasser, B. D., and Kramer, E. J., "Microscopic Mechanisms of Craze Growth and Fracture," *Phil. Mag.*, *A*, Vol. 39, No. 4, 1979, pp. 469-495.

3 Kramer, E. J., "Crazing," Proc. of the Int. Spring School of Plastic Deformation of Amorphous and Semicrystalline Materials, Froelich, D., ed., Les Houches, France, Apr. 19-29, 1982.

4 Farrar, N. R., and Kramer, E. J., "Microstructure and Mechanics of Crazes in Oriented Polystyrene," *Polymer*, Vol. 22, 1981, pp. 691-698.

5 Brown, H. R., and Kramer, E. J., "Craze Microstructure From Small-Angle X-Ray Scattering (SAXS)," *J. Macromol. Sci-Phys.*, *B*, Vol. 19, 1981, pp. 487-522.

6 Donald, A. M., and Kramer, E. J., "The Mechanism of Craze-Tip Advance in Glassy Polymers," *Phil. Mag.*, *A*, Vol. 43, No. 4, 1981, pp. 857-870.

7 Hull, D., "The Microstructure and Properties of Crazes," in *Deformation and Fracture of High Polymers*, Kausch, Hassell, and Jaffee, eds., Plenum Press, 1973, pp. 171-189.

8 Wellinghoff, S., and Baer, E., "The Mechanism of Crazing in Polystyrene," *J. Macromol. Sci.-Phys.*, B11.(3), 1975, pp. 367-387.

9 Beahan, P., Bevis, M., and Hull, D., "Fracture Processes in Polystyrene," *Proc. Royal Soc.*, London, Series *A*, Vol. 343, 1975, pp. 525-535.

10 Morgan, R. P., and O'Neal, J. E., "The Durability of Epoxies," *Polym.-Plas. Technol. Eng.*, Vol. 10, No. 1, 1978, pp. 49-116.

11 Marshall, G. P., Culver, L. E., and Williams, J. G., "Craze Growth in Polymethylmethacrylate: A Fracture Mechanics Approach," *Proc. Royal Soc.*, London, Series *A*, Vol. 319, 1970, pp. 165-187.

12 Verheuplen-Heymens, N., and Bauwens, J. C., "Effects of Stress and Temperature on Dry Craze Growth Kinetics During Low-Stress Creep of Polycarbonate," *J. Materials Sci.*, Vol. 11, 1976, pp. 1-6.

13 Andrews, E. H., Levy, G. M., and Willis, J., "Environmental Crazing in a Glassy Polymer: The Role of Solvent Absorption," *J. Materials Sci.*, Vol. 8, 1973, pp. 1000-1008.

14 Weidmann, G. W., and Williams, J. G., "Crazing and Creep Behavior of PMMA in Methanol," *Polymer*, Vol. 16, 1975, pp. 921-935.

15 Williams, J. G., and Marshall, G. P., "Thermal and Environmental Effects on Craze Growth and Fracture," in *Deformation and Fracture of High Polymers*, Kausch, Hassell, and Jaffee, eds., Plenum Press, New York, 1973, pp. 557-583.

16 Yaffee, M. B., and Kramer, E. J., "Plasticization Effects on Environmental Craze Microstructure," *J. Materials Sci.*, Vol. 16, 1981, pp. 2130-2136.

17 Williams, J. G., and Marshall, G. P., "Environmental Crack and Craze Growth Phenomena in Polymers," *Proc. Royal Soc.*, London, Series *A*, Vol. 342, 1975, pp. 55-77.

18 Hoare, J., and Hull, D., "Craze Yielding and Stress-Strain Characteristics of Craze in Polystyrene," *Phil. Mag.*, Vol. 26, 1972, pp. 443-455.

19 Andrews, E. H., and Bevan, L., "Mechanics and Mechanism of Environmental Crazing in a Polymeric Glass," *Polymer*, Vol. 13, 1972, pp. 337-346.

20 Passaglia, E., "Relaxation of Stresses in Crazes at Crack Tips and Rate of Craze Extension," *Polymer*, Vol. 23, 1982, pp. 754-760.

21 Warren, W. E., "The Stress and Displacement Fields at the Tip of Crazes in Glassy Polymers," Sandia National Labs, Report under Contract DE-AC04-76DP00789, communicated privately, June 1982.

22 Atkinson, C., "An Iterative Scheme for Solving Problems Relating to Cracks Opening Under a Displacement Dependent Internal Stress," *Int. J. of Fracture Mechanics*, Vol. 6, No. 2, June 1970, pp. 193-197.

23 Gladwell, G. M. L., *Contact Problems in the Classical Theory of Elasticity*, Sijthoff & Noordhoff, 1980.

24 Sneddon, I. H., *The Use of Integral Transforms*, McGraw-Hill, New York, 1972, p 235.

25 Gakhov, F. D., *Boundary Value Problems*, Pergamon Press, 1966, Chapter 8.

Downloaded 02 May 2010 to 171.66.16.25. Redistribution subject to ASME license or copyright; see http://www.asme.org/terms/Terms_Use.cfm

26 Muskhelishvili, N. I., *Singular Integral Equations*, Noordhoff, 1953, Chapter 4.
27 Erdelyi, Magnus, Oberhettinger, and Tricomi, "Tables of Integral Transforms," Bateman Manuscript Project, Vol. 2, McGraw-Hill, New York, 1954, Expression 15.2.23, p. 250.
28 Gradshteyn, I. S., and Ryzhik, I. M., *Tables of Integrals, Series and Products*, Academic Press, New York, 1965, Equation 3.621, Number 3, p. 369.
29 Barenblatt, G. I., "The Mathematical Theory of Equilibrium Cracks in Brittle Fracture," *Advances in Applied Mechanics*, Vol. VII, Academic Press, New York, 1962, pp. 59–129.
30 Atkinson, K. E., *A Survey of Numerical Methods for the Solution of Fredholm Integral Equations of the Second Kind*, SIAM Publication, 1976, pp. 88–95; 106–114.

APPENDIX

The Numerical Scheme

To solve for $\chi(x)$ we identify equation (15) as a Fredholm integral equation of the second kind, with a logarithmic singularity. The solution to (15) is obtained numerically, employing the Nyström method [30]. For this purpose, define $L(x,s) = k(s)\sqrt{(1-s^2)/(1-x^2)}$ and employ (16) to identify the four following integrals

$$I_1 = -\frac{1}{\pi}\int_0^1 L(x,s)\chi(s)\ln|x-s|\,ds$$

$$I_2 = -\frac{1}{\pi}\int_0^1 L(x,s)\chi(s)\ln(x+s)\,ds \qquad (A\text{-}1)$$

$$I_3 = \frac{1}{\pi}\int_0^x L(x,s)\chi(s)\ln(1-s)\,ds$$

$$I_4 = \frac{1}{\pi}\int_0^x L(x,s)\chi(s)\ln(1+s)\,ds$$

The integration of remaining terms on the right side of (16) is straightforward.

The evaluation of $I_1 - I_4$ in (A-1) was accomplished by means of "nodal weights" w_{ij}. We will illustrate the determination of those weights for I_1. The remaining values are obtained analogously.

Following Nyström's method, we divide the interval [0, 1] into n subintervals. Let us consider n equal subintervals $h = 1/n$. Denote $s_i = ih$, $s_j = jh$ $(i, j = 0, 1, 2, \ldots n)$.

We relate s_i to the variable x, and s_j to the integration variable s. Accordingly we have n values of s_i and $n+1$ values of s_j in I_1. For $x = s_n = 1$ the operative expression must be derived from (19), which can be accomplished by means of the trapezoidal rule.

Discretize I_1 as follows

$$I_1 = -\frac{1}{\pi}\sum_{j=1}^{n}\int_{s_{j-1}}^{s_j} L(x,s)\chi(s)\ln|x-s|\,ds \qquad (A\text{-}2)$$

At the nodal points $x=s_i$, $s=s_j$ denote $L(x,s)\chi(s) = L(s_i,s_j)\chi(s_j) = L_{ij}\chi_j$.[4] Over each subinterval $[s_{j-1}, s_j]$ employ the linear interpolation

$$L(x,s)\chi(s) \simeq L_{i,j-1}\chi_{j-1} + \frac{L_{ij}\chi_j - L_{i,j-1}\chi_{j-1}}{s_j - s_{j-1}}(s-s_{j-1})$$

$$= \frac{1}{h}[L_{i,j-1}(s_j-s)\chi_{j-1} + L_{ij}(s-s_{j-1})\chi_j] \qquad (A\text{-}3)$$

Since all L_{ij} are known and χ_j, although unknown, are constants, the evaluation of each subintegral in (A-2) reduces to the evaluation of

$$I^{ij}_{1,1} = \int_{s_{j-1}}^{s_j}(s_j - s)\ln|s_i - s|\,ds \qquad (A\text{-}4)$$

and

$$I^{ij}_{1,2} = \int_{s_{j-1}}^{s_j}(s - s_{j-1})\ln|s_i - s|\,ds \qquad (A\text{-}5)$$

Let $s = s_{j-1} + \mu h = (j-1+\mu)h$, then

$$I^{ij}_{1,1} = h^2\int_0^1(1-\mu)\ln\{h\,|i-j+1-\mu|\}\,d\mu$$

$$= h^2\left[\frac{1}{2}\ln h + \int_0^1(1-\mu)\ln|i-j+1-\mu|\,d\mu\right]$$

Similarly

$$I^{ij}_{1,2} = h^2\left[\frac{1}{2}\ln h + \int_0^1 \mu\ln|i-j+1-\mu|\,d\mu\right]$$

Define

$$\psi_1(p) = \int_0^1 \ln|p-\mu|\,d\mu = p\ln|p| - (p-1)\ln|p-1| - 1 \qquad (A\text{-}6)$$

$$\varphi_1(p) = \int_0^1 \mu\ln|p-\mu|\,d\mu = \frac{1}{2}\left[(1-p^2)\ln|p-1| + p^2\ln|p| - p - \frac{1}{2}\right] \qquad (A\text{-}7)$$

Then

$$I^{ij}_{1,1} = h^2\left[\frac{1}{2}\ln h + \psi_1(i-j+1) - \varphi_1(i-j+1)\right] \qquad (A\text{-}8)$$

$$I^{ij}_{2,1} = h^2\left[\frac{1}{2}\ln h + \varphi_1(i-j+1)\right] \qquad (A\text{-}9)$$

Incorporation of (A-8) and (A-9) in (A-2), together with (A-3) yields

$$I^i_1 = -\frac{1}{\pi}\sum_{j=0}^{n} w^{(1)}_{ij}L_{ij}\chi_j \quad 0 \le i \le n-1 \qquad (A\text{-}10)$$

where

$$w^{(1)}_{ij} = \beta_{ij} + \alpha_{i(j+1)} \quad 1 \le j \le n-1$$
$$w^{(1)}_{i0} = \alpha_{i1} \qquad (A\text{-}11)$$
$$w^{(1)}_{in} = \beta_{in}$$

In (A-11)

$$\alpha_{ij} = \frac{1}{2}h\ln h + h[\psi_1(i-j+1) - \varphi_1(i-j+1)] \qquad (A\text{-}12)$$

$$\beta_{ij} = \frac{1}{2}h\ln h + h\varphi_1(i-j+1) \qquad (A\text{-}13)$$

To evaluate I_2, I_3, and I_4 define

$$\psi_2(p) = \int_0^1 \ln(p+\mu)\,d\mu = (p+1)\ln(p+1) - p\ln p - 1$$

$$\varphi_2(p) = \int_0^1 \mu\ln(p+\mu)\,d\mu = \frac{1}{2}\left[(1-p^2)\ln(p+1) + p^2\ln p + p - \frac{1}{2}\right]$$

[4] No summation is implied over a repeated index.

Downloaded 02 May 2010 to 171.66.16.25. Redistribution subject to ASME license or copyright; see http://www.asme.org/terms/Terms_Use.cfm

$$\psi_3(p)=\int_0^1 ln(p-\mu)\,d\mu=(1-p)\,ln(p-1)+p\,lnp-1$$

$$\varphi_3(p)=\int_0^1 \mu ln(p-\mu)\,d\mu=\frac{1}{2}\left[(1-p)^2 ln(p-1)+p^2 lnp-p-\frac{1}{2}\right]$$

We then obtain

$$I_2^i=-\frac{1}{\pi}\sum_{j=0}^{n} w_{ij}^{(2)}L_{ij}\chi_j \quad 0\le i\le n-1 \tag{A-14}$$

where

$$\begin{aligned} w_{ij}^{(2)}&=\gamma_{ij}+\eta_{i(j+1)}, \quad 1\le j\le n-1\\ w_{i0}^{(2)}&=\eta_{i1}\\ w_{in}^{(2)}&=\gamma_{in}\end{aligned} \tag{A-15}$$

In (A-15)

$$\eta_{ij}=\frac{1}{2}h\ ln\ h+h[\psi_2(i+j-1)-\varphi_2(i+j-1)]$$

$$\gamma_{ij}=\frac{1}{2}h\ ln\ h+h\varphi_2(i+j-1) \tag{A-16}$$

Also, combining I_3^i and I_4^i we obtain

$$I_3^i+I_4^i=\frac{1}{\pi}\sum_{j=0}^{n}\hat{w}_{ij}L_{ij}\chi_j \tag{A-17}$$

where

$$\begin{aligned} \hat{w}_{00}&=0\\ \hat{w}_{i0}&=(\rho_1+\eta_{n1})L_{i0} \quad 1\le j\le n-1\\ \hat{w}_{ii}&=(\zeta_i+\gamma_{ni})L_{ii} \quad 1\le i\le n-1\\ \hat{w}_{ij}&=(\zeta_j+\rho_{j+1}+\gamma_{nj}+\eta_{n,j+1})L_{ij} \quad 1\le j\le i-1,\ 2\le i\le n-1\end{aligned} \tag{A-18}$$

In (A-18)

$$\begin{aligned} \zeta_j&=\frac{1}{2}h\ ln\ h+h\varphi_3(n-j+1)\\ \rho_j&=\frac{1}{2}h\ ln\ h+h[\psi_3(n-j+1)-\varphi_3(n-j+1)]\end{aligned} \tag{A-19}$$

The integration of the remaining terms on the right side of (16) is achieved by a straightforward application of the trapezoidal rule to yield

$$\frac{1}{\pi}\sum_{j=0}^{n} w_{ij}^{R}L_{ij}\chi_j \tag{A-20}$$

For the sake of brevity we omit the expressions for w_{ij}^R. Denote

$$A_{ij}=\frac{1}{\pi}\left(-w_{ij}^{(1)}-w_{ij}^{(2)}-\hat{w}_{ij}+w_{ij}^{R}\right)L_{ij} \quad 0\le j\le n,\ 0\le i\le n-1 \tag{A-21}$$

and

$$A_{nj}=\begin{cases}\dfrac{h}{\pi}k_0 & j=0\\ 2\dfrac{h}{\pi}k_j & 1\le j\le n-1\\ \dfrac{h}{\pi}k_n & j=n\end{cases} \tag{A-22}$$

Then (15) can be approximated by the linear algebraic system

$$\sum_{j=0}^{n}(\lambda\delta_{ij}+A_{ij})\chi_j=1 \quad (i,j=0,1,\ldots,n) \tag{A-23}$$

As noted earlier, the nondimensional displacements and stresses within the craze are given by $v_i=(1-s_i^2)^{1/2}\chi_i$ and $\sigma_i=k_i v_i$, respectively. The nondimensional stress intensity factor is given by χ_n.

Downloaded 02 May 2010 to 171.66.16.25. Redistribution subject to ASME license or copyright; see http://www.asme.org/terms/Terms_Use.cfm

Constitutive Restrictions for Idealized Elastic-Viscoplastic Materials

P. M. Naghdi
Department of Mechanical Engineering,
University of California,
Berkeley, Calif. 94720
Honorary Mem. ASME

This paper is concerned mainly with restrictions on constitutive equations of idealized elastic-viscoplastic materials in the presence of finite deformation. The development is confined to the purely mechanical theory utilizing a constitutive model that includes unloading and allows for suitable definition of plastic strain. With the use of a physically plausible assumption concerning non-negative work in a closed cycle of deformation, two local inequalities are derived which place restrictions on the nonlinear constitutive response functions of the idealized material. Further implications of these inequalities relating the various response functions are dicussed. In the absence of rate effects in the stress response, the results correspond to those appropriate for rate-independent plasticity.

1 Introduction

Within the framework of a purely mechanical *rate-dependent* theory of plasticity, the present paper is concerned with restrictions on constitutive equations of finitely deformed, *idealized*, elastic-viscoplastic materials. The idealization is motivated by a constitutive *model* capable of describing material response during both loading and unloading and accommodates a suitable definition of plastic strain. In particular, the stress constitutive equation is characterized by a nonlinear rate-dependent response (see equations (17) and (18)) while the remaining constitutive equations of the theory, such as the rate of plastic strain and rate of work hardening, are of the same form as those of the rate-independent plasticity in the presence of finite deformation. The latter results (summarized in Section 2) are based on the work of Green and Naghdi [1, 2], but formulated here in a strain space setting as proposed by Naghdi and Trapp [3]. A work inequality was derived previously by Naghdi and Trapp [4] from a physically plausible work assumption.[1] An examination of the derivation of the work inequality in [4] reveals that it is also valid for rate-dependent materials even though originally it was used for rate-independent elastic-plastic materials. With the use of this work inequality, two local inequalities are derived which place restrictions on the nonlinear constitutive response functions of the idealized material. One of these is a restriction on the rate of plastic strain and has the same form as that appropriate for rate-independent plasticity, but the other is a restriction on the rate-dependent part of the stress-response.

Background information on elastic-viscoplastic and more general rate-dependent materials can be found in the articles by Perzyna [8], by Campbell [9], and by Klepaczko and Duffy [10], where a large number of both theoretical and experimental papers are cited. One particular category which has attracted considerable attention from time to time is one in which the theory attempts to describe material behavior during loading with the initial response prior to yield regarded as elastic. In such rate-dependent theories an important feature, which seems to have been dealt with from various points of view (see, e.g., [11–15]), is the prediction of an increase in the linear range of the stress-strain response with increasing strain which, in turn, leads to the prediction of higher initial yield stress at higher strain rates. The interpretations of experimental results in this area seem inconclusive and do not appear to include any discussion about the nature of unloading or a suitable definition of plastic strain. In order to provide motivation for a constitutive model of the idealized rate-dependent material, consider a standard one-dimensional tension or compression test in which the strain may be moderately large or even large. Let E and S stand, respectively, for the component E_{11} of the Lagrangian strain tensor and the component S_{11} of the symmetric Piola-Kirchhoff stress tensor. Figure 1 shows the familiar plot of stress versus strain of an elastic-viscoplastic material[2] at various strain rates such as $\dot{E}_1, \dot{E}_2, \ldots$, where a superposed dot designates differentiation with respect to time. In the linear range OA the material is elastic and the point A representing the elastic limit is assumed to be coincident with

[1] The work inequality in [4] is derived in the context of finite deformation and in a strain space setting. Its relationship to the postulates of Drucker [5, 6] and Il'iushin [7] is indicated in [4, Sections 1 and 3] and need not be repeated here.

Contributed by the Applied Mechanics Division for publication in the JOURNAL OF APPLIED MECHANICS.

Discussion on this paper should be addressed to the Editorial Department, ASME, United Engineering Center, 345 East 47th Street, New York, N.Y. 10017, and will be accepted until two months after final publication of the paper itself in the JOURNAL OF APPLIED MECHANICS. Manuscript received by ASME Applied Mechanics Division, December, 1982; final revision, July, 1983.

[2] Although the stress-strain response shown in Fig. 1 is plotted in the S-E plane, the corresponding parts of engineering stress versus engineering strain or true stress versus true strain exhibit similar features.

Copyright © 1984 by ASME
Downloaded 02 May 2010 to 171.66.16.25. Redistribution subject to ASME license or copyright; see http://www.asme.org/terms/Terms_Use.cfm

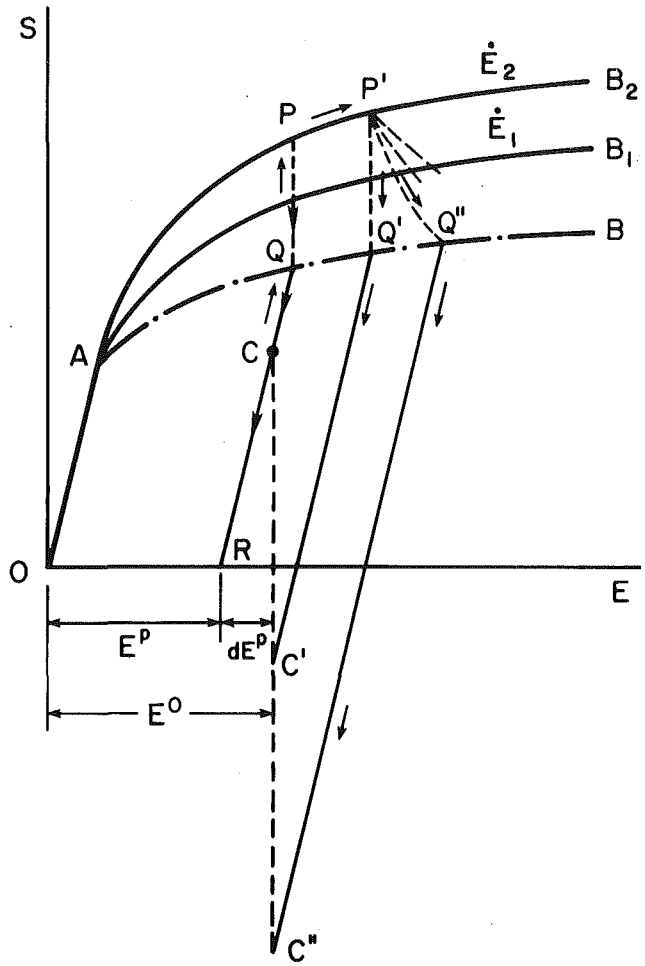

Fig. 1 Idealized mechanical response of an elastic-viscoplastic material at various strain rates. The curves OAB_1 and OAB_2 represent the material response at higher rates of strain associated with rate-dependent model, while the curve OAB represents the so-called "static response" of the idealized rate-independent model and may be viewed as representing the material response when the strain rate approaches zero. The dashed line curves to the right of $P'Q'$, including $P'Q''$, represent unloading with various degrees of deceleration (the most rapid path being $P'Q'$) from a point P' on curve OAB_2. The instantaneous unloading from P and P' take place, respectively, along the rapid paths PQ and $P'Q'$. Also shown are elastic unloading from a point Q and the identification of plastic strain by OR along the E-axis. The values of the total strain and the plastic strain are the same for every point along the dashed curves PQ and $P'Q'$.

the initial yield. Since the deformation in the range OA is reversible, unloading takes place along OA. For loading above A the deformation is irreversible and the rate-independent material strain hardens along AQB. Unloading from a point such as Q is assumed to take place elastically along QR, which is generally taken to be parallel to OA. There are other features associated with the rate-independent response such as the lower compressive yield limit, but these need not be discussed here.

It is reasonable to assume that for sufficiently low strain rate, i.e., as the strain rate $\dot{E}$ tends to zero, the rate-dependent response of the material approaches that of the rate-independent model represented by OA in Fig. 1. At higher rates of strain, the rate-dependent response of the material would be represented by OAB_1 when the strain rate is $\dot{E}_1$ and by OAB_2 when the strain rate is $\dot{E}_2$ $(>\dot{E}_1)$ and so on. Again, with reference to Fig. 1, consider a point P on the response curve $OAPB_2$ and through P draw a dashed line parallel to the S-axis intersecting the curve OAB at Q. Let E and E^p denote, respectively, the total strain and the plastic strain at Q on the rate-independent response curve OAB. Then, as indicated in Fig. 1, the segment OR represents the plastic strain at Q. In general, deceleration from a point such as P' on the curve OAB_2 would proceed along a dashed curve such as $P'Q'$ to the right of $P'Q'$ and such processes would be represented by dashed curves that end on the curve OAB representing the rate-independent response. As the process of deceleration takes place at a faster and faster rate, the dashed line $P'Q''$ is approached in the limits. The vertical dashed curve PQ or $P'Q'$ may be referred to as a *rapid path* using a terminology introduced in [14]. Clearly, every point along a line such as PQ experiences the same total strain E and the same amount of plastic strain E^p and this notion of rapid path enables one to define plastic strain for rate-dependent materials. Again, with reference to Fig. 1, reloading from a point along RQ at a given rate of strain (say for example at the rate $\dot{E}_2$) would proceed along RQ until one reaches Q and then, consistent with the idealization indicated, there has to be an allowance for jump in the value of the stress in order to reach the point P. Thereafter, as indicated in Fig. 1, further plastic deformation at the rate $\dot{E}_2$ will continue along PB_2.

It is worth summarizing here the main features of the idealized constitutive model as follows: (1) The constitutive model is capable of describing the rate-dependent material response during both loading and unloading; (2) it allows for a suitable definition of plastic strain; (3) for sufficiently low strain rates (i.e., as the strain rate tends to zero), the rate-dependent response of the material approaches that of the response of the rate-independent model; (4) the stress constitutive equation during loading is composed of two parts, one part of which has the same form as that for the rate-independent response and the second part is linear in the rate of plastic strain and hence depends explicitly on the rate of strain; (5) the second part of the stress response during loading referred to in (4) represents a jump in stress during loading; and (6) the constitutive model accommodates also a jump in stress during loading at initiation of yield[3] as indicated in Fig. 2, but through a simple assumption that the jump in stress diminishes with decreasing plastic strain the model would then represent a material behavior corresponding to that shown in Fig. 1.

It should be evident from the discussion of the preceding paragraph that the jump in stress for the idealized model is intimately related to the definition of plastic strain and the notion of unloading. Moreover, it should be noted that the proposed idealized model has a *genuine* rate-independent elastic range (this is different from a viscoelastic range which is rate-dependent). Hence, the interior of the yield surface in strain space cannot depend on strain rate although the interior of the yield surface in stress space can depend on rates by virtue of the stress constitutive equations of the theory. Further, it may be emphasized that the jump in stress admitted in the idealized model is a *temporal* jump only and will always have continuous spatial variation (with respect to material position), even though it admits temporal discontinuity. In this connection, it may be recalled also that there are no time derivatives of the stress in the differential equations of motion (see equation (6)) so that the spatially continuous jump in stress would not cause any difficulties in numerical computations.

We close this section with some comments about the strain cycle used in the calculations of Section 3 and the constitutive restrictions obtained in Section 4. The spatially homogeneous strain cycle (21) used in obtaining the estimate for the integral on the left-hand side of (20) is not smooth and corresponds to $CQPP'Q'C'$ in Fig. 1. The use of (21) simplifies the calculations, but the final conclusions in Section 3 would be

[3] For additional related remarks, see also [15].

Downloaded 02 May 2010 to 171.66.16.25. Redistribution subject to ASME license or copyright; see http://www.asme.org/terms/Terms_Use.cfm

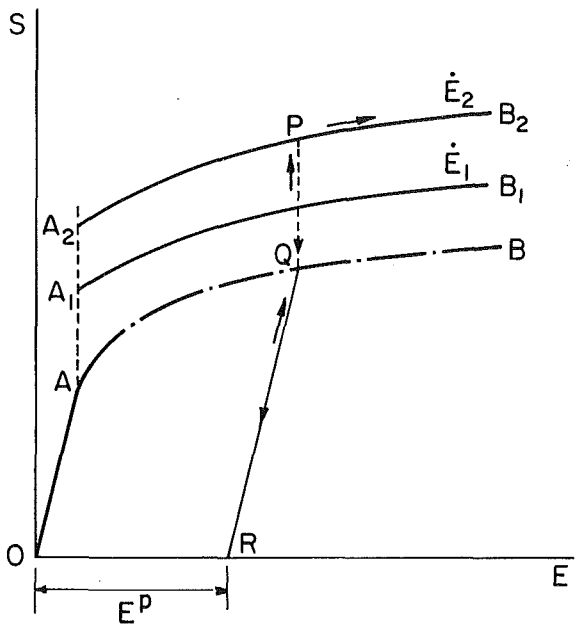

Fig. 2 An idealized one-dimensional response with features similar to those of Fig. 1 but allowing also for a jump in stress at initial yield

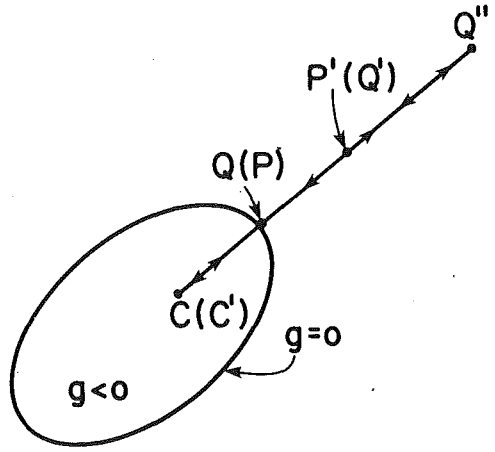

Fig. 3 The loading surface $g = 0$ in strain space and the paths of strain cycle represented by the sequence (21). From C to P' the strain rate has a constant value M represented by the slope of the line segment CQP'. From P' to Q'' again the strain rate has a fixed direction parallel to M but with decreasing magnitude until it attains the zero value at Q'' (see also Fig. 1). In the reverse direction from Q'' to a point along $Q''C$ (corresponding to $Q''C''$ in Fig. 1) the strain rate is parallel to $-$M but with increasing magnitude from zero until the strain rate reaches the constant value $-$M at a point where the strain has the same value as that at Q'. Thereafter, the unloading continues at the constant strain rate $-$M until the strain returns to its value at C.

the same if one employs instead a more elaborate strain cycle that would allow for a period of constant deceleration along a path such as $P'Q''$ in Fig. 1 and then allow $CPP'Q''C''$ to approach in the limit $CQPP'Q'C'$. The conclusions reached in Section 3 lead to two local inequalities whose implications are further discussed in Section 4. One of these [see $(44)_1$] places restriction on the plastic strain rate and has the same form as that appropriate for rate-independent plasticity. The other inequality [see $(44)_2$] leads to a restriction on the nonlinear rate-dependent part of the stress response and enables us to replace the constitutive equation (17*b*) by either of the expressions $(50)_{1,2}$.

2 General Background and Preliminaries

Consider a body with material points X and identify the material point X with its position $\mathbf{X}$ in a fixed reference configuration in a Euclidean three-space. Let $\mathbf{x}$ denote the place occupied by X in the present configuration at time t. Then, a motion of the body is defined by a vector function χ which assigns position $\mathbf{x}$ to each $\mathbf{X}$ at each instant of time, i.e., $\mathbf{x} = \chi(\mathbf{X},t)$. We assume that the vector function χ is single-valued and continuously differentiable with respect to its arguments as many times as may be required in the subsequent analysis, except possibly at singular points, curves, and surfaces. The deformation gradient $\mathbf{F}$ at $\mathbf{X}$ relative to the reference configuration is given by

$$\mathbf{F} = \mathbf{F}(\mathbf{X},t) = \frac{\partial \chi(\mathbf{X},t)}{\partial \mathbf{X}}, \quad \det \mathbf{F} \neq \mathbf{0}. \tag{1}$$

We define a symmetric strain tensor $\mathbf{E}$ by

$$\mathbf{E} = \tfrac{1}{2}(\mathbf{F}^T\mathbf{F} - \mathbf{I}), \tag{2}$$

where $\mathbf{F}^T$ stands for the transpose of $\mathbf{F}$ and $\mathbf{I}$ is the unit tensor. Also, the velocity $\mathbf{v}$ and the rate of strain are defined by

$$\mathbf{v} = \dot{\mathbf{x}}, \quad \dot{\mathbf{E}} = \mathbf{F}^T\,\mathbf{D}\,\mathbf{F}, \tag{3}$$

where

$$\mathbf{D} = \tfrac{1}{2}(\mathbf{L} + \mathbf{L}^T), \quad \mathbf{L} = \dot{\mathbf{F}}\,\mathbf{F}^{-1}, \tag{4}$$

a superposed dot denotes the material time derivative with respect to the present time t holding $\mathbf{X}$ fixed and $\mathbf{F}^{-1}$ is the inverse of $\mathbf{F}$.

Let $\mathfrak{R}$ be the region of space occupied by the body in the present configuration at time t, and designate the boundary of $\mathfrak{R}$ by a closed surface $\partial\mathfrak{R}$. Similarly, let $\mathfrak{R}_0$ be the corresponding region of space occupied by the body in the reference configuration, and designate the boundary of $\mathfrak{R}_0$ by a closed surface $\partial\mathfrak{R}_0$. Let $\mathbf{N}$ be the outward unit normal to $\partial\mathfrak{R}_0$ and let ${}_R\mathbf{t}$ be the surface force vector that acts across $\partial\mathfrak{R}$ but is measured per unit area of the surface $\partial\mathfrak{R}_0$ in the reference configuration. We denote the nonsymmetric Piola-Kirchhoff stress tensor by $\mathbf{P}$, the symmetric Piola-Kirchhoff stress tensor by $\mathbf{S}$, the body force per unit mass by $\mathbf{b}$, and the mass density in the reference configuration by ρ_0, and recall the relations

$${}_R\mathbf{t} = \mathbf{P}\,\mathbf{N}, \quad \mathbf{P} = \mathbf{F}\,\mathbf{S}, \quad \mathbf{S} = \mathbf{S}^T, \tag{5}$$

and the differential equations of motion in the form

$$\mathrm{Div}\,\mathbf{P} + \rho_0\mathbf{b} = \rho_0\dot{\mathbf{v}}, \tag{6}$$

where Div stands for the divergence operator with respect to the place $\mathbf{X}$ keeping t fixed.

Rate-Independent Theory. By way of background and for later reference, we now summarize the main results governing the purely mechanical, rate-independent theory of elastic-plastic continua contained in the work of Green and Naghdi [1, 2] and Naghdi and Trapp [3]. Thus, in addition to the strain tensor $\mathbf{E}$ defined by (2), at each point of the continuum we assume the existence of a plastic strain specified by a second-order tensor $\mathbf{E}^p$ and a measure of work-hardening specified by the scalar function κ, and introduce the stress constitutive assumption

$$\mathbf{S} = \hat{\mathbf{S}}(\mathfrak{U}), \quad \mathfrak{U} = (\mathbf{E},\mathbf{E}^p,\kappa). \tag{7}$$

We assume that, for fixed values of $\mathbf{E}^p$ and κ, the expression $(7)_1$ is invertible in the form

$$\mathbf{E} = \hat{\mathbf{E}}(\mathfrak{V}), \quad \mathfrak{V} = (\mathbf{S},\mathbf{E}^p,\kappa). \tag{8}$$

We use a strain-space formulation of plasticity and, as in the paper of Casey and Naghdi [16], also regard the loading criteria of the strain-space formulation as primary. Thus, we admit the existence of a continuously differentiable scalar-valued yield (or loading) function $g(\mathfrak{U})$ such that

$$g(\mathfrak{U}) = 0 \tag{9}$$

represents a closed orientable hypersurface $\partial\mathcal{E}$ of dimension five enclosed in a region $\mathcal{E}$ of strain space. The function g is

Downloaded 02 May 2010 to 171.66.16.25. Redistribution subject to ASME license or copyright; see http://www.asme.org/terms/Terms_Use.cfm

chosen so that $g(\mathfrak{U}) < 0$ for all points in the interior of the region $\mathcal{E}$.

Corresponding to a motion χ, with each particle of the body we associate a smooth oriented curve C_e in strain space. The curve C_e is called a strain trajectory. Along the strain trajectory C_e, the time rates of $\mathbf{E}^p$ and κ are assumed to have the forms [3]:

$$\dot{\mathbf{E}}^p = \begin{cases} 0 \quad \text{if} \quad g<0, & (a) \\ 0 \quad \text{if} \quad g=0, \quad \hat{g}<0, & (b) \\ 0 \quad \text{if} \quad g=0, \quad \hat{g}=0, & (c) \\ \mathfrak{M}\,\dot{\mathbf{E}} = \lambda \hat{g} \boldsymbol{\rho} \quad \text{if} \quad g=0, \quad \hat{g}>0, & (d) \end{cases} \tag{10}$$

and

$$\dot{\kappa} = \underset{\sim}{\mathcal{C}} \cdot \dot{\mathbf{E}}^p, \tag{11}$$

where $\underset{\sim}{\mathcal{C}}$ and $\mathfrak{M}$ are, respectively, a symmetric second-order and a fourth-order tensor function of the variables $(7)_2$,

$$\hat{g} = \frac{\partial g}{\partial \mathbf{E}} \cdot \dot{\mathbf{E}}, \tag{12}$$

$$\mathfrak{M} = \lambda \boldsymbol{\rho} \otimes \frac{\partial g}{\partial \mathbf{E}}, \tag{13}$$

and where λ and $\boldsymbol{\rho}$ are, respectively, a scalar valued and a symmetric second-order tensor-valued function of the variables $\mathfrak{U}$ and the symbol $\otimes$ denotes tensor product. The conditions involving g and $\hat{g}$ in (10) are the loading criteria of the strain-space formulation. Using conventional terminology, these four conditions in the order listed correspond to (*a*) an elastic state (or point in strain space for which $g < 0$); (*b*) unloading from an elastic-plastic state, i.e., a point in strain space for which $g = 0$; (*c*) neutral loading from an elastic-plastic state; and (*d*) loading from an elastic-plastic state. We assume that the coefficient of $\hat{g}$ in (10*d*), after inserting (13), is nonzero on the yield surface; and, without loss in generality, we set $\boldsymbol{\rho} \neq 0$, $\lambda > 0$. The stipulation that during loading the strain trajectory remains on the yield surface $\partial\mathcal{E}$ so that $\dot{g} = 0$ (with $g = 0$, $\hat{g} > 0$) yields the so-called "consistency" condition given by

$$1 + \lambda \boldsymbol{\rho} \cdot \left(\frac{\partial g}{\partial \mathbf{E}^p} + \frac{\partial g}{\partial \kappa} \underset{\sim}{\mathcal{C}} \right) = 0, \tag{14}$$

where (10*d*), (13), and (11) have been used.

For a given loading function $g(\mathfrak{U})$, with the help of $(8)_1$, we can obtain a corresponding function $f(\mathfrak{V})$ by means of the formula

$$g(\mathfrak{U}) = f(\mathbf{E}(\mathfrak{V}), \mathbf{E}^p, \kappa) = f(\mathfrak{V}). \tag{15}$$

Because of the smoothness of $(8)_1$, for fixed values of $\mathbf{E}^p$ and κ, the equation

$$f(\mathfrak{V}) = 0 \tag{16}$$

represents a hypersurface $\partial\mathcal{S}$ of dimension five in stress space having the same geometrical properties as the hypersurface $\partial\mathcal{E}$ in strain space. The region enclosed by $\partial\mathcal{S}$ is denoted by $\mathcal{S}$. It follows from (15) that a point in strain space belongs to the region $\mathcal{E}$ (i.e., $g(\mathfrak{U}) < 0$) if and only if the corresponding point in stress space satisfies $f(\mathfrak{V}) < 0$ and hence belongs to $\mathcal{S}$. With the use of constitutive equation $(8)_1$, loading conditions for stress space can be derived from loading criteria of strain space in (10) as discussed by Casey and Naghdi [16]. We do not record these conditions as they are not needed in the development that follows.

Rate-Dependent Theory. Motivation for *idealized* one-dimensional response of a rate-dependent material representing an idealized elastic-viscoplastic model was provided in Section 1. Keeping this background in mind, we now introduce a constitutive assumption appropriate for the stress response of idealized elastic-viscoplastic materials in the form

$$\mathbf{S} = \begin{cases} {}_1\mathbf{S} & \text{during unloading and neutral loading when } g=0,\ \hat{g}\leq 0, \quad (a) \\ {}_1\mathbf{S} + \underset{\sim}{\mathcal{S}}\,\dot{\mathbf{E}}^p & \text{during loading when } g=0,\ \hat{g}>0, \quad (b) \end{cases} \tag{17}$$

where the second-order tensor ${}_1\mathbf{S}$ and the fourth-order tensor $\underset{\sim}{\mathcal{S}}$ are assumed to depend on the variables $\mathfrak{U}$, i.e.,

$${}_1\mathbf{S} = {}_1\mathbf{S}(\mathfrak{U}), \quad \underset{\sim}{\mathcal{S}} = \underset{\sim}{\mathcal{S}}(\mathfrak{U}), \tag{18}$$

and satisfy obvious symmetries. The stress response characterized by (17) and (18) is linear in the strain rate $\dot{\mathbf{E}}$ through the constitutive equation (10*d*) during loading. During unloading and neutral loading, the stress response has the same form as that of the rate-independent theory of plasticity discussed earlier in this section. Also, the second part of the stress response (17*b*) during loading, namely $\underset{\sim}{\mathcal{S}}\,\dot{\mathbf{E}}^p$, represents the jump in $\mathbf{S}$ from a point such as Q in Fig. 1 and will assume different values depending on the rate of strain with which loading is progressed.

The constitutive equation $(17)_2$ does, of course, accommodate during loading a jump in stress at initial yield corresponding to point A as indicated schematically in Fig. 2. However, it is not necessary to ascribe to such generality and it is sufficient to focus attention on a material behavior for which the jump in stress diminishes to the value zero with decreasing plastic strain as depicted in Fig. 1.

3 Non-Negative External Work in a Cycle of Homogeneous Deformation

Although the work assumption introduced by Naghdi and Trapp [4] was originally used to derive constitutive restrictions for rate-independent materials only, the work assumption itself may be invoked for any material and will be utilized in this section to obtain restrictions on constitutive equations for plastic strain rate and the stress response (17). Consider a closed cycle of spatially homogeneous motion in the closed time interval[4] $[t_1, t_2]$, $(t_1 < t_2)$. We designate such a smooth spatially homogeneous closed cycle of deformation by $\mathcal{C}(t_1, t_2)$ and recall the following work assumption [4]: *The external work done on the body by surface tractions and by body forces in any smooth spatially homogeneous closed cycle is nonnegative*, i.e.,

$$\int_{t_2}^{t_1} \int_{\partial\mathcal{R}_0} {}_R\mathbf{t} \cdot \mathbf{v}\, dA + \int \rho_0 \mathbf{b} \cdot \mathbf{v}\, dV\, d \geq 0, \tag{19}$$

for all cycles $\mathcal{C}(t_1, t_2)$. In (19), dA and dV denote the elements of area and volume in the reference configuration, and all other symbols were introduced earlier in Section 2. Also, it should be noted that given any smooth strain trajectory C_e, a smooth homogeneous motion can always be found such that at every particle of the body the strain in the homogeneous motion equals that on the strain trajectory. A motion of this kind can be maintained by a suitable choice of the body force field in the balance of linear momentum (6). As shown in [4,

[4] Recall that a homogeneous motion is one whose deformation gradient is independent of the material coordinates so that, in a spatially homogeneous motion, the strain tensor $\mathbf{E}$ is a function of time only. For a closed spatially homogeneous cycle in the closed time interval $[t_1, t_2]$, the position vector $\mathbf{x}$ and the strain $\mathbf{E}$ assume the same values at times t_1 and t_2.

Downloaded 02 May 2010 to 171.66.16.25. Redistribution subject to ASME license or copyright; see http://www.asme.org/terms/Terms_Use.cfm

Section 3], the work assumption (19) implies that for any homogeneous body undergoing a smooth homogeneous cycle of deformation $\mathcal{C}(t_1, t_2)$

$$\int_{t_1}^{t_2} \mathbf{S}\cdot\dot{\mathbf{E}}\, dt \geq 0 \tag{20}$$

at every particle of the body. As can be seen from the details of the derivation in [4], the work inequality (20) is valid for both rate-independent and rate-dependent materials.

To obtain the desired restrictions on plastic strain rate given by (10*d*) and (13) and on the stress response (17*b*), we consider now the following special spatially homogeneous strain cycle[5]:

$$\mathbf{E}(t) = \begin{cases} \mathbf{E}^0 = \mathbf{E}^y - \beta\mathbf{M}, & t \leq 1-\beta, \quad (a) \\ \mathbf{E}^y + \mathbf{M}(t-1), & 1-\beta \leq t < 1, \quad (b) \\ \mathbf{E}^y + \mathbf{M}(t-1), & 1 \leq t < 1+\dfrac{1}{n}, \quad (c) \\ \mathbf{E}^y - \mathbf{M}\left(t-1-\dfrac{2}{n}\right), & 1+\dfrac{1}{n} \leq t < 1+\dfrac{2}{n}, \quad (d) \\ \mathbf{E}^y - \mathbf{M}\left(t-1-\dfrac{2}{n}\right), & 1+\dfrac{2}{n} \leq t < 1+\dfrac{2}{n}+\beta, \quad (e) \\ \mathbf{E}^0, & 1+\dfrac{2}{n}+\beta \leq t. \quad (f) \end{cases} \tag{21}$$

In (19), $\mathbf{E}^0$ is an existing state of strain inside the loading surface in the six-dimensional strain space such that $g(\mathbf{E}^0, \mathbf{E}^p, \kappa) < 0$ for values of $t < 1-\beta$, E^y designates the values of the strain tensor on the loading surface satisfying the equation $g(\mathbf{E}^y, \mathbf{E}^p, \kappa) = 0$ at time $t = 1$, the parameter β represents the time duration that it takes for the strain $\mathbf{E}$ to attain the value $\mathbf{E}^y$ from $\mathbf{E}^0$, $\mathbf{M}$ $(=\dot{\mathbf{E}})$ is a constant (second-order) strain rate tensor such that $\mathbf{E}^y + a\mathbf{M}$ is outside the loading surface for all $0 < a \leq 1$, with

$$\frac{\partial g}{\partial \mathbf{E}}\cdot\mathbf{M} > 0 \quad \text{at} \quad \mathbf{E} = \mathbf{E}^y. \tag{22}$$

In general, the strain rate $\dot{\mathbf{E}}$ which is directed along the tangent to the path may take any desired value; but, in the strain cycle (21), we have assumed the constant values

$$\dot{\mathbf{E}} = \begin{cases} \mathbf{M}, \ 1-\beta \leq t < 1+\dfrac{1}{n}, & (b, c) \\ -\mathbf{M}, \ 1+\dfrac{1}{n} \leq t < 1+\dfrac{2}{n}+\beta, & (d, e) \end{cases} \tag{23}$$

so that the path is a straight line as indicated in Fig. 3. At time $t = 1-\beta$, the strain begins to increase from $\mathbf{E}^0$ at a constant strain rate $\mathbf{M}$ until it reaches the value $\mathbf{E}^y$ at time $t = 1$ and β represents the time duration that it takes for the strain to reach $\mathbf{E}^y$ from $\mathbf{E}^0$. During the time interval specified in (21*b*) the loading takes place elastically at a constant strain rate $\mathbf{M}$ noted also in $(23)_1$ until it reaches a state of strain $\mathbf{E}^y$ on the loading surface (corresponding to point Q in Fig. 1). Moreover, depending on the magnitude of the strain rate, at the end of the interval in (21*b*) the constitutive model admits an instantaneous jump in stress (corresponding, for example, to the jump in stress from Q to P in Fig. 1). During the next interval specified in (21*c*) with $n \geq 1$, the loading continues into the viscoplastic range at the same constant rate of strain; and, at the end of this interval, the strain has a value $\mathbf{E}^y + 1/n\,\mathbf{M}$ (corresponding to a point such as P' in Fig. 1). Thereafter, unloading takes place during the interval (21*d*,*e*) with a reverse strain rate $-\mathbf{M}$ until the strain returns to $\mathbf{E}^0$ (corresponding to $P'Q'C'$ in Fig. 1).

The nature of the homogeneous strain cycle discussed in the foregoing requires further elaboration. The cycle (21) is not smooth. In fact, at the end of the interval in (21*c*), the strain rate changes instantaneously from $\mathbf{M}$ to zero corresponding to a "rapid path" depicted by the dashed line $P'Q'$ in Fig. 1. It is possible to introduce a suitable "rounding" of the corners so that the strain rate is continuous during the entire cycle. For example, a period of constant deceleration can be introduced following the interval in (21*c*) in such a manner that the strain rate decreases from $\mathbf{M}$ to zero (corresponding to dashed line paths such as $P'Q''$ indicated in Fig. 1) and then reaches the value $-\mathbf{M}$ in the early portion of $Q''C''$. If the time interval of such constant deceleration is taken to be shorter and shorter, then in the limit this deceleration process approaches the rapid path (corresponding to $P'Q'$ in Fig. 1). Since the basic argument and the final results will not change, such additional consideration is not needed. It should also be noted that while the time derivatives of the strain $\mathbf{E}$ are not defined at $t = 1-\beta$, $1 + 1/n$, $1 + 2/n + \beta$, the one-sided derivatives at these values, namely the right and left-sided derivatives, do exist.

We now proceed to obtain a reduction of the work inequality (20). Thus, in the context of the strain cycle (21) and with the use of the stress response (17), we first observe that (20) can be written as

$$\int_{1-\beta}^{1+\frac{2}{n}+\beta} {}_1\mathbf{S}\cdot\dot{\mathbf{E}}\, dt + \int_{1-\beta}^{1+\frac{2}{n}+\beta} \dot{\mathbf{E}}\cdot\underset{\sim}{\mathfrak{S}}\,\dot{\mathbf{E}}^p\, dt \geq 0. \tag{24}$$

Since $\dot{\mathbf{E}}^p$ is nonzero only during loading, i.e., in the plastic region, and since plastic strain rate occurs only during the time interval indicated in (21*c*), the limits of integration of the second integral in (24) can be replaced by 1 and $1 + 1/n$, respectively. Further, by writing $\dot{\mathbf{E}}$ as $\dot{(\mathbf{E}-\mathbf{E}^0)}$ and after integrating the first integral in (24) by parts, we obtain the inequality

$$-\int_{1-\beta}^{1+\frac{2}{n}+\beta} (\mathbf{E}-\mathbf{E}^0)_1\dot{\mathbf{S}}\, dt + \int_1^{1+\frac{1}{n}} \dot{\mathbf{E}}\cdot\underset{\sim}{\mathfrak{S}}\,\dot{\mathbf{E}}^p\, dt \geq 0. \tag{25}$$

Our objective in the remainder of this section is to obtain local inequalities from (25). To this end, we first examine the second integral in (25) which after substitution from (21*c*) can be shown to yield[6]

$$\int_1^{1+\frac{1}{n}} \dot{\mathbf{E}}\,\underset{\sim}{\mathfrak{S}}\,\dot{\mathbf{E}}^p\, dt = \int_1^{1+\frac{1}{n}} \mathbf{M}\cdot\underset{\sim}{\mathfrak{S}}\,\mathfrak{M}\,\dot{\mathbf{E}}\, dt$$

$$= \frac{1}{n}\,\mathbf{M}\cdot\underset{\sim}{\mathfrak{S}}^y\mathfrak{M}^y\mathbf{M} + 0\left(\frac{1}{n^2}\right). \tag{26}$$

In writing the result $(26)_2$, a function of $1/n$ defined by the integral $(26)_1$ has been expanded in Taylor series about $t = 1$, a superscript y is used to denote the value of any function on the loading surface when $\mathbf{E} = \mathbf{E}^y$ at $t = 1$, e.g.,

$$\underset{\sim}{\mathfrak{S}}^y = \underset{\sim}{\mathfrak{S}}(\mathfrak{U}(1)), \tag{27}$$

[5] For given values of $\mathbf{E}^0$ and $\mathbf{M}$, the strain cycle (21) depends simultaneously on the two parameters β and n. It can be noted that sequences of strain cycles of the form (21) can also be constructed in which β and n vary independently of one another.

[6] For details of the result $(26)_2$ and related estimates, see Appendix *A*.

Downloaded 02 May 2010 to 171.66.16.25. Redistribution subject to ASME license or copyright; see http://www.asme.org/terms/Terms_Use.cfm

and the symbol 0 on the right-hand side of $(26)_2$ designates the usual order symbol, i.e., a function f is said to be of $0(\epsilon^m)$ if there is a positive constant $\mathcal{C}$ such that $|f| \leq \mathcal{C}|\epsilon^m|$ as $\epsilon \to 0$.

For the strain cycle (21), the first integral on the left-hand side of (25) can be written as

$$\int_{1-\beta}^{1+\frac{2}{n}+\beta} (\mathbf{E}-\mathbf{E}^0)\cdot {}_1\dot{\mathbf{S}}\, dt = \int_{1-\beta}^{1+\frac{2}{n}+\beta} F\, dt + \int_1^{1+\frac{1}{n}} (\mathbf{E}-\mathbf{E}^0)\cdot\left[\frac{\partial_1\mathbf{S}}{\partial\mathbf{E}^p}\dot{\mathbf{E}}^p + \frac{\partial_1\mathbf{S}}{\partial\kappa}\dot{\kappa}\right]dt + \int_{1-\beta}^{1+\frac{2}{n}+\beta} (\mathbf{E}-\mathbf{E}^0)\cdot\frac{\partial_1\mathbf{S}^y}{\partial\mathbf{E}}\dot{\mathbf{E}}\, dt, \tag{28}$$

where the lower and upper limits of integration of the second integral on the right-hand side of (28) have been replaced by 1 and $1 + 1/n$, respectively, since the plastic strain rate $\dot{\mathbf{E}}^p \neq 0$ only during the time interval $1 \leq t < 1 + 1/n$. Also, F in (28) is a scalar function defined by

$$F = (\mathbf{E}-\mathbf{E}^0)\cdot\left[\frac{\partial_1\mathbf{S}}{\partial\mathbf{E}} - \frac{\partial_1\mathbf{S}^y}{\partial\mathbf{E}}\right]\dot{\mathbf{E}}, \tag{29}$$

$\partial_1\mathbf{S}^y/\partial\mathbf{E}$ is the value of the fourth-order tensor function $\partial_1\mathbf{S}/\partial\mathbf{E}$ evaluated on the loading surface $\partial\mathcal{E}$ when $\mathbf{E} = \mathbf{E}^y$ at $t = 1$ and where the quantity $(\mathbf{E}-\mathbf{E}^0)\cdot(\partial_1\mathbf{S}^y/\partial\mathbf{E})\,\dot{\mathbf{E}}$, which occurs in (29) and the last integral in (28), has been added to and subtracted from the integrand on the left-hand side of (28). Since the second-order tensor $\partial_1\mathbf{S}^y/\partial\mathbf{E} = \partial_1\mathbf{S}/\partial\mathbf{E}\,|_{\mathbf{E}=\mathbf{E}^y}$ is fixed and since the strain cycle (21) is symmetric about $t = 1 + 1/n$ (see also Fig. 3), it is easily verified that:

$$\text{The third integral on the right-hand side of (28)} \equiv 0. \tag{30}$$

Next, we consider the second integral on the right-hand side of (28) and obtain

$$\int_1^{1+\frac{1}{n}} (\mathbf{E}-\mathbf{E}^0)\cdot\left\{\frac{\partial_1\mathbf{S}}{\partial\mathbf{E}^p}\dot{\mathbf{E}}^p + \frac{\partial_1\mathbf{S}}{\partial\kappa}\dot{\kappa}\right\}dt = \int_1^{1+\frac{1}{n}} (\mathbf{E}-\mathbf{E}^0)\cdot\left\{\frac{\partial_1\mathbf{S}}{\partial\mathbf{E}^p} + \frac{\partial_1\mathbf{S}}{\partial\kappa}\otimes\mathfrak{Q}\right\}\dot{\mathbf{E}}^p\, dt = \frac{1}{n}(\mathbf{E}^y-\mathbf{E}^0)\cdot\mathfrak{K}^y\mathfrak{N}^y\mathbf{M} + 0\left(\frac{1}{n^2}\right), \tag{31}$$

where the integral has been expanded in Taylor series about $t = 1$ and where

$$\mathfrak{K} = \frac{\partial_1\mathbf{S}}{\partial\mathbf{E}^p} + \frac{\partial_1\mathbf{S}}{\partial\kappa}\otimes\mathfrak{Q}, \quad \mathfrak{K}^y = \mathfrak{K}(\mathfrak{U}(1)). \tag{32}$$

We now turn our attention to the first integral on the right-hand side of (28) and for convenience write this as

$$\int_{1-\beta}^{1+\frac{2}{n}+\beta} F\, dt = \int_{1-\beta}^{1} F\, dt + \int_1^{1+\frac{1}{n}} F\, dt + \int_{1+\frac{1}{n}}^{1+\frac{2}{n}} F\, dt + \int_{1+\frac{2}{n}}^{1+\frac{2}{n}+\beta} F\, dt. \tag{33}$$

Recalling the expression (29) and after substitution for $\mathbf{E} = \mathbf{E}^y + \mathbf{M}(t-1)$ from (21b) the first integral on the right-hand side of (33) results in

$$\int_{1-\beta}^{1} F\, dt = \int_{1-\beta}^{1} [(\mathbf{E}^y-\mathbf{E}^0) + (t-1)\mathbf{M}]\cdot\left\{(t-1)\frac{\partial}{\partial\mathbf{E}}\left(\frac{\partial_1\mathbf{S}}{\partial\mathbf{E}}\right)\Big|_{t=1}\mathbf{M} + 0((t-1)^2)\right\}\mathbf{M}\, dt = 0(\|\mathbf{E}^y-\mathbf{E}^0\|^3), \tag{34}$$

where $\|\mathbf{E}\|$ denotes the norm of the second-order tensor $\mathbf{E}$ and where in obtaining $(34)_3$ we have expanded $\partial_1\mathbf{S}/\partial\mathbf{E}$ (which occurs in F) in Taylor series about $t = 1$, made use of the fact that $\dot{\mathbf{E}}^p = 0$ during the time interval $(1-\beta, 1)$ and noted that the first term in the expansion cancels that which arises from the second term in (29). The next three integrals on the right-hand side of (33) may be evaluated similarly but some of these involve more detailed calculations. Thus,

$$\int_1^{1+\frac{1}{n}} F\, dt = \left[\frac{1}{2n^2}(\mathbf{E}^y-\mathbf{E}^0) + \frac{1}{3n^3}\mathbf{M}\right]\cdot({}_1\mathfrak{L}^y + {}_2\mathfrak{L}^y)\mathbf{M} + 0\left(\frac{1}{n^4}, \frac{1}{n^3}\|\mathbf{E}^y-\mathbf{E}^0\|\right), \tag{35}$$

$$\int_{1+\frac{1}{n}}^{1+\frac{2}{n}} F\, dt = -\frac{1}{n^2}(\mathbf{E}^y-\mathbf{E}^0)\cdot({}_1\mathfrak{L}^y + {}_2\mathfrak{L}^y)\mathbf{M} + 0\left(\frac{1}{n^2}\right), \tag{36}$$

$$\int_{1+\frac{2}{n}}^{1+\frac{2}{n}+\beta} F\, dt = -\frac{1}{2n}(\mathbf{E}^y-\mathbf{E}^0)\cdot{}_2\mathfrak{L}^y(\mathbf{E}^y-\mathbf{E}^0) + 0\left(\frac{1}{n^2}, \|\mathbf{E}^y-\mathbf{E}^0\|^3\right), \tag{37}$$

where

$${}_1\mathfrak{L} = {}_1\mathfrak{L}(\mathfrak{U},\mathbf{M}) = \frac{\partial}{\partial\mathbf{E}}\left(\frac{\partial_1\mathbf{S}}{\partial\mathbf{E}}\right)\mathbf{M}, \quad {}_1\mathfrak{L}^y = ({}_1\mathfrak{L})_{t=1},$$

$${}_2\mathfrak{L} = {}_2\mathfrak{L}(\mathfrak{U},\mathbf{M}) = \frac{\partial}{\partial\mathbf{E}^p}\left(\frac{\partial_1\mathbf{S}}{\partial\mathbf{E}}\right)\mathfrak{N}\mathbf{M} + \frac{\partial}{\partial\kappa}\left(\frac{\partial_1\mathbf{S}}{\partial\mathbf{E}}\right)\mathfrak{Q}\cdot\mathfrak{N}\mathbf{M}, \quad {}_2\mathfrak{L}^y = ({}_2\mathfrak{L})_{t=1}. \tag{38}$$

Also, with reference to (35)–(37) the following should be noted: In obtaining (35) the function $\partial_1\mathbf{S}/\partial\mathbf{E}$ is expanded in Taylor's series about $t = 1$, in the case of (36) the expansion is first made about $t = 1 + 1/n$ and again about $t = 1$, while in the case of (37) Taylor's series expansion is first made about $t = 1 + 2/n$ and subsequently about $t = 1 + 1/n$ and $t = 1$.

Introducing (30) and (31), as well as (34)–(37), in (28) and combining the result with (26), from (25) follows the inequality

$$\frac{1}{n}\mathbf{M}\cdot\mathfrak{L}^y\mathfrak{N}^y\mathbf{M} - \frac{1}{n}(\mathbf{E}^y-\mathbf{E}^0)\cdot\mathfrak{K}^y\mathfrak{N}^y\mathbf{M} + 0\left(\frac{1}{n^2}, \|\mathbf{E}^y-\mathbf{E}^0\|^2\right) \geq 0, \tag{39}$$

which must hold for all n and all values of $\|\mathbf{E}^y-\mathbf{E}^0\|$ independent of one another and for all choices of $\mathbf{M}$ such that (22) is satisfied. Consider now a special case of (39) in which $\mathbf{E}^0$ is allowed to approach $\mathbf{E}^y$ at $t = 1$. In this case, the time parameters $\beta \to 0$ while n and the strain rate $\mathbf{M}$ at $\mathbf{E}^y$ remain fixed. Then, after multiplying (39) by n and taking the limit as $\mathbf{E}^0 \to \mathbf{E}^y$, there results

Downloaded 02 May 2010 to 171.66.16.25. Redistribution subject to ASME license or copyright; see http://www.asme.org/terms/Terms_Use.cfm

$$\mathbf{M}\cdot\underset{\sim}{\mathcal{S}}^{y}\underset{\sim}{\mathcal{M}}^{y}\mathbf{M}+0\left(\frac{1}{n}\right)\geq 0. \tag{40}$$

Consider next a nested sequence of strain cycles with progressively larger n, each of which (with $\mathbf{E}^0 = \mathbf{E}^y$ and $\beta = 0$) meets the condition (40). Then, in the limit as $n\to\infty$, we conclude that

$$\mathbf{M}\cdot\underset{\sim}{\mathcal{S}}^{y}\underset{\sim}{\mathcal{M}}^{y}\mathbf{M}\geq 0. \tag{41}$$

Returning to (39) and remembering that $\underset{\sim}{\mathcal{S}}^{y}$, $\underset{\sim}{\mathcal{M}}^{y}$ and $\underset{\sim}{\mathcal{K}}^{y}$ are all independent of the strain rate $\mathbf{M}$, we consider a limiting case in which $\mathbf{M}$ becomes smaller and smaller while $\mathbf{E}^0 = \mathbf{E}^y - \beta\mathbf{M}$ remains fixed, i.e., the limiting case in which $\mathbf{M}\to\mathbf{0}$ while $\beta\mathbf{M}$ remains finite. In order to effect such a limiting case, we first replace $\mathbf{M}$ in (39) by $\alpha\mathbf{M}$, α being a positive scalar, and after multiplying by n/α and taking the limit as $\alpha\to 0$ we obtain

$$-(\mathbf{E}^y-\mathbf{E}^0)\cdot\underset{\sim}{\mathcal{K}}^{y}\underset{\sim}{\mathcal{M}}^{y}\mathbf{M}+0\left(\frac{1}{n},\|\mathbf{E}^y-\mathbf{E}^0\|^2\right)\geq 0. \tag{42}$$

Consider next a nested sequence of strain cycles with $\mathbf{E}^0$ fixed but n becoming progressively larger. In the limit as $n\to\infty$, an inequality of the same form as (42) results but with the second term replaced by $0(\|\mathbf{E}^y-\mathbf{E}^0\|^2)$. Applying the latter inequality to a further sequence of strain cycle in which $\|\mathbf{E}^y-\mathbf{E}^0\|$ is allowed to approach zero, in the limit as $\|\mathbf{E}^y-\mathbf{E}^0\|\to 0$, we obtain

$$(\mathbf{E}^y-\mathbf{E}^0)\cdot\underset{\sim}{\mathcal{K}}^{y}\underset{\sim}{\mathcal{M}}^{y}\mathbf{M}\leq 0. \tag{43}$$

Since $\mathbf{E}^y-\mathbf{E}^0 = \beta\mathbf{M}$, we observe that after dividing through by the positive scalar β the inequality (43) can also be written as $\mathbf{M}\cdot\underset{\sim}{\mathcal{K}}^{y}\underset{\sim}{\mathcal{M}}^{y}\mathbf{M}\leq 0$.

The inequalities (41) and (43) are consequences of the work assumption (19) and place restrictions on the response functions $\underset{\sim}{\mathcal{S}}$ and $\underset{\sim}{\mathcal{K}}$. It should be emphasized that these restrictions hold in *all* motions, even though they have been deduced from consideration of homogeneous motions. This is because the response functions that occur in (41) and (43) depend only on the local kinematical variables $(7)_2$ and are independent of their rates and their spatial gradients.

4 Restrictions on Constitutive Equations

We discuss in this section some implications of the inequalities (41) and (43). Recalling the structure of the plastic strain rate given by (10*d*) and (13), as well as the remark following (43), it is easily seen that the two inequalities (43) and (41) can be rewritten, respectively, in the forms

$$\dot{\mathbf{E}}\cdot\underset{\sim}{\mathcal{K}}\dot{\mathbf{E}}^{p}\leq 0,\quad \dot{\mathbf{E}}\cdot\underset{\sim}{\mathcal{S}}\dot{\mathbf{E}}^{p}\geq 0, \tag{44}$$

where it is understood that the various functions in $(44)_{1,2}$ are evaluated on the loading surface (9). If we substitute the expression $\dot{\mathbf{E}}^p = \lambda\boldsymbol{\rho}\hat{g}$ for the plastic strain rate in the last two results, then after dividing by $\hat{g}$ (which is a positive scalar) we obtain from $(44)_{1,2}$ the inequalities[7]

$$\dot{\mathbf{E}}\cdot\lambda\underset{\sim}{\mathcal{K}}\boldsymbol{\rho}\leq 0,\quad \dot{\mathbf{E}}\cdot\lambda\underset{\sim}{\mathcal{S}}\boldsymbol{\rho}\geq 0. \tag{45}$$

By a procedure similar to that used previously by Naghdi and Trapp [4, Section 5], it can be shown that the inequalities $(45)_{1,2}$ imply

$$\lambda\underset{\sim}{\mathcal{K}}\boldsymbol{\rho}=-\gamma_1\frac{\partial g}{\partial\mathbf{E}},\quad \lambda\underset{\sim}{\mathcal{S}}\boldsymbol{\rho}=\gamma_2\frac{\partial g}{\partial\mathbf{E}}, \tag{46}$$

where the right-hand sides of $(46)_{1,2}$ are evaluated on the loading surface $\partial\mathcal{E}$ and where the scalar-valued coefficients $\gamma_1 = \gamma_1(\mathcal{U})$, $\gamma_2 = \gamma_2(\mathcal{U})$ satisfy the conditions $\gamma_1\geq 0$, $\gamma_2\geq 0$. According to $(46)_{1,2}$ each of the two second-order tensors $\underset{\sim}{\mathcal{K}}\boldsymbol{\rho}$ and $\underset{\sim}{\mathcal{S}}\boldsymbol{\rho}$ are directed along the normal to the loading surface $\partial\mathcal{E}$, the former being directed inward and the latter outward. A brief outline of the proof in the case of $(46)_2$ is given at the end of Appendix *A* [between (*A*10) and (*A*12)], which also corrects a part of the line of argument of the proof in [4, p. 41]; see, in this connection, the footnote in the last paragragh of Appendix *A*. As to be expected, the results in (46) include that appropriate for the rate-independent theory of plasticity. Indeed, in the absence of the rate-dependent part of the stress response $\underset{\sim}{\mathcal{S}}$ (see equation (17)), we are left only with the restriction $(46)_1$ which is equivalent to the inequality (4.32) in [4].

Inspection of $(46)_{1,2}$ reveals that their right-hand sides are scalar multiples of each other. Hence, a similar relationship must exist between the quantities on the left-hand sides of $(46)_{1,2}$. Thus, in order to effect a result of this type, we first divide both sides of $(46)_1$ by $-\gamma_1$ and substitute the resulting expression for $\partial g/\partial\mathbf{E}$ into (4.5) and obtain

$$\lambda\underset{\sim}{\mathcal{S}}\boldsymbol{\rho}=-\gamma\left(\frac{\partial_1\mathbf{S}}{\partial\mathbf{E}^p}+\frac{\partial_1\mathbf{S}}{\partial\kappa}\otimes\underset{\sim}{\mathcal{C}}\right)\lambda\boldsymbol{\rho}, \tag{47}$$

where use has been made of $(32)_1$ and the scalar-valued function $\gamma = \gamma(\mathcal{U})$ is defined by

$$\gamma=\frac{\gamma_2}{\gamma_1}>0. \tag{48}$$

The result (47) holds only on the loading surface $\partial\mathcal{E}$. If we multiply (47) by the scalar $\hat{g}$ and make use of (10*d*) and (13), we arrive at

$$\underset{\sim}{\mathcal{S}}\dot{\mathbf{E}}^{p}=-\gamma\left(\frac{\partial_1\mathbf{S}}{\partial\mathbf{E}^p}+\frac{\partial_1\mathbf{S}}{\partial\kappa}\otimes\underset{\sim}{\mathcal{C}}\right)\dot{\mathbf{E}}^{p}. \tag{49}$$

The preceding result indicates a relationship between the rate-dependent part of the stress response $\underset{\sim}{\mathcal{S}}$ and those of the rate-independent response ${}_1\mathbf{S}$ in (16) and the work-hardening response $\underset{\sim}{\mathcal{C}}$ in (11). Although (47) is valid only during loading and by (10) the plastic strain rate $\dot{\mathbf{E}}^p$ is also nonzero only during loading, the expression (49) may be regarded as valid throughout the motion of the idealized elastic-viscoplastic body.

With the help of (49) and $(46)_2$, the second part of the constitutive equation for the stress given by (17*b*) can be written as

$$\begin{aligned}\mathbf{S}&={}_1\mathbf{S}-\gamma\underset{\sim}{\mathcal{K}}\dot{\mathbf{E}}^{p}\\&={}_1\mathbf{S}-\gamma_2\frac{\partial g}{\partial\mathbf{E}}\hat{g}\ \text{during loading when}\ g=0,\ \hat{g}>0,\end{aligned} \tag{50}$$

where the fourth-order tensor $\underset{\sim}{\mathcal{K}}$ is defined by $(32)_1$. Next, suppose that $\underset{\sim}{\mathcal{K}}$ is invertible in the sense that for any two symmetric second-order tensors $\mathbf{a}$ and $\mathbf{b}$, $\underset{\sim}{\mathcal{K}}\mathbf{a} = \mathbf{b}$ implies

$$\mathbf{a}=\underset{\sim}{\mathcal{K}}^{-1}\mathbf{b}. \tag{51}$$

It then follows from $(46)_1$ that

$$\lambda\boldsymbol{\rho}=-\gamma_1\underset{\sim}{\mathcal{K}}^{-1}\frac{\partial g}{\partial\mathbf{E}}. \tag{52}$$

It may be of interest to observe that after multiplying (52) by the scalar $\hat{g}$ defined by (12) and recalling once more that $\dot{\mathbf{E}}^p = \lambda\boldsymbol{\rho}\hat{g}$, the expression for the plastic strain rate can be written as

$$\dot{\mathbf{E}}^{p}=-\gamma_1\left(\underset{\sim}{\mathcal{K}}^{-1}\frac{\partial g}{\partial\mathbf{E}}\right)\hat{g}. \tag{53}$$

Acknowledgment

The results reported here were obtained in the course of research sponsored by the U.S. Office of Naval Research under Contract N00014-75-C-0148, Project NR 064-436, with the University of California, Berkeley.

[7] The scalar λ (already assumed to be positive) can be deleted from both inequalities in (45). However, it is more convenient to retain λ in $(45)_{1,2}$ for later developments.

Downloaded 02 May 2010 to 171.66.16.25. Redistribution subject to ASME license or copyright; see http://www.asme.org/terms/Terms_Use.cfm

References

1 Green, A. E., and Naghdi, P. M., "A General Theory of an Elastic-Plastic Continuum," *Archive for Rational Mechanics and Analysis*, Vol. 18, 1965, pp. 251–281.

2 Green, A. E., and Naghdi, P. M., "A Thermodynamic Development of Elastic-Plastic Continua," *Proceedings, IUTAM Symposium on Irreversible Aspects of Continuum Mechanics and Transfer of Physical Characteristics in Moving Fluids*, Springer-Verlag, 1966, pp. 117–131.

3 Naghdi, P. M., and Trapp, J. A., "The Significance of Formulating Plasticity With Reference to Loading Surfaces in Strain Space," *International Journal of Engineering Science*, Vol. 13, 1975, pp. 785–797.

4 Naghdi, P. M., and Trapp, J. A., "Restrictions on Constitutive Equations of Finitely Deformed Elastic-Plastic Materials," *Quarterly Journal of Mechanics and Applied Mathematics*, Vol. 28, 1975, pp. 25–46.

5 Drucker, D. C., "A More Fundamental Approach to Plastic Stress-Strain Relations," *Proceedings of the First U.S. National Congress on Applied Mechanics* (Chicago 1951), New York, 1952, pp. 487–491.

6 Drucker, D. C., "A Definition of Stable Inelastic Material," ASME JOURNAL OF APPLIED MECHANICS, Vol. 26, 1959, pp. 101–106.

7 Il'iushin, A. A., "On the Postulate of Plasticity," *Journal of Applied Mathematics and Mechanics* (translation of *Prikladnaya Mathematika i Mekhanika*), Vol. 25, 1961, pp. 746–752.

8 Perzyna, P., "Fundamental Problems in Viscoplasticity," in *Advances in Applied Mechanics*, Vol. 9, Yih, C. S., ed., Academic Press, New York, 1966, pp. 243–377.

9 Campbell, J. D., "Dynamic Plasticity: Macroscopic and Microscopic Aspects," *Materials Science and Engineering*, Vol. 12, 1973, pp. 3–21.

10 Klepaczko, J., and Duffy, J., "Strain Rate History Effects in Body-Centered-Cubic Metals," in *Mechanical Testing for Deformation Model Development*, Rohde, R. W., and Swearengen, J. C., eds., Special Technical Publication 765, American Society for Testing and Materials, Philadelphia, 1982, pp. 251–268.

11 Malvern, L. E., "The Propagation of Longitudinal Waves of Plastic Deformation in a Bar of Material Exhibiting a Strain-Rate Effect," ASME JOURNAL OF APPLIED MECHANICS, Vol. 18, 1951, pp. 203–208.

12 Wilkins, M. L., and Guinan, M. W., "Impact of Cylinders on a Rigid Boundary," *Journal of Applied Physics*, Vol. 44, 1973, pp. 1200–1206.

13 Rubin, M. B., "A Thermoelastic-Viscoplastic Model with a Rate-Dependent Yield Strength," ASME JOURNAL OF APPLIED MECHANICS, Vol. 49, 1982, pp. 305–311.

14 Naghdi, P. M., and Murch, S. A., "On the Mechanical Behavior of Viscoelastic/Plastic Solids," ASME JOURNAL OF APPLIED MECHANICS, Vol. 30, 1963, pp. 321–328.

15 Naghdi, P. M., "Some Remarks on Rate-Dependent Plasticity," in the D. C. Drucker Anniversary Volume, *Mechanics of Material Behavior*, Elsevier, Amsterdam, to appear.

16 Casey, J., and Naghdi, P. M., "On the Characterization of Strain-Hardening in Plasticity," ASME JOURNAL OF APPLIED MECHANICS, Vol. 48, 1981, pp. 285–296.

APPENDIX A

We include here some mathematical details in connection with the estimates obtained in Section 3, as well as an outline of the proof of the results (46) in Section 4. In providing the details of the estimates in Section 3, we make extensive use of Taylor series expansion of functions of the form

$$G(s)=\int_{s_0}^{s} F(t)\,dt, \tag{A1}$$

where the integrand F is continuous and at least twice differentiable in the interval $s_0 \le t \le s$. For the special case in which F has the product form

$$F(t)=f(t)g(t), \tag{A2}$$

the Taylor series expansion of (A1) about $t = s_0$ is given by

$$\begin{aligned} G(s) &= (s-s_0)f(s_0)g(s_0) \\ &+ \frac{1}{2!}(s-s_0)^2[f'(s_0)g(s_0)+f(s_0)g'(s_0)] \\ &+ \frac{1}{3!}(s-s_0)^3[f''(s_0)g(s_0)+2f'(s_0)g'(s_0) \\ &+ f(s_0)g''(s_0)]+0((s-s_0)^4), \end{aligned} \tag{A3}$$

where the prime denotes differentiation with respect to time t and 0 denotes the order symbol defined following (27).

In the calculations that follow, we need the expressions for the second time derivative of plastic strain $\mathbf{E}^p$. For convenience, we record, in the following, these expressions in component form referred to the basis vector of rectangular Cartesian coordinates. Thus, the rectangular Cartesian component form of the constitutive equation (10*d*) reads as

$$\dot{E}^p_{KL}=\mathfrak{M}_{KLMN}\dot{E}_{MN}, \tag{A4}$$

where Latin indicates take the values 1,2,3 and the usual convention for summation over repeated indices is used. Repeated differentiation of (A4) with respect to t yields

$$\ddot{E}^p_{KL}=\mathfrak{M}_{KLMN}\ddot{E}_{MN}+\mathfrak{D}_{KLMNRS}\dot{E}_{MN}\dot{E}_{RS}, \tag{A5}$$

where

$$\begin{aligned} \mathfrak{D}_{KLMNRS} &= \frac{\partial \mathfrak{M}_{KLMN}}{\partial E_{RS}}+\frac{\partial \mathfrak{M}_{KLMN}}{\partial E^p_{PQ}}\mathfrak{M}_{PQRS} \\ &+ \frac{\partial \mathfrak{M}_{KLMN}}{\partial \kappa}\mathfrak{C}_{PQ}\mathfrak{M}_{PQRS}, \end{aligned} \tag{A6}$$

and where $\mathfrak{M}_{KLMN}$ and $\mathfrak{C}_{PQ}$ are, respectively, the rectangular Cartesian components of the tensor $\mathfrak{M}$ and $\mathfrak{C}$ in (13) and (11).

Consider now the estimate of the integral on the left-hand side of (26). With the help of (A3), (A5), and (A6), the left-hand side of (26) when expanded about $t = 1$ gives

$$\begin{aligned} \text{L.H.S. of } (26)_1 &= \frac{1}{n}[\mathbf{M}\cdot\underset{\sim}{\mathfrak{S}}\dot{\mathbf{E}}^p]_{t=1}+\frac{1}{2n^2}[\mathbf{M}\underset{\sim}{\dot{\mathfrak{S}}}\dot{\mathbf{E}}^p \\ &+ \mathbf{M}\cdot\underset{\sim}{\mathfrak{S}}\ddot{\mathbf{E}}^p]_{t=1}+0\left(\frac{1}{n^3}\right) \\ &= \frac{1}{n}\mathbf{M}\cdot\underset{\sim}{\mathfrak{S}}^y\mathfrak{M}^y\mathbf{M}+\frac{1}{2n^2}[\mathbf{M}\underset{\sim}{\mathfrak{J}}^y\mathfrak{M}^y\mathbf{M} \\ &+ \mathbf{M}\cdot\underset{\sim}{\mathfrak{S}}^y\mathfrak{N}\mathbf{M}]+0\left(\frac{1}{n^3}\right) \\ &= \text{R.H.S. of } (26)_2, \end{aligned} \tag{A7}$$

where

$$\begin{aligned} \dot{\underset{\sim}{\mathfrak{S}}} &= \mathfrak{J}(\mathfrak{U},\dot{\mathbf{E}})=\frac{\partial \underset{\sim}{\mathfrak{S}}}{\partial \mathbf{E}}\dot{\mathbf{E}}+\frac{\partial \underset{\sim}{\mathfrak{S}}}{\partial \mathbf{E}^p}\mathfrak{M}\dot{\mathbf{E}}+\frac{\partial \underset{\sim}{\mathfrak{S}}}{\partial \kappa}\underset{\sim}{\mathfrak{C}}\cdot\mathfrak{M}\dot{\mathbf{E}}, \\ \dot{\mathfrak{M}} &= \mathfrak{N}(\mathfrak{U},\dot{\mathbf{E}})=\frac{\partial \mathfrak{M}}{\partial \mathbf{E}}\dot{\mathbf{E}}+\frac{\partial \mathfrak{M}}{\partial \mathbf{E}^p}\mathfrak{M}\dot{\mathbf{E}}+\frac{\partial \mathfrak{M}}{\partial \kappa}\underset{\sim}{\mathfrak{C}}\cdot\mathfrak{M}\dot{\mathbf{E}}, \end{aligned} \tag{A8}$$

and where as in (27) an attached superscript y indicates the quantity is evaluated at $t = 1$. The estimate in (31) can be evaluated similarly.

We now turn our attention to the estimate in (34). Here the term $\partial_1\mathbf{S}/\partial\mathbf{E}$, which occurs in the integrand on the left-hand side of $(34)_1$, has been expanded in Taylor series about $t = 1$ to obtain

$$\begin{aligned} \frac{\partial_1\mathbf{S}}{\partial\mathbf{E}} &= \frac{\partial_1\mathbf{S}^y}{\partial\mathbf{E}}+(t-1)\left(\frac{\dot{\overline{\partial_1\mathbf{S}}}}{\partial\mathbf{E}}\right)_{t=1} \\ &+ \tfrac{1}{2}(t-1)^2\left(\frac{\ddot{\overline{\partial_1\mathbf{S}}}}{\partial\mathbf{E}}\right)_{t=1}+0((t-1)^3) \\ &= \frac{\partial_1\mathbf{S}^y}{\partial\mathbf{E}}+(t-1)\left[\frac{\partial}{\partial\mathbf{E}}\left(\frac{\partial_1\mathbf{S}}{\partial\mathbf{E}}\right)\dot{\mathbf{E}}\right]_{t=1} \\ &+ \tfrac{1}{2}(t-1)^2\left[\frac{\partial}{\partial\mathbf{E}}\left(\frac{\partial^2{}_1\mathbf{S}}{\partial\mathbf{E}\partial\mathbf{E}}\right)\dot{\mathbf{E}}\dot{\mathbf{E}}\right]_{t=1}+0((t-1)^3), \end{aligned} \tag{A9}$$

where use has been made of the fact that during the interval $1-\beta \le t < 1$ only elastic loading takes place. After introducing (A9) in the integrand on the left-hand side of $(34)_1$, integrating the resulting expression and remembering that $\beta\mathbf{M} = \mathbf{E}^y - \mathbf{E}^0$ for the interval in (21*a*), we arrive at the estimate

Downloaded 02 May 2010 to 171.66.16.25. Redistribution subject to ASME license or copyright; see http://www.asme.org/terms/Terms_Use.cfm

$(34)_2$. The estimates for the integrals in (35)-(37) may be obtained similarly.

In the rest of this Appendix we provide an outline of the proof for one of the normality conditions in (46), namely $(46)_2$. The proof (by contradiction) follows the line of argument used previously for rate-independent plasticity Naghdi and Trapp [4, Section 5][8]: Suppose that $(46)_2$ does not hold at a regular point (say a point P) of the loading surface $\partial\mathcal{E}$. Then, the second-order tensor $\lambda\underline{\mathbf{S}}\boldsymbol{\rho}$ is not directed along the normal to the loading surface and must be expressible in the form

$$\lambda\underline{\mathbf{S}}\boldsymbol{\rho}=\gamma_2\frac{\partial g}{\partial \mathbf{E}}+\mathbf{V}, \tag{A10}$$

where $\mathbf{V}$ is a nonzero vector in six-dimensional strain space laying in the hyperplane tangent to the loading surface at P. Substitution of (A10) into (44) gives

$$\gamma_2\dot{\mathbf{E}}\cdot\frac{\partial g}{\partial \mathbf{E}}+\dot{\mathbf{E}}\cdot\mathbf{V}\geq\mathbf{0}, \tag{A11}$$

which must hold for all arbitrary values of $\dot{\mathbf{E}}$. Choose

$$\dot{\mathbf{E}}=\alpha\frac{\partial g}{\partial \mathbf{E}}-\delta\mathbf{V}, \tag{A12}$$

where the arbitrary coefficients α and δ are nonzero and positive. After introducing (A12) into (A11), observing that $(\partial g/\partial\mathbf{E})\cdot\mathbf{V}=0$, dividing (A11) by the scalar δ, and taking the limit as $\delta\to\infty$, we arrive at the result $\mathbf{V}\cdot\mathbf{V}\leq 0$. But, this is a contradiction since $\mathbf{V}\cdot\mathbf{V}=\|\mathbf{V}\|^2>0$ for $\mathbf{V}\neq\mathbf{0}$. We conclude, therefore, that $\mathbf{V}=\mathbf{0}$ and hence (A10) reduces to $(46)_2$ at all regular points of the loading surface. Next, with the use of the reduced form of (A12), substitution of $(46)_2$ into the inequality $(45)_2$ after also observing that $(\partial g/\partial\mathbf{E})\cdot(\partial g/\partial\mathbf{E})>0$ determines the sign of γ_2 as

$$\gamma_2=\gamma_2(\mathfrak{U})\geq 0. \tag{A13}$$

The proof for the normality condition $(46)_1$ is similar along with $\gamma_1=\gamma_1(\mathfrak{U})\geq 0$.

[8] The statement following equation (5.4) of [4] is incorrect but this does not affect the line of argument for the proof or the final result. Strictly speaking, the temporary notation $\mathbf{G}$ introduced in (5.1) of [4] should be defined as the right-hand side of (5.1) divided by the scalar $\hat{g}$. Then, the inequality (5.3) of [4] remains valid and the scalar-valued coefficient γ would be a function of the variables $\mathfrak{U}$ as stated following (5.4) of [4].

Downloaded 02 May 2010 to 171.66.16.25. Redistribution subject to ASME license or copyright; see http://www.asme.org/terms/Terms_Use.cfm

Impact Force of a Rigid-Plastic Missile

M. P. White
Department of Civil Engineering,
University of Massachusetts,
Amherst, Mass. 01003
Fellow ASME

A cylindrical missile, assumed to be of a rigid-plastic material strikes a nonyielding target normally and end-on. Above a certain (critical) velocity the nose of the missile disintegrates or spatters, and below that velocity the nose flattens to a mushroom form. The contact force decreases with decreasing velocity during impact but experiences a jump as the critical velocity is passed during slowdown. This paper gives a method of calculating the critical velocity and the contact force as function of time, as well as the time variations of the other parameters of the impact process.

1 Introduction

It is known from experience that a lead bullet striking a rigid target at high velocity disintegrates, while a similar bullet at low velocity is somewhat distorted but remains in one piece. It was discovered during World War II (or perhaps much earlier), both in the field and in the course of terminal ballistic firing, that some projectiles have critical impact velocities above which breakup occurs. Breakup is accompanied by impaired performance.

This paper treats the idealized case of a rigid-plastic cylindrical missile striking an unyielding obstacle. It is shown that a critical impact velocity exists which separates two quite different modes of missile behavior. Above that critical velocity the missile spatters or flows laterally along the face of the target while below it the missile remains coherent. Just above the critical velocity the impact force is smaller than just below it, and by a significant amount.

In elastic impact of a slender missile, waves of stress and strain travel back and forth along it at the elastic wave speed c, where $c^2 = E/\rho$ (Young's modulus/density). The initial impact stress is related to the impact velocity by $\sigma = VE/c$. If the elastic limit stress is exceeded, the propagation pattern becomes extremely complicated with elastic and inelastic waves interacting with each other [1–3]. G. I. Taylor [2] showed that (*a*) if the elastic wave speed c is large compared to the inelastic speed(s) and to the impact velocity, and (*b*) if the impact velocity is well above that required to reach the elastic limit, then a good approximate analysis is obtained by assuming the elastic modulus E to be infinite, i.e., by treating the material of the missile as rigid-plastic. Lee and Tupper [3] in analyzing missile impact by both the "exact" and the G. I. Taylor approximate methods, and then comparing these predictions both with each other and with experiment, obtained good agreement all around.

The primary objective of this paper is to present a method of predicting the time history of the force on an unyielding target during impact by a cylindrical missile of rigid-plastic material, with or without strain hardening. This paper is an extension of work reported by Lee and Tupper [3] and by White and Griffis [4].

The assumption of rigid-plastic behavior simplifies the analysis considerably and introduces significant errors only for relatively low-velocity impact, perhaps less than two or three times the velocity to initiate yielding.

Figure 1 shows the assumed form of the rigid-plastic stress-strain relation in compression. ϵ is "engineering strain" (or nominal strain), change of length divided by the original length and σ is "engineering stress" (or nominal stress), axial force divided by the original cross-sectional area A_0, compression being positive. Incompressibility is assumed, so that α, the ratio of the cross-sectional area A to the original area A_0, is related to the strain ϵ by $\alpha(1 - \epsilon) = 1$. In compression, because the cross section increases with strain, the engineering stress-strain relation is concave upward. There is assumed to

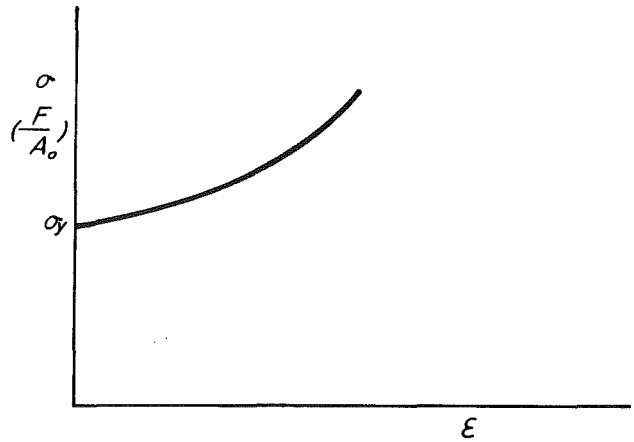

Fig. 1 Compression stress-strain relation

Contributed by the Applied Mechanics Division for presentation at the 1984 PVP Conference and Exhibition, Joint with Applied Mechanics Division and Materials Division, San Antonio, Texas, June 17–21, 1984 of THE AMERICAN SOCIETY OF MECHANICAL ENGINEERS.

Discussion on this paper should be addressed to the Editorial Department, ASME, United Engineering Center, 345 East 47th Street, New York, N.Y. 10017, and will be accepted until two months after final publication of the paper itself in the JOURNAL OF APPLIED MECHANICS. Manuscript received by ASME Applied Mechanics Division, July, 1982; final revision, April, 1983. Paper No. 84-APM-3.

Copies will be available until February, 1985.

Copyright © 1984 by ASME
Downloaded 02 May 2010 to 171.66.16.25. Redistribution subject to ASME license or copyright; see http://www.asme.org/terms/Terms_Use.cfm

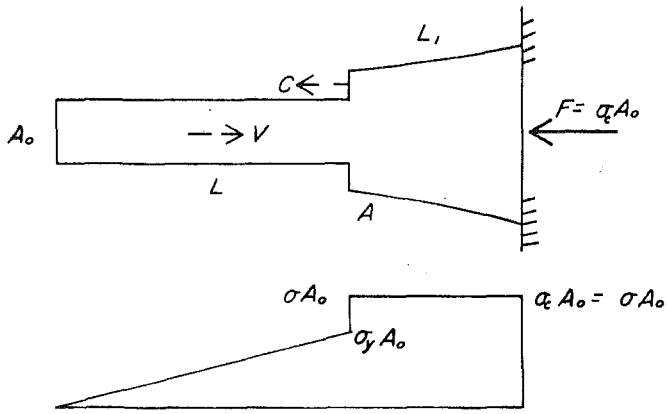

Fig. 2 (*a*) Mechanics of Mode *I* impact, and (*b*) internal force

be no rate-of-strain effect. For certain materials (e.g., some steels) and for moderate amounts of deformation, it is permissible to neglect strain hardening, i.e., to assume that the "true" stress remains constant. In this case, the engineering stress-strain relation becomes $\sigma = \sigma_y \alpha = \sigma_y/(1 - \epsilon)$, where σ_y is the constant "true" yield stress.

Two different modes of behavior are possible, as was shown by White and Griffis [4]. Up to a certain critical velocity the missile flattens or mushrooms, but remains coherent. Above that velocity the material of the missile spatters or flows laterally parallel to the surface of the target like a stream of fluid. When the impact velocity is such that the flowing mode occurs, it must be followed by the mushrooming mode as the missile slows down.

2 Mode I—Mushrooming Mode

This case has been discussed by Lee and Tupper [3] with the purpose of predicting the final strain distribution in a missile. In the present paper equations (1)–(7) and (6′)–(9′) are equivalent to expressions developed in [3].

Figure 2(*a*) illustrates the mechanics of the mushrooming mode and Fig. 2(*b*) shows the distribution of internal force along the missile during impact. The nose of the missile has shortened to a length L_1, is of nonuniform cross section and has come to rest against the target. The rear portion of the missile, of cross section A_0 and decreasing length L, moves at a diminishing velocity V toward the target. The boundary between the static front and the moving tail is advancing away from the target. This boundary is, in fact, both a shock front with a stress discontinuity and a location where the cross section jumps from A_0 to A. The axial force within the missile is zero at the free end and increases linearly to the yield point ($\sigma_y A_0$) just at the shock front where it jumps to a higher level. The internal force is then uniform between that point and the target. However, it changes with time.

2.1 Analysis of Mushrooming Mode. With the help of Fig. 2 the following equations are derived:

$$dL/dt + \alpha dL_1/dt = 0 \quad \text{(conservation of material)}$$

$$dL/dt + V + dL_1/dt = 0 \quad \text{(geometric compatibility)}$$

$$\sigma_y = -\rho L\, dV/dt \quad \text{(equilibrium of tail portion)}$$

$$\sigma = -\rho\, d(VL)/dt \quad \text{(rate of change of momentum)}$$

After introducing the following parameters, $\beta^2 = \sigma_y/\rho$, $\tau = \beta t/L_0$, $\xi = L/L_0$, $\xi_1 = L_1/L_0$, $\eta = V/\beta$ and letting $\dot{\xi}$ indicate $d\xi/d\tau$, etc., these equations become

$$\dot{\xi} + \alpha\dot{\xi}_1 = 0 \tag{1}$$

$$\dot{\xi} + \dot{\xi}_1 + \eta = 0 \tag{2}$$

$$\xi\eta = -1 \tag{3}$$

$$d(\xi\eta)/d\tau = -\frac{\sigma}{\sigma_y} \tag{4}$$

Also

$$\epsilon = \frac{\alpha - 1}{\alpha} \tag{5}$$

For a given stress-strain function, a relation between the dimensionless tail velocity η and the stress σ or strain ϵ just following the shock front can be obtained with help of the preceding equations, namely,

$$\left(\frac{\sigma}{\sigma_y} - 1\right)\epsilon = \eta^2 \tag{6}$$

This expression is valid during the entire Mode *I* slowing-down period, including the initial instant, of course. Eliminating $\dot{\xi}_1$ and $d\tau$ from equations (1)–(3), and using equation (5) result in

$$2\epsilon\frac{d\xi}{\xi} = 2\eta\, d\eta = d\eta^2$$

Combining the last two expressions and integrating, gives

$$ln\ \xi^2 = \frac{\sigma}{\sigma_y} - ln\ \epsilon + \frac{1}{\sigma_y}\int\frac{\sigma d\epsilon}{\epsilon} + C$$

Since ξ is initially unity, this becomes

$$\xi^2 = e^{(E - E_i)} \tag{7}$$

where E is a function of σ (or of ϵ) and can be obtained from the stress-strain relation as follows:

$$E = \frac{\sigma}{\sigma_y} - ln\ \epsilon + \frac{1}{\sigma_y}\int\frac{\sigma d\epsilon}{\epsilon} \tag{8}$$

The subscript i indicates an initial value, e.g., V_i = velocity at beginning of a phase. (It should be noted that an equivalent development is found in [3].)

Equations(6)–(8) relate ξ and η with the stress and strain following the shock front during the entire Mode *I* impact phase. With equation (3) these expressions give the time dependence of η and hence of all other variables,

$$\tau = -\int_{\eta_i}^{\eta} \xi\, d\eta \tag{9}$$

The nose length is found with the help of equations (1) and (5),

$$\xi_1 = -\int_1^{\xi} (1 - \epsilon)\, d\xi \tag{10}$$

or from equations (1) and (2), if preferred,

$$\xi_1 = \int_0^{\tau} \frac{\eta d\tau}{\alpha - 1} \tag{10}$$

Since the strain following the shock front is now known as a function of time it is possible to calculate α, the variation of the cross section there as well.

Finally, the (engineering) contact stress on the target σ_c ($= F/A_0$) equals σ, the stress following the shock front which is a known function of time.

As will be shown later, Mode *I* impact occurs only when $0 < \eta \leq 1$, or when $V \leq \beta$, whre $\beta^2 = \sigma_y/\rho$.

2.2 Mode *I*—Constant True Stress (No Strain Hardening). If there is no strain hardening, the true stress is constant and the engineering stress is proportional to the cross-sectional area where strain is occurring, i.e., $\sigma = \alpha\sigma_y = \sigma_y/(1 - \epsilon)$. Then the relations just derived can be determined explicitly [3]. Note that all radicals are positive.

$$\eta = (\alpha - 1)/\sqrt{\alpha} = \epsilon/\sqrt{1 - \epsilon} \tag{6′}$$

$$\alpha = 1 + \eta^2/2 + \eta\sqrt{1 + \eta^2/4} \tag{6″}$$

Downloaded 02 May 2010 to 171.66.16.25. Redistribution subject to ASME license or copyright; see http://www.asme.org/terms/Terms_Use.cfm

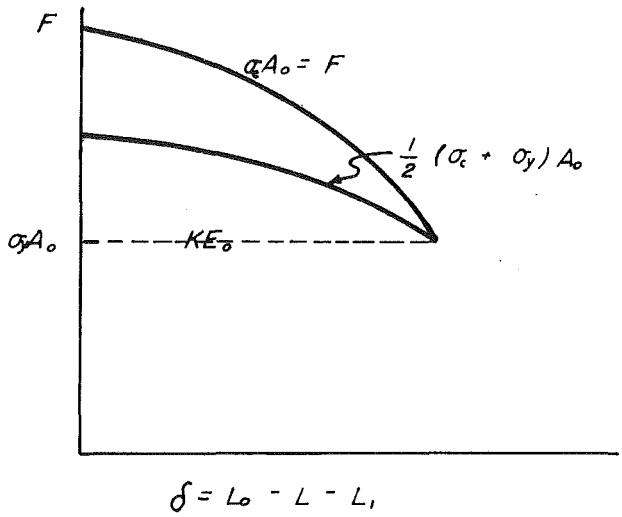

Fig. 3 Missile force versus shortening (Mode *I*)

$$\epsilon = \eta\sqrt{1+\eta^2/4} - \eta^2/2 \qquad (6''')$$

$$\xi^2 = \frac{\alpha e^{\alpha}}{\alpha_i e^{\alpha} i} = \frac{1-\epsilon_i}{1-\epsilon}\,\frac{e^{1/(1-\epsilon)}}{e^{1/(1-\epsilon_i)}} \qquad (7')$$

$$\tau = \frac{G_i - G}{\sqrt{\alpha_i e^{\alpha_i/2}}} \qquad (9')$$

where

$$G = \frac{1}{2}\int_1^{\alpha} e^{\alpha/2}\left(\frac{\alpha+1}{\alpha}\right)d\alpha$$

and by virtue of equation (6′) G can also be expressed as a function of η. Figure 5 gives $G(\eta) = G(\alpha)$.

Finally, the impact contact stress is

$$\sigma_c = \sigma = \sigma_y \alpha = \sigma_y/(1-\epsilon)$$

2.3 Mode *I*—Work and Energy Relations. Since no energy escapes from the zone of impact and no work is done on the target, the loss of kinematic energy must equal the energy absorbed in plastic deformation of the missile (including a portion converted to heat). With reference to the engineering stress-strain relation of Fig. 1, a slow change of state absorbs energy per unit volume equal to the area beneath the curve between the initial and final states. However, this is not true for a sudden change such as that associated with a shock wave, as here. In this case, the energy absorbed equals the trapezoidal area defined by the secant connecting the initial and final states [4]. Consequently, the absorbed energy in a length ΔL of the missile is

$$\Delta E = A_0 \Delta L\,(\sigma + \sigma_y)\,\epsilon/2$$

and the τ-rate of energy absorption is

$$\dot{E} = A_0 L_0 \dot{\xi}\,\epsilon(\sigma + \sigma_y)/2$$

With the help of equations (1), (2), and (5) one obtains

$$\dot{E} = A_0 L_0\,\eta\,(\sigma + \sigma_y)/2$$

The residual kinetic energy at any time is

$$KE = \rho A_0 L\,V^2/2 = \rho A_0 L_0 \beta^2 \xi \eta^2/2$$

Its τ-derivative is

$$K\dot{E} = \rho A_0 L_0 \beta^2 \eta(\dot{\xi}\eta + 2\xi\dot{\eta})/2$$

Adding equation (3) to equation (4), noting that $\sigma_y/\rho = \beta^2$, and substituting in the preceding expression gives

$$K\dot{E} = -A_0 L_0 \eta(\sigma + \sigma_y)/2$$

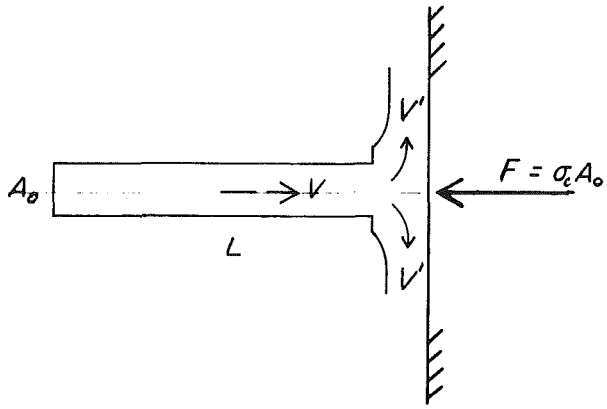

Fig. 4 Mechanics of Mode *II* impact

which confirms that the loss of kinetic energy equals the plastic work. It is to be noted that the rate of loss of kinetic energy (or the absorption of deformation energy) does not equal the contact force multiplied by the residual velocity of the tail of the missile, but rather is equal to that velocity multiplied by the *average* of the static yield force and the dynamic contact force $(\sigma_y + \sigma_c)A_0/2$. This means that the area beneath the curve of missile force-missile shortening exceeds the initial kinetic energy. In fact, that kinetic energy equals the area beneath a curve having ordinates midway between the actual missile force and a horizontal line representing the static yield load, as shown by the shaded area of Fig. 3.

3 Mode *II*—Flowing Impact

Although the mathematical expressions derived in the Mode *I* analysis have solutions for any impact velocity, it is known from experience that at sufficiently high velocities ductile materials spatter or flow parallel to the target surface. White and Griffis [4] discussed and analyzed the several possible modes of behavior for a steady-state situation (e.g., a missile of very great length or a very long rod subjected to a constant force or to constant velocity compression at the end). The present analysis treats missiles of finite length. Figure 4 illustrates the postulated mechanics of flowing impact. The rear portion of the missile is moving toward the target and encounters what can be termed a standing shock wave, i.e., a discontinuity of force, velocity, and cross section which is stationary relative to the target but has a velocity $c = V$ relative to the moving tail. In passing through the shock front the material experiences an increase of cross section to A and a corresponding decrease in velocity from V to V'. The material then flows away laterally from the zone of impact.

3.1 Analysis of Flowing Mode. The symbols used here are the same as those of the Mode *I* analysis with the addition of V', the velocity of material after passing through the shock front, and the Lagrangian wave speed c. (The Lagrangian speed is measured in a coordinate system which is, as it were, built into the missile, moving with it and shrinking or stretching as the missile is compressed or extended locally.)

Referring to Fig. 4 one obtains the following equations:

$$A_0 V = A\,V' \quad \text{(continuity)}$$

$$V - c = 0 \quad \text{(standing shock relative to tail)}$$

$$V' - c(1-\epsilon) = 0 \quad \text{(standing shock relative to nose)}$$

$$dL/dt = -c \quad \text{(geometry)}$$

$$\sigma_y = -\rho L\,dV/dt \quad \text{(equilibrium of tail portion)}$$

$$\sigma_y + \rho V^2 = \sigma + \rho V V' \quad \text{(equilibrium across shock front)}$$

Downloaded 02 May 2010 to 171.66.16.25. Redistribution subject to ASME license or copyright; see http://www.asme.org/terms/Terms_Use.cfm

$$F/A_0 = \sigma_c = \sigma_y + \rho V^2 \quad \text{(rate of change of momentum)}$$

Using the parameters already defined, together with $\eta' = V'/\beta$ and the relation $c = V$, one obtains

$$\eta = \alpha\,\eta' \tag{11}$$

$$\eta = c/\beta \tag{12}$$

$$\eta' = (1-\epsilon)\,\eta \tag{13}$$

$$\dot{\xi} = -\eta \tag{14}$$

$$\xi\,\dot{\eta} = -1 \tag{15}$$

$$\sigma/\sigma_y = 1 + \eta(\eta - \eta') \tag{16}$$

$$\sigma_c/\sigma_y = 1 + \eta^2 \tag{17}$$

Combining equations (14) and (15) gives

$$d\xi/\xi = \eta d\eta$$

Integrating this and noting that $\eta = \eta_i$ when $\xi = 1$, one obtains

$$\xi^2 = e^{(\eta^2 - \eta_i^2)} \tag{18}$$

where

$$\eta_i = V_i/\beta$$

At the same time

$$d\tau = -\xi d\eta = -e^{1/2(\eta^2 - \eta_i^2)} d\eta$$

which leads to

$$\tau = (H_i - H)\; e^{-\eta_i^2/2} \tag{19}$$

where

$$H = \int_1^{\eta} e^{\eta^2/2}\, d\eta$$

The function $H\ (\eta)$ is shown in Fig. 6 for $1.0 \le \eta \le 2.4$. Expressions for the other parameters of the process can be developed with help of the previous equations. From equations (13) and (16) one gets

$$\frac{\sigma - \sigma_y}{\sigma_y} = \eta^2 \epsilon \quad \text{or} \quad \frac{\sigma - \sigma_y}{\epsilon} = \rho V^2 \tag{20}$$

Either one of equations (20) together with the stress-strain relation determines the stress and the strain just following the shock front. The velocity of material just after passing through the shock front is also the velocity of the escaping material and is given by equation (13) when η and ϵ have been determined. Finally, the contact force is found from equation (17), namely,

$$\sigma_c/\sigma_y = 1 + \eta^2 \quad \text{or} \quad \sigma_c = \sigma_y + \rho V^2 \tag{17}$$

Note that these equations have no meaning for $\eta < 1.0$.

3.2 Mode *II*—Constant True Stress (No Strain Hardening). With no strain hardening, the engineering stress-strain relation in compression is

$$\sigma = \frac{\sigma_y}{1-\epsilon}$$

The principal change in the relations just developed is in equation (20), which becomes

$$\eta^2 = \frac{1}{1-\epsilon} = \alpha, \quad \text{or} \quad V^2 = \frac{\sigma_y}{(1-\epsilon)\rho} = \alpha\frac{\sigma_y}{\rho} \tag{20'}$$

Also

$$\eta'^2 = 1 - \epsilon = 1/\eta^2, \quad \text{or} \quad V'^2 = (1-\epsilon)\,\sigma_y/\sigma \tag{13'}$$

equations (17)–(19) are unchanged, as is Fig. 6.

3.3 Mode *II*—Work and Energy Relations. As the tail of the missile decelerates, the lost kinetic energy is absorbed by three different mechanisms:

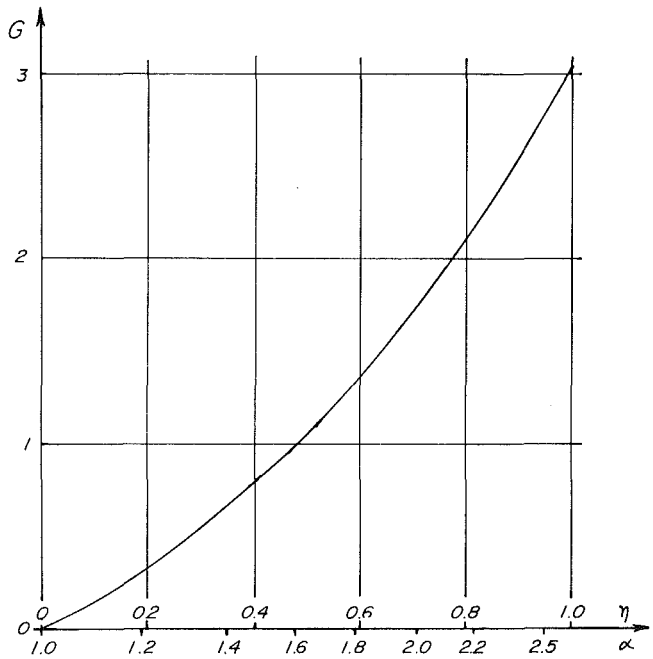

Fig. 5 $G(\eta) = G(\alpha)$ Mode I impact—no strain hardening

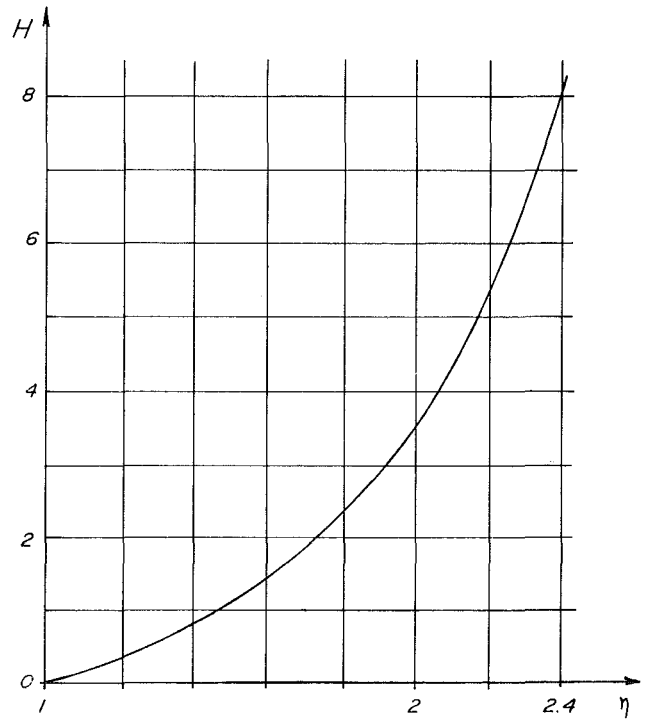

Fig. 6 $H(\eta)$ Mode II impact

(*a*) plastic deformation inside the shock front;

(*b*) kinetic energy carried away by the escaping material; and

(*c*) work done by the moving stress σ acting on the escaping flow.

This process is described by the following equation in which the four terms on the left correspond, respectively, to the rate of change of the kinetic energy of the tail and the three absorbing mechanisms.

Downloaded 02 May 2010 to 171.66.16.25. Redistribution subject to ASME license or copyright; see http://www.asme.org/terms/Terms_Use.cfm

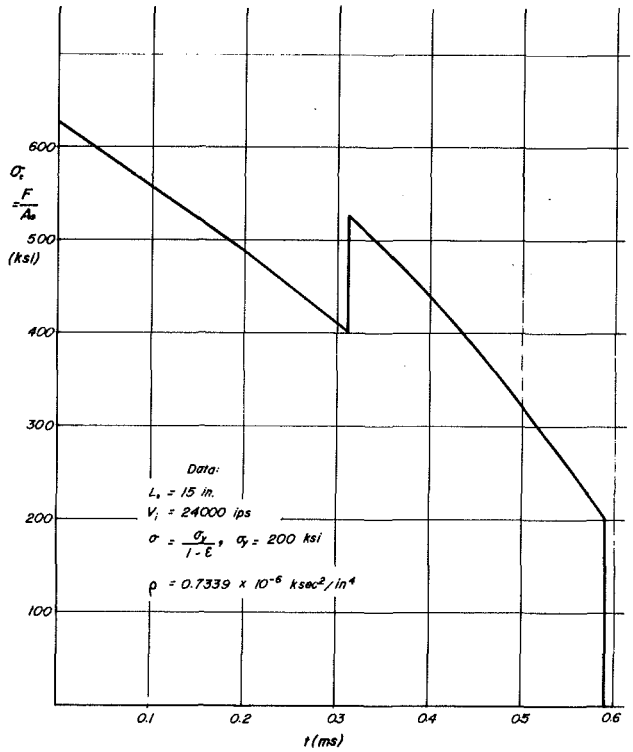

Fig. 7 Missile impact stress

$$\frac{d}{dt}(\rho A_0 L V^2/2) + \left(\frac{\sigma+\sigma_y}{2}\right)\epsilon A_0 V + \rho\frac{A_0}{2} VV'^2 + \sigma A_0 V' = \Delta E$$

Introducing dimensionless parameters results in

$$\eta^2\dot{\xi} + 2\xi\eta\dot{\eta} + \left(\frac{\sigma}{\sigma_y}+1\right)\epsilon\eta + \eta\eta'^2 + 2\frac{\sigma}{\sigma_y}\eta' = \Delta e$$

When σ/σ_y is eliminated (equation (16)), $\dot{\xi}$ (equation (14)), $\dot{\eta}$ (equation (15)), and η' (equation (13)) the result, $\Delta e = 0$, shows that the lost kinetic energy is indeed divided among the three mechanisms considered.

4 Calculation Procedure

For $V_i \leq \beta$ the missile mushrooms and the Mode *I* analysis is used. Equation (6) (6′) establishes the initial stress and strain in the nose and also the dependence of stress and strain just behind the shock front on the velocity of the tail while the latter is coming to rest. Equation (7) (7′) relates the length of the tail portion to the stress or strain behind the shock. The time dependence of all these variables is determined by equation (9) (9′). Equation (10) allows the growth of the front section to be calculated.

When $V_i > \beta$ the initial phase is Mode *II*, which is followed by Mode *I* as soon as the tail velocity drops below β. The time variation of the tail velocity V in the range $V_i \geq V \geq \beta$ is given by equation (19). Equation (20) (20′) relates the stress and strain just following the shock front to the velocity of the tail. Likewise, equation (18) gives the length of the tail as function of its velocty. The velocity of the escaping material is determined from equation (13) (13′). Equation (17) gives the time variation of the contact force.

When the tail velocity drops below β, Mode *I* response takes over, the initial conditions being determined by the final conditions of the preceding phase. Thus, the new initial velocity $V_i' = \beta$ and the initial missile length L_0' is the length of tail remaining at the end of the flowing mode.

It should be noted that as the critical velocity $V = \beta$ is passed there is a discontinuity in the contact force relation, the mushroom-stage force being the larger. Thus, the generally decreasing impact force is interrupted by a sudden jump at $V = \beta$. For a missile having constant "true" stress σ_y, the engineering contact stress is 2 σ_y at the close of the flowing mode and jumps to 2.618 σ_y at the start of the mushrooming mode.

4.1 Example. A 15 in. (0.381 m) missile, nonstrain hardening, with σ_y = 200 ksi (1.379 × 10^6 kPa), ρ = 0.7339 × 10^{-6} kip-sec^2-in.$^{-4}$ (7841 kg/m^3), V_i = 24,000 ips (609.6 m/s) strikes a rigid boundary head-on. Then β = 16,500 ips (419.3 m/s) and η_i = 1.4538. Phase *I* (Mode *II*) lasts 0.311 ms and Phase *II* (Mode *I*) 0.278 ms. At the end of Phase *I* about 43 percent of the length and mass of the missile have disappeared. The initial contact (engineering) stress is 622 ksi (4.289 × 10^6 kPa); the stress decreases to 400 ksi (2.758 × 10^6 kPa) during Phase *I*, jumps to 524 ksi (3.613 × 10^6 kPa), then drops to 200 ksi (1.379 × 10^6 kPa) by the end of the impact process. The force history is shown in Fig. 7.

References

1 White, M. P., and Griffis, L., "The Permanent Strain in a Uniform Bar due to Longitudinal Impact," ASME Journal of Applied Mechanics, Vol. 14, 1947, pp. *A*-377–*A*-343 (also U.S. Govt. Report OSRD 742, July 1942).

2 Taylor, G. I., "The Plastic Wave in a Wire Extended by an Impact Load," British Official Report RC 329, June 1942.

3 Lee, E. H., and Tupper, S. J., "Analysis of Plastic Deformation in a Steel Cylinder Striking a Rigid Target," ASME Journal of Applied Mechanics, Vol. 21, 1954, pp. 63–70.

4 White, M. P., and Griffis, L., "The Propagation of Plasticity in Uniaxial Compression," ASME Journal of Applied Mechanics, Vol. 15, 1948, pp. 256–260.

Downloaded 02 May 2010 to 171.66.16.25. Redistribution subject to ASME license or copyright; see http://www.asme.org/terms/Terms_Use.cfm

Constitutive Relations for Fiber-Reinforced Inelastic Laminated Plates

J. Aboudi

Y. Benveniste

Department of Solid Mechanics, Materials and Structures, Faculty of Engineering, Tel-Aviv University, Ramat-Aviv, 69978, Israel.

Effective stress-strain relations for inelastic unidirectional composites developed previously are used to derive the gross constitutive behavior of inelastic laminates in which every lamina is fiber-reinforced. The laminated plate is subjected to stretching and bending deformation and the strain field is described by the Love-Kirchhoff hypothesis. The distribution of the resulting stresses across the thickness is necessarily nonlinear and a Legendre expansion formalism is used to determine the stress field. Results are given for cross-ply symmetric laminates under pure cylindrical bending.

Introduction

In the analysis of inelastic fiber-reinforced laminated plates two essential problems arise: the first problem is the representation of the fiber-reinforced lamina by means of an appropriate effective constitutive law; the second problem consists in the determination of the gross behavior of the laminate.

As far as the micromechanics analysis of the lamina is considered, several attempts have been made for the modeling and description of inelastic fibrous composites. In previous papers [1, 2], the average behavior of unidirectional fiber-reinforced composites, whose constituents are elastic-viscoplastic, work-hardening materials, has been formulated. Numerous comparisons have been given in these papers with other analytical, numerical, and experimental approaches, exhibiting the reliability of the theory and thus providing strong evidence in its applicability and potential use.

It is well known that gross behavior of perfectly elastic laminated plates under combined bending and stretching deformations can be carried out in a quite straightforward manner. This is due to the fact that once the strain field is prescribed in the framework of an appropriate plate theory (e.g., Love-Kirchhoff), the stress field is immediately determined by the explicit strain-stress relations of the lamina, (see Christensen [3], for example). In inelastic laminates, however, such a direct determination of the stress field from the strain distribution is not possible due to the complexity of the nonlinear constitutive relations which appear as rate-type path-dependent laws. Furthermore, although the Love-Kirchhoff hypothesis may be adequate in describing the deformation field across the plate, the stress distribution is necessarily nonlinear and needs to be determined by an appropriate method. Similar difficulties are encountered in the theory of inelastic homogeneous shells where Wempner and Hwang [4] employed the Legendre polynomials to approximate the distribution of the stresses across the thickness of the shell.

The present paper is concerned with the determination of the constitutive laws describing the gross behavior of inelastic fiber-reinforced laminated plates. Each lamina is modeled by the effective constitutive law for elastic-viscoplastic unidirectional composites developed in [1]. The gross behavior of the laminated plate in bending and stretching deformation is determined by approximating the stress distribution across the thickness of each layer by a series of Legendre polynomials. The method of determination of the coefficients in these series is direct and does not rely on the balance of work concept used in [4] for homogeneous shells. It should be noted here that in the special case when the laminated plate, under plane stress conditions, is subjected to pure stretching only, the Legendre expansion procedure is not necessary; see for example reference [5].

In the first section of the paper we develop the constitutive relations of the inelastic laminated plate in which the deformation field is described by the Love-Kirchhoff hypothesis. These constitutive laws relate the linear strain field to the stress field in each lamina as obtained by the Legendre expansions. Due to the presence of the inelastic effects, the implementation of these relations is carried out incrementally in a stepwise manner. The description of the micromechanics, resulting in an effective law for each lamina, is given in the Appendix.

The developed theory is applied in the second section to the specific case of pure cylindrical bending of cross-ply symmetric laminates. Moment- curvature relations are given for unidirectional and three-layered cross-ply laminates made of titanium fibers and aluminum matrix, both exhibiting elastic-viscoplastic behavior.

Contributed by the Applied Mechanics Division for publication in the JOURNAL OF APPLIED MECHANICS.

Discussion on this paper should be addressed to the Editorial Department, ASME, United Engineering Center, 345 East 47th Street, New York, N.Y. 10017, and will be accepted until two months after final publication of the paper itself in the JOURNAL OF APPLIED MECHANICS. Manuscript received by ASME Applied Mechanics Division, February, 1983; final revision, July, 1983.

Copyright © 1984 by ASME

Downloaded 02 May 2010 to 171.66.16.25. Redistribution subject to ASME license or copyright; see http://www.asme.org/terms/Terms_Use.cfm

1 Constitutive Equations for the Laminated Plate

Let us consider a fiber reinforced laminated plate in which every lamina has a width of $2h_k$ with $k = 1, 2, \ldots K$ where K represents the total number of the layering. For combined bending and stretching deformations, the displacements can be assumed to be in the following form according to the Love-Kirchhoff theory:

$$u_x(x,y,z,t) = u_0(x,y,t) - z\frac{\partial w_0}{\partial x}(x,y,t)$$

$$u_y(x,y,z,t) = v_0(x,y,t) - z\frac{\partial w_0}{\partial y}(x,y,t)$$

$$u_z(x,y,z,t) = w_0(x,y,t) \tag{1}$$

where the functions u_0, v_0 and w_0 are the displacements at a reference surface $z = 0$ of a coordinate system (x,y,z) with z perpendicular to the layering and t denotes the time.

A local coordinate system located at the midplane of every lamina is now defined as $(x,y,z^{(k)})$ with $k = 1, 2, \ldots K$. In terms of this local coordinate system the displacement in equation (1) can now be written as:

$$u_x^{(k)} = u_0 - (z^{(k)} + l_k)\frac{\partial w_0}{\partial x}$$

$$u_y^{(k)} = v_0 - (z^{(k)} + l_k)\frac{\partial w_0}{\partial y}$$

$$w_z^{(k)} = w_0 \tag{2}$$

with l_k being the ordinate of the midplane of the kth layer from the plane $z = 0$ and where the dependence of the displacements on x, y, and t has been omitted in the notation for simplicity.

The infinitesimal strains ϵ_{mn} with $m,n = x,y$, are now given in every layer by

$$\epsilon_{mn}^{(k)} = \epsilon_{mn(0)}^{(k)} + z^{(k)}\epsilon_{mn(1)}^{(k)} \tag{3}$$

where

$$\epsilon_{xx(0)}^{(k)} = \frac{\partial u_0}{\partial x} - l_k\frac{\partial^2 w_0}{\partial x^2}, \epsilon_{xx(1)}^{(k)} = -\frac{\partial^2 w_0}{\partial x^2}$$

$$\epsilon_{yy(0)}^{(k)} = \frac{\partial v_0}{\partial x} - l_k\frac{\partial^2 w_0}{\partial y^2}, \epsilon_{yy(1)}^{(k)} = -\frac{\partial^2 w_0}{\partial y^2}$$

$$\epsilon_{xy(0)}^{(k)} = \left[\left(\frac{\partial u_0}{\partial y} + \frac{\partial v_0}{\partial x}\right)/2\right] - l_k\frac{\partial^2 w_0}{\partial x \partial y}, \epsilon_{xy(1)}^{(k)} = -\frac{\partial^2 w_0}{\partial x \partial y} \tag{4}$$

Introducing the nondimensionalization

$$\zeta^{(k)} = z^{(k)}/(h_k/2),$$

the following form for the strains is obtained

$$\epsilon^{(k)} = \mathbf{e}_{(0)}^{(k)} + \sqrt{3}\mathbf{e}_{(1)}^{(k)}\zeta^{(k)} \tag{5}$$

where

$$\epsilon^{(k)} = \{\epsilon_{xx}^{(k)}, \epsilon_{yy}^{(k)}, \epsilon_{xy}^{(k)}\}$$

$$\mathbf{e}_{(0)}^{(k)} = \{\epsilon_{xx(0)}^{(k)}, \epsilon_{yy(0)}^{(k)}, \epsilon_{xy(0)}^{(k)}\}$$

$$\mathbf{e}_{(1)}^{(k)}, = \{\epsilon_{xx(1)}^{(k)}, \epsilon_{yy(1)}^{(k)}, \epsilon_{xy(1)}^{(k)},\}[h_k/(2\sqrt{3})] \tag{5}$$

and no summation is implied on k.

Every layer of the laminated plate is a unidirectional fiber-reinforced composite with the constituents separately obeying a unified elastic-viscoplastic law as formulated in the work of Bodner and Partom [6]. To proceed with the formulation of the constitutive behavior of the laminated plate, an effective elastic-viscoplastic law describing every fiber-reinforced layer is needed. Such an average constitutive theory for a unidirectional fiber-reinforced inelastic medium has been developed by Aboudi in [1] and a brief summary of it is given in the Appendix for completeness. According to this constitutive law, and for the special case of plane stress, the average stresses and strains are related by:

$$\epsilon^{(k)} = \mathbf{E}^{(k)}\sigma^{(k)} + \mathbf{F}^{(k)} \tag{6}$$

where $\sigma^{(k)}$ is defined by

$$\sigma^{(k)} = \{\sigma_{xx}^{(k)}, \sigma_{yy}^{(k)}, \sigma_{xy}^{(k)}\},$$

$\mathbf{E}^{(k)}$ is a 3×3 matrix which consists of the effective elastic (initial) moduli of the composite and $\mathbf{F}^{(k)}$, denoted by,

$$\mathbf{F}^{(k)} = \{F_{xx}^{(k)}, F_{yy}^{(k)}, F_{xy}^{(k)}\}$$

represents the inelastic strains whose description is given in the Appendix.

Equation (6) is described in the Appendix in the material coordinates (x_1, x_2, x_3) of the lamina in which the fibers are aligned in the x_1-direction, with the plane stress plane being defined by $x_3 = 0$. In this material coordinate system the constants $\mathbf{E}^{(k)}$ and the functions $\mathbf{F}^{(k)}$ are denoted by $\mathbf{D}^{(k)}$ and $\mathbf{H}^{(k)}$, respectively. The relations between $(\mathbf{E}^{(k)}, \mathbf{F}^{(k)})$ and $(\mathbf{D}^{(k)}, \mathbf{H}^{(k)})$ are obtaind by using the standard transformation between the (x_1, x_2, x_3) and (x,y,z) coordinate systems.

The description of the strains $\epsilon^{(k)}$ is given in the framework of the Love-Kirchhoff theory by equation (5). To proceed with the formulation of a laminated plate theory, a description of the stresses across the plate is needed. It is well known that the essential difficulty in developing plate and shell theories of inelastic homogeneous materials lies in the formulation of the global constitutive equations, see [4]. Although the Love-Kirchhoff hypothesis may be adequate as a first approximation to the deformation field, a linear dependence of the stresses across the plate is certainly not sufficient, and a higher order distribution needs to be considered. In their work on homogeneous elastic-plastic shells Wempner and Hwang [4] have used a Legendre polynomial expansion for the stresses. It is shown in their work that an expansion in the stresses including six terms in the Legendre polynomials may be needed to formulate a theory of shells compatible with the Love-Kirchhoff hypothesis. In [4] the balance of work has been used to establish the coefficients in the expansion of the stresses.

In the present paper where a fiber-reinforced laminated plate is considered, we also employ the Legendre expansion formalism to develop the constitutive relations. The method of derivation however is different than the one adopted in [4] and a more direct and simpler approach is proposed instead of the balance of work.

Let us assume the following expansion for the stresses:

$$\sigma^{(k)} = (1+2n)^{1/2}\tau_{(n)}^{(k)}P_n(\zeta^{(k)}) \tag{7}$$

where $\tau_{(n)}^{(k)}$, defined by

$$\tau_{(n)}^{(k)} = \{\tau_{xx(n)}^{(k)}, \tau_{yy(n)}^{(k)}, \tau_{xy(n)}^{(k)}\}$$

are the coefficients of the expansion in the Legendre polynomials $P_n(\zeta^{(k)})$. In the preceding equation, summation is applied by the repeated index $n = 0, 1, 2, \ldots N$ and there is no sum on k. Equation (7), together with (5), is now introduced in (6), each side multiplied by $P_m(\zeta^{(k)})$, and then integrated between -1 and $+1$ with respect to $\zeta^{(k)}$. Making use of the orthogonality property of the Legendre polynomials yields:

$$\mathbf{e}_{(m)}^{(k)} = \mathbf{E}^{(k)}\tau_{(m)}^{(k)} + \mathbf{R}_{(m)}^{(k)} \qquad m = 0, 1, 2, \ldots, N \tag{8}$$

where

$$\mathbf{R}_{(m)}^{(k)} = [(2m+1)^{1/2}/2]\int_{-1}^{+1}\mathbf{F}_{(m)}^{(k)}P_m(\zeta^{(k)})d\zeta^{(k)} \tag{9}$$

Downloaded 02 May 2010 to 171.66.16.25. Redistribution subject to ASME license or copyright; see http://www.asme.org/terms/Terms_Use.cfm

Table 1 Elastic and inelastic constants for titanium and aluminum

	E(GPa)	ν	n^*	m^*	Z_0(MPa)	Z_1(MPa)	D_0^{-1}(sec)
Titanium	120	0.34	1	350	1000	1400	10^{-4}
Aluminum	68	0.33	5	10	25	150	10^{-4}

in which $\mathbf{e}^{(k)}_{(m)} = 0$ for $m \geq 2$. Again no sum is implied on k and m. Solving equation (8) for $\tau^{(k)}_{(m)}$ yields

$$\tau^{(k)}_{(m)} = \mathbf{C}^{(k)}(\mathbf{e}^{(k)}_{(m)} - \mathbf{R}^{(k)}_{(m)}) \tag{10}$$

where $\mathbf{C}^{(k)} = (\mathbf{E}^{(k)})^{-1}$. This equation determines the coefficients $\tau^{(k)}_{(m)}$ once the coefficients $\mathbf{e}^{(k)}_{(m)}$ and the functions $\mathbf{R}^{(k)}_{(m)}$ are known at any instant.

The field variables of the laminated plate are determined by an incremental procedure which is carried out step-by-step in time. In this procedure suppose that at two consecutive times t and $t + \Delta t$, the strains $\epsilon^{(k)}_{xx}$, $\epsilon^{(k)}_{xy}$, $\epsilon^{(k)}_{yy}$, and therefore the coefficients $e^{(k)}_{xx(m)}$, $e^{(k)}_{xy(m)}$, $e^{(k)}_{yy(m)}$ are known, and the functions $\mathbf{R}^{(k)}_{(m)}$ have been calculated from the previous step so that they are also known at time t. The stresses at the same time t are calculated by using (7) in conjunction with (10). In addition, the stresses at $t + \Delta t$ are approximated by using the same equations but with the available values of $\mathbf{R}^{(k)}_{(m)}$ at time t. Using the value of these stresses at t and $t + \Delta t$, the functions $\mathbf{F}^{(k)}_{(m)}$ at $t + \Delta t$ are calculated by the procedure described in the last paragraph of the Appendix. Having obtained $\mathbf{F}^{(k)}_{(m)}$ at $t + \Delta t$, $\mathbf{R}^{(k)}_{(m)}$ at $t + \Delta t$ is readily computed from (9) by performing a numercial integration across the lamina and the stepwise procedure can thus be continued.

2 Application: Pure Cylindrical Bending of Symmetric Cross-Ply Laminates

As an illustration of the previously formulated constitutive equations, we will develop in this section the moment-curvature relations for for symmetric cross-ply laminates in pure cylindrical bending. Results are given for composite laminae made of aluminum matrix and reinforced by titanium fibers. The Young's modulus $(E)_{\text{Ti}}$, $(E)_{\text{Al}}$ and Poisson's ratios ratios $(\nu)_{\text{Ti}}$, $(\nu)_{\text{Al}}$ determine the behavior of both constituents in the elastic range. In the inelastic range, the constituents are described by the unified theory of viscoplasticity of Bodner and Partom for isotropic work-hardening materials (see reference [6]). In the framework of this theory the elastic-viscoplastic material is specified in the inelastic range by five constants: Z_0, Z_1, m^*, n^*, and D_0. Z_0 is related to the "yield stress" of a uniaxial stress strain curve of the material and Z_1 is proportional to the ultimate stress. The material parameter m^* represents the rate of work hardening and the rate sensitivity of the material is controlled by the constant n^*. Finally D_0 is the limiting strain rate and usually can be chosen as $D_0^{-1} = 10^{-4}$ sec, serving as a reference measure of time. In Table 1, the elastic and inelastic parameters of titanium and aluminum are given. The volume fraction of the reinforcement is chosen as 50 percent in all the given examples.

In the first part of this section the special case of unidirectionally reinforced plates are considered. In the second part results are given for symmetric cross-ply laminates composed of three layers.

2(a) A Unidirectionally Reinforced Plate. Since there is only one layer in this case, $K = 1$, and no superscripts will be used in all the field variables. For the case of pure cylindrical bending with no dependence in the y-direction, the curvature of the mid-plane is defined by

$$\kappa = -\frac{\partial^2 w_0}{\partial x^2} \tag{11}$$

Therefore the only nonvanishing strain coefficient in equation (5) is given by

$$e_{xx(1)} = (h\kappa)/(2\sqrt{3}). \tag{12}$$

The resultant moment (per unit length in the y-direction) is written as

$$M = \int_{-h/2}^{h/2} \sigma_{xx} z \, dz, \tag{13}$$

so that using the expansion for σ_{xx} given in (7) we obtain

$$M = (h^2/2)\tau_{xx(1)}. \tag{14}$$

Two problems are of interest: in the first problem κ is given as a function of time and the variation of M as a function of κ is desired; in the second problem M is given as a function of time and the variation of κ as a function of M to be computed. In the first problem where κ is given, the strain field is described by equation (12), $\tau_{xx(1)}$ is computed at any time by using the stepwise procedure explained in the preceding section, and M can be determined through equation (13). It should be noted that the solution to the first problem does not in fact necessitate the Legendre expansion formalism. In other words, the curvature being given, the strain field is known from (12), the stresses can be calculated directly from (6), and the moment M is readily obtained by performing the integration in (13). Such a "direct" scheme cannot, however, be used in the inverse problem in which M is given and κ is desired and thus the Legendre expansion formalism becomes necessary. Furthermore, the "direct" scheme is not applicable in almost all problems of bending of plates in which the deformation field is not known a priori (as in boundary value problems of plates under loading).

Let us now return to the bending problem of the fiber-reinforced plate. First consider the case in which the reinforcement direction coincides with the x-axis, see Fig. (1*a*). In the first problem a constant rate of curvature $\dot{\kappa}$ is prescribed and the resultant moment M is to be calculated. It turns out that for the range of curvatures chosen in this paper, six terms in the Legendre expansions (i.e., $N = 5$) and 20 intervals in the numerical integration of equation (9) were sufficient for satisfactory accurate results. The accuracy of the obtained results was checked by computing the moment M by applying the "direct" procedure as described in the foregoing. The agreement between the two different approaches was excellent and indistinguishable up to the scale of the exhibited plots.

In Fig. (2) the nondimensional moment $M^* = M/[(E)_{Ti}h^2/2]$ versus the nondimensional curvature $\kappa^* = \kappa h/2$ is given for a unidirectional plate in which the fibers are in the x-direction. Two values are chosen for the constant rates of curvature: $\dot{\kappa}^* = 10/\text{sec}$, $\dot{\kappa}^* = 0.01/\text{sec}$. Also shown in the figure are the resulting moments for the same curvature rates in the case when the layer is made of pure titanium and pure aluminum.

Consider now the inverse problem in which M is prescribed and κ is to be determined. As mentioned before this problem necessitates the use of Legendre expansion formalism since the "direct" scheme is not applicable. For this situation once M is prescribed $\tau_{xx(1)}$ is readily obtained from (14), the corresponding $e_{xx(1)}$ is determined from (8) in the process of the incremental procedure, and thus κ is finally obtained from (12). In Fig. (3) the curvature κ^* is given versus the applied moment M^* for the constant moment rates $\dot{M}^* = 10/\text{sec}$, $\dot{M}^* = 0.1/\text{sec}$.

Downloaded 02 May 2010 to 171.66.16.25. Redistribution subject to ASME license or copyright; see http://www.asme.org/terms/Terms_Use.cfm

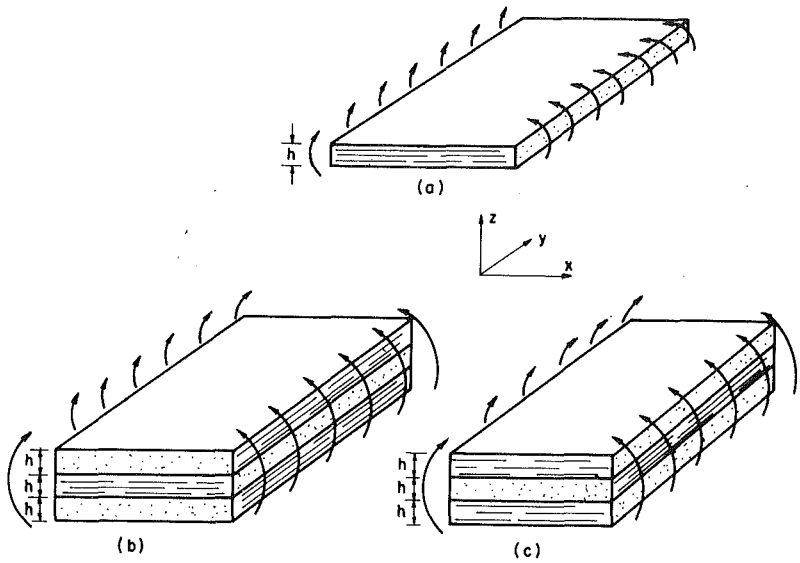

Fig. 1(*a*) Unidirectional fiber-reinforced plate. (*b*) cross-ply laminated plate (90 deg/0 deg/90 deg and (*c*) cross-ply laminated plate (0 deg/90 deg/0 deg)

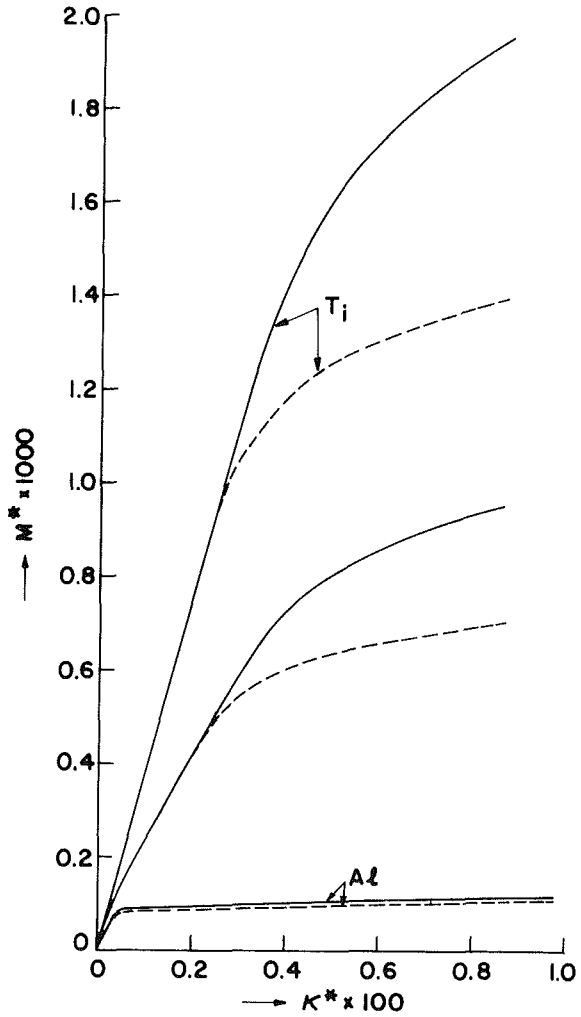

Fig. 2 Moment versus curvature for unidirectional fiber-reinforced plates in which the fibers are aligned in the x-direction, and for plates made of single materials of titanium only and aluminum only. The rates of applied curvature are $\dot{\kappa}^* = 10$/sec (——) and $\dot{\kappa}^* = 0.01$/sec (------).

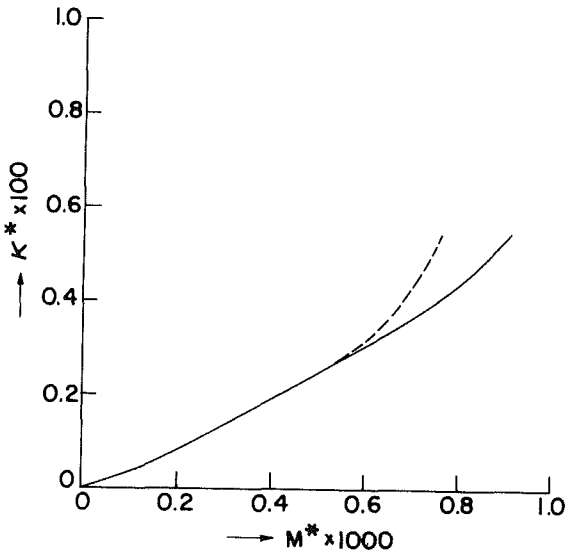

Fig. 3 Curvature versus moment for a unidirectional fiber-reinforced plate with fibers aligned in the x-direction. The rates of applied moment are $\dot{M}^* = 10$/sec (——) and $\dot{M}^* = 0.1$/sec (------).

2(*b*) Cross-Ply Laminates. Consider a three-layered cross-ply laminate in which the fibers are in the x and y-direction, and each lamina has the same width h (see Fig. 1(*b*) and 1(*c*)). The following two situations are considered.

(*i*) The middle lamina is reinforced in the x direction and the extreme layers in the y-direction (90 deg/0 deg/90 deg), Fig. 1(*b*).

(*ii*) The middle lamina is reinforced by fibers in the y-direction and the extreme layers in the x-direction (0 deg/90 deg/0 deg), Fig. 1(*c*).

In the considered pure cylindrical bending situation for a prescribed curvature κ, the shear coefficients $e^{(k)}_{xx(m)}$ are given by:

$$e^{(1)}_{xx(0)} = 0, \quad e^{(1)}_{xx(1)} = (\kappa h)/2\sqrt{3},$$
$$e^{(2)}_{xx(0)} = \pm \kappa h, \quad e^{(2)}_{xx(1)} = \kappa h/2\sqrt{3} \tag{15}$$

where the superindex $k = 1$ represents the middle layer and $k = 2$ stands for the extreme layers of the symmetric laminate (the plus and minus signs denote the upper and lower layers, respectively).

Downloaded 02 May 2010 to 171.66.16.25. Redistribution subject to ASME license or copyright; see http://www.asme.org/terms/Terms_Use.cfm

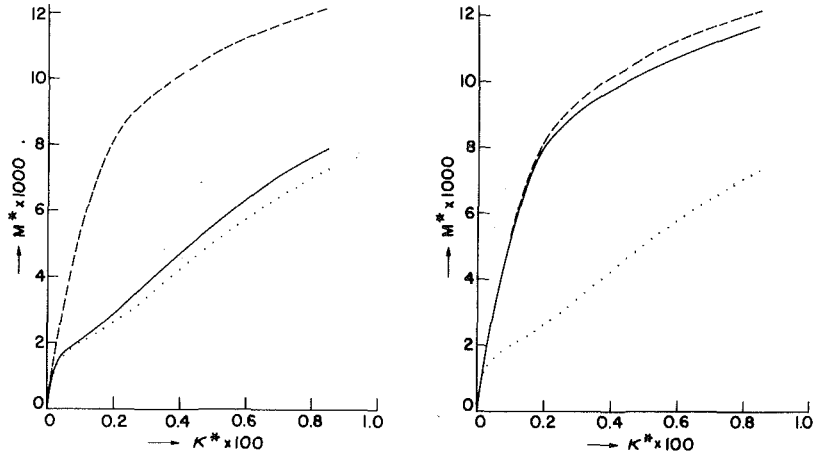

Fig. 4(*a*) Comparison between the moment-curvature relations of a cross-ply laminated plate (90 deg/0 deg/90 deg) (——) and unidirectional reinforced plates in which the fibers are oriented in the x-direction (------) and y-direction (· · ·). The rate of applied curvature is $\dot{\kappa}^* = 10$/sec. (*b*) comparison between the moment-curvature relations of a cross-ply lamianted plate (0 deg/90 deg/0 deg) (——) and unidirectional reinforced plates in which the fibers are oriented in the x-direction (------) and y-direction (· · ·). The rate of applied curvature is $\dot{\kappa}^* = 10$/sec.

The resulting moment of the three-layered laminate is given by

$$M = \int_{-h/2}^{h/2} \sigma_{xx}^{(1)} z^{(1)} dz^{(1)} + 2\int_{-h/2}^{h/2} \sigma_{xx}^{(2)} (h + z^{(2)}) dz^{(2)} \qquad (16)$$

which reduces by the Legendre expansion formalism to the following form

$$M = (h^2/2\sqrt{3})\tau_{xx(1)}^{(1)} + 2h^2 \tau_{xx(0)}^{(2)} + (h^2/\sqrt{3})\tau_{xx(1)}^{(2)} \qquad (17)$$

As before, when the strain coefficients in (15) are given, the stress coefficients in (17) can be determined and the moment M is thus known.

In Fig. 4(*a*), the moment-curvature relation is shown for the cross-ply laminated plate of Fig. 1(*b*) with $\dot{\kappa}^* = 10$ sec. The graph is compared with the two situations of unidirectionally reinforced plates in the x and y-directions, respectively, both of thickness $3h$. Similarly, we present in Fig. 4(*b*), the results for the cross-ply laminate of Fig. 1(*c*). In both cases the effect of the cross-ply arrangement is exhibited by comparison with unidirectional reinforcements.

Acknowledgment

This research was sponsored by the Air Force Office of Scientific Research/AFSC under Grant AFOSR-80-0214, through the European Office of Aerospace Research and Development (EOARD), U.S. Air Force.

References

1 Aboudi, J., "A Continuum Theory for Fiber-Reinforced Elastic-Viscoplastic Composites," *Int. J. Eng. Sci.*, Vol. 20, 1982, pp. 605-621.

2 Aboudi, J., "Effective Behavior of Inelastic Fiber-Reinforced Composites," *Int. J. Eng. Sci.*, Vol. 22, 1984.

3 Christensen, R. M., *Mechanics of Composite Materials*, Wiley, New York, 1979.

4 Wempner, G., and Hwang, C. M., "A Derived Theory of Elastic-Plastic Shells," *Int. J. Solids Structures*, Vol. 13, 1977, pp. 1123-1132.

5 Bahei-EL-Din, Y. A., and Dvorak, G. J., "Plasticity Analysis of Laminated Composite Plates, ASME JOURNAL OF APPLIED MECHANICS," Vol. 49, 1982, pp. 740-746.

6 Bodner, S. R., and Partom, Y., "Constitutive Equations for Elastic-Viscoplastic Strain Hardening Material," ASME JOURNAL OF APPLIED MECHANICS, Vol. 42, 1975, pp. 385-389.

APPENDIX

Micromechanics of the Inelastic Fiber-Reinforced Material

In this Appendix we present the effective constitutive equations for the inelastic unidirectional composite in a state of plane stress.

Consider a composite material that consists of a viscoplastic matrix reinforced by unidirectional viscoplastic fibers of square cross section. The fibers extend in the x_1-direction and are arranged in a square array in the x_2 and x_3 directions, see Fig. A.1(*a*). Let d_1 denote the dimension of the square fibers and d_2 represent the spacing of the fibers within the matrix in the x_2 and x_3 directions. Due to the assumed square arrangement, we consider a representative cell as shown in Fig. A.1(*b*). The cell is divided into four subcells α, $\beta = 1,2$ (in this appendix, repeated α or β do not imply summation), and four local system of coordinates x_1, $\bar{x}_2^{(\alpha)}$, $\bar{x}_3^{(\beta)}$ are introduced whose origins are located at the center of each subcell.

The displacement in each subcell are expressed in the form

$$u_i^{(\alpha\beta)} = W_i^{(\alpha\beta)} + \bar{x}_2^{(\alpha)} W_{i(1,0)}^{(\alpha\beta)} + \bar{x}_3^{(\beta)} W_{i(0,1)}^{(\alpha\beta)} \quad i = 1,2,3 \qquad (A.1)$$

where $W_i^{(\alpha\beta)}$ are the displacement components of the center of the subcell and $W_{i(1,0)}^{(\alpha\beta)}$, $W_{i(0,1)}^{(\alpha\beta)}$ characterize the linear dependence of the displacements on the local coordinates within the subcell.

The components of the small strain tensor are given by

$$\epsilon_{ij}^{(\alpha\beta)} = \frac{1}{2}\left[\partial_i u_j^{(\alpha\beta)} + \partial_j u_i^{(\alpha\beta)}\right] \quad i,j = 1,2,3 \qquad (A.2)$$

where in (*A*.2), the differentiation in the x_2 and x_3 directions should be with respect to the local coordinates $\bar{x}_2^{(\alpha)}$ and $\bar{x}_3^{(\beta)}$, respectively.

The continuity conditions of the displacements across the interfaces of the subcells yield [1]

$$W_i^{(11)} = W_i^{(12)} = W_i^{(21)} = W_i^{(22)} \equiv W_i,$$

$$d_1 W_{i(1,0)}^{(1\beta)} + d_2 W_{i(1,0)}^{(2\beta)} = (d_1 + d_2)\frac{\partial}{\partial x_2} W_i, \qquad (A.3)$$

$$d_1 W_{i(0,1)}^{(\alpha 1)} + d_2 W_{i(0,1)}^{(\alpha 2)} = (d_1 + d_2)\frac{\partial}{\partial x_3} W_i.$$

Downloaded 02 May 2010 to 171.66.16.25. Redistribution subject to ASME license or copyright; see http://www.asme.org/terms/Terms_Use.cfm

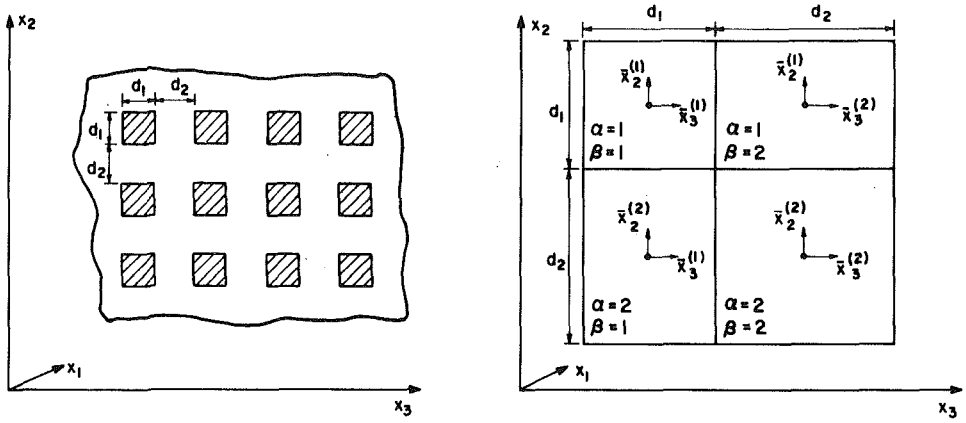

Fig. A.1(a) A fiber-reinforced composite in which the square fibers are oriented in the x_1-direction and arranged in a square array in x_2 and x_3 directions. (b) A representative cell.

The total rate of small strain is expressed as the superposition of elastic (reversible) and plastic (irreversible) components

$$\dot{\epsilon}_{ij}^{(\alpha\beta)} = \dot{\epsilon}_{ij}^{EL(\alpha\beta)} + \dot{\epsilon}_{ij}^{PL(\alpha\beta)} \quad i,j=1,2,3 \tag{A.4}$$

The elastic strain rates are related to the stress rates by Hooke's law for isotropic materials (i.e., elastic isotropy of each constituent is assumed),

$$\dot{\epsilon}_{ij}^{EL(\alpha\beta)} = \dot{\sigma}_{ij}^{(\alpha\beta)}/(2\mu_{\alpha\beta}) - (\nu_{\alpha\beta}/E_{\alpha\beta})\dot{\sigma}_{kk}^{(\alpha\beta)}\,\delta_{ij} \tag{A.5}$$

where $\mu_{\alpha\beta}$, $\nu_{\alpha\beta}$, $E_{\alpha\beta}$ are, respectively, the shear modulus, Poisson's ratio, and Young's modulus of the material, and δ_{ij} is the Kronecker delta. The plastic strain rates are given by the unified theory of Bodner-Partom [6]. In the framework of this unified theory the material behavior is represented by a single set of constitutive equations without a yield criterion, nor loading or unloading conditions. Plastic deformation always exists, but it is negligibly small when the material behavior should be essentially elastic.

Let $\bar{\epsilon}_{ij}$ denote the average strains in the composites. They are given by [1]

$$\bar{\epsilon}_{ij} = \frac{1}{2}\left[\frac{\partial}{\partial x_i} W_j + \frac{\partial}{\partial x_j} W_i\right] \tag{A.6}$$

The average stresses, $\bar{\sigma}_{ij}$, in the composite are determined from the average stresses in the subcells, $S_{ij}^{(\alpha\beta)}$, in the form

$$\bar{\sigma}_{ij} = \frac{1}{A}\sum_{\alpha,\beta=1}^{2} A_{\alpha\beta} S_{ij}^{(\alpha\beta)} \tag{A.7}$$

with

$$S_{ij}^{(\alpha\beta)} = \frac{1}{A_{\alpha\beta}}\int_{-d_\alpha/2}^{d_\alpha/2}\int_{-h_\beta/2}^{h_\beta/2} \sigma_{ij}^{(\alpha\beta)} dx_2^{-(\alpha)} dx_3^{-(\beta)}$$

where $A_{\alpha\beta} = d_\alpha d_\beta$ and $A = (d_1 + d_2)^2$. The expressions for $S_{ij}^{(\alpha\beta)}$ are given in [1, equations (49)]. For the plane stress situation ($x_1 - x_2$ plane) considered here, the relevent expressions of $S_{ij}^{(\alpha\beta)}$ are given by

$$S_{11}^{(\alpha\beta)} = \lambda_{\alpha\beta}\left[\frac{\partial}{\partial x_1} W_1 + W_{2(1,0)}^{(\alpha\beta)} + W_{3(0,1)}^{(\alpha\beta)}\right] + 2\mu_{\alpha\beta}\left[\frac{\partial}{\partial x_1} W_1 - L_{11}^{(\alpha\beta)}\right],$$

$$S_{22}^{(\alpha\beta)} = \lambda_{\alpha\beta}\left[\frac{\partial}{\partial x_1} W_1 + W_{2(1,0)}^{(\alpha\beta)} + W_{3(0,1)}^{(\alpha\beta)}\right] + 2\mu_{\alpha\beta}\left[W_{2(1,0)}^{(\alpha\beta)} - L_{22}^{(\alpha\beta)}\right],$$

$$S_{33}^{(\alpha\beta)} = \lambda_{\alpha\beta}\left[\frac{\partial}{\partial x_1} W_1 + W_{2(1,0)}^{(\alpha\beta)} + W_{3(0,1)}^{(\alpha\beta)}\right] + 2\mu_{\alpha\beta}\left[W_{3(0,1)}^{(\alpha\beta)} - L_{33}^{(\alpha\beta)}\right],$$

$$S_{12}^{(\alpha\beta)} = \mu_{\alpha\beta}\left[\frac{\partial}{\partial x_1} W_2 + W_{1(1,0)}^{(\alpha\beta)} - 2L_{12}^{(\alpha\beta)}\right], \tag{A.8}$$

$\bar{\sigma}_{33} = 0$, with $\lambda_{\alpha\beta}$, and $\mu_{\alpha\beta}$ being the Lamé constants. In (A.8), $L_{ij}^{(\alpha\beta)}$ involve the inelastic effects in the subcell. Their evolution law is given by

$$\dot{L}_{ij}^{(\alpha\beta)} = \Lambda_{\alpha\beta}\hat{S}_{ij}^{(\alpha\beta)} \tag{A.9}$$

with $\hat{S}_{ij}^{(\alpha\beta)} = S_{ij}^{(\alpha\beta)} - S_{kk}^{(\alpha\beta)}\,\delta_{ij}/3$ being the deviator of $S_{ij}^{(\alpha\beta)}$. In (A.9), $\Lambda_{\alpha\beta}$ is the flow rule function (which depends on $S_{ij}^{(\alpha\beta)}$) whose exact form is given in the framework of the Bodner-Partom unified theory in reference [1].

The relevant continuity conditions of the displacement for the plane stress situation follow from (A.3):

$$d_1 W_{1(1,0)}^{(1\beta)} + d_2 W_{1(1,0)}^{(2\beta)} = (d_1 + d_2)\frac{\partial}{\partial x_2} W_1,$$

$$d_1 W_{2(1,0)}^{(1\beta)} + d_2 W_{2(1,0)}^{(2\beta)} = (d_1 + d_2)\frac{\partial}{\partial x_2} W_2,$$

$$d_1 W_{3(0,1)}^{(\alpha 1)} + d_2 W_{3(0,1)}^{(\alpha 2)} = (d_1 + d_2)\frac{\partial}{\partial x_3} W_3, \tag{A.10a,b,c}$$

The conditions for the continuity of the stresses across the subcells interfaces give [1]

$$S_{12}^{(1\beta)} = S_{12}^{(2\beta)}, S_{22}^{(1\beta)} = S_{22}^{(2\beta)}, S_{33}^{(\alpha 1)} = S_{33}^{(\alpha 2)}. \tag{A.11a,b,c,}$$

Equations (A.10) and (A.11) together with the evolution laws (A.9) suffice for the determination of the average behavior of the unidirectional reinforced material as shown in the sequel.

The average strain in the composite can be represented in the form:

$$\bar{\epsilon} = \mathbf{D}\bar{\sigma} + \mathbf{H} \tag{A.12}$$

where

$$\bar{\epsilon} = \{\bar{\epsilon}_{11}, \bar{\epsilon}_{22}, \bar{\epsilon}_{12}\},$$

$$\bar{\sigma} = \{\bar{\sigma}_{11}, \bar{\sigma}_{22}, \bar{\sigma}_{12}\},$$

and

$$\mathbf{H} = \{H_{11}, H_{22}, H_{12}\}. \tag{A.13}$$

In (A.12), $\mathbf{D}$ is a 3×3 matrix which consists of the effective elastic (initial) moduli and $\mathbf{H}$ represents the inelastic strains in the unidirectional composite. The vanishing elements of $\mathbf{D}$ are: $D_{13} = D_{31} = D_{23} = D_{32} = 0$. The elements D_{11}, $D_{12} = D_{21}$, D_{22} are obtained (after setting the inelastic variables equal to zero) by eliminating the eight microstructure variables $W_{2(1,0)}^{(\alpha\beta)}$, $W_{3(0,1)}^{(\alpha\beta)}$, and $\partial/\partial x_3\ W_3$, from the nine equations (A.10b,c), (A.11b,c), and $\bar{\sigma}_{33} = 0$. The solution for D_{33} can be readily obtained in the form

Downloaded 02 May 2010 to 171.66.16.25. Redistribution subject to ASME license or copyright; see http://www.asme.org/terms/Terms_Use.cfm

$$D_{33} = 1/(2\bar{G}_A) \tag{A.14}$$

where

$$\bar{G}_A = \frac{\mu_2}{d_1 + d_2} \frac{\mu_1(d_1^2 + d_2^2 + d_1 d_2) + \mu_2 d_1 d_2}{\mu_1 d_2 + \mu_2 d_1} \tag{A.15}$$

is the effective axial elastic shear modulus, and μ_1, μ_2 are the elastic rigidities of the fiber and matrix, respectively (i.e., $\mu_1 = \mu_{11}$ and $\mu_2 = \mu_{\alpha\beta}$ otherwise).

The determination of the inelastic strains, **H**, is carried out by an incremental procedure as follows. Suppose that the effective stresses, $\bar{\sigma}$, are given at two consecutive times t and $t + \Delta t$, and it is required to compute H at time $t + \Delta t$ (Δt is an increment in time). It is assumed that $L_{ij}^{(\alpha\beta)}$ have been obtained at time t by integrating their evolution equation (*A*.9). Therefore we have 16 algebraic equations: (*A*.10), (*A*.11), and the known expressions for $\bar{\sigma}_{11}$, $\bar{\sigma}_{22}$, $\bar{\sigma}_{12}$ together with $\bar{\sigma}_{33} = 0$. In these equations, the 16 unknowns are: $W_{1(1,0)}^{(\alpha\beta)}$, $W_{2(1,0)}^{(\alpha\beta)}$, $W_{3(0,1)}^{(\alpha\beta)}$, $\bar{\epsilon}_{11}$, $\bar{\epsilon}_{22}$, $\bar{\epsilon}_{33}$, and $\bar{\epsilon}_{12}$, with $\bar{\epsilon}_{12} = \partial/\partial x_2$ $W_1 = \partial/\partial x_1$ W_2 in (*A*.8) and (*A*.10*a*) to exclude rotation dependence in pure shear of the constitutive equations. These readily determine $S_{ij}^{(\alpha\beta)}$ at time t so that $\dot{L}_{ij}^{(\alpha\beta)}(t)$ are known from (*A*.9). Consequently, $L_{ij}^{(\alpha\beta)}$ can be predicted, tentatively, at time $t + \Delta t$ using the improved Euler-Cauchy integration procedure. Using the predicted values of $L_{ij}^{(\alpha\beta)}$ and the known values of $\bar{\sigma}$ at $t + \Delta t$, the corrected values of $L_{ij}^{(\alpha\beta)}$ can be obtained by repeating the foregoing process which also provides $\bar{\epsilon}$ at $t + \Delta t$. Accordingly, the inelastic strains, **H**, can be computed at time $t + \Delta t$ by using (*A*.12).

Downloaded 02 May 2010 to 171.66.16.25. Redistribution subject to ASME license or copyright; see http://www.asme.org/terms/Terms_Use.cfm

W. Wojewódzki
Assistant Professor.

R. Bukowski
Research Assistant.

Institute of Structural Mechanics,
Warsaw Technical University,
Al. Armii Ludowej 16,
PL-00-637 Warsaw, Poland

Influence of the Yield Function Nonlinearity and Temperature in Dynamic Buckling of Viscoplastic Cylindrical Shells

A viscoplastic theory of dynamic buckling is developed for cylindrical shells subjected to uniform radially inward impulses. The influence of the yield function nonlinearity and elevated temperature on the magnitude of displacements, buckling mode, and threshold impulse is investigated. Asymmetrical and axisymmetrical modes of buckling are considered. The asymmetrical mode is proved to exist. The obtained theoretical results are compared with existing experiments.

Introduction

The material viscosity exerts a considerable influence on the dynamic buckling of shells and must therefore be taken into account in theoretical analyses.

Experimental investigations in the uniaxial stress state show that the function $\sigma(\dot{\epsilon})$ varies nonlinearly. Bodner and Symonds [1] pointed out that the power function describes the experimental results in a satisfactory manner. In a certain strain-rate range this curve may be linearized in two different ways (Fig. 1). The first linearization consists in drawing of a line tangent to the curve at the point where the strain rate is at its maximum. The equation of this tangent expressing a linear law of viscoplastic flow was used by Florence [2–4] for the solution of the buckling problem of a cylindrical shell loaded by radial pressure impulse. The second approximation results from the interpretation of Perzyna's equation [5] in the uniaxial stress state for $\delta = 1$, and is represented in Fig. 1 by the straight lines with a slope determined by σ_0/γ^*. In the triaxial stress state this case corresponds to the linear function $\phi(F) = F$ where F denotes the static yield function. Such constitutive equations were applied by Wojewódzki [6, 7] to analyze the dynamic instability of shells of revolution. Material viscosity was found to influence considerably the buckling process and, in particular its duration, the magnitude of final deformation, the buckling mode, and critical impulse. Comparison of the computed values for buckling modes with the experimental findings for shells made of mild steel, reported in [2], has shown that the theoretical results are sometimes much below the experimental ones. Those discrepancies are caused mainly by the assumption of the linear function $\phi(F)$.

Dynamic buckling of cylindrical and spherical shells made of an elastic-plastic or a rigid-plastic material with linear strain hardening without viscous effects has been considered in numerous papers: Abrahamson and Goodier [8], Anderson and Lindberg [9], Vaughan and Florence [10], Struiver [11], Jones et al. [12, 13], and others. Dynamic instability of structures is discussed at length by Grybos in his monograph [14].

The present paper aims at taking the function $\phi(F) = F^\delta$ and analyzing the influence of such nonlinearity on the buckling of shells. In the uniaxial stress state this case corresponds to the power function $\sigma(\dot{\epsilon})$ suggested by Bodner and Symonds [1]. A thin cylindrical shell will be considered, loaded by a uniform radially inward impulse pressure. The influence of elevated temperature will also be shown. The obtained theoretical results will be compared with some available experimental data.

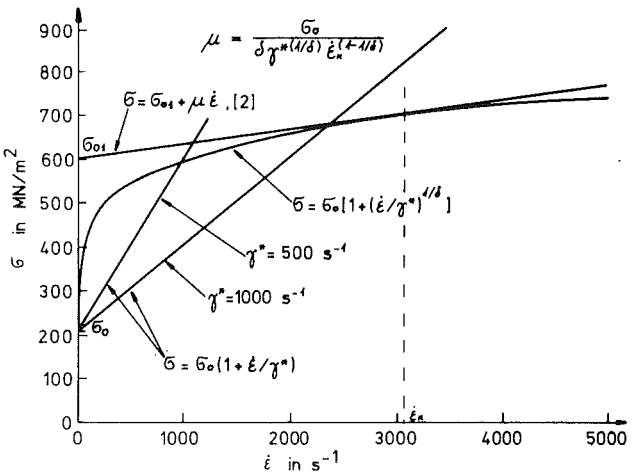

Fig. 1 Uniaxial curve $\sigma(\dot{\epsilon})$ and linearizations

Contributed by the Applied Mechanics Division for publication in the JOURNAL OF APPLIED MECHANICS.

Discussion on this paper should be addressed to the Editorial Department, ASME, United Engineering Center, 345 East 47th Street, New York, N.Y. 10017, and will be accepted until two months after final publication of the paper itself in the JOURNAL OF APPLIED MECHANICS. Manuscript received by ASME Applied Mechanics Division, September, 1982; final revision, May, 1983.

Copyright © 1984 by ASME
Downloaded 02 May 2010 to 171.66.16.25. Redistribution subject to ASME license or copyright; see http://www.asme.org/terms/Terms_Use.cfm

Basic Equations

Geometric Equations. The coordinate system, notation, and dimensions used to describe the shell are all shown in Fig. 2. According to the Kirchhoff-Love hypothesis the components of the strain rate tensor are (dots denote time differentiation)

$$\dot{\epsilon}_x = \frac{\partial \dot{u}}{\partial x} - z\frac{\partial^2 \dot{w}}{\partial x^2}, \quad \dot{\epsilon}_\vartheta = \frac{1}{a}\left(\frac{\partial \dot{v}}{\partial \vartheta} - \dot{w}\right) - \frac{z}{a^2}\left(\frac{\partial^2 \dot{w}}{\partial \vartheta^2} + \frac{\partial \dot{v}}{\partial \vartheta}\right),$$

$$\dot{\epsilon}_{x\vartheta} = \dot{\epsilon}_{\vartheta x} = \frac{1}{2a}\left(a\frac{\partial \dot{v}}{\partial x} + \frac{\partial \dot{u}}{\partial \vartheta}\right) - \frac{z}{a}\left(\frac{\partial^2 \dot{w}}{\partial x \partial \vartheta} + \frac{1}{2}\frac{\partial \dot{v}}{\partial x} - \frac{1}{2a}\frac{\partial \dot{u}}{\partial \vartheta}\right). \tag{1}$$

Constitutive Equations. The influence of work hardening, strain rate, and temperature on the material response can be described by the following equations given by Perzyna and Wierzbicki [5, 15]:

$$\dot{\epsilon}_{ij} = \frac{\gamma(\theta)}{2}\langle\phi(F)\rangle\frac{S_{ij}}{J_2^{1/2}}, \quad F = \frac{J_2^{1/2}}{k(\theta)} - 1,$$

$$\langle\phi(F)\rangle = \begin{cases} \phi(F) & \text{for } F > 0, \\ 0 & \text{for } F \le 0, \end{cases} \tag{2}$$

where $\dot{\epsilon}_{ij}$ is the strain rate tensor, $J_2 = 1/2\, S_{ij}S_{ij}$ denotes the second invariant of stress deviator S_{ij}, $k(\theta) = \sigma_0(\theta)/3^{1/2}$, $\sigma_0(\theta)$ is the static yield stress, $\gamma(\theta)$ is the viscosity coefficient of the material, and θ denotes the temperature. The nonlinear function $\phi(F) = F^\delta$ will be assumed where F denotes the static yield function and δ is the material constant. The elastic strains are omitted and the material is incompressible, $\dot{\epsilon}_{ii} = \dot{\sigma}_{ii}/3K + \alpha_0\dot{\theta} = 0$, where K is the modulus of volume expansion and α_0 denotes the coefficient of thermal expansions. Experimental results confirmed a suitability of the description of the behavior of metals with only two quantities k and γ dependent on the temperature and ϕ itself independent of it, see [15]. In the uniaxial stress state we get from (2) the equation $\sigma/\sigma_0(\theta) = 1 + (\dot{\epsilon}/\gamma^*(\theta))^{1/\delta}$, $\gamma^* = \gamma/3^{1/2}$, shown in Fig. 1. The functions $k(\theta)$ and $\gamma(\theta)$ for mild steel, established on the basis of experimental results of Maiden, Campbell [16], and Manjoine [17] have the form ($\delta = 5$)

$$k(\theta) = 119.51\exp[0.45(288/\theta - 1)], \quad [\text{MPa}],$$
$$\gamma(\theta) = 60.24[1 + 2.6((220-\theta)/273)^2], [5s^1], \tag{3}$$

where the temperature θ is expressed in [K].

The shell operates at constant temperature and no constraints are imposed on the deformation. This results in no arising the stresses due to the coefficient of thermal expansion of the material. The applied impulse is regarded to be accidental one.

In the state of compressive viscoplastic flow, the resulting homogeneous deformation (i.e., decreasing of the shell radius under unchanged circular symmetry conditions) is, in general, unstable since any small perturbation of the deformation exhibits a tendency to increase during the subsequent deformation process. The perturbations are caused by the displacement and loading imperfections. A characteristic feature of dynamic buckling is the significance of inertial effects in restraining the growth of buckling mode amplitudes at an early stage of the motion. These effects result in the yielding before the instabilities become dominant.

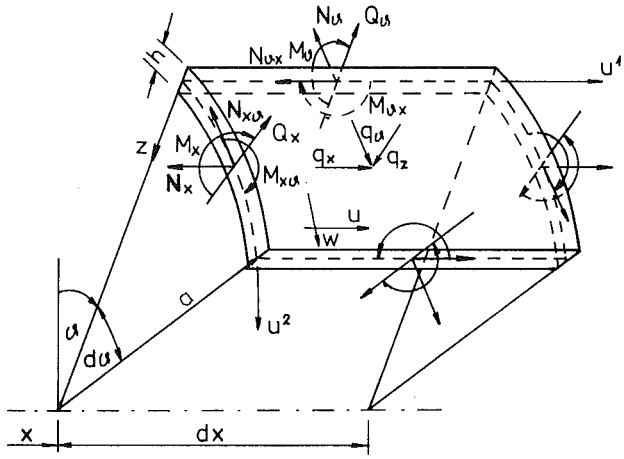

Fig. 2 Shell element notation

Analytically, the problem is formulated as a superposition of small perturbations on the basic unperturbed motion. Thus

$$u = u_0(x,t) + u_p(x,\vartheta,t), \quad v = v_p(x,\vartheta,t),$$
$$w = w_0(t) + w_p(x,\vartheta,t). \tag{4}$$

The amplitudes of perturbed motion are restricted to be so small that the homogeneous compressive deformation predominates over local bending.

Assuming $\sigma_{33} = 0$, $\dot{\epsilon}_{13} = \dot{\epsilon}_{23} = 0$, according to the Kirchhoff-Love theory of shells, we get from (2), for $J_2^{1/2} > k$ the following nonlinear equations:

$$\sigma_{\alpha\beta} = A(\dot{\epsilon}_{\alpha\beta} + \dot{\epsilon}_{\rho\rho}\delta_{\alpha\beta}),$$

$$\delta_{\alpha\beta} = \begin{cases} 1, & \alpha = \beta, \\ 0, & \alpha \ne \beta, \end{cases} \quad \alpha,\beta,\rho = 1,2 \tag{5}$$

where

$$A = \frac{k}{\dot{I}_2^{1/2}}\left[1 + \left(\frac{2\dot{I}_2^{1/2}}{\gamma}\right)^{1/\delta}\right],$$

$$\dot{I}_2 = \frac{1}{2}(\dot{\epsilon}_{\alpha\beta} + \dot{\epsilon}_{\rho\rho}\delta_{\alpha\beta})\dot{\epsilon}_{\alpha\beta}. \tag{6}$$

$\dot{I}_2$ is the second invariant of the strain rate deviator. The loading criterion $J_2^{1/2} > k$ is equivalent to $\dot{I}_2 > 0$.

The constitutive equations (5) can be linearized by their expansion into Taylor's series in three variables in the vicinity of predominant state of strain rate $\dot{\epsilon}^0_{\alpha\beta}$ and by retaining two terms only. We obtain:

$$\sigma_{\alpha\beta} = A^0(\dot{\epsilon}_{\alpha\beta} + \dot{\epsilon}_{\rho\rho}\delta_{\alpha\beta}) + B^0[(\dot{\epsilon}^0_{\gamma\varphi} + \dot{\epsilon}^0_{\rho\rho}\delta_{\gamma\varphi})(\dot{\epsilon}_{\gamma\varphi} - \dot{\epsilon}^0_{\gamma\varphi})](\dot{\epsilon}^0_{\alpha\beta} + \dot{\epsilon}^0_{\delta\delta}\delta_{\alpha\beta}) \tag{7}$$

where

$$A^0 = \frac{k}{\dot{I}_2^{0\,1/2}}\left[1 + \left(\frac{2\dot{I}_2^{0\,1/2}}{\gamma}\right)^{1/\delta}\right],$$

$$B^0 = \frac{k}{2}(\dot{I}_2^0)^{-3/2}\left[-1 + \frac{1-\delta}{\delta}\left(\frac{2\dot{I}_2^{0\,1/2}}{\gamma}\right)^{1/\delta}\right],$$

$$\dot{I}_2^0 = \frac{1}{2}(\dot{\epsilon}^0_{\beta\gamma} + \dot{\epsilon}^0_{\alpha\alpha}\delta_{\beta\gamma})\dot{\epsilon}^0_{\beta\gamma}, \quad \alpha,\beta,\ldots = 1,2. \tag{8}$$

Dynamic Equilibrium Equations. The following equations of equilibrium are employed, [18], Fig. 2:

$$\frac{\partial(A_\nabla N_\alpha)}{\partial u^\alpha} + \frac{\partial(A_\alpha N_{\nabla\alpha})}{\partial u^\nabla} + (-1)^\alpha(\bar{r}_\alpha N_{\alpha\nabla} - \bar{r}_\nabla N_\nabla) + (-1)^\nabla(\bar{q}_\alpha Q_\alpha + \bar{p}_\nabla Q_\nabla) + aP^\alpha = 0,$$

Downloaded 02 May 2010 to 171.66.16.25. Redistribution subject to ASME license or copyright; see http://www.asme.org/terms/Terms_Use.cfm

$$a\frac{\partial Q_x}{\partial x}+\frac{\partial Q\vartheta}{\partial\vartheta}-\tilde{q}_1N_x-\tilde{p}_2N_{\vartheta x}+\tilde{p}_1N_{x\vartheta}+\tilde{q}_2N_\vartheta+aP^3=0,$$

$$\frac{\partial(A_\nabla M_{\alpha\nabla})}{\partial u^\alpha}-\tilde{r}_\alpha M_\alpha+(-1)^\alpha\left(\frac{\partial(A_\alpha M_\nabla)}{\partial u^\nabla}+\tilde{r}_\nabla M_{\nabla\alpha}-aQ_\nabla\right)=0,$$

$$\tilde{p}_1M_x+\tilde{p}_2M_\vartheta-\tilde{q}_1M_{x\vartheta}+\tilde{q}_2M_{\vartheta x}+a(N_{\vartheta x}-N_{x\vartheta})=0, \tag{9}$$

where

$u^1=x,\ u^2=\vartheta,\ A_1=1,\ A_2=a,\ \alpha=1,2$ or x,ϑ;

$$\nabla=3-\alpha,\ \tilde{p}_1=\frac{\partial}{\partial x}\left(\frac{\partial w}{\partial\vartheta}+v\right),\ \tilde{p}_2=-\tilde{p}_1,\ \tilde{q}_1=-a\frac{\partial^2 w}{\partial x^2},$$

$$\tilde{q}_2=1+\frac{1}{a}\frac{\partial^2 w}{\partial\vartheta^2}+\frac{\partial v}{\partial\vartheta},\ \tilde{r}_1=a\frac{\partial^2 v}{\partial x^2},\ \tilde{r}_2=\frac{\partial}{\partial x}\left(\frac{\partial v}{\partial\vartheta}-w\right),$$

$$P^1=q_x-\rho h\ddot{u},\ P^2=q_y-\rho h\ddot{v},\ P^3=q_z-\rho h\ddot{w} \tag{10}$$

and ρ denotes the density of material. The resultant forces and moments obtained from (7) and (1) have the form:

$$N_\alpha=\int_{-\frac{h}{2}}^{\frac{h}{2}}\sigma_\alpha dz=N_\alpha^0+D_\alpha a\frac{\partial\dot{u}_p}{\partial x}+D_{\alpha+1}\left(\frac{\partial\dot{v}_p}{\partial\vartheta}-\dot{w}_p\right),$$

$$N_{x\vartheta}=N_{\vartheta x}=\int_{-\frac{h}{2}}^{\frac{h}{2}}\sigma_{x\vartheta}dz=D_0\left(a\frac{\partial\dot{v}_p}{\partial x}+\frac{\partial\dot{u}_p}{\partial\vartheta}\right), \tag{11}$$

$$M_\alpha=\int_{-\frac{h}{2}}^{\frac{h}{2}}\sigma_\alpha z dz=-\frac{h^2}{12}\left[D_\alpha a\frac{\partial^2\dot{w}_p}{\partial x^2}+\frac{D_{\alpha+1}}{a}\left(\frac{\partial^2\dot{w}_p}{\partial\vartheta^2}+\frac{\partial\dot{v}_p}{\partial\vartheta}\right)\right],$$

$$M_{x\vartheta}=-M_{\vartheta x}=-\int_{-\frac{h}{2}}^{\frac{h}{2}}\sigma_{x\vartheta}z dz=\frac{h^2}{6}D_0\left(\frac{\partial^2\dot{w}_p}{\partial x\partial\vartheta}+\frac{1}{2}\frac{\partial\dot{v}_p}{\partial x}-\frac{1}{2a}\frac{\partial\dot{u}_p}{\partial\vartheta}\right),$$

where

$$D_0=A^0h/2a,\quad D_1=4D_0+\kappa_1^2B^0h/a,$$

$$D_2=2D_0+\kappa_1\kappa_2B^0h/a,\quad D_3=4D_0+\kappa_2^2B^0h/a,$$

$$\kappa_\alpha=(3-\alpha)\frac{\partial\dot{u}_0}{\partial x}+\alpha\frac{\dot{w}_0}{a}, \tag{12}$$

and

$$N_\alpha^0=2D_0a\kappa_\alpha,\quad N_{\alpha\eta}^0=0,\quad M_\alpha^0=M_{\alpha\eta}^0=0,\quad \alpha,\eta=1,2. \tag{13}$$

The indices 0 and p denote the unperturbed and perturbed quantities, respectively.

Differential Equations of Motion

Unperturbed Motion. Substituting (13) into (9) gives the set of two strongly nonlinear equations describing the unperturbed motion. The solution is to be found by numerical integration. However, the problem can be simplified by taking the relation

$$\alpha_1=-\dot{\epsilon}_x/\dot{\epsilon}_\vartheta\quad\text{for}\quad z=0,\quad 0\le\alpha_1\le 1/2. \tag{14}$$

The change of the value α_1 from 1/2 to 0 corresponds to the variation of the length of the shell from very short to infinitely long. The relation was originally proposed in [10]. On the basis of experimental tests on cylindrical shells the relation $\alpha_1=\frac{1}{2}\exp(-l/4a)$ was determined. In [3] the different relation was proposed, $\alpha_1=\frac{1}{2}[\cosh(\sqrt{3}l/4a)]^{-1}$. The values of α_1 calculated from these two relations do not differ appreciably and the discrepancies involved have negligible influence on numerical results. From (14) we obtain $\partial\dot{u}_0/\partial x=\alpha_1\dot{w}_0/a$. The shell is subjected to the radial pressure impulse, thus $q_x^0=0$. The longitudinal deformation occurs freely during motion, there being no axial restraint and no axial forces at the ends of the shell. Longitudinal inertia will also be disregarded. In such situations equations (9) reduce to the equation

$$N_\vartheta^0+a(q_z^0(t)-\rho h\ddot{w}_0)=0. \tag{15}$$

Let us consider the shell loaded by an ideal radial impulse pressure (uniform initial velocity V_0).

In this case $q_z^0(t)=0$ and we infer from (15) that $w_0(t)$ must be a solution to the nonlinear (for $\delta\neq 1$) initial value problem

$$\ddot{w}_0+c\dot{w}_0^{1/\delta}=-\beta,\quad w_0(0)=0,\quad \dot{w}_0(0)=V_0, \tag{16}$$

where

$$c=\left(\frac{2}{\gamma}\right)^{1/\delta}\frac{(2-\alpha_1)kR^{(1-\delta)/2\delta}}{\rho a^{(1+\delta)/\delta}},$$

$$\beta=\frac{(2-\alpha_1)k}{a\rho R^{1/2}},\quad R=\alpha_1^2-\alpha_1+1.$$

Introducing a parameter

$$\frac{dw_0^*(\zeta)}{dt}=(-\zeta)^\delta \tag{17}$$

into (16), we obtain

$$t(\zeta)=(-1)^{\delta-1}\frac{\delta}{\beta}\int_{-V_0^{1/\delta}}^{\zeta}\frac{\zeta^{\delta-1}}{1-\frac{c}{\beta}\zeta}d\zeta$$

$$=(-1)^\delta\frac{\delta\beta^{\delta-1}}{c^\delta}\left\{\sum_{i=1}^{\delta-1}\frac{1}{\delta-i}\left[\left(\frac{c}{\beta}\zeta\right)^{\delta-i}-\left(-\frac{c}{\beta}V_0^{1/\delta}\right)^{\delta-i}\right]+ln\frac{1-\frac{c}{\beta}\zeta}{1+\frac{c}{\beta}V_0^{1/\delta}}\right\}. \tag{18}$$

From (17) and (18) we get the parametric solution to the equation (16),

$$w_0^*(\zeta)=(-1)^\delta\frac{\delta}{\beta}\int_{-V_0^{1/\delta}}^{\zeta}\frac{\zeta^{2\delta-1}}{1-\frac{c}{\beta}\zeta}d\zeta$$

$$=(-1)^{\delta-1}\frac{\delta\beta^{2\delta-1}}{c^{2\delta}}\left\{\sum_{i=1}^{2\delta-1}\frac{1}{2\delta-i}\left[\left(\frac{c}{\beta}\zeta\right)^{2\delta-i}-\left(-\frac{c}{\beta}V_0^{1/\delta}\right)^{2\delta-i}\right]+ln\frac{1-\frac{c}{\beta}\zeta}{1+\frac{c}{\beta}V_0^{1/\delta}}\right\} \tag{19}$$

where $w_0^*(\zeta)\equiv w_0(t(\zeta))$ and $-V_0^{1/\delta}\le\zeta\le 0$. The motion ceases at the instant $t=t_f$, $(\zeta=0)$, when $\dot{w}_0(t)=0$. Thus

Downloaded 02 May 2010 to 171.66.16.25. Redistribution subject to ASME license or copyright; see http://www.asme.org/terms/Terms_Use.cfm

$$t_f = (-1)^{\delta+1}\frac{\delta\beta^{\delta-1}}{c^\delta}\left[\sum_{i=1}^{\delta-1}\frac{1}{\delta-i}\left(-\frac{c}{\beta}V_0^{1/\delta}\right)^{\delta-i} + ln\left(1+\frac{c}{\beta}V_0^{1/\delta}\right)\right] \tag{20}$$

and the final displacements

$$w_{0f}^* = (-1)^{\delta}\frac{\delta\beta^{2\delta-1}}{c^{2\delta}}\left[\sum_{i=1}^{2\delta-1}\frac{1}{2\delta-i}\left(-\frac{c}{\beta}V_0^{1/\delta}\right)^{2\delta-i} + ln\left(1+\frac{c}{\beta}V_0^{1/\delta}\right)\right]. \tag{21}$$

For $\delta = 1$ the initial value problem (16) becomes linear and has an explicit form solution.

Perturbed Motion. The total displacements are described by (4). The perturbed displacements are assumed to be much smaller than the unperturbed ones. Eliminating shear forces from (9), neglecting the terms with products of perturbation quantities and the sixth equation, we get

$$\begin{aligned}
&a\frac{\partial N_x}{\partial x} + \frac{\partial N_{\vartheta x}}{\partial \vartheta} - \left(\frac{\partial^2 v}{\partial x\partial\vartheta} - \frac{\partial w}{\partial x}\right)N_\vartheta^0 + aP_x = 0,\\
&a\frac{\partial N_{x\vartheta}}{\partial x} + \frac{\partial N_\vartheta}{\partial\vartheta} + \frac{\partial M_{x\vartheta}}{\partial x} - \frac{\partial M\vartheta}{a\partial\vartheta} + a\frac{\partial^2 v}{\partial x^2}N_x^0 + aP_\vartheta = 0,\\
&a\frac{\partial^2 M_x}{\partial x^2} + \frac{\partial^2 M_\vartheta}{a\partial\vartheta^2} + \frac{\partial^2 M_{\vartheta x}}{\partial x\partial\vartheta} - \frac{\partial^2 M_{x\vartheta}}{\partial x\partial\vartheta}\\
&\quad + a\frac{\partial^2 w}{\partial x^2}N_x^0 + N_\vartheta + \frac{1}{a}\left(\frac{\partial v}{\partial\vartheta} + \frac{\partial^2 w}{\partial\vartheta^2}\right)N_\vartheta^0 + aP_z = 0.
\end{aligned} \tag{22}$$

On substituting (11), (4), and (13) in (22) and on accounting for (15) and $q_x = q_x^p(x,\vartheta,t)$, $q_\vartheta = q_\vartheta^p(x,\vartheta,t)$, $q_z = q_z^0(t) + q_z^p(x,\vartheta,t)$, we obtain the following equations of the viscoplastic flow buckling:

$$\begin{aligned}
&\ddot{u}_p - \frac{1}{\rho h}\left[-D_2\frac{\partial\dot{w}_p}{\partial x} + (D_0+D_2)\frac{\partial^2\dot{v}_p}{\partial x\partial\vartheta} + \frac{D_0}{a}\frac{\partial^2\dot{u}_p}{\partial\vartheta^2} + D_1 a\frac{\partial^2\dot{u}_p}{\partial x^2}\right.\\
&\quad \left. - 2(\alpha_1-2)D_0\left(\frac{\partial^2 v_p}{\partial x\partial\vartheta} - \frac{\partial w_p}{\partial x}\right)\frac{\dot{w}_0}{a} + q_x^p\right] = 0,\\
&\ddot{v}_p - \frac{1}{\rho h}\left[\frac{h^2}{12a}(2D_0+D_2)\frac{\partial^3\dot{w}_p}{\partial x^2\partial\vartheta} + \frac{h^2}{12a^3}D_3\frac{\partial^3\dot{w}_p}{\partial\vartheta^3} - \frac{D_3}{a}\frac{\partial\dot{w}_p}{\partial\vartheta}\right.\\
&\quad + (D_0+D_2)\frac{\partial^2\dot{u}_p}{\partial x\partial\vartheta} + aD_0\frac{\partial^2\dot{v}_p}{\partial x^2} + \frac{D_3}{a}\frac{\partial^2\dot{v}_p}{\partial\vartheta^2}\\
&\quad \left. + 2(2\alpha_1-1)D_0\dot{w}_0\frac{\partial^2 v_p}{\partial x^2} + q_\vartheta^p\right] = 0,\\
&\ddot{w}_p - \frac{1}{\rho h}\left\{-\frac{D_3}{a}\dot{w}_p + \frac{D_3}{a}\frac{\partial\dot{v}_p}{\partial\vartheta} + D_2\frac{\partial\dot{u}_p}{\partial x} - \frac{h^2}{12a^2}\left[D_1 a^3\frac{\partial^4\dot{w}_p}{\partial x^4}\right.\right.\\
&\quad + \frac{D_3}{a}\frac{\partial^4\dot{w}_p}{\partial\vartheta^4} + 2(2D_0+D_2)a\frac{\partial^4\dot{w}_p}{\partial x^2\partial\vartheta^2}\\
&\quad \left. + (2D_0+D_2)a\frac{\partial^3\dot{v}_p}{\partial x^2\partial\vartheta} + \frac{D_3}{a}\frac{\partial^3\dot{v}_p}{\partial\vartheta^3} - 2D_0\frac{\partial^3\dot{u}_p}{\partial x\partial\vartheta^2}\right]\\
&\quad + 2(2\alpha_1-1)D_0\dot{w}_0\frac{\partial^2 w_p}{\partial x^2} + 2(\alpha_1-2)D_0\frac{\dot{w}_0}{a^2}\\
&\quad \left.\left(\frac{\partial^2 w_p}{\partial\vartheta^2} + \frac{\partial v_p}{\partial\vartheta}\right) + q_z^p\right\} = 0.
\end{aligned} \tag{23}$$

The terms $h^2/12a^2$ occurring in the second equation of (23) were disregarded as small in comparison with unity.

The displacement and loading perturbations can be assumed in the form of Fourier series

$$\begin{aligned}
\begin{matrix} u_p \\ q_x^p \end{matrix} &= \sum_{m=1}^{M}\sum_{n=0}^{N}\begin{matrix} u_{mn}(t) \\ q_{mn}^x(t) \end{matrix}\sin\alpha_m x\cos n\vartheta,\\
\begin{matrix} v_p \\ q_\vartheta^p \end{matrix} &= \sum_{m=0}^{M}\sum_{n=1}^{N}\begin{matrix} v_{mn}(t) \\ q_{mn}^\vartheta(t) \end{matrix}\cos\alpha_m x\sin n\vartheta,\\
\begin{matrix} w_p \\ q_z^p \end{matrix} &= \sum_{m=0}^{M}\sum_{n=0}^{N}\begin{matrix} w_{mn}(t) \\ q_{mn}^z(t) \end{matrix}\cos\alpha_m x\cos n\vartheta,
\end{aligned} \tag{24}$$

where $\alpha_m = m\Pi/l$, m, and $2n$ denote the number of half-waves in longitudinal and circumferential directions, respectively.

Substituting (24) into (23), we find the following equations for the amplitudes $u_{mn}(t)$, $v_{mn}(t)$, and $w_{mn}(t)$:

$$\begin{aligned}
&\ddot{u}_{mn} + \frac{1}{\rho h}\left[\left(\frac{n^2}{a}D_0 + a\alpha_m^2 D_1\right)\dot{u}_{mn} + n\alpha_m(D_0+D_2)\dot{v}_{mn}\right.\\
&\quad \left. - \alpha_m D_2\dot{w}_{mn} + 2(\alpha_1-2)\alpha_m D_0\frac{\dot{w}_0}{a}(w_{mn} - nv_{mn}) - q_{mn}^x\right] = 0,\\
&\ddot{v}_{mn} + \frac{1}{\rho h}\left\{n\alpha_m(D_0+D_2)\dot{u}_{mn} + \left(\alpha_m^2 aD_0 + \frac{n^2}{a}D_3\right)\dot{v}_{mn}\right.\\
&\quad - n\left[\frac{h^2}{12a}\left(\alpha_m^2(2D_0+D_2) + \frac{n^2}{a^2}D_3\right) + \frac{D_3}{a}\right]\dot{w}_{mn}\\
&\quad \left. + 2(2\alpha_1-1)\alpha_m^2 D_0\dot{w}_0 v_{mn} - q_{mn}^\vartheta\right\} = 0,\\
&\ddot{w}_{mn} + \frac{1}{\rho h}\left\{\left(\frac{n^2\alpha_m h^2}{6a^2}D_0 - \alpha_m D_2\right)\dot{u}_{mn}\right.\\
&\quad - \frac{n}{a}\left[D_3 + \frac{h^2}{12a^2}((2D_0+D_2)a^2\alpha_m^2 + n^2 D_3)\right]\dot{v}_{mn}\\
&\quad + \left[\frac{1}{a}D_3 + \frac{h^2}{12a^2}\left(a^3\alpha_m^4 D_1 + \frac{n^4}{a}D_3\right.\right.\\
&\quad \left.\left. + 2an^2\alpha_m^2(2D_0+D_2)\right)\right]\dot{w}_{mn} + 2D_0\dot{w}_0\left[(2\alpha_1-1)\alpha_m^2\right.\\
&\quad \left.\left. + \frac{n^2}{a^2}(\alpha_1-2)\right]w_{mn} - 2(\alpha_1-2)nD_0\frac{\dot{w}_0}{a^2}v_{mn} - q_{mn}^z\right\} = 0.
\end{aligned} \tag{25}$$

The coefficients of these equations are functions of time and are determined by the solution for the unperturbed motion.

In the general case the solution of equations (25) for given initial conditions can be easily obtained by numerical integration.

Bearing in mind the form of the solution (24), the initial conditions must also be expressed in the form of Fourier series. For the ideal radial impulse pressure $q_x^p = q_\vartheta^p = q_z^p = 0$ and we assume the following set of initial values:

$$\begin{aligned}
&u_{mn}(0) = 0, \quad v_{mn}(0) = 0, \quad w_{mn}(0) = a_{mn} = \bar{a}h,\\
&\dot{u}_{mn}(0) = 0, \quad \dot{v}_{mn}(0) = 0, \quad \dot{w}_{mn}(0) = b_{mn} = \bar{b}V_0
\end{aligned} \tag{26}$$

where $\bar{a}$ and $\bar{b}$ are constants.

Downloaded 02 May 2010 to 171.66.16.25. Redistribution subject to ASME license or copyright; see http://www.asme.org/terms/Terms_Use.cfm

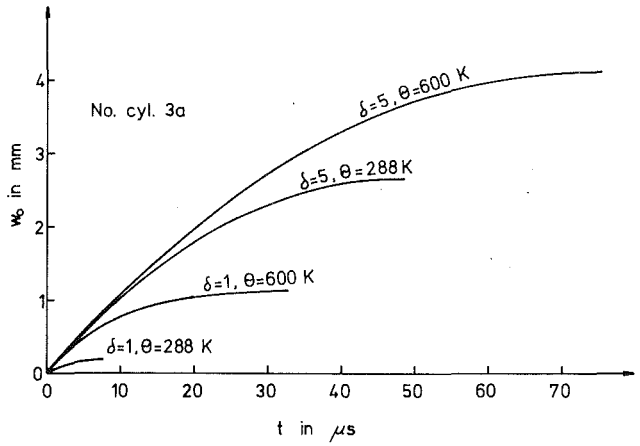

Fig. 3 Unperturbed displacement w_0 versus time for the two values of material coefficient δ and temperature θ

From the general case given by (23) some special cases of buckling modes can be obtained. The equation of the unperturbed motion will remain the same in each case. Differences will only occur in the perturbed motion.

Special Cases of Buckling Mode

General Mode For $u_p = v_p = 0$. The total displacements are expressed by

$$u=\alpha_1 w_0(t)x/a, \quad v=0, \quad w=w_0(t)+w_p(x,\vartheta,t) \tag{27}$$

The equations for the amplitudes (25) reduce to the equation

$$\ddot{w}_{mn}+\frac{1}{\rho h}\left\{\left[\frac{D_3}{a}+\frac{h^2}{12a^2}\left(a^3\alpha_m^4 D_1+\frac{n^4}{a}D_3\right.\right.\right.$$

$$\left.+2an^2\alpha_m^2(2D_0+D_2)\right]\dot{w}_{mn}+2D_0\dot{w}_0\left[(2\alpha_1-1)\alpha_m^2\right.$$

$$\left.\left.+\frac{n^2}{a^2}(\alpha_1-2)\right]w_{mn}-q^z_{mn}\right\}=0. \tag{28}$$

Asymmetrical Mode. The total displacements are taken in the form

$$u=\alpha_1 w_0(t)x/a, \quad v=v_p(\vartheta,t), \quad w=w_0(t)+w_p(\vartheta,t). \tag{29}$$

Substituting $u_p = 0$, $\partial/\partial x = 0$, and $m = 0$ into the equations of the general mode, suitable formulas will be derived for the case considered. The equations of amplitudes (25) become

$$\ddot{v}_n+\frac{1}{\rho h}\left[-\frac{D_3}{a}n\left(\frac{h^2}{12a^2}n^2+1\right)\dot{w}_n+n^2\frac{D_3}{a}\dot{v}_n-q^\vartheta_n\right]=0,$$

$$\ddot{w}_n+\frac{1}{\rho h}\left[\frac{D_3}{a}\left(\frac{h^2}{12a^2}n^4+1\right)\dot{w}_n-\frac{D_3}{a}n\left(\frac{h^2}{12a^2}n^2+1\right)\dot{v}_n\right.$$

$$\left.+2(\alpha_1-2)D_0 n\frac{\dot{w}_0}{a^2}(nw_n-v_n)-q^z_n\right]=0. \tag{30}$$

The obtained solution reduces for $v_p = 0$ to the specific simple form,

$$\ddot{w}_n+\frac{1}{\rho h}\left[\frac{D_3}{a}\left(\frac{h^2}{12a^2}n^4+1\right)\dot{w}_n\right.$$

$$\left.+2(\alpha_1-2)D_0 n^2\frac{\dot{w}_0}{a^2}w_n-q^z_n\right]=0. \tag{31}$$

Axisymmetrical Mode. In this case the total displacements in the perturbed motion are described by the functions:

$$u=\alpha_1 w_0(t)x/a+u_p(x,t), \quad v=0, \quad w=w_0(t)+w_p(x,t). \tag{32}$$

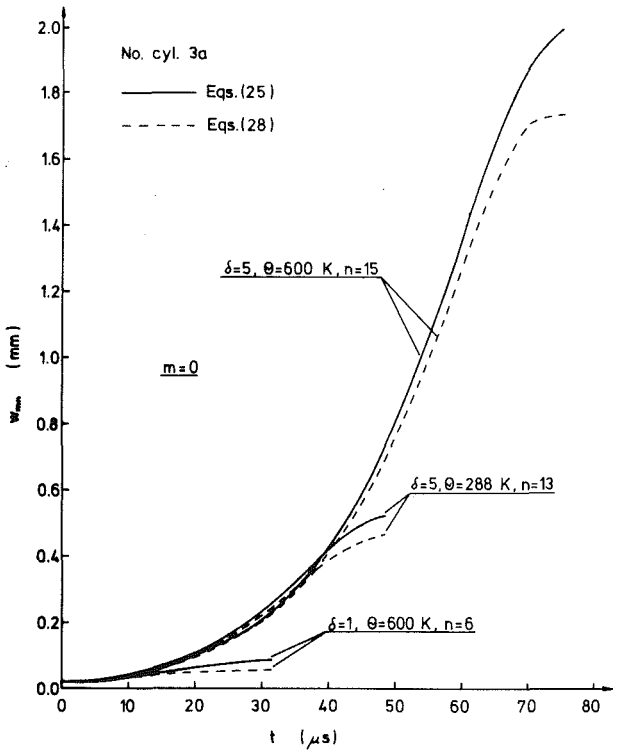

Fig. 4(a) Time variation of the amplitude w_{mn} for the two values of δ and θ

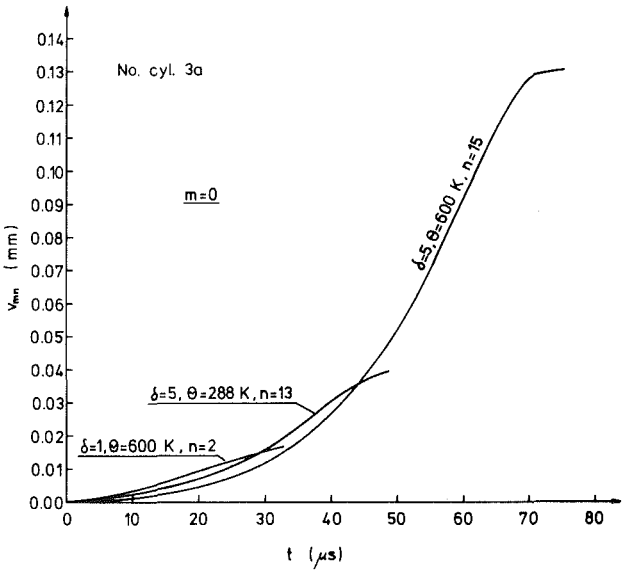

Fig. 4(b) Time variation of the amplitude v_{mn} for the two values of δ and θ

Equations of the perturbed motion can be obtained from the general solution by putting $v_p = 0$, $\partial/\partial\vartheta = 0$, $n = 0$. The equations of amplitudes (25) reduce to

$$\ddot{u}_m+\frac{1}{\rho h}\left[D_1 a\alpha_m^2\dot{u}_m-D_2\alpha_m\dot{w}_m\right.$$

$$\left.+2(\alpha_1-2)D_0\alpha_m\frac{\dot{w}_0}{a}w_m-q^x_m\right]=0,$$

$$\ddot{w}_m+\frac{1}{\rho h}\left[-D_2\alpha_m\dot{u}_m+\left(D_3\frac{1}{a}+\frac{h^2 a}{12}D_1\alpha_m^4\right)\dot{w}_m\right.$$

$$\left.+2(2\alpha_1-1)D_0\alpha_m^2\dot{w}_0 w_m-q^z_m\right]=0. \tag{33}$$

Downloaded 02 May 2010 to 171.66.16.25. Redistribution subject to ASME license or copyright; see http://www.asme.org/terms/Terms_Use.cfm

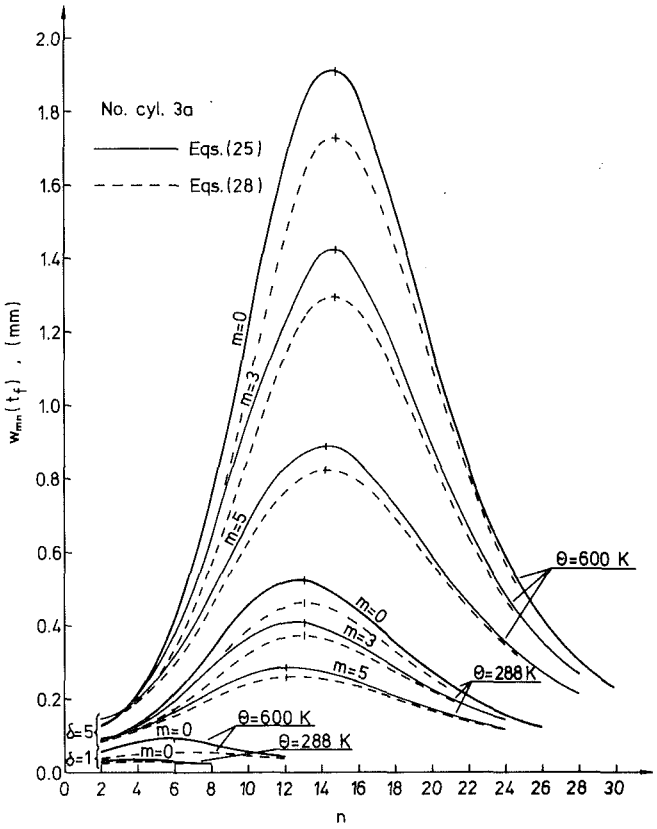

Fig. 5(a) Final amplitudes of perturbed displacement $w_{mn}(t_f)$ versus the number of half-waves in longitudinal and circumferential directions m and n for the two values of δ and θ

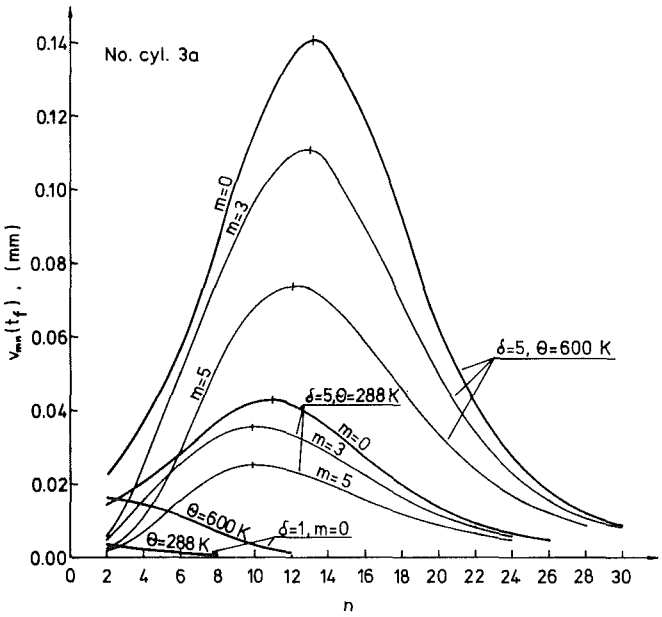

Fig. 5(b) Final amplitudes of perturbed displacement $v_{mn}(t_f)$ versus the number of half-waves in longitudinal and circumferential directions m and n for the two values of δ and θ

The problem may be furthermore simplified by assuming $u_p = 0$. In this case we obtain

$$\ddot{w}_m + \frac{1}{\rho h}\left[\left(\frac{D_3}{a} + \frac{h^2 a}{12} D_1 \alpha_m^4\right)\dot{w}_m + 2(2\alpha_1 - 1)D_0 \alpha_m^2 \dot{w}_0 w_m - q_m^z\right] = 0. \tag{34}$$

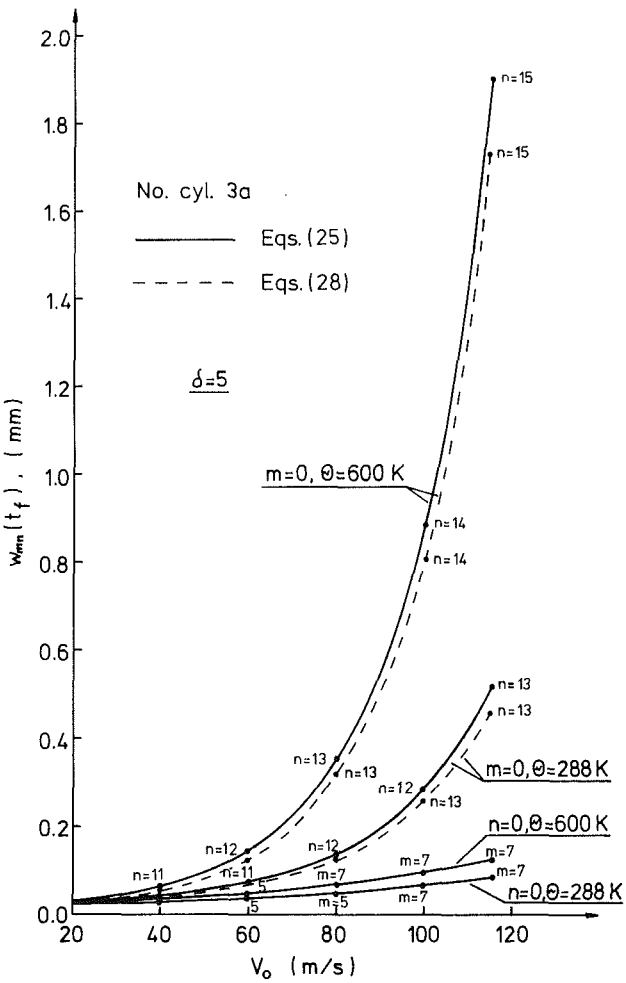

Fig. 6 Maximum amplitudes of perturbed displacement $w_{mn}(t_f)$ versus applied impulse V_0. Asymmetrical ($m = 0$) and axisymmetrical ($n = 0$) buckling mode.

Discussion of Results and Comparison With Experiments

The equation of unperturbed motion and the equations of amplitudes have been solved numerically employing the Merson procedure. The following material data for shells made of mild steel 1015 were assumed: $\sigma_0 = 206.9$ MPa, $\rho = 7.78$ Mg/m^3, $\gamma^* = 40.4$ s^{-1}, and $\delta = 5$, [2]. The theoretical results obtained are compared with the experimental data given in [2, 3]. Some of the numerical results for loading by the ideal radial impulse pressure and for $\bar{a} = 0.01$, $\bar{b} = 0.01$, and $\alpha_1 = 0.17$ are presented diagrammatically. In Fig. 3 a substantial influence of the material constant δ and the temperature θ on the magnitude of unperturbed radial displacement w_0 is shown. In Figs. 4 and 5 the amplitudes of perturbed displacements w_{mn} and v_{mn} are given as functions of t, δ, θ, and n. Again, the pronounced influence of these parameters is readily observed. The solution to equations (25) is indicated by a solid line, the solution to equation (28), accounting for the radial displacement only, by a broken line.

The amplitudes w_{mn} and v_{mn} are seen to reach their largest values for $m = 0$ and $u_{mn} = 0$. The unperturbed displacements w_0 are many times greater than w_{mn}. Similarly $w_{mn} >> v_{mn}$ and it is the growth of w_{mn} that mainly causes the instability of the shell. In this type of buckling the loss of stability is not quite instantaneous, the process needs the increment of loading and some time to develop. Since the values of w_{mn} and v_{mn} are the largest and $u_p = 0$ for $m = 0$,

Downloaded 02 May 2010 to 171.66.16.25. Redistribution subject to ASME license or copyright; see http://www.asme.org/terms/Terms_Use.cfm

Table 1 Comparison of the theoretical and experimental results

No. of cyl.	Radius a cm	Thickness h cm	a/h	Length l cm	Experiment [2] Impulse V_0 m/s	Final strain ε_u %	Buckling mode n	Theory Final strain ε_u, % $\delta=5$	$\delta=1$	Buckling mode n $\delta=5$	$\delta=1$	Duration of motion t_f, μs $\delta=5$	$\delta=1$
1a	3.795	0.107	35.6	15.24	85.19	4.9	26	4.86	0.41	21	5	37.5	7.3
2a	3.815	0.167	22.8	15.24	105.71	9.5	19	7.16	0.53	17	4	45.6	7.8
3a	3.779	0.226	16.7	15.24	115.60	9.3	13	8.33	0.59	13	3	48.7	7.8
4a	3.835	0.366	10.5	15.24	116.36	8.7	9	7.98	0.63	9	3	49.8	8.0

the generators of the cylindrical shell remain straight. This conclusion is verified by the experimental observations [2, 9].

The values of w_{mn} obtained from the equation (28), where $u_p = v_p = 0$, attain their largest values also for $m = 0$ and are smaller than those calculated from the set of equations (25), Figs. 4(*a*), 5(*a*), and 6. For cylinder 3*a* and $\theta = 288$ K the decrease of $w_{mn}(t_f)$ is equal to 20 percent and 8.9 percent for $\delta = 1$ and $\delta = 5$, respectively. It causes that the threshold impulse determined is larger than that obtained from equations (25).

In Fig. 6 the variation of $w_{mn}(t_f)$ is shown as a function of impulse applied for the asymmetrical, $m = 0$, and the axisymmetrical buckling mode, $n = 0$. It can be seen that for the given load the shell buckles exhibiting asymmetrical wrinkled shape. The numbers at the dots distributed along the curves denote the critical modes. The function $w_{mn}(t_f)$ is monotonously increasing and the absence of extremum makes it impossible to accurately determine the critical impulse, Fig. 6. The function $w_{mn}(t_f)$ attains large values in a certain narrow interval of the impulse variation; hence it is natural to determine the approximate critical value as the abcissa of such a point on the curve at which a small increment of the pulse begins to produce considerable increments of the deflection amplitude.

The comparison of some theoretical results with the experimental data [2, 3] is given in Table 1. For the shells made of mild steel ($\delta = 5$) reasonable agreement can be seen for the buckling modes and for the final strains. For $\delta = 1$ and $\gamma^* = 40.4\ s^{-1}$ the straight line being the interpretation of equations (2) in the uniaxial stress state (see Fig. 1), has a large slope and is a poor approximation of the real curve ($\delta = 5$). It causes a substantial difference between the results for $\delta = 1$ and $\delta = 5$. The differences will become smaller for larger values of γ^*. Florence's approximation, Fig. 1, is more accurate for the larger strain-rate range and the obtained results [3] are close to the results given in this paper for the nonlinear case, $\delta = 5$. The numerical results, not included in this paper, show the increase in mode number with shell length. This observation is in a general accordance with the results presented in Fig. 10 of reference [13].

Conclusions

The nonlinearity of the function $\phi(F)$ as well as elevated temperature and the initial imperfections considerably decrease the buckling resistance of shell. It is proved that the asymmetrical mode of buckling occurs for the cylindrical shell subjected to uniform radially inward impulse, what is in accord with the experimental observations reported in the literature. Accounting for the circumferential displacement leads to an increase in the radial perturbed displacement. This increase is found to be 9 percent for the temperature range from 288 K to 600 K. It results in diminish the threshold impulse.

The theory is applicable to viscoplastic shells in which final strains are large compared with the elastic strains. Reasonable agreement with the available experimental results suggests that the theory describes the buckling process in a satisfactory manner.

References

1 Bodner, S. R., Symonds, P. S., "Experimental and Theoretical Investigations of the Plastic Deformation of Cantilever Beams Subjected to Impulsive Loading," ASME JOURNAL OF APPLIED MECHANICS, Vol. 29, 1962, pp. 719–728.

2 Florence, A. L., "Buckling of Viscoplastic Cylindrical Shells Due to Impulsive Loading," *AIAA Journal*, Vol. 6, No. 3, 1968, pp. 532–537.

3 Florence, A. L., "Dynamic Buckling of Viscoplastic Cylindrical Shells," in: *Inelastic Behavior of Solids*, Kanninen, et al., eds., McGraw-Hill, London, 1970.

4 Florence, A. L., and Abrahamson, G. R., "Critical Velocity for Collapse of Viscoplastic Cylindrical Shells Without Buckling," ASME JOURNAL OF APPLIED MECHANICS, Vol. 44, 1977, pp. 89–94.

5 Perzyna, P., "The Constitutive Equations for Rate Sensitive Plastic Materials," *Quarterly of Applied Mathematics*, Vol. 20, 1963, pp. 321–332.

6 Wojewódzki, W., "Buckling of Short Viscoplastic Cylindrical Shells Subjected to Radial Impulse," *International Journal of Non-Linear Mechanics*, Vol. 8, 1973, pp. 325–343.

7 Wojewódzki, W., "Buckling of Viscoplastic Cylindrical Shells Subjected to Radial Impulse and Temperature," Reprints of the 2nd International Conference on "Structural Mechanics in Reactor Technology," Vol. V, Part L 6/7, Berlin, Germany, Sept. 10–14, 1973, pp. 1–12.

8 Abrahamson, G. R., and Goodier, J. N., "Dynamic Plastic Flow Buckling of a Cylindrical Shell From Uniform Radial Impulse," *Proceedings of Fourth U.S. National Congress on Applied Mechanics*, University of California, ASME, 1962, pp. 939–950.

9 Anderson, D. L., and Lindberg, H. E., "Dynamic Pulse Buckling of Cylindrical Shells Under Transient Lateral Pressure," *AIAA Journal*, Vol. 6, No. 4, 1968, pp. 589–598.

10 Vaughan, H., and Florence, A. L., "Plastic Flow Buckling of Cylindrical Shells Due to Impulsive Loading," ASME JOURNAL OF APPLIED MECHANICS, Vol. 37, 1970, pp. 171–179.

11 Stuiver, W., "On the Buckling of Rings Subjected to Impulsive Pressures," ASME JOURNAL OF APPLIED MECHANICS, Vol. 32, 1965, pp. 511–518.

12 Jones, N., and Ahn, C. S., "Dynamic Elastic and Plastic Buckling of Complete Spherical Shells," *International Journal of Solid Structures*, Vol. 10, 1974, pp. 1357–1374.

13 Jones, N., and Okawa, D. M., "Dynamic Plastic Buckling of Rings and Cylindrical Shells," *Nuclear Engineering and Design*, Vol. 37, 1976, pp. 125–147.

14 Gryboś, R., *Stability of Structures Under Blast Loading*, PWN, Warsaw, 1980, in Polish.

15 Perzyna, P., and Wierzbicki, T., "Temperature Dependent and Strain Rate Sensitive Plastic Materials," *Archives for Mechanics*, Vol. 1, 1964, pp. 135–143.

16 Maiden, C. J., and Campbell, J. D., "The Static and Dynamic Strength of a Carbon Steel at Low Temperatures," *Philosophical Magazine*, Vol. 3, 1958, pp. 872–885.

17 Manjoine, M. J., "Influence of Rate of Strain and Temperature on Yield Stresses of Mild Steel," ASME JOURNAL OF APPLIED MECHANICS, Vol. 11, 1944, pp. 211–218.

18 Love, A. E., *A Treatise on the Mathematical Theory of Elasticity*, 4th Ed., Cambridge University Press, 1927, Chapter 24.

Downloaded 02 May 2010 to 171.66.16.25. Redistribution subject to ASME license or copyright; see http://www.asme.org/terms/Terms_Use.cfm

G. W. Hedstrom
L. Thigpen
B. P. Bonner

Lawrence Livermore National Laboratory,
Livermore, Calif. 94550

P. H. Worley
Computer Science Department,
Stanford University,
Stanford, Calif. 94305

Regularization and Inverse Problems in Viscoelasticity

The method of constrained regularization is used to invert for retardation spectra and attenuation from the creep data of a commercial-grade lucite material. Four different criteria for choosing a regularization parameter in the solution of the first-kind integral equation are examined. Although the spectra are different, computations using each criterion give essentially the same attenuation curve for a range of frequencies. These results show that reliable estimates of the attenuation may be obtained from inversion of creep data using the method of constrained regularization.

Introduction

In two previous papers [1, 2], Butler's [3] method of constrained regularization was used to obtain retardation spectra and attenuation from creep experiments. In this method the regularization or smoothing parameter depends on an estimate of the standard deviation of the data. It was concluded in the preceding works [1, 2] that although Butler's method did not guarantee an optimum solution to first-kind integral equations, the technique does provide significant improvements over more direct methods [4, 5] when the data are noisy. The choice of a suitable regularization parameter is still the main difficulty in implementing regularization, because Butler's algorithm deliberately makes it too large and because the algorithm requires an estimate of the standard deviation of the data.

The objective of the present investigation is to examine different techniques used to choose the regularizing parameters in order to broaden our understanding of how the solution to first-kind integral equations is affected by different levels of smoothing. In the following, the equations representing the creep function and dynamic viscoelastic functions are summarized. Four methods to determine an optimum regularization parameter are then discussed and applied to the inversion of creep response data for retardation spectra of a commercial-grade lucite specimen. The methods used are those of Butler [3], Wahba [6], and two heuristics derived for this study by Worley. We find that for this set of data there is a wide range of regularization parameters which give solutions consistent with the data. Thus, the solution is not uniquely determined by the data, a phenomenon that is common among integral equations of the first kind [7]. We also computed the quality factor as a function of frequency and found that is is essentially independent of the regularization parameter, so long as the solution is consistent with the data.

Summary of Equations

The creep function $J(t)$ may be written in terms of the strain retardation spectrum $\chi(\tau)$ by a first-kind integral equation [1, 2, 8]

$$J(t)=J_0+\int_0^\infty \chi(\tau)(1-e^{-t/\tau})\,d\tau, \quad t\geq 0 \tag{1}$$

where J_0 is the instantaneous elastic compliance, t is the time, τ is the strain retardation time, and $\chi(\tau)$ is the retardation spectrum. From equation (1) it may be observed that the retardation spectrum completely characterizes the creep experiment. For convenience we write equation (1)

$$Kf=\int_0^\infty k(t,s)f(s)\,ds=g(t), \tag{2}$$

where we have used the following change of variables

$$s=1/\tau \tag{3}$$

$$\chi(\tau)=s^2 f(s), \tag{4}$$

and

$$g(t)=J(\infty)-J(t). \tag{5}$$

With these definitions, equation (2) is seen to be a Fredholm integral equation of the first kind with an exponential kernel, i.e., $k(t,s)=e^{-st}$.

The attenuation and dispersion are determined from Fourier transforming the creep function $J(t)$,

$$J'(\omega)=J_0+\int_0^\infty \frac{\chi(\tau)}{1+\omega^2\tau^2}\,d\tau, \tag{6}$$

$$J''(\omega)=\int_0^\infty \chi(\tau)\frac{\omega\tau}{1+\omega^2\tau^2}\,d\tau, \tag{7}$$

and

$$Q^{-1}(\omega)=J''(\omega)/J'(\omega), \tag{8}$$

Contributed by the Applied Mechanics Division for publication in the JOURNAL OF APPLIED MECHANICS.

Discusson on this paper should be addressed to the Editorial Department, ASME, United Engineering Center, 345 East 47th Street, New York, N.Y. 10017, and will be accepted until two months after final publication of the paper itself in the JOURNAL OF APPLIED MECHANICS. Manuscript received by ASME Applied Mechanics Division, March, 1983; final revision, September, 1983.

Copyright © 1984 by ASME
Downloaded 02 May 2010 to 171.66.16.25. Redistribution subject to ASME license or copyright; see http://www.asme.org/terms/Terms_Use.cfm

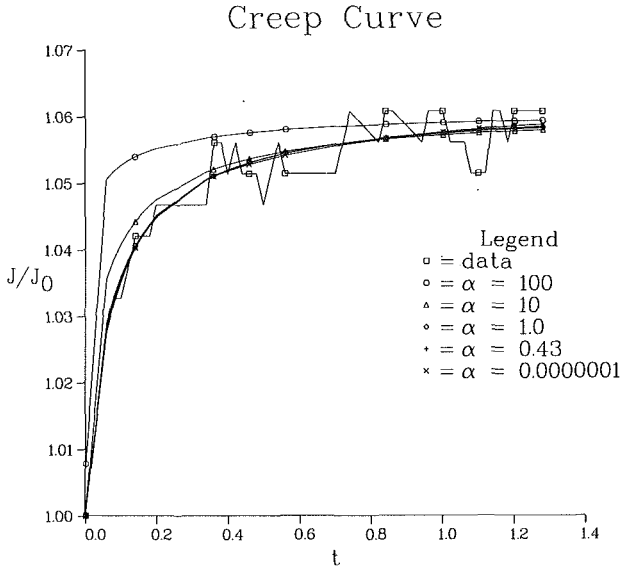

Fig. 1 Data curves

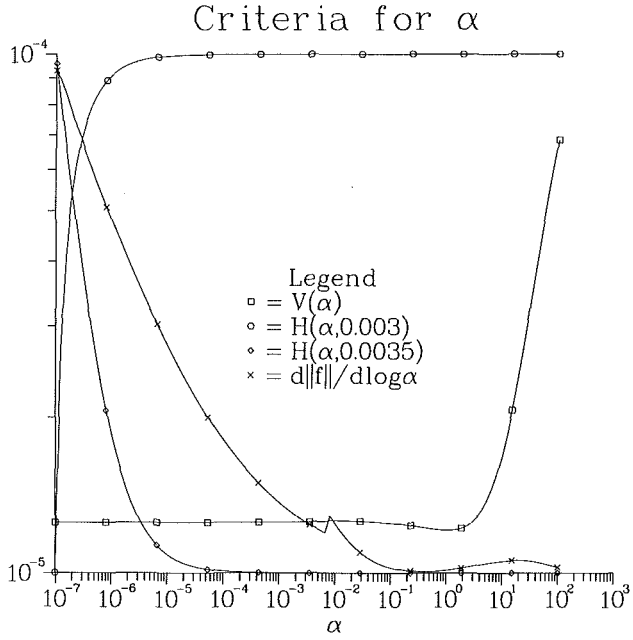

Fig. 2 Criteria for optimal α

where $J'(\omega)$ is the storage compliance and is a measure of the dispersion, $J''(\omega)$ is the loss compliance, and $Q^{-1}(\omega)$ is the inverse quality factor, associated with energy dissipation. A comparison of equations (2), (6), and (7) shows that the retardation function $\chi(\tau)$ satisfies Fredholm integral equations with different kernels in terms of either the creep function or the dynamic viscoelastic functions. Conversely, the viscoelastic behavior is completely determined by the retardation spectrum $\chi(\tau)$.

This summarizes the equations used in the present work. In the following, we discuss the solution to equation (2) using four techniques for determining regularization (or smoothing) parameters. We solve equation (2) instead of equation (6) or equation (7) for $\chi(\tau)$ because our data is obtained from creep experiments.

Solution Procedure

We seek an approximate solution to the integral equation

$$\int_0^\infty e^{-ts} f(s)\,ds = g(t) \quad 0 < t < \infty, \tag{9}$$

for positive f. Imperceptible changes in $g(t)$ can give rise to large-amplitude, high-frequency oscillation in the solution $f(s)$ to equation (9). In fact, equation (9) is ill-posed and any direct numerical solution technique will give rise to solutions that mimic this unstable behavior. The problem can be stabilized by the imposition of contraints as well as by regularization [7]. In what follows, we use Tihonov regularization [7] in addition to a positivity constraint on the solution. This technique has been discussed in detail by Butler [3] and Wahba [6].

The approximate solution f_α for discrete data is the solution that minimizes the function

$$\psi(f) = \sum_{i=1}^{N} w_i^2 \left(\int_D k(t_i,s) f(s)\,ds - g(t_i) \right)^2 + \alpha \|f\|^2 \tag{10}$$

subject to the constraint $f(s) \geq 0$. Here, w_i^2 are weights inversely proportional to measurement error variances in $g(t_i)$, $\alpha \geq 0$ is the smoothing parameter, and $\|\cdot\|$ denotes the Euclidean R^N vector norm.

The details describing the minimization of the function $\psi(f)$ for a given α have been discussed in a previous paper [1]. Here our emphasis is on different methods of choosing an optimum α and how the different choices affect the solution f_α.

We first review briefly the method used by Butler [3] to choose a smoothing parameter; see also [1]. In this method, the optimal smoothing parameter is chosen to be the α that minimizes a function that is an estimator of the solution error less an additive constant that is independent of the smoothing parameter. The function to be minimized is given by

$$H(\alpha) = \|f_\alpha\|^2 - 2g \cdot c + 2\sigma\sqrt{N}\|c\| \tag{11}$$

where c is a solution vector to the equation

$$(Kf - g) + \alpha c = 0,$$
$$f(s) = \max\{0, \Sigma c_j k(t_j,s)\}, \tag{12}$$

and σ is the measurement error variance of the data which is assumed to be known. If the data prediction error for the least squares solution ($\alpha = 0$) is greater than σ, then $H(\alpha)$ is minimized by $\alpha = 0$. If the identically zero solution ($\alpha = \infty$) gives a data prediction error less than σ, then $H(\alpha)$ has its minimum at $\alpha = \infty$. These extreme cases indicate that σ is too small or too large for the method to work. We will see that for some data the value of α that minimizes $H(\alpha)$ may be exceedingly sensitive to the value of σ.

For a set of α, a solution f_α that minimizes $\psi(f)$ in equation (10) is obtained for the data depicted in Fig. 1. This data is for creep of a commercial-grade lucite, and the experiment is described in [2]. $H(\alpha)$ is then obtained from equation (11) for each α. These results are plotted in Fig. 2 as $H(\alpha)$ versus α for two values of σ. Note that in Fig. 2 the vertical scales have been adjusted to enable us to plot the curves together. The optimum α is chosen as the α that minimizes $H(\alpha)$. For $\sigma = 0.003$ the optimal smoothing parameter was $\alpha_{opt} = 10^{-7}$, because we chose 10^{-7} as our smallest value of α. For $\sigma = 0.0035$ we obtained $\alpha_{opt} = 100$, but it is presumably even larger. For these values of α the corresponding values of $J(t) = J(\infty) - g(t)$ are compared with the data in Fig. 1. It is clear that $\alpha = 10^{-7}$ gives a solution that is consistent with the data, while $\alpha = 100$ does not. The spectrum $\chi(\tau)$ for $\alpha = 10^{-7}$ is shown as a dashed curve in Fig. 3.

The second technique we used to determine an optimal smoothing parameter is the generalized cross validation method of Wahba [6]. Detailed discussion of the method is given in Wahba's papers. Wahba pointed out that the complete method is expensive computationally and suggested an approximation to the general method. In this paper we

Downloaded 02 May 2010 to 171.66.16.25. Redistribution subject to ASME license or copyright; see http://www.asme.org/terms/Terms_Use.cfm

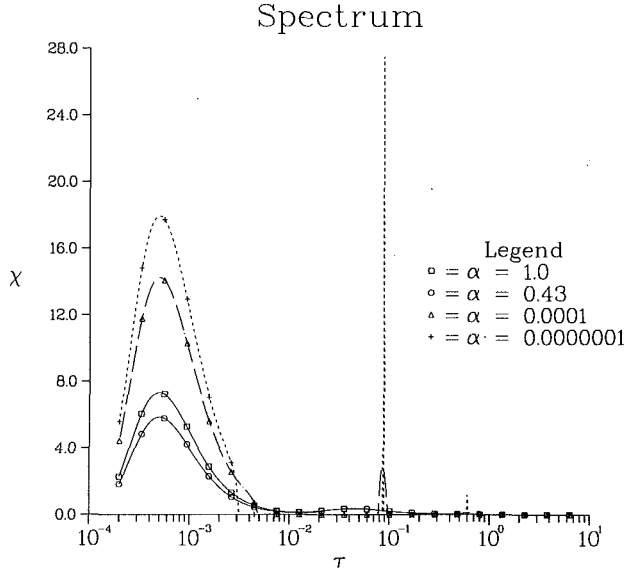

Fig. 3 Spectra

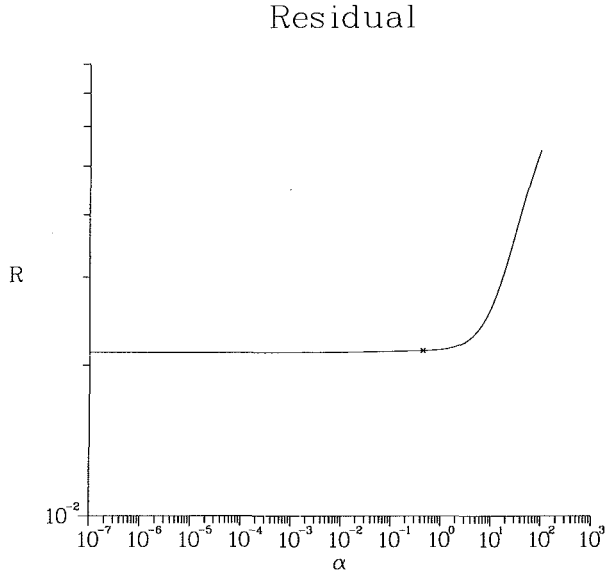

Fig. 5 Residual

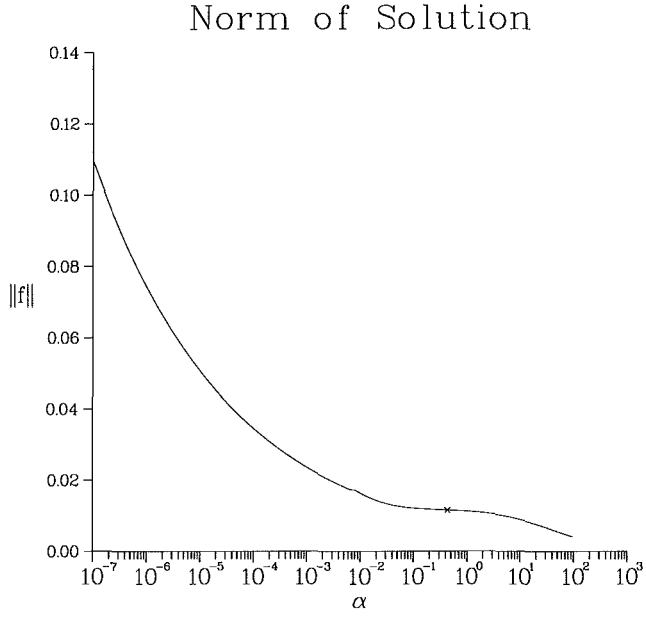

Fig. 4 Norm of f_α

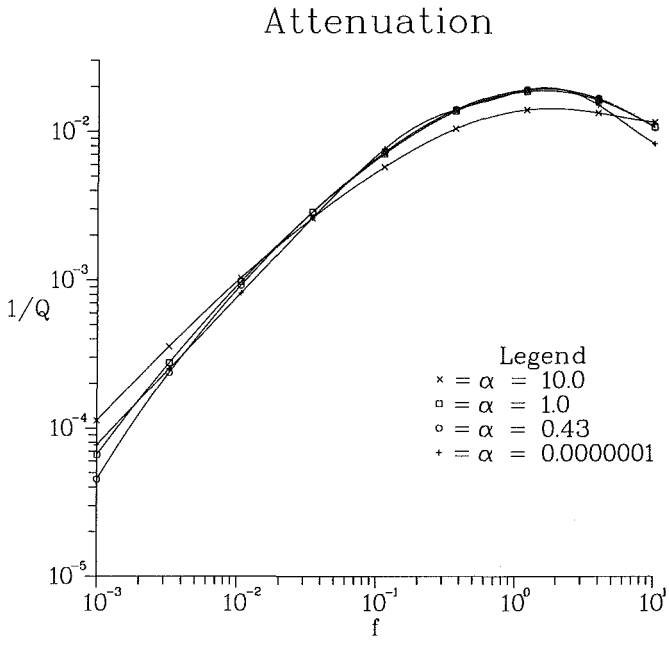

Fig. 6 Q-inverse

present results using this approximation to the generalized cross validation method for determining the optimal smoothing parameter. The optimal α is taken as the solution that minimizes the function

$$V(\alpha) = \frac{N\alpha^2 \|c\|^2}{[Tr(I - M(M+\alpha I)^{-1}]^2} \tag{13}$$

where Tr represents the trace of a matrix and the components of M are

$$M_{ij} = \int_{\text{supp} f} e^{-st_i} e^{-st_j} ds. \tag{14}$$

By evaluating $V(\alpha)$ for a range of α's, we found that the minimum occurs at $\alpha = 1$. The graph of $V(\alpha)$ is shown in Fig. 2. The solution $\chi(\tau)$ for $\alpha = 1$ is shown in Fig. 3, and the corresponding function $J(t)$ is depicted in Fig. 1.

The third method we tried for determining the optimal smoothing parameter is termed differential smoothing. The function to be minimized for small α is

$$\frac{d}{d\log\alpha} \|f_\alpha\|. \tag{15}$$

This function is plotted in Fig. 2 and gives an optimal $\alpha_{\text{opt}} = 0.43$.

The corresponding spectrum $\chi(\tau)$ is shown in Fig. 3, and the comparison with the data is given in Fig. 1. This measure is motivated by an examination of the graph of $\|f_\alpha\|$ as a function of log α, see Fig. 4. A common attribute of our problems has been a range of α for which $\|f_\alpha\|$ is relatively insensitive. This flat portion of the curve indicates the location of a good smoothing parameter α, if the steeper portion of the curve for smaller values of α is interpreted as arising from oscillatory noise in f_α.

The final technique is also empirical, and it is motivated by the data approximation error curve, Fig. 5, of

$$R = \| \int_0^\infty e^{-ts} f(s)\, ds - g(t) \|$$

as a function of α. Curves of this shape are common in our trials. The data can not be matched exactly by the mathematical model, so we never get $R = 0$. Instead, we find a range of α over which the data is matched nearly equally well.

Downloaded 02 May 2010 to 171.66.16.25. Redistribution subject to ASME license or copyright; see http://www.asme.org/terms/Terms_Use.cfm

For our data this range is $10^{-7} \leq \alpha \leq 1$ in Fig. 5 (see also Fig. 1). If we are concerned about high-frequency noise in the solution, we should take α as large as possible within this interval of a good match to the data. A rough estimator of the knee of the curve in Fig. 5 gives an opitmal $\alpha = 0.39$. Because the solution for $\alpha = 0.39$ differs so little from that for $\alpha = 0.43$, we have not shown it in Figs. 1 and 3.

Four methods have been used to determine an optimal smoothing parameter. Although each method gives a different solution to the integral equation, a direct computation using each solution matches the data. This is clearly shown in Figs. 1 and 3. Thus, if we are interested in the distribution function $\chi(\tau)$, all we can really say is that each candidate is equally valid. However, in the present investigation the main interest is in the inverse quality factor $Q^{-1}(\omega/2\pi)$. This is plotted in Fig. 6, which shows that although different optimal smoothing parameters produce large variations in the retardation spectra, the inverse quality factors for the range of α's ($10^{-7} \leq \alpha \leq 1$) is only slightly different for a range of frequencies.

Summary and Conclusions

The main interest of this paper has been in examining different methods of determining smoothing parameters for solution of a first-kind integral equation in viscoelasticity by the method of constrained regularization. Our results clearly demonstrate that a solution to a first kind integral equation that well approximates the data in a direct computation may not be unique. There may be other physical grounds, however, to prefer one solution over the others. For the lucite studied here, we prefer the solution for $\alpha = 10^{-7}$ on the grounds that the peak near $\tau = 0.09$ in Fig. 3 probably represents the commonly observed β-relaxation [9]. Without this extra physical information, a mathematician concerned about high-frequency noise would be inclined to choose α near 0.43 or 1.0 for this data.

Acknowledgments

The authors wish to thank Lydia Burrow for the excellent and timely typing. This work was performed under the auspices of the U.S. Department of Energy by the Lawrence Livermore National Laboratory under Contract Number W-7405-ENG-48.

References

1 Thigpen, L., Hedstrom, G. W., and Bonner, B. P., "Inversion of Creep Response for Retardation Spectra and Dynamic Viscoelastic Functions," ASME JOURNAL OF APPLIED MECHANICS, Vol. 50, 1983, pp. 361–366.

2 Thigpen, L., Hedstrom, G. W., and Bonner, B. P., "An Inverse Problem in Viscoelasticity," *Review of Progress in Quantitative NDE*, Vol. 2*B*, Thompson, D. O., and Chimenti, D. E., eds., Plenum Press, New York, 1983, pp. 897–905.

3 Bulter, J. P., Reeds, J. A., and Dawson, S. V., "Estimating Solutions of First Kind Integral Equations With Nonnegative Constraints and Optimal Smoothing," *SIAM Journal of Numerical Analysis*, Vol. 18, 1981, pp. 381–397.

4 Schapery, R. A., "Approximate Methods of Transform Inversion for Viscoelastic Stress Analysis," *Proceedings of the 4th U.S. National Congress on Applied Mechanics*, Vol. 2, 1962, pp. 1075–1085.

5 Swanson, S. R., "Approximate Laplace Transform in Dynamic Viscoelasticity," ASME JOURNAL OF APPLIED MECHANICS, Vol. 47, 1980, pp. 769–774.

6 Wahba, G., "Constrained Regularization for Ill-Posed Linear Operator Equations, with Applications in Meterology and Medicine," in *Statistical Decision Theory and Related Topics III*, Vol. 2, Gupta, Shanti S., and Berger, James O., eds., Academic Press, New York, 1982, pp. 383–418.

7 Tihonov, A. N., "Solution of Incorrectly Formulated Problems and the Regularization Method," *Soviet Mathematics Doklady*, Vol. 4, 1963, pp. 1035–1038.

8 Nowick, A. S., and Berry, B. S., *Anelastic Relaxation in Crystalline Solids*, Academic Press, New York, 1972.

9 McCrum, N. G., Read, B. E., and Williams, G., *Anelastic and Dielectric Effects on Polymeric Solids*, Wiley, New York, 1967.

Downloaded 02 May 2010 to 171.66.16.25. Redistribution subject to ASME license or copyright; see http://www.asme.org/terms/Terms_Use.cfm

48 Hour Multiaxial Creep and Creep Recovery of 2618 Aluminum Alloy at 200°C

J.-L. Ding
Research Assistant.

W. N. Findley
Professor of Engineering.
Fellow ASME

Division of Engineering,
Brown University,
Providence, R.I. 02912

Data are reported from 48 hour constant multiaxial stress creep followed by 48 hour creep recovery with the magnitudes of the effective stress ranging from 34.5 MPa (5.00 ksi) to 175.5 MPa (25.46 ksi). They differed from a previous data set in the much longer constant-stress durations and the inclusion of data from low stress creep, compression creep, and short term aging tests. Data were represented by a viscous-viscoelastic model in which the time-dependent strain was resolved into recoverable and nonrecoverable components. Previous stress-strain relations for constant stress creep and recovery were modified to include the current experimental observations of the nonexistence of creep limits, negligible aging effects, and symmetry in tension and compression. The time dependence was represented by a power of time with different exponents for the recoverable and nonrecoverable components. A homogeneous function of maximum shear stress was developed to represent the full range of stress dependence of the nonrecoverable time-dependent components; the third-order multiple integral representation was used for the recoverable component.

Introduction

Past experimental work in creep under multiaxial stress was reviewed in [1].

In previous work at Brown University on 2618-T61 aluminum alloy [2–5], a constitutive relation in which the total strain was decomposed into elastic, time-independent plastic, viscoelastic, and time-dependent nonrecoverable components was developed based on a series of short term (2 h creep period), relatively high stress creep tests with different creep and recovery durations; see [2]. It was reported that there appeared to be creep limits below which the creep strains did not occur or were negligible. It was also shown that the two time-dependent strain components had the same time dependence and their relative proportion might be taken to be independent of stress.

In the present work, a series of constant duration creep and recovery tests were performed whose stress levels were evenly distributed from those causing little creep strain in 48 hours to those causing tertiary creep in less than one hour. They were used not only to check the behavior below the apparent creep limits but also to check the applicability of previous results to longer term primary creep. Two aging tests were also performed to study the aging effects within the time span of the tests performed. Two compression tests were used to compare the creep behavior in tension and compression. The purpose of these works was to refine and to extend the viscous-viscoelastic constitutive relations and to provide a systematic data basis for other theoretical approaches and for more understanding of multiaxial creep behavior.

In subsequent papers, data for variable states of stress will be presented together with predictions based on the present data using two different types of constitutive relations with different hardening natures.

Material and Specimen

The material employed in the present work was aluminum forging alloy 2618-T61 which was the same kind of material as that in previous work [2–6], but obtianed 14 years later from the same source, probably from a different batch. A repeat of the test shown in Fig. 3 of [3] performed on the current batch showed a small increase in creep rate compared to that of the earlier batch; possibly within material variability. A comparison of the chemical compositions of these two batches is shown in Table 1.

Table 1 Chemical compositions of the previous and the current lots of 2618–T61 aluminum alloy

Composition wt. percent	Cu	Fe	Mg	Ni	Ti	Si	Mn
previous	2.2	1.1	1.6	1.05	0.07		
current	2.2	0.99	1.55	1.38	0.06	0.27	0.07

Contributed by the Applied Mechanics Division for presentation at the 1984 PVP Conference and Exhibition, Joint with Applied Mechanics Division and Materials Division, San Antonio, Texas, June 17–21, 1984 of THE AMERICAN SOCIETY OF MECHANCIAL ENGINEERS.

Discussion on this paper should be addressed to the Editorial Department, ASME, United Engineering Center, 345 East 47th Street, New York, N.Y. 10017, and will be accepted until two months after final publication of the paper itself in the JOURNAL OF APPLIED MECHANICS. Manuscript received by ASME Applied Mechancis Division, January, 1983; final revision July, 1983. Paper No. 84-APM-11.

Copies will be available until February, 1985.

Copyright © 1984 by ASME
Downloaded 02 May 2010 to 171.66.16.25. Redistribution subject to ASME license or copyright; see http://www.asme.org/terms/Terms_Use.cfm

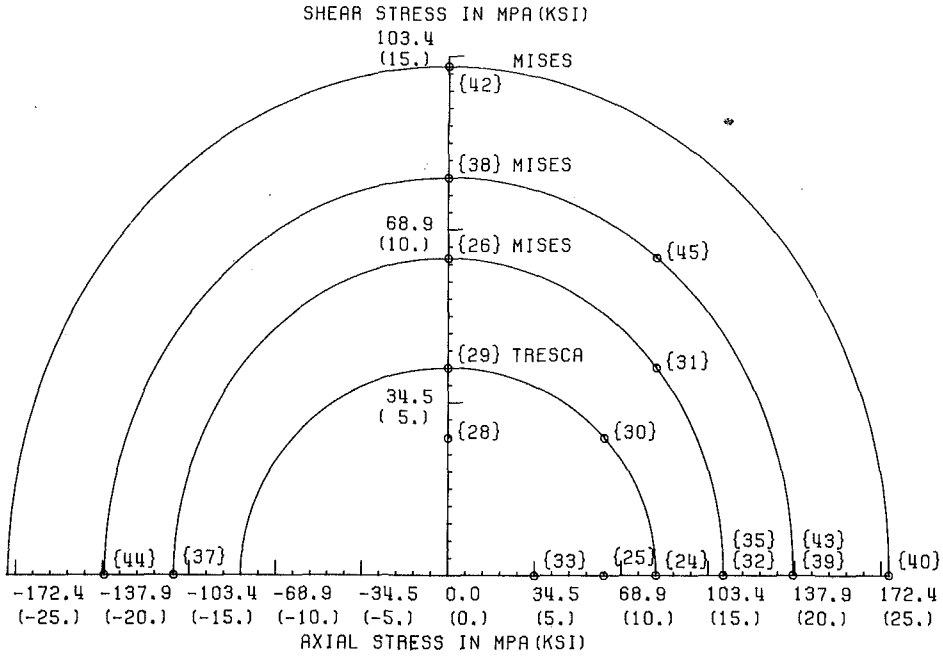

Fig. 1 Test numbers and stress surfaces

Table 2 Numerical results for 2 hour creep and recovery data

					Eq. (1)			Eq. (3)			Eq. (4)
Test	Tension, σ		Torsion, τ		ϵ°_{ij},	ϵ^{+}_{ij},	N	A_{ij},	ϵ^{+VE}_{ij},	n_1	$\frac{E}{\epsilon_{ij}}$,
No.	MPa	(ksi)	MPa	(ksi)	10^{-4}	$10^{-5}/hr^N$		10^{-4}	$10^{-5}/hr^{n_1}$		10^{-4}
T28	0	(0)	27.37	(3.97)	5.720	4.167	0.2318	-2.412	1.704	0.7901	6.162
CT30	62.05	(9.00)	27.37	(3.97)	5.494	4.843	0.2636	0.565	1.554	0.4919	5.687
T29	0	(0)	41.37	(6.00)	8.420	6.922	0.2730	1.643	2.370	0.3337	8.564
CT31	82.74	(12.00)	41.37	(6.00)	8.587	9.134	0.3097	2.757	6.739	0.1322	8.347
A33	34.47	(5.00)	0	(0)	5.186	1.386	0.4131	0.606	1.472	0.3163	5.184
A25	62.05	(9.00)	0	(0)	9.861	3.884	0.3787	1.280	3.509	0.1974	9.807
CA30	62.05	(9.00)	27.37	(3.97)	9.692	5.340	0.3648	1.761	9.256	0.0723	9.154
A24	82.74	(12.00)	0	(0)	12.660	7.380	0.3560	1.797	3.243	0.3712	12.900
CA31	82.74	(12.00)	41.37	(6.00)	12.890	9.698	0.3178	3.029	7.999	0.1593	12.560
CA45	82.74	(12.00)	63.23	(9.17)	12.350	20.030	0.2427	6.204	10.870	0.1773	12.340
T26	0	(0)	63.23	(9.17)	13.000	16.060	0.3162	5.180	11.880	0.1322	12.560
CT45	82.74	(12.00)	63.23	(9.17)	13.580	22.750	0.3043	9.412	20.670	0.0954	12.020
T38	0	(0)	79.22	(11.49)	17.690	33.580	0.2552	12.960	14.660	0.1618	16.600
A32	109.49	(15.88)	0	(0)	16.960	12.910	0.3258	3.569	6.834	0.2931	16.820
A37*	-109.49	(-15.88)	0	(0)	17.250	15.620	0.3235	4.752	7.872	0.1854	16.970
A35**	109.49	(15.88)	0	(0)	16.630	15.050	0.2923	3.328	8.452	0.2372	16.780
A39	137.21	(19.9)	0	(0)	21.380	27.030	0.2983	8.267	14.970	0.1990	21.610
A44*	-137.21	(-19.9)	0	(0)	21.030	32.300	0.2487	8.820	13.290	0.2050	21.170
A43**	137.21	(19.9)	0	(0)	21.370	35.500	0.2399	9.370	25.580	0.1104	20.260
T42	0	(0)	101.35	(14.7)	22.18	90.58	0.2824	220.100	155.800	0.0292	7.456
A40	175.54	(25.46)	0	(0)	28.430	59.490	0.2839	90.17	42.520	0.1088	26.550

*Compression test

**Aging test

Note: For test 42, the creep duration considered was 0.808 hours.

Specimens were thin-walled tubes of circular cross section machined from 63.5 mm dia. extruded rod. The nominal outside diameter, wall thickness, and gage length were 25.4, 1.52, and 101.6 mm (1.00, 0.06, and 4.00 in.), respectively. A more complete description of material and specimen is given in [2].

Experimental Apparatus and Procedures

The combined tension and torsion creep machine used in these experiments and the procedures for performance and data acquistion were described in [2–7].

A compression machine employed in the present work was described in [8].

The temperature control and measurement systems were the same for both machines described in [2–8]. Except for aging tests, the specimen was soaked at the test temperature of 200°C for approximately 18 hours prior to testing. All experiments were performed at a test temperature of 200°C. The variation of temperature was within ± 0.3°C both with time and position within the gage length.

Experimental Results

The test numbers and the stress levels under which the creep tests were performed are shown in Fig. 1. The magnitudes of the stress levels are given in Table 2. Three Mises stress curves whose magnitudes of effective stress defined by $\sigma^2 + 3\tau^2 = (\sigma_{eff})^2$ for combined tension σ and torsion τ stresses can be constructed through these stress points. The magnitudes of the three effective stresses are 109.5 MPa (15.88 ksi), 137.2 MPa (19.90 ksi), and 175.5 MPa (25.46 ksi), respectively. One

Downloaded 02 May 2010 to 171.66.16.25. Redistribution subject to ASME license or copyright; see http://www.asme.org/terms/Terms_Use.cfm

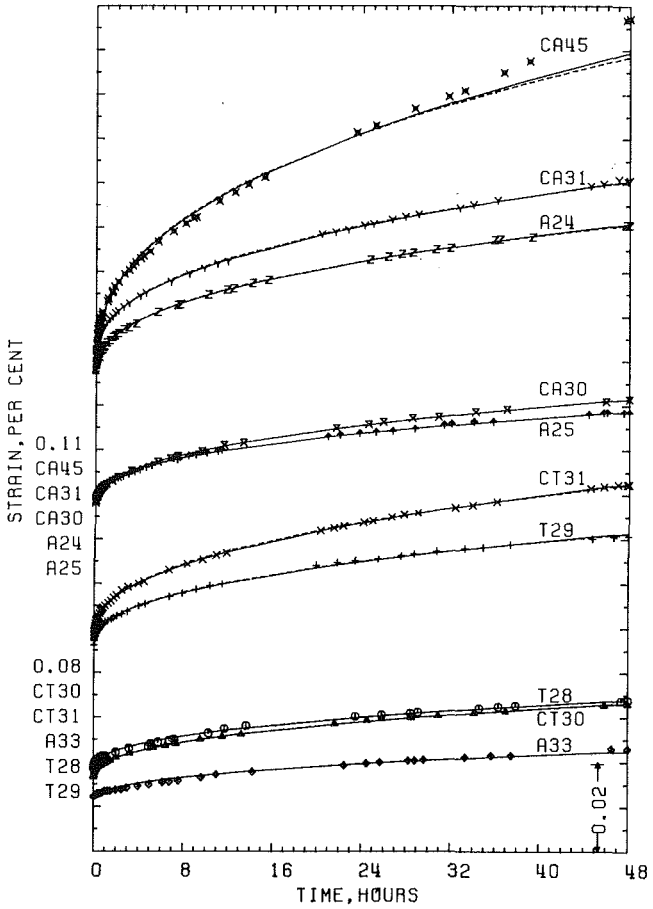

Fig. 2 Creep strains versus time. Solid lines are equation (2); dotted lines are equation (1). Numbers identify the tests listed in Table 2 with stress values.

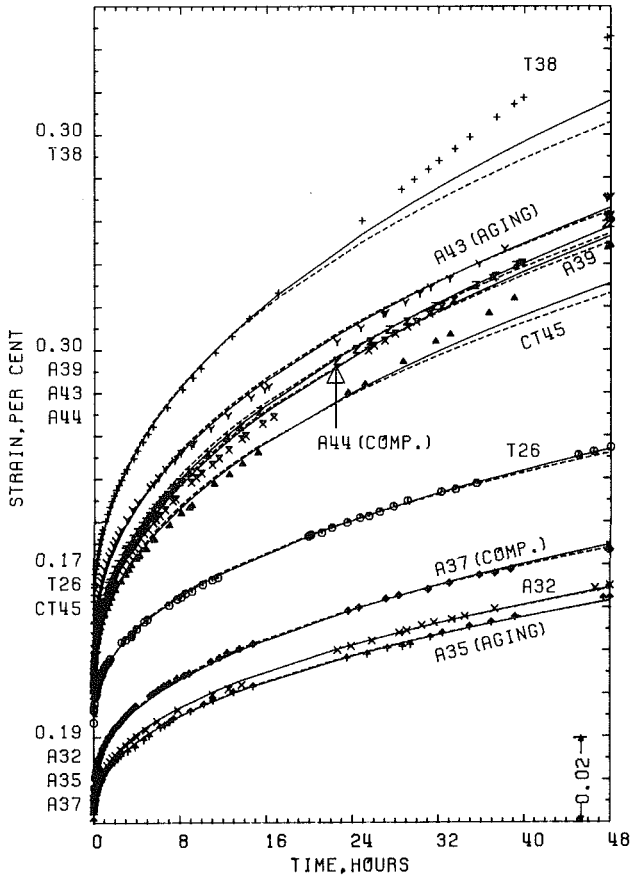

Fig. 4 Creep strains versus time. Solid lines are equation (2); dotted lines are equation (1). Numbers identify the tests listed in Table 2 with stress values.

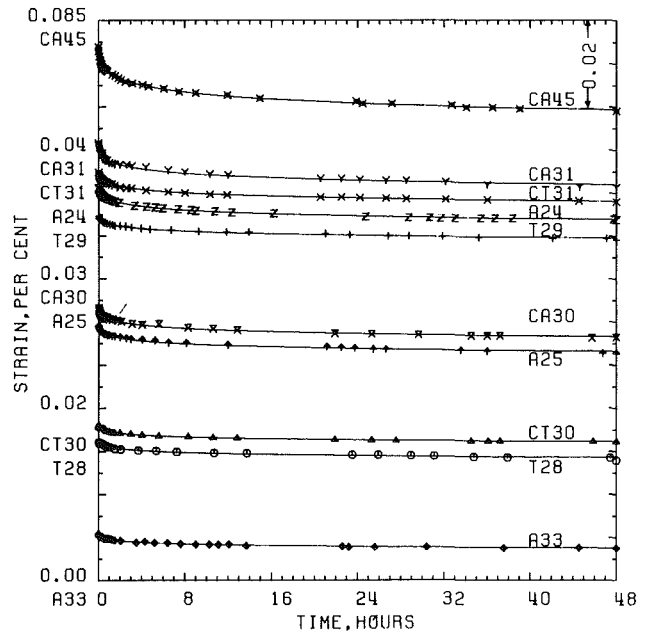

Fig. 3 Recovery strains versus time. Solid lines are equation (3). Numbers identify the tests listed in Table 2 with stress values.

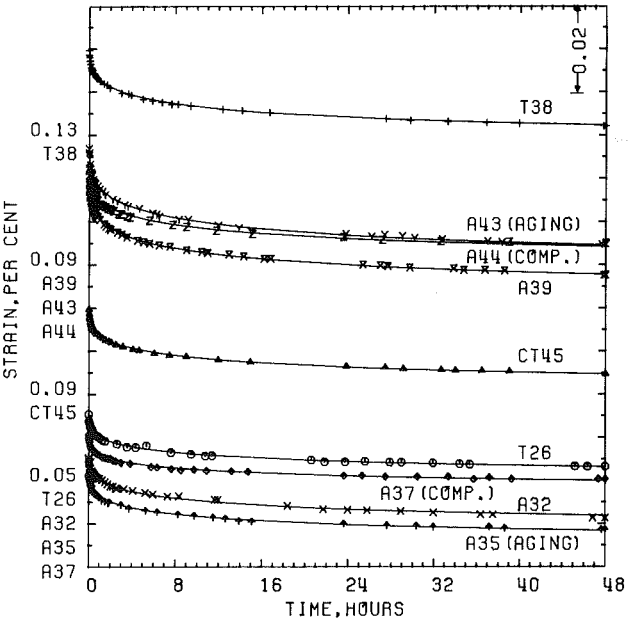

Fig. 5 Recovery strains versus time. Solid lines are equation (3). Numbers identify the tests listed in Table 2 with stress values.

Tresca curve defined by $\sigma^2 + 4\tau^2 = (82.7 \text{ MPa})^2 (12.00 \text{ ksi})^2$ can also be constructed through these stress points. Each combined tension and torsion test was interrelated with at least one pure axial creep test and one pure shear test. The test durations were all 48 hours for both creep and creep recovery except for test 42 whose creep period only lasted for 36.02 hours with a recovery period of 36 hours.

All the creep and recovery data are shown in Figs. 2–6 in which symbol A represents pure axial tests; symbol T represents pure shear tests, and symbols CA and CT represent the axial and the shear strains, respectively, in combined

Downloaded 02 May 2010 to 171.66.16.25. Redistribution subject to ASME license or copyright; see http://www.asme.org/terms/Terms_Use.cfm

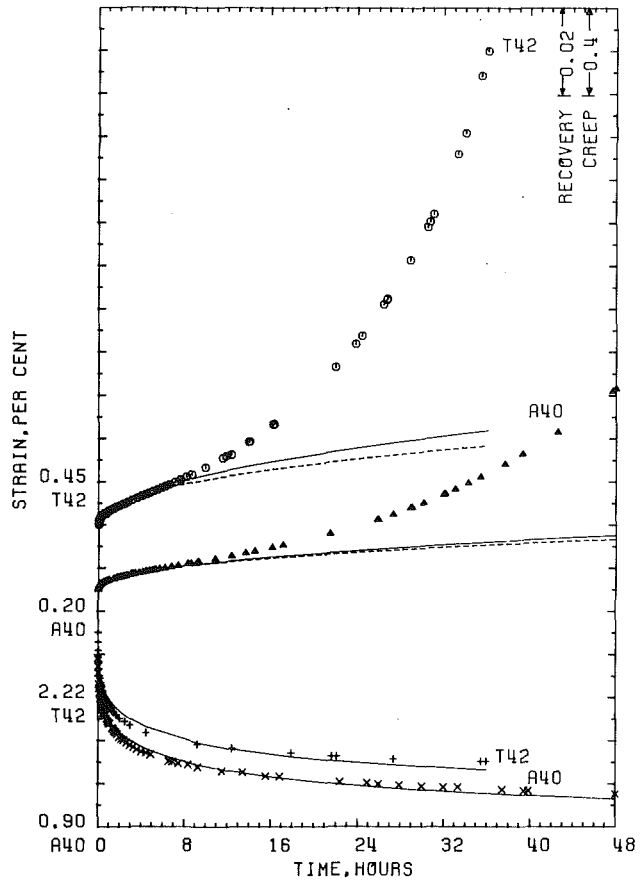

Fig. 6 Creep and recovery strains versus time for tests 40 and 42; solid lines are equation (2) for creep, equation (3) for recovery; dotted lines are equation (1). Numbers identify the tests listed in Table 2 with stress values.

tension-torsion tests. Figure 6 shows that the effective stress of 175.5 MPa (25.46 ksi) was high enough to cause tertiary creep in less than 1 hour for pure shear stress state.

Analysis of the Creep and Recovery Data

In the viscous-viscoelastic model, the total strain was decomposed into elastic (ϵ^E), plastic (ϵ^P), viscoelastic (ϵ^{VE}), and time-dependent nonrecoverable (ϵ^V) components. These components were taken to be independent of each other and additive.

In current work, the total strain ϵ_{ij} was well represented (except for tertiary creep) by the expression:

$$\epsilon_{ij} = \epsilon_{ij}^0 + \epsilon_{ij}^+ t^N, \tag{1}$$

where t is time and ϵ_{ij}^0 and ϵ_{ij}^+ are stress dependent.

Considering both the time-dependent strain components ϵ^{VE} and ϵ^V to be represented by power functions of time with different stress dependences, the total strain during creep was expressed as:

$$\epsilon_{ij} = \epsilon_{ij}^E + \epsilon_{ij}^P + \epsilon_{ij}^{+VE} t^{n_1} + \epsilon_{ij}^{+V} t^{n_2}. \tag{2}$$

The strain during creep recovery from creep at constant stress for time t_1 was the following according to the superposition principle,

$$\epsilon_{ij} = A_{ij} + \epsilon_{ij}^{+VE}\{t^{n_1} - (t-t_1)^{n_1}\}, \tag{3}$$

where A_{ij} is equal to $\epsilon_{ij}^{+V} t_1^{n_2} + \epsilon_{ij}^P$, t_1 is the creep duration, and ϵ^V is by definition not recoverable.

The elastic strain during load removal was

$$\epsilon_{ij}^E = \epsilon_{ij}|_{t=t_1} - A_{ij} - \epsilon_{ij}^{+VE} t_1^{n_1}, \tag{4}$$

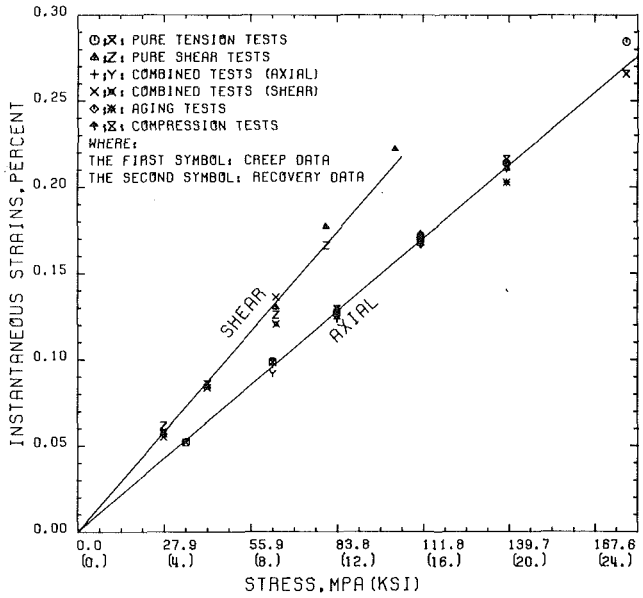

Fig. 7 ϵ_{ij}^0 and ϵ_{ij}^E in Table 2 versus stress

whre the first term came from the creep data and the last two terms were obtained from the recovery data.

To obtain the most accurate values of the instantaneous responses upon loading and unloading, only the first 2 hours of creep and recovery data were used to compute ϵ_{ij}^0 in equation (1) and ϵ_{ij}^E in equation (4). For test 42, only the data within 0.808 hours was used. The reuslts are shown in Table 2 and the instantaneous responses are plotted in Fig. 7 except for the value of ϵ_{ij}^E for test 42, which was erratic. The average values of N and n_1 in Table 2 are 0.301 and 0.229, respectively.

The data distribution shown in Fig. 7 is nearly linear which implies that time-independent plastic strain components are small or zero. Neglecting tests 40 and 42 because of their deviations in ϵ_{ij}^E and ϵ_{ij}^0, the inverse slopes of the best fitting straight lines yield the elastic moduli for tension E and for torsion G of 6.50×10^4 MPa (9.43×10^3 ksi) and 2.38×10^4 MPa (3.45×10^3 ksi), respectively, which are consistent with previous findings [2].

The recoverable viscoelastic component ϵ^{VE} was determined from the recoverable data by using equation (3). Neglecting tests 40 and 42, the time exponent n_1 was found to be independent of stress, as in [2], and the average value was $n_1 = 0.223$; see Table 3. This value of n_1 was nearly the same (0.244) as previously determined [2].

To determine the nonrecoverable time-dependent component ϵ^V, the recoverable strain ϵ^{VE} was first subtracted from the creep data using the relation $\epsilon_{ij}^{VE} = \epsilon_{ij}^{+VE} t^{0.223}$. Before calculating the ϵ^V components, the data in the secondary and tertiary stages were first eliminated because these stages were not described by equation (1). The cutoff point for primary creep was taken to correspond to a maximum shear strain of the ϵ^V component equal to 0.08 percent. The maximum shear strain of ϵ^V under combined tension and torsion stress states was defined by $[((3/4)\epsilon_{11}^V)^2 + (\epsilon_{12}^V)^2]^{1/2}$ with incompressibility of ϵ_{ij}^V and coincidence of the strain rate direction with the stress deviator assumed, as discussed in a later section. The cutoff times corresponding to this criterion are given in the note for Table 3. The criterion resulted from the following considerations: Since equation (3) could describe very well the whole recovery data even for those tests in which secondary and tertiary stages showed up, see Figs. 5 and 6, it appeared that ϵ^V dominated in these stages. So the criterion was based only on ϵ^V.

Downloaded 02 May 2010 to 171.66.16.25. Redistribution subject to ASME license or copyright; see http://www.asme.org/terms/Terms_Use.cfm

Table 3 Numerical results for 48 hour creep and recovery data

	Eq. (1)	Eq. (1) with N=0.407		Eq. (3)	Eq. (3) with n_1=0.223		Eq. (4) with n_1=0.223	Eq. (2)	Eq. (2) with n_1=0.223; n_2=0.496	
Test No.	N	ϵ^{o}_{ij}, 10^{-4}	ϵ^{+}_{ij}, $10^{-5}/hr^{N}$	n_1	A_{ij}, 10^{-4}	ϵ^{+VE}_{ij}, $10^{-5}/hr^{n1}$	ϵ^{E}_{ij}, 10^{-4}	n_2	$\epsilon^{E}_{ij} + \epsilon^{P}_{ij}$, 10^{-4}	ϵ^{+V}_{ij}, $10^{-5}/hr^{n2}$
T28	0.4519	5.815	3.245	0.3309	0.763	2.455	6.034	0.5701	5.743	1.559
CT30	0.3972	5.624	3.479	0.2593	1.130	2.407	5.594	0.4772	5.562	1.733
T29	0.4038	8.580	5.246	0.2936	1.826	3.227	8.479	0.4726	8.512	2.723
CT31	0.4115	8.762	7.159	0.1867	2.641	4.169	8.599	0.4799	8.686	3.775
A33	0.5757	5.103	2.344	0.2887	0.673	2.052	5.132	0.8002	5.030	1.059
A25	0.4247	9.841	4.195	0.3233	1.176	3.637	9.802	0.5504	9.718	1.884
CA30	0.4110	9.722	5.020	0.2766	1.495	4.064	9.681	0.5223	9.596	2.330
A24	0.4200	12.700	6.969	0.2730	2.199	4.623	12.760	0.5080	12.590	3.526
CA31	0.4224	13.010	8.339	0.2094	2.975	5.556	12.780	0.5197	12.870	4.203
CA45$^{\Delta}$	0.4513	12.840	14.500	0.2046	6.081	8.775	12.550	0.5793	12.660	7.631
T26	0.4324	13.240	13.160	0.1654	5.039	6.981	13.030	0.5003	13.150	7.161
CT45$^{\Delta}$	0.4459	13.800	19.690	0.1513	9.109	9.092	13.160	0.5393	13.730	11.240
T38$^{\Delta}$	0.2952	18.440	24.540	0.1774	12.810	10.580	16.980	0.3366	18.360	14.570
A32	0.4268	17.120	11.020	0.2660	3.850	8.463	16.660	0.5421	16.870	5.263
A37*	0.3781	17.570	12.060	0.1531	4.755	6.113	17.130	0.4252	17.510	6.614
A35**	0.4022	17.010	10.650	0.1757	3.519	8.021	16.800	0.4995	16.770	5.123
A39$^{\Delta}$	0.4572	21.700	22.380	0.1917	8.271	12.800	21.810	0.5649	21.480	11.920
A44$^{*\Delta}$	0.4042	21.880	22.410	0.1414	9.003	10.670	21.390	0.4698	21.810	12.520
A43$^{*\Delta}$	0.3798	22.480	22.250	0.1676	8.927	13.390	21.450	0.4665	22.230	11.580
T42$^{\Delta}$	0.2437	23.000	89.580	0.0259	219.600	19.320	20.960	0.2491	23.130	69.620
A40$^{\Delta}$	0.3055	29.310	49.530	0.0834	89.900	18.710	28.860	0.3508	29.200	31.440

*Compression test

**Aging test

Note: 1. The duration within which data were taken into analysis were 33.083, 17.000, 0.808 and 6.800 hours for the creep steps of tests 45, 38, 42, and 40 respectively. All the others are the whole test durations, i.e. 48 hours for both the creep and the recovery step except for test 42 whose recovery step lasted 36 hours.

2. The elastic responses ϵ^{E}_{ij} from Table 2 were taken into account in computing N and n_2 for tests indicated by Δ by including in the data set the elastic strain at t=0 calculated from E and G.

The creep data in the primary stage, after subtracting ϵ^{VE}, were used in equation (2) to determine ϵ^{+V}_{ij} and n_2; see Table 3. The exponent n_2 was found to be independent of stress, as in [2], and to have an average value of 0.496.

The primary creep data were also fitted by equation (1) to obtain ϵ^{+}_{ij} and N; see Table 3. The average N was found to be 0.407. The results obtained through the foregoing procedures are plotted in Figs. 2–6 in which equations (2) and (3) are represented by solid lines for creep and recovery data, respectively, and equation (1) is represented by dotted lines for creep data only.

Unlike results in previous work [2], the values of n_1 and n_2 were found to be different, even though both were independent of stress. Contrary to the results for 304 stainless steel [9, 10], increasing the time period of creep data employed in analysis had the effect of increasing the time exponents; compare the values of N in Table 2 with those in Table 3. However, the value of n_1 (recoverable) was nearly independent of the time duration of data employed, n_1 = 0.229 and 0.223 for 2 and 48 hours, respectively. Since the exponent n_2 was independent of stress even for the primary part of tests, which subsequently showed secondary and tertiary stages, the current value of n_2 may be satisfactory for the entire primary stage (generally more than 48 hours for low stress) as long as aging effects are negligible.

The small differences between the instantaneous responses determined from 2 hours and 48 hours of data for a few high stress tests will be neglected in the subsequent analysis, and the values obtained from 2 hours of data will be used. This will cause small discrepancies between the experimental data and the theoretical predictions at the very beginning of a few high stress tests.

Symmetry in Tension and Compression

Only a few data (see [11 pp. 257–261]) have been published for compression creep. These data showed that short term creep is symmetrical in tension and compression. Comparing the curves for tests 32 and 37, 39 and 44 in Fig. 4, also the corresponding values of ϵ^{+}_{ij}, ϵ^{+VE}_{ij}, and ϵ^{+V}_{ij} in Table 3, shows that the total creep strains are close to each other in tension and compression throughout the test durations (the compression strains are somewhat greater than the tension). The viscoelastic components of strain ϵ^{VE} in tension are a little higher than those in compression which results in smaller strain for the ϵ^{V} component in tension in the viscous-viscoelastic model. This may be true material behavior. However, since the differences did not increase with stress and the proportion of the viscoelastic component in the total strain was small, the differences were neglected in the current work. This would induce deviations between the experimental data and theoretical predictions of about, 10 percent for ϵ^{VE} and 5 percent for ϵ^{V} in the viscous-viscoelastic model. Symmetry is not expected through the secondary and tertiary stages for constant load creep tests; see [11, p. 258].

Aging Effects

Two aging tests were performed in the current work. The pretest soaking durations were 312 hours and 114 hours for tests 35 and 43, respectively, Figs. 4 and 5. The whole test durations for nearly all the tests performed in the current research are within this range.

Comparing test 35 (aged 312 h) with test 32 (aged 18 h) at the same stress, and test 43 (aged 114 h) with test 39 (aged 18 h) at the same stress show that there are no significant aging effects within 300 hours. However, a previous test reported in [2] showed that aging for 1103 hours had a considerable softening effect.

Creep Rates and Creep Surfaces

A widely used representation for the multiaxial primary creep rate is

$$\dot{\epsilon}_{ij} = F_a(J_2)\sigma'_{ij}t^m \tag{5}$$

where σ'_{ij} is the stress deviator and $J_2 = \frac{1}{2}\sigma'_{ij}\sigma'_{ij}$ is the second invariant of the stress deviator; see [12, 13]. This expression implies that the creep deformation is incompressible and the

Downloaded 02 May 2010 to 171.66.16.25. Redistribution subject to ASME license or copyright; see http://www.asme.org/terms/Terms_Use.cfm

creep rate tensor has the same direction as the applied stress deviator, that is, normal to the Mises surface. Furthermore, taking squares of both sides of (5) yields $\frac{1}{2}\dot{\epsilon}_{ij}\dot{\epsilon}_{ij} = [F_a(J_2)]^2(J_2)t^{2m}$. Thus the magnitude of the strain rate tensor defined by $(\frac{1}{2}\,\dot{\epsilon}_{ij}\dot{\epsilon}_{ij})^{\frac{1}{2}}$ is constant along a Mises stress surface at a given time. A surface defined by a constant value of $(\frac{1}{2}\dot{\epsilon}_{ij}\dot{\epsilon}_{ij})^{\frac{1}{2}}$ could be explained as a surface of constant rate of energy dissipation. In previous work [6, 14, 15], the creep surface was defined as the stress surface for which creep rate tensors had equal magnitudes following creep for a given time at constant stress. If equation (5) is true for any given stress states, it implies that the creep surface may be represented by a Mises stress surface and the material hardens isotropically. This follows from the fact that creep under the given stress state reduces the strain rate for any other state of stress in an isotropic fashion since the magnitude of the strain rate tensor $(\frac{1}{2}\,\dot{\epsilon}_{ij}\dot{\epsilon}_{ij})^{\frac{1}{2}}$ is constant at a given time along a J_2 curve. A strain hardening model can be obtained by expressing t in terms of the accumulated effective strain as discusssed in [13].

The creep surface may be related to the state variable theories, the flow rules of most of which were expressed as:

$$\dot{\epsilon}_{ij} = F_b(J_2', K)\,\Sigma_{ij}, \tag{6}$$

where $\Sigma_{ij} = \sigma_{ij}' - \alpha_{ij}$, J_2' is the second invariant of Σ_{ij}, and K and α_{ij} are the scalar and the tensorial state variables, respectively. These flow rules imply that the strain rate tensor has the same direction as Σ_{ij} and the creep surface defined by constant strain rate magnitude can be represented by $J_2' = \frac{1}{2}\Sigma_{ij}\Sigma_{ij} = \text{constant}$.

Anisotropic creep surfaces may be introduced by (6). Since α_{ij} defines the center of the creep surface, nonzero values of α_{ij} result in kinematic movement of the creep surface. Furthermore, squaring both sides of (6) yields $\frac{1}{2}\dot{\epsilon}_{ij}\dot{\epsilon}_{ij} = [F_b(J_2', K)]^2\,J_2'$. Thus surfaces of constant J_2' imply constant magnitudes of strain rate tensors.

Although it is quite impossible to draw any conclusion about the hardening natures of the material from constant stress creep data, equation (5) can be evaluated by comparing the creep rates of different creep tests whose stress levels are equated by the Mises relation. According to equation (5), the ratio $\dot{\epsilon}_{11}/\dot{\epsilon}_{12}$ should equal $2/\sqrt{3}$ for a pure axial creep test and the corresponding pure shear test whose stress levels lie on the same Mises surface. However, a comparison of the values of ϵ_{ij}^{+} and ϵ_{ij}^{+V} in Table 3 for axial and shear tests on the same Mises curve showed that none of these data satisfied this requirement. They actually showed the opposite tendencies, i.e., shear creep rates were higher than axial creep rates. The data for 304 stainless steel also showed the same thing [9, 10, 14].

To eliminate this disagreement, $F_a(J_2)$ in equation (5) was replaced by F_c as a function of maximum shear stress $\tau_{\max}$,

$$\dot{\epsilon}_{ij} = F_c(\tau_{\max})\sigma_{ij}'t^m. \tag{7}$$

Equation (7) shows that tensors $\dot{\epsilon}_{ij}$ and σ_{ij}' have the same directions, which is normal to a Mises surface. Taking the maximum of the shear stress on the right-hand side of (7) and the maximum of the shear strain rate on the left-hand side shows that the maximum shear strain rates are a function of the maximum shear stress and time only. Thus at any given time the maximum shear strain rates are constant along a Tresca curve. If equation (7) is true for any given state of stress, it implies that a creep surface defined by normality of the strain rate vector is not the same as that defined by a constant value of $(\frac{1}{2}\dot{\epsilon}_{ij}\dot{\epsilon}_{ij})^{\frac{1}{2}}$, as discussed in [15]. Furthermore, the rate ratio $\dot{\epsilon}_{11}/\dot{\epsilon}_{12}$ for a pure axial creep test and a pure shear test whose stress levels are the same according to the Tresca relation should be 4/3. Comparing the values of ϵ_{ij}^{+V} and ϵ_{ij}^{+} of tests 29 (pure torsion) with those of test 24 (pure tension) which are on the same Tresca curve, see Fig. 1, yields ratios that are almost exactly 4/3, i.e., 1.295 for ϵ_{ij}^{+V} and 1.33 for ϵ_{ij}^{+}, respectively. A subsequent section show that equation (7) can describe the whole set of constant stress creep data quite well. However, a disadvantage of this type of expression is that it cannot be derived from a potential theory.

It should be noticed that neither (5) nor (7) can specify exactly the initial creep surface because the initial creep rate is very rapid, infinite as described by the power of time. Also their agreement with constant stress creep data does not guarantee that the material has an isotropic hardening nature. Other more complicated stress histories such as non-proportional loadings are necessary for this determination. However, the degree of agreement of (5) and (7) with data does give some indications of the suitability of using a Mises or Tresca relation to extend the constitutive relations from uniaxial to multiaxial stress states.

The Stress Dependence of ϵ^{VE} and ϵ^{V}

In previous work [2–5], the stress dependences of the time-dependent components were represented by a third-order multiple integral representation combined with creep limits below which creep does not occur or is negligible. However, the current data at stresses as low as 34.5 MPa (5.00 ksi) shows that there is creep below the transition previously called a creep limit. Furthermore, the creep behavior below the apparent creep limits is very nearly linear. Therefore, in the following analysis, no creep limits will be included.

The third-order multiple integral representation yields the following expressions [2] for the stress-dependent coefficients ϵ_{11}^{+VE} and ϵ_{12}^{+VE} under constant combined tension and torsion stress, i.e.,

$$\epsilon_{11}^{+VE} = F_1^{+}\sigma + F_2^{+}\sigma^2 + F_3^{+}\sigma^3 + F_4^{+}\sigma\tau^2 + F_5^{+}\tau^2, \tag{8}$$

$$\epsilon_{12}^{+VE} = G_1^{+}\tau + G_2^{+}\tau^3 + G_3^{+}\sigma\tau + G_4^{+}\sigma^2\tau, \tag{9}$$

where F_i^{+} and G_i^{+} are constants.

Because of symmetry in tension versus compression, F_2^{+} and G_3^{+} are zero. Also, F_5^{+} is zero since there occurred negligible axial creep strain during pure shear creep tests except for test 42 in which a small amount of axial strain was detected in the tertiary stage, which might be due to geometrical change caused by the large deformation in shear.

By use of the method of least squares, the values of F_1^{+}, F_3^{+} and G_1^{+}, G_3^{+} were determined from pure tension and pure torsion creep data, respectively. Then the values of F_4^{+} and G_4^{+} were determined from combined tension and torsion data. The details of these procedures can be found in [2, 16]. The constants for ϵ^{+VE} determined through these procedures are shown in Table 4. Equations (8) and (9) are represented by solid lines for pure axial and pure shear tests and dotted lines for combined tension and torsion tests in Fig. 8.

However, it was found that the coefficients for the ϵ^{V} component (ϵ^{+V}) were not well described by equations like (8) and (9). Apparently terms of higher order than these would be required to describe the stress dependence of ϵ^{V}, which would be impractical. In experimental results for 304 stainless steel

Table 4 Constants for equations (8) and (9)

F_1^{+}	4.634×10^{-7}, per MPa-h^{n_1}	3.195×10^{-6}, per ksi-h^{n_1}
F_3^{+}	1.964×10^{-11}, per MPa^3-h^{n_1}	6.437×10^{-9}, per ksi^3-h^{n_1}
F_4^{+}	1.156×10^{-10}, per MPa^3-h^{n_1}	3.789×10^{-8}, per ksi^3-h^{n_1}
G_1^{+}	5.938×10^{-7}, per MPa-h^{n_1}	4.094×10^{-6}, per ksi-h^{n_1}
G_2^{+}	1.261×10^{-10}, per MPa^3-h^{n_1}	4.133×10^{-8}, per ksi^3-h^{n_1}
G_4^{+}	3.542×10^{-11}, per MPa^3-h^{n_1}	1.161×10^{-8}, per ksi^3-h^{n_1}

Note: $F_2^{+} = F_5^{+} = G_3^{+} = 0$, $n_1 = 0.223$

Downloaded 02 May 2010 to 171.66.16.25. Redistribution subject to ASME license or copyright; see http://www.asme.org/terms/Terms_Use.cfm

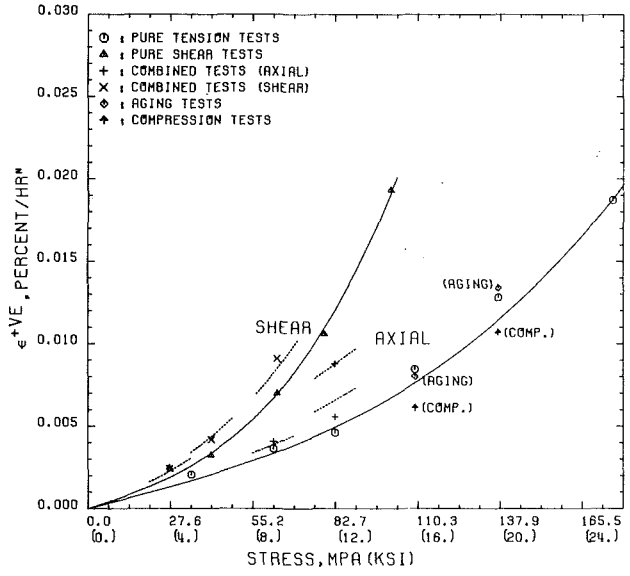

Fig. 8 ϵ_{ij}^{+VE} **versus stress. The solid lines and the dotted lines represent the multiple integral representations with the constants shown in Table 4.**

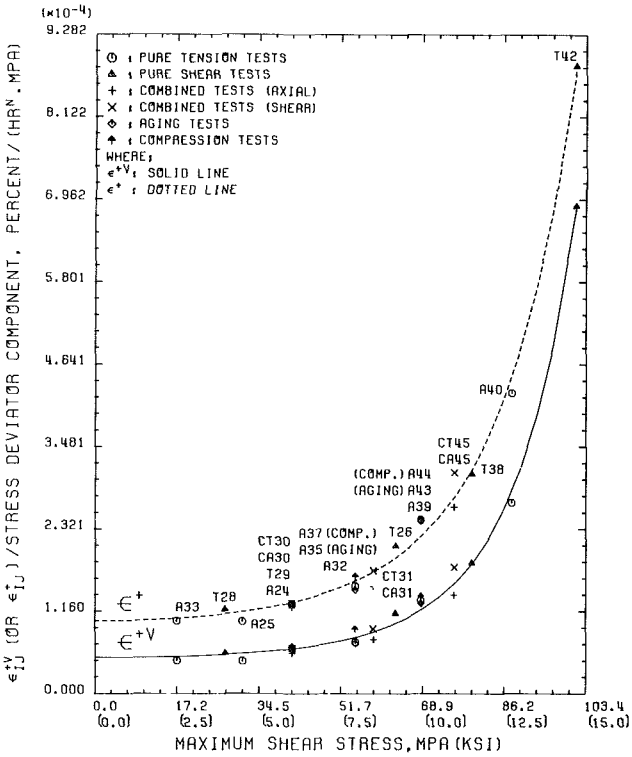

Fig. 9 $\epsilon_{ij}^{+V}/\sigma_{ij}'$ **and** $\epsilon_{ij}^{+}/\sigma_{ij}'$ **versus maximum shear stress. The dotted line and the solid line represent equations (12) and (11), respectively.**

[9, 10], the data were separated ino linear and nonlinear regions to deal with this situation. Here, because of the agreements with tests 24 and 29 as discussed in the preceding section, equation (7) was employed to represent the ϵ^V component. Under constant stress, ϵ^V can then be expressed by

$$\epsilon_{ij}^{V} = F(\tau_{\max})\sigma_{ij}' t^n, \tag{10}$$

where $\tau_{\max}$ is the maximum shear stress, σ_{ij}' is the stress deviator, and $F(\tau_{\max})\sigma_{ij}'$ represents the stress dependence of ϵ_{ij}^{+V}. The incompressibility of ϵ_{ij}^{V} is a corollary of this expression.

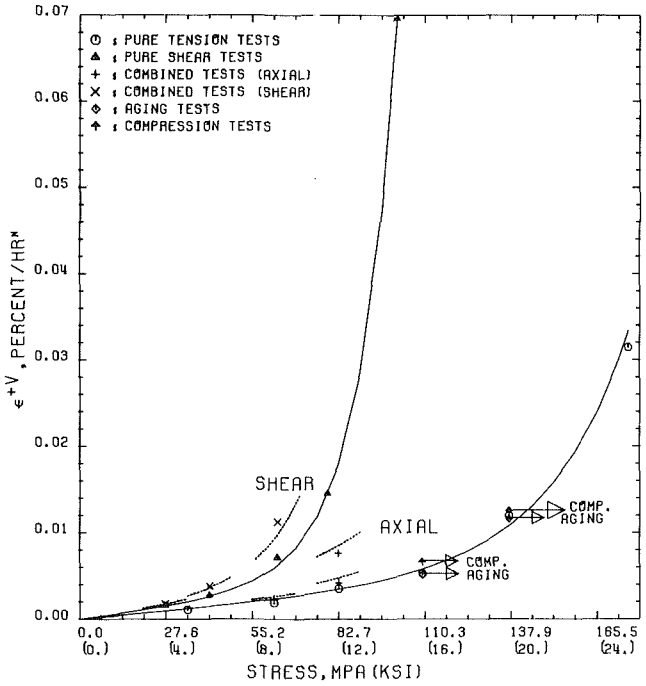

Fig. 10 ϵ_{ij}^{+V} **versus stress. The solid lines and the dotted lines represent** $F(\tau_{\max})\sigma_{ij}'$ **with** $F(\tau_{\max})$ **expressed by equation (11).**

For combined tension σ and torsion τ stress states, σ_{ij}' is equal to zero except for $\sigma_{11}' = (2/3)\sigma$, $\sigma_{22}' = \sigma_{33}' = (-1/3)\sigma$, $\sigma_{12}' = \sigma_{21}' = \tau$. Also τ_{max} is equal to $[(\sigma/2)^2 + \tau^2]^{1/2}$. To check the validity of equation (10), ϵ_{ij}^{+V} (in Table 3)/σ_{ij}' was plotted versus $\tau_{\max}$, also ϵ_{ij}^{+} (in Table 3)/σ_{ij}' was plotted versus $\tau_{\max}$ for a possible viscoplastic approach. These plots are shown in Fig. 9 as the lower and the upper data sets, respectively. Even though there seemed to be some deviations for combined tension and torsion tests, the data showed a homogeneous relationship in $F(\tau_{\max})$. On the other hand, if equation (5) was employed, then $F(\tau_{\max})$ in equation (10) should be replaced by $F(J_2)$. A plot of $\epsilon_{ij}^{+}/\sigma_{ij}'$ versus J_2 would show the invalidity of this expression. For example, tests T26 and A32 are on the same Mises curve, see Fig. 1. Two other pairs T38 and A39, T42 and A40 are also on the same Mises curves. However, their values are not the same as requried by F as a function of J_2. They are far apart as may be observed in Fig. 9.

The functions $F(\tau_{\max})$ were found to represent the data best using the following expressions:
for ϵ_{ij}^{+V},

$$F(\tau_{\max}) = 3.616 \times 10^{-5} \times \{1 + 0.3914 \times \exp[2.108 \times 10^5 \times (\tau_{\max}/G)^2]\}, \text{ percent per MPa} - \text{hr}^{0.496}; \tag{11}$$

and for ϵ_{ij}^{+},

$$F(\tau_{\max}) = 6.219 \times 10^{-5} \times \{1 + 0.6433 \times \exp[1.633 \times 10^5 \times (\tau_{\max}/G)^2]\}, \text{ percent per MPa} - \text{hr}^{0.407}, \tag{12}$$

where G is the shear modulus determined in a previous section. Equations (11) and (12) are shown, respectively, as the solid and the dotted lines in Fig. 9.

If the exponential term in (11) or (12) is expanded in a Taylor series and multiplied by σ_{ij}', the first two terms of equations (11) or (12) reduce to the same form as (8) and (9) with $F_2^+ = F_5^+ = G_3^+ = 0$. However, in this case, the coefficients for ϵ_{11}^{+V} and ϵ_{12}^{+V} are not independent of each other because incompressibility was assumed in equation (9).

The stress dependence of ϵ_{ij}^{+V} represented by $F(\tau_{\max})\sigma_{ij}'$ are shown in Fig. 10 as the solid lines for pure axial and pure shear tests and as dotted lines for combined tension and torsion tests. The agreement with the test data are quite good.

Downloaded 02 May 2010 to 171.66.16.25. Redistribution subject to ASME license or copyright; see http://www.asme.org/terms/Terms_Use.cfm

Conclusions

48 hour creep and recovery data over a wide range of multiaxial stress states showed that creep limits did not exist and that aging effects were negligible up to 300 hours. The time dependence was resolved into recoverable and nonrecoverable components having different time dependences and stress dependences. A third-order polynomial in stress was found inadequate to describe the stress dependence of the nonrecoverable component. Creep was symmetrical in tension versus compression. The strain rate magnitudes defined by maximum shear strain rate are the same at any given time for those creep tests whose stress levels are the same according to the Tresca relation. The creep behavior at low stresses, which can closely be approximated by a linear relationship, is different from that at high stress.

The stress-strain relations for constant stress creep and recovery employed the multiple integral representation for the recoverable component of strain and a function of the maximum shear stress multiplied by the stress deviator for the nonrecoverable component of strain. A function of the second invariant of the stress deviator (Mises relation) was not applicable.

Acknowledgment

This work was supported by the Army Research Office, Research Grant Number DAAG29-81-K-0138. The material was contributed by the Aluminum Company of America. The authors are grateful to R. M. Reed for assistance in experiments.

References

1 Findley, W. N., Cho, U. W., and Ding, J. L., "Creep of Metals and Plastic Under Combined Stresses, A Review," ASME *Journal of Engineering Materials and Technology*, Vol. 101, 1979, p. 365.

2 Findley, W. N., and Lai, J. S., "Creep and Recovery of 2618 Aluminum Alloy Under Combined Stress With a Respresentation by a Viscous-Viscoelastic Model," ASME JOURNAL OF APPLIED MECHANICS, Vol. 45, 1978, pp. 507–514.

3 Lai, J. S., and Findley, W. N., "Creep of 2618 Aluminum Under Step Stress Changes Predicted by a Viscous-Viscoelastic Model," ASME JOURNAL OF APPLIED MECHANICS, Vol. 47, 1980, pp. 21–26.

4 Findley, W. N., and Lai, J. S., "Creep of 2618 Aluminum Under Side Steps of Tension and Torsion and Stress Reversal Predicted by a Viscous-Viscoelastic Model," ASME JOURNAL OF APPLIED MECHANICS, Vol. 48, 1981, pp. 47–54.

5 Lai, J. S., and Findley, W. N., "Simultaneous Stress Relaxation in Tension and Creep in Torison of 2618 Aluminum at Elevated Temperature," ASME JOURNAL OF APPLIED MECHANICS, Vol. 49, 1982, pp. 19–25.

6 Blass, J. J., and Findley, W. N., "Short Time Biaxial Creep of an Aluminum Alloy With Abrupt Changes of Temperature and State of Stresses," ASME JOURNAL OF APPLIED MECHANICS, Vol. 38, 1971, pp. 489–501.

7 Findley, W. N., and Gjelsvik, A., "A Biaxial Testing Machine for Plasticity; Creep or Relaxation Under Variable Principal Stress Ratios," *Proceedings, American Society for Testing and Materials*, Vol. 62, 1962, pp. 1103–1118.

8 Findley, W. N., "A Compressive Creep Machine," ASTM *Journal of Testing and Evaluation*, Vol. 10, July 1982, pp. 179–180.

9 Cho, U. W., and Findley, W. N., "Creep and Creep Recovery of 304 Stainless Steel Under Combined Stress With a Representation by a Viscous-Viscoelastic Model," ASME JOURNAL OF APPLIED MECHANICS, Vol. 47, 1980, pp. 755–761.

10 Cho, U. W., and Findley, W. N., "Creep and Creep Recovery of 304 Stainless Steel at Low Stresses With Effects of Aging on Creep and Plastic Strains," ASME JOURNAL OF APPLIED MECHANICS, Vol. 48, pp. 785–790.

11 Robotnov, Yu. N., *Creep Problems in Structural Members*, North-Holland, Amsterdam, 1969.

12 Henderson, J., "An Investigation of Multiaxial Creep Characteristics of Metals," ASME *Journal of Engineering Materials and Technology*, Vol. 101, 1979, p. 356.

13 Kraus, H., *Creep Analysis*, Wiley, New York, 1980.

14 Mark, R., and Findley, W. N., "Concerning a Creep Surface Derived From a Multiple Integral Representation for 304 Stainless Steel Under Combined Tension and Torsion," ASME JOURNAL OF APPLIED MECHANICS, Vol. 45, 1978, pp. 773–780.

15 Findley, W. N., Lai, J. S., and Nolte, K. G., "Concerning a Creep Surface for an Aluminum Alloy," ASME JOURNAL OF APPLIED MECHANICS, Vol. 38, 1971, pp. 1091–1094.

16 Findley, W. N., Lai, J. S., and Onaran, K., *Nonlinear Creep and Relaxation of Viscoelastic Materials, With an Introduction to Linear Viscoelasticity*, North-Holland, Amsterdam, 1976.

Downloaded 02 May 2010 to 171.66.16.25. Redistribution subject to ASME license or copyright; see http://www.asme.org/terms/Terms_Use.cfm

Multiaxial Creep of 2618 Aluminum Under Proportional Loading Steps

J.-L. Ding
Research Assistant.

W. N. Findley
Professor of Engineering.
Fellow ASME

Division of Engineering,
Brown University,
Providence, R.I. 02912

Creep data of 2618-T61 aluminum alloy under multistep multiaxial proportional loadings at 200°C (392°F) are reported. Two viscoplastic flow rules were developed using constant stress creep and creep recovery data. One was based on the accumulated strain (isotropic strain hardening), and the other on a tensorial state varible (kinematic hardening). Data were represented by two models: a nonrecoverable viscoplastic model, and a viscous-viscoelastic model in which the time-dependent strain was resolved into recoverable (viscoelastic) and nonrecoverable components. The modified superposition principle was used to predict the viscoelastic strain component under variable stress states. The experiments showed that the viscous-viscoelastic model with either isotropic strain hardening or kinematic hardening gave very good predictions of the material responses. Isotropic strain hardening was best in some step-down stress states. The viscoelastic component accounted for not only the recovery strain but also the transient creep strain upon reloadings and step-up loadings.

Introduction

There have been great advances in the development of constitutive relations suitable for material used in design for high temperature. However, all suffer from a lack of experimental data to evaluate them [1].

Classically, most constitutive relations were based on the strain hardening rule. Some modifications have to be made for this approach to simulate the anisotropic nature observed in most structural materials, see [2, 3] and [4, Chapter 2].

In recent theories, state variables have been introduced to incorporate the anisotropic nature. The formulations usually consist of a flow rule that describes the interrelations between strain rate, applied stress, and state variable, and an evolution rule that describes the rate of change of the state variables with deformation and metallurgical effects. The evolution rule was generally based on the Bailey-Orowan model [5], and in most cases a tensorial state variable (back stress) was associated with the kinematic hardening nature and a scalar state variable with the isotropic hardening nature, see [6–8]. Nearly all theories used the Mises relation to extend their applicability from uniaxial to multiaxial stress states, and except for Hart's work [8], they are all based on the viscoplastic approach.

In previous work at Brown University on 2618–T61 aluminum [9–12], a viscous-viscoelastic model (*VV*) with strain-hardening nature was developed and compared with a series of short-term creep tests under various stress histories. The stress-strain relations were refined in [13] through a set of 48 hour creep and recovery data under constant multiaxial stress states including aging and compression tests. In current work, the previous strain-hardening flow rule (*SH*) was refined and another kinematic hardening rule (*KH*) was derived from the stress-strain relations reported in [13]. In addition to the *VV* model, a viscoplastic model (*VP*) in which all the time-dependent strain was assumed nonrecoverable was also developed to show the role of the viscoelastic component. A set of 300-hour creep experiments under multiaxial multistep proportional loadings were compared with: a *VV* model with *SH* nature (*VV-SH*); a *VV* model with *KH* nature (*VV-KH*); a *VP* model with *SH* nature (*VP-SH*); and a *VP* model with *KH* nature (*VP-KH*). Future work will consider more complicated stress states such as nonproportional loadings, stress reversals, and mixed stress relaxation and multiaxial creep.

Material, Specimen, Apparatus, and Procedures

The material employed in the present work was aluminum alloy 2618–T61 which came from the same batch as that reported in [13]. A more complete description of material and specimen were given in [9, 13]. The combined tension and torsion machine and the compression machine used for these experiments were described in [14] and [15], respectively. The temperature control system and the data acquisition procedures were described in [9, 14, 15]. All the tests were performed at a test temperature of 200°C.

Contributed by the Applied Mechanics Division for presentation at the 1984 PVP Conference and Exhibition, Joint With Applied Mechanics Division and Materials Division, San Antonio, Texas, June 17–21, 1984 of THE AMERICAN SOCIETY OF MECHANICAL ENGINEERS.

Discussion on this paper should be addressed to the Editorial Department, ASME, United Engineering Center, 345 East 47th Street, New York, N.Y. 10017, and wil be accepted until two months after final publication of the paper itself in the JOURNAL OF APPLIED MECHANICS. Manuscript received by ASME Applied Mechanics Division, January, 1983; final revision, July, 1983. Paper No. 84-APM-12.

Copies will be available until February, 1985.

Copyright © 1984 by ASME
Downloaded 02 May 2010 to 171.66.16.25. Redistribution subject to ASME license or copyright; see http://www.asme.org/terms/Terms_Use.cfm

Experimental Results

Eight tests are reported here whose loading programs and the resulting total strain versus time are shown in Figs. 1–7. The total duration of each test was around 300 h. The letter A preceeding the test number represents a pure tension or compression test, T represents a pure torsion test, and CA, CT represent the axial part and the torsion part, respectively, in a combined tension and torsion test. The first two periods of each test were constant stress creep followed by creep recovery. These were used for determining the stress-strain-time relations for constant stress states, as reported in [13]. Test 23, Fig. 1, was not shown in [13] because some friction was detected in the strain measuring system during the first period and small adjustments were made during period 2 to save the following steps.

The loading direction remained constant for each test. The magnitudes changed abruptly in the following ways: step up followed by step down as in Fig. 2, step down followed by step up as in Fig. 3 and 7, and step down followed by reloading and step down as in Fig. 1, 4–6. Test A37, Fig. 6, is a compression test with the loading program exactly the same as that of tension test A32 shown in the same figure. The symmetry in tension and compression as discussed in [13] can be reaffirmed from Fig. 6. Another compression test is A44, Fig. 7.

The loading program for test 31 (CA31 or CT31), Fig. 5, is basically the same as that for test A32 with equal magnitudes of effective stress defined by $\sigma^2 + 3\tau^2 = (\sigma_{\text{eff}})^2$ for each pair of corresponding steps.

The third period for all the tests except test A24, Fig. 2 was reloaded to the same stress as the first period. This always resulted in some transient creep strain upon reloading to the previous creep stress level. Also all the step-up steps resulted in transient creep. Partial unloading resulted in the following: if the reduction was small enough there was a period of strain recovery followed by new creep within 24 h or less, as in period 6, Figs. 1 and 2; period 4, Fig. 3; period 7, Figs. 5(*a*), 5(*b*) and 6. However, in period 4, Fig. 7 a reduction of stress similar to that of period 4, Fig. 3 but at much higher stress yielded continuous strain recovery during the period of observation.

When the stress was reduced in one or two steps to about one-half there was a short strain recovery period followed by a long period with no strain change, as in period 7, Figs. 1 and 2; period 4 Figs. 4, 5, and 6; period 7, Fig. 4; and period 9, Fig. 7. If the stress was reduced in several steps to a sufficiently small proportion of the initial stress, continuous slow strain recovery was observed as in period 8, Figs. 1, 5, and 6; period 5, Figs. 3 and 7.

Stress-Strain-Time Relations for Constant Stress States

In the *VV* model, the total strain ϵ_{ij} during constant stress creep was represented as:

$$\epsilon_{ij} = \epsilon_{ij}^E + \epsilon_{ij}^{+VE} t^{n_1} + \epsilon_{ij}^{+V} t^{n_2}, \tag{1}$$

where ϵ_{ij}^E is the time-independent elastic strain, $\epsilon_{ij}^{+VE} t^{n_1} = \epsilon_{ij}^{VE}$ is the viscoelastic component, and $\epsilon_{ij}^{+V} t^{n_2} = \epsilon_{ij}^{V}$ is the time-dependent nonrecoverable component for the *VV* model. n_1 and n_2 are 0.223 and 0.496, respectively, see [13]. Time-independent plastic strain was negligible for this material at the stresses employed. In the *VP* model, the total strain ϵ_{ij} during creep is

$$\epsilon_{ij} = \epsilon_{ij}^E + \epsilon_{ij}^{+} t^N, \tag{2}$$

where $\epsilon_{ij}^{+} t^N = \epsilon_{ij}^{V}$ is the time-dependent strain for the *VP* model, and N was found to be 0.407, [13]. The elastic moduli for tension E and for torsion G were found to be 6.50×10^4 MPa (9.43×10^3 ksi) and 2.38×10^4 MPa (3.45×10^3 ksi), respectively. The third-order multiple integral representation yields the following expressions for the stress-dependent coefficients ϵ_{11}^{+VE} and ϵ_{12}^{+VE} under constant combined tension and torsion stress, i.e.,

$$\epsilon_{11}^{+VE} = F^{VE}(\sigma,\tau) = F_1^+ \sigma + F_3^+ \sigma^3 + F_4^+ \sigma\tau^2, \tag{3}$$

$$\epsilon_{12}^{+VE} = G^{VE}(\sigma,\tau) = G_1^+ \tau + G_2^+ \tau^3 + G_4^+ \sigma^2 \tau, \tag{4}$$

where F_i^+ and G_i^+ are constants whose values are given in [13].

A function F_a (or F_b) of maximum shear stress $\tau_{\max}$ multiplied by the stress deviator σ_{ij}', was developed to represent the stress dependence of ϵ_{ij}^{+V} or ϵ_{ij}^{+} as follows,

$$\epsilon_{ij}^{+V} = \sigma_{ij}' F_a(\tau_{\max}), \tag{5}$$

where

$$F_a(\tau_{\max}) = 3.616 \times 10^{-5} \times \{1 + 0.3914 \times \exp[2.108 \times 10^5 \times (\tau_{\max}/G)2]\},$$

percent per MPa-hr$^{0.496}$ and

$$\epsilon_{ij}^{+} = \sigma_{ij}' F_b(\tau_{\max}), \tag{6}$$

where

$$F_b(\tau_{\max}) = 6.219 \times 10^{-5} \times \{1 + 0.6433 \times \exp[1.633 \times 10^5 \times (\tau_{\max}/G)^2]\},$$

percent per MPa-hr$^{0.407}$,

where G is the shear modulus. Equations (5) and (6) represent the data best of several different formulations considered, such as power function and hyperbolic sine.

Weakening Effects

In previous work [13], secondary and tertiary creep stages were observed when the magnitude of the effective stress was 137.2 MPa (19.90 ksi) or higher. It was also reported that there were no significant aging effects in this precipitation hardened material in 300 hours. The onset of the secondary and tertiary stages could be caused by a combination of several other weakening effects such as static recovery, dynamic recovery, grain boundary shearing, and intercrystalline fracture. In current work, these possible weaking effects were neglected in the theoretical analysis, which did not consider the occurrence of secondary and tertiary stages.

Constitutive Equations for Variable Stress States

Viscoelastic Strain, ϵ_{ij}^{VE}. By the modified superposition principle [9, 16, 17] the viscoelastic strain for a varying stress is given by

$$\epsilon = \int_0^t \frac{\partial f[\sigma(\xi), t-\xi]}{\partial \sigma(\xi)} \dot{\sigma}(\xi) d\xi, \tag{7}$$

where the strain at constant stress is given by $\epsilon = f(\sigma,t)$.

For a series of m steps in stress as in the present test programs, the strain was described by the following form from equation (7)

$$\begin{aligned} \epsilon_{11}^{VE} = {} & F^{VE}(\sigma_1,\tau_1)[t^{n_1} - (t-t_1)^{n_1}] + \ldots \\ & + F^{VE}(\sigma_{m-1},\tau_{m-1})[(t-t_{m-2})^{n_1} \\ & - (t-t_{m-1})^{n_1}] + F^{VE}(\sigma_m,\tau_m)(t \\ & - t_{m-1})^{n_1}, \quad t_{m-1} < t. \end{aligned} \tag{8}$$

Similarly, ϵ_{12}^{VE} was obtained by replacing $F^{VE}(\sigma,\tau)$ by $G^{VE}(\sigma,\tau)$ in equation (8).

Time-Dependent Nonrecoverable Strain, ϵ_{ij}^{V}. Two flow rules, isotropic strain hardening and kinematic hardening, were developed here for ϵ_{ij}^{V} under variable stress states. The derivation was based on the assumption that the hardening nature of the material under variable stress states was the same as that under constant stress states.

Downloaded 02 May 2010 to 171.66.16.25. Redistribution subject to ASME license or copyright; see http://www.asme.org/terms/Terms_Use.cfm

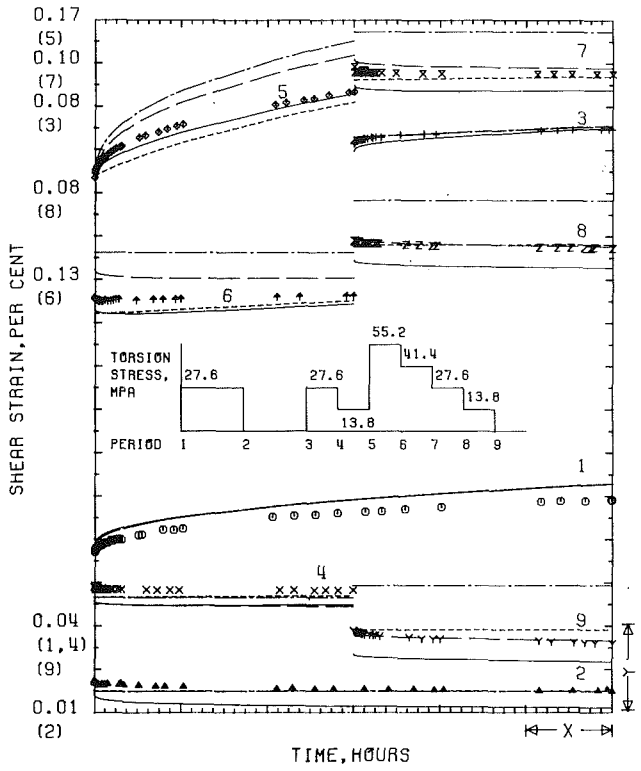

Fig. 1 Test T23. X = 8 h, Y = 0.02 percent. Durations are 48 h for periods 1-2, 24 h otherwise. Numbers in parenthesis on the ordinate indicate the creep period to which the ordinate number applies. Solid lines: viscous-viscoelastic with isotropic strain hardening (*VV – SH*); dashed lines: viscous-viscoelastic with kinematic hardening (*VV-KH*); dotted lines: viscoplastic with isotropic strain hardening (*VP – SH*); dot-dashed lines: viscoplastic with kinematic hardening (*VP – KH*).

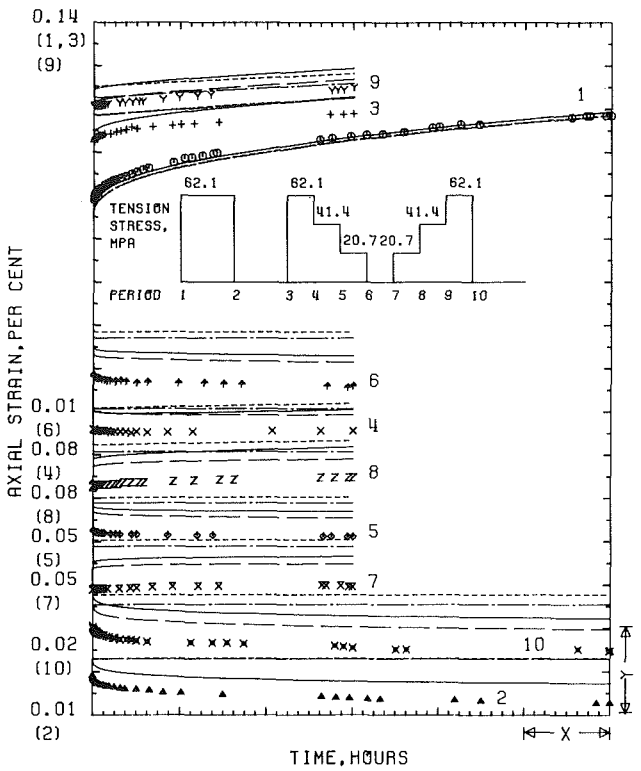

Fig. 3 Test A25. X = 8 h, Y = 0.02 percent. Durations are 48 h for periods 1-2, 24 h otherwise. See capition of Fig. 1 for keys.

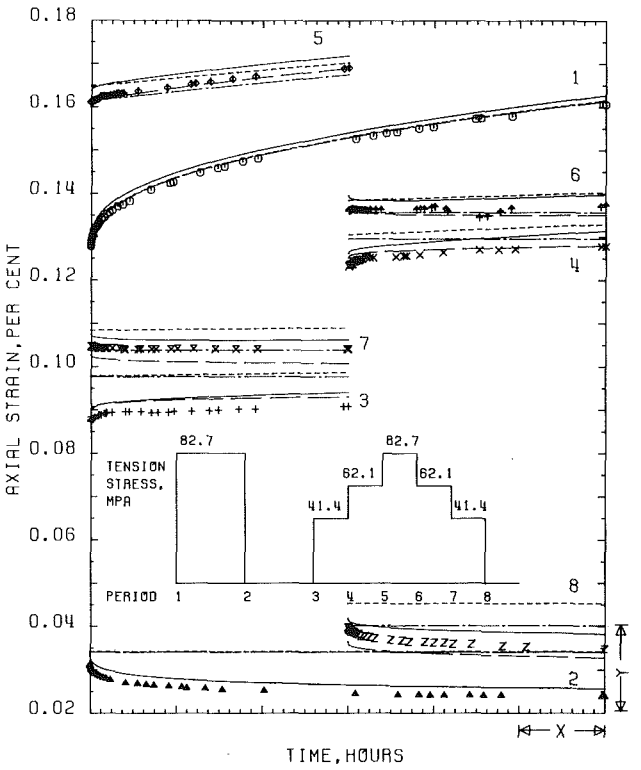

Fig. 2 Test A24. X = 8 h, Y = 0.02 percent. Durations are 48 h for periods 1-2, 24 h otherwise. See caption of Fig. 1 for key to theory curves.

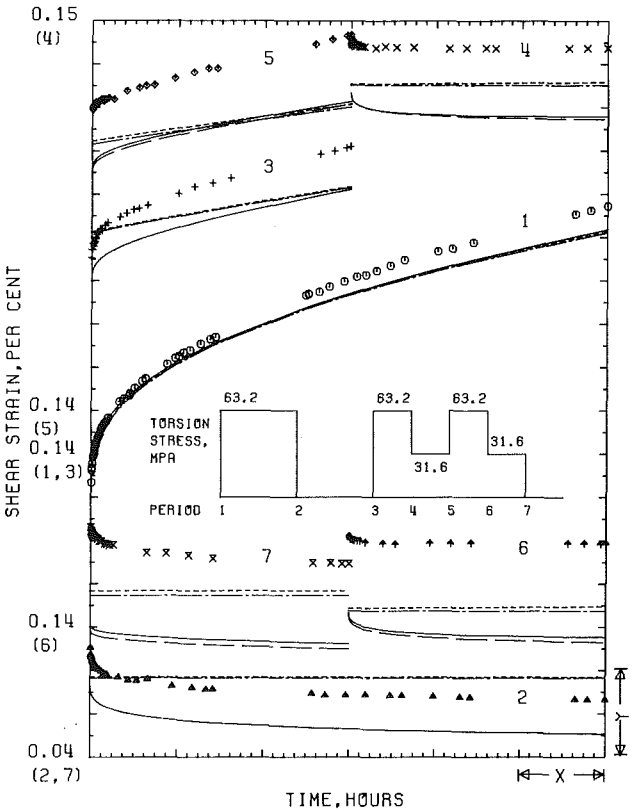

Fig. 4 Test T26. X = 8 h, Y = 0.02 percent. Durations are 48 h for periods 1-2, 24 h otherwise. See caption of Fig. 1 for keys.

Downloaded 02 May 2010 to 171.66.16.25. Redistribution subject to ASME license or copyright; see http://www.asme.org/terms/Terms_Use.cfm

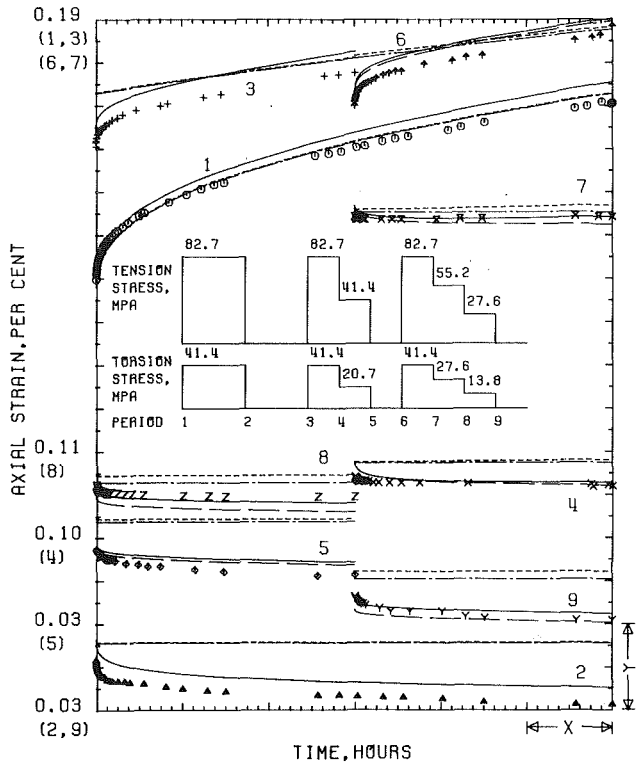

Fig. 5(a) Test CA31. X = 8 h, Y = 0.02 percent. Durations are 48 h for periods 1-2, 24 h otherwise. See caption of Fig. 1 for keys.

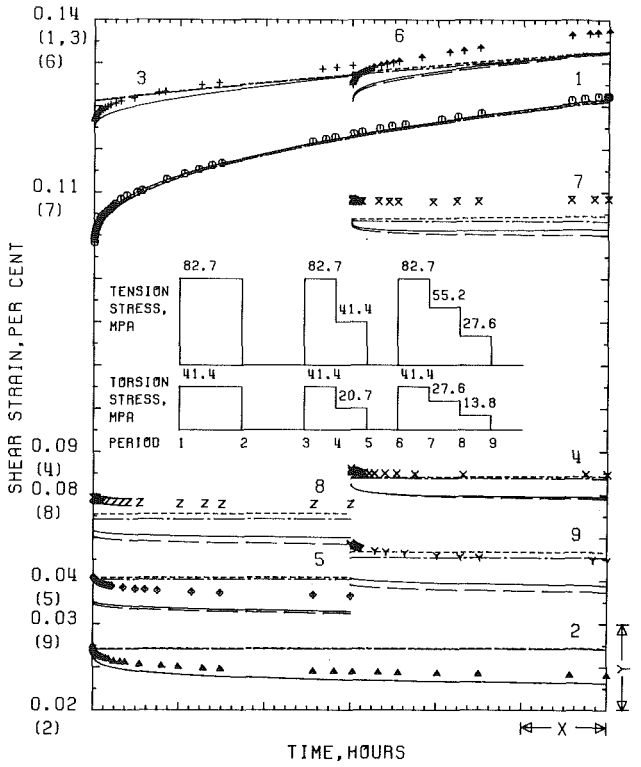

Fig. 5(b) Test CT31. X = 8h, Y = 0.02 percent.

Fig. 5

Development of the Isotropic Strain-Hardening Flow Rule (*SH*): Here only the case for the ϵ_{ij}^{V} (*VP* model) is discussed. The derivations are exactly the same for the ϵ_{ij}^{V} (*VV* model) except for different values of the time exponents and different relationships for $F(\tau_{max})$.

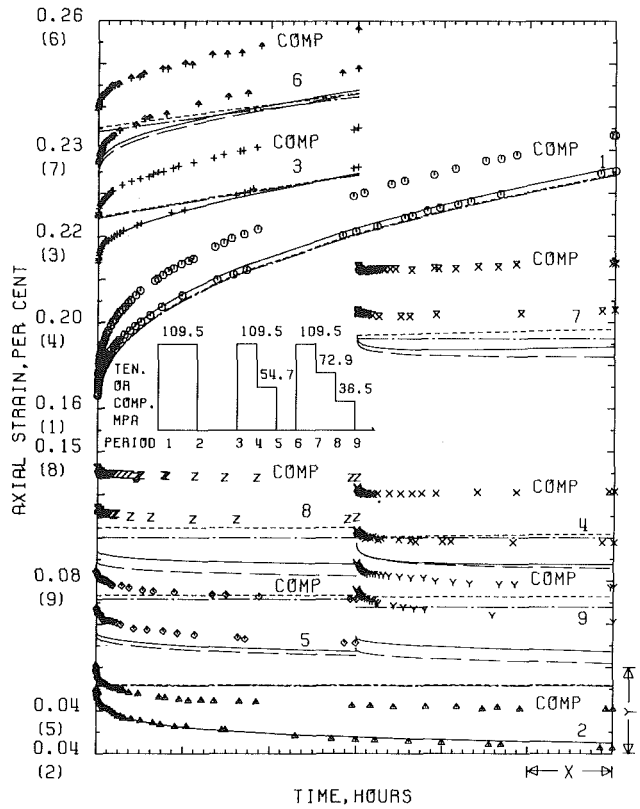

Fig. 6 Tests A32, a tension creep test, and A37, a compression creep test (designated by COMP). X = 8 h, Y = 0.02 percent. Durations are 48 h for periods 1-2, 24 h otherwise. See caption of Fig. 1 for keys.

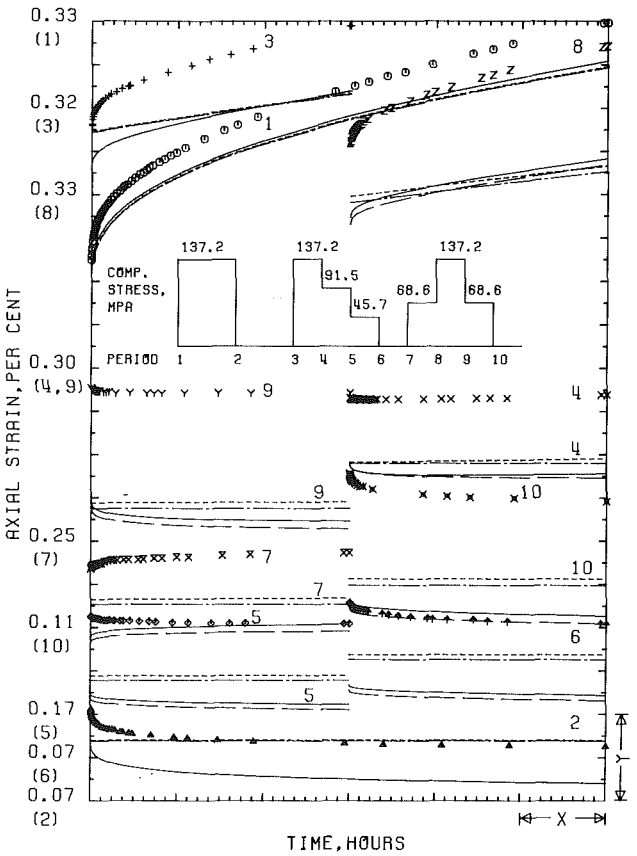

Fig. 7 Test A44, a compression creep test. X = 8 h, Y = 0.04 percent. Durations are 48 h for periods 1-2, 24 h otherwise. See caption of Fig. 1 for keys.

Downloaded 02 May 2010 to 171.66.16.25. Redistribution subject to ASME license or copyright; see http://www.asme.org/terms/Terms_Use.cfm

As shown in [13], ϵ_{ij}^V under constant stress creep can be expressed as:

$$\epsilon_{ij}^V = F(\tau_{\max})\sigma'_{ij}t^N. \tag{9}$$

Differentiating both sides with respect to time yields

$$\dot{\epsilon}_{ij}^V = NF(\tau_{\max})\sigma'_{ij}t^{N-1}. \tag{10}$$

To obtain an isotropic strain hardening flow rule the t in equation (10) was expressed in terms of the accumulated strain as follows. Taking the maximum of shear strain on the left-hand side of equation (9) and the maximum of the shear stress on the right-hand side yields the following expression:

$$\tfrac{1}{2}\gamma_{\max} = \tau_{\max}F(\tau_{\max})t^N, \tag{11}$$

from which,

$$t = \{(\tfrac{1}{2}\gamma_{\max})/[\tau_{\max}F(\tau_{\max})]\}^{1/N}, \tag{12}$$

where $\frac{1}{2}\gamma_{\max}$ is the maximum shear strain (engineering shear strain $\gamma = 2\epsilon_{12}$). In equations (11) and (12), the choice of the Tresca relation, i.e., maximum shear strain and maximum shear stress, instead of a Mises relation, i.e., the second invariant of the strain and stress deviators, came from the observation that the maximum shear strain rates are constant at any given time for those creep tests whose stress levels are the same according to the Tresca relation as discussed in [13]. For combined tension σ and torsion τ stress states, $\tau_{\max}$ is equal to $[(\sigma/2)^2 + \tau^2]^{1/2}$ and $\frac{1}{2}\gamma_{\max}$ equals $\{[(3/4)\epsilon_{11}^V]^2 + (\epsilon_{12}^V)^2\}^{1/2}$. Substituting t from equation (12) into equation (10) yielded the isotropic strain-hardening flow rule,

$$\dot{\epsilon}_{ij}^V = \sigma'_{ij}NF(\tau_{\max})\{(\tfrac{1}{2}\gamma_{\max})/[\tau_{\max}F(\tau_{\max})]\}^{(N-1)/N}, \tag{13}$$

where $F(\tau_{\max})$ is as follows: for the *VP* model, $F(\tau_{\max})$ is $F_b(\tau_{\max})$, equation (6). For the *VV* model, N is replaced by n_2 and $F(\tau_{\max})$ is $F_a(\tau_{\max})$, equation (5). This flow rule is isotropic due to the fact that an increment of $\gamma_{\max}$ contributed from any strain component induces a hardening effect in all directions.

For creep tests under multistep proportional loadings in which the loading direction is constant throughout the test, equation (13) can be integrated explicitly to obtain the strain components at any given time. This can be seen by using a multistep combined tension (σ) and torsion (τ) test as an example in which σ'_{ij} is equal to zero except $\sigma'_{11} = (2/3)\sigma$, $\sigma'_{22} = \sigma'_{33} = (-1/3)\sigma$, and $\sigma'_{12} = \sigma'_{21} = \tau$. From equation (13) a constant loading direction implies a constant strain rate direction and thus constant strain direction, i.e.,

$$\tau/[(2/3)\sigma] = \epsilon_{12}^V/\epsilon_{11}^V = k, \tag{14}$$

where k is a constant for each test. From equation (14), $\frac{1}{2}\gamma_{\max}$ and $\tau_{\max}$ can be expressed as:

$$\tfrac{1}{2}\gamma_{\max} = \{[(3/4)\epsilon_{11}^V]^2 + (\epsilon_{12}^V)^2\}^{1/2} = \epsilon_{11}^V \times [k^2 + (9/16)]^{1/2}, \tag{15}$$

$$\tau_{\max} = [(\sigma/2)^2 + \tau^2]^{1/2} = [(2/3)\sigma][k^2 + (9/16)]^{1/2} \tag{16}$$

and and $\dot{\epsilon}_{11}^V$ can be obtained by substituting equations (15) and (16) into equation (13), i.e.,

$$\dot{\epsilon}_{11}^V = N(\epsilon_{11}^V)^{(N-1)/N}[(2\sigma/3)F(\tau_{\max})]^{1/N}. \tag{17}$$

Integrating equation (17) with respect to time yields

$$\epsilon_{11}^V = \left\{\int_0^t [(2\sigma(\xi)/3)F(\tau_{\max}(\xi))]^{1/N}d\xi\right\}^N. \tag{18}$$

For a series of m steps in stress, equation (18) becomes

$$\begin{aligned}\epsilon_{11}^V = \{&[(2\sigma_1/3)F(\tau_{\max(1)})]^{1/N}(t_1) + \ldots \\ &+ [(2\sigma_{m-1}/3)F(\tau_{\max(m-1)})]^{1/N}(t_{m-1} - t_{m-2}) \\ &+ [(2\sigma_m/3)F(\tau_{\max(m)})]^{1/N} \\ &\times (t - t_{m-1})\}^N, \quad t_{m-1} < t.\end{aligned} \tag{19}$$

A similar form can be obtained for ϵ_{12}^V with $2\sigma/3$ replaced by τ. The preceding expressions are exactly the same as those reported in [10, 16] with the stress-dependent coefficients replaced by $F(\tau_{\max})\sigma'_{ij}$.

Development of the Kinematic Hardening Flow Rule (KH): Neglecting the weakening effects mentioned in a previous paragraph, a general form of the kinematic hardening model can be expressed as:

$$\dot{\epsilon}_{ij}^V = [H_1(||\Sigma_{ij}||)]\Sigma_{ij}/||\Sigma_{ij}|| \text{ (flow rule)}, \tag{20}$$

and

$$\dot{\alpha}_{ij} = H_2(||\alpha_{ij}||, ||\dot{\epsilon}_{ij}^V||)\dot{\epsilon}_{ij}^V \text{ (evolution rule)}, \tag{21}$$

where H_1 and H_2 are functions of the specified arguments, $\Sigma_{ij} = \sigma'_{ij} - \alpha_{ij}$, σ'_{ij} is the stress deviator, α_{ij} is the state variable (back stress), and $||\Sigma_{ij}||$, $||\alpha_{ij}||$, $||\dot{\epsilon}_{ij}^V||$ are the magnitudes of the corresponding stress tensors, which in principle can be defined by either Mises or Tresca relations; see [6–8]. By symmetry in tension and compression and the indifference of creep strain to the stress direction, as implied by equations (3)–(6), it is reasonable to assume the initial values of α_{ij} are all zero.

In a pure torsion test, σ'_{ij} is equal to zero except for $\sigma'_{12} = \sigma'_{21} = \tau$, which implies, according to equatins (20) and (21), that all the tensorial components are zero except for $\dot{\epsilon}_{12}^V = \dot{\epsilon}_{21}^V \neq 0$, $\dot{\alpha}_{12} = \dot{\alpha}_{21} \neq 0$, $\epsilon_{12}^V = \epsilon_{21}^V \neq 0$, $\alpha_{12} = \alpha_{21} = \alpha \neq 0$, and that $||\Sigma_{ij}||$, $||\alpha_{ij}||$, and $||\dot{\epsilon}_{ij}^V||$ are equal to $|\tau - \alpha|$, $|\alpha|$, and $|\dot{\epsilon}_{12}^V|$, respectively. Equations (20) and (21) thus reduce to the following forms:

$$\dot{\epsilon}_{12}^V = H_1(\tau - \alpha), \tag{22}$$

$$\dot{\alpha} = H_2(\alpha, \dot{\epsilon}_{12}^V)\dot{\epsilon}_{12}^V. \tag{23}$$

Since the initial value of α is zero, the initial shear creep rate is a function of shear stress only, according to equation (22), i.e., $\dot{\epsilon}_{12(t=0)}^V = H_1(\tau)$. Therefore function H_1 can be specified by the relationship between the initial shear creep rates and shear stresses.

However, the initial creep rates are so rapid as to be indeterminant, possibly infinite according to equations (1), and (2). To obtain a reasonable estimation of an initial creep rate, the first two hours of creep data of all the tests reported in [13] were fitted by equation (1) with $n_1 = 0.223$ to obtain n_2 for use in ϵ^V (*VV* model) and by equation (2) to obtain N for use in ϵ^V (*VP* model). The averages of n_2 and N are 0.330 and 0.292, respectively. Because only the values of ϵ_{ij}^{+V} and ϵ_{ij}^+ with n_2 and N fixed are involved in the creep rate estimations, the values of n_2 and N for individual tests are not shown here.

Refitting the 2 hour data by equations (1) and (2), with n_2 and N equal to 0.330 and 0.292, respectively, yields the values of ϵ_{ij}^{+V} in equation (1) and ϵ_{ij}^+ in equation (2) which are shown in Table 1. Instead of the initial creep rate (infinite) an "early" value of creep rate was used in determining H_1. The "early" creep rates could be calculated either by $n_2\epsilon_{ij}^{+V}t_1^{n_2-1}$ (or $N\epsilon_{ij}^+t_1^{N-1}$) or by $\epsilon_{ij}^{+V}t_1^{n_2}/t_1$ (or $\epsilon_{ij}^+t_1^N/t_1$), where t_1 is a small time such as 1 sec. In either case it can be seen that the ratios of creep rates for different tests depend only on ϵ_{ij}^{+V} or ϵ_{ij}^+. Different approaches or choices of t_1 can only result in a different constant multiplier for H_1 whose effect will be discussed in a later section. The initial creep rates based on the first approach with $t_1 = 1$ sec are shown in Table 1.

The relationships between initial shear creep rates and τ were found to be best represented by the following expressions: For the *VV* model,

$$\dot{\epsilon}_{12(t=0)}^V = C_1\sinh(\tau/K_1), \tag{24}$$

or, for the *VP* model,

$$\dot{\epsilon}_{12(t=0)}^V = C_2\sinh(\tau/K_2), \tag{25}$$

Downloaded 02 May 2010 to 171.66.16.25. Redistribution subject to ASME license or copyright; see http://www.asme.org/terms/Terms_Use.cfm

Table 1 Estimation of the "early" Shear Creep rates

TEST NO.	SHEAR STRESS,		ϵ_{12}^{+V}, (in Eq. (1) with $n_1 = 0.223$, $n_2 = 0.330$)	ϵ_{12}^{+}, (in Eq. (2) with $N = 0.292$)	$\dot{\epsilon}_{12}^{V}$ at $t = 0$, (from $n_2 \epsilon_{12}^{+V} t_1^{n_2-1}$, $t_1 = 1$ sec)	$\dot{\epsilon}_{12}^{V}$ at $t = 0$, (from $N\epsilon_{12}^{+} t_1^{N-1}$ $t_1 = 1$ sec)
	MPa	(ksi)	$10^{-4}/h^{n_2}$	$10^{-4}/h^{N}$	$10^{-2}/h$	$10^{-2}/h$
T28	27.4	(3.97)	0.1417	0.3592	0.1129	0.3456
T29	41.4	(6.00)	0.3629	0.6608	0.2891	0.6358
T26	63.2	(9.17)	1.034	1.699	0.8237	1.635
T38	79.2	(11.49)	2.404	3.514	1.915	3.381
T42	101.4	(14.70)	7.544	9.564	6.009	9.202

where K_1, K_2, are 19.34 MPa (2.805 ksi) and 22.23 MPa (3.225 ksi), respectively; and C_1, C_2 are equal to 0.06371 and 0.1929 in percent/h, respectively; see Fig. 8.

According to equation (20) and (22) the flow rules for pure torsion loadings can then be expressed as:

$$\dot{\epsilon}_{12(I)}^{V} = C_1 \sinh[(\tau - \alpha)/K_1], \quad (VV), \tag{26}$$

or

$$\dot{\epsilon}_{12(I)}^{V} = C_2 \sinh[(\tau - \alpha)/K_2], \quad (VP) \tag{27}$$

To obtain the evolution rule, an interrelation between $\dot{\alpha}$, α, and $\dot{\epsilon}_{12}^{V}$ during deformation was derived from constant stress shear creep tests. Here, ϵ^{V} (VP model) is used as an example; the same method applies for ϵ^{V} (VV model) except for different constants. From equation (27) it follows that: for any stress histories,

$$\tau - \alpha = K_2 \ ln\{(\dot{\epsilon}_{12}^{V}/C_2) + [(\dot{\epsilon}_{12}^{V}/C_2)^2 + 1]^{1/2}\}. \tag{28}$$

For pure torsion, creep tests in which τ is constant, differentiating equation (28) with respect to time yields:

$$\dot{\alpha} = -K_2 \ddot{\epsilon}_{12}^{V}/[(\dot{\epsilon}_{12}^{V})^2 + C_2^2]^{1/2}. \tag{29}$$

The evolution rule can be obtained by expressing $\ddot{\epsilon}_{12}^{V}$ in equation (29) in terms of α and $\dot{\epsilon}_{12}^{V}$. Recalling that the creep strain can be expressed by $\epsilon_{12}^{V} = \epsilon_{12}^{+} t^N$ in the VP model, the following results were obtained by consecutive differentiation with respect to time:

$$\dot{\epsilon}_{12}^{V} = N \epsilon_{12}^{+} t^{N-1}, \tag{30}$$

$$\ddot{\epsilon}_{12}^{V} = N(N-1)\epsilon_{12}^{+} t^{N-2}, \tag{31}$$

From (30) and (31),

$$\ddot{\epsilon}_{12}^{V} = [(N-1)/t]\dot{\epsilon}_{12}^{V}$$
$$= (N-1)(\epsilon_{12}^{+} N)^{1/(N-1)} (\dot{\epsilon}_{12}^{V})^{-1/(N-1)} \dot{\epsilon}_{12}^{V}. \tag{32}$$

ϵ_{12}^{+} in equation (32) is equal to $\tau F_b(\tau)$ according to equation (6). Substituting τ from equation (28) makes $\ddot{\epsilon}_{12}$ in (32) a function of α and $\dot{\epsilon}_{12}$ only. Introducing equation (32) into equation (29) yields the evolution rule; i.e., the relation between $\dot{\alpha}$, α,, $\dot{\epsilon}_{12}^{V}$ during creep. Even though the evolution rule for hardening was derived from creep tests at constant stress it was assumed that the same hardening nature would be applicable for other stress histories.

For the VV model the evolution rule is the same as the VP model except N is replaced by n_2 and ϵ_{12}^{+} is replaced by $\epsilon_{12}^{+V} = \tau F_a(\tau)$ from equation (5).

As mentioned earlier, different approaches for estimation of the initial creep rates resulted in different values of C_1 (or C_2). Since equations (27) and (29) (with equation (32) inserted in equation (29)) were both derived from constant stress creep tests, the kinematic hardening rule, equations (27) and (29), describes the creep curves very well regardless of values of C_1 (or C_2) employed. But different values of C_1 (or C_2) result in different values of α during creep according to equation (28). However, $\dot{\epsilon}_{12}^{V}$ in equation (28) is very small compared to C_1 (or C_2) except at the very beginning of a test. Thus differences in C_1 (or C_2) are generally unimportant.

Isotropic hardening effects can also be taken into consideration in equation (26) or (27) by developing an evolution rule for K_1 (or K_2) as in [6, 7].

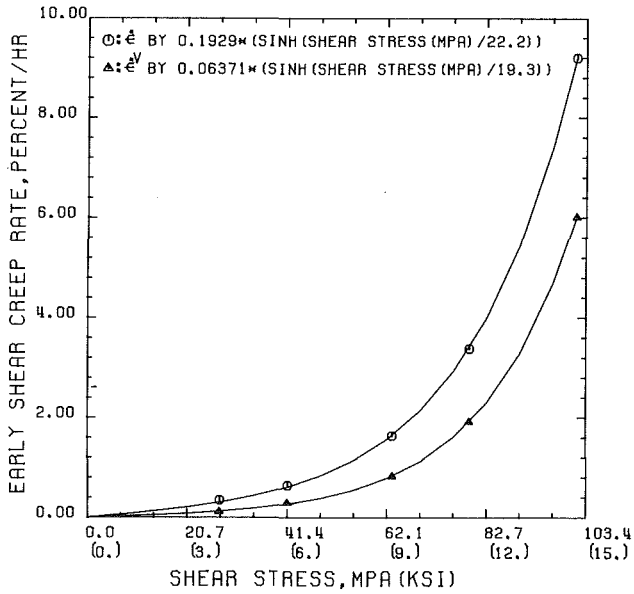

Fig. 8 Early shear creep rates versus shear stresses.

Kinematic Hardening Rules for Multiaxial Stress States

Equations (27), (29), and (32) can be extended to multiaxial stress states as follows. For ϵ_{ij}^{V} (VP model),

$$\dot{\epsilon}_{ij}^{V} = C_2(\Sigma_{ij}/||\Sigma_{ij}||)\sinh(||\Sigma_{ij}||/K_2), \tag{33}$$

$$\dot{\alpha}_{ij} = -\frac{K_2(N-1)(b_1 N)^{1/(N-1)} ||\dot{\epsilon}_{ij}^{V}||^{-1/(N-1)}}{(||\dot{\epsilon}_{ij}^{V}||^2 + C_2^2)^{1/2}} \dot{\epsilon}_{ij}^{V}, \tag{34}$$

where $b_1 = b_2 F_b(b_2)$ and

$$b_2 = ||\alpha_{ij}|| + K_2 l_n\{(||\dot{\epsilon}_{ij}^{V}||/C_2) + [(||\dot{\epsilon}_{ij}^{V}||/C_2)^2 + 1]^{1/2}\}.$$

Similar expressions can be obtained for ϵ_{ij}^{V} (VV model) with N replaced by n_2 and F_b by F_a, equation (5). The magnitude quantities $||\Sigma_{ij}||$, $||\alpha_{ij}||$, and $||\dot{\epsilon}_{ij}^{V}||$ are defined by maximum shear stress and maximum shear strain rate, respectively, in accord with the previous experimental observation that the maximum shear strain rates are constant at any given time for those creep tests whose stresses are equal according to the Tresca relation [13].

The validity of these multiaxial relations can be checked by viewing the data and theory for the first step of each of the pure tension and the combined tension and torsion tests shown in Figs. 1-7. The dashed and dash-dot lines represent the results predicted by the foregoing multiaxial relations for VV and VP models, respectively.

Since this paper deals only with multistep proportional loadings, $\dot{\epsilon}_{ij}^{V}$ was taken to be zero whenever Σ_{ij} was smaller than zero, i.e., ϵ_{ij}^{V} was frozen. More complicated stress histories will be discussed in subsequent papers.

Predictions by the Theories

In summary, two theoretical models are presented: VV and VP. In each model the time-dependent nonrecoverable strain was represented by either the SH flow rule, equation (13), or by the KH flow rule, equations (33) and (34). Equation (13) can be integrated explicitly for proportional loadings as shown by equation (19) for ϵ_{11}^{V}. The modified superposition principle was used for representing the viscoelastic component under variable stress states as shown by equation (8) for ϵ_{11}^{VE}. An IMSL subroutine DVERK based on the Runge-Kutta-

Downloaded 02 May 2010 to 171.66.16.25. Redistribution subject to ASME license or copyright; see http://www.asme.org/terms/Terms_Use.cfm

Table 2 Applied stress deviator (σ'_{ij}) in each period and back stress (α_{ij}) at the end of the period

TEST NO.	STRESS, MPa	PERIOD									
		1	2	3	4	5	6	7	8	9	10
T23	σ'_{12}	27.579	0.000	27.600	13.790	55.158	41.369	27.600	13.790	0.000	
	α_{12}(VV)	27.547	27.547	27.553	27.553	55.024	55.024	55.024	55.024	55.024	
	α_{12}(VP)	27.565	27.565	27.568	27.568	55.096	55.096	55.096	55.096	55.096	
A24	σ'_{11}	55.158	0.000	27.579	41.369	55.158	41.369	27.579	0.000		
	α_{11}(VV)	55.084	55.084	55.084	55.084	55.098	55.098	55.098	55.098		
	α_{11}(VP)	55.125	55.125	55.125	55.125	55.132	55.132	55.132	55.132		
A25	σ'_{11}	41.369	0.000	41.369	27.579	13.790	0.000	13.790	27.579	41.369	0.000
	α_{11}(VV)	41.319	41.319	41.328	41.328	41.328	41.328	41.328	41.328	41.334	41.334
	α_{11}(VP)	41.346	41.346	41.351	41.351	41.351	41.351	41.351	41.351	41.354	41.354
T26	σ'_{12}	63.200	0.000	63.200	31.600	63.200	31.600	0.000			
	α_{12}(VV)	63.057	63.057	63.082	63.082	63.097	63.097	63.097			
	α_{12}(VP)	63.134	63.134	63.146	63.146	63.153	63.153	63.153			
CA31	σ'_{11}	55.158	0.000	55.158	27.579	0.000	55.158	36.772	18.386	0.000	
	α_{11}(VV)	55.056	55.056	55.123	55.123	55.123	55.086	55.086	55.086	55.086	
	α_{11}(VP)	55.114	55.114	55.075	55.075	55.075	55.129	55.129	55.129	55.129	
CT31	σ'_{12}	41.369	0.000	41.369	20.684	0.000	41.369	27.579	13.790	0.000	
	α_{12}(VV)	41.292	41.292	41.306	41.306	41.306	41.315	41.315	41.315	41.315	
	α_{12}(VP)	41.335	41.335	41.342	41.342	41.342	41.347	41.347	41.347	41.347	
A32 and A37*	σ'_{11}	72.970	0.000	72.970	36.485	0.000	72.970	48.647	24.323	0.000	
	α_{11}(VV)	72.846	72.846	72.869	72.869	72.869	72.883	72.883	72.883	72.883	
	α_{11}(VP)	72.915	72.915	72.927	72.927	72.927	72.934	72.934	72.934	72.934	
A44*	σ'_{11}	91.471	0.000	91.471	60.980	30.490	0.000	45.736	91.471	45.736	0.000
	α_{11}(VV)	91.240	91.240	91.283	91.283	91.283	91.283	91.283	91.308	91.308	91.308
	α_{11}(VP)	91.375	91.375	91.396	91.396	91.396	91.396	91.396	91.408	91.408	91.408

*Compression test

Note: 1. In pure tension tests, $\alpha_{ij} = 0$ except $\alpha_{22} = \alpha_{33} = -(1/2)\alpha_{11} \neq 0$

2. In pure torsion tests, $\alpha_{ij} = 0$ except $\alpha_{12} = \alpha_{21} \neq 0$

3. In combined tension and torsion tests, $\alpha_{ij} = 0$ except $\alpha_{12} = \alpha_{21} \neq 0$, $\alpha_{22} = \alpha_{33} = -(1/2)\alpha_{11} \neq 0$

Verner fifth and sixth-order method with automatic time step control was used for the numerical integration.

The results are shown in Figs. 1–7 in which *VV-SH* are represented by solid lines, VP-SH by dotted lines, VV-KH by dashed lines, and VP-KH by dash-dot lines. The back stresses α_{ij} at the end of each period are shown in Table 2.

Discussion

A comparison of the theoretical results with experimental data shows that both *VV-SH* and *VV-KH* give very good predictions of the material responses. Since the nonrecoverable strains were frozen in the *KH* models whenever Σ_{ij} was smaller than zero, *VV-SH* is better than *VV-KH* in some periods such as period 6 of Fig. 1. Adding a linear evolution rule for K_1 or K_2 in the *KH* rules was tried, but did not result in a smaller α_{ij} at the beginning of these periods as required in order for the applied stress to induce further creep. This might be an inherent disadvantage for the state variable approach.

Since the ϵ^{VE} component was not included in either *VP-SH* or *VP-KH*, they could not predict the recovery strains and the transient creep strains upon reloadings such as observed in period 3 of Figs. 3 and 4, etc. Most of the work of other investigators based on VP models used a "static recovery" term (representing annealing after cold work) in the evolution rule to simulate the transient strains, see [18]. The present work shows that the ϵ^{VE} component can account for these behaviors without introducing annealing effects into the analysis.

Conclusions

Two viscoplastic flow rules based on different hardening natures, i.e., isotropic strain hardening (*SH*) and kinematic hardening (*KH*), were developed from constant stress creep and recovery data. Under multistep proportional loadings, the isotropic strain-hardening flow rule can be integrated explicitly to obtain all the strain components at any given time. Associated with each hardening rule, data are represented by two theoretical models: a viscous-viscoelastic (*VV*) model and a viscoplastic (*VP*) model. The viscoelastic component in the *VV* model was described by the third-order multiple integral representation combined with the modified superposition principle. The agreements of the *VV* models with the experimental observations are generally very good. *VV-SH* is better than *VV-KH* in some step down stress states. The viscoelastic component is essential in accounting for not only the recovery strain but also the transient creep strain upon reloadings and step-up loadings.

Acknowledgment

This work was supported by the Army Research Office, Research Grant Number DAAG29-81-K-0138. The material was contributed by the Aluminum Company of America. The authors are grateful to R. M. Reed for assistance in experiments and C. P. Capece for typing the manuscript.

References

1 Findley, W. N., Cho, U. W., and Ding, J. L., "Creep of Metals and Plastic Under Combined Stresses, A Review," ASME *Journal of Engineering Materials and Technology*, Vol. 101, 1979, p. 365.

2 Murakami, S., and Ohno, N., "A Constitutive Equation of Creep Based on the Concept of a Creep-Hardening Surface," *Int. J. Solids Structures*, Vol. 18, No. 7, 1982, pp. 597–609.

3 Ohashi, Y., Ohno, N., and Kawai, M., "Evaluation of Creep Constitutive Equations for Type 304 Stainless Steel Under Repeated Multiaxial

Downloaded 02 May 2010 to 171.66.16.25. Redistribution subject to ASME license or copyright; see http://www.asme.org/terms/Terms_Use.cfm

Loading," ASME *Journal of Engineering Materials and Technology*, Vol. 104, 1982, pp. 159–164.

4 Kraus, H., *Creep Analysis*, Wiley, New York, 1980.

5 Orowan, E., "The Creep of Metals," *J. West Scot. Iron & Steel Inst.*, Vol. 54, 1946, pp. 45–53.

6 Miller, A. K., "An Inelastic Constitutive Model for Monotonic, Cyclic, and Creep Deformation: Part 1—Equations Development and Analytical Procedures and Part 2—Applications to Type 304 Stainless Steel," ASME *Journal of Engineering Materials and Technology*, Vol. 98, 1976, p. 97.

7 Kreig, R. D., Swearengen, J. C., and Rohde, R. W., "A Physically Based Internal Variable Model for Rate Dependent Plasticity," in "Inelastic Behavior of Pressure Vessel and Piping Components," PVP-PE-028, ASME, 1978, p. 15.

8 Hart, E. W., "Constitutive Relations for the Nonelastic Deformation of Metals," ASME *Journal of Engineering Materials and Technology*, Vol. 98, 1976, p. 193.

9 Findley, W. N., and Lai, J. S., "Creep and Creep Recovery of 2618 Aluminum Alloy Under Combined Stress With a Representation by a Viscous-Viscoelastic Model," ASME JOURNAL OF APPLIED MECHANICS, Vol. 45, 1978, pp. 507–514.

10 Lai, J. S., and Findley, W. N., "Creep of 2618 Aluminum Under Step Stress Changes Predicted by a Viscous-Viscoelastic Model," ASME JOURNAL OF APPLIED MECHANICS, Vol. 47, 1980, pp. 21–26.

11 Findley, W. N., and Lai, J. S., "Creep of 2618 Aluminum Under Side Steps of Tension and Torsion and Stress Reversal Predicted by a Viscous-Viscoelastic Model," ASME JOURNAL OF APPLIED MECHANICS, Vol. 48, 1981, pp. 47–54.

12 Lai, J. S., and Findley, W. N., "Simultaneous Stress Relaxation in Tension and Creep in Torsion of 2618 Aluminum at Elevated Temperature," ASME JOURNAL OF APPLIED MECHANICS, Vol. 49, 1982, pp. 19–25.

13 Ding, J. L., and Findley, W. N., "48 Hour Multiaxial Creep and Creep Recovery of 2618 Aluminum Alloy at 200°C," To appear in JOURNAL OF APPLIED MECHANICS, Vol. 51, 1984, pp. 00–00.

14 Findley, W. N., and Gjelsvik, A., "A Biaxial Testing Machine for Plasticity, Creep or Relaxation Under Variable Principal Stress Ratios," *Proceedings, American Society for Testing and Materials*, Vol. 62, 1962, pp. 1103–1118.

15 Findley, W. N., "A Compressive Creep Machine," *ASTM Journal of Testing and Evaluation*, Vol. 10, July 1982, pp. 179–180.

16 Cho, U. W., and Findley, W. N., "Creep and Plastic Strains of 304 Stainless Steel at 593°C Under Step Stress Changes, Considering Aging," ASME JOURNAL OF APPLIED MECHANICS, Vol. 49, 1982, pp. 297–304.

17 Findley, W. N., Lai, J. S., and Onaran, K., *Nonlinear Creep and Relaxation of Viscoelastic Materials, With an Introduction to Linear Viscoelasticity*, North-Holland, Amsterdam, 1976.

18 Matlock, D. K., Harrigan, W. C., Jr., and Nix, W. D., "On the Importance of Including Recovery in Phenomenological Theories of Plastic Flow in Metal," *Acta Metallurgica*, Vol. 20, 1972, pp. 661–668.

Downloaded 02 May 2010 to 171.66.16.25. Redistribution subject to ASME license or copyright; see http://www.asme.org/terms/Terms_Use.cfm

Nonlinear Bending and Collapse of Long, Thin, Open Section Beams and Corrugated Panels

R. C. Benson
Associate Professor,
Department of Mechanical Engineering,
University of Rochester,
Rochester, N.Y. 14627
Mem. ASME

Long, thin, open section beams and corrugated panels undergo a cross section flattening when bent longitudinally. This leads to a "soft" nonlinear moment-curvature response and geometrical instability. The problem is analyzed by means of a closed, convergent sequence of algebraic and integral equations which are tractable on modern microcomputers. The shape of the cross section is unrestricted, save that it be thin, symmetrical, and not self-penetrating. Results for circular section and angle section beams are obtained and compared with the existing literature. Example results for a wide, corrugated panel are also obtained. Bifurcations in the deformed cross section are found to occur.

1 Introduction

The title problem, in many guises, is familiar to most readers. The most common example is that of the extendible tape measure, which winds off a spool and yet has substantial resistance to longitudinal bending due to the large area moment of inertia of its curved cross section. A representative geometry is shown in Fig. 1. During bending, the cross section flattens, as a second-order effect, and "soft," longitudinal moment-curvature relationships, of the sort seen in Figs. 2–4, are produced. Geometric instability occurs when the moment reaches a local maximum, and strain energy is released for increased curvature. This phenomenon is sometimes known as the "Brazier effect" after the author of a 1927 article [1] on the nonlinear bending and collapse of thin, circular tubes.

Because of the desire to design with lightweight structures, interest in the Brazier effect has remained strong. Wood [2] in 1958 added internal pressure to the circular tube problem. Shortly thereafter Reissner [3], and Reissner and Weinitschke [4] extended the analysis by series expansions that have first-order terms corresponding to linear theory and second-order terms corresponding to Brazier/Wood theory. Among recent papers on the pressurized tube are those by Spence and Toh [5] who use ellipses to model out-of-round cross sections, and Fabian [6] who analyzes failure due to axial wrinkling as well as cross section flattening.

An early study of the Brazier effect in open section beams is by Ashwell [7], who provides a detailed analysis of the pure bending of beams with shallow circular sectors as cross sections, and small but non-negligible thicknesses. Bisplinghoff [8] studies the same geometry, adding torsion to the problem. These contributions are important in setting limits on the range of validity of the pure bending results (e.g. open section beams are not observed to bend symmetrically for reversed bending moment). Rimrott [9] examines the bending of circular tubes with longitudinal slits and Meck [10] studies the bending and twisting of angle sections.

The articles described here are but a few of a large and excellent literature. The reader desiring a comprehensive review is referred to the paper by Axelrad [11]. Collectively these works provide an ample research base for the analysis of many lightweight structures; airplane struts and underwater

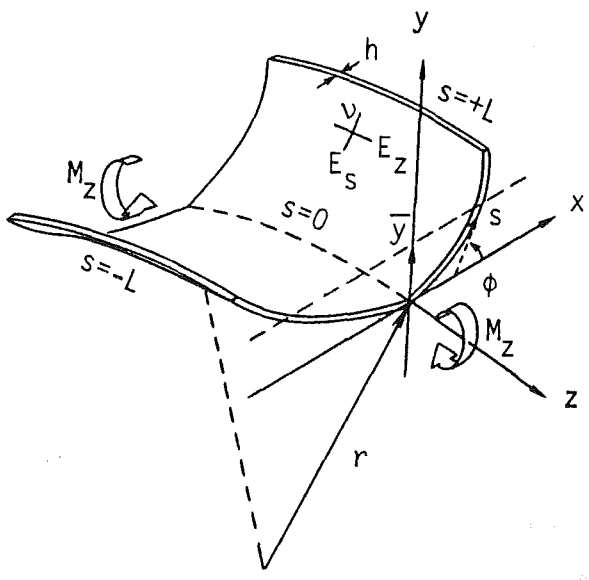

Fig. 1 Geometry

Contributed by the Applied Mechanics Division for presentation at the 1984 PVP Conference and Exhibition, Joint with Applied Mechanics Division and Materials Division, San Antonio, Texas, June 17–21, 1984, of THE AMERICAN SOCIETY OF MECHANICAL ENGINEERS.

Discussion on this paper should be addressed to the Editorial Department, ASME, United Engineering Center, 345 East 47th Street, New York, N.Y. 10017, and will be accepted until two months after final publication of the paper itself in the JOURNAL OF APPLIED MECHANICS. Manuscript received by ASME Applied Mechanics Division, January, 1983; final revision, June, 1983. Paper No. 84-APM-4.

Copyright © 1984 by ASME
Downloaded 02 May 2010 to 171.66.16.25. Redistribution subject to ASME license or copyright; see http://www.asme.org/terms/Terms_Use.cfm

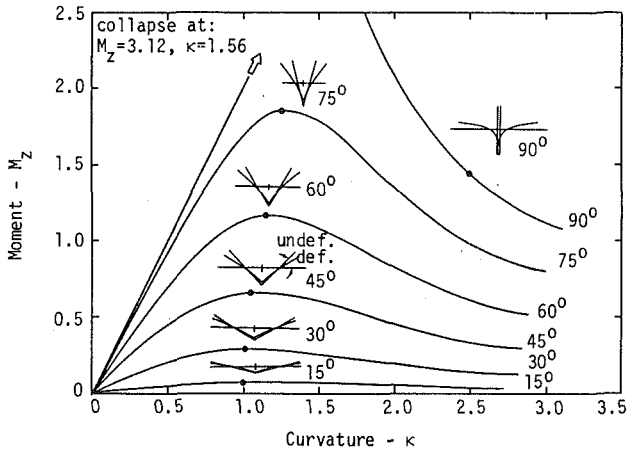

Fig. 2 Angle section

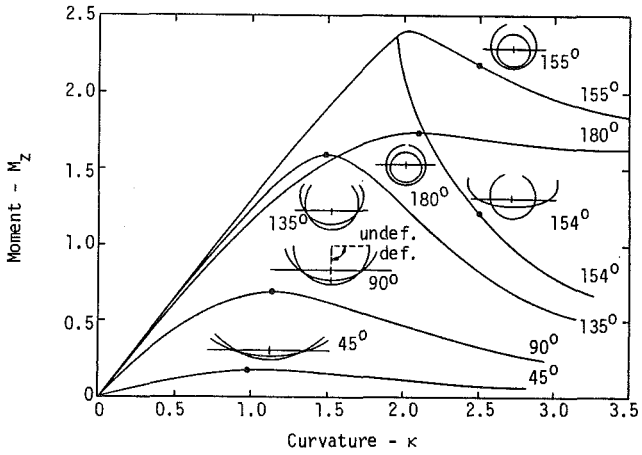

Fig. 3 Circular section

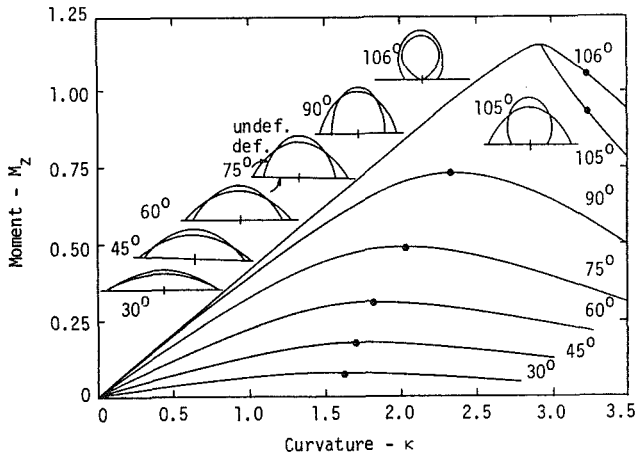

Fig. 4 Corrugated panel

pipelines are two examples. Limiting the range of applicability is the fact that most authors invoke kinematical conditions for the beam's cross section (typically a circle or parabola) so that closed form results may be obtained. This precludes direct application to nonstandard geometries such as might be found in a corrugated panel or a tape-reading device. (It is common design practice to impart a slight cross curvature to tapes that must be fed across open spaces.)

The only cross section restrictions to be made here are that the shape be thin, symmetrical, and not self-penetrating. What results is a set of algebraic and integral equations which, though lacking a closed form solution, may be applied to a wide range of geometries, and which yield favorable results when tested on standard geometries. Numerical calculations are facilitated by casting the equations in a form so that they may be evaluated sequentially rather than simultaneously. Convergence is achieved by iterating a sufficient number of times. Example results are produced for angle section beams, for comparison with Meck [10], and circular section beams, for comparison with Ashwell [7] and Rimrott [8]. A third example is that of a corrugated panel.

2(*a*) Governing Equations for Open Section Beams

Figure 1 shows the geometry of the open section beam. A point in the midsurface of the symmetric beam is located by specifying its distance z along the longitudinal centerline, and arclength s in the plane perpendicular to z. At the centerline $s=0$, and at the free edges $s=\pm L$. The beam is very thin, $h<<L$, so that midsurface calculations suffice for distance measurements. In the cross section, Cartesian coordinates x and y are chosen so that y points along the line of symmetry and $x=y=0$ at the centerline. At s, a tangent to the cross section forms an angle $\phi(s)$ with the x axis, and the Cartesian coordinates of this point are

$$x(s)=\int_0^s \cos\phi(t)\,dt, \quad y(s)=\int_0^s \sin\phi(t)\,dt. \tag{1),(2}$$

The neutral axis is at a distance

$$\bar{y}=(1/L)\int_0^L y(s)\,ds, \tag{3}$$

and the area moment of inertia about this axis is

$$I=2h\int_0^L [y(s)-\bar{y}]^2 ds+(h^3/6)\int_0^L [\cos\phi(s)]^2 ds.$$

The first and second integrals represent the respective contributions to the beam's moment of inertia from corrugation and beam thickness. For a flat cross section, $y(s)\equiv 0$, the expected result, $I = Lh^3/6$, is obtained. In this paper, however, the focus is on the former effect, with the assumption that

$$h^2<<(1/L)\int_0^L [y(s)-\bar{y}]^2 ds,$$

so that the moment of inertia expression simplifies to

$$I\approx 2h\int_0^L [y(s)-\bar{y}]^2 ds. \tag{4}$$

The bending moment, M_z, changes the longitudinal curvature of the beam by an amount κ (measured at the neutral axis). This is found from the classical beam equilibrium equation

$$M_z=E_z I\kappa, \tag{5}$$

where E_z is the elastic modulus in the longitudinal direction. If the beam originally had longitudinal curvature κ_0, then the new radius of curvature is

$$r=1/(\kappa_0+\kappa).$$

Along longitudinal fibers there is generated an inernal force per unit cross length, denoted $N(s)$. For

$$(1/L)\int_0^L [y(s)-\bar{y}]^2 ds<<r^2$$

this reaction may be reasonably assumed to be proportional to the vertical distance from the neutral axis

$$N(s)=(M_z h/I)[y(s)-\bar{y}]. \tag{6}$$

Due to the longitudinal curvature of the beam, $N(s)$, in turn, induces a vertical shear force per unit midsurface area that is given by

$$\rho(s)=N(s)/r=E_z h\kappa(\kappa_0+\kappa)[y(s)-\bar{y}]. \tag{7}$$

The deformation in the cross direction is found from the

Downloaded 02 May 2010 to 171.66.16.25. Redistribution subject to ASME license or copyright; see http://www.asme.org/terms/Terms_Use.cfm

equations of the elastica [12] for large inextensional bending. These are as follows.

$$M_s(s) = \int_s^L [x(s) - x(t)]\rho(t)\,dt, \tag{8}$$

$$\phi(s) = \phi_0(s) + (1/D)\int_0^s M_s(t)\,dt, \tag{9}$$

$$D = (E_s h^3)/[12(1-\nu^2)].$$

Here $M_s(s)$ is the bending moment per unit longitudinal length acting on the cross section, $\phi_0(s)$ is the tangent angle of the undeformed cross setion, D is the plate bending rigidity per unit longitudinal length, E_s is the elastic modulus in the cross direction, and ν is Poisson's ratio. It will also prove convenient to define a material constant, γ, which represents a combined Poisson effect and measure of orthotropy

$$\gamma = [(1-\nu^2)E_z/E_s]^{1/2}.$$

The problem is reduced to its most compact form by the following nondimensionalization (reusing symbols)

$$\frac{s}{L}\to s, \frac{x}{L}\to x, \frac{y}{L}\to y, \frac{\bar{y}}{L}\to \bar{y}, \frac{I}{hL^3}\to I, \frac{M_z h}{DL\gamma}\to M_z,$$

$$\frac{\kappa L^2\gamma}{h}\to\kappa, \frac{\kappa_0 L^2\gamma}{h}\to\kappa_0, \frac{NhL}{D\gamma}\to N, \frac{\rho L^3}{D}\to\rho, \frac{M_s L}{D}\to M_s.$$

Then the nondimensional counterparts to equations (1)–(9) are obtained by setting $L = h = D = 1$ and $E_z = 12$. All quantities in equations (1)–(9) may depend on z, however gradients in z should be small since longitudinal shear effects are neglected.

2(b) Governing Equations for Corrugated Panels

Through the specification of $\phi_0(s)$, the equations of the last section can be used to model beams with very complicated cross sections. Many beams of structural interest, however, have symmetries that recommend labor-saving modifications of equations (1)–(9). Specifically, a corrugated panel with a repeating, serpentine, cross section

$$\phi(s \pm L) = -\phi(s) = \phi(-s),$$

is examined. Here L stands for the arclength of half a cycle of corrugation (not the distance to the free edge as used in Section 2(a)). It is assumed that the panel has many corrugation cycles so that edge effects at the outer reaches of the cross section may be neglected. Under these circumstances the neutral axis of the corrugated panel never moves, and quarter cycle, $0 \le s \le L/2$, calculations are sufficient for complete knowledge of the deformed geometry. To modify the equations of the last section for the present application, equations (2), (3), and (8) become, respectively,

$$y(s) = -\int_s^{L/2} \sin\phi(t)\,dt, \quad \bar{y} \equiv 0, \tag{11),(12}$$

$$M_s(s) = [x(L/2) - x(s)]\int_0^{L/2} \rho(t)\,dt + \int_s^{L/2} [x(s) - x(t)]\rho(t)\,dt \tag{13}$$

Equations (1), (4)–(7), and (9) are unchanged, as is the nondimensionalizing scheme.

2(c) Numerical Solution

Equations (1)–(9) (or the equivalent corrugated panel equations) have been cast in a form that is most conducive to numerical solution. Only function evaluations and integrations need be performed. Convergence is achieved by evaluating the equations sequentially, rather than simultaneously, and iterating a sufficient number of times. A special root-finding algorithm is not required. It was the author's experience that convergence was rapid and monotonic when the specified curvature, κ, was less than the buckling value, κ_b. For $\kappa > \kappa_b$ the convergence was slower and usually oscillatory. At approximately $\kappa = 3\kappa_b$ convergence broke down. This appears to be due to the accuracy of the computer that was used, and thus has no physical interpretation. With M_z used as the independent variable the prebuckle solution, $\kappa < \kappa_b$ was always obtained. Solving the equations in sequence permits the use of a computer with only modest storage capability. The results of this paper, for example, were obtained on a microcomputer with 16,000 eight-bit words of storage space [13].

3(a) Description of the Example Geometries – General Results

The equations of this paper are tested on three example geometries; an angle section beam, a circular section beam, and a sinusoidal corrugated panel. Moment-curvature results are plotted in Figs. 2, 3, and 4, respectively. The two open section beam examples were chosen because they already have some coverage in the literature, thus permitting comparison with present results. In addition, the cross sections are of such standard shape that structures engineers should find a number of applications for which the results may be directly applied. The corrugated panel example is included because it is representative of a nonstandard geometry, as mentioned in the Introduction.

The initial, nondimensional, cross section geometry of an angle section is determined by the root angle of one of its leaves, ψ_r. See, for example, the 45 deg drawing of Fig. 2. A circular section has its initial, nondimensional, cross section determined by the sweep angle of one of its leaves, ψ_s. The 90 deg drawing of Fig. 3 illustrates this. By the present nondimensionalization ψ_s also represents the initial cross curvature of the circular section. Either of the initial beam geometries, or a mixture of both, may be described by the slope angle function

$$\phi_0(s) = \psi_r + \psi_s s.$$

For the corrugated panel, the initial cross section geometry is generated by the function

$$\phi_0(s) = -\psi_c \sin(\pi s),$$

where ψ_c is the slope of the panel as it crosses the neutral axis. This is illustrated by the 75 deg drawing of Fig. 4. All three of the example cases have zero initial longitudinal curvature, $\kappa_0 = 0$.

Each curve of Figs. 2–4 is accompanied by a drawing that shows the beam or panel in the undeformed state and a selected deformed state. These drawings are to scale and are superimposed on a common neutral axis. A dot on the moment-curvature graph marks the point of the illustrated deformed state. This is the buckle geometry in most cases; a post-buckled geometry for the rest.

3(b) Angle Section Results

Angle sections ranging from $\psi_r = 15$ to $\psi_r = 90$ deg are examined in Fig. 2. While it is hard to imagine any structural value of a 90 deg angle section, the curve is nonetheless interesting as it forms an envelope to the other curves. With vertical leaves, the 90 deg angle section does not initially exhibit cross section flattening as a moment is applied. Rather, internal compression builds up until the leaves collapse, as in Euler buckling of a column. By the numerical method of section 2(c), the 90 deg angle section was found to buckle at $M_{zb} = 3.12$ and $\kappa_b = 1.56$. An independent check by an Euler buckling analysis gave identical answers.

For the lower set of curves of Fig. 2, comparison is made with Meck [10]. In his paper Meck provides a convenient

Downloaded 02 May 2010 to 171.66.16.25. Redistribution subject to ASME license or copyright; see http://www.asme.org/terms/Terms_Use.cfm

Table 1: Comparison with Meck [10]

ψ_r(deg)	Present M_{zb}	Meck's $M_{zb}(\nu=1/3)$
0	0	0
15	0.0736	0.0706
30	0.294	0.282
45	0.659	0.635
60	1.175	1.129
75	1.872	1.765
90	3.12	2.54

Table 2: Comparison with Ashwell [7]

ψ_s(deg)	Present M_{zb}	Ashwell's $M_{zb}(\nu=1/3)$
0	0	0
15	0.0192	0.0221
30	0.0768	0.0797
45	0.173	0.150
60	0.304	0.207

approximation for the buckling moment as a function of the root angle and Poisson's ratio. His equation (19), in the present nondimensional notation is

$$M_{zb}=1.071\left[\frac{1-\nu^2}{1-0.68\nu^2}\right]^{1/2}\psi_r{}^2.$$

Here ψ_r is expressed in radians. Meck claims that the formula is good to within 3 percent error for angles up to 70 deg. A comparison with present results is made in Table 1. The match is quite good (and even better for $\nu = 0$), and it speaks well for Meck's kinematic assumption that the angle section deforms in the cross section as two rigid leaves connected by an elastic hinge at the root.

Theoretically the angle section beam exhibits a symmetry for reversed bending, $M_z(-\kappa)=-M_z(\kappa)$, and numerical results bear this out. However, the beam cannot physically support a bending that puts into compression the fibers at the free edge. Rather these fibers will suffer a local buckling, and the beam will deform torsionally for even small negative bending moments. Torsion is not treated here, but readers may consult Bisplinghoff [8] for an investigation of combined bending and torsion of a cambered plate. Axial wrinkling for $0<M_z<M_{zb}$ could also occur when the free edges are in tension and the centerline compression is great. This is the sort of problem studied by Fabian [6]. The steep angle sections $\psi_r = 75$ deg and $\psi_r = 90$ deg would seem to be candidates for axial wrinkling. Structural engineers should regard these geometries more as limiting conditions, rather than as sound design.

3(*c*) Circular Section Results

Circular sections ranging from $\psi_s = 45$ to $\psi_s = 180$ deg are examined in Fig. 3. It will be noted that the beams divide into two post-buckle categories; those with leaves that collapse outward, and those with leaves that collapse inward. The transition occurs at $\psi_s = 155$ deg. With nearly identical initial geometries, the prebuckle curves for $\psi_s = 154$ deg and $\psi_s = 155$ deg are indistinguishable in Fig. 3. However, near the buckling point, $\kappa_b \approx 2$, the curves bifurcate. The $\psi_s = 154$ deg leaves collapse outward with a dramatic moment of inertia loss, whereas the $\psi_s = 155$ deg leaves collapse inward to form a relatively stiff tube with overlapping leaves.

The other inward collapsing geometry shown in Fig. 3 is the $\psi_s = 180$ deg tube or "slit tube." This has a very flat moment-curvature response in the post-buckle region. From a peak of $M_{zb} = 1.722$ at $\kappa_b = 2.047$, the moment drops only to $M_z = 1.635$ at $\kappa \pm 3.5$ (where the graph ends). One should take care, however, in accepting the moment-curvature results for inward collapsing tubes, as no account has been taken for the leaves interfering with each other. In actuality the leaves will rub against each other for an effective increase in the stiffness of the tube. The $\psi_s = 180$ deg deformed geometry at $\kappa = 3.5$, in particular, has a pronounced interference (0.07 nondimensional units along the neutral axis), so the moment reported above may be significantly undervalued. The $\psi_s = 180$ deg buckle geometry, however, has a very slight interference, which is barely discernible in Fig. 3. The same may be said of the post-buckle illustration for $\psi_s = 155$ deg. In these cases the interleaf rubbing is probably slight, and the calculated bending moment reasonably accurate.

Comparison of the present results has been made with Ashwell [7] for shallow circular sections. Ashwell gives an expression for the buckling moment, his equation (29), which when simplified for very small thicknesses and cast in present terms, becomes

$$M_{zb}=0.334\frac{\sin^3(\psi_s)}{\psi_s}.$$

This expression is based on a parabolic approximation for the cross section of a shallow circular section. Ashwell recommends that (in present terms) the sweep angle, ψ_s, be less than 10.3 deg, to insure that the maximum error in curvature is no greater than 5 percent. A comparison with present results is made in Table 2. The match is good to within 15 percent through $\psi_s = 45$ deg.

At the other extreme, comparison has been made with Rimrott [9] for the $\psi_s = 180$ deg slit tube. He reports a nondimensional buckling load of $M_{zb} = 2.177$ as compared to $M_{zb} = 1.722$ found here. The disparity is about 25 percent. Rimrott cautions that, near buckling, his analysis neglects terms that are not very small, "and the theory must therefore be considered to be of an approximate nature, at least where loading into the region near instability is studied." It would also appear from Rimrott's Fig. 3 that his placement of the neutral axis neglects the effect from overlapping leaves. As noted for the angle section, the present formulation will yield symmetric results for reversed bending. The same restrictions apply, however, on accepting a result that has the outer fibers on the free edge in compression.

3(*d*) Corrugated Panel Results

The corrugated panel results exhibit three features worth noting. The first is that, like the angle section and circular section, the buckling moment for the corrugated panel is simply approximated by a proportionality with the square of a descriptive angle; specifically

$$M_{zb}\approx 0.281\psi_c{}^2.$$

Similar to the circular section, the corrugated panel can collapse in on itself. The bifurcation between inward and outward collapsing geometries occurs for $\psi_c \approx 105$ deg. This is illustrated in Fig. 4. Unlike the angle section and circular section, the corrugated panel may accept reversed bending, as effects at the free edge have been neglected.

4 Summary

The equations of equilibrium for a classical problem in nonlinear beam bending have been cast in a form that renders the problem convergent by a closed sequence of algebraic and integral calculations. The only restrictions placed on the cross section geometry, either before or after deformation, are that it be thin, symmetrical, and not self-penetrating. Results for three example geometries have been obtained by numerical calculation on a microcomputer, and comparisons have been made with the existing literature. Cross section bifurcations are found to occur.

Acknowledgment

This work was supported by the Xerox Corporation. For that, the author is most grateful.

Downloaded 02 May 2010 to 171.66.16.25. Redistribution subject to ASME license or copyright; see http://www.asme.org/terms/Terms_Use.cfm

References

1 Brazier, L. G., "On the Flexure of Thin Cylindrical Shells and Other Thin Sections," *Proceediongs of the Royal Society of London*, Series *A*, Vol. 116, 1927, pp. 104–114.

2 Wood, J. D., "The Flexure of a Uniformly Pressurized, Circular, Cylindrical Shell," ASME *Journal of Applid Mechanics*, Vol. 25, 1958, pp. 453–458.

3 Reissner, E., "On Finite Bending of Pressurized Tubes," ASME JOURNAL OF APPLIED MECHANICS, Vol. 26, 1959, pp. 386–392.

4 Reissner, E., and Weinitschke, H. J., "Finite Pure Bending of Circular Cylindrical Tubes," *Quarterly of Applied Mathematics*, Vol. 20, 1963, pp. 305–319.

5 Spence, J., and Toh, S. L., "Collapse of Thin Orthotropic Elliptical Cylindrical Shells Under Combined Bending and Pressure Loads," ASME JOURNAL OF APPLIED MECHANICS, Vol. 26, 1959, pp. 363–371.

6 Fabian, O., "Collapse of Cylindrical, Elastic Tubes Under Combined Bending, Pressure and Axial Loads," *International Journal of Solids and Structures*, Vol. 13, 1977, pp. 1257–1270.

7 Aswell, D. G., "A Characteristic Type of Instability in the Large Deflections of Elastic Plates," *Proceedings of the Royal Society of London*, Series *A*, Vol. 214, 1952, pp. 98–118.

8 Bisplinghoff, R. L., "Finite Deflections of Thin Cambered Elastic Plates," *Journal of the Franklin Institute*, Vol. 268, Oct. 1959, pp. 270–277.

9 Rimrott, F. P. J., "Two Secondary Effects in Bending of Slit Thin-Walled Tubes," ASME *Journal of Applied Mechanics*, Vol. 323, 1966, pp. 75–78.

10 Meck, H. R., "Instability of an Angle Section Beam Under an Applied Bending Moment," *International Journal of Mechanical Science*, Vol. 11, 1969, pp. 199–207.

11 Axelrad, E. L., "Flexible Shells," *Proceedings of the XV International Congress of Theoretical and Applied Mechanics*, F. P. J., Rimrott, and B., Tabarrok, eds., North-Holland, 1980, pp. 45–50.

12 Frisch-Fay, R., *Flexible Bars*, Butterworth, 1962.

13 Osborne, A., and Donahue, C. S., *PET/CBM Personal Computer Guide*, 2nd ed., McGraw-Hill, New York, 1980.

Downloaded 02 May 2010 to 171.66.16.25. Redistribution subject to ASME license or copyright; see http://www.asme.org/terms/Terms_Use.cfm

M. W. Johnson, Jr.
Professor,
Department of Engineering Mechanics,
The University of Wisconsin,
Madison, Wis. 53706
Mem. ASME

T. J. Urbanik
Research Engineer,
Forest Products Laboratory,
Forest Service,
U.S. Department of Agriculture,
Madison, Wis. 53705

A Nonlinear Theory for Elastic Plates With Application to Characterizing Paper Properties

A theory of thin plates which is physically as well as kinematically nonlinear is developed and used to characterize elastic material behavior for arbitrary stretching and bending deformations. It is developed from a few clearly defined assumptions and uses a unique treatment of strain energy. An effective strain concept is introduced to simplify the theory to a special theory having fewer parameters and being capable of characterizing paper. A procedure is given for matching the special theory to edgewise compressive data of paperboard.

1 Introduction

Our primary objective is to develop a theory of thin elastic plates which allows physical as well as kinematic nonlinearity. In the following section this theory is developed using an asymptotic analysis of the three-dimensional equations of finite elasticity. Plate stress-strain relations and equilibrium equations are derived. These equations are adequate for the analysis of engineering problems involving finite deformation and anisotropic nonlinear material behavior.

Our current interest is to use our plate stress-strain relations to characterize the elastic properties of paper. In Section 3 we develop a simple special set of stress-strain relations through the introduction of an effective strain. The material parameters in this special theory can be determined from experimental data currently available. In Section 4 comparison of our theory with data on paper is presented. The special theory seems capable of modeling the available experimental data sufficiently well for engineering purposes.

There is only a small literature on elastic plate theory which allows physical as well as geometrical nonlinearity. Completely general theories are presented by Naghdi [1] and Wempner [2]. The theory given here is developed by the scaling-asymptotic technique [3]. The analysis has the desirability of using a few assumptions that are clearly defined. Further contributions of our approach are its unique treatment of the strain energy and the use of an effective strain measure which allows the material properties to be characterized by a small number of coefficients. We note that the effective strain concept has been found useful in plasticity theory [4].

In a previous work [5] on the strength of corrugated fiberboard it was found necessary to model paper as a nonlinear elastic material. The need for a nonlinear model has also been shown by Moody [6]. While the model used in [5] proved successful for the problem considered there, we stress that it is ad hoc to that problem and does not provide a general theory that can be applied to a wide range of engineering problems. Our purpose here is to provide such a theory.

2 Derivation of Plate Equations

We start with the equations of nonlinear three-dimensional elasticity and simplify them by a scaling argument appropriate for a thin plate. The resulting equations are then partially integrated to yield two-dimensional plate equations. The resulting plate equations represent a generalization of the von-Karman equations [7] to account for nonlinear anisotropic stress-strain relations as well as nonlinear kinematics.

The basic equations of nonlinear three-dimensional elasticity [7] are the equation of equilibrium,

$$\frac{\partial P_{ij}}{\partial x_i} = 0 \tag{2.1}$$

the stress-strain relations

$$P_{ij} = T_{ik}\left(\delta_{jk} + \frac{\partial u_j}{\partial x_k}\right), \quad T_{ij} = \frac{\partial H(E)}{\partial E_{ij}} \tag{2.2}$$

and the strain-displacement relations

$$2E_{ij} = \frac{\partial u_i}{\partial x_j} + \frac{\partial u_j}{\partial x_i} + \frac{\partial u_k}{\partial x_i}\frac{\partial u_k}{\partial x_j} \tag{2.3}$$

In the foregoing, P is the Piola-Kirchhoff stress tensor of the first kind, E is the material strain tensor, H is the strain energy density, $\mathbf{u}$ is the displacement, and x_i are Cartesian material coordinates. The equations are written in terms of Cartesian components and the summation convention is used.

Let the middle surface on the undeformed plate be $x_3 = 0$, the thickness of the plate be h, and the lateral length scale be L. For a thin plate $\epsilon = h/L$ is a small parameter. We assume that coordinates, displacement components, and strain components are scaled the same as in the von-Karman theory,

Contributed by the Applied Mechanics Division for publication in the JOURNAL OF APPLIED MECHANICS.
Discussion on this paper should be addressed to the Editorial Department, ASME, United Engineering Center, 345 East 47th Street, New York, N.Y. 10017, and will be accepted until two months after final publication of the paper itself in the JOURNAL OF APPLIED MECHANICS. Manuscript received by ASME Applied Mechanics Division, June, 1982; final revision, July, 1983.

Copyright © 1984 by ASME
Downloaded 02 May 2010 to 171.66.16.25. Redistribution subject to ASME license or copyright; see http://www.asme.org/terms/Terms_Use.cfm

$$x_1, x_2 - 0(L), \quad x_3 - 0(h) \tag{2.4}$$

$$u_1, u_2 - 0(\epsilon h), u_3 - 0(h) \tag{2.5}$$

$$\left.\begin{aligned} &E_{11}, E_{22}, E_{12}, E_{33} - 0(\epsilon^2) \\ &E_{13}, E_{23} - 0(\epsilon^3) \end{aligned}\right\} \tag{2.6}$$

With this scaling, the lowest order terms in the strain displacement relations (2.3) are

$$\left.\begin{aligned} E_{11} &= \frac{\partial u_1}{\partial x_1} + \frac{1}{2}\left(\frac{\partial u_3}{\partial x_1}\right)^2 \\ E_{22} &= \frac{\partial u_2}{\partial x_2} + \frac{1}{2}\left(\frac{\partial u_3}{\partial x_2}\right)^2 \\ E_{12} &= \frac{1}{2}\left(\frac{\partial u_1}{\partial x_2} + \frac{\partial u_2}{\partial x_1} + \frac{\partial u_3}{\partial x_1}\frac{\partial u_3}{\partial x_2}\right) \end{aligned}\right\} \tag{2.7}$$

$$\left.\begin{aligned} 0 &= \frac{\partial u_1}{\partial x_3} + \frac{\partial u_3}{\partial x_1} + \frac{\partial u_3}{\partial x_1}\frac{\partial u_3}{\partial x_3} \\ 0 &= \frac{\partial u_2}{\partial x_3} + \frac{\partial u_3}{\partial x_2} + \frac{\partial u_3}{\partial x_2}\frac{\partial u_3}{\partial x_3} \\ 0 &= \frac{\partial u_3}{\partial x_3}\left(1 + \frac{1}{2}\frac{\partial u_3}{\partial x_3}\right) \end{aligned}\right\} \tag{2.8}$$

Equations (2.8) can be partially integrated to yield:

$$\left.\begin{aligned} u_3 &= w(x_1, x_2) \\ u_1 &= U_1(x_1, x_2) - x_3\frac{\partial w}{\partial x_1} \\ u_2 &= U_2(x_1, x_2) - x_3\frac{\partial w}{\partial x_2} \end{aligned}\right\} \tag{2.9}$$

where U_1, U_2, and w are components of displacement of the middle surface. With (2.9) equations (2.7) take the form

$$\left.\begin{aligned} E_{11} &= \epsilon_1 - \kappa_1 x_3 \\ E_{22} &= \epsilon_2 - \kappa_2 x_3 \\ E_{12} &= \epsilon_{12} - \kappa_{12} x_3 \end{aligned}\right\} \tag{2.10}$$

where ϵ_1, ϵ_2, and ϵ_{12} are middle surface strain components and κ_1, κ_2, and κ_{12} are middle surface curvature components given by:

$$\left.\begin{aligned} \epsilon_1 &= \frac{\partial U_1}{\partial x_1} + \frac{1}{2}\left(\frac{\partial w}{\partial x_1}\right)^2 \\ \epsilon_2 &= \frac{\partial U_2}{\partial x_2} + \frac{1}{2}\left(\frac{\partial w}{\partial x_2}\right)^2 \\ \epsilon_{12} &= \frac{1}{2}\left(\frac{\partial U_1}{\partial x_2} + \frac{\partial U_2}{\partial x_1} + \frac{\partial w}{\partial x_1}\frac{\partial w}{\partial x_2}\right) \end{aligned}\right\} \tag{2.11}$$

$$\kappa_1 = \frac{\partial^2 w}{\partial x_1^2}, \quad \kappa_2 = \frac{\partial^2 w}{\partial x_2^2}, \quad \kappa_{12} = \frac{\partial^2 w}{\partial x_1 \partial x_2} \tag{2.12}$$

Next, let p have the dimension of stress. The following scaling of the stress components is consistent with the equilibrium equations (2.1).

$$\left.\begin{aligned} &P_{11}, P_{22}, P_{21}, P_{12} - 0(p) \\ &P_{31}, P_{13}, P_{23}, P_{32} - 0(\epsilon p) \\ &P_{33} - 0(\epsilon^2 p) \end{aligned}\right\} \tag{2.13}$$

The terms in each of the equilibrium equations are the same order so that all terms are to be retained. Define force and moment resultants by

$$N_{ij} = \int_{-h/2}^{h/2} P_{ij}\, dx_3, \quad M_{ij} = \int_{-h/2}^{h/2} P_{ij} x_3\, dx_3 \tag{2.14}$$

where the integrations are taken over the plate thickness in the undeformed configuration. We assume the surface conditions,

$$\left.\begin{aligned} &P_{31}(h/2) = P_{31}(-h/2) = 0 \\ &P_{32}(h/2) = P_{32}(-h/2) = 0 \\ &P_{33}(h/2) - P_{33}(-h/2) = q(x_1, x_2) \end{aligned}\right\} \tag{2.15}$$

That is, there is an applied surface load in the three-direction. Integration of the three-dimensional equilibrium equations and use of conditions (2.15) yield the plate force equilibrium equations:

$$\left.\begin{aligned} &\frac{\partial N_{11}}{\partial x_1} + \frac{\partial N_{21}}{\partial x_2} = 0 \\ &\frac{\partial N_{12}}{\partial x_1} + \frac{\partial N_{22}}{\partial x_2} = 0 \\ &\frac{\partial N_{13}}{\partial x_1} + \frac{\partial N_{23}}{\partial x_2} + q = 0 \end{aligned}\right\} \tag{2.16}$$

Next, multiply the first two equations of (2.1) by x_3 and integrate to obtain the equations of plate moment equilibrium

$$\left.\begin{aligned} &\frac{\partial M_{11}}{\partial x_1} + \frac{\partial M_{21}}{\partial x_2} = N_{31} \\ &\frac{\partial M_{12}}{\partial x_1} + \frac{\partial M_{22}}{\partial x_2} = N_{32} \end{aligned}\right\} \tag{2.17}$$

The stress-strain relations (2.2) are equivalent to the work principle

$$\dot{H} = P_{ki}\dot{F}_{ik} \tag{2.18}$$

where

$$F_{ij} = \delta_{ij} + \partial u_i / \partial x_j \tag{2.19}$$

is the deformation gradient tensor and the dot indicates the material time derivative.

Equations (2.2) cannot be approximated directly to obtain plate stress-strain relations because E_{33} is the same order of magnitude as E_{11}, E_{22}, and E_{12}. That is, if E_{33} is retained in the stress-strain relations, the result is an inconsistent theory. The way to resolve this problem is to use the reciprocal stress-strain relation written in terms of the complementary energy. Assume that the stress-strain relation (2.2) is uniquely invertible for strain E in terms of tensor T. Define complementary energy $H_C(T)$ by the Legendre transformation:

$$H_C(T) = T_{ij}E_{ij} - H(E) \tag{2.20}$$

Note that

$$E_{ij} = \frac{\partial H_C(T)}{\partial T_{ij}} \tag{2.21}$$

We now assume H_C is correctly approximated by retaining only the lowest order components of T. This is appropriate if H_C is a polynomial, for example. Noting that the components of T have the same scaling in ϵ as the components of P, we obtain

$$H_C(T) \sim \bar{H}_C(T_{11}, T_{22}, T_{12}) \tag{2.22}$$

$$E_{11} = \frac{\partial \bar{H}_C}{\partial T_{11}}, \quad E_{22} = \frac{\partial \bar{H}_C}{\partial T_{22}}, \quad E_{12} = \frac{\partial \bar{H}_C}{\partial T_{12}} \tag{2.23}$$

We note that approximation (2.22) cannot be adequate if E_{13},

Downloaded 02 May 2010 to 171.66.16.25. Redistribution subject to ASME license or copyright; see http://www.asme.org/terms/Terms_Use.cfm

E_{23}, or E_{33} is to be obtained from (2.21). We further assume that equations (2.23) can be uniquely inverted to give T_{11}, T_{22}, and T_{12} in terms of E_{11}, E_{22}, and E_{12}. Using (2.22) and noting that

$$T_{ij}E_{ij} \sim T_{11}E_{11} + T_{22}E_{22} + 2T_{12}E_{12} \tag{2.24}$$

we use (2.20) to approximate the strain energy function as follows

$$H(E) \sim \bar{H}(E_{11}, E_{22}, E_{12}) = T_{\alpha\beta}E_{\alpha\beta} - \bar{H}_C(T_{11}, T_{22}, T_{12}) \tag{2.25}$$

where Greek indices take on the values 1, 2. It is important that $\bar{H}(E_{11}, E_{22}, E_{12}) \neq H(E_{11}, E_{22}, E_{12}, 0, 0, 0)$.

We next make an appropriate thin plate approximation by expanding $\bar{H}$ in a Taylor series in x_3 about $x_3 = 0$ and keeping the leading terms.

$$H(E) \sim \bar{H}(\epsilon_1, \epsilon_2, \epsilon_{12}) + \frac{\partial \bar{H}}{\partial x_3}\bigg|_0 x_3 + \frac{1}{2}\frac{\partial^2 \bar{H}}{\partial x_3^2}\bigg|_0 x_3^2 \tag{2.26}$$

Use of a chain rule and equation (2.10) yields:

$$\begin{aligned}\frac{\partial^2 \bar{H}}{\partial x_3^2}\bigg|_0 &= \bar{H}_{11}\kappa_1^2 + \bar{H}_{22}\kappa_2^2 + \bar{H}_{33}\kappa_{12}^2 \\ &\quad + 2\bar{H}_{12}\kappa_1\kappa_2 + 2\bar{H}_{13}\kappa_1\kappa_{12} + 2\bar{H}_{23}\kappa_2\kappa_{12}\end{aligned} \tag{2.27}$$

where $\bar{H}_{11}(\epsilon_1, \epsilon_2, \epsilon_{12})$, $\bar{H}_{12}(\epsilon_1, \epsilon_2, \epsilon_{12})$, etc., are given by

$$\bar{H}_{11} = \frac{\partial^2 \bar{H}}{\partial \epsilon_1^2}, \quad \bar{H}_{12} = \frac{\partial^2 \bar{H}}{\partial \epsilon_1 \partial \epsilon_2}, \text{ etc.} \tag{2.28}$$

The integrated form of the work principle (2.18) is

$$\dot{\Sigma} = \int_{-h/2}^{h/2} P_{ji}\partial \dot{u}_i/\partial x_j \, dx_3 \tag{2.29}$$

where

$$\Sigma = \int_{-h/2}^{h/2} H \, dx_3 \tag{2.30}$$

is the plate strain energy density. Using (2.26), we obtain

$$\begin{aligned}\Sigma(\epsilon_1, \epsilon_2, \epsilon_{12}, \kappa_1, \kappa_2, \kappa_{12}) &\sim h\bar{H}(\epsilon_1, \epsilon_2, \epsilon_{12}) \\ &\quad + \frac{1}{24}h^3 \frac{\partial^2 \bar{H}}{\partial x_3^2}\bigg|_0\end{aligned} \tag{2.31}$$

Introducing forms (2.9) for the displacement components in (2.29) and using definitions (2.14) for force and moment resultants yields:

$$\begin{aligned}&\left(\frac{\partial \Sigma}{\partial \epsilon_1} - N_{11}\right)\frac{\partial \dot{U}_1}{\partial x_1} + \left(\frac{\partial \Sigma}{\partial \epsilon_2} - N_{22}\right)\frac{\partial \dot{U}_2}{\partial x_2} \\ &+ \left(\frac{1}{2}\frac{\partial \Sigma}{\partial \epsilon_{12}} - N_{21}\right)\frac{\partial \dot{U}_1}{\partial x_2} + \left(\frac{1}{2}\frac{\partial \Sigma}{\partial \epsilon_{12}} - N_{12}\right)\frac{\partial \dot{U}_2}{\partial x_1} \\ &+ \left(\frac{\partial \Sigma}{\partial \epsilon_1}\frac{\partial w}{\partial x_1} + \frac{1}{2}\frac{\partial \Sigma}{\partial \epsilon_{12}}\frac{\partial w}{\partial x_2} + N_{31} - N_{13}\right)\frac{\partial \dot{w}}{\partial x_1} \\ &+ \left(\frac{\partial \Sigma}{\partial \epsilon_2}\frac{\partial w}{\partial x_2} + \frac{1}{2}\frac{\partial \Sigma}{\partial \epsilon_{12}}\frac{\partial w}{\partial x_1} - N_{23} + N_{32}\right)\frac{\partial \dot{w}}{\partial x_2} \\ &+ \left(\frac{\partial \Sigma}{\partial \kappa_1} + M_{11}\right)\frac{\partial^2 \dot{w}}{\partial x_1^2} + \left(\frac{\partial \Sigma}{\partial \kappa_2} + M_{22}\right)\frac{\partial^2 \dot{w}}{\partial x_2^2} \\ &+ \left(\frac{\partial \Sigma}{\partial \kappa_{12}} + M_{12} + M_{21}\right)\frac{\partial^2 \dot{w}}{\partial x_1 \partial x_2} = 0\end{aligned} \tag{2.32}$$

Assuming that the rates in (2.32) are independent and arbitrary, leads us to set each of their coefficients to zero. These are the desired plate stress-strain relations. If Σ is approximated by (2.31) with the second derivative given by (2.27), these plate stress-strain relations take the form

$$\left.\begin{aligned}N_{11} &= h\frac{\partial \bar{H}}{\partial \epsilon_1}, \quad N_{22} = h\frac{\partial \bar{H}}{\partial \epsilon_2} \\ N_{12} &= N_{21} = \frac{1}{2}h\frac{\partial \bar{H}}{\partial \epsilon_{12}}\end{aligned}\right\} \tag{2.33}$$

$$\left.\begin{aligned}M_{11} &= -\frac{1}{12}h^3[\bar{H}_{11}\kappa_1 + \bar{H}_{12}\kappa_2 + \bar{H}_{13}\kappa_{12}] \\ M_{22} &= \frac{1}{12}h^3[\bar{H}_{12}\kappa_1 + \bar{H}_{22}\kappa_2 + \bar{H}_{23}\kappa_{12}] \\ M_{12} + M_{21} &= -\frac{1}{12}h^3[\bar{H}_{13}\kappa_1 + \bar{H}_{23}\kappa_2 + \bar{H}_{33}\kappa_{12}]\end{aligned}\right\} \tag{2.34}$$

$$\left.\begin{aligned}N_{13} &= N_{31} + h\frac{\partial \bar{H}}{\partial \epsilon_1}\frac{\partial w}{\partial x_1} + \frac{1}{2}h\frac{\partial \bar{H}}{\partial \epsilon_{12}}\frac{\partial w}{\partial x_2} \\ N_{23} &= N_{32} + h\frac{\partial \bar{H}}{\partial \epsilon_2}\frac{\partial w}{\partial x_2} + \frac{1}{2}h\frac{\partial \bar{H}}{\partial \epsilon_{12}}\frac{\partial w}{\partial x_1}\end{aligned}\right\} \tag{2.35}$$

where we have dropped higher order terms. Combining equations (2.33) and (2.35) yields

$$\left.\begin{aligned}N_{13} &= N_{31} + N_{11}\frac{\partial w}{\partial x_1} + N_{21}\frac{\partial w}{\partial x_2} \\ N_{23} &= N_{32} + N_{12}\frac{\partial w}{\partial x_1} + N_{22}\frac{\partial w}{\partial x_2}\end{aligned}\right\} \tag{2.36}$$

It is interesting that $N_{12} = N_{21}$ but $N_{13} \neq N_{31}$ and $N_{23} \neq N_{32}$.

The basic plate equations are the strain-displacement equations (2.11) and (2.12). the equilibrium equations (2.16) and (2.17), and the stress-strain relations (2.33), (2.34), and(2.36). These are 19 equations in 20 variables. To resolve this apparent discrepancy, we derive a combined equation of transverse equilibrium by substituting expressions (2.17) for N_{31} and N_{32} into equations (2.36) and then substituting the resulting expressions for N_{13} and N_{23} into equation $(2.16)_3$. The result is

$$\begin{aligned}&\frac{\partial^2 M_{11}}{\partial x_1^2} + \frac{\partial^2}{\partial x_1 \partial x_2}(M_{12} + M_{21}) + \frac{\partial^2 M_{22}}{\partial x_2^2} \\ &\quad + \frac{\partial}{\partial x_1}\left(N_{11}\frac{\partial w}{\partial x_1} + N_{12}\frac{\partial w}{\partial x_2}\right) \\ &\quad + \frac{\partial}{\partial x_2}\left(N_{22}\frac{\partial w}{\partial x_2} + N_{21}\frac{\partial w}{\partial x_1}\right) + q = 0\end{aligned} \tag{2.37}$$

The equations are now reduced to 15 in number: equations (2.11), (2.12), $(2.16)_1$, $(2.16)_2$, (2.33), (2.34), and (2.37). The variables are also 15 in number: ϵ_1, ϵ_2, ϵ_{12}, κ_1, κ_2, κ_{12}, U_1, U_2, w, N_{11}, N_{12}, $= N_{21}$, N_{22}, M_{11}, M_{22}, $M_{12} + M_{21}$. Note that equation (2.37) is also obtained in the von-Karman theory.

Our particular interest in what follows is with the stress-strain relations (2.33) and (2.34) which express the nonlinear elastic mechanical properties of the plate. These properties are determined by the strain energy density $\bar{H}$ which is a function only of the middle surface strains ϵ_1, ϵ_2, and ϵ_{12}. Linear isotropic plate theory corresponds to the strain energy

$$\bar{H} = \frac{\mathrm{E}}{2(1-\nu^2)}(\epsilon_1 + \epsilon_2)^2 - \frac{\mathrm{E}}{1+\nu}(\epsilon_1\epsilon_2 - \epsilon_{12}^2) \tag{2.38}$$

where E is Young's modulus and ν Poisson's ratio. Linear orthotropic plate theory corresponds to

$$\bar{H} = \frac{\mathrm{E}_1}{2(1-\nu_1\nu_2)}(\epsilon_1^2 + \nu_2\epsilon_1\epsilon_2)$$

Downloaded 02 May 2010 to 171.66.16.25. Redistribution subject to ASME license or copyright; see http://www.asme.org/terms/Terms_Use.cfm

$$+\frac{E_2}{2(1-\nu_1\nu_2)}(\epsilon_2^2+\nu_1\epsilon_1\epsilon_2)+2G\epsilon_{12}^2 \tag{2.39}$$

where E_1 and E_2 are Young's moduli, ν_1, ν_2 Poisson's ratios, and G the shear modulus. Note that the moduli satisfy $\nu_2 E_1 = \nu_1 E_2$. Equations (2.38) and (2.39) are obtained, of course, by starting with the expressions for the three-dimensional strain energy density $H(E)$ and following the steps indicated from equations (2.20) to (2.25).

For orthotropic (rhombic) material symmetry it can be shown that $\bar{H}$ depends on variable ϵ_{12} as the square of that variable; that is

$$\bar{H}(\epsilon_1,\epsilon_2,\epsilon_{12}^2) \tag{2.40}$$

The proof of this is given in [8]. This symmetry is appropriate to paper or wood.

We note that the constitutive equations (2.34) are linear in curvature components with stiffness moduli that depend only on middle-surface strain components. This form is consistent with the original scaling assumptions (2.4), (2.5), and (2.6) on which this entire plate theory is based. In each equation only terms of lowest order in ϵ are retained. One could produce terms in (2.34) that are nonlinear in curvature components by retaining additional terms in the expansion (2.26) but that would be inconsistent with the approximations made in the kinematic and equilibrium equations.

It is important that middle-surface strains are small, being of order ϵ^2, but general nonlinear, anisotropic constitutive behavior is retained. In fact, this is how the present theory represents an extension of the von-Karman theory.

We remark that equations (2.36) can also be derived from the fact that tensor T_{ij}, defined in equation (2.2), is symmetric. This symmetry has been built into the preceding anlaysis because T_{ij} is defined as $\partial H/\partial E_{ij}$ and E_{ij} is symmetric by definition.

From equation (2.2),

$$P_{ij} = T_{ik}F_{jk}$$

which inverts to give

$$T_{ij} = P_{ik}F_{jk}^{-1}$$

The symmetry condition $T_{ij} = T_{ji}$ leads to the following equation to be satisfied by tensor P_{ij}.

$$P_{ki}F_{jk} = F_{ik}P_{kj}$$

or

$$P_{ji}+P_{ki}\frac{\partial u_j}{\partial x_k} = P_{ij}+\frac{\partial u_i}{\partial x_k}P_{kj} \tag{2.41}$$

Equation (2.41) is an identity when $i = j$. For $i \neq j$, if we use scalings (2.5) and (2.13), drop higher order terms and write $u_3 = w(x_1, x_2)$. Equation (2.41) yields

$$\left.\begin{aligned} &P_{12} = P_{21}\\ &P_{13} = P_{31}+P_{11}\frac{\partial w}{\partial x_1}+P_{21}\frac{\partial w}{\partial x_2}\\ &P_{23} = P_{32}+P_{12}\frac{\partial w}{\partial x_1}+P_{22}\frac{\partial w}{\partial x_2}\end{aligned}\right\} \tag{2.42}$$

The integration of these equations over the thickness of the plate yields $N_{12} = N_{21}$ and equations (2.36).

We also note that tensor T_{ij} is related to the Cauchy stress tensor C_{ij} by

$$C_{ij} = \frac{\rho}{\rho_0}F_{ik}T_{km}F_{jm}$$

where ρ and ρ_0 are densities of the deformed and undeformed body. The symmetry of C_{ij}, and hence of T_{ij}, follows from the law of moment equilibrium in continuum mechanics. In this sense, equations (2.36) represent plate equilibrium equations. In linear plate theory, five equilibrium equations of the form (2.16) and (2.17) are used. Equations (2.36) represent additional equilibrium equations[1] that arise in the present theory because of the use of the nonsymmetric stress tensor P_{ij}.

3 A Special Plate Theory

As pointed out in the foregoing the nonlinear elastic properties of a thin plate are described by equations (2.33) and (2.34) in terms of a single function, the strain energy density $\bar{H}$. $\bar{H}$ is a function of three variables, the middle-surface strains ϵ_1, ϵ_2, ϵ_{12}. To completely determine $\bar{H}$, it would be necessary to have a complete set of data on biaxial stretching and shear of the plate. Since such data is not yet available for paper, we formulate a simpler set of stress-strain relations in this section based on an assumed structure for the strain energy density function. All the parameters in these equations can be determined from experimental data that is now available on paper. Beyond this, the modified theory is interesting in its own right.

Note that, for linear orthotropic elasticity the plate strain energy function (2.39) can be written in the form

$$\bar{H} = \frac{\nu_2 E_1}{2(1-\nu_1\nu_2)}e \tag{3.1}$$

where e is given by

$$e = \nu_2^{-1}\epsilon_1^2+\nu_1^{-1}\epsilon_2^2+2\epsilon_1\epsilon_2+c\epsilon_{12}^2 \tag{3.2}$$

Constant c is related to the shear modulus G by

$$c = \frac{4(1-\nu_1\nu_2)}{\nu_1 E_2}G \tag{3.3}$$

The quantity $\epsilon_g = \sqrt{e}$ is an "effective strain" measure, a measure of the magnitude of strain at a point in the material.

For nonlinear orthotropic material behavior we construct an approximate theory by assuming that the plate strain energy function is a function of the single variable e as it is in the linear theory, $\bar{H}(e)$. Constants ν_1, ν_2, and c as well as the functional form of $\bar{H}(e)$ are to be found by comparison with the data. The material functions in (2.33) and (2.34) now take the form

$$\left.\begin{aligned} &N_{11} = h\bar{H}'(e)2(\nu_2^{-1}\epsilon_1+\epsilon_2)\\ &N_{22} = h\bar{H}'(e)2(\nu_1^{-1}\epsilon_2+\epsilon_1)\\ &N_{12} = N_{21} = h\bar{H}'(e)c\epsilon_{12}\end{aligned}\right\} \tag{3.4}$$

$$\left.\begin{aligned} &\bar{H}_{11} = \bar{H}''(e)4(\nu_2^{-1}\epsilon_1+\epsilon_2)^2+2\nu_2^{-1}\bar{H}'(e)\\ &\bar{H}_{22} = \bar{H}''(e)4(\nu_2^{-1}\epsilon_2+\epsilon_1)^2+2\nu_1^{-1}\bar{H}'(e)\\ &\bar{H}_{12} = \bar{H}''(e)4(\nu_2^{-1}\epsilon_1+\epsilon_2)(\nu_1^{-1}\epsilon_2+\epsilon_1)+2\bar{H}'(e)\\ &\bar{H}_{33} = \bar{H}''(e)4c^2\epsilon_{12}^2+2c\bar{H}'(e)\\ &\bar{H}_{13} = \bar{H}''(e)4(\nu_2^{-1}\epsilon_1+\epsilon_2)c\epsilon_{12}\\ &\bar{H}_{23} = \bar{H}''(e)4(\nu_1^{-1}\epsilon_2+\epsilon_1)c\epsilon_{12}\end{aligned}\right\} \tag{3.5}$$

For uniaxial extension in the two direction, we have $N_{11} = 0$ which leads to $\epsilon_1 = -\nu_2\epsilon_2$. That is, constant ν_2 is the Poisson ratio associated with two-direction extension. Similarly, ν_1 is the Poisson ratio associated with one-direction extension. It is interesting that, while this theory is nonlinear, it predicts constant Poisson ratios. With $\epsilon_{12} = 0$, equations (3.4) and (3.5) take the following form for two-direction uniaxial extension:

[1] We thank Professor Gerald Wempner for pointing this out.

Downloaded 02 May 2010 to 171.66.16.25. Redistribution subject to ASME license or copyright; see http://www.asme.org/terms/Terms_Use.cfm

$$e=(\nu_1^{-1}-\nu_2)\epsilon_2^2 \tag{3.6}$$

$$N_{22}=2h(\nu_1^{-1}-\nu_2)\bar{H}'(e)\epsilon_2 \tag{3.7}$$

$$\left.\begin{aligned}
&\bar{H}_{11}=2\nu_2^{-1}\bar{H}'(e)\\
&\bar{H}_{22}=4(\nu_1^{-1}-\nu_2)^2\bar{H}''(e)\epsilon_2^2+2\nu_1^{-1}\bar{H}'(e)\\
&\bar{H}_{12}=2\bar{H}'(e),\quad \bar{H}_{33}=2c\bar{H}'(e)\\
&\bar{H}_{13}=\bar{H}_{23}=0
\end{aligned}\right\} \tag{3.8}$$

Similar relations hold for uniaxial extension in the one direction. The axial stress-strain relation is, in this case:

$$N_{11}=2h(\nu_2^{-1}-\nu_1)\bar{H}'(e)\epsilon_1 \tag{3.9}$$

where

$$e=(\nu_2^{-1}-\nu_1)\epsilon_1^2.$$

Either extension in the two direction or in the one direction can be used to determine the function $\bar{H}(e)$. To use (3.7), we combine it with (3.6) to obtain

$$\frac{d\bar{H}}{d\epsilon_2}=\sigma_2(\epsilon_2) \tag{3.10}$$

where σ_2 is the axial stress in uniaxial extension. With $\sigma_2(\epsilon_2)$ given experimentally, we can integrate (3.10) to find function $\bar{H}$. Substituting this form for $\bar{H}$ back into (3.4) and (3.5) determines the stress-strain relations once constant c has been found. If extension in the one direction is used to determine $\bar{H}$ the relevant equation is:

$$\frac{d\bar{H}}{d\epsilon_1}=\sigma_1(\epsilon_1) \tag{3.11}$$

One interesting relationship predicted by this special theory says that the stress σ_1 in uniaxial extension in the one direction is related to the stress σ_2 in uniaxial extension in the two direction by

$$\epsilon_1\sigma_1(\epsilon_1)=\epsilon_2\sigma_2(\epsilon_2) \tag{3.12}$$

when the corresponding strains are related by

$$\sqrt{\nu_1}\epsilon_1=\sqrt{\nu_2}\epsilon_2 \tag{3.13}$$

These relations are compared with experimental data for paper in Section 4. They provide a critical test of the special plate theory. A complete test of this theory will be possible if and when biaxial stress-strain data are available.

Any strain energy function of form (2.40) describes an orthotropic material. Hence, the special strain energy form of this section given by $\bar{H}(e)$ where e is given by (3.2) describes a particular orthotropic material.

4 Application to Paper Properties

This section compares the Special Plate Theory to data on paper. We identify the one direction with the machine direction (M.D.) of paper and the two directions with the cross machine direction (C.D.). Our current application of the theory is as part of a theory to predict the behavior of paperboard in a corrugated fiberboard structure. We therefore limit strains to those normally encountered in paperboard during the compressive loading of fiberboard boxes. Up to these strains we can adequately assume that compression and tension stress-strain curves are identical.

Average values for Poisson ratios ν_1 and ν_2 are given by Kellicutt for Fourdrinier kraft paperboards [11]. These values are

$$\nu_1=0.328,\ \nu_2=0.219 \tag{4.1}$$

An effective Poisson ratio, $\nu = 0.268$, defined as the geometric mean $\nu=\sqrt{\nu_1\nu_2}$, was used in the engineering calculations of [5] and [10].

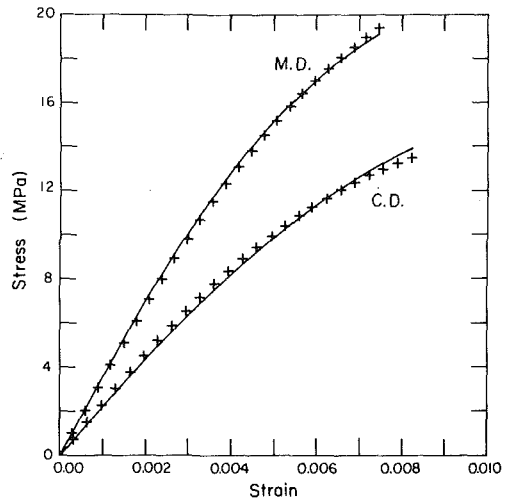

Fig. 1 Stress-strain curves for linerboard material. The crosses represent the average fit of equation (4.3) to tests of 18 C.D. specimens and the average fit to tests of 18 M.D. specimens. The curves represent a fit of equation (4.7) to the data.

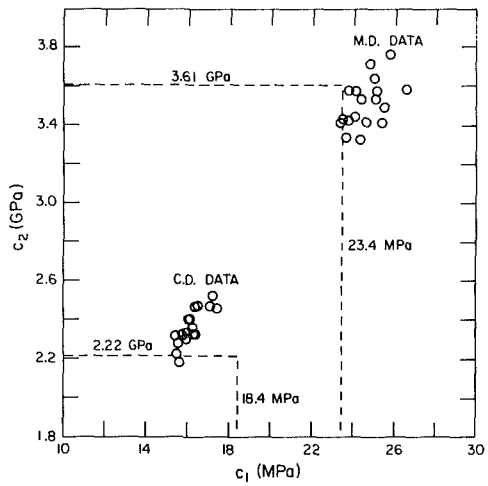

Fig. 2 Values of c_1 and c_2. The points are obtained by fitting equation (4.3) to tests of 18 C.D. specimens and 18 M.D. specimens. The dashes represent the values obtained from the regression analysis of equation (4.7).

Poisson ratios for several papers tested in tension have been measured by Göttsching and Baumgarten [12] and by Baum and Bornhoeft [13]. The range of values found is large, ν_1 ranging from 0.15–0.50, and ν_2 from 0.04–0.20. There is a large scatter in the results given in [12], which illustrates the difficulty in the measurement of Poisson ratios.

Experimental values of the initial shear modulus G for several papers are given by Setterholm, Benson, and Kuenzi [14]. These values range from 1.23 to 1.47 GPa. For situations where the shear modulus is not known, some writers [15] recommend the formula

$$G=\frac{\sqrt{E_1E_2}}{2(1+\sqrt{\nu_1\nu_2})}=\frac{\sqrt{\nu_1/\nu_2}E_2}{2(1+\sqrt{\nu_1\nu_2})} \tag{4.2}$$

where E_1 and E_2 are initial Young's moduli. For the stress-strain data on several papers given in [5] and with ν_1 and ν_2 given by equation (4.1), equation (4.2) predicts G values from 1.01–1.59 GPa, which are not unreasonable when compared to the results in [14].

The prediction of constant Poisson ratios is confirmed up to the strains of interest by tensile data given by Göttsching and Baumgarten [12]. For several papers (Figs. 3, 4, 6, 7, 10 of reference [12]), the Poisson ratios are almost constant. For

Downloaded 02 May 2010 to 171.66.16.25. Redistribution subject to ASME license or copyright; see http://www.asme.org/terms/Terms_Use.cfm

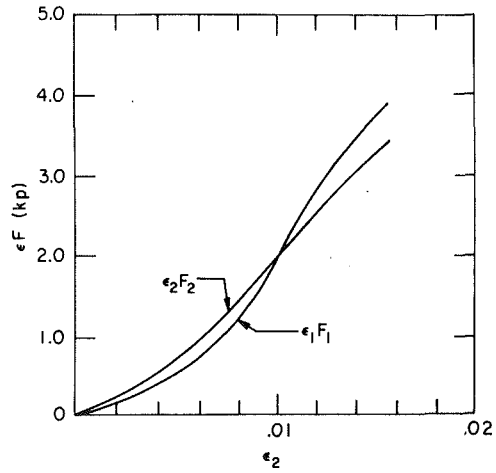

Fig. 3 Curves of $\epsilon_1 F_1$ and $\epsilon_2 F_2$ determined from data given in [12]. $\nu_1 = 0.42$, $\nu_2 = 0.11$. The theory of equations (3.12) and (3.13) predicts that the two curves should be identical.

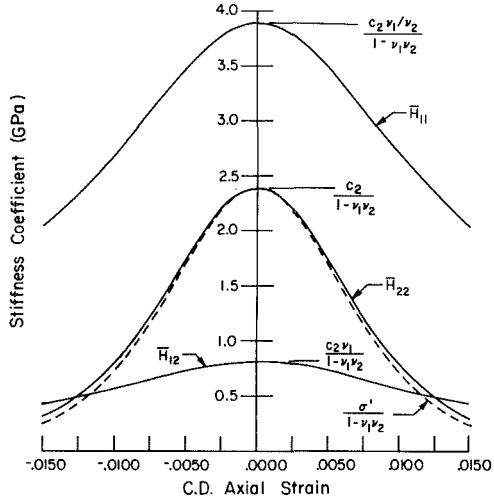

Fig. 4 Form of the plate stiffness coefficients in uniaxial strain. $c_1 = 18.4$ MPa, $c_2 = 2.22$ GPa, $A = 1.63$, $\nu = 0.268$ ($\nu_1 = 0.342$, $\nu_2 = 0.210$). Also shown is the tangent modulus coefficient $\sigma'/(1-\nu_1\nu_2)$ used as an approximation to $\bar{H}_{22}$ in [5].

the other papers tested, there is only a small deviation, so that assuming constant Poisson ratios would seem an adequate engineering approximation. In fact, throughout reference [12], Poisson's ratio is implicitly assumed to be constant, that is, independent of strain.

An empirical relation for the compressive stress-strain relation $\sigma(\epsilon)$ is given in [5]. This relation makes use of three parameters. A more accurate formula, which uses only two parameters, is given in [9] along with a procedure for matching the formula to data. That formula is

$$\sigma(\epsilon) = c_1 \tanh(c_2\epsilon/c_1) \tag{4.3}$$

where c_1 and c_2 are parameters to be determined from the data. While (4.3) can be identified with either the C.D. or M.D. stress-strain curves, we here match it with the C.D. two direction.

$$\sigma_2(\epsilon_2) = c_1 \tanh(c_2\epsilon_2/c_1) \tag{4.4}$$

Equation (3.10) then reads

$$\frac{d\bar{H}}{d\epsilon_2} = c_1 \tanh(c_2\epsilon_2/c_1)$$

Integrating this equation yields the strain energy density function

$$\bar{H} = (c_1^2/c_2)\log\cosh(c_2\epsilon_2/c_1)$$

Replacing ϵ_2 by e according to equation (3.6) gives the strain energy density in terms of e.

$$\bar{H}(e) = (c_1^2/c_2)\log\cosh\left(\frac{c_2}{c_1}\sqrt{\frac{\nu_1 e}{1-\nu_1\nu_2}}\right) \tag{4.5}$$

For uniaxial deformation in the one direction, the stress-strain relation is given by equation (3.11). Using equations (3.9) and (4.5), we obtain

$$\sigma_1(\epsilon_1) = N_{11}/h = c_1\sqrt{\frac{\nu_1}{\nu_2}}\tanh\left(\frac{c_2}{c_1}\sqrt{\frac{\nu_1}{\nu_2}}\epsilon_1\right) \tag{4.6}$$

Stress-strain data have been taken at the Forest Products Laboratory for linerboard material tested in edgewise compression. Eighteen C.D. specimens and 18 M.D. specimens have been tested. The results of an analysis of these data are shown on Figs. 1 and 2. While it makes some sense to determine c_1 and c_2 by fitting (4.3) to C.D. data only, we have found that a good fit to both C.D. and M.D. data can be made with the single equation

$$\sigma = q_1 c_1 \tanh(c_2\epsilon/c_1) + q_2 c_1\sqrt{A}\tanh\left(\frac{c_2}{c_1}\sqrt{A}\epsilon\right) \tag{4.7}$$

where A stands for the ratio ν_1/ν_2. Equation (4.7) reduces to (4.4) when $q_1 = 1$, $q_2 = 0$, and to (4.6) when $q_1 = 0$, $q_2 = 1$.

Values of c_1, c_2, and A are determined from a nonlinear regression analysis of (4.7) using σ as the dependent variable and ϵ, q_1, and q_2 as the independent variables. For C.D. data we use $q_1 = 1$, $q_2 = 0$, and for M.D. data $q_1 = 0$, $q_2 = 1$. The values of c_1 and c_2 obtained, which are C.D. values, are c_1(C.D.) = 18.4 MPa and c_2(C.D.) = 2.22 GPa. The value of A obtained is $A = 1.628$.

From equations (4.3), (4.4), and (4.6) we see that

$$\left.\begin{aligned} c_1(\text{M.D.}) &= \sqrt{A}\, c_1(\text{C.D.}) \\ c_2(\text{M.D.}) &= A\, c_2(\text{C.D.}) \end{aligned}\right\} \tag{4.8}$$

These equations are equivalent to equations (3.12) and (3.13) of the special theory. We use them and the preceding results for c_1(C.D.) and c_2(C.D.) to obtain c_1(M.D.) = 23.4 MPa and c_2(M.D.) = 3.61 GPa. These parameter values are used in equation (4.3) to plot the curves in Fig. 1 which show good agreement with the data.

On Fig. 2 are shown values of c_1 and c_2 obtained by matching equation (4.3) to the 18 C.D. and 18 M.D. stress-strain curves. These are compared with values of c_1 and c_2 obtained from equation (4.7). Figures 1 and 2 are a good test of the special theory and especially of relations (3.12) and (3.13) predicted by the special theory.

In Fig. 8 of reference [12] are given load and lateral contraction data for tensile tests in the machine and cross-machine directions of offset printing paper. These results can also be used to check prediction (3.12) and (3.13). The Poisson ratios determined from Fig. 8 of [12] are $\nu_1 = 0.42$ and $\nu_2 = 0.11$. The check of equation (3.12) is shown in Fig. 3. There is especially good agreement for strains less than 0.01. Note that the data are not given in terms of stress, but rather in tensile force. Thus, forces rather than stresses have been used in equation (3.12) and on Fig. 3. This is justified because the widths of all test specimens are the same and it was assumed that the thicknesses of M.D. and C.D. specimens were the same.

The plate stiffness coefficients appear in constitutive equations (2.34) and are given by equations (3.5) for the special theory. With the strain energy given by equation (4.5), equations (3.5) take the following form for uniaxial extension in the two direction.

Downloaded 02 May 2010 to 171.66.16.25. Redistribution subject to ASME license or copyright; see http://www.asme.org/terms/Terms_Use.cfm

$$\left.\begin{aligned}
\bar{H}_{11} &= \frac{c_1 \nu_1/\nu_2}{1-\nu_1\nu_2}\,\frac{\tanh(c_2\epsilon_2/c_1)}{\epsilon_2} \\
\bar{H}_{22} &= \frac{c_2}{\cosh^2(c_2\epsilon_2/c_1)} + \frac{\nu_1\nu_2 c_1}{1-\nu_1\nu_2}\,\frac{\tanh(c_2\epsilon_2/c_1)}{\epsilon_2} \\
\bar{H}_{12} &= \frac{c_1\nu_1}{1-\nu_1\nu_2}\,\frac{\tanh(c_2\epsilon_2/c_1)}{\epsilon_2} \\
\bar{H}_{33} &= c\,\bar{H}_{12}, \quad \bar{H}_{13} = \bar{H}_{23} = 0
\end{aligned}\right\} \tag{4.9}$$

The variation of stiffness components (4.9) with axial strain is illustrated in Fig. 4. There are no experimental data available to compare with these predictions of the theory.

Acknowledgment

This research is supported by the U.S. Department of Agriculture, Forest Products Laboratory, Madison, Wisconsin.

References

1 Naghdi, P. M., "The Theory of Shells and Plates," in S. Flügge's *Encyclopedia of Physics*, Volume VI *a*/2, Truesdell, S., ed., Springer-Verlag, 1972, pp. 425–640.

2 Wempner, G., *Mechanics of Solids*, McGraw-Hill, 1973.

3 Rutten, H. S., *Asymptotic Approximation in the Three-Dimensional Theory of Thin and Thick Elastic Shells*, Nederlandse Boekdruk Industrie N. V., 's - Hertogenbosch, 1971.

4 Mendelson, A., *Plasticity: Theory and Application*, Macmillan, 1968, p. 116.

5 Johnson, M. W., Jr., Urbanik, T. J., and Denniston, W. E., "Optimum Fiber Distribution in Singlewall Corrugated Fiberboard," USDA Forest Service Research Paper FPL 348, Forest Products Laboratory, Madison, Wis., 1979.

6 Moody, R. C., "Edgewise Compression Strength of Corrugated Fiberboard as Determined by Local Instability," USDA Forest Service Research Paper FPL 46, Forest Products Laboratory, Madison, Wis., 1965.

7 Fung, Y. C., *Foundation of Solid Mechanics*, Prentice-Hall, Englewood Cliffs, N.J., 1965, Chapter 16.

8 Green, A. E., and Adkins, J. E., *Large Elastic Deformation*, Oxford Press, 1960, p. 14.

9 Urbanik, T. J., "A Method for Analyzing Analoque Plots of Paperboard Stress-Strain Data," *Tappi*, Vol. 65, 1982, pp. 104–108.

10 Urbanik, T. J., "Effect of Paperboard Stress-Strain Characteristics on Strength of Singlewall Corrugated Fiberboard: A Theoretical Approach," USDA For. Serv. Res. Pap. FPL 401, For. Prod. Lab., Madison, Wis., 1981.

11 Kellicutt, K. Q., and Landt, E. F., "Basic Design Data for the Use of Fiberboard in Shipping Containers," USDA For. Serv. Rep. No. 1911. For. Prod. Lab., Madison, Wis., 1958.

12 Göttsching, L., and Baumgarten, H. L., "Triaxial Deformation of Paper Under Tensile Load," in *The Fundamental Properties of Paper Related to Its Uses*, Vol. 1, Technical Division of the British Paper and Board Industry Federation, 1976, pp. 227–252.

13 Baum, G. A., and Bornhoeft, L. R., "Estimating Poisson Ratios in Paper Using Ultrasonic Techniques," *Tappi*, Vol. 62, 1979, pp. 87–90.

14 Setterholm, V. C., Benson, R., and Kuenzi, E. W., "Method for Measuring Edgewise Shear Properties of Paper," *Tappi*, Vol. 51, 1968, pp. 196–202.

15 Panc, V., *Theories of Elastic Plates*, Noordhoff International, 1975, p. 399.

Downloaded 02 May 2010 to 171.66.16.25. Redistribution subject to ASME license or copyright; see http://www.asme.org/terms/Terms_Use.cfm

M. Sathyamoorthy
Associate Professor,
Department of Mechanical
and Industrial Engineering,
Clarkson College of Technology,
Potsdam, N.Y. 13676
Assoc. Mem. ASME

M. E. Prasad
Engineer,
Simmonds Precision,
Norwich, N.Y. 13815

A Multiple-Mode Approach to Large-Amplitude Vibration of Moderately Thick Elliptical Plates

Based on a multiple-mode analysis, solutions to the nonlinear equations of motion are presented for elliptical plates in terms of variations of nonlinear periods with amplitudes of vibration. The governing equations are written in terms of lateral displacement w and stress function F and the effects of transverse shear deformation and rotatory inertia are incorporated into these equations. For the multiple-mode approach considered in this paper, an exact solution to the stress function is determined. Effects of geometric nonlinearity, shear deformation, rotatory inertia, plate geometry, and modal interaction on the vibration behaviors of elliptical plates are investigated in detail.

Introduction

The study of geometrically nonlinear behavior of plates of various planforms has been the subject of several investigations for many years [1, 2]. Several solutions are available in literature for nonlinear static and post-buckling problems. Large-amplitude vibration studies on thin plates have also been carried out by several researchers. Among theories accounting for the effects of geometric nonlinearity on dynamic problems, the most widely used is the dynamic von Kármán theory given by Herrmann [3]. In the case of elliptical plates, a few solutions are available for the nonlinear dynamic cases with the most recent one formulated by Sathyamoorthy [4] for clamped isotropic plates. Sathyamoorthy and Chia [5] have also presented solutions for the nonlinear dynamic cases involving orthotropic elliptical plates. Using Berger approximation Banerjee [6] studied the large-amplitude vibration behavior of an isotropic elliptical plate. All these analyses, however, are based on a single-mode approximation and none of these investigations take into account the effects of transverse shear deformation and rotatory inertia which are important for moderately thick plates.

A discussion on various nonlinear theories applicable for moderately thick plates can be found in earlier papers by Sathyamoorthy and Chia [7, 8]. It has also been shown that the effects of transverse shear and rotatory inertia play a significant role in the large-amplitude vibration behavior of moderately thick plates of various geometries [7, 8]. Analytical work so far carried out is based mainly on single-mode approximations and is often done with the aid of either von Kármán-type nonlinear equations or Berger-type approximation. Finite element methods have recently been used by Reddy, Huang, and Chao [9–11] in the investigations concerning fundamental modes for moderately thick plates. Chia and Prabhakara [12, 13] used generalized double Fourier series for the multiple-mode vibration analysis of orthotropic as well as laminated rectangular plates and concluded that the coupling of vibrating modes has a significant effect on the nonlinear frequencies. The analysis, however, is restricted to thin plates since the effects of transverse shear and rotatory inertia have been ignored in the formulation.

This paper is analytically concerned with the large-amplitude flexural vibration of moderately thick plates of elliptical geometry with clamped boundaries. Nonlinear equations of motion derived earlier in [7] in terms of the lateral displacement w and stress function F have been used in this work. The effects of transverse shear and rotatory inertia have been incorporated into these equations by means of tracing constants T_s representing the effect of transverse shear and R_i that of rotatory inertia. A solution for w is carefully chosen in the polynomial separable form to satisfy the out-of-plane boundary conditions of the plate configuration. The assumed multiple mode in this case is a product of two known space functions and two unknown time functions. An exact solution to the stress function F is obtained by solving one of the two nonlinear governing equations with the aid of a semi-inverse method. The stress function thus determined is a polynomial of the twelfth degree and consists of 27 appropriate coefficients. All the nonlinear boundary conditions are satisfied completely in the process of determining F. Since the mode shape w and the stress function F are known in an explicit form, the equation of transverse motion is satisfied by integrating the error function over the area of the plate. After a very laborious manipulation, two time-differential equations are obtained in terms of the two unknown time

Contributed by the Applied Mechanics Division for presentation at the 1984 ASME Applied Mechanics, Bioengineering, and Fluids Engineering Conference, San Antonio, Texas, June 17–21, 1984 of THE AMERICAN SOCIETY OF MECHANICAL ENGINEERS.

Discussion on this paper should be addressed to the Editorial Department, ASME, United Engineering Center, 345 East 47th Street, New York, N.Y. 10017, and will be accepted until two months after final publication of the paper itself in the JOURNAL OF APPLIED MECHANICS. Manuscript received by ASME Applied Mechanics Division, March, 1983; final revision, June, 1983. Paper No. 84-APM-6.

Copies will be available until February, 1985.

Copyright © 1984 by ASME
Downloaded 02 May 2010 to 171.66.16.25. Redistribution subject to ASME license or copyright; see http://www.asme.org/terms/Terms_Use.cfm

functions. These two modal equations contain a total of 40 coefficients which depend on the elastic constants and geometric plate parameters of the plate. Runge-Kutta numerical integration method has been conveniently used to solve these two modal equations. Numerical results for nonlinear periods are presented for elliptical plates for different sizes and thicknesses including the effects of transverse shear and rotatory inertia. Similar results can be readily generated for thin elliptical plates by equating each of the tracing constants to zero. Present results are in excellent agreement with all available solutions in the literature for special cases such as thin plates and represent a significant improvement in understanding the nonlinear vibration behavior of elliptical plates.

Governing Equations

For a rectilinearly orthotropic elliptical plate of semimajor axis a and semiminor axis b and uniform thickness h the two coupled nonlinear equations that take into account the effects of transverse shear deformation and rotatory inertia are [7]

$$F_{,\zeta\zeta\zeta\zeta}+k^2r^4F_{,\eta\eta\eta\eta}+2m^2r^2F_{,\zeta\zeta\eta\eta}=E_yr^2(w^2_{,\zeta\eta}-w_{,\zeta\zeta}w_{,\eta\eta}) \quad (1)$$

$$\begin{aligned}a_1(\tilde{I}_{,\zeta\zeta\zeta\zeta}+r^4\tilde{I}_{,\eta\eta\eta\eta})+a_2r^2\tilde{I}_{,\zeta\zeta\eta\eta}+a_3a^4\tilde{I}_{,tttt}\\+a_4a^2(\tilde{I}_{,\zeta\zeta tt}+r^2\tilde{I}_{,\eta\eta tt})+a_5a^2(\tilde{I}_{,\zeta\zeta}+r^2\tilde{I}_{,\eta\eta})\\+a_6a^4\tilde{I}_{,tt}-a^4\tilde{I}+a_7a^6(w_{,\zeta\zeta tt}+r^2w_{,\eta\eta tt})\\+a_8a^4(w_{,\zeta\zeta\zeta\zeta}+r^4w_{,\eta\eta\eta\eta})+a_9a^4r^2w_{,\zeta\zeta\eta\eta}\\+a_{10}a^4r^2w_{,\zeta\zeta\eta\eta tt}+a_{11}a^4(w_{,\zeta\zeta\zeta\zeta tt}+r^4w_{,\eta\eta\eta\eta tt})\\+a_{12}a^6(w_{,\zeta\zeta tttt}+r^2w_{,\eta\eta tttt})+a_{13}a^2(w_{,\zeta\zeta\zeta\zeta\zeta\zeta}+r^6w_{,\eta\eta\eta\eta\eta\eta})\\+a_{14}a^2(r^2w_{,\zeta\zeta\zeta\zeta\eta\eta}+r^4w_{,\eta\eta\eta\eta\zeta\zeta})=0\end{aligned} \quad (2)$$

where

$$\tilde{I}=a^4[q(\zeta,\eta)-\rho hw_{,tt}]+r^2(F_{,\eta\eta}w_{,\zeta\zeta}+F_{,\zeta\zeta}w_{,\eta\eta}-2F_{,\zeta\eta}w_{,\zeta\eta})$$

$$\zeta=\frac{x}{a},\quad \eta=\frac{y}{b},\quad r=\frac{a}{b}$$

$$k^2=E_y/E_x,\quad q^2=\nu_{xy},\quad m^2=(k^2-q^4-2p^2q^2)/p^2$$

$$p^2=G_{xy}\nu'/E_x,\quad \nu'=1-\nu_{xy}\nu_{yx}$$

and a comma denotes the partial differentiation with respect to the corresponding coordinate. E_x, E_y, ν_{xy}, ν_{yx}, and G_{xy} are the orthotropic material constants of the plate and ρ is the mass density. The coefficients $a_1, \ldots a_{14}$ are completely defined in reference [7] and are functions of aspect ratio r, orthotropic material constants k^2, q^2, p^2, and tracing constants T_s and R_i. It is a matter of simple exercise to show that equations (1) and (2) will readily reduce to the well-known von Kármán equations when the effects of transverse shear rotatory inertia are neglected, i.e., $T_s=R_i=0$.

Equations (1) and (2) constitute a set of two equations applicable for the large-amplitude flexural vibrations of moderately thick plates wherein the effects of transverse shear and rotatory inertia have been included as mentioned before. These equations can be readily used for thin plates by setting T_s and R_i to zero. Additional special cases are the ones where transverse shear is included but not rotatory inertia, ie., $T_s=1$, $R_i=0$; rotatory inertia is included but not the transverse shear, i.e., $T_s=0$, $R_i=1$. Equations (1) and (2) can be modified to account for these special cases.

For the elliptical plate considered here, the clamped immovable boundary conditions are represented by means of the following equations

$$u^0=v^0=0;\quad w=w_{,\zeta}=w_{,\eta}=0 \quad \text{along} \quad 1-\zeta^2-\eta^2=0 \quad (3)$$

where u^0, v^0, and w are the displacement components of the midsurface of the plate along the coordinate directions. The preceding boundary conditions in u^0 and v^0 can be transformed in terms of the lateral displacement w and stress function F as

$$u^0=\int u^0_{,\zeta}d\zeta=\int\left(c_{11}r^2F_{,\eta\eta}-c_{12}F_{,\zeta\zeta}-\frac{1}{2}w^2_{,\zeta}\right)d\zeta=0 \quad (4)$$

$$v^0=\int v^0_{,\eta}d\eta=\int\left(\frac{c_{22}}{r^2}F_{,\zeta\zeta}-c_{12}F_{,\eta\eta}-\frac{1}{2}w^2_{,\eta}\right)d\eta=0 \quad (5)$$

along the boundary and where

$$c_{11}=k^2\nu'/E_x',\quad c_{12}=q^2\nu'/E_x',\quad c_{22}=\nu'/E_x'$$
$$E_x'=E_x(k^2-q^4)$$

Equations (1) and (2) will have to be solved in conjunction with boundary conditions (4) and (5).

Analytical Solution

Solutions to equations (1) and (2) are sought in terms of polynomial functions which would satisfy all the in-plane and out-of-plane boundary conditions. An expression for the lateral mode w is assumed in the following separable form consisting of unknown time functions $A(\tau)$ and $B(\tau)$.

$$w(\zeta,\eta,\tau)=h(\zeta^2+\eta^2-1)^2[A(\tau)+B(\tau)(\zeta^2+\eta^2-1)] \quad (6)$$

Clearly, this mode shape satisfies all the out-of-plane boundary conditions given in equation (3). In equation (6) τ is the nondimensional time defined as $\tau^2=t^2(E_x/\rho a^2)$. Equation (6) is substituted in equation (1) and an expression for stress function is taken in the following polynomial form.

$$\begin{aligned}F(\zeta,\eta,\tau)=b_1\zeta^{12}+b_2\zeta^{10}\eta^2+b_3\zeta^8\eta^4+b_4\zeta^6\eta^6\\+b_5\zeta^4\eta^8+b_6\zeta^2\eta^{10}+b_7\eta^{12}+b_8\zeta^{10}+b_9\zeta^8\eta^2\\+b_{10}\zeta^6\eta^4+b_{11}\zeta^4\eta^6+b_{12}\zeta^2\eta^8+b_{13}\eta^{10}\\+b_{14}\zeta^8+b_{15}\zeta^6\eta^2+b_{16}\zeta^4\eta^4+b_{17}\zeta^2\eta^6\\+b_{18}\eta^8+b_{19}\zeta^6+b_{20}\zeta^4\eta^2+b_{21}\zeta^2\eta^4\\+b_{22}\eta^6+b_{23}\zeta^4+b_{24}\zeta^2\eta^2+b_{25}\eta^4\\+b_{26}\zeta^2+b_{27}\eta^2\end{aligned} \quad (7)$$

The 27 coefficients b_1–b_{27} in equation (7) are uniquely determined as follows. By substituting equations (6) and (7) in equation (1) and comparing the coefficients of like terms on both sides, 15 simultaneous algebraic equations are generated. Boundary conditions given by equations (4) and (5) are now satisfied by substituting equations (6) and (7) and performing the integrations as indicated. This procedure results in an additional set of 12 equations in terms of b_i. Combining these two sets of simultaneous equations and solving them for the 27 unknown coefficients b_i, the stress function F in equation (7) is completely known. It must be noted that the semi-inverse procedure used here enables one to solve equation (1) exactly for the lateral mode given in equation (6). It is possible to obtain such exact solutions for any number of appropriate additional modes included in equation (6). The complexity of the solution procedure, however, increases enormously for each additional mode included. For the present two-mode case, no attempt has been made here to define the coefficients b_i explicitly since the algebra is tedious and these coefficients are very lengthy.

Having the stress function F, completely defined, it is now required to satisfy the equation of motion in the lateral direction of the vibrating plate, namely equation (2). The procedure involves multiplying equation (2) by the two spatial

Downloaded 02 May 2010 to 171.66.16.25. Redistribution subject to ASME license or copyright; see http://www.asme.org/terms/Terms_Use.cfm

functions $(\zeta^2+\eta^2-1)^2$ and $(\zeta^2+\eta^2-1)^3$ and integrating the resulting expressions over the area of the plate. Performing these integrations, a set of two coupled ordinary nonlinear time-differential equations are obtained in terms of the time

Table 1 Numerical values for elastic constants

Material	$\frac{E_x}{E_y}$	ν_{xy}	$\frac{G_{xy}}{E_x}$	$\frac{G_{yz}}{E_x}$
Glass-Epoxy	3	0.25	0.2	0.1
Boron-Epoxy	10	0.22	0.033	0.0165
Graphite-Epoxy	40	0.25	0.015	0.0075

Table 2 Nondimensional frequency parameter $\lambda^2=\omega a^2(\rho/D)^{1/2}$ for elliptical plates

(a/b)	Single-mode	Multiple-mode	References 15,16
0.5	7.012	6.937	6.937
1.0	10.328	10.217	10.217
1.5	17.393	17.206	17.206
2.0	28.048	27.746	27.746

Table 3 Comparison of load-deflection valves for elliptical plates with $r=2$

w_o^*	Values of q_o^*		
	Single-Mode	Multiple-Mode	Reference 17
0	0	0	0
0.5	24.14	24.52	24.16
1.0	63.43	67.05	65.60
1.5	133.04	148.91	153.60
2.0	248.12	298.47	285.40

Table 4 Comparison of period ratios T/T_0 for glass-epoxy elliptical plates with $r=1.5$ ($T_s=R_i=0$)

w_o^*	Single-Mode	Multiple-Mode	Reference 5
0	1.0000	1.0000	1.0000
0.5	0.9601	0.9583	0.9589
1.0	0.8649	0.7878	0.8642
1.5	0.7555	0.6093	0.7549
2.0	0.6554	0.5362	0.6562

Table 5 Coefficients of modal equations (8) and (9) for boron-epoxy elliptical plate with $r=2$ ($T_s=R_i=1$)

i	A_i	B_i	A_i	B_i
	$\beta=10$		$\beta=30$	
1	0.049009	0.061646	0.000605	0.000761
2	-0.138734	-0.181347	-0.001713	-0.002239
3	0.135773	0.183904	0.001676	0.002270
4	-0.045995	-0.064458	-0.000568	-0.000796
5	1.101922	1.224363	0.122436	0.136040
6	-0.918265	-1.049455	-0.102029	-0.116606
7	2.982468	3.731926	0.276422	0.347454
8	-8.351297	-11.085650	-0.781359	-1.023445
9	8.123972	11.343490	0.764071	1.039129
10	-2.713010	-4.000415	-0.258359	-0.364513
11	60.621450	67.897590	55.220320	61.416190
12	-50.922770	-59.239590	-46.061750	-52.758170
13	39.402700	49.156690	28.032820	35.200790
14	-110.401200	-148.429400	-79.144620	-103.830600
15	107.272500	153.705500	77.360970	105.563100
16	-35.733100	-54.811900	-26.109260	-37.062220
17	743.175000	835.837400	5531.398000	6157.414000
18	-626.872500	-743.245800	-4618.023000	-5300.570000
19	56.951900	56.951900	56.951900	56.951900
20	-57.288200	-82.917290	-44.332670	-69.961540

Table 6 Values of period ratios T/T_0 for isotropic and orthotropic elliptical plates with $r=2$ (multiple-mode solution)

w_o^*	$\beta=20$			$T_s=R_i=0$		
	Isotropic	GE	GrE	Isotropic	GE	GrE
0	1.0296	1.0359	1.1040	1.0000	1.0000	1.0000
0.5	0.9810	0.9854	1.0252	0.9588	0.9581	0.9586
1.0	0.7825	0.7790	0.7479	0.7912	0.7887	0.7908
1.5	0.6162	0.6157	0.6211	0.6101	0.6071	0.6084
2.0	0.5405	0.5450	0.5545	0.5358	0.5331	0.5340

Downloaded 02 May 2010 to 171.66.16.25. Redistribution subject to ASME license or copyright; see http://www.asme.org/terms/Terms_Use.cfm

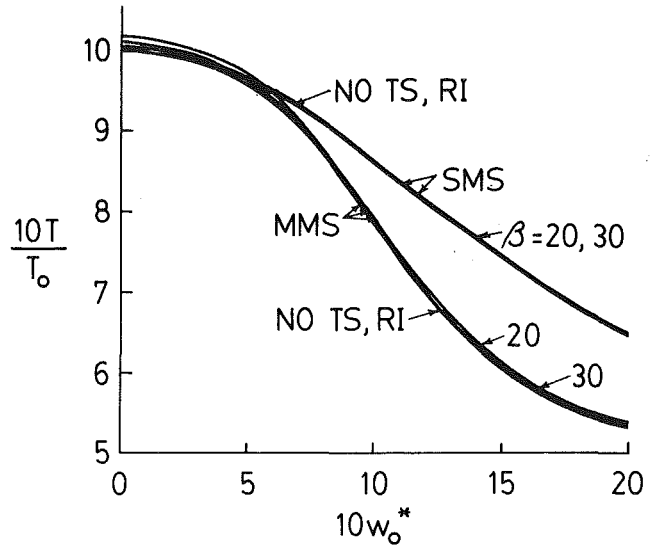

Fig. 1 Variation of period ratio with amplitude for isotropic plates with $r = 1.5$; MMS = multiple-mode solution SMS = single-mode solution

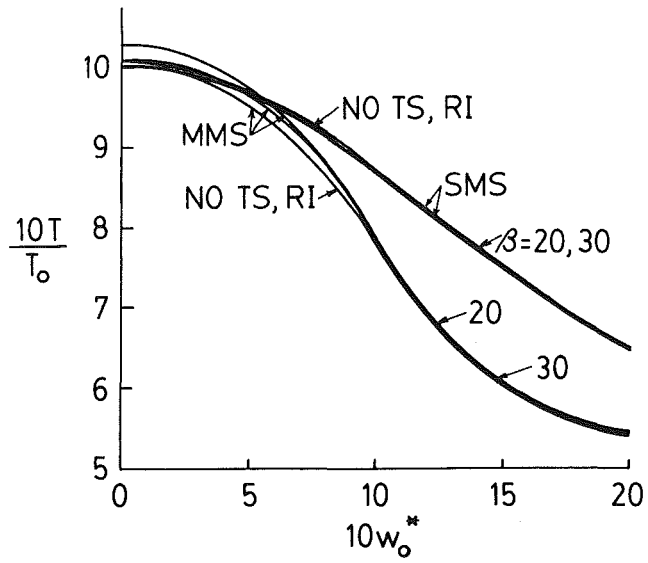

Fig. 2 Relation between period ratio and amplitude for glass-epoxy plates with $r = 1.5$; MMS = multiple-mode solution SMS = single-mode solution

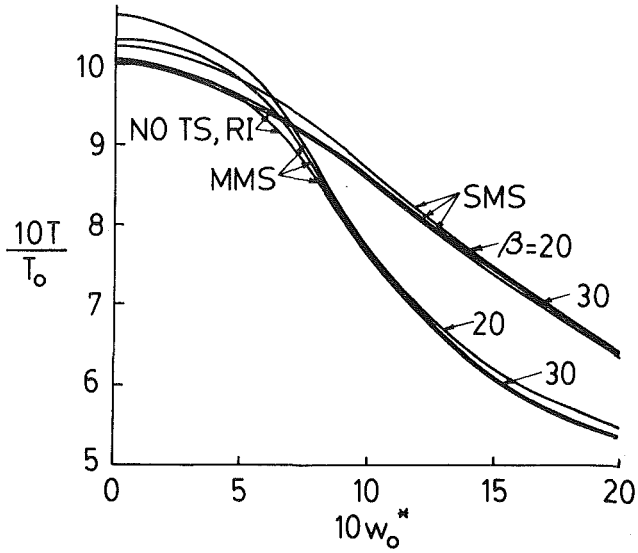

Fig. 3 Variation of period ratio with amplitude for boron-epoxy plates with $r = 1.5$; MMS = multiple-mode solution SMS = single-mode solution

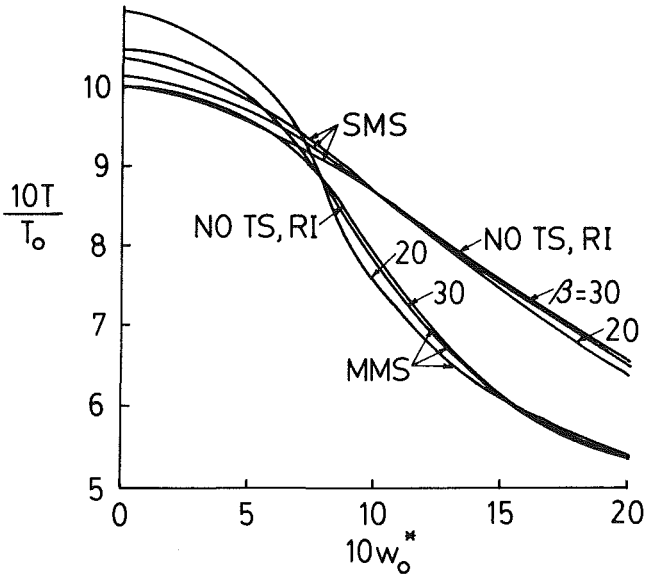

Fig. 4 Relation between period ratio and amplitude for graphite-epoxy plates with $r = 1.5$; MMS = multiple-mode solution SMS = single-mode solution

functions $A(\tau)$ and $B(\tau)$. These equations are

$$A_1(A^3)_{,\tau\tau\tau\tau} + A_2(A^2B)_{,\tau\tau\tau\tau} + A_3(AB^2)_{,\tau\tau\tau\tau} + A_4(B^3)_{,\tau\tau\tau\tau} + A_5(A)_{,\tau\tau\tau\tau\tau\tau} + A_6(B)_{,\tau\tau\tau\tau\tau\tau} + A_7(A^3)_{,\tau\tau} + A_8(A^2B)_{,\tau\tau} + A_9(AB^2)_{,\tau\tau} + A_{10}(B^3)_{,\tau\tau} + A_{11}(A)_{,\tau\tau\tau\tau} + A_{12}(B)_{,\tau\tau\tau\tau} + A_{13}A^3 + A_{14}A^2B + A_{15}AB^2 + A_{16}B^3 + A_{17}(A)_{,\tau\tau} + A_{18}(B)_{,\tau\tau} + A_{19}A + A_{20}B = q_0^* \quad (8)$$

$$B_1(A^3)_{,\tau\tau\tau\tau} + B_2(A^2B)_{,\tau\tau\tau\tau} + B_3(AB^2)_{,\tau\tau\tau\tau} + B_4(B^3)_{,\tau\tau\tau\tau} + B_5(A)_{,\tau\tau\tau\tau\tau\tau} + B_6(B)_{,\tau\tau\tau\tau\tau\tau} + B_7(A^3)_{,\tau\tau} + B_8(A^2B)_{,\tau\tau} + B_9(AB^2)_{,\tau\tau} + B_{10}(B^3)_{,\tau\tau} + B_{11}(A)_{,\tau\tau\tau\tau} + B_{12}(B)_{,\tau\tau\tau\tau} + B_{13}A^3 + B_{14}A^2B + B_{15}AB^2 + B_{16}B^3 + B_{17}(A)_{,\tau\tau} + B_{18}(B)_{,\tau\tau} + B_{19}A + B_{20}B = q_0^* \quad (9)$$

It must be noted that these two modal equations have been nondimensionalized with respect to τ. For reasons of saving space, the nonlinear coefficients A_i and B_i are not defined in this paper. However, some typical numerical values for these coefficients are tabulated later considering certain plate and material parameters as well as tracing constants. The nondimensional load q_0^* in equations (8) and (9) is given by $q_0^* = q_0\beta^4/E_x$ where β is the thickness parameters, a/h, and q_0 is the intensity of uniformly distributed load. Equations (8) and (9) are to be used for the analysis of moderately thick elliptical plates. At this stage it is also possible to specialize these two equations to three other possible combinations of the effects of transverse shear and rotatory inertia, i.e., $T_s = 1$, $R_i = 0$; $T_s = 0$, $R_i = 1$; and $T_s = R_i = 0$. Of the three possible combinations, the one that is interesting corresponds to the equations applicable to a thin elliptical plate when $T_s = R_i = 0$. Equating these tracing constants to zero in the nondimensional coefficients A_i and B_i in equations (8) and (9), a set of two simplified equations are obtained as follows.

$$A_{13}A^3 + A_{14}A^2B + A_{15}AB^2 + A_{16}B^3 + A_{17}(A)_{,\tau\tau} + A_{18}(B)_{,\tau\tau} + A_{19}A + A_{20}B = q_0^* \quad (10)$$

Downloaded 02 May 2010 to 171.66.16.25. Redistribution subject to ASME license or copyright; see http://www.asme.org/terms/Terms_Use.cfm

$$B_{13}A^3 + B_{14}A^2B + B_{15}AB^2 + B_{16}B^3 + B_{17}(A)_{,\tau\tau} + B_{18}(B)_{,\tau\tau} + B_{19}A + B_{20}B = q_0^* \quad (11)$$

Equations (10) and (11) are applicable to thin plates whereas such equations for moderately thick plates are given by equations (8) and (9). These two sets of equations can further be specialized for nonlinear static problems by treating A and B as time independent and therefore they constitute a set of nonlinear algebraic equations with nondimensional load q_0^* appearing in each set. Turning the attention to the solutions of modal equations (8)–(11) where A and B are time dependent, an IMSL subroutine, which is based on the Runge-Kutta-Verner integration technique, is employed to obtain numerical results. Integration is carried out with time step size $\Delta\tau = 0.001$ and initial conditions $A(0) = 0$, 0.5, 1.0, 1.5, 2.0; $A_{,\tau}(0) = 0; B(0) = 0$; and $B_{,\tau}(0) = 0$.

Numerical Results and Discussion

Numerical results are presented for moderately thick as well as thin orthotropic elliptical plates made of glass-epoxy (*GE*), boron-epoxy (*BE*) and graphite-epoxy (*GrE*) materials. Results for isotropic plates are also included. The elastic constants for all these materials are tabulated in Table 1. The ratios of G_{xz}/E_x are assumed to be the same as those of G_{xy}/E_x and the ratios of G_{yz}/E_x are taken to be one-half of the ratios of G_{xz}/E_x [14]. The ratios of the nonlinear period T of vibration, including the effects of transverse shear and rotatory inertia, to the corresponding linear period T_0 of the classical plate ($T_s = R_i = 0$) are computed for various plate aspect ratios, thickness parameters, and material constants at different nondimensional amplitudes of vibration. For moderately thick plates, the nonlinear periods are dependent on the thickness parameter β whereas they are independent of β for classical thin plates.

Fundamental linear frequencies have been computed using one-term and two-term mode shapes given in equation (6). The nondimensional frequency parameter λ^2 obtained on the basis of single and multiple modes are tabulated in Table 2 and comparisons are made with existing solutions. Good agreement is found between the two sets of values. It must be pointed out here that a two-term mode shape has been used in reference [15]. In the case of classical thin plates undergoing large deflections, load-deflection values are obtained by solving equations (10) and (11) after dropping the time-dependent terms. Nondimensional loads q_0^* are obtained for various values of nondimensional deflection w_0^* considering single and multiple terms in the expression for w in equation (6). w_0^* is defined as the ratio of the maximum deflection to the thickness of the plate. These results have been compared in Table 3 with those of Nash and Cooley [17] for isotropic elliptical plates with an aspect ratio of 2. In the case of or[thotropic material, the present results for glass-epoxy elliptical plates with an aspect ratio of 2. In the case of orthotropic material, the present results for glass-epoxy elliptical plate is in close agreement with references [5, 18] but been extended for orthotropic plates in [18]. Similar results are presented in Table 4 for nonlinear vibration of a thin, orthotropic elliptical plate and compared with those of reference [5]. All these results are in close agreement with the available results in the literature for thin plates. In the case of moderately thick plates no such solutions are available for comparison.

Equations (8) and (9) which are applicable for moderately thick plates ($T_s = R_i = 1$) are very complex and therefore cannot be solved without any further simplifications. The coefficients A_i and B_i in these equations are evaluated for certain geometric and plate parameters and are shown in Table 5. Many of these coefficients vanish for thin plates

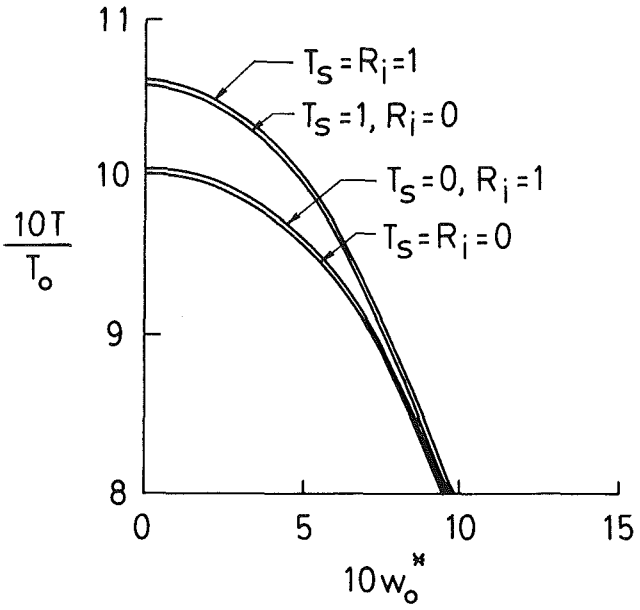

Fig. 5 Combined effects of transverse shear and rotatory inertia on boron-epoxy plate with $r = 1.5$ and $\beta = 20$ (multiple-mode solution)

($T_s = R_i = 0$) resulting in a simple set of time-differential equations as shown in equations (10) and (11). A close look at the values of the coefficients A_i and B_i in Table 5 indicates that it is reasonable to ignore the terms containing A_1 to A_{10} and B_1 to B_{10} in equations (8) and (9) without introducing any appreciable error in the numerical results. Results obtained by retaining these coefficients in the linearized version of equations (8) and (9) indicate that this is a reasonable assumption. With this simplification in mind, equations (8) and (9) are numerically integrated using the Runge-Kutta-Verner method to obtain T and T_0 for various values of nondimensional amplitude w_0^*. Period ratios T/T_0 are obtained for various values of the geometric plate parameters and material constants. These results are graphically presented in Figs. 1–4 considering single-mode (SMS) as well as multiple-mode (MMS) approaches. Similar results are tabulated in Table 6 using only multiple-mode approach. In all the cases investigated here, the period-amplitude behavior is of hardening type for both moderately thick and thin plates. The period ratios do not change significantly with the thickness parameters. However, there is a significant difference in numerical values between single-mode and multiple-mode solutions. Period ratios are higher at any given amplitude when the effects of transverse shear and rotatory inertia are accounted for. These effects, however, are found to be predominant at small amplitudes of vibration. The use of tracing constants makes it possible to investigate the individual effects of the transverse shear deformation and rotatory inertia. For various combinations of T_s and R_i, the period-amplitude curves are given in Fig. 5. It is clear that the effect of transverse shear is much more important than the effect of rotatory inertia, while both of them contribute to an increase in the numerical value of the period ratio at any given amplitude.

Summary and Conclusions

The problem of large-amplitude vibration of an orthotropic elliptical plate is solved here with the aid of a generalized set of von Kármán-type nonlinear dynamic equations. Effects of transverse shear and rotatory inertia have been included and a multiple-mode approach is used to investigate the nonlinear static as well as dynamic behavior of moderately thick and thin plates. Exact solution to one of the nonlinear governing

Downloaded 02 May 2010 to 171.66.16.25. Redistribution subject to ASME license or copyright; see http://www.asme.org/terms/Terms_Use.cfm

equations is reported and it is possible to extend this approach for several additional lateral modes. For both thick and thin plates the effect of coupling between modes is found to be significant.

References

1 Sathyamoorthy, M., "Nonlinear Vibrations of Plates—A Review," *The Shock and Vibration Digest*, Vol. 15, 1983, pp. 3-16.

2 Chia, C. Y., *Nonlinear Analysis of Plates*, McGraw-Hill, New York, 1980.

3 Herrmann, G., "Influence of Large Amplitudes on Flexural Motions of Elastic Plates," NACA TN-3578, 1955.

4 Sathyamoorthy, M., "Nonlinear Vibration of Elliptical Plates," *Journal of Sound and Vibration*, Vol. 70, 1980, pp. 458-460.

5 Sathyamoorthy, M., and Chia, C. Y., "Large Amplitude Vibration of Orthotropic Elliptical Plates," *Acta Mechanica*, Vol. 37, 1980, pp. 247-258.

6 Banerjee, B., "Large Amplitude Free Vibrations of Elliptic Plates," *Journal of the Physical Society of Japan*, Vol. 23, 1967, pp. 1169-1172.

7 Sathyamoorthy, M., and Chia, C. Y., "Effect of Transverse Shear and Rotatory Inertia on Large Amplitude Vibration of Anisotropic Skew Plates, I—Theory," ASME JOURNAL OF APPLIED MECHANICS, Vol. 47, 1980, pp. 128-132.

8 Sathyamoorthy, M., "Effects of Large Amplitude, Transverse Shear and Rotatory Inertia on Vibration of Orthotropic Elliptical Plates," *International Journal of Nonlinear Mechanics*, Vol. 16, 1981, pp. 327-335.

9 Reddy, J. N., and Huang, C. L., "Large Amplitude Free Vibrations of Annular Plates of Varying Thickness," *Journal of Sound and Vibration*, Vol. 79, 1981, pp. 387-396.

10 Reddy, J. N., and Chao, W. C., "Large Deflection and Large Amplitude Free Vibrations of Laminated Composite Material Plates," *Computers and Structures*, Vol. 13, 1981, pp. 341-347.

11 Reddy, J. N., and Chao, W. C., "Nonlinear Oscillations of Laminated Anisotropic Rectangular Plates," ASME JOURNAL OF APPLIED MECHANICS, Vol. 49, 1982, pp. 396-402.

12 Prabhakara, M. K., and Chia, C. Y., "Nonlinear Flexural Vibration of Orthotropic Rectangular Plates," *Journal of Sound and Vibration*, Vol. 52, 1977, pp. 511-518.

13 Chia, C. Y., and Prabhakara, M. K., "A General Mode Approach to Nonlinear Flexural Vibrations of Laminated Rectangular Plates," ASME JOURNAL OF APPLIED MECHANICS, Vol. 45, 1978, pp. 623-628.

14 Wu, C. I., and Vinson, J. R., "On the Nonlinear Oscillations of Plates Composed of Composite Materials," *Journal of Composite Material*, Vol. 3, 1969, pp. 548-561.

15 McNitt, R. P., "Free Vibration of a Clamped Elliptical Plate," *Journal of Aerospace Sciences*, Vol. 29, 1962, pp. 1124-1125.

16 Leissa, A. W., "Vibration of Plates," NASA SP-160, 1969.

17 Nash, W. A., and Cooley, I. D., "Large Deflections of a Clamped Elliptical Plate Subjected to Uniform Pressure," ASME JOURNAL OF APPLIED MECHANICS, Vol. 26, 1959, pp. 291-293.

18 Prabhakara, M. K., and Chia, C. Y., "Bending of Elliptical Orthotropic Plates With Large Deflection," Acta Mechanica, Vol. 21, 1975, pp. 29-40.

Downloaded 02 May 2010 to 171.66.16.25. Redistribution subject to ASME license or copyright; see http://www.asme.org/terms/Terms_Use.cfm

A. K. Mallik
Professor,
Department of Mechanical Engineering.

S. B. Kulkarni
Graduate Student.

K. S. Ram
Professor and Head,
Nuclear Engineering Program.

Indian Institute of Technology,
Kanpur, India 208016

Parametric Instability of a Periodically Supported Pipe Without and With Vibration Absorbers

Parametric instability of a periodically supported pipe without and with dynamic absorbers is investigated. A method based on the notion of propagation constant is used. This method requires no prior knowledge of the mode shapes and renders the amount of computation independent of the number of spans. Numerical results are presented for single and two-span pipes. Effective control of the instability regions by means of dynamic absorbers is also demonstrated.

1 Introduction

Pipelines conveying fluid at high pressure and velocity are encountered in various fields of engineering. It is well known that if the velocity of fluid flowing through a pipe is not constant but has harmonic fluctuations over and above a constant mean value, then the pipe experiences parametric instabilities in its transverse motion. The instability regions of a single-span pipe, with different end conditions, have been studied in detail [1, 2]. In these works, a Ritz-Galerkin procedure was used for the determination of the instability regions. This method requires prior knowledge about the mode shapes and when extended to the case of a multispan pipe, encounters numerical difficulties as well [3]. In fact, the computational efforts increases progressively with the number of spans. For the case of a multispan pipe with identical spans, hereafter referred to as a periodically supported pipe, a wave approach was proposed in reference [3]. This approach renders the computational effort independent of the number of spans. Use of conventional vibrations absorbers to control the parametric instabilities was demonstrated both for a single-span pipe [4] and a periodically supported pipe [5].

In references [3-5], the equation of motion given by Cehn [1] was used. The error in this equation was pointed out by Paidoussis and Isid [2]. Furthermore, for a periodically supported pipe the wave approach was used in an ad hoc manner by decoupling two different types of waves. One of these gave the lower boundary while the other yielded the upper boundary of the instability regions. As a result, the instability boundaries were not determined accurately and especially, the effect of the fluid-pipe mass ratio parameter was not accounted for correctly [6].

The major objective of the present paper is to investigate the parametric instability regions of a periodically supported pipe without and with vibration absorbers after incorporating

(*i*) the correct equation of motion which calls for a series solution, and

(*ii*) the correct application of the coupled waves to result in both the upper and the lower boundaries

simultaneously. The analysis and the numerical results are presented for the principal primary instabilities of single-span and two-span pipes. The discrepancy between these results and those presented in references [3-5] depend on the values of the different parameters involved. The method can readily be extended for the determination of other primary and secondary instability regions as well.

2 Theoretical Analysis

2.1 Equation of Motion. Consider an N-span, horizontal pipe on identical, line supports, a distance l appart (Fig. 1). In the nondimensional form, the equation for the transverse motion of the pipe in any span is [2]

$$\frac{\partial^4 \bar{w}}{\partial \xi^4} + u^2 \frac{\partial^2 \bar{w}}{\partial \xi^2} + \left[\gamma(1-\xi)\frac{\partial u}{\partial \tau}\right]\frac{\partial^2 \bar{w}}{\partial \xi^2} + 2\gamma u \frac{\partial^2 \bar{w}}{\partial \xi \partial \tau} + \frac{\partial^2 \bar{w}}{\partial \tau^2} = 0, \quad 0 \le \xi \le 1 \tag{1}$$

The symbols used in (1) are explained in the following:

$\bar{w} = w/l$ where w is the transverse displacement of the pipe; $\xi = x/l$ with x measured from the left support in each span along the length of the pipe; u is the nondimensional fluid velocity $= (m_f/EI)^{1/2} Vl$ where m_f is the mass of the fluid per unit length of the pipe, EI is the flexural stiffness of the pipe, and V is the fluid velocity; γ is the fluid-pipemass ratio parameter $= [m_f/(m_f + m_p)]^{1/2}$ where m_p is the mass of the

Contributed by the Applied Mechanics Division for publication in the JOURNAL OF APPLIED MECHANICS.

Discussion on this paper should be addressed to the Editorial Department, ASME, United Engineering Center, 345 East 47th Street, New York, N.Y. 10017, and will be accepted until two months after final publication of the paper itself in the JOURNAL OF APPLIED MECHANICS. Manuscript received by ASME Applied Mechanics Division, March, 1982; final revision September, 1983.

Copyright © 1984 by ASME
Downloaded 02 May 2010 to 171.66.16.25. Redistribution subject to ASME license or copyright; see http://www.asme.org/terms/Terms_Use.cfm

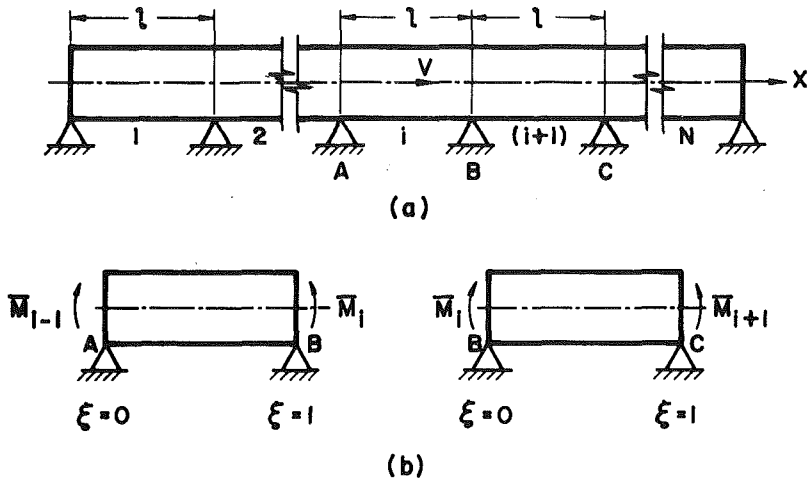

Fig. 1 *(a)* A periodically supported *N*-span pipe, and *(b)* two adjacent spans of the pipe

pipe per unit length; $\tau = t\,[EI/(m_f + m_p)]^{1/2}/l^2$ is the nondimensional time with t denoting the time.

In deriving (1), the damping in the pipe material, the external damping to the pipe motion, the axial tension in the pipe, and any effect of the pressurization of the flowing fluid are neglected.

Let

$$u = u_0(1 + \delta \cos \Omega\tau) \tag{2}$$

where the nondimensional frequency $\Omega = \omega l^2\,[(m_f + m_p)/EI]^{1/2}$ with ω as the radian frequency of the harmonic fluctuation of the fluid velocity which has a mean value $u_0 \cdot \delta$ is called the excitation parameter.

Substituting (2) in (1), one gets

$$\frac{\partial^4 \bar{w}}{\partial \xi^4} + [u_0^2(1 + \delta \cos \Omega\tau)^2 - \gamma u_0 \delta\Omega(1-\xi)\sin\Omega\tau]\frac{\partial^2 \bar{w}}{\partial \xi^2}$$

$$+ 2\gamma u_0(1 + \delta \cos \Omega\tau)\frac{\partial^2 \bar{w}}{\partial \xi \partial \tau} + \frac{\partial^2 \bar{w}}{\partial \tau^2} = 0 \tag{3}$$

Our objective is to determine the regions of parametric instabilities of this equation in the $\Omega - \delta$ space.

2.2 Determination of Regions of Parametric Instabilities. The regions of primary instabilities of equations of type (3) are bounded by periodic solutions of period $2T$; where $T = 2\pi/\Omega$. At the boundaries of the regions of principal primary instabilities $\bar{w}$ can quite accurately be expressed as [7]

$$\bar{w}(\xi,\tau) = X(\xi)\,\sin\frac{\Omega\tau}{2} + Y(\xi)\,\cos\frac{\Omega\tau}{2} \tag{4}$$

Substituting (4) into (3) and equation coefficients of $\sin \Omega\tau/2$ and $\cos \Omega\tau/2$ to zero, one gets

$$X'''' + u_0^2\left(1 - \delta + \frac{\delta^2}{2}\right)X'' - \frac{\Omega^2}{4}X - \frac{\gamma u_0 \delta\Omega}{2}\left[(1-\xi)Y'' - \left(1 - \frac{2}{\delta}\right)Y'\right] = 0 \tag{5}$$

and

$$Y'''' + u_0^2\left(1 + \delta + \frac{\delta^2}{2}\right)Y'' - \frac{\Omega^2}{4}y - \frac{\gamma u_0 \delta\Omega}{2}\left[(1-\xi)X'' - \left(1 + \frac{2}{\delta}\right)X'\right] = 0 \tag{6}$$

where the prime denotes differentation with respect to ξ. For a given value δ, the values of Ω, from which (5) and (6) are satisfied in every span along with all the boundary (or continuity) conditions imposed at the supports, determine the bounding frequencies of the principal primary instability.

2.3 Wave Approach for Determination of Bounding Frequencies. A notation of propagation constant, similar to that used for a periodically supported beam [8], is developed in the following manner. Consider any two consecutive intermediate spans, say the ith and the $(i+1)$th as shown in Fig. 1(*b*). Let $\bar{M}_{i-1}$ and $\bar{M}_i$ be, respectively, the nondimensional bending moments at the end A and B of the ith span. The nondimensional bending moment is defined as $Ml/(EI)$ where M is the actual bending moment. With the transverse deflection of the pipe given by (4), these moments can also be written in the form

$$\bar{M}_{i-1} = \bar{M}_{i-1}^X \sin\frac{\Omega\tau}{2} + \bar{M}_{i-1}^Y \cos\frac{\Omega\tau}{2} \tag{7}$$

Similarly, the slope of the pipe at the support B can be expressed as

$$\theta_B = \theta_B^X \sin\frac{\Omega\tau}{2} + \theta_B^Y \cos\frac{\Omega\tau}{2} \tag{8}$$

Using receptances, the slope components can be expressed in terms of the moment components as follows:

$$\theta_B^X = \beta_{rr}^{XX}\bar{M}_i^X + \beta_{rr}^{XY}\bar{M}_i^Y + \beta_{r1}^{XY}\bar{M}_{i-1}^X + \beta_{r1}^{XY}\bar{M}_{i-1}^Y \tag{9}$$

and

$$\theta_B^Y = \beta_{rr}^{YX}\bar{M}_i^X + \beta_{rr}^{YY}\bar{M}_i^Y + \beta_{r1}^{YX}\bar{M}_{i-1}^X + \beta_{r1}^{YY}\bar{M}_{i-1}^Y \tag{10}$$

where the receptance β_{r1}^{XY} represents the amplitude of the sinusoidally (X) varing slope at the right-hand end (r) due to a unit consinussoidal (Y) moment at the left-hand end (1) of the same span. The frequency of both the slopes and the moments is $\Omega/2$. Thus, for every receptance the first superscript and the subscript refer, respectively, to the nature and the location of the slope and likewise the second ones refer to the unit applied moment. The method of determining receptances from (5) and (6) is elaborated in Appendix A.

Since these receptance functions are the same for each identical span, considering the $(i+1)$th span one can write

$$\theta_B^X = \beta_{11}^{XX}\bar{M}_i^X + \beta_{11}^{XY}\bar{M}_i^Y + \beta_{1r}^{XX}\bar{M}_{i+1}^X + \beta_{1r}^{XY}\bar{M}_{i+1}^Y \tag{11}$$

and

$$\theta_B^Y = \beta_{11}^{YX}\bar{M}_i^X + \beta_{11}^{YY}\bar{M}_i^Y + \beta_{1r}^{XY}\bar{M}_{i+1}^X + \beta_{1r}^{YY}\bar{M}_{i+1}^Y \tag{12}$$

Equating (9) with (11) and (10) with (12), the following coupled difference equations (similar to three moment equation) are obtained:

Downloaded 02 May 2010 to 171.66.16.25. Redistribution subject to ASME license or copyright; see http://www.asme.org/terms/Terms_Use.cfm

$$\beta_{r1}^{XX}\bar{M}_{i-1}^{X}+(\beta_{rr}^{XX}-\beta_{11}^{XX})\bar{M}_{i}^{X}-\beta_{1r}^{XX}\bar{M}_{i+1}^{X}$$
$$=\beta_{1r}^{XY}\bar{M}_{i+1}^{X}+(\beta_{11}^{XY}-\beta_{rr}^{XY})\bar{M}_{i}^{Y}-\beta_{r1}^{XY}\bar{M}_{i-1}^{X} \quad (13a)$$

and

$$\beta_{r1}^{YX}\bar{M}_{i-1}^{X}+(\beta_{rr}^{YX}-\beta_{11}^{YX})\bar{M}_{i}^{X}-\beta_{1r}^{YX}\bar{M}_{i+1}^{X}$$
$$=\beta_{1r}^{YY}\bar{M}_{i+1}^{Y}+(\beta_{11}^{YY}-\beta_{rr}^{YY})\bar{M}_{i}^{Y}-\beta_{r1}^{YY}\bar{M}_{i-1}^{Y} \quad (13b)$$
$$\text{for } i=1,2,\ldots,(N-1)$$

Solution to (13a) and (13b) is sought in the form

$$\frac{\bar{M}_{i+1}^{X}}{\bar{M}_{i}^{X}}=\frac{\bar{M}_{i}^{X}}{\bar{M}_{i-1}^{X}}=\frac{\bar{M}_{i+1}^{Y}}{\bar{M}_{i}^{Y}}=\frac{\bar{M}_{i}^{Y}}{\bar{M}_{i-1}^{Y}}=e^{\mu}$$
$$\text{for} \quad i=1,2,\ldots(N-1) \quad (14)$$

where μ is termed as the propagation constant.

Substitution of (14) into (13a) and (13b) leads to

$$[\beta_{1r}^{XX}e^{2\mu}+(\beta_{11}^{XX}-\beta_{rr}^{XX})e^{\mu}-\beta_{r1}^{XX}]\bar{M}_{i}^{X}$$
$$+[\beta_{1r}^{XY}e^{2\mu}+(\beta_{11}^{XY}-\beta_{rr}^{XY})e^{\mu}-\beta_{r1}^{XY}]\bar{M}_{i}^{Y}=0 \quad (15a)$$

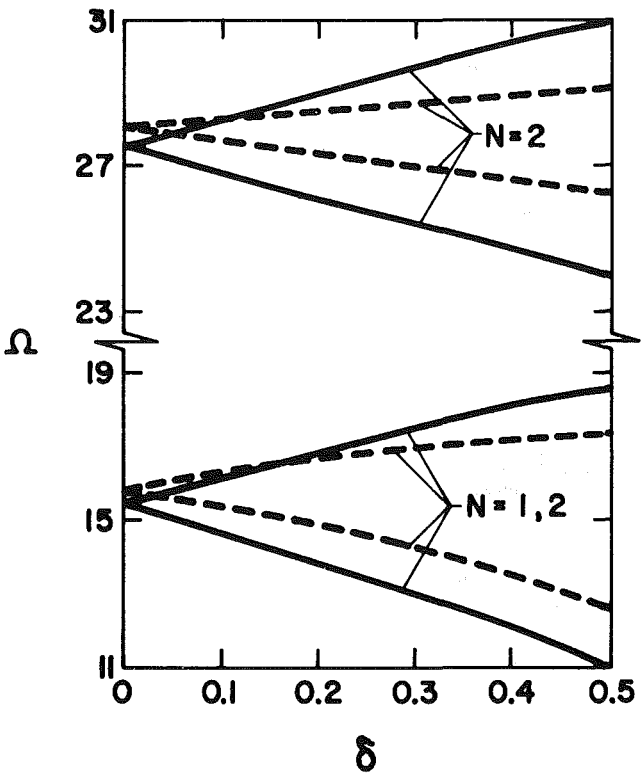

Fig. 2 Regions of principal primary instability of single and two-span pipe for $u_0 = 0.6\pi$, ____ $\gamma = 0.8$, - - - - $\gamma = 0$

and

$$[\beta_{1r}^{YX}e^{2\mu}+(\beta_{11}^{YX}-\beta_{rr}^{YX})e^{\mu}-\beta_{r1}^{YX}]\bar{M}_{i}^{X}$$
$$+[\beta_{1r}^{YY}e^{2\mu}+(\beta_{11}^{YY}-\beta_{rr}^{YY})e^{\mu}-\beta_{r1}^{YY}]\bar{M}_{i}^{Y}=0 \quad (15b)$$

So, for nontrivial solutions of $\bar{M}_i^X$ and $\bar{M}_i^Y$ one obtains

$$[\beta_{1r}^{XX}e^{2\mu}+(\beta_{11}^{XX}-\beta_{rr}^{XX})e^{\mu}-\beta_{r1}^{XX}][\beta_{1r}^{YY}e^{2\mu}$$
$$+(\beta_{11}^{YY}-\beta_{rr}^{YY})e^{\mu}-\beta_{r1}^{YY}]-$$
$$-[\beta_{1r}^{XY}e^{2\mu}+(\beta_{11}^{XY}-\beta_{rr}^{XY})e^{\mu}-\beta_{r1}^{XY}\beta_{1r}^{YX}e^{2\mu}$$
$$+(\beta_{11}^{YX}-\beta_{rr}^{YX})e^{\mu}-\beta_{r1}^{YX}]=0 \quad (16)$$

At any frequency Ω four values of the propagation constant (say μ_j with $j=1,2,3,4$) can be evaluated from (16).

Now (15a) is used to define

$$R_j=\left(\frac{\bar{M}_i^Y}{\bar{M}_i^X}\right)_j=-\frac{\beta_{1r}^{XX}e^{2\mu_j}+(\beta_{11}^{XX}-\beta_{rr}^{XX})e^{\mu_j}-\beta_{r1}^{XX}}{\beta_{1r}^{XY}e^{2\mu_j}+(\beta_{11}^{XY}-\beta_{rr}^{XY})e^{\mu_j}-\beta_{r1}^{XY}}$$
$$\text{for } j=1,2,3,4 \quad (17)$$

At this stage the only boundary conditions that still remain to be satisfied are zero moments at the end supports which can be written as follows:

$$\sum_{j=1}^{4}(\bar{M}_0^X)_j=0$$
$$\sum_{j=1}^{4}(\bar{M}_0^Y)_j=\sum_{j=1}^{4}R_j(\bar{M}_0^X)_j=0 \quad \text{(using (17))}$$
$$\sum_{j=1}^{4}(\bar{M}_N^X)_j=\sum_{j=1}^{4}e^{N\mu_j}(\bar{M}_0^X)_j=0 \quad \text{(using (14))}$$
$$\sum_{j=1}^{4}(\bar{M}_N^Y)_j=\sum_{j=1}^{4}R_j\,e^{N\mu_j}(\bar{M}_0^X)=0 \quad (18)$$

Again for nontrivial solution of (18) the following condition must be satisfied

$$F(\Omega)=\begin{vmatrix}1 & 1 & 1 & 1\\ R_1 & R_2 & R_3 & R_4\\ e^{N\mu_1} & e^{N\mu_2} & e^{N\mu_3} & e^{N\mu_4}\\ R_1e^{N\mu_1} & R_2e^{N\mu_2} & R_3e^{N\mu_3} & R_4e^{N\mu_4}\end{vmatrix}=0 \quad (19)$$

Hence finally, the zeroes of $F(\Omega)$ determine the boundaries of the principal primary instabilities.

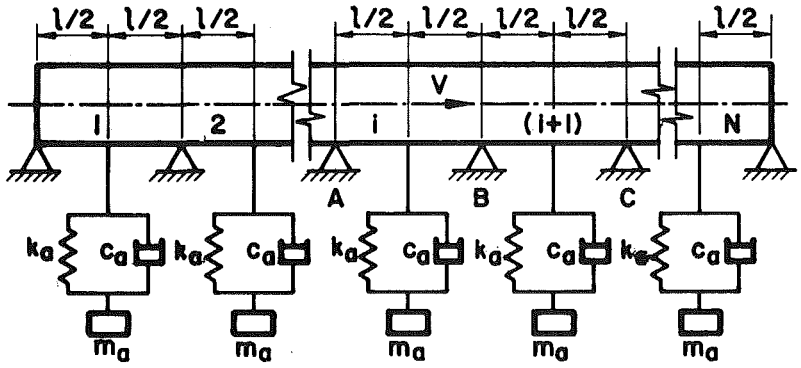

Fig. 3 A periodically supported N-span pipe with absorbers

Downloaded 02 May 2010 to 171.66.16.25. Redistribution subject to ASME license or copyright; see http://www.asme.org/terms/Terms_Use.cfm

3 Numerical Results and Discussions

The determinant $F(\Omega)$ is found to be either entirely real or entirely imaginary. The zeros of $F(\Omega)$ are determined by a change in the sign of $F(\Omega)$ whether real or imaginary. Figure 2 shows some regions of principal primary instability for a single-span and a two-span pipe. The results for a single-span pipe are in perfect agreement with those reported in reference [2]. Results for $\gamma = 0$ are also included in the same figure. It should be noted that, with $\gamma = 0$ equations (5) and (6) are decoupled and two separate pairs of propagation constants (say $\pm \mu_X$ and $\pm \mu_Y$) are determined, on each from (5) and (6), respectively. In this special case, the computational effort is much less, since no cross-receptance with different superscripts are to be evaluated. Furthermore, in such cases it can be shown [6] that, one of the bounding frequencies of the instability zones are given by those at which

$$Re(\mu_X) = 0$$

and

$$|Im(\mu_X)| = \frac{j\pi}{N}; \quad j = 0,1,2, \ldots N \tag{20a}$$

while the corresponding other bounding frequencies are obtained from

$$Re(\mu_Y) = 0$$

and

$$|Im(\mu_Y)| = \frac{j\pi}{N}; \quad j = 0,1,2, \ldots N \tag{20b}$$

As noted in reference [3], in each set given (20*a*) and (20*b*), the highest frequencies are to be discarded. The difference in the results with and without γ were not correctly reported in reference [3].

The proposed method can readily be extended for the determination of secondary and other primary regions of instability by replacing (4) appropriately. This is achieved by including higher harmonics of periods T and $2T$ in equation (4). In every case the computational effort remains independent of the number of spans and all the instability regions corresponding to a particular harmonic are obtained simultaneously.

4 Control of Instability Boundaries by Dynamic Vibration Absorbers

Let us now consider an N-span periodically supported pipe with identical vibration absorbers attached to the midpoint of every span as shown in Fig. 3. The method outlined in Section 2 can readily be applied by changing only the receptances. Equations (5) and (6) are now valid in every half of each span. The continuity of deflection, slope, and bending moment and the jump in the shear force values across the absorber are to be used while evaluating the receptances. This is given in Appendix *B*. Results given in Section 3 can be obtained from the present analysis after putting $\Gamma_a = 0$.

Figure 4 indicates how drastically the presence of the absorbers affects the instability regions of a two-span pipe. Corresponding to every instability region without the absorbers, two new but relatively smaller domains of instability are resulted when the absorbers are attached to the pipe. Parametric investigations [6] suggest that all the absorber parameters, viz, Γ_a, ζ_a, and σ_a affect the instability boundaries significantly. The presence of damping (ζ_a) in the absorbers shifts the onset of instability to a critical excitation parameter. Almost the entire domain of instability (without the absorbers) can be rendered stable by a careful choice of the absorber parameters. In fact, optimum absorber parameters including the location should be chosen so as to satisfy a desired objective, like (*i*) minimizing the domain of unstable region in a specified Ω-δ space or, (*ii*) maximizing the critial value of the excitation parameter for the onset of instability etc.

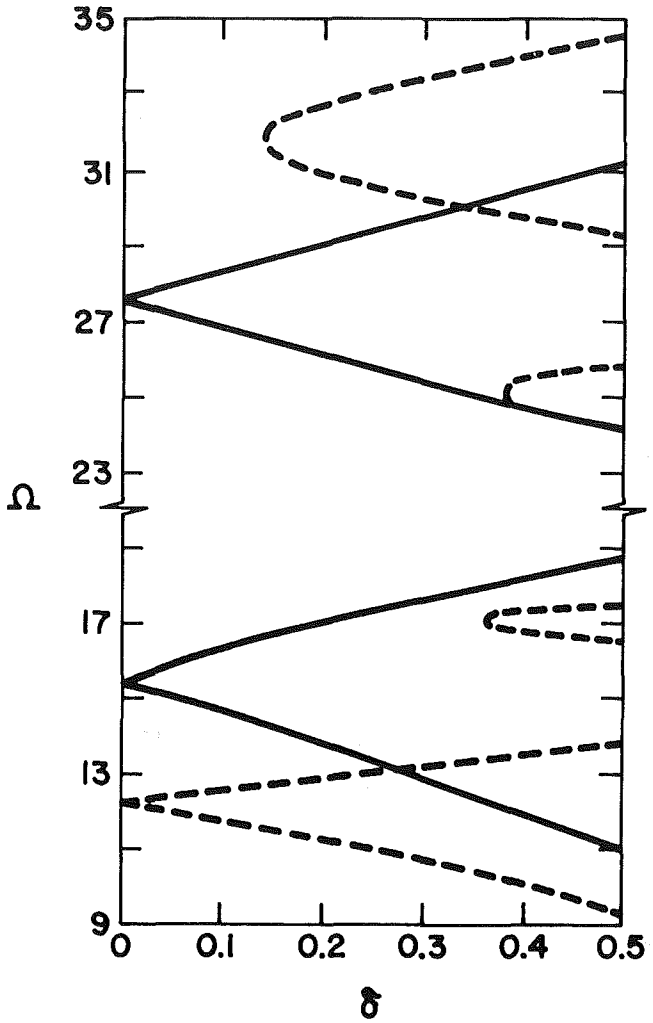

Fig. 4 Regions of principal primary instability of a two-span pipe without and with absorers. $u_0 = 0.6\pi$, $\gamma = 0.8$ ____ without absorbers. - - - - with absorbers. $\Gamma_a = 0.2$, $\sigma_a = 1.0$, $\zeta_a = 0.01$.

5 Conclusions

The notion of propagation constant can be used profitably for studying the parametric instability of a periodically supported pipe with and without the absorbers. The amount of computational effort remains independent of the number of spans in the pipe. All the unstable regions associated with a particular harmonic are obtained simultaneously. The method can readily be extended for the determination of unstable regions associated with higher harmonics. The improved analysis with the correct governing equation predicts the effect of the fluid-pipe mass ratio parameter (γ) correctly. Dynamic vibration absorbers can be used for effective control of the parametric instabilities of a pipe conveying fluid.

References

1 Chen, S. S., "Dynamic Stability of a Tube Conveying Fluid," *Journal of the Engineering Mechanics Division*, Proceedings of the American Society of Civil Engineers, Vol. 97, 1971, pp. 1469-1485.

2 Paidoussis, M. P., and Issid, N. T., "Dynamic Stability of Pipes Conveying Fluid," *Journal of Sound and Vibration*, Vol. 33, 1974, pp. 267-294.

3 Singh, K., and Mallik, A. K., "Parametric Instabilities of a Periodically Supported Pipe Conveying Fluid," *Journal of Sound and Vibration*, Vol. 62, 1979, pp. 379-397.

Downloaded 02 May 2010 to 171.66.16.25. Redistribution subject to ASME license or copyright; see http://www.asme.org/terms/Terms_Use.cfm

4 Singh, K., and Mallik, A. K., "Use of Dynamic Absorbers to Control Parametric Instabilities of a Pipe," ASME JOURNAL OF APPLIED MECHANICS, Vol. 45, 1978, pp. 949-951.

5 Mallik, A. K., and Narayanan, S., "Control of Parametric Instabilities of a Periodically Supported Pipe With Dynamic Absorber," *Proceedings of the International Conference on Recent Advances in Structrual Dynamics*, University of Southhampton, U.K., 1980, pp. 661-676.

6 Kulkarni, S., "Parametric Instability of a Periodically Supported Pipe Conveying Fluid," M. Tech. Thesis, Indian Institute of Technology, Kanpur, Sept., 1981.

7 Bolotin, V. V., *The Dynamic Stability of Elastic System*, Holden Day Inc., San Francisco, 1964.

8 Mead, D. J., "Free Wave Propagation in Periodically Supported Infinite Beams," *Journal of Sound and Vibration*, Vol. 11, 1970, pp. 181-197.

APPENDIX A

Determination of Receptances Without Absorber

Considering the span AB shown in Fig 1(b), let the solutions to (5) and (6) be given by

$$X(\xi)=\sum_{m=0}^{K} g_m(1-\xi)^m \tag{21}$$

and

$$Y(\xi)=\sum_{m=0}^{K} h_m(1-\xi)^m \tag{22}$$

Substituting these into (5) and (6) and equation like powers of $(1-\xi)$, one gets the following recursive relations:

$$\frac{(m+4)!}{m!}g_{m+4}\frac{(m+2)!}{m!}(a_2-a_3)g_{m+2}-a_1g_m - (m+1)[b_1(m+1)-b_2]h_{m+1}=0 \tag{23}$$

and

$$\frac{(m+4)!}{m!}h_{m+4}\frac{(m+2)!}{m!}(a_2+a_3)h_{m+2}-a_1h_m - (m+1)[b_1(m+1)-b_2]g_{m+1}=0 \tag{24}$$

where $m = 0, 1, 2, \ldots . (K-4)$,

with,

$$a_1=\frac{\Omega^2}{4},\ b_1=\frac{\gamma u_0\delta\Omega}{2},\ a_2=u_0^2\left(1+\frac{\delta^2}{2}\right),$$
$$b_2=\gamma u_0\delta \quad \text{and} \quad a_3=u_0^2\delta.$$

Now, if a nondimensional, unit X-wise moment is applied at the end A then eight boundary conditions are

$$\begin{aligned} &X(0)=Y(0)=X(1)=Y(1)=0\\ &X''(1)=Y''(1)=0\\ &Y''(0)=0 \quad \text{and} \quad X''(0)=-1 \end{aligned} \tag{25}$$

The unknown coefficients (g_0 to g_K) and (h_0 to h_K) can be solved from (23)-(25). Thereafter, the following four receptances are evaluated as

$$\beta_{11}^{XX}=X'(0)=-\sum_{m=1}^{K} mg_m$$

$$\beta_{11}^{YX}=Y'(0)=-\sum_{m=1}^{K} mh_m$$

$$\beta_{r1}^{XX}=X'(1)=-g_1$$

and

$$\beta_{r1}^{YX}=Y'(1)=-h_1 \tag{26}$$

Similarly, applying unit Y-wise moment at A and X and Y-wise moments at B in turn, all the required receptances are obtained. Using reciprocity for dynamic receptances it is easy to show that

$$\begin{aligned} &\beta_{r1}^{XX}=-\beta_{1r}^{XX},\ \beta_{11}^{XY}=\beta_{11}^{XY},\ \beta_{r1}^{YX}=-\beta_{r1}^{XY},\\ &\beta_{r1}^{YX}=-\beta_{r1}^{XY},\ \beta_{rr}^{YX}=\beta_{rr}^{XY},\ \beta_{r1}^{YY}=-\beta_{1r}^{YY} \end{aligned} \tag{27}$$

The series solutions (21) and (22) are truncated at proper values of K so that by including more number of terms the receptance values do not change by more than 1 percent. In the range of the parameter values used in the present work, $K = 16$ was found to be sufficient for Ω up to 40. For still higher frequencies larger values of K were demanded for the desired accuracy.

APPENDIX B

Determination of Receptances With Absorbers

In this case (4) is written separately for the left and the right half of the span as

$$\bar{w}_L=X_L(\xi)\sin\frac{\Omega\tau}{2}+Y_L(\xi)\cos\frac{\Omega\tau}{2} \quad 0\le\xi\le\frac{1}{2}$$

and

$$\bar{w}_R=X_R(\xi)\sin\frac{\Omega\tau}{2}+Y_R(\xi)\cos\frac{\Omega\tau}{2} \quad \frac{1}{2}\le\xi\le 1 \tag{28}$$

Assuming solutions for X_L, X_R, and Y_R in the form similar to (21) and (22), 4 $(K+1)$ number of unknown constants are involved. These constants are determined through 4 $(k-3)$ number of recursive relations along with 16 boundary conditions for a specified type of unit moment at one end. For example, with $1X$-wise moment at A the 16 boundary conditions are [6]

$$X_L(0)=Y_L(0)=X_R(1)=Y_R(1)=0,$$
$$X_R''(1)=Y_R''(1)=Y_L''(0)=0,\ X_L''(0)=-1$$

$$X_L\left(\frac{1}{2}\right)=X_R\left(\frac{1}{2}\right),\ X_L'\left(\frac{1}{2}\right)=X_R'\left(\frac{1}{2}\right),\ X_L''\left(\frac{1}{2}\right)=X_R''\left(\frac{1}{2}\right)$$

$$Y_L\left(\frac{1}{2}\right)=Y_R\left(\frac{1}{2}\right),\ Y_L'\left(\frac{1}{2}\right)=Y_R'\left(\frac{1}{2}\right),\ Y_L''\left(\frac{1}{2}\right)=Y_R''\left(\frac{1}{2}\right)$$

$$\left(1-\frac{\Omega^2}{4\sigma_a^2\pi^4}\right)\left[X_L'''\left(\frac{1}{2}\right)-X_R'''\left(\frac{1}{2}\right)\right]+\frac{\Omega\zeta_a}{2}\left[Y_R'''\left(\frac{1}{2}\right)-Y_L'''\left(\frac{1}{2}\right)\right]+\frac{\Gamma_a\Omega^2}{4}\left[X_L\left(\frac{1}{2}\right)-\frac{\Omega\zeta_a}{2}Y_L\left(\frac{1}{2}\right)\right]=0$$

and

$$\frac{\Omega\zeta_a}{2}\left[X_L'''\left(\frac{1}{2}\right)-X_R'''\left(\frac{1}{2}\right)\right]+\left(1-\frac{\Omega^2}{4\sigma_a^2\pi^4}\right)\left[Y_L'''\left(\frac{1}{2}\right)-Y_R'''\left(\frac{1}{2}\right)\right]+\frac{\Gamma a\Omega^2}{4}\left[Y_L\left(\frac{1}{2}\right)-\frac{\zeta\Omega_a}{2}X_L\left(\frac{1}{2}\right)\right]=0 \tag{29}$$

Once the solutions to X_L, X_R, X_L, and Y_R are obtained, the receptances are determined easily as explained in Appendix A. The absorber parameters are nondimensionalized as follows:

Γ_a = mass ratio of the absorber with m_a as the absorber mass; $= m_a/\{(m_f+m_p)l\}$

σ_a = tuning ratio of the absorber where k_a is the spring constant of the absorber; $= [\{k_a(m_f+m_p)\}/(m_aEI)]^{1/2}l^2/\pi^2$

ζ_a = damping ratio of the absorber with c_a as the viscous damping coefficient of the absorber. $= c_a/[\sigma_a\pi^2(k_am_a)^{1/2}]$

Downloaded 02 May 2010 to 171.66.16.25. Redistribution subject to ASME license or copyright; see http://www.asme.org/terms/Terms_Use.cfm

Friction, Restitution, and Energy Loss in Planar Collisions

R. M. Brach
Department of Aerospace and Mechanical Engineering, University of Notre Dame, Notre Dame, Ind. 46556
Mem. ASME

Both particle and rigid body planar collisions are covered in this paper. For particles, the classical equations for oblique impacts are derived using Newton's laws along with definitions of the coefficient of restitution and equivalent coefficient of friction. A general expression is obtained for the kinetic energy loss explicity containing the two coefficients. This expression for energy loss as a function of the friction coefficient possesses a maximum. The value of the friction coefficient at the maximum is a limiting value which can be used to determine whether or not sliding exists at separation. The maximum energy loss is independent of the physical mechanism of generation of tangential forces (friction) and serves as an upper bound for two-particle collisions. It is shown that to properly formulate and solve the rigid body problem, a moment must be considered at the common "point" of impact. A moment coefficient of restitution must be defined. This leads to six linear algebraic equations from which the six final velocity components can be calculated. An analytical solution is obtained for the general rigid body problem. In a reduced form, it is used to solve the problem of a single rigid body impacting a rigid barrier. This solution is then applied to a classical textbook problem. As shown for particle impacts, the concepts of limiting friction coefficient and maximum energy loss apply to rigid body impacts.

Introduction

Adaptation of Newton's laws in the form of impulse and momentum variables to study collisions have been included in almost every dynamics textbook ever written. Few texts present more than basic equations and solutions for velocity changes of particles. Some mention impacts of rigid bodies and provide one or two simple examples. None formulate properly the planar, rigid body collision problem. In fact, a general formulation [1, 2] and solution appears not to have been accomplished until recently. The proper role and meaning of the classical coefficient of restitution is discussed thoroughly in only a few books. The proper role and interpretation of a coefficient of friction for oblique impacts is seldom mentioned. As a result, the question of whether or not sliding takes place and whether or not sliding exists at separation remains vague.

A classical approach for particle impacts follows; final velocity components are treated as unknowns. The initial velocity components are assumed known as is the mass of each particle. The coefficient of restitution is used in the solution and later is related to the forces of deformation of the particles. An equivalent coefficient of friction is defined. Proper use of this friction coefficient allows a unique determination of the existence of sliding at separation of particles. An upper bound on the energy lost in a collision of two particles is also obtained.

An analysis of the planar problem of the collision of two rigid bodies is presented. Again, a classical view is taken of the problem where the final velocity components are the unknowns. Three components exist for each rigid body for a total of six unknowns. Six equations can be derived only if a moment is included at the area of contact of the two bodies. This leads to the definition of a new coefficient called the moment coefficient of restitution. Although the problem has six unknowns, the six equations are algebraic and linear, permitting an analytical solution.

The formulation of collison problems using the concepts of impulse and momentum are somewhat unusual and unique in the field of dynamics. Generally, dynamical problems are initial value problems and their solution requires integration of differential equations. Since the impulse/momentum equations represent a first integral of the motion (under specific circumstances), the solutions are algebraic. This simplicity results in a tradeoff however, in that no trajectory information is obtained; only before-and-after velocities can be computed. Since the velocity changes can be used to determine energy changes, important and fundamental results are often provided.

Equations for a Planar, Two-Particle Collision

The equations presented in this section are those commonly found in many dynamics tests in one form or another. Although the theory of particle impacts is simple and commonly applied, it is presented here because its simplicity

Contributed by the Applied Mechanics Division for publication in the JOURNAL OF APPLIED MECHANICS.
Discussion on this paper should be addressed to the Editorial Department, ASME, 345 East 47th Street, New York, N.Y. 10017, and will be accepted until two months after final publication of the paper itself in the JOURNAL OF APPLIED MECHANICS. Manuscript received by ASME Applied Mechanics Division, February, 1983; final revision, August, 1983.

Copyright © 1984 by ASME
Downloaded 02 May 2010 to 171.66.16.25. Redistribution subject to ASME license or copyright; see http://www.asme.org/terms/Terms_Use.cfm

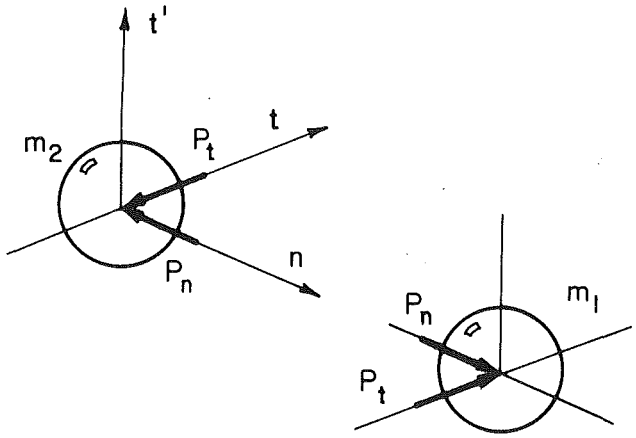

Fig. 1 Free body diagrams of colliding particles

permits a thorough coverage of the dependence of energy loss on friction and restitution. This simplicity is lost later in the rigid body problem equations, yet the concepts do not change substantially. Only planar collisions are treated since extension to three-dimensional collisions appears straightforward. The coefficients of restitution and friction are introduced here with the equations, but a discussion of their properties and meaning is deferred until the topic of energy is treated in the next section.

Figure 1 shows free body diagrams of two particles. A normal-tangential coordinate system is chosen such that the lines through the particle centers is the normal axis. The tangential axis, t, is perpendicular to the normal axis and lies in the plane of the initial velocities. Velocity symbols will be double subscripted with the first subscript indicating the particle number and the second, the coordinate direction. Capital, or uppercase, symbols indicate final velocities; small, or lowercase, symbols indicate initial velocities. For example, V_{1n} is the final velocity component of particle 1 along the normal, n, axis; v_{2t} is the initial velocity component of particle 2 in the tangential direction.

Conservation of momentum for the system of two particles along the normal axis gives

$$m_1 V_{1n} + m_2 V_{2n} = m_1 v_{1n} + m_2 v_{2n} \tag{1}$$

Conservation of momentum of the system of two particles in the tangential direction gives

$$m_1 V_{1t} + m_2 V_{2t} = m_1 v_{1t} + m_2 v_{2t} \tag{2}$$

A coefficient of restitution, e, is used commonly to represent energy loss of the collision. It is defined as

$$e = -(V_{1n} - V_{2n})/(v_{1n} - v_{2n})$$

where $0 \le e \le 1$. This gives a third equation

$$V_{1n} - V_{2n} = -e(v_{1n} - v_{2n}) \tag{3}$$

Finally, tangential velocity changes are governed by the tangential impulse, P_t, developed during the collision. An equivalent coefficient of friction, μ, is defined such that

$$\mu = P_t/P_n \tag{4}$$

In some applications, μ may correspond directly to a coefficient of dynamic sliding friction. The preceding definition does not impose any limitations and permits modeling of such diverse processes as a stone skipping over water or a hard particle plowing through a softer material. The tangential and normal impulses can be obtained directly for the free body diagrams of Fig. 1. Thus

$$P_n = m_1(V_{1n} - v_{1n}) = -m_2(V_{2n} - v_{2n}) \tag{5}$$

and

$$P_t = m_1(V_{1t} - v_{1t}) = -m_2(V_{2t} - v_{2t}) \tag{6}$$

Using linear combinations of these last two equations along with equation (4) provides a fourth equation which can be written in the form

$$\mu m_1 V_{1n} - m_1 V_{1t} - \mu m_2 V_{2n} + m_2 V_{2t} = \mu m_1 v_{1n} - m_1 v_{1t} - \mu m_2 v_{2n} + m_2 v_{2t} \tag{7}$$

The foregoing set of equations is incomplete because no provisions are made to determine whether or not sliding (relative tangential motion) continues throughout the duration of contact (including separation). Relative tangential motion always exists at the beginning of contact as long as $|v_{2t} - v_{1t}| > 0$. If this motion ceases during the duration of contact, then

$$V_{1t} - V_{2t} = 0 \tag{8}$$

Further discussion of the choice of equation (7) or equation (8) is deferred to the next section. For now, equation (7) and (8) are treated as alternatives and the solutions are found for both cases. Equations (1)–(3) and (7) or the alternative, equation (8), to equation (7) form a set of four linear algebraic equations for which the four unknown velocity components can be solved.

It will prove enlightening for the rigid body problem to place the equations in matrix form. If done for the particle equations in the foregoing, the following equation results: (using equation (7)):

$$\begin{bmatrix} m_1 & 0 & m_2 & 0 \\ 0 & m_1 & 0 & m_2 \\ -1 & 0 & +1 & 0 \\ \mu m_1 & -m_1 & -\mu m_2 & m_2 \end{bmatrix} \begin{Bmatrix} V_{1n} \\ V_{1t} \\ V_{2n} \\ V_{2t} \end{Bmatrix} = \begin{bmatrix} m_1 & 0 & m_2 & 0 \\ 0 & m_1 & 0 & m_2 \\ e & 0 & -e & 0 \\ \mu m_1 & -m_1 & -\mu m_2 & m_2 \end{bmatrix} \begin{Bmatrix} v_{1n} \\ v_{1t} \\ v_{2n} \\ v_{2t} \end{Bmatrix} \tag{9}$$

If the momentum change variables are defined to replace the velocity variables, a different, more convenient set of equations is obtained:

$$\begin{bmatrix} 1 & 0 & 1 & 0 \\ 0 & 1 & 0 & 1 \\ -1/m_1 & 0 & 1/m_2 & 0 \\ \mu & -1 & -\mu & 1 \end{bmatrix} \begin{Bmatrix} U_{1n} \\ U_{1t} \\ U_{2n} \\ U_{2t} \end{Bmatrix} = \begin{bmatrix} 0 & 0 & 0 & 0 \\ 0 & 0 & 0 & 0 \\ -(1+e) & 0 & (1+e) & 0 \\ 0 & 0 & 0 & 0 \end{bmatrix} \begin{Bmatrix} v_{1n} \\ v_{1t} \\ v_{2n} \\ v_{2t} \end{Bmatrix} \tag{9a}$$

where $U_{1n} = m_1(V_{1n} - v_{1n})$, $U_{1t} = m_1(V_{1t} - v_{1t})$, $U_{2n} = m_2(V_{2n} - v_{1n})$ and $U_{2t} = m_2(V_{2t} - v_{2t})$.

The solutions can be written in several different forms. The

Downloaded 02 May 2010 to 171.66.16.25. Redistribution subject to ASME license or copyright; see http://www.asme.org/terms/Terms_Use.cfm

following seem to best display the symmetry of the physical problem:

$$V_{1n} = v_{1n} + m_2(1+e)\,(v_{2n} - v_{1n})/(m_1 + m_2) \tag{10}$$

$$V_{1t} = v_{1t} + \mu m_2(1+e)\,(v_{2n} - v_{1n})/(m_1 + m_2) \tag{11}$$

$$V_{2n} = v_{2n} - m_1(1+e)\,(v_{2n} - v_{1n})/(m_1 + m_2) \tag{12}$$

and

$$V_{2t} = v_{2t} - \mu m_1(1+e)\,(v_{2n} - v_{1n})/(m_1 + m_2) \tag{13}$$

The solutions for momentum-change variables can be obtained directly from these equations by transposing v_{1n}, v_{1t}, v_{2n}, and v_{2t} to the left-hand side of each equation, respectively, and multiplying by the proper mass.

Equation (8) is used in place of equation (7) when sliding does not exist at separation. The corresponding matrix equations in this case are

$$\begin{bmatrix} m_1 & 0 & m_2 & 0 \\ 0 & m_1 & 0 & m_2 \\ -1 & 0 & +1 & 0 \\ 0 & +1 & 0 & -1 \end{bmatrix} \begin{Bmatrix} V_{1n} \\ V_{1t} \\ V_{2n} \\ V_{2t} \end{Bmatrix} = \begin{bmatrix} m_1 & 0 & m_2 & 0 \\ 0 & m_1 & 0 & m_2 \\ e & 0 & -e & 0 \\ 0 & 0 & 0 & 0 \end{bmatrix} \begin{Bmatrix} v_{1n} \\ v_{1t} \\ v_{2n} \\ v_{2t} \end{Bmatrix} \tag{14}$$

and

$$\begin{bmatrix} 1 & 0 & 1 & 0 \\ 0 & 1 & 0 & 1 \\ -1/m_1 & 0 & 1/m_2 & 0 \\ 0 & 1/m_1 & 0 & -1/m_2 \end{bmatrix} \begin{Bmatrix} U_{1n} \\ U_{1t} \\ U_{2n} \\ U_{2t} \end{Bmatrix} = \begin{bmatrix} 0 & 0 & 0 & 0 \\ 0 & 0 & 0 & 0 \\ (1+e) & 0 & -(1+e) & 0 \\ 0 & -1 & 0 & +1 \end{bmatrix} \begin{Bmatrix} v_{1n} \\ v_{1t} \\ v_{2n} \\ v_{2t} \end{Bmatrix} \tag{15}$$

The solutions of equation (14) and (15) for the final normal velocity components are identical to equation (10) and (11). The final tangential velocity component solutions are:

$$V_{1t} = v_{1t} + m_2(v_{2t} - v_{1t})/(m_1 + m_2) \tag{16}$$

and

$$V_{2t} = v_{2t} - m_1(v_{2t} - v_{1t})/(m_1 + m_2) \tag{17}$$

Again, the solutions for U_{1t} and U_{2t} are the last term of each of equation (16) and (17), multiplied by m_1 and m_2, respectively.

Restitution, Friction, and Energy Loss

There is an important advantage of introducing the coefficient of restitution into the collision problem as done in the preceding section. It serves as a means of allowing kinetic energy to be lost yet its equation is linear in the velocity components. Any equation containing kinetic energy explicitly would be nonlinear and the ease of obtaining a solution is lost. Because of the importance of energy, a relationship is found here between e, μ, and the energy loss. An energy conservation equation can be written as:

$$\frac{1}{2}m_1(V_{1t}^2 + V_{1n}^2) + \frac{1}{2}m_2(V_{2n}^2 + V_{2t}^2) + T_L = \frac{1}{2}m_1(v_{1t}^2 + v_{1n}^2) + \frac{1}{2}m_2(v_{2n}^2 + v_{2t}^2) \tag{18}$$

where T_L is the energy converted to other forms such as sound, light, heat, and/or permanent strain. Substitution of the solutions for the final velocity components into equation (18) can give the energy loss in terms of initial velocities, particle masses, and coefficients. Using the "sliding" solution, equations (10)-(13) gives

$$T_L = \frac{1}{2}\bar{m}(v_{2n} - v_{1n})^2(1+e)[(1-e) + 2\mu r - (1+e)\mu^2] \tag{19}$$

where $\bar{m} = m_1 m_2/(m_1 + m_2)$ and $r = (v_{2t} - v_{1t})/(v_{2n} - v_{1n})$. If the collision is colinear or frictionless, $\mu = 0$ and

$$T_L = \frac{1}{2}\bar{m}(1-e^2)(v_{2n} - v_{1n})^2 \tag{20}$$

This form of equation (19) has been obtained by many others including [3].

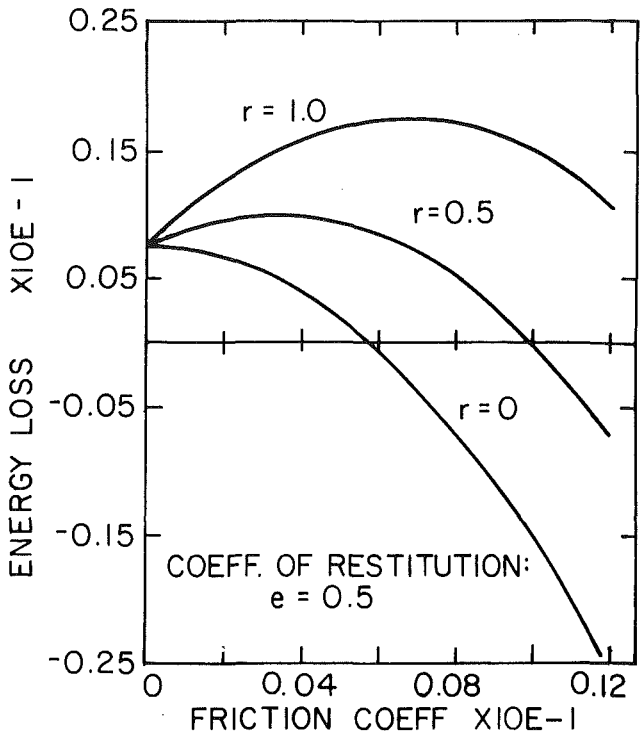

Fig. 2 Energy loss as a function of friction

Friction. Consider the role of the equivalent friction coefficient μ in the dissipation of energy. First, define a nondimensional energy loss T_L' such that

$$T_L' = (1+e)[(1-e) + 2\mu r - (1+e)\mu^2] \tag{21}$$

Plots of $T_L'(\mu)$ for typical values of e and treating r as a parameter have the form shown in Fig. 2. The existence of a maximum proves worth pursuing. Intuitively, for a given collision, one expects a larger friction coefficient along with the condition of sliding to dissipate more energy. This is only true to a point, however, since with high enough friction, sliding will cease prior to separation. Any amount of friction

Downloaded 02 May 2010 to 171.66.16.25. Redistribution subject to ASME license or copyright; see http://www.asme.org/terms/Terms_Use.cfm

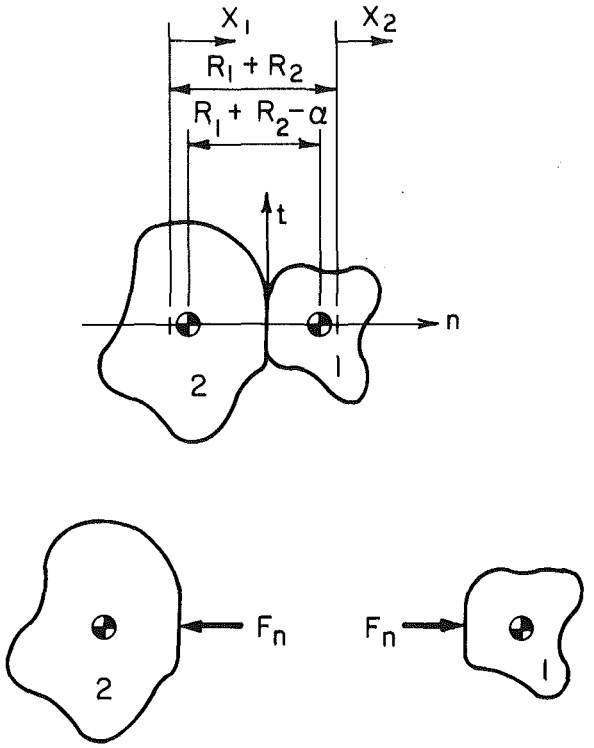

Fig. 3 Local forces and displacements of colliding particles

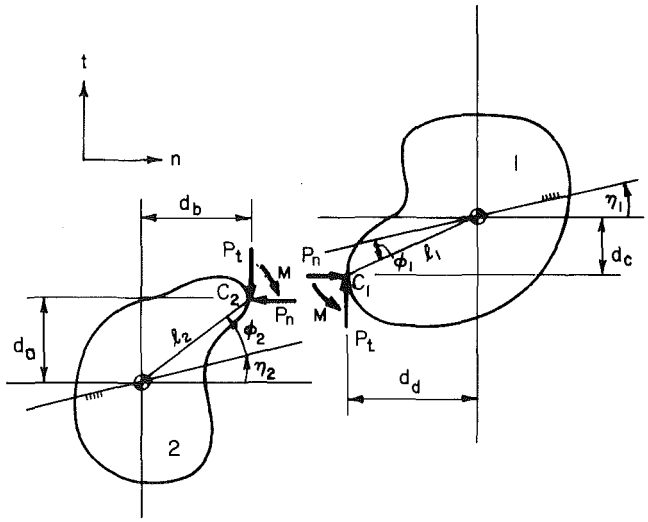

Fig. 4 Free body diagrams of colliding rigid bodies

higher than the amount which causes sliding to cease will have no further effect. Namely sliding will still cease prior to separation with V_{1t} still equal to V_{2t}. If, for a given collision, sliding at separation does not occur, yet the "sliding solution," equations (10)–(13) are used with a large value of μ, the results are incorrect. This incorrect solution will have excessive tangential velocity changes, perhaps even velocity reversals. The latter can occur only if the friction "created" energy rather than dissipated it. Consequently, the peak in each curve of Fig. 2 corresponds to a maximum value of friction (for a given e and r) below which sliding takes place through separation and above which $V_{1t} = V_{2t}$. The stationary value of T_L', equation (21), occurs at a friction coefficient of

$$\mu_m = \frac{r}{1+e} \tag{22}$$

To summarize, if $\mu < \mu_m$, sliding exists at separation and equations (10)–(13) provide the final velocities. If $\mu \geq \mu_m$, sliding ceases during the collision, the final tangential velocities are equal and the final velocities are given by equations (10), (12), (16), and (17). Note that for colinear impacts, $v_{1t} = v_{2t} = 0$ and $\mu_m = 0$.

Because of the form of the curves in Fig. 2 and the preceding reasoning, a maximum energy loss exists. This maximum provides an upper bound to the energy loss of a two-particle collision. This is $(T_L)_m$, found by substituting μ_m into equation (19). This is

$$(T_L)_m = \frac{1}{2}\bar{m}(v_{2n} - v_{1n})^2(1 - e^2 + r^2) \tag{23}$$

or

$$(T_L)_m = \frac{1}{2}\bar{m}[(v_{2t} - v_{1t})^2 + (1-e^2)(v_{2n} - v_{1n})^2] \tag{23a}$$

Note that this upper bound is independent of the physical process that creates the tangential impulse.

Restitution. To discuss the role and meaning of the coefficient of restitution, it is convenient to consider normal impacts only. This is legitimate since the normal velocity changes are independent of μ; see equations (10) and (12). Another convenience is to introduce the mass center displacements of the particles during contact using a single relative coordinate as done by Timoshenko [4]. Figure 3 shows the relative normal displacement, $\alpha = x_1 - x_2$, of the particle's mass centers. Although the shape of the particles can play an important role, it will not be considered here. The equation of motion of the particles are

$$m_1\ddot{x}_1 = -F_n \tag{24}$$

and

$$m_2\ddot{x}_2 = -F_n \tag{25}$$

Multiplication of equation (24) by $m_2/(m_1+m_2)$ and equation (24) by $m_1/(m_1+m_2)$ and subtracting gives

$$\bar{m}\ddot{\alpha} + F(\dot{\alpha},\alpha,\tau) = 0 \tag{26}$$

where $F_n = F(\dot{\alpha},\alpha,\tau)$ and τ is time. Multiplication by $\dot{\alpha}$ and integration over the contact duration with $\dot{\alpha}(\tau_1) = \dot{\alpha}_1$ and $\dot{\alpha}(\tau_2)$,

$$\frac{1}{2}\bar{m}\dot{\alpha}_2^2 - \frac{1}{2}\bar{m}\dot{\alpha}_1^2 + \int F(\dot{\alpha},\alpha,\tau)\,d\alpha = 0 \tag{27}$$

The first two terms represent the kinetic energy change of the particles during the collision (not including frictional losses). Using equation (20), this can be written as

$$\frac{1}{2}\bar{m}(1-e^2)(v_{2n} - v_{1n})^2 - \int F(\dot{\alpha},\alpha,\tau)\,d\alpha = 0$$

or

$$e^2 = 1 - \frac{2}{\bar{m}(v_{2n} - v_{1n})^2}\int F(\dot{\alpha},\alpha,\tau)\,d\alpha \tag{28}$$

This expression shows that the coefficient of restitution is directly related to the energy lost due to deformation of particles during contact. If particle geometry and material behavior is simple, equation (28) can be integrated. See, for example, the use of Hertz's static equations applied by Timoshenko [4] to the problem of the impact of two spheres. In that example, the integral is zero and $e = 1$ and the impact is elastic. Another model [5] uses viscous dissipation.

Impact of Two Rigid Bodies in a Plane

Numerous examples exist of solutions of specific rigid body

Downloaded 02 May 2010 to 171.66.16.25. Redistribution subject to ASME license or copyright; see http://www.asme.org/terms/Terms_Use.cfm

impact problems. Most of these are for idealized situations such as a sphere rolling over a rigid step, a pendulum impacted at a point, etc. A relatively long and cumbersome semigraphical solution method [3] has been proposed. But until recently [1, 2] the proper formulation of the general, two-dimensional rigid body impact problem appears not to have been published. In this section, the equations of this problem will be reviewed; six linear equations are obtained which involve the six unknown final velocity components of the two rigid bodies. In addition, it is shown that these equations can be solved analytically.

In the impact problem of two particles, it is common to neglect the impulse of all forces other than the common interparticle force. Usually this is a reasonable assumption because collisions occur over short time durations and the impact force is relatively large. When working with rigid body collisions this same assumption is made but an additional effect comes into play. It is usually necessary to assume a short contact duration so that changes in angular orientation of both rigid bodies are small. This assumption does not affect the solution of the equations as much as it does the application. Consequently it is not pursued here.

Consider the two free body diagrams shown in Fig. 4. Note that in addition to the force impulse components, P_n, and P_t, a moment impulse, M, is shown at the point of impact, C (shown as C_1 in body 1 and C_2 in body 2). It appears to have been a common procedure to neglect the effects of any moments between two colliding bodies. Neglecting M may be valid in many problems but is certainly not true in general. Neglecting a common moment impulse may be invalid for two reasons. In all real collisions, the impact force occurs over a surface, not a point. The impulse components P_n and P_t represent the impulses of the components of the resultant of a surface force whose exact location not only may not be accurately known but that usually changes during the contact duration. Consequently, uncertainty in the selection of point C, the "center of impact," demands an equivalent force system which must include a moment. Secondly, impact equations may be used to model collisions where a physical mechanism exists to transmit a moment such as mating parts whose contact prohibits relative rotation. Consequently any general formulation must include a common impulse M.

Equations of Rigid Body Impacts. Again, from the aspect of the classical impact problem, it is assumed that the initial velocities are known and the final velocities are to be computed. Three final velocity components exist for each rigid body for motion in a plane for a total of six unknowns. Momentum-change variables will be introduced again after the full set of equations is derived and a matrix equation is introduced.

Conservation of linear momentum of the system in the direction of the normal coordinate, n, can be written:

$$m_1 V_{1n} + m_2 V_{2n} = m_1 v_{1n} + m_2 v_{2n} \tag{29}$$

Likewise, conservation of linear momentum in the tangential direction is:

$$m_1 V_{1t} + m_2 V_{2t} = m_1 v_{1t} + m_2 v_{2t} \tag{30}$$

The final and initial relative normal velocity components are again related by the coefficient of restitution. For rigid bodies, the relationship is between velocity components at the point of contact where the deformation occurs. This is:

$$V_{1n} + d_c\Omega_1 - V_{2n} + d_a\Omega_2 = -e(v_{1n} + d_c\omega_1 - v_{2n} + d_a\omega_2) \tag{31}$$

where

$$d_a = l_2\sin(\eta_2 + \phi_2) \quad \text{and} \quad d_c = l_1\sin(\eta_1 + \phi_1) \tag{32}$$

Similarly,

$$d_b = l_2\cos(\eta_2 + \phi_2) \quad \text{and} \quad d_d = l_1\cos(\eta_1 + \phi_1) \tag{33}$$

Also for use shortly, note that the linear impulse components can be written as:

$$P_n = \frac{1}{2}m_1(V_{1n} - v_{1n}) - \frac{1}{2}m_2(V_{2n} - v_{2n}) \tag{34}$$

and

$$P_t = \frac{1}{2}m_1(V_{1t} - v_{1t}) - \frac{1}{2}m_2(V_{2t} - v_{2t}) \tag{35}$$

As in the point mass problem, an equivalent friction coefficient can be defined by equation (4). Using equations (34) and (35), this gives

$$-\mu m_1 V_{1n} + m_1 V_{1t} + \mu m_2 V_{2n} - m_2 V_{2t} = -\mu m_1 v_{1n} + m_1 v_{1t} + \mu m_2 v_{2n} - m_2 v_{2t} \tag{36}$$

A fifth equation is obtained by summing moments about the mass center of each rigid body, eliminating the unknown moment impulse M and using equations (34) and (35). The resulting expression is:

$$-d_{13}m_1 V_{1n} + d_{24}m_1 V_{1t} + d_{13}m_2 V_{2n} - d_{24}m_2 V_{2t} + I_1\Omega_1 + I_2\Omega_2 = -d_{13}m_1 v_{1n} + d_{24}m_1 v_{1t} + d_{13}m_2 v_{2n} - d_{24}m_2 v_{2t} + I_1\omega_1 + I_2\omega_2 \tag{37}$$

where

$$d_{13} = (d_a + d_c)/2 \quad \text{and} \quad d_{24} = (d_b + d_d)/2 \tag{38}$$

At this point, a sixth equation is necessary. As in the two-particle impact problems, energy loss due to contact deformation has already been accounted for by introduction of the coefficient of restitution e, equation (31). But in a general formulation, energy loss due to change in rotational energy must be treated independently. It is conceivable that a perfectly elastic impact (at the contact point) may occur along with a rotational constraint. Consequently a moment coefficent of restitution (or simply moment coefficient), e', is introduced. To determine the form of the proper equation, first consider the following. From equation (5).

$$P_n = -m_2(V_{2n} - v_{2n}) = +\bar{m}(1+e)(v_{2n} - v_{1n})$$

where equation (12) has been used. Using equation (3) it is possible to write

$$eP_n/\bar{m} = -(1+e)(V_{2n} - V_{1n}) \tag{39}$$

This expression confirms that for $e = 0$, $V_{2n} = V_{1n}$; furthermore, it is already known $e = 1$ corresponds to a perfectly elastic impact. Note however that for the unrealistic value of $e = -1$, $P_n = 0$. (A value of $P_n = 0$ may be interpreted as no impact, since by equation (4), $P_n = 0$ implies $P_t = 0$.) The same form as equation (39) wil be used to define the moment coefficient, e'; that is

$$e'M/\bar{I} = -(1+e')(\Omega_2 - \Omega_1) \tag{40}$$

where $\bar{I} = I_1 I_2/(I_1 + I_2)$. Note that for $e' = 0$, $\Omega_2 = \Omega_1$ and corresponds to a perfectly inelastic angular impact, independently of e. When $e' = -1$, $M = 0$ and corresponds to previous solutions of rigid body impact problems where the moment has been neglected. That $e' = 1$ corresponds to a perfectly elastic angular impact can be seen after solutions are obtained. Summing moments about the mass centers of each rigid body gives

$$I_1(\Omega_1 - \omega_1) = P_n d_c - P_t d_d + M \tag{41}$$

and

Downloaded 02 May 2010 to 171.66.16.25. Redistribution subject to ASME license or copyright; see http://www.asme.org/terms/Terms_Use.cfm

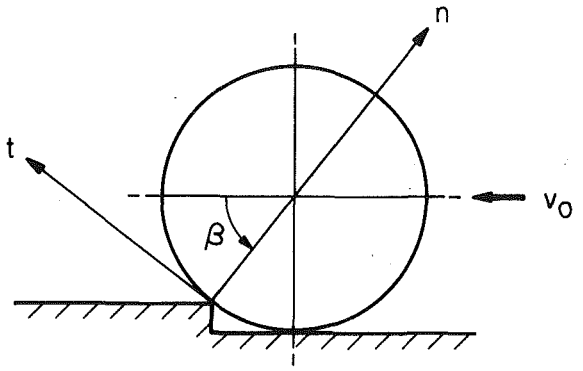

Fig. 5 Rolling cylinder impacting a rigid step

$$I_2(\Omega_2-\omega_2)=P_n d_a-P_t d_b-M \tag{42}$$

From these,

$$M/I_1=(\Omega_1-\omega_1)-P_n d_c/I_1+P_t d_d/I_1$$

and

$$M/I_2=-(\Omega_2-\omega_2)+P_n d_a/I_2-P_t d_b/I_2 \tag{43}$$

Substitution of the expressions for M from equation (43) into equation (40) and using equations (34) and (35) provides a sixth equation. That is

$$\begin{aligned}-e'\gamma m_1 V_{1n}+e'\delta m_1 V_{1t}+e'\gamma m_2 V_{2n}-e'\delta m_2 V_{2t}-\Omega_1+\Omega_2\\ =-e'\gamma m_1 v_{1n}+e'\delta m_1 v_{1t}+e'\gamma m_2 v_{2n}-e'\delta m_2 v_{2t}\\ +e'\omega_1-e'\omega_2\end{aligned} \tag{44}$$

where

$$\gamma=\left(\frac{d_c}{I_1}-\frac{d_a}{I_2}\right)/2 \quad \text{and} \quad \delta=\left(\frac{d_d}{I_1}-\frac{d_b}{I_2}\right)/2 \tag{45}$$

Equations (29)–(31), (36), (37) and (44) are six linear algebraic equations whose solution furnishes the six unknown final velocity components of a rigid body collision. These can be written in matrix form where

$$\begin{bmatrix} m_1 & 0 & m_2 & 0 & 0 & 0\\ 0 & m_1 & 0 & m_2 & 0 & 0\\ 1 & 0 & -1 & 0 & d_c & d_a\\ -\mu m_1 & m_1 & \mu m_2 & -m_2 & 0 & 0\\ -d_{13}m_1 & d_{24}m_1 & d_{13}m_2 & -d_{24}m_2 & I_1 & I_2\\ -e'\gamma m_1 & e'\delta m_1 & e'\gamma m_2 & -e'\delta m_2 & -1 & +1 \end{bmatrix} \begin{Bmatrix} V_{1n}\\ V_{1t}\\ V_{2n}\\ V_{2t}\\ \Omega_1\\ \Omega_2 \end{Bmatrix}$$

$$= \begin{bmatrix} m_1 & 0 & m_2 & 0 & 0 & 0\\ 0 & m_1 & 0 & m_2 & 0 & 0\\ -e & 0 & e & 0 & -ed_c & -ed_a\\ -\mu m_1 & m_1 & \mu m_2 & -m_2 & 0 & 0\\ -d_{13}m_1 & d_{24}m_1 & d_{13}m_2 & -d_{24}m_2 & I_1 & I_2\\ -e'\gamma m_1 & e'\delta m_1 & e'\gamma m_2 & -e'\delta m_2 & e' & -e' \end{bmatrix} \begin{Bmatrix} v_{1n}\\ v_{1t}\\ v_{2n}\\ v_{2t}\\ \omega_1\\ \omega_2 \end{Bmatrix} \tag{46}$$

Transforming the variables to momentum-changes simplifies equation (46) considerably. That is, let $U_{in} = m_i(V_{in}-v_{in})$, $U_{it} = m_i(V_{it}-v_{it})$, and $W_i = I_i(\Omega_i-\omega_i)$; $i = 1, 2$. Then equation (46) becomes

$$\begin{bmatrix} 1 & 0 & 1 & 0 & 0 & 0\\ 0 & 1 & 0 & 1 & 0 & 0\\ 1/m_1 & 0 & -1/m_2 & 0 & d_c/I_1 & d_a/I_2\\ -\mu & 1 & \mu & -1 & 0 & 0\\ -d_{13} & d_{24} & d_{13} & -d_{24} & 1 & 1\\ -e'\gamma & e'\delta & e'\gamma & -e'\delta & -1/I_1 & 1/I_2 \end{bmatrix} \begin{Bmatrix} U_{1n}\\ U_{1t}\\ U_{2n}\\ U_{2t}\\ W_1\\ W_2 \end{Bmatrix}$$

$$= \begin{Bmatrix} B_1\\ B_2\\ B_3\\ B_4\\ B_5\\ B_6 \end{Bmatrix} = \begin{Bmatrix} 0\\ 0\\ -(1+e)(v_{1n}-v_{2n}+d_c\omega_1+d_a\omega_2)\\ 0\\ 0\\ (1+e')(\omega_1-\omega_2) \end{Bmatrix} \tag{47}$$

Note that equations (46) and (47) reduce to the particle problem, equations (14) and (15), when all dimensions are zero and rotations vanish.

Solution of Rigid Body Impact Equations. Equation (47) is not difficult to solve. Let each of the individual component equations be referred to as (*a*), (*b*), . . . (*f*) respectively. Multiplying (*c*) by m_2 and adding to (*a*) gives

$$U_{1n}=\bar{m}B_3-\frac{\bar{m}d_c}{I_1}W_1-\frac{\bar{m}d_a}{I_2}W_2 \tag{48}$$

Multiplying (*d*) by d_{24}, subtracting from (*e*) and using equation (48) gives

$$\left[1+2(d_{13}-\mu d_{24})\frac{\bar{m}d_c}{I_1}\right]W_1+\left[1+2(d_{13}-\mu d_{24})\frac{\bar{m}d_a}{I_1}\right]W_2 =2(d_{13}-\mu d_{24})\bar{m}B_3 \tag{49}$$

Multiplying (*d*) by $e'\delta$, subtracting from (*f*) and using equation (48) gives

$$[-1+2e'(\gamma-\mu\delta)\bar{m}d_c]\,W_1/I_1+[1+2e'(\gamma-\mu\delta)\bar{m}d_a]W_2/I_2 =B_6+2e'(\gamma-\mu\delta)\bar{m}B_3 \tag{50}$$

Equations (49) and (50) are two independent simultaneous equations for W_1 and W_2. Their solution can be used with equation (48) to provide U_{1n} and with (*a*), U_{2n}. Written in the form of final velocities, these are:

$$\begin{aligned}V_{1n}=v_{1n}-\bar{m}(1+e)(v_{2n}-v_{1n})/m_1\\ +\bar{m}[d_c(\Omega_1+e\omega_1)+d_a(\Omega_2+e\omega_2)]/m_1\end{aligned} \tag{51}$$

and

$$\begin{aligned}V_{2n}=v_{2n}-\bar{m}(1+e)(v_{2n}-v_{1n})/m_2\\ +\bar{m}[d_c(\Omega_1+e\omega_1)+d_a(\Omega_2+e\omega_2)]/m_2\end{aligned} \tag{52}$$

The fourth of the matrix equations, (*d*) shows that $U_{1t} = \mu U_{1n}$ and $U_{2t} = \mu U_{2n}$. Expressed in final velocities, these are

$$\begin{aligned}V_{1t}=v_{1t}+\mu\bar{m}(1+e)(v_{2n}-v_{1n})/m_1\\ -\mu\bar{m}[d_c(\Omega_1+e\omega_1)+d_a(\Omega_2+e\omega_2)]/m_1\end{aligned} \tag{53}$$

$$\begin{aligned}V_{2t}=v_{2t}-\mu\bar{m}(1+e)(v_{2n}-v_{1n})/m_2\\ -\mu\bar{m}[d_c(\Omega_1+e\omega_1)+d_a(\Omega_2+e\omega_2)]/m_2\end{aligned} \tag{54}$$

Equations (51)–(54) contain the final angular velocities as obtained from solution to equations (49) and (50). Among

Downloaded 02 May 2010 to 171.66.16.25. Redistribution subject to ASME license or copyright; see http://www.asme.org/terms/Terms_Use.cfm

other variables, Ω_1 and Ω_2 will be functions of e', I_1, and I_2 which do not appear explicitly in equations (51)–(54).

A general expression for energy loss, analogous to equation (19) for particle collisions is extremely lengthy and complicated. It is not written here. By intuition, it is expected that energy loss varies with friction in a fashion analogous to the particle solution, possessing a maximum at the limiting value of the friction coefficient. This is borne out by examination of special cases and numerical results. A general expression for the limiting friction coefficient, μ_m, and an energy loss bound are extremely lengthy. These expressions can be obtained more readily for special cases as is done in the next section.

Impact of a Rigid Body With a Rigid Barrier

A special case of the foregoing, which possesses a reasonable amount of practicality, is the problem of a rigid body impacting a rigid surface. If mass 1 is chosen as that of interest, the proper equations can be obtained from the foregoing by letting $m_2 \to \infty$, $I_2 \to \infty$, $l_2 = 0$, and $V_{2n} = V_{2t} = \Omega_2 = 0$. Only three unknowns remain. Since momentum is no longer conserved for mass 1 alone, equations (29), (30), and (37) are not applicable. With mass 2 becoming unbounded as indicated above, equations (31), (36), and (44) become, respectively,

$$V_{1n} + d_c\Omega_1 = -e(v_{1n} + d_c\omega_1) \tag{55}$$

$$-\mu V_{1n} + V_{1t} = -\mu v_{1n} + v_{1t} \tag{56}$$

and

$$-e'\gamma m_1 V_{1n} + e'\delta m_1 V_{1t} - \Omega_1 = -e'\gamma m_1 v_{1n} + e'\delta m_1 v_{1t} + e'\omega_1 \tag{57}$$

These equations, easily solved for the unknowns, are valid for both sliding at separation as well as for zero final tangential velocity at the contact point. The latter case will occur if the limiting value of friction, μ_m, is used in the equation and corresponds to the case where $\mu \geq \mu_m$. An expression for μ_m can be obtained by finding the stationary point of the energy loss or by using the definition of μ and the solution of equations (55), (57), and $V_{1t} = d_d\Omega_1 = 0$ in place of equation (56). This is

$$\mu_m = \frac{v_{1t} - d_d\Omega_1}{d_c(\Omega_1 - \omega_1) + (1+e)(v_{1n} + d_c\omega_1)} \tag{58}$$

where

$$\Omega_1 = -e'\frac{\omega_1(I_1 + m_1 d_c^2) + m_1 d_d v_{1t} - (1+e)m_1 d_c(v_{1n} + d_c\omega_1)}{I_1 - e' m_1 l_1^2} \tag{59}$$

Rolling Cylinder Impacting a Step. A rigid body impact problem often used as an example [6] is illustrated in Fig. 5. It is assumed that the cylinder is rolling without slip prior to it impact with the rigid step. Ordinarily it is assumed that the impact is totally inelastic and that final motion is characterized by rotation about the edge of the step. A solution can be obtained easily without these assumptions. Let the cylinder's center have a velocity v_0 and let $\eta_1 = \phi_1 = 0$, $d_c = 0$, $d_d = R$, $v_{1n} = -v_0\cos\beta$, $v_{1t} = v_0\sin\beta$, and $\omega_1 = v_0/R$.

The final velocities are

$$\Omega_1 = e'\frac{v_0}{R}[2\mu(1+e)\cos\beta - 1] \tag{60}$$

$$V_{1n} = ev_0\cos\beta \tag{61}$$

$$V_{1t} = v_0[\sin\beta + \mu(1+e)\cos\beta] \tag{62}$$

The limiting value of the friction coefficient is found from equation (58)

$$\mu_m = \frac{e' + \sin\beta}{(2e'-1)(1+e)\cos\beta} \tag{63}$$

This solution permits many more options to be examined in contrast to the classical solution. The latter occurs for $e' = -1$ (no moment), $e = 0$, and $\mu = \mu_m$. Substitution of these into equation (60)–(62) gives the proper solution. If $\beta \to 0$, the step may prove insurmountable to the cylinder, particularly if the friction coefficient is negligibly small. Again assuming no moment ($e' = -1$) this case gives $V_{1n} \sim ev_0$, $V_{1t} \sim 0$, and $\Omega_1 \sim v_0/R$. Another physically possible case is if the cylinder is impaled by the edge of the step and gets stuck. In this case $e = 0$, $e' = 0$, and $\mu = \mu_m$. As a result, $\Omega_1 = V_{1n} = V_{1t} = 0$, which may appear rather uninteresting. However, note that this is an example of a case which cannot be solved without the existence of a moment at the point of impact, i.e., $M \neq 0$.

Conclusions

The concepts of impulse and momentum have been used since Newton's time to calculate velocity changes of colliding particles. Although the actual velocity changes seemed simple enough to calculate, the question of the existence of a nonzero relative tangential velocity at separation and its relationship to an equivalent friction coefficient has apparently never been firmed up. The fact that a limiting friction coefficient value, μ_m, must exist is not startling but its correspondence to a stationary value of kinetic energy loss seems never to have been recognized. The facts that μ_m can be expressed simply and is independent of the final velocities and is independent of the friction mechanism makes it easy to calculate. This also furnishes a convenient expression for an upper bound on energy loss.

The concepts of a limiting friction coefficient and maximum energy loss carry over to rigid body impacts. Although the rigid body problem can now be solved analytically, the general expressions for μ_m and T_L are very cumbersome. The analytical solution is tractable when solving for velocity changes; general equations have been furnished. These equations have been applied to experimental collisions of vehicles [9] with typical coefficients found by the method of least squares.

Solution of the rigid body problem was achieved using the concept of a moment coefficient of restitution. As the classical, linear coefficient, e, is related to energy loss, e' is probably related to rotational energy losses. The precise relationship is not easily demonstrated however. As e is an artifice to simplify the solution of particle impact equations, e' is the same for the rigid body problems.

An obvious next step is the three-dimensional rigid body impact problem. Its formulation and solution is by no means from the foregoing, although some direction is indicated. The existence of torsional moments has been recognized by others [7, 8] and hints that more than one moment coefficient may be necessary.

References

1 Brach, R. M., "An Impact Moment Coefficient for Vehicle Collision Analysis," Trans. SAE 770014, 1977.

2 Brach, R. M., "Moments Between Impacting Rigid Bodies," ASME *Journal of Mechanical Design*, Vol. 103, Oct. 1981, pp. 812–817.

3 Goldsmith, W., *Impact*, Edward Arnold, London, 1960.

4 Timoshenko, S., and Goodier, J. W., *Theory of Elasticity*, McGraw-Hill, New York, 1951.

5 Sachs, H. K., "On a One-Dimensional Model of Vehicle Crashworthiness," *Israel J. of Tech.*, Vol. 12, 1974, pp. 138–144.

6 Timoshenko, S., and Young, D. H., *Advanced Dynamics*, McGraw-Hill, New York, 1948.

7 Horak, F., "Impact of a Rough Ball Spinning Round Its Vertical Diameter Onto a Horizontal Plane," *Trans. of the Faculty of Mech. and Elec. Eng. of the Tech. Univ. of Prague*, Czechoslovakia, 1948.

8 Andrews, James, "A Mechanical Analysis of a Special Class of Rebound Phenomena," *Med. and Sci. in Sports and Exercise*, Vol. 15, No. 3, 1983.

9 Brach, R. M., "Identification of Vehicle and Collision Impact Parameters from Crash Tests," ASME Tech. Conf., Dearborn, Mich., Sept. 1983.

Downloaded 02 May 2010 to 171.66.16.25. Redistribution subject to ASME license or copyright; see http://www.asme.org/terms/Terms_Use.cfm

T. W. Lee
Associate Professor.
Mem. ASME

E. Akbil[1]
Former Research Assistant.

Department of Mechanical and
Aerospace Engineering,
Rutgers University,
New Brunswick, N.J. 08903

General Characteristics of the Motion of Multiple-Pode Joints

This paper presents an analytical method on the investigation of the motion characteristics of a class of spatial mechanical components involving the ball-and-trunnion type of joint, namely, the multiple-pode joint. Algebraic derivations of the input-output equation and explicit relations for motion parameters are presented for these joints as well as their shaft couplings. From this general displacement analysis, some insights into the basic nature and behavior of the multiple-pode joint are observed and interpreted. The creation of shaft couplings using these joints and their functional analysis are also illustrated in several cases.

Introduction

The multiple-pode joint, developed about 1910 [1], has been rediscovered and redeveloped throughout the years, and has found a wide application in different types and makes of modern vehicles. Generally, there are two kinds – the two-pode and the tripode joints. The motion characteristics of the two-pode shaft couplings are essentially similar to that of the Hooke's joint which has nonconstant velocity characteristics. The tripode joint, on the other hand, provides an approximate constant-velocity (CV) transmission. It is used to connect intersecting shafts or (when in series) nonintersecting shafts, allowing length variations caused by the motion of the supporting system of shafts. Therefore, the joint is particularly suitable for use as the shaft coupling of front-wheel drive vehicles. Since constant velocity transmission is essential for minimizing speed fluctuations and vibrations at the front-end of these vehicles under higher speeds, the tripode joint, consequently, has been the subject of many recent investigations and a summary of them is given in [2, 3].

This investigation concerns the general characteristics of the motion of all multiple-pode joints. There are several questions of practical concern regarding the motion of pode joints, which remain unanswered. First, why can the evolution of the tripode from two-pode driving element provide a nearly nonvarying velocity characteristic? Second, if increasing one pode in the case of the tripode results in better motion characteristics, can joints with more than three podes be used to make further improvement? Third, how would the different types of pode joints and their combinations with various pode joints or CV joints effect the function of the compound coupling? All these questions are of fundamental nature, and therefore, warrant an investigation.

This paper deals with these problems from an analytical viewpoint by performing a general displacement analysis of the multipode joint. Such an investigation, as it will be shown here, yields similar findings to those recently reported by the authors [3] from another approach, i.e., considered purely from the kinematic structure and functional analysis of the multiple-pode joint. Therefore a correspondence is demonstrated between the displacement equation of the pode joints and their kinematic graph structures. Furthermore, the result of this analytical investigation provides explicit expressions in terms of motion as well as design parameters and is essential for the understanding and formulation of the mechanics, and subsequently, the design of these joints.

Definitions

A pode joint, as used in this investigation, refers to any joint that has *raceways* (grooves or slots) parallel to its shaft axis and a *spider* or a *yoke* with radially and equally spaced *legs* as carriers of intermediate elements (such as spherical or cylindrical rollers, etc.) which remain perpendicular to the other shaft.

Pode joints that fit the preceding definition can be divided into two broad categories: (1) *End-motion* type pode joints, and (2) *fixed-end* or *tulip* type pode joints.

The end-motion type pode joint refers to the case where the carrier legs are fixed to the *moving shaft*, which is referred to as the *spider shaft*, and moving shaft means that the shaft axis can have both rotation and translation. The plane of the legs in this case is called the *spider plane*. An arbitrary plane perpendicular to the *fixed shaft axis* or *pot axis* is called the *pot plane*. The equally spaced raceways, therefore, are said to be on the *pot side* and they remain parallel to the pot axis.

In the fixed-end or tulip type pode joints, the legs are fixed to a *housing* and the plane of the legs is perpendicular to the fixed axis. The moving shaft, in this case, is referred to as the *tulip shaft* and its axis as the *tulip axis*. In this case, the plane of the legs is assumed to be fixed. The raceways are parallel to the tulip axis and they are said to be on the *tulip side*.

[1] Present address: Gonyeli-Nicosia, Mersin-10, Turkey.

Contributed by the Applied Mechanics Division for publication in the JOURNAL OF APPLIED MECHANICS.

Discussion on this paper should be addressed to the Editorial Department, ASME, United Engineering Center, 345 East 47th Street, New York, N. Y. 10017, and will be accepted until two months after final publication of the paper itself in the JOURNAL OF APPLIED MECHANICS. Manuscript received by ASME Applied Mechanics Division, January, 1983.

Copyright © 1984 by ASME
Downloaded 02 May 2010 to 171.66.16.25. Redistribution subject to ASME license or copyright; see http://www.asme.org/terms/Terms_Use.cfm

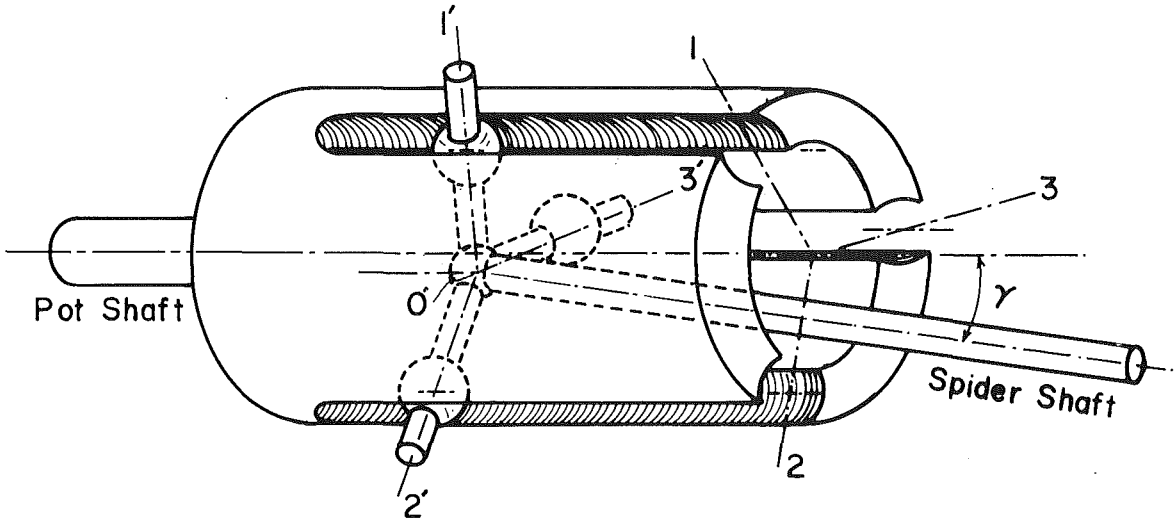

Fig. 1 Elements of a tripode joint with cylindrical raceways

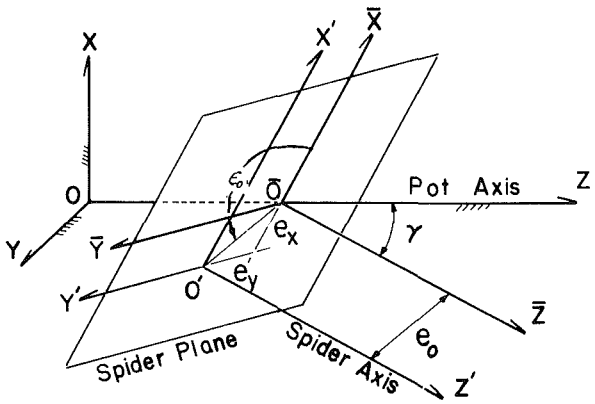

Fig. 2 Reference frames

Structurally, the fixed-end type joint can be thought of as a kinematic inversion of the end-motion type pode joint.

Yet another classification of pode joints can be made according to the number of raceways, legs, or intermediate elements present within the joint. For example, a pode-joint with three equally spaced raceways, three coplanar legs, and three rollers as intermediate members is called a tripode joint. In this classification, type or structure is disregarded.

For a better understanding of the displacement analysis some additional definitions are considered to be useful which are given in the following:

Coordinate Frames. The coordinate frames used in obtaining the displacement equations of several pode joints are shown in Fig. 2. In the case of end-motion type pode joints, the selection of these reference frames can be described as follows.

(*i*) The fixed frame X, Y, Z is chosen on the pot side where the Z-axis is the pot axis and the XY-plane is the pot plane.

(*ii*) The two moving frames are chosen on the spider side. The first one, denoted by X', Y', Z', has its origin at the spider center O'. The Z'-axis lies along the spider shaft axis, and the $X'Y'$-plane is the spider plane. Without losing generality, the Y'-axis is chosen parallel to the common perpendicular of the Z and the Z' axes. The second moving frame, denoted as $\bar{X}$, $\bar{Y}$, and $\bar{Z}$, has axes $\bar{X}$, $\bar{Y}$, and $\bar{Z}$ parallel to the X', Y', and Z' axes, respectively. Since the origin $\bar{O}$ is at the intersection of the spider plane and the Z-axis, $\bar{X}$ and $\bar{Y}$ axes lie in the spider plane.

In the fixed-end type joints, the Z-axis is chosen perpendicular to the plane of the legs at the intersection point of their axis, i.e., O. The Z'-axis is the tulip shaft axis and instead of a spider plane, a plane perpendicular to tulip axis is considered. Selection of O' and consequently $\bar{O}$, are arbitrary. Otherwise, the coordinate frames described in the foregoing equally apply to fixed-end type pode joints.

Spider Center, O'. In the case of the end-motion type pode joints, the intersection point of the axes of the legs is referred to as the spider center and it is denoted by O'. In the fixed-end type pode joints, this point is not uniquely defined. Therefore, in this case, O' refers to a point on the tulip-axis, which is chosen in the vicinity of the joint center, O.

Spider Rays. The radial centerline of each of the spider legs in the spider plane are called "spider rays." In Fig. 1, these are shown as 1′, 2′, and 3′ (end-motion type pode joints).

Pot Rays. The rays that intersect the centerlines of the grooves and the pot axis in the pot plane. In Fig. 1, these are shown as 1, 2, and 3 (end-motion type pode joints).

For the fixed-end type pode joints, considering an inverted case, similar definitions can be given.

Angular Offset, ϵ_0. The angular position of $\bar{O}O'$ in the positive sense of Z'-axis and from positive $\bar{X}$ axis is denoted as ϵ_0 and, referring to Fig. 2, it is given by

$$\tan(\pi-\epsilon_0)=\frac{e_y}{e_x}$$

Eccentricity, e_0. The radial offset distance between O' and the Z-axis in the moving plane (e.g., for end-motion type joints, the spider plane) is denoted as e_0 (Fig. 2).

Displacement Angle-Input, θ. The input displacement angle, θ, is measured in the positive sense of Z-axis and from positive X-axis to a pot ray (or in the tulip type to a leg axis) which is arbitrarily selected as ray number 1.

Displacement Angle-Output, ψ. Output displacement ψ is measured in the positive sense of the Z'-axis (moving axis) and from the positive X'-axis to a spider ray, which corresponds to the pot ray number 1, in the moving plane.

True Offset, ρ_0. The shortest distance from O' to the Z-axis is denoted by ρ_0 and given by

$$\rho_0=\sqrt{a_0^2+b_0^2}$$

where, a_0 and b_0 are the X and Y coordinates of O'.

Downloaded 02 May 2010 to 171.66.16.25. Redistribution subject to ASME license or copyright; see http://www.asme.org/terms/Terms_Use.cfm

Assumptions

The following assumptions apply to all pode joints.

(1) The centerline of each of the raceways remains parallel to and a constant radial distance (R or r) from their respective shaft axis (pot or tulip axis) and they are on mutually intersecting and equally spaced planes (say "slot planes").

(2) The carrier legs are equally spaced with a constant dividing angle ν and are coplanar, where the plane of the legs remains perpendicular to the moving shaft axis.

(3) The ball or roller centers must remain at a constant distance (R or r) from one of the shaft axis, i.e., constant pitch radius.

(4) In the case of shaft couplings involving pode joints, the length of the intermediate shaft (spider or tulip shaft), l, is assumed to be constant.

(5) Clearance between joints, elasticity, and deflection of links are not considered.

Basic Approach

In the study of spatial mechanisms, the most fundamental and dependable information usually comes from the displacement analysis. The input-output displacement equation provides information leading to the motion characteristics of the mechanism. Furthermore, in the cases where the general degree-of-freedom equation does not seem to be applicable, the displacement equation gives the only basis for a mobility analysis [4, 5]. In addition, displacement analysis offers physical insight which is helpful to the understanding and the design of the mechanism and is otherwise difficult to obtain.

The approach which is used in the derivation of displacement relations of pode joints, first involves a proper selection of coordinate frames – the moving as well as the fixed coordinates. Using these coordinates, the position and the locus of the geometric centers of the intermediate elements (spherical or cylindrical rollers, sliding blocks, etc.) on both the fixed and moving systems, therefore, can be analytically represented. Through coordinate transformations, displacement relationships between the input and output shafts and relationships for various components of the pode joint can then be obtained.

In the following, a general formulation of the displacement analysis is presented first. Then, based on these formulations the input-output displacement equations and equations for other variable parameters of four major types of pode joints are derived. From these general expressions and considering a specific number of raceways, displacement relations of several pode joints (up to six-pode joints) are obtained and the results are given. A comparative study of two-pode and tripode joints is presented. Finally, the results of the general derivations are applied to shaft couplings involving pode joints.

Displacement Analysis

Part 1 Pode Joints. Referring to Fig. 3, the parameters α, β, and γ are the angles of the spider (or tulip) shaft axis, Z', with respect to X, Y, and Z axes, respectively. In addition, let l_i, m_i, and n_i ($i = 1, 2, 3$) be the direction cosines of X', Y', and Z' with respect to X, Y, and Z axes (subscripts 1, 2, and 3 correspond to the axis X', Y', and Z', respectively). The orientation of the output shaft, i.e., the Z' axis can be described by two parameters, say γ and τ. The direction cosines l_i, m_i, and n_i can be represented as follows:

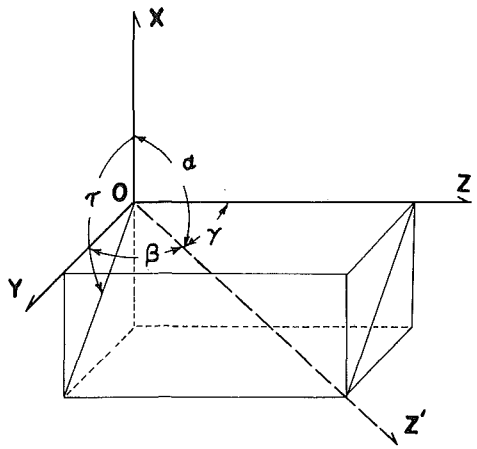

Fig. 3 Geometrical interpretation of the parameter, τ

$$\begin{bmatrix} l_1 & l_2 & l_3 \\ m_1 & m_2 & m_3 \\ n_1 & n_2 & n_3 \end{bmatrix} = \begin{bmatrix} -\cos\gamma\cos\tau & \sin\tau & \sin\gamma\cos\tau \\ -\cos\gamma\sin\tau & -\cos\tau & \sin\gamma\sin\tau \\ \sin\gamma & 0 & \cos\gamma \end{bmatrix} \quad (1)$$

For the coordinate transformation involving translation and rotation, we can write

$$\left.\begin{aligned} X' &= l_1(X-a_0)+m_1(Y-b_0)+n_1(Z-c_0) \\ Y' &= l_2(X-a_0)+m_2(Y-b_0)+n_2(Z-c_0) \\ Z' &= l_3(X-a_0)+m_3(Y-b_0)+n_3(Z-c_0) \end{aligned}\right\} \quad (2)$$

or

$$\left.\begin{aligned} X &= l_1X'+l_2Y'+l_3Z'+a_0 \\ Y &= m_1X'+m_2Y'+m_3Z'+b_0 \\ Z &= n_1X'+n_2Y'+n_3Z'+c_0 \end{aligned}\right\} \quad (3)$$

where l_i, m_i, and n_i ($i = 1, 2, 3$) are given in equation (1) and the origin O' of the X'-Y'-Z' system has coordinates (a_0, b_0, c_0) relative to X-Y-Z system.

Similarly, for the $\bar{X}$-$\bar{Y}$-$\bar{Z}$ system whose origin $\bar{O}$ has the coordinates (O, O, Z^*), we can write

$$\left.\begin{aligned} \bar{X} &= l_1X+m_1Y+n_1(Z-Z^*) \\ \bar{Y} &= l_2X+m_2Y+n_2(Z-Z^*) \\ \bar{Z} &= l_3X+m_3Y+n_3(Z-Z^*) \end{aligned}\right\} \quad (4)$$

Using equation (1) and the coordinate transformation between the two moving frames, relationships between a_0, b_0, e_x, and e_y can be found. These are given by

$$\left.\begin{aligned} e_x &= -(a_0\cos\tau+b_0\sin\tau)/\cos\gamma \\ e_y &= a_0\sin\tau-b_0\cos\tau \end{aligned}\right\} \quad (5)$$

or

Downloaded 02 May 2010 to 171.66.16.25. Redistribution subject to ASME license or copyright; see http://www.asme.org/terms/Terms_Use.cfm

$$\left.\begin{aligned} a_0 &= e_y \sin\tau - e_x \cos\gamma \cos\tau \\ b_0 &= e_y \cos\tau + e_x \cos\gamma \sin\tau \end{aligned}\right\} \quad (6)$$

where e_x and e_y represent the coordinates of point O' on the moving frame $\bar{X}$-$\bar{Y}$-$\bar{Z}$.

The Z-coordinate of the origin O', c_0, depends on the placement of the origin O along Z-axis. For a single pode joint c_0, therefore, can be considered as arbitrary.

Equations (1)–(6) provide the coordinate transformation for any point between the fixed and the moving frames. For a point on the $X'Y'$- or the $\bar{X}\bar{Y}$-plane, therefore we can write

$$\left.\begin{aligned} X' &= -\frac{(X\cos\tau + Y\sin\tau)}{\cos\tau} - e_x \\ Y' &= (X\sin\tau - Y\cos\tau) - e_y \end{aligned}\right\} \quad (7)$$

and letting $Z' = 0$,

$$Z - c_0 = -(X\cos\tau + Y\sin\tau)\tan\gamma - e_x \sin\gamma \quad (8)$$

Similarly, for points on the XY-plane, we have

$$\left.\begin{aligned} X &= -\frac{\cos\tau}{\cos\gamma}X' + \sin\tau\, Y' - c_0 \tan\gamma\cos\tau + a_0 \\ Y &= -\frac{\sin\tau}{\cos\gamma}X' - \cos\tau\, Y' - c_0 \tan\gamma\sin\tau + b_0 \end{aligned}\right\} \quad (9)$$

and from $Z = 0$

$$Z' = -X'\tan\gamma - \frac{c_0}{\cos\gamma} \quad (10)$$

To derive the input-output displacement relationships, the positions of spherical roller centers must be related to the rotations of the shafts, namely θ and ψ. The position of the ball centers can be written in polar notation as

$$\left.\begin{aligned} X_i &= R_i\cos\theta_i \\ Y_i &= R_i\sin\theta_i \\ Z_i &= Z_i \end{aligned}\right\} \quad i = 1, 2, \ldots, n \quad (11)$$

and

$$\left.\begin{aligned} X'_i &= r_i\cos\psi_i \\ Y'_i &= r_i\sin\psi_i \\ Z'_i &= Z_i \end{aligned}\right\} \quad i = 1, 2, \ldots, n \quad (12)$$

where n denotes the number of pots or raceways and, depending on the type of the pot joint in consideration, either R_i or r_i are constant.

Recalling the first two assumptions, for the angular position of each ball center, we can write

$$\left.\begin{aligned} \theta_i &= \theta + m\nu \\ \psi_i &= \psi + m\nu \end{aligned}\right\} \quad i = 1, 2, \ldots, n \quad (13)$$

where ν denotes the constant dividing angle ($\nu = 360$ deg/n), $m = i - 1$ is an integer ($m = 1, 2, \ldots, n-1$), and i denotes the particular ball center.

The general expressions developed so far apply to all pode joints. In the following, general displacement relations of pode joints according to the type is first presented. Then, displacement analysis for each of the pode joints considering both the type and the number of raceways are performed.

1 General Displacement Relations for n-Pode Joints. The displacement analysis can either be based on the number of raceways (slots or grooves) present within the joint or with respect to the type of pairing elements of the joint, such as R (revolute joint), C (cylindrical joint), E (plane joint), S_G (ball in cylinder or sphere-groove joint), and S_p (sphere-plane joint), etc. [2]. The latter approach provides some general expressions, which then can be reduced to obtain the specific input-output displacement relations for the individual case with specific number of raceways and, therefore, it is preferred.

1.1 Pode Joints With Cylindrical Raceways and Spherical Rollers ($S_G - C$ Pairs). Substituting equations (11)–(13) into equation (7), and eliminating the variable radii r_i, the general input-output displacement relations of an n-pode joint with cylindrical grooves become

$$\frac{R}{2}\frac{(1-\cos\gamma)}{\cos\gamma}(D\cos 2m\nu + E\sin 2m\nu) + \frac{(1+\cos\gamma)}{\cos\gamma}F = S\cos m\nu - T\sin m\nu \quad (14)$$

where m and ν are as defined in equation (13) and D, E, F, S, and T are given in Table 1.

Expression given by (14) provides n equations that can be solved for various parameters for a given pode joint, for instance two-pode ($\nu = 180$ deg) or tripode ($\nu = 120$ deg), etc.

Similarly, for the axial and radial relative displacements of the ball centers, using equations (5)–(8) and (11)–(13), we obtain

$$Z_i - c_0 = R\tan\gamma(A\cos m\nu - B\sin m\nu) - e_x\sin\gamma \quad (15)$$

and

$$r_i = -\frac{[R(A\sin m\nu + B\cos m\nu) + e_y]}{\sin(\psi + m\nu)} \quad (16)$$

where i refers to the particular roller center ($i = 1, 2, \ldots, n$).

The coordinates of the origin O' in $\bar{X}-\bar{Y}-\bar{Z}$ and $X-Y-Z$ systems are given in equations (5) and (6), respectively. These variable parameters (a_0, b_0, e_x, and e_y) can be determined from the n equations given by equation (14).

1.2 Pode Joints With Straight Raceways and Spherical Rollers ($S_p - R$) or (S_p) Pairs. In this case it is assumed that the distance between each ball center (r_i) and the moving origin (O') be constant, i.e., $r_i = r$, however, its distance from the fixed origin O (i.e., R_i) can be varied. Since the motion of the ball centers are again confined to the spider plane ($X'Y'$-plane), equations (7) and (8) can still be used. After substitutions and eliminating R_i, we obtain the input-output displacement relation for each of the carrier legs. These n equations can be expressed in the following form:

$$\frac{r}{2}(1-\cos\gamma)(D\cos 2m\nu + E\sin 2m\nu) + (1+\cos\gamma)F = U\sin m\nu - V\cos m\nu \quad (17)$$

where D, E, F, U, and V are given in Table 1.

The relative axial displacement for each of the ball centers, equation (15) remains to be the same, except, in this case R is to be replaced by R_i.

The radial displacement, however, is with respect to the fixed axis, Z. A general expression for each of the ball centers, in this case, becomes

Downloaded 02 May 2010 to 171.66.16.25. Redistribution subject to ASME license or copyright; see http://www.asme.org/terms/Terms_Use.cfm

Table 1 Coefficients for general displacement relations of pode joints

$A=\cos\tau\cos\theta+\sin\tau\sin\theta$
$B=\cos\tau\sin\theta-\sin\tau\cos\theta$
$D=A\sin\psi+B\sin\psi$
$E=A\cos\psi-B\sin\psi$
$F=A\sin\psi-B\cos\psi$
$G=A\cos\psi+B\sin\psi$

and

$S=e_y\cos\psi-e_x\sin\psi$
$T=e_y\sin\psi+e_x\cos\psi$
$U=B\,e_y+A\,e_x\cos\gamma$
$V=A\,e_y-B\,e_x\cos\gamma$

$$R_i=-\frac{r\sin(\psi+m\nu)+e_y}{A\sin m\nu+B\cos m\nu} \tag{18}$$

For the coordinates of O', equations (5) and (6) are still valid.

1.3 Pode Joints With Straight Raceways and (C_P-R) or $(E-R)$ Pairs. The general expressions for these cases are identical to the previous case of the (S_P-R) pairs. In these joints, however, there are more constraints imposed on the rotational degrees of freedom. This is because each of the radially positioned axes of the spider legs has to stay in their respective planes which are referred to as the slot planes.

1.4 The Tulip Type Pode Joints With Cylindrical Grooves and Spherical Rollers $(C-S_G)$ Pairs. In these joints, the distance from the tulip center (O') to the ball centers, r, remains invariant, i.e., constant pitch radius. The plane of the legs is taken to be the XY-plane, therefore, equations (9) and (10) are used for point transformations.

The general input-output displacement relations for a n-pode joint can be derived as follows, referring to Table 1,

$$\frac{r}{2}\frac{(1-\cos\gamma)}{\cos\gamma}(D\cos 2m\nu+E\sin 2m\nu)-\frac{(1+\cos\gamma)}{\cos\gamma}F = U\sin m\nu-V\cos m\nu + c_0\tan\gamma(A\sin m\nu+B\cos m\nu) \tag{19}$$

The axial relative motion of the ball centers along the tulip axis (i.e., the Z'-axis) is given by

$$Z'_i=-r\tan\gamma\cos(\psi+m\nu)-c_0/\cos\gamma \tag{20}$$

For the radial displacement of the ball centers with respect to the fixed axis (i.e., the Z-axis), we can write

$$R_i=\frac{r}{2}\frac{(1-\cos\gamma)}{\cos\gamma}(D\sin 2m\nu-E\cos 2m\nu)-\frac{(1+\cos\gamma)}{\cos\gamma}G - (U\cos m\nu+V\sin m\nu) - c_0\tan\gamma(A\cos m\nu-B\sin m\nu) \tag{21}$$

The preceding four cases cover most of the pode joints having constant pitch radius. The treatment of the straight slot situations in the tulip type pode joints, however, are omitted. This is because in these joints, the controlling of the interference between the housing and the tulip may have some practical problems. A general treatment of the displacement analysis of these joints, nevertheless, follows essentially a similar approach as the previous cases.

2 A Summary of the Motion Characteristics of Pode Joints. The displacement relations for each type of pode joint (up to six-pode joints) with a specific number of raceways, can be reduced from the general expressions given in the last section. The results of these analyses are summarized in Table 2. In the following, some notable observations on the motion characteristics of multiple-pode joints are presented.

(1) In two-pode joints, the eccentricity, e_0, is arbitrary. Therefore, in the intersecting shaft problem, the eccentricity related parameters, i.e., a_0, b_0, e_x, e_y, and e_0 can all be set to zero.

(2) The input-output displacement characteristics of the tulip type two-pode (Case *I-iii*) and the other two cases of two-pode joints [(*i*) and (*ii*)] are similar, except there is a 90 deg phase angle difference.

(3) Tripode joints cannot be used in the fixed joint angle (γ) application.

(4) The tripode jont with cylindrical slots has a smaller orbital radius (or eccentricity) as compared with other types of tripodes. This can be seen from a comparison of the orbital motion characteristics shown in Table 2. The cylindrical slot case, therefore, appears to have better motion characteristics than the other types of tripodes.

(5) It is found that the four, five, and six-pode joints cannot operate in angled shaft positions (Table 2).

THEROEM: *The pode joint with more than three podes and with constant pitch radius cannot be used for coupling two shafts at angled positions.*

3 A Comparative Study on the Motion Characteristics of Two-Pode and Tripode Joints. In an attempt to answer the question of why the evolution of two-pode to tripode joint gives rise to a nearly CV transmission, a comparative study on the motion characteristics of the two joints must be performed. First, a comparative basis should be established for the input-output displacement equations of the two-pode and the tripode joints. For the tripode joint from equations (26) and (57), we have

$$\tan\psi=\left(1+2\frac{e_0}{R}\right)\cos\gamma\frac{B}{A} \tag{69}$$

For the two-pode case, the input-output expression is,

$$\tan\psi=\cos\gamma\frac{B}{A} \tag{70}$$

A comparison of equations (69) and (70) implies that the improved motion characteristics of the tripode are due to the inherent obital motion.

Furthermore, let us examine other motion characteristics, such as the maximum radial displacements of two-pode and tripode cases (considering a two-pode application without eccentricity), from equations (38) and (42), respectively, we have

$$r_{\max}=\frac{R}{\cos\gamma}\quad\text{(two-pode)} \tag{71}$$

and

$$r_{\max}=\frac{R}{\cos\gamma}\frac{(3-\cos\gamma)}{2}\quad\text{(tripode)} \tag{72}$$

Also, for the axial strokes of the balls, from equations (46) and (49), respectively, we obtain,

$$(Z_i-c_0)_{\max}=R\tan\gamma\quad\text{(two-pode)} \tag{73}$$

and

$$(Z_i-c_0)_{\max}=R\tan\gamma\frac{(3-\cos\gamma)}{2}\quad\text{(tripode)} \tag{74}$$

From equations (71)-(74) it is concluded that the use of three equally spaced podes, rather than two, increases both the radial and axial displacements by the same factor, σ,

$$\sigma_r=\sigma_z=\sigma=\frac{3-\cos\gamma}{2} \tag{75}$$

Downloaded 02 May 2010 to 171.66.16.25. Redistribution subject to ASME license or copyright; see http://www.asme.org/terms/Terms_Use.cfm

Table 2 Displacement relations of various pode joints

Joint name and type		Input-output displacement equation	equation no.	Relative radial displacement equation	equation no.
I. Two-pode joints ($n=2$, $\nu=180$ deg)					
(*i*) End-motion type with cylindrical raceways	(*a*)	General[1]: $\psi=\tan^{-1}(f_1\cos\gamma)$	(22)	$r_i = \dfrac{-(RB\cos m\nu+e_y)}{\sin(\psi+m\nu)}$	(38)
	(*b*)	Special[2]: $\psi=\tan^{-1}(\cos\gamma\tan\theta)$	(23)		
(*ii*) With straight raceways				$R_i = -\dfrac{r\sin(\psi+m\nu)+e_y}{B\cos m\nu}$	(39)
(*iii*) Tulip type with cylindrical raceways	(*a*)	General: $\psi=\tan^{-1}(f_1/\cos\gamma)$	(24)	$R_i = \dfrac{f_2 r\cos m\nu}{\sin\gamma\cos\gamma\sin(\theta+m\nu)}$	(40)
	(*b*)	Special: $\psi=\tan^{-1}(\tan\theta/\cos\gamma)$	(25)	$R_i = \dfrac{r\cos m\nu\sin\psi}{\sin(\theta+m\nu)}$	(41)
II. Tripode joints ($n=3$, $\nu=120$ deg)					
(*i*) End-motion type with cylindrical raceways	(*a*)	General: $\psi=\tan^{-1}(f_1)$	(26)	$r_i = \dfrac{R}{2}\left[\dfrac{1+\cos\gamma}{\cos\gamma} + 2\dfrac{(1-\cos\gamma)}{\cos\gamma}\cos 2(\psi+m\nu)\right]$	(42)
(*ii*) With straight raceways	(*b*)	Special: $\psi=\theta$	(27)	$R_i = \dfrac{r}{2}[(1+\cos\gamma) - 2(1-\cos\gamma)\cos 2(\psi+m\nu)]$	(43)
(*iii*) Tulip type with cylindrical raceways	(*a*)	General: $\psi=\tan^{-1}(f_1)$	(28)	$R_i = \dfrac{r}{2}\left[\dfrac{(1+\cos\gamma)}{\cos\gamma} + 2\dfrac{(1-\cos\gamma)}{\cos\gamma}\cos 2(\psi+m\nu)\right] + c_0\tan\psi\cos(\psi+m\nu)$	(44)
	(*b*)	Special: $\psi=\theta$	(29)		
III. Four-pode joints ($n=4$, $\nu=90°$) All types		$\tan\psi=f_1\cos\gamma$	(30)		
	and	$\tan\psi=f_1/\cos\gamma$	(31)		
	or	$\sin^2\gamma=0$	(32)		
IV. Five-pode joints ($n=5$, $\nu=72°$) All Types		$\cos\gamma=1$	(33)		
	or	$\cos\gamma=\dfrac{3-2\cos^2\psi}{1+2\cos^2\psi}$	(34)	${}^3r_i$ = constant	(45)
V. Six-pode joints ($n=6$, $\nu=60°$) All types		$\tan\psi=f_1$	(35)		
		$\tan\psi=f_1\cos\gamma$	(36)		
	or	$\cos\gamma=1$	(37)		

[1] General refers to arbitrary shaft positions defined by α, β, and γ.
[2] Special refers to fixed joints angle (γ) situation, i.e., $\beta=90$ deg.
Note 1: $i=1, 2, n$ and $m=i-1$.
Note 2: $A=\cos\alpha\cos\theta+\cos\beta\sin\theta$.
$B=\cos\alpha\sin\theta-\cos\beta\cos\theta$
$f_1=B/A$
$f_2=\cos\beta\cos\psi+\cos\alpha\cos\gamma\sin\psi$
[3] For most practical purposes, these radial displacements are assumed to be constant.

The comparison of other types of two-pode and tripode joints can be achieved in a similar way which would yield the same factor, σ, where in the tulip type of tripode joints, the minor contribution due to the term involving c_0 (equation (44)) is assumed to be negligible.

Based on the foregoing analysis, the following observations can be made:

(1) The extreme values of the radial and the axial displacements of the tripode joints are greater than the corresponding values of the two-pode and they all differ by a factor of σ. This factor increases with increasing joint angle (γ) assuming both joints have the same pitch radius (either R or r).

(2) It can be interpreted that from the evolution of the two-pode to the tripode, the speed fluctuations present at the two-pode on the output shaft are "distributed" into the radial and axial directions of the tripode. The increases of the displacement along these directions, therefore, can be explained by the orbital motion inherent to tripode joints, which helps the reduction of speed fluctuation.

(3) The results of the analytical study given in the foregoing imply that the factor σ may have a physical significance which could be a subject for further investigation.

Part 2 Compound Coupling. Having developed the input-output displacement equation for each individual pode joint of various types, we are now interested in the realistic case of combining these joints, perhaps with other CV joints as compound joints for shaft coupling. The tripode joint, for instance, cannot function alone [3]. Therefore, the study

Downloaded 02 May 2010 to 171.66.16.25. Redistribution subject to ASME license or copyright; see http://www.asme.org/terms/Terms_Use.cfm

Table 2 (Continued)

Joint name and type	Relative axial displacement equation	equation no.	Relations for orbital parameters	equation no.
I. Two-pode joints ($n=2$, $\nu=180$ deg)				
(*ii*) End-motion type with cylindrical raceways	$Z_i - c_0 = -RA\tan\gamma\cos m\nu - e_x\sin\gamma$	(46)	$\frac{b_0}{a_0} = \tan\theta$	
(*ii*) With straight raceways	$Z_i - c_0 = -R_i A\tan\gamma\cos m\nu - e_x\sin\gamma$	(47)	$\frac{e_y}{e_x} = \tan\psi \quad e_0 \neq 0$	(53)
(*iii*) Tulip type with cylindrical raceways	$Z_i = -r\tan\gamma\cos(\psi+m\nu) - c_0/\cos\gamma$	(48)	$a_0\sin\theta - b_0\cos\theta = c_0 B\tan\gamma$ $e_x = -\frac{a_0\cos\alpha + b_0\cos\beta}{\sin\gamma\cos\gamma}$ $e_y = \frac{a_0\cos\beta - b_0\cos\alpha}{\sin\gamma}$	(54) (55) (56)
II. Tripode Joints ($n=3$, $\nu=120°$) (*i*) End-motion type with cylindrical raceways	$Z_i - c_0 = \frac{R}{2}\tan\gamma[2\cos(\psi+m\nu) + (1-\cos\gamma)\cos 3\psi]$	(49)	$e_0 = \frac{R}{2}\frac{(1-\cos\gamma)}{\cos\gamma}$ $\epsilon = 3\psi + \pi$, $\rho_0 = e_0(\sin^2 3\psi + \cos^2\gamma\cos^2 3\psi)$	(57) (58)
(*ii*) With straight raceways	$Z_i - c_0 = R_i\tan\gamma\cos(\psi+m\nu) + \frac{r}{2}(1-\cos\gamma)\tan\gamma\cos 3\psi$	(50)	$a_0 = -\frac{r}{2}(1-\cos\gamma)\cos(2\psi+\theta)$ $b_0 = -\frac{r}{2}(1-\cos\gamma)\sin(2\psi+\theta)$ $e_x = -\frac{r}{2}\frac{(1-\cos\gamma)}{\cos\gamma}\cos 3\psi$ $e_y = -\frac{r}{2}(1-\cos\gamma)\sin 3\psi$	(59) (60) (61) (62)
(*iii*) Tulip type tripode with cylindrical raceways	$Z_i = -\frac{r}{2}\tan\gamma[2\cos(\psi+m\nu) + (1-\cos\gamma)\cos 3\psi]$	(51)	$^5a_0 = \rho(\cos^2\gamma\cos\Delta\cos 3\psi - \sin\Delta\sin 3\psi)$ $b_0 = \rho(\cos^2\gamma\sin\Delta\cos 3\psi + \cos\Delta\sin 3\psi)$ $e_x = \frac{r}{2}[(1-\cos\gamma)\cos 3\psi - c_0\sin\gamma]/\cos^2\gamma$ $e_y = -\frac{r}{2}\frac{(1-\cos\gamma)}{\cos\gamma}\sin 3\psi$	(63) (64) (65) (66)
III. Four-Pode Joints ($n=4$, $\nu=90$ deg) All types			$e_x\sin\psi = e_y\cos\psi$	(67)
IV. Five-Pode Joints ($n=5$, $\nu=72°$)	$^4Z_i = c_0$	(52)	and $e_y\cos\psi = -e_y\sin\psi$	(68)
V. Six-Pode Joints ($n=6$, $\nu=60$ deg) All types			or $a_0 = b_0 = e_x = e_y = e_0 = 0$	

[4]In four, five, and six-pode joints axial displacement is possible only for $\gamma = 0$ cases, where c_0 refers to the axial position of O'.
[5]$\Delta = \phi - \psi$; $\rho_0 = (r/2)(1-\cos\gamma)/\cos\gamma$; $c_0 = 0$.

presented in this section would provide us with the basic formulations that are needed for function as well as structure analysis of these couplings. The displacement analysis of the tripode-Rzeppa combination have been reported [2]. In the following, the two-pode-two-pode and tripode-tripode combinations are investigated.

1 Displacement Relations for the Two-Pode-Two-Pode Shaft Coupling. As an illustration, we consider the combination of an end-motion type and a fixed-motion (tulip) type two-pode couplings, with cylindrical raceways and spherical rollers.

Letting γ_1 be the operating angle for the first pode joint, and α_2, β_2, and γ_2 denote the direction angles of the output shaft with respect to X', Y' and Z' axes of the moving frame, respectively, and assuming intersecting shaft situations, we have, for the end-motion type, from equation (23)

$$\tan\psi_1 = \cos\gamma_1\tan\theta_1 \tag{76}$$

and for the tulip type, from equation (24)

$$\tan\psi_2 = \frac{1}{\cos\gamma_2}\frac{(\cos\alpha_2\sin\theta_2 - \cos\beta_2\cos\theta_2)}{(\cos\alpha_2\cos\theta_2 + \cos\beta_2\sin\theta_2)} \tag{77}$$

Downloaded 02 May 2010 to 171.66.16.25. Redistribution subject to ASME license or copyright; see http://www.asme.org/terms/Terms_Use.cfm

where θ_1 and θ_2 denote the input and output shaft angular displacements, respectively, and ψ_1 and ψ_2 both refer to the spider shaft angular displacement. Depending on the connection, therefore, the angular displacements can be either $\psi_1 = \psi_2$ or $\psi_1 = -\psi_2$ or, with a 90 deg phasing, $\psi_2 = 90 \pm \psi_1$ are taken.

Substituting ψ_2 and θ_2 for the case of 90 deg phasing, and equating, after simplification, the input-output displacement equation of the system becomes

$$\tan \theta_2 = \frac{k_1 + k_2 \tan \theta_1}{1 - k_1 k_2 \tan \theta_1} \tag{78}$$

where,

$$\left.\begin{aligned} k_1 &= \cos\beta_2 / \cos\alpha_2 \\ k_2 &= \cos\gamma_1 / \cos\gamma_2 \end{aligned}\right\} \tag{79}$$

When input and output shafts are parallel, operating angles γ_1 and γ_2 become equal and β can be set to a right angle, therefore, a CV transmission is obtained. Otherwise, even at the same operating angles, when the shafts are not parallel, CV transmission is not possible.

For the other two-pode-two-pode combinations, similar expressions can be obtained. The combination of any of these two-pode joints with a CV joint (e.g., Rzeppa or Birfield joint) does not provide a CV transmission.

In this general treatment, the direction angles are arbitrarily selected, for specific applications, the values of these angles can be related to or determined by the mechanism proportions. Otherwise, they can be considered as a part of design specifications.

2 Displacement Relations for the Tripode-Tripode Shaft Coupling. Possible combinations of a tripode-tripode shaft coupling must employ one end-motion and one fixed-end type of tripode joints and this combination has been used in some recent foreign compact front-wheel drive vehicles. As an illustration, the combination of the type with cylindrical raceways and spherical rollers is considered.

Letting the direction angles of the spider shaft with respect to the fixed coordinate X, Y, and Z be denoted as α_1, β_1, and γ_1, and the direction angles of the output shaft with respect to the moving coordinates X', Y', and Z' be denoted as α_2, β_2, and γ_2, respectively, then from equations (26) and (28), we have

$$\tan \psi_i = \frac{\cos \alpha_i \sin \theta_i - \cos \beta_i \cos \theta_i}{\cos \alpha_i \cos \theta_i + \cos \beta_i \sin \theta_i}, \quad i = 1, 2. \tag{80}$$

Depending on the kind of arrangement, being face-to-face or back-to-back, the angular displacements of the spider shaft can be either $\psi_2 = -\psi_1$ or $\psi_2 = \psi_1$, respectively. As before, θ_1 and θ_2 denote the input and output angular displacements.

We have from equation (80)

$$\tan(\theta_1 - \theta_2) = s/t \tag{81}$$

where

$$\left.\begin{aligned} s &= \cos \beta_1 \cos \alpha_2 - \cos \alpha_1 \cos \beta_2 \\ t &= \cos \alpha_1 \cos \alpha_2 + \cos \beta_1 \cos \beta_2 \end{aligned}\right\} \tag{82}$$

Noting that when $\psi_2 = -\psi_1$, the negative and positive signs of the expressions of s and t are reversed.

From equation (81), the input-output displacement equation is

$$\tan \theta_2 = \frac{\tan \theta_1 - s/t}{1 + (s/t) \tan \theta_1} \tag{83}$$

When the input and output shafts are parallel, $\cos \beta_1$ and $\cos \beta_2$ become zero, therefore, $\theta_2 = \theta_1$, and a CV transmission is achieved. Also, for $\gamma_1 = \gamma_2$, even when the shafts are not parallel, CV transmission will be possible.

In general, the operating angles for each joint are to be specified. Then the remaining parameters are determined from the mechanism proportions.

The analysis of yet another type of common combination in practice, the tripode-Rzeppa coupling has been performed [2]. It was concluded in [2, 3] that the combination of any tripode joint with another CV joint does not provide a true CV transmission. However, in low angle applications, variations are generally very small, and can be considered as an approximate CV coupling [2].

Conclusions

Possibly the most significant contribution of this investigation is the development of an analytical method on the displacement analysis of a class of complicated spatial mechanical components. Unlike most spatial mechanisms studied on the record, which are usually of the linkage-type involving familiar joints such as revolute, cylindrical joints, etc., the pode joints involve a large number of unconventional joints that have relative motions and generally do not have their linkage-equivalents. Therefore, the pode joint is difficult to analyze. The results of this investigation also provide much information on the motion characteristics of pode joints. One of the most interesting findings is on the comparative study of the motion characteristics of the two-pode and tripode joints, which offers much physical insight. Another important conclusion was reached in the form of a theorem concerning the pode joints with four or more raceways. The result of this investigation indicates that the tripode joint is best suited to angled shaft applications among all the other pode joints. Furthermore, it illustrates, in the case of the pode joints, the correspondence between the displacement equation and mobility, and therefore, demonstrates that the displacement analysis offers a basis for the mobility analysis as well as the development of motion characteristics of a mechanism. The analytical method presented here can lend itself to further development, for instance, involving the dual-number elements in (3×3) matrices [5], and application to the displacement analysis of other spatial mechanical components and mechanisms of realistic complexity.

Acknowledgments

The authors are grateful to the National Science Foundation for the support of this research through grant MEA-80-06783-03 to Rutgers University.

References

1 Zock, A. E., "Flexible Joint for Shafts," U.S. Patent No. 981, 736, Jan. 17, 1911.

2 Akbil, E., "Kinematic Synthesis of Spatial Mechanisms with Prescribed Entire-Motion Characteristics," Doctoral dissertation, School of Engineering, Rutgers University, Oct. 1982.

3 Akbil, E., and Lee, T. W., "Kinematic Structure and Functional Analysis of Shaft Couplings Involving Pode Joints," ASME *Journal of Mechanisms, Transmissions, and Automation in Design*, to appear.

4 Wallace, D. M., and Freudenstein, F., "Displacement Analysis of the Generalized Clemens Coupling, the *R-R-S-R-R*, Spatial Linkage," ASME *Journal of Engineering for Industry*, May 1975, pp. 575-580.

5 Yang, A. T., "Displacement Analysis of Spatial Five-Link Mechanisms Using (3×3) Matrices With Dual-Number Elements," ASME *Journal of Engineering for Industry*, Feb. 1969, pp. 152-157.

Downloaded 02 May 2010 to 171.66.16.25. Redistribution subject to ASME license or copyright; see http://www.asme.org/terms/Terms_Use.cfm

Journal of Applied Mechanics

Design Data and Methods

Vibration Frequencies of Tapered Bars With End Mass

J. H. Lau[1]

Introduction

In references [1-2], useful results have been presented by Conway, Dubil, and Becker for the first five transverse vibrational resonant frequencies of truncated-cone beams having various combinations of classical boundary conditions (free, clamped, and simply supported). Recently, considerable effort has been directed toward the evaluation of the natural frequencies of tapered beams with nonclassical boundary conditions such as spring and end mass, e.g., references [3-5]. A detailed literature review of this subject has been given by Downs [6].

In the present paper, Conway's results for a cantilever beam are extended to include a concentrated mass at the free end. Numerical values for the first five eigenfrequencies are presented in tabular form for a wide range of values of the beam dimensions and the concentrated mass. The results provided herein may be applied to beams with solid or hollow rectangular and circular cross sections.

Analysis

The partial differential equation governing the motion for small-amplitude, free transverse vibrations of the beam shown in Fig. 1 is

$$[EI(x)v'']'' + m(x)\ddot{v} = 0 \tag{1}$$

where E is Young's modulus, I is the moment of inertia, v is the deflection, m is the mass per unit length of the beam, $(')$ $= \partial/\partial x$ and $(\dot{})$ $= \partial/\partial t$.

The boundary conditions are as follows:

At $x = L_0$

$$v'' = 0; (EI(x)v'')' = -M\ddot{v} \tag{2}$$

At $x = L_1$

$$v = 0; v' = 0, \tag{3}$$

where M is the concentrated mass.

Using the standard method of separation of variables one assumes

$$v(x,t) = V(x)T(t), \tag{4}$$

then equation (1) leads to two ordinary differential equations,

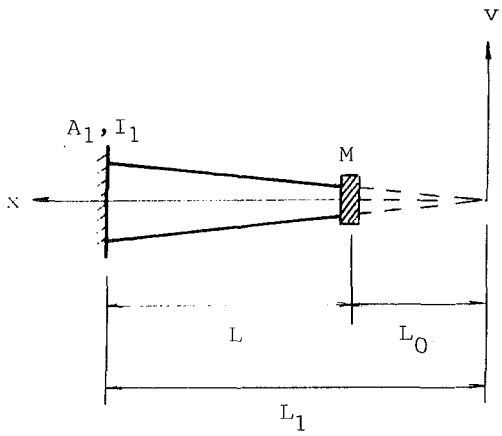

Fig. 1 Tapered beam with end mass

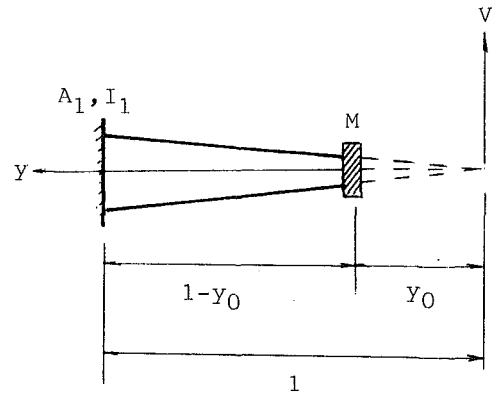

Fig. 2 Dimensionless coordinate for tapered beam

$$\ddot{T} + p^2 T = 0 \tag{5}$$

and

$$[EI(x)V'']'' - m(x)p^2 V = 0. \tag{6}$$

The boundary conditions become

At $x = L_0$

$$V'' = 0; [EI(x)V'']' = p^2 MV \tag{7}$$

At $x = L_1$

$$V = 0; V' = 0, \tag{8}$$

where p is the circular frequency of vibration.

For the structural system under consideration (Fig. 1)

[1] MTS, Sandia National Laboratories, Alburquerque, N. Mex. 87185. Formerly, Bechtel Power Corporation, San Francisco Calif. 94119. Manuscript received by ASME Applied Mechanics Division, January, 1983.

Copyright © 1984 by ASME
Downloaded 02 May 2010 to 171.66.16.25. Redistribution subject to ASME license or copyright; see http://www.asme.org/terms/Terms_Use.cfm

Table 1 Values of Q for $\bar{M}=0$

	Mode				
y_0	1	2	3	4	5
0.1	2.68419	4.32206	6.09293	7.96900	9.90786
0.2	2.48926	4.28783	6.31139	8.44048	10.62205
0.3	2.34718	4.31754	6.54297	8.86120	11.22275
0.4	2.23809	4.36633	6.76301	9.23817	11.74885
0.5	2.15062	4.42127	6.96986	9.58190	12.22252
0.6	2.07817	4.47772	7.16482	9.89975	12.65692
0.7	2.01666	4.53382	7.34950	10.19682	13.06052
0.8	1.96345	4.58876	7.52531	10.47678	13.43915
0.9	1.91669	4.64222	7.69341	10.74233	13.79699
1.0	1.87510	4.69409	7.85476	10.99554	14.13717

Table 2 Values of Q for $\bar{M}=0.2$

	Mode				
y_0	1	2	3	4	5
0.1	1.10212	3.15637	5.11296	7.10001	9.10876
0.2	1.29695	3.31638	5.45913	7.65757	9.88171
0.3	1.41336	3.46089	5.75049	8.11207	10.50084
0.4	1.48992	3.59643	6.01266	8.51076	11.03690
0.5	1.54127	3.72491	6.25635	8.87359	11.51935
0.6	1.57524	3.84671	6.48690	9.21107	11.96382
0.7	1.59681	3.96180	6.70713	9.52936	12.37965
0.8	1.60936	4.07015	6.91860	9.83234	12.77289
0.9	1.61530	4.17182	7.12218	10.12251	13.14762
1.0	1.61640	4.26706	7.31837	10.40156	13.50670

Table 3 Values of Q for $\bar{M}=0.4$

	Mode				
y_0	1	2	3	4	5
0.1	0.92869	3.15207	5.11131	7.09909	9.10815
0.2	1.09856	3.30136	5.45278	7.65382	9.87911
0.3	1.20610	3.43098	5.73653	8.10341	10.49466
0.4	1.28282	3.54948	5.98853	8.49516	11.02548
0.5	1.34001	3.66057	6.22005	8.84917	11.50105
0.6	1.38332	3.76604	6.43711	9.17624	11.93714
0.7	1.41618	3.86680	6.64329	9.48294	12.34332
0.8	1.44093	3.96331	6.84085	9.77360	12.72590
0.9	1.45924	4.05581	7.03125	10.05118	13.08929
1.0	1.47241	4.14443	7.21549	10.31781	13.43668

Table 4 Values of Q for $\bar{M}=0.6$

	Mode				
y_0	1	2	3	4	5
0.1	0.83974	3.15064	5.11076	7.09879	9.10795
0.2	0.99509	3.29631	5.45065	7.65256	9.87824
0.3	1.09534	3.42067	5.73179	8.10049	10.49259
0.4	1.16882	3.53275	5.98021	8.48985	11.02160
0.5	1.22551	3.63669	6.20725	8.84072	11.49478
0.6	1.27031	3.73472	6.41907	9.16396	11.92787
0.7	1.30608	3.82810	6.61942	9.46622	12.33047
0.8	1.33471	3.91761	6.81076	9.75189	12.70895
0.9	1.35757	4.00369	6.99473	10.02406	13.06777
1.0	1.37567	4.08665	7.17252	10.28498	13.41021

Table 5 Values of Q for $\bar{M}=0.8$

	Mode				
y_0	1	2	3	4	5
0.1	0.78174	3.14993	5.11048	7.09864	9.10785
0.2	0.92717	3.29377	5.44958	7.65193	9.87781
0.3	1.02193	3.41545	5.72941	8.09903	10.49154
0.4	1.09233	3.52417	5.97599	8.48716	11.01966
0.5	1.14759	3.62425	6.20071	8.83643	11.49161
0.6	1.19217	3.71808	6.40976	9.15769	11.92316
0.7	1.22867	3.80712	6.60695	9.45760	12.32390
0.8	1.25876	3.89227	6.79480	9.74059	12.70022
0.9	1.28360	3.97412	6.97506	10.00979	13.05659
1.0	1.30409	4.05308	7.14898	10.26749	13.39631

Table 6 Values of Q for $\bar{M}=1.0$

	Mode				
y_0	1	2	3	4	5
0.1	0.73947	3.14950	5.11032	7.09854	9.10779
0.2	0.87751	3.29225	5.44894	7.65155	9.87755
0.3	0.96797	3.41230	5.72798	8.09815	10.49092
0.4	1.03572	3.51895	5.97345	8.48555	11.01848
0.5	1.08945	3.61661	6.19674	8.83384	11.48970
0.6	1.13335	3.70777	6.40407	9.15389	11.92031
0.7	1.16983	3.79396	6.59928	9.45234	12.31991
0.8	1.20042	3.87617	6.78492	9.73366	12.69489
0.9	1.22619	3.95507	6.96277	10.00099	13.04974
1.0	1.24792	4.03114	7.13413	10.25662	13.38776

Table 7 Values of Q for $\bar{M}=3.0$

	Mode				
y_0	1	2	3	4	5
0.1	0.56219	3.14836	5.10988	7.09830	9.10763
0.2	0.66808	3.28818	5.44723	7.65054	9.87685
0.3	0.73854	3.40382	5.72413	8.09579	10.48924
0.4	0.79247	3.50478	5.96659	8.48121	11.01534
0.5	0.83643	3.59561	6.18599	8.82686	11.48456
0.6	0.87359	3.67898	6.38855	9.14358	11.91262
0.7	0.90570	3.75657	6.57814	9.43802	12.30910
0.8	0.93389	3.82956	6.75736	9.71464	12.68037
0.9	0.95889	3.89876	6.92806	9.97659	13.03093
1.0	0.98123	3.96482	7.09160	10.22621	13.36409

Table 8 Values of Q for $\bar{M}=5.0$

	Mode				
y_0	1	2	3	4	5
0.1	0.49484	3.14813	5.10979	7.09825	9.10760
0.2	0.58822	3.28736	5.44688	7.65034	9.87671
0.3	0.65054	3.40212	5.72336	8.09532	10.48891
0.4	0.69844	3.50190	5.96521	8.48034	11.01471
0.5	0.73771	3.59130	6.18381	8.82546	11.48353
0.6	0.77113	3.67299	6.38538	9.14149	11.91107
0.7	0.80024	3.74867	6.57379	9.43510	12.30690
0.8	0.82603	3.81953	6.75163	9.71073	12.67741
0.9	0.84913	3.88642	6.92076	9.97155	13.02707
1.0	0.87002	3.94998	7.08254	10.21986	13.35920

$$A(x) = \left(\frac{x}{L_1}\right)^2 A_1;$$

$$I(x) = \left(\frac{x}{L_1}\right)^4 I_1, \tag{9}$$

where A_1 and I_1 are, respectively, the cross-sectional area and moment of inertia at $x = L_1$. It is convenient to introduce a new variable y defined by (Fig. 2)

$$y = \frac{x}{L_1} \tag{10}$$

Then equations (6)–(8) become

$$\frac{1}{y^2}\frac{d^2}{dy^2}\left(y^4\frac{d^2V}{dy^2}\right) - q^4V = 0 \tag{11}$$

At $y = y_0 = L_0/L_1$

$$\frac{d^2V}{dy^2} = 0;\ \frac{d}{dy}\left(y^4\frac{d^2V}{dy^2}\right) = \bar{M}q^4(1-y_0)V \tag{12}$$

At $y = 1$

$$V = 0;\ \frac{dV}{dy} = 0, \tag{13}$$

where

$$q^4 = \rho A_1 L_1^4 p^2/EI_1 \tag{14}$$

and

$$\bar{M} = M/\rho A_1 L \tag{15}$$

ρ is the mass density of the beam.

The general solution to equation (11) is

Downloaded 02 May 2010 to 171.66.16.25. Redistribution subject to ASME license or copyright; see http://www.asme.org/terms/Terms_Use.cfm

Table 9 Values of Q for $\bar{M}=0$

	Mode				
y_0	1	2	3	4	5
0.1	0.45494	3.14804	5.10975	7.09823	9.10758
0.2	0.54085	3.28702	5.44673	7.65025	9.87665
0.3	0.59827	3.40138	5.72303	8.09511	10.48876
0.4	0.64248	3.50066	5.96462	8.47997	11.01444
0.5	0.67882	3.58944	6.18287	8.82485	11.48308
0.6	0.70982	3.67040	6.38401	9.14059	11.91040
0.7	0.73693	3.74524	6.57191	9.43384	12.30596
0.8	0.76103	3.81516	6.74915	9.70905	12.67614
0.9	0.78272	3.88101	6.91759	9.96937	13.02541
1.0	0.80243	3.94344	7.07860	10.21712	13.35709

Table 10 Values of Q for $\bar{M}=9.0$

	Mode				
y_0	1	2	3	4	5
0.1	0.42725	3.14798	5.10973	7.09822	9.10757
0.2	0.50797	3.28682	5.44665	7.65021	9.87662
0.3	0.56195	3.40098	5.72285	8.09500	10.48868
0.4	0.60356	3.49997	5.96429	8.47976	11.01429
0.5	0.63780	3.58840	6.18235	8.82451	11.48284
0.6	0.66707	3.66895	6.38325	9.14009	11.91003
0.7	0.69270	3.74332	6.57086	9.43314	12.30544
0.8	0.71555	3.81271	6.74777	9.70811	12.67543
0.9	0.73616	3.87797	6.91582	9.96815	13.02448
1.0	0.75494	3.93976	7.07639	10.21558	13.35591

$$V=y^{-1}[C_1J_2(z)+C_2Y_2(z)+C_3I_2(z)+C_4K_2(z)] \tag{16}$$

where

$$z=2q\sqrt{y} \tag{17}$$

In equation (16), J_2 and Y_2 are the second-order Bessel functions of first and second kind, [7], respectively; while I_2 and K_2 are the modified Bessel functions of second order and of first and second kind, respectively.

Substituting equation (16) in equations (12) and (13) results in the frequency determinant equation

$$\begin{vmatrix} J_4(a) & Y_4(a) & I_4(a) & K_4(a) \\ a_{21} & a_{22} & a_{23} & a_{24} \\ J_2(b) & Y_2(b) & I_2(b) & K_2(b) \\ J_3(b) & Y_3(b) & -I_3(b) & K_3(b) \end{vmatrix} = 0 \tag{18}$$

where

$$\begin{aligned} a_{21} &= J_3(a)-\bar{M}q(1-y_0)y_0^{-2.5}J_2(a) \\ a_{22} &= Y_3(a)-\bar{M}q(1-y_0)y_0^{-2.5}Y_2(a) \\ a_{23} &= I_3(a)-\bar{M}q(1-y_0)y_0^{-2.5}I_2(a) \\ a_{24} &= -K_3(a)-\bar{M}q(1-y_0)y_0^{-2.5}K_2(a) \\ a &= 2q\sqrt{y_0} \\ b &= 2q \end{aligned} \tag{19}$$

Equation (18) degenerates to the clamped-free case of [1, 2], if $\bar{M}=0$.

Numerical Results

To find the roots of equation (18), the Bessel functions were replaced by their approximate polynomial equivalents [8], and the roots were then found by using the method of Successive Bisection with $\epsilon = 10^{-7}$ [9]. In order to initiate the iterative process, the roots were first bracketed by means of a straight search process.

Once the roots have been obtained, the frequency of the structural system can be determined by equation (14) as

$$f=\frac{Q^2}{2\pi L^2}\sqrt{\frac{EI_1}{\rho A_1}} \tag{20}$$

where the frequency parameter, $Q = q(1-y_0)$, for a wide range of values of beam dimensions and concentrated mass are shown in Tables 1–10.

Summary

Based on Euler theory, the first five natural frequencies have been tabulated for a nonuniform cantilever beam with a mass at the free end. The reliability of the present results have been verified by checking the clamped-free case, $\bar{M}=0$, with [1, 2]; and the limiting case, $y_0 = 1$, with [10]. The last case is corresponding to a uniform cantilever beam with end mass. The results reported herein may be useful for several engineering situations: e.g., a mast antenna structure, and a tower-tank structure.

References

1 Conway, H. D., Becker, E. C. H., and Dubil, J. F. "Vibration Frequencies of Tapered Bars and Circular Plates," ASME JOURNAL OF APPLIED MECHANICS, Vol. 31, 1964, pp. 329–331.

2 Conway, H. D., and Dubil, J. F. "Vibration Frequencies of Truncated-Cone and Wedge Beams," ASME JOURNAL OF APPLIED MECHANICS, Vol. 32, 1965, pp. 932–934.

3 Lee, T. W., "Transverse Vibrations of a Tapered Beam Carrying a Concentrated Mass," ASME JOURNAL OF APPLIED MECHANICS, Vol. 43, 1976, pp. 366–367.

4 Goel, R. P., "Transverse Vibrations of Tapered Beams," *Journal of Sound and Vibration*, Vol. 47, 1976, pp. 1–7.

5 Mabie, H. H., and Rogers, C. B., "Transverse Vibrations of Double-Tapered Cantilever Beams With End Support and With End Mass," *Journal of Acoustical Society of America*, Vol. 55, May 1974, pp. 986–991.

6 Downs, B., "Transverse Vibrations of Cantilever Beams Having Unequal Breadth and Depth Tapers," ASME JOURNAL OF APPLIED MECHANICS, Vol. 44, 1977, pp. 737–742.

7 Watson, G. N., *A Treatise on the Theory of Bessel Functions*, Cambridge, England, 1952.

8 Abramowitz, M., and Stegun, I. A., *Handbook of Mathematical Functions*, Dover, New York, 1970.

9 McCalla, T. R., *Introduction to Numerical Methods and FORTRAN Programming*, Wiley, New York, 1967.

10 Laura, P. A. A., Pombo, J. L., and Susemihl, E. A., "A Note on the Vibrations of a Clamped-Free Beam With a Mass at the Free End," *Journal of Sound and Vibration*, Vol. 37, 1974, pp. 161–168.

Downloaded 02 May 2010 to 171.66.16.25. Redistribution subject to ASME license or copyright; see http://www.asme.org/terms/Terms_Use.cfm

Vibration Frequencies and Mode Shapes for a Constrained Cantilever

J. H. Lau[1]

Introduction

In [1], Rutenberg has presented the results of the first three eigenfrequencies of a uniform cantilever beam with a rotational constraint at some point. In the present paper, Rutenberg's results are extended to include an additional spring to against translation (Fig. 1). Numerical values for the first five natural frequencies are presented in tabular form for a wide range of values of the translational and rotational stiffness ratios. Exact expressions for the mode shapes are also provided for engineering practice convenience.

Analysis

The differential equations for small-amplitude, free vibration of the constrained beam (Fig. 1) executing harmonic oscillations are given by

$$EI\frac{d^4y_1}{du^4} - mp^2y_1(u) = 0 \quad 0 \le u \le zL \tag{1}$$

$$EI\frac{d^4y_2}{dv^4} - mp^2y_2(v) = 0 \quad 0 \le v \le (1-z)L \tag{2}$$

where, E = Young's modulus; I = second moment of the cross-sectional area; L = length of the beam; m = mass per unit length of the beam, p = circular frequency of the constrained system; and $0 \le z \le 1$.

The general solutions to equations (1) and (2) are, respectively,

$$y_1(u) = A\sin(qu) + B\cos(qu) + C\sinh(qu) + D\cosh(qu) \quad 0 \le u \le zL \tag{3}$$

and

$$y_2(v) = Q\sin(qv) + F\cos(qv) + G\sinh(qv) + H\cosh(qv) \quad 0 \le v \le (1-z)L \tag{4}$$

where

$$q^4 = \frac{mp^2}{EI} \tag{5}$$

The boundary conditions are as follows:

At $u = 0$:

$$y_1 = \frac{dy_1}{du} = 0 \tag{6}$$

At $u = zL$, and $v = 0$:

$$y_1 = y_2; \quad \frac{dy_1}{du} = \frac{dy_2}{dv};$$

$$EI\frac{d^3y_1}{du^3} = Ky_1 + EI\frac{d^3y_2}{dv^3} \tag{7}$$

$$EI\frac{d^2y_1}{du^2} = -k\frac{dy_1}{du} + EI\frac{d^2y_2}{dv^2}$$

At $v = (1-z)L$:

$$\frac{d^2y_2}{dv^2} = \frac{d^3y_2}{dv^3} = 0 \tag{8}$$

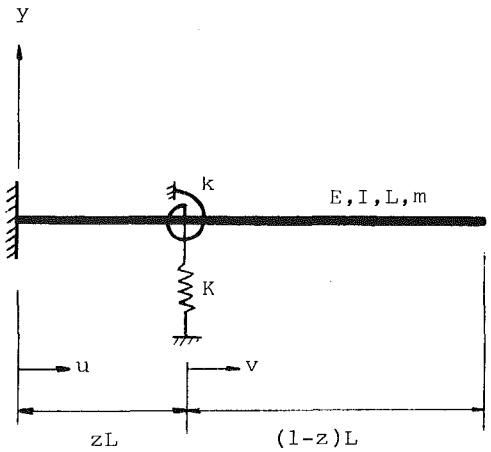

Fig. 1 Translationally and rotationally constrained cantilever beam

where K and k are the translational and rotational stiffnesses, respectively. Substituting equations (3) and (4) in equations (6)–(8), leads to the following frequency equation

$$\begin{aligned}
&[-2a^3(\sin(a)+\sinh(a)) \\
&\quad +\bar{K}(sh-s)(\bar{sh}+\bar{s}) + a^2\bar{k}(\bar{c}+\bar{ch})(c-ch)]. \\
&[\ 2a^3(\sin(a)+\sinh(a)) \\
&\quad +\bar{K}(ch-c)(\bar{c}+\bar{ch}) + a^2\bar{k}(s+sh)(\bar{s}-\bar{sh})] \\
&\quad +[\ 2a^3(\cos(a)+\cosh(a)) \\
&\quad -\bar{K}(ch-c)(\bar{sh}+\bar{s}) + a^2\bar{k}(s+sh)(\bar{c}+\bar{ch})]. \\
&[-2a^3(\cos(a)+\cosh(a)) \\
&\quad +\bar{K}(sh-s)(\bar{c}+\bar{ch}) + a^2\bar{k}(c-ch)(\bar{sh}-\bar{s})] = 0
\end{aligned} \tag{9}$$

where

$$\begin{aligned}
&s = \sin(b); \quad sh = \sinh(b); \quad c = \cos(b); \\
&ch = \cosh(b); \quad \bar{s} = \sin(a-b); \quad \bar{sh} = \sinh(a-b); \\
&\bar{c} = \cos(a-b); \quad \bar{ch} = \cosh(a-b); \quad a = qL; \quad b = az,
\end{aligned} \tag{10}$$

and

$$\bar{K} = \frac{KL^3}{EI}; \quad \bar{k} = \frac{kL}{EI} \tag{11}$$

have been introduced.

Numerical Results

To find the roots of equation (9), a straight search process is first adopted to bracket the roots, and the roots were then found by using the method of false position with $\epsilon = 10^{-7}$ [2].

Tables 1–5 show the values of the first five frequency parameter, $a = qL$, for $\bar{K}$ and $\bar{k} = 0, 1, 10, 100, 1000$, and 10000, and $z = 0.2, 0.4, 0.6, 0.8$, and 1.0.

[1] MTS, Sandia National Laboratories, Alburquerque, N. Mex. 87185. Formerly, Bechtel Power Corporation, San Francisco Calif. 94119. Manuscript received by ASME Applied Mechanics Division, January, 1983.

Copyright © 1984 by ASME
Downloaded 02 May 2010 to 171.66.16.25. Redistribution subject to ASME license or copyright; see http://www.asme.org/terms/Terms_Use.cfm

Table 1.1 Values of qL for $Z = 0.2$ (mode 1)

$\bar{K}$ \ $\bar{k}$	0.0	1.0	10.0	100.0	1000.0	10000.0
0.00	1.87510	1.92466	2.12534	2.30140	2.33413	2.33769
1.00	1.87572	1.92516	2.12549	2.30142	2.33414	2.33769
10.00	1.88118	1.92955	2.12684	2.30154	2.33418	2.33773
100.00	1.92730	1.96721	2.13892	2.30271	2.33457	2.33806
1000.00	2.09381	2.10996	2.19522	2.30942	2.33691	2.34005
10000.00	2.19789	2.20449	2.24472	2.31787	2.34013	2.34282

Table 1.2 Values of qL for $Z = 0.2$ (mode 2)

$\bar{K}$ \ $\bar{k}$	0.0	1.0	10.0	100.0	1000.0	10000.0
0.00	4.69409	4.74374	5.03755	5.52582	5.65969	5.67532
1.00	4.69497	4.74457	5.03811	5.52604	5.65983	5.67546
10.00	4.70277	4.75195	5.04313	5.52796	5.66112	5.67668
100.00	4.77440	4.81966	5.08944	5.54591	5.67313	5.68806
1000.00	5.14801	5.17475	5.34033	5.64947	5.74398	5.75537
10000.00	5.52057	5.53253	5.61044	5.77779	5.83634	5.84369

Table 1.3 Values of qL for $Z = 0.2$ (mode 3)

$\bar{K}$ \ $\bar{k}$	0.0	1.0	10.0	100.0	1000.0	10000.0
0.00	7.85476	7.87435	8.01592	8.41615	8.59232	8.61586
1.00	7.85551	7.87511	8.01669	8.41692	8.59307	8.61661
10.00	7.86227	7.88190	8.02362	8.42381	8.59981	8.62332
100.00	7.92788	7.94773	8.09057	8.48997	8.66441	8.68767
1000.00	8.41088	8.43090	8.57181	8.94475	9.10085	9.12142
10000.00	9.22942	9.24388	9.34335	9.59102	9.68953	9.70233

Table 1.4 Values of qL for $Z = 0.2$ (mode 4)

$\bar{K}$ \ $\bar{k}$	0.0	1.0	10.0	100.0	1000.0	10000.0
0.00	10.99554	10.99581	10.99776	11.00363	11.00653	11.00694
1.00	10.99597	10.99624	10.99820	11.00409	11.00700	11.00741
10.00	10.99982	11.00010	11.00212	11.00821	11.01121	11.01164
100.00	11.03834	11.03871	11.04145	11.04966	11.05371	11.05428
1000.00	11.41583	11.41773	11.43146	11.47221	11.49191	11.49466
10000.00	12.84594	12.85825	12.94631	13.19293	13.30253	13.31725

Table 1.5 Values of qL for $Z = 0.2$ (mode 5)

$\bar{K}$ \ $\bar{k}$	0.0	1.0	10.0	100.0	1000.0	10000.0
0.00	14.13717	14.14562	14.20430	14.35412	14.41483	14.42275
1.00	14.13732	14.14577	14.20444	14.35424	14.41494	14.42286
10.00	14.13871	14.14714	14.20572	14.35528	14.41589	14.42380
100.00	14.15272	14.16102	14.21865	14.36583	14.42550	14.43328
1000.00	14.30679	14.31361	14.36104	14.48260	14.53216	14.53865
10000.00	16.11917	16.12019	16.12702	16.14274	16.14860	16.14934

Table 2.1 Values of qL for $Z = 0.4$ (mode 1)

$\bar{K}$ \ $\bar{k}$	0.0	1.0	10.0	100.0	1000.0	10000.0
0.00	1.87510	2.00933	2.48428	2.88536	2.96256	2.97103
1.00	1.88303	2.01557	2.48692	2.88642	2.96341	2.97186
10.00	1.94760	2.06706	2.50929	2.89554	2.97068	2.97894
100.00	2.27905	2.34774	2.64827	2.95500	3.01835	3.02538
1000.00	2.65388	2.68652	2.85005	3.05046	3.09608	3.10124
10000.00	2.73595	2.76267	2.90012	3.07611	3.11727	3.12195

Downloaded 02 May 2010 to 171.66.16.25. Redistribution subject to ASME license or copyright; see http://www.asme.org/terms/Terms_Use.cfm

Table 2.2 Values of qL for $Z = 0.4$ (mode 2)

$\bar{K}$ \ $\bar{k}$	0.0	1.0	10.0	100.0	1000.0	10000.0
0.00	4.69409	4.70350	4.75949	4.85329	4.87941	4.88249
1.00	4.69860	4.70804	4.76414	4.85807	4.88422	4.88730
10.00	4.73862	4.74826	4.80542	4.90046	4.92679	4.92988
100.00	5.08767	5.09893	5.16422	5.26793	5.29569	5.29893
1000.00	6.44373	6.46655	6.59724	6.79561	6.84595	6.85174
10000.00	7.04720	7.08148	7.28627	7.62957	7.72363	7.73462

Table 2.3 Values of qL for $Z = 0.4$ (mode 3)

$\bar{K}$ \ $\bar{k}$	0.0	1.0	10.0	100.0	1000.0	10000.0
0.00	7.85476	7.88730	8.08744	8.44155	8.54119	8.55286
1.00	7.85533	7.88786	8.08795	8.44198	8.54161	8.55328
10.00	7.86049	7.89292	8.09252	8.44589	8.54536	8.55701
100.00	7.91408	7.94554	8.13989	8.48624	8.58405	8.59551
1000.00	8.56849	8.59002	8.72795	8.99043	9.06710	9.07613
10000.00	10.39927	10.43306	10.66299	11.14374	11.27404	11.28836

Table 2.4 Values of qL for $Z = 0.4$ (mode 4)

$\bar{K}$ \ $\bar{k}$	0.0	1.0	10.0	100.0	1000.0	10000.0
0.00	10.99554	11.03161	11.29414	12.03219	12.34323	12.38368
1.00	10.99562	11.03168	11.29420	12.03224	12.34327	12.38373
10.00	10.99629	11.03234	11.29476	12.03266	12.34369	12.38415
100.00	11.00314	11.03902	11.30043	12.03695	12.34788	12.38834
1000.00	11.08180	11.11554	11.36399	12.08208	12.39071	12.43107
10000.00	12.06586	12.07579	12.15857	12.52271	12.74153	12.77259

Table 2.5 Values of qL for $Z = 0.4$ (mode 5)

$\bar{K}$ \ $\bar{k}$	0.0	1.0	10.0	100.0	1000.0	10000.0
0.00	14.13717	14.13799	14.14424	14.16621	14.17913	14.18108
1.00	14.13734	14.13816	14.14441	14.16637	14.17929	14.18124
10.00	14.13889	14.13971	14.14594	14.16784	14.18072	14.18266
100.00	14.15444	14.15524	14.16132	14.18263	14.19512	14.19700
1000.00	14.31835	14.31897	14.32363	14.33945	14.34841	14.34973
10000.00	16.09368	16.09377	16.09440	16.09577	16.09625	16.09631

Table 3.1 Values of qL for $Z = 0.6$ (mode 1)

$\bar{K}$ \ $\bar{k}$	0.0	1.0	10.0	100.0	1000.0	10000.0
0.00	1.87510	2.06655	2.60876	2.94992	3.00458	3.01037
1.00	1.90646	2.09119	2.62383	2.96251	3.01690	3.02267
10.00	2.13029	2.27625	2.74618	3.06734	3.11984	3.12542
100.00	2.93657	3.02369	3.37790	3.67938	3.73240	3.73808
1000.00	3.57232	3.65356	4.03322	4.44670	4.53275	4.54227
10000.00	3.67174	3.75239	4.13617	4.56947	4.66230	4.67264

Table 3.2 Values of qL for $Z = 0.6$ (mode 2)

$\bar{K}$ \ $\bar{k}$	0.0	1.0	10.0	100.0	1000.0	10000.0
0.00	4.69409	4.73154	4.94831	5.27292	5.35322	5.36239
1.00	4.69745	4.73476	4.95083	5.27478	5.35497	5.36413
10.00	4.72779	4.76380	4.97370	5.29173	5.37090	5.37994
100.00	5.02875	5.05468	5.21296	5.47466	5.54328	5.55120
1000.00	6.50096	6.51977	6.63418	6.82770	6.87985	6.88590
10000.00	7.16288	7.19107	7.36797	7.69284	7.78663	7.79768

Downloaded 02 May 2010 to 171.66.16.25. Redistribution subject to ASME license or copyright; see http://www.asme.org/terms/Terms_Use.cfm

Table 3.3 Values of qL for $Z = 0.6$ (mode 3)

$\bar{K}$ \ $\bar{k}$	0.0	1.0	10.0	100.0	1000.0	10000.0
0.00	7.85476	7.88329	8.06553	8.41378	8.51683	8.52902
1.00	7.85522	7.88375	8.06595	8.41415	8.51719	8.52938
10.00	7.85941	7.88788	8.06978	8.41753	8.52044	8.53262
100.00	7.90312	7.93102	8.10963	8.45244	8.55412	8.56615
1000.00	8.47891	8.49948	8.63454	8.90724	8.99049	9.00039
10000.00	10.33018	10.36151	10.57627	11.03887	11.17078	11.18555

Table 3.4 Values of qL for $Z = 0.6$ (mode 4)

$\bar{K}$ \ $\bar{k}$	0.0	1.0	10.0	100.0	1000.0	10000.0
0.00	10.99554	11.03009	11.28246	12.00043	12.30634	12.34626
1.00	10.99562	11.03017	11.28253	12.00049	12.30640	12.34631
10.00	10.99634	11.03088	11.28314	12.00096	12.30686	12.34678
100.00	11.00367	11.03805	11.28935	12.00577	12.31153	12.35145
1000.00	11.08673	11.11913	11.35818	12.05604	12.35920	12.39898
10000.00	12.05526	12.06588	12.15315	12.52003	12.73501	12.76545

Table 3.5 Values of qL for $Z = 0.6$ (mode 5)

$\bar{K}$ \ $\bar{k}$	0.0	1.0	10.0	100.0	1000.0	10000.0
0.00	14.13717	14.13804	14.14466	14.16773	14.18116	14.18317
1.00	14.13734	14.13822	14.14483	14.16789	14.18132	14.18333
10.00	14.13890	14.13978	14.14638	14.16937	14.18276	14.18476
100.00	14.15462	14.15547	14.16191	14.18428	14.19726	14.19920
1000.00	14.32009	14.32074	14.32566	14.34220	14.35148	14.35285
10000.00	16.09876	16.09886	16.09953	16.10098	16.10149	16.10155

Table 4.1 Values of qL for $Z = 0.8$ (mode 1)

$\bar{K}$ \ $\bar{k}$	0.0	1.0	10.0	100.0	1000.0	10000.0
0.00	1.87510	2.07404	2.45029	2.59156	2.60974	2.61161
1.00	1.95026	2.13046	2.48409	2.61940	2.63687	2.63867
10.00	2.40287	2.50532	2.73864	2.83611	2.84894	2.85026
100.00	3.82712	3.84606	3.88307	3.89618	3.89781	3.89798
1000.00	4.67897	4.81699	5.30157	5.54922	5.57824	5.58115
10000.00	4.68230	4.82670	5.40219	5.81882	5.87974	5.88603

Table 4.2 Values of qL for $Z = 0.8$ (mode 2)

$\bar{K}$ \ $\bar{k}$	0.0	1.0	10.0	100.0	1000.0	10000.0
0.00	4.69409	4.85644	5.59037	6.25503	6.36381	6.37514
1.00	4.69414	4.85655	5.59075	6.25561	6.36442	6.37575
10.00	4.69459	4.85753	5.59420	6.26091	6.36996	6.38132
100.00	4.70206	4.87246	5.63557	6.31920	6.43036	6.44192
1000.00	6.20838	6.25650	6.62687	7.20711	7.30973	7.32023
10000.00	7.15257	7.21529	7.68878	8.78617	9.07182	9.09899

Table 4.3 Values of qL for $Z = 0.8$ (mode 3)

$\bar{K}$ \ $\bar{k}$	0.0	1.0	10.0	100.0	1000.0	10000.0
0.00	7.85476	7.90049	8.25443	9.24250	9.60592	9.65030
1.00	7.85508	7.90080	8.25463	9.24254	9.60593	9.65031
10.00	7.85798	7.90355	8.25640	9.24294	9.60608	9.65044
100.00	7.88786	7.93185	8.27455	9.24690	9.60755	9.65166
1000.00	8.24674	8.27293	8.49493	9.28874	9.62186	9.66352
10000.00	9.46537	9.46702	9.48155	9.58454	9.71318	9.73699

Downloaded 02 May 2010 to 171.66.16.25. Redistribution subject to ASME license or copyright; see http://www.asme.org/terms/Terms_Use.cfm

Table 4.4 Values of qL for $Z = 0.8$ (mode 4)

$\bar{K}$ \ $\bar{k}$	0.0	1.0	10.0	100.0	1000.0	10000.0
0.00	10.99554	10.99802	11.01764	11.09925	11.15641	11.16553
1.00	10.99585	10.99833	11.01796	11.09961	11.15677	11.16589
10.00	10.99865	11.00114	11.02085	11.10277	11.16006	11.16919
100.00	11.02691	11.02950	11.05002	11.13463	11.19313	11.20241
1000.00	11.32579	11.32951	11.35848	11.46925	11.53855	11.54908
10000.00	12.86383	12.87327	12.94353	13.16846	13.28259	13.29859

Table 4.5 Values of qL for $Z = 0.8$ (mode 5)

$\bar{K}$ \ $\bar{k}$	0.0	1.0	10.0	100.0	1000.0	10000.0
0.00	14.13717	14.14303	14.18541	14.30839	14.36521	14.37295
1.00	14.13730	14.14316	14.18553	14.30849	14.36530	14.37304
10.00	14.13845	14.14430	14.18661	14.30941	14.36614	14.37387
100.00	14.15006	14.15584	14.19758	14.31869	14.37465	14.38227
1000.00	14.27810	14.28303	14.31861	14.42158	14.46915	14.47564
10000.00	16.02278	16.02320	16.02606	16.03305	16.03581	16.03617

Table 5.1 Values of qL for $Z = 1$ (mode 1)

$\bar{K}$ \ $\bar{k}$	0.0	1.0	10.0	100.0	1000.0	10000.0
0.00	1.87510	2.05395	2.29117	2.35644	2.36415	2.36493
1.00	2.01000	2.14907	2.34704	2.40368	2.41042	2.41111
10.00	2.63892	2.66623	2.71468	2.73095	2.73297	2.73317
100.00	3.64054	3.68184	3.78882	3.84032	3.84749	3.84824
1000.00	3.89780	4.00421	4.35620	4.58450	4.62047	4.62427
10000.00	3.92374	4.03808	4.42292	4.67543	4.71512	4.71932

Table 5.2 Values of qL for $Z = 1$ (mode 2)

$\bar{K}$ \ $\bar{k}$	0.0	1.0	10.0	100.0	1000.0	10000.0
0.00	4.69409	4.86860	5.28872	5.47087	5.49503	5.49753
1.00	4.70379	4.87680	5.29328	5.47404	5.49803	5.50051
10.00	4.79377	4.95203	5.33488	5.50295	5.52539	5.52770
100.00	5.61600	5.65171	5.75618	5.81301	5.82126	5.82212
1000.00	6.87629	6.91393	7.08432	7.25212	7.28464	7.28819
10000.00	7.05070	7.11325	7.41534	7.73343	7.79572	7.80252

Table 5.3 Values of qL for $Z = 1$ (mode 3)

$\bar{K}$ \ $\bar{k}$	0.0	1.0	10.0	100.0	1000.0	10000.0
0.00	7.85476	7.96567	8.35306	8.59821	8.63508	8.63895
1.00	7.85682	7.96760	8.35436	8.59905	8.63587	8.63973
10.00	7.87565	7.98518	8.36607	8.60673	8.64295	8.64675
100.00	8.08409	8.17596	8.48887	8.68705	8.71725	8.72042
1000.00	9.55253	9.55375	9.55931	9.56499	9.56613	9.56625
10000.00	10.15498	10.19578	10.42747	10.76056	10.84018	10.84919

Table 5.4 Values of qL for $Z = 1$ (mode 4)

$\bar{K}$ \ $\bar{k}$	0.0	1.0	10.0	100.0	1000.0	10000.0
0.00	10.99554	11.07815	11.43213	11.72565	11.77512	11.78038
1.00	10.99629	11.07888	11.43267	11.72599	11.77543	11.78069
10.00	11.00310	11.08544	11.43754	11.72908	11.77822	11.78345
100.00	11.07484	11.15414	11.48760	11.76071	11.80679	11.81170
1000.00	11.95100	11.97059	12.05527	12.13342	12.14805	12.14964
10000.00	13.22183	13.24789	13.40959	13.70052	13.78416	13.79405

Downloaded 02 May 2010 to 171.66.16.25. Redistribution subject to ASME license or copyright; see http://www.asme.org/terms/Terms_Use.cfm

Table 5.5 Values of qL for $Z = 1$ (mode 5)

$\bar{K}$ \ $\bar{k}$	0.0	1.0	10.0	100.0	1000.0	10000.0
0.00	14.13717	14.20285	14.52434	14.85354	14.91516	14.92182
1.00	14.13752	14.20320	14.52462	14.85371	14.91532	14.92197
10.00	14.14072	14.20632	14.52711	14.85527	14.91669	14.92333
100.00	14.17355	14.23833	14.55237	14.87103	14.93063	14.93707
1000.00	14.58153	14.62730	14.83802	15.04656	15.08638	15.09071
10000.00	16.22802	16.24184	16.33098	16.51330	16.57317	16.58052

Determination of Mode Shapes

Corresponding to each frequency, the mode shape may be obtained by equations (3) and (4) with the following expressions for the coefficients

$$B=gA;\quad C=-A;\quad D=-gA;\quad Q=(c-g.s+M)A;$$
$$F(s+g.c-N)A;\quad G=(-ch-g.sh-M)A;$$
$$H=(-sh-g.ch+N)A, \tag{12}$$

where

$$M=\frac{\bar{K}}{2a^3}[(s-sh)+g(c-ch)];$$

$$N=\frac{\bar{k}}{2a}[(c-ch)-g(s+sh)]; \tag{13}$$

$$g=\frac{-2a^3(\sin(a)+\sinh(a))+\bar{K}(sh-s)(\bar{s}\bar{h}+\bar{s})+a^2\bar{k}(\bar{c}+\bar{c}\bar{h})(c-ch)}{2a^3(\cos(a)+\cosh(a))-\bar{K}(ch-c)(\bar{s}\bar{h}+\bar{s})+a^2\bar{k}(s+sh)(\bar{c}+\bar{c}\bar{h})},$$

and A defines the amplitude of motion, The constants c, s, ch, sh, $\bar{s}$, $\bar{c}\bar{h}$, and $\bar{s}\bar{h}$ have been defined in equation (10).

Summary

Exact expressions for mode shapes and extensive tabular results for eigenfrequencies of a cantilever beam with intermediate elastic constraints have been presented. The reliability of the present results have been verified by checking 10 degenerate cases with published results [3, 4].

References

1 Rutenberg, A., "Vibration Frequencies for a Uniform Cantilever With a Rotational Constraint at a Point," ASME JOURNAL OF APPLIED MECHANICS, Vol. 45, 1978, pp. 422–423.

2 McCalla, T. R., *Introduction to Numerical Methods and FORTRAN Programming*, Wiley, New York, 1967.

3 Gorman, D. J., *Free Vibration Analysis of Beams and Shafts*, Wiley, New York, 1975.

4 Blevins, R. D., *Formulas For Natural Frequency And Mode Shape*, Van Nostrand, New York, 1979.

Downloaded 02 May 2010 to 171.66.16.25. Redistribution subject to ASME license or copyright; see http://www.asme.org/terms/Terms_Use.cfm

Journal of Applied Mechanics

Brief Notes

A Brief Note is a short paper that presents a specific solution of technical interest in mechanics but which does not necessarily contain new general methods or results. A Brief Note should not exceed 1500 words *or equivalent* (a typical one-column figure or table is equivalent to 250 words; a one line equation to 30 words). Brief Notes will be subject to the usual review procedures prior to publication. After approval such Notes will be published as soon as possible. The Notes should be submitted to the Technical Editor of the JOURNAL OF APPLIED MECHANICS. Discussions on the Brief Notes should be addressed to the Editorial Department, ASME, United Engineering Center, 345 East 47th Street, New York, N. Y. 10017, or to the Technical Editor of the JOURNAL OF APPLIED MECHANICS. Discussions on Brief Notes appearing in this issue will be accepted until two months after publication. Readers who need more time to prepare a Discussion should request an extension of the deadline from the Editorial Department.

Instability of Laminated Cylinders in Torsion

D. Shaw[1] and G. J. Simitses[1]

Introduction

A Galerkin-type solution, for the buckling analysis of a perfect geometry, laminated, circular, cylindrical thin shell subjected to pure torsion, is presented. The torsion is applied through the reference surface, which is the midsurface of the laminate and the boundaries are classical simple supports (*SS*-3). The analysis is based on Donnell-type nonlinear kinematic relations and linearly elastic material behavior. It is assumed that a primary state exists and that it is axisymmetric. This primary state can be obtained by solving the field equations. Through perturbation of the governing field equations a set of (linearized) buckling equations is obtained, along with the related boundary conditions. A Galerkin procedure is employed for solving the buckling equations. Thus, the problem is reduced to an eigen-boundary-value problem. Critical torsional loads are obtained for several boron/epoxy configurations of symmetric, antisymmetric, and asymmetric stacking. In addition, approximate buckling modes are established for both positive and negative torsion.

Governing Equations and Solution Procedure

The geometry and sign convention are the same as those employed in [1]. The governing equations for a general laminated circular cylindrical shell, with or without orthogonal stiffeners, without geometric imperfections, and subjected to a pure torsion, consist of two coupled partial nonlinear differential equations in the transverse displacement component $w(x,y)$ and an Airy stress (resultant) function $F(x,y)$. One of the equations characterizes transverse equilibrium and the other characterizes in-plane compatibility. These equations are taken from [1] by setting $\bar{N}_{xx}=q=w^{\circ}(x,y)=0$, where $\bar{N}_{xx}$ denotes the uniform axial compression, q lateral pressure, and $w^{\circ}(x,y)$ an initial geometric imperfection.

It is assumed that, under the action of pure torsion, a primary state exists, which is axisymmetric (all three reference surface displacement components, u, v, and w, are independent of the circumferential coordinate y). Note that for symmetric construction (regular angle-ply or cross-ply with odd number of plies, for example) a membrane state exists and, therefore, the foregoing is not an assumption. How reasonable this assumption is, depends on the nature and magnitude of the coupling stiffnesses $[B_{ij}]$. Primary state quantities are denoted by a caret. With this assumption, the field equations become

$$b_{21}\hat{F},_{xxxx}+d_{11}\hat{w},_{xxxx}+\hat{F},_{xx}/R=0 \tag{1}$$

$$a_{22}\hat{F},_{xxxx}+b_{21}\hat{w},_{xxxx}+\hat{w},_{xx}/R=0 \tag{2}$$

where

$$[a_{ij}]=[A_{ij}]^{-1};\quad [b_{ij}]=[A_{ij}]^{-1}[B_{ij}]$$
$$[d_{ij}]=[B_{ij}][b_{ij}]-[D_{ij}] \tag{3}$$

and $[A_{ij}]$, $[B_{ij}]$, and $[D_{ij}]$ are the extensional, coupling, and flexural stiffnesses appearing in the usual lamination theory.

The expressions for the simply supported boundary conditions ($SS-3$) are given in the following in terms of w and F (at $x=0, L$).

$$w=0;\quad F,_{yy}=0;\quad b_{21}F,_{xx}+d_{11}w,_{xx}=-b_{31}\bar{N}_{xy};$$
$$a_{22}F,_{xx}+b_{21}w,_{xx}=-a_{23}\bar{N}_{xy}, \tag{4}$$

where $\bar{N}_{xy}$ is the applied torsional stress resultant. For more details see [1]. One can solve for the primary path parameters, $\hat{w}$ and $\hat{F}$ by employing equations (1), (2), and (4).

Next, the buckling equations are obtained through a perturbation of the nonlinear governing equations [1]. The dependent variable, w and F, are replaced by the sum of the primary state parameters, $\hat{w}$ and $\hat{F}$, and small additional quantities, w^1 and F^1, necessary to represent the buckled state. Moreover, the related boundary conditions for the buckling equations are also obtained in the same manner. Note that since the additional quantities can be made as small as one wishes, only the linear terms in w^1 and F^1 are retained.

The buckling equations and related boundary conditions are:

$$\begin{aligned}&b_{21}F^1,_{xxxx}+(2b_{23}-b_{31})F^1,_{xxxy}+(b_{11}-2b_{33}\\&+b_{22})F^1,_{xxyy}+(2b_{13}-b_{32})F^1,_{xyyy}+b_{12}F^1,_{yyyy}\\&+d_{11}w^1,_{xxxx}+(2d_{31}+2d_{13})w^1,_{xxxy}+(d_{12}+4d_{33}\\&+d_{21})w^1,_{xxyy}+(2d_{32}+2d_{23})w^1,_{xyyy}+d_{22}w^1,_{yyyy}\\&+\frac{F^1,_{xx}}{R}+\hat{F},_{xx}w^1,_{yy}+\hat{w},_{xx}F^1,_{yy}+2\bar{N}_{xy}w^1,_{xy}=0\end{aligned} \tag{5}$$

[1] Research Associate and Professor, Mem. ASME, respectively, School of Engineering Science and Mechanics, Georgia Institute of Technology, Atlanta, Ga. 30332.

Manuscript received by ASME Applied Mechanics Division, June, 1982; final revision, May, 1983.

Copyright © 1984 by ASME
Downloaded 02 May 2010 to 171.66.16.25. Redistribution subject to ASME license or copyright; see http://www.asme.org/terms/Terms_Use.cfm

$$a_{22}F^{\mathrm{I}}{}_{,xxxx} - 2a_{23}F^{\mathrm{I}}{}_{,xxxy} + (2a_{12}+a_{33})F^{\mathrm{I}}{}_{,xxyy} - 2a_{13}F^{\mathrm{I}}{}_{,xyyy} + a_{11}F^{\mathrm{I}}{}_{,yyyy} + b_{21}w^{\mathrm{I}}{}_{,xxxx} + (2b_{23} - b_{31})w^{\mathrm{I}}{}_{,xxxy} + (b_{11} - 2b_{33} + b_{22})w^{\mathrm{I}}{}_{,xxyy} + (2b_{13} - b_{32})w^{\mathrm{I}}{}_{,xyyy} + b_{12}w^{\mathrm{I}}{}_{,yyyy} + \frac{w^{\mathrm{I}}{}_{,xx}}{R} + \hat{w}_{,xx}w^{\mathrm{I}}{}_{,yy} = 0 \tag{6}$$

$$\text{at } x=0,L \begin{cases} w=0; & b_{21}F^{\mathrm{I}}{}_{,xx} + b_{31}F^{\mathrm{I}}{}_{,xy} + d_{11}w^{\mathrm{I}}{}_{,xx} + 2d_{13}w^{\mathrm{I}}{}_{,xy} = 0; \\ F_{,yy}=0; & a_{22}F^{\mathrm{I}}{}_{,xx} + a_{23}F^{\mathrm{I}}{}_{,xy} + b_{12}w^{\mathrm{I}}{}_{,xx} + 2b_{23}w^{\mathrm{I}}{}_{,xy} = 0. \end{cases} \tag{7}$$

The Galerkin procedure is employed for both equations. The following approximate series are used for generating the Galerkin integrals. Note that the boundary conditions are satisfied by each term in the series.

$$w^{\mathrm{I}} = \sum_{n=1}^{N}\sum_{i=1}^{M}\left(A_{in}\cos\frac{ny}{R} + B_{in}\sin\frac{ny}{R}\right)\left[\frac{L}{i\pi}\sin\frac{i\pi x}{L} - \frac{L}{(i+2)\pi}\sin\frac{(i+2)\pi x}{L}\right]$$

$$F^{\mathrm{I}} = \sum_{n=1}^{N}\sum_{i=1}^{M}\left(C_{in}\cos\frac{ny}{R} + D_{in}\sin\frac{ny}{R}\right)\left[\frac{L}{i\pi}\sin\frac{i\pi x}{L} - \frac{L}{(i+2)\pi}\sin\frac{(i+2)\pi x}{L}\right] \tag{8}$$

Substitution of the preceding expressions, equations (8), into the buckling equations results into a set of systems of linear homogeneous algebraic equations in A_{in}, B_{in}, C_{in}, and D_{in} for each n (decoupled with respect to n). Assuming that the lowest eigenvalue corresponds to the critical load, $\bar{N}_{xy_{\mathrm{cr}}}$, a computer program has been written to this effect. The Georgia Tech high-speed digital computer CDC-CYBER-170/760 is used for generating results. Note that a minimization with respect to n is performed in order to find the lowest eigenvalue.

Numerical Results and Conclusions

First, results are obtained by the present scheme and they are compared to those generated by employing the methodology of [2], for an isotropic geometry.

$$L = 10.16 \text{ cm (4 in.)}; \; L/R = 1; \quad R/h = 1000$$

$$E = 7.24 \times 10^7 \text{ kN/m}^2 (10.5 \times 10^6 \text{ psi}); \quad \mu = 0.3$$

The critical loads are:

$$\bar{N}_{xy_{\mathrm{cr}}} \text{(present)} = 1029.66 \text{ N/m (5.88 lbs/in.)}$$

$$\bar{N}_{xy_{\mathrm{cr}}} \text{([2])} = 1048.92 \text{ N/m (5.99 lbs/in.)}$$

A fairly complete list of references is presented in [2] with regard to torsional buckling of cylinders (with various constructions).

The new geometries considered in the investigation represent variations of the one reported in [3]. Each lamina is orthotropic (boron/epoxy; AVCO 5505) with the following properties:

$$E_{11} = 2.0690 \times 10^8 \text{ kN/m}^2 (30 \times 10^6 \text{ psi}); \; \mu_{12} = 0.21;$$

$$E_{22} = 0.1862 \times 10^8 \text{ kN/m}^2 (2.7 \times 10^6 \text{ psi});$$

$$R = 190.5 \text{ cm (7.5 in.)};$$

$$G_{12} = 0.04482 \times 10^8 \text{ kN/m}^2 (0.65 \times 10^6 \text{ psi});$$

$$L = 381 \text{ cm (15 in.)};$$

$$h_{\mathrm{ply}} = 0.013462 \text{ cm (0.0053 in.)};$$

$$(h_{\mathrm{ply}} = h_k - h_{k-1} \text{ for } k = 1,2,3,4) \tag{9}$$

Five different stacking combinations of the four-ply laminate compromise the various geometries, $I-i$, $i=1, 2, \ldots 5$. These are

$I-1$: 45 deg/ −45 deg/ −45 deg/45 deg;

$I-2$: 45 deg/ −45 deg/45 deg/ −45 deg; $I-3 = -I-2$;

$I-4$: 90 deg/60 deg/30 deg/0 deg;

$I-5$: 0 deg/30 deg/60 deg/90 deg. (10)

where the first number denotes the orientation of the fibers of the outermost ply with respect to x, and the last of the innermost. A pure torsion is applied through the midsurface of the four-ply laminate.

Some of the generated results are shown in Table 1. For each geometry, the critical torsion (for both positive and negative application, clockwise and counterclockwise at the end $x=L$), the minimizing value of n (full number of circumferential waves), and the values of the coefficients A_{in} and B_{in} (normalized with respect to B_{2n}) are shown. Note that the A_{in} and B_{in}, when substituted into the first of equations (8), yield the buckling mode. It was concluded that $M=5$ suffices for determining critical loads.

Note that geometry $I-1$ is symmetric (with respect to the midsurface), geometries $I-2$ and $I-3$ antisymmetric, and geometries $I-4$ and $I-5$ asymmetric. For the symmetric geometry ($I-1$), the positive direction critical torsion is 6987 N/m (39.9 lbs/in.), while the negative critical torsion is 13,220 N/m (75.5 lbs/in.). The respective reported [3] experimental values are 4640 N/m (26.5 lbs/in.) for the positive direction and 11,508 N/m (65.72 lbs/in.) for the negative. This suggests that the geometric imperfection in the tested cylinder [3] is such that the configuration is more sensitive to it, when loaded in the positive direction, than in the negative (the ratio of the experimental to theoretical value is 0.664 for the former and 0.87 for the latter). The difference in response is understandable, because of the anisotropy. The antisymmetric geometries, $I-2$ and $I-3$, yield the same response when loaded to each other. Note that the positive direction critical load for $I-2$ is the same as the negative direction critical load for $I-3$ (the same is true for the buckling mode). Also, observe that the two (± direction) critical loads are very close (9534 N/m and 9454 N/m). This is due to the fact that the extensional, $[A_{ij}]$, and flexural, $[D_{ij}]$, stiffness have the same form as if the shell were isotropic. The difference from isotropy is the existence of some small (in value) terms in the coupling, $[B_{ij}]$, stiffnesses.

Finally, for the asymmetric configurations, $I-4$ and $I-5$ the response is completely different when each geometry is loaded in the positive and in the negative direction. Although the $[A_{ij}]$ and $[D_{ij}]$ stiffnesses, for the two configurations, are the same and only the signs are different in the $[B_{ij}]$ stiffness, the geometries behave (radically) differently.

Acknowledgment

This work is sponsored by the Air Force Office of Scientific Research, Department of the Air Force, under Grant No. AFOSR-81-0227. This financial support is gratefully acknowledged.

References

1 Sheinman, I., Shaw, D., and Simitses, G. J., "Nonlinear Analysis of Axially-Loaded Laminated Cylindrical Shells," *Proceedings of the Symposium on Advances and Trends in Structural and Solid Mechanics*, Washington, D. C., Oct. 4-7, 1982.

2 Simitses, G. J., "Buckling of Eccentrically Stiffened Cylinders under Torsion," *AIAA J.*, Vol. 6, No. 10, 1968, pp. 1856-1860.

Downloaded 02 May 2010 to 171.66.16.25. Redistribution subject to ASME license or copyright; see http://www.asme.org/terms/Terms_Use.cfm

Table 1 Numerical results

Geometry	Minimizing n	$N_{xy_{cr}}$ in N/m (lbs/in.)	A_1	B_1	A_2	B_2	A_3	B_3	A_4	B_4	A_5	B_5
$I-1$	12	6987 (39.90)	−0.3353	0.	0.	1.0	0.7520	0.	0.	0.2038	0.3439	0.
	9	−13220 (−75.50)	0.7627	−0.1954	0.2561	1.0	0.0980	−0.0251	0.1185	0.4626	0.0225	0.0058
I−2	10	9534 (54.45)	−0.5830	0.	0.	1.0	0.1696	0.	0.	0.4230	0.1023	0.
	10	−9454 (−53.99)	0.5804	0.	0.	1.0	−0.1753	0.	0.	0.4218	−0.1063	0.
$I-3$	10	9454 (53.99)	−0.5830	0.	0.	1.0	−0.1753	0.	0.	0.4218	−0.1063	0.
	10	−9534 (54.45)	0.5804	0.	0.	1.0	0.1696	0.	0.	0.4230	0.1023	0.
$I-4$	13	8597 (49.01)	−0.3290	0.0226	0.0685	1.0	0.7107	0.0487	0.0189	0.2759	0.4182	−0.0287
	12	−7790 (−44.59)	0.3431	0.	0.	1.0	0.7355	0.	0.	0.10374	−0.2708	0.
$I-5$	13	13082 (74.71)	−0.4035	−0.0062	0.0153	1.0	0.5681	0.0087	0.0056	0.3666	0.3994	0.0061
	12	−7846 (−44.81)	0.3413	0.0183	0.0536	1.0	−0.8158	−0.0437	0.0010	0.0184	−0.263	−0.0141

Downloaded 02 May 2010 to 171.66.16.25. Redistribution subject to ASME license or copyright; see http://www.asme.org/terms/Terms_Use.cfm

3 Wilkins, D. J., and Love, T. S., "Combined Compression Torsion Tests of Laminated Composite Cylindrical Shells," AIAA/ASME/SAE 15th Structures, Structural Dynamics, and Materials Conference, Las Vegas, Nev., 1974, AIAA Paper No. 73-379.

Effect of Imperfections on the Vibrations of Loaded Structures

I. Elishakoff,[1] V. Birman,[1] and J. Singer[1]

Introduction

Since the classic dissertation [1] by Koiter in 1945, numerous studies have been devoted to the influence of initial imperfections on the buckling load of different structures, whose load-carrying capacity is often reduced by tens of percent. These studies were extended to vibration problems by Rosen and Singer [2, 3], Lipovski and Tokarenko [4], and Nash [5] in isotropic cylindrical shells, while stiffened shells were treated by Singer and Prucz [6]. An interesting conclusion of these papers was that the natural frequency is also significantly lowered or raised due to initial imperfections.

In this study a simple model structure is used to demonstrate imperfection sensitivity in vibrations. Closed formulas are derived for the natural frequency of axially compressed symmetric, asymmetric, and nonsymmetric structures.

Consider the simple model suggested by Budiansky and Hutchinson [7], a three-hinge rigid rod system constrained laterally by a nonlinear spring, shown in Fig. 1. We suppose that the restoring force F is related to the additional displacement x by

$$F=k_1\xi+k_2\xi^2+k_3\xi^3 \tag{1}$$

where $\xi=x/L$. Denoting the nondimensional initial imperfection by $\bar{\xi}=\bar{x}/L$, the equilibrium requirement yields

$$\lambda(\xi+\bar{\xi})=0.5F\sqrt{1-(\xi+\bar{\xi})^2}=0.5(k_1\xi+k_2\xi^2 +k_3\xi^3)\sqrt{1-(\xi+\bar{\xi})^2} \tag{2}$$

and for small values of ξ, the following result is obtained:

$$\lambda(\xi+\bar{\xi})=\lambda_c[\xi+a\xi^2+b\xi^3+\ \ldots\ ]+0(\xi^2\bar{\xi}) \tag{3}$$

$$\lambda_c=k_1/2,\quad a=k_2/k_1,\quad b=(k_3/k_1)-0.5 \tag{4}$$

Structures with $a=0$, $b\neq 0$ are designated as symmetric, those with $a\neq 0$, $b=0$ as asymmetric, and those with $a\neq 0$, $b\neq 0$ as nonsymmetric. Let us first recapitulate how initial imperfections influence the buckling load, i.e., the maximum load the imperfect structure can sustain. As was shown in reference [7], a symmetric structure is imperfection-sensitive (in the sense that the presence of imperfections reduces the buckling load) both at $\bar{\xi}>0$ and $\bar{\xi}<0$ for $b<0$, and imperfection-insensitive for $b>0$. For an imperfection-sensitive structure with respect to buckling the following formula holds, relating the static buckling load λ to the initial imperfection parameter $\bar{\xi}$:

$$(1-\lambda_s/\lambda_c)^{3/2}-(3\sqrt{3}/2)\,|\bar{\xi}\,|\sqrt{-b}\lambda_s/\lambda_c=0 \tag{5}$$

An asymmetric structure is imperfection-sensitive with respect to buckling at $a\bar{\xi}<0$ and insensitive otherwise, the expression for λ_s being

$$(1-\lambda_s/\lambda_c)^2+4a\bar{\xi}\lambda_s/\lambda_c=0 \tag{6}$$

The nonsymmetric structure ($ab\neq 0$) was considered by Elishakoff [8]. The structure turned out to be imperfection-sensitive for $b<0$ irrespective of the sign of a and $\bar{\xi}$, and insensitive for $b>0$ and $a\bar{\xi}>0$. For $b>0$ and $a\bar{\xi}<0$ there are two subcases: for $a^2\geq 3b$ the structure is imperfection-sensitive; for $a^2<3b$ sensitivity is attained if $\bar{\xi}$ is less than some critical initial imperfection, defined by equation (20) of reference [8].

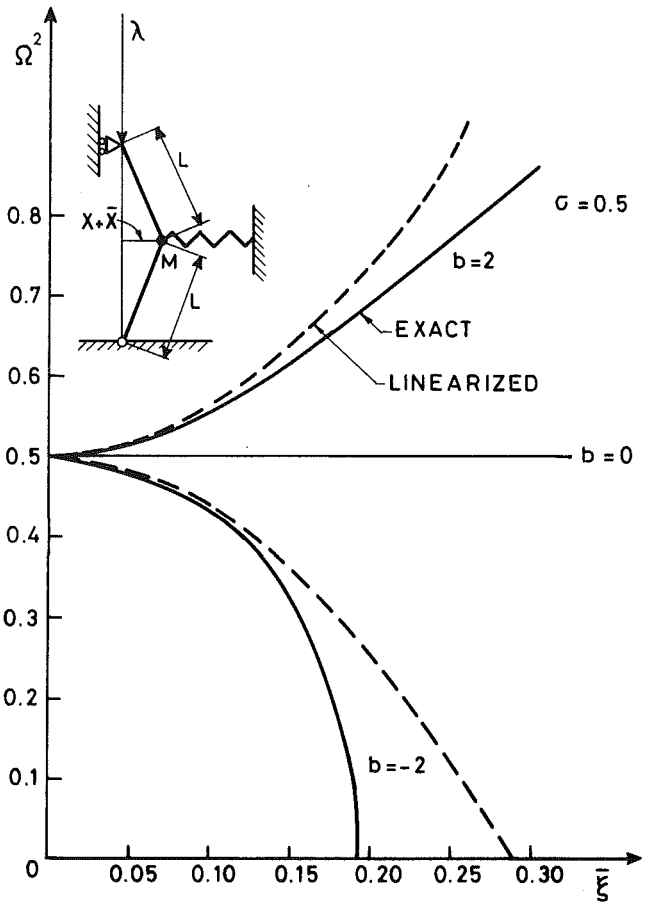

Fig. 1 Mode structure and relative natural frequency versus initial imperfection parameter for symmetric structure ($\sigma=0.5$)

In what follows, formulas analogous to equations (5), (6), and equation (20) of reference [8] are derived for the natural frequency.

Symmetric Structure

The static state described by equation (3) will be hereinafter referred to as basic and indicated by a circumflex, namely

$$\lambda(\hat{\xi}+\bar{\xi})=\lambda_c(\hat{\xi}+b\hat{\xi}^3+\ \ldots\ ) \tag{7}$$

Then, following references [2–4], small vibrations are superimposed on the basic state, so that now

$$\chi(t)=\hat{\xi}+w(t) \tag{8}$$

The corresponding dynamic equation is obtained from equation (30) of reference [9]:

$$(ML/k_1)d^2\chi/dt^2+(1-\lambda/\lambda_c)\chi+b\chi^3=(\lambda/\lambda_c)\bar{\xi} \tag{9}$$

Substituting equation (8) into equation (9), omitting nonlinear terms with respect to $w(t)$, and using equation (7), one obtains

$$(1/\omega_1^2)d^2w/dt^2+(1-\sigma)w+3b\hat{\xi}^2w=0,$$
$$\omega_1=(k_1/ML)^{1/2},\quad \sigma=\lambda/\lambda_c \tag{10}$$

where ω_1 is the natural frequency of the corresponding linear structural model, and σ is the nondimensional axial load. For free vibrations we have $w(t)=We^{i\omega t}$, which upon substituting into equation (10) yields

[1] Department of Aeronautical Engineering, Technion-Israel Institute of Technology, 32000 Haifa, Israel.

Manuscript received by ASME Applied Mechanics Division, August, 1982; final revision, May, 1983.

Downloaded 02 May 2010 to 171.66.16.25. Redistribution subject to ASME license or copyright; see http://www.asme.org/terms/Terms_Use.cfm

3 Wilkins, D. J., and Love, T. S., "Combined Compression Torsion Tests of Laminated Composite Cylindrical Shells," AIAA/ASME/SAE 15th Structures, Structural Dynamics, and Materials Conference, Las Vegas, Nev., 1974, AIAA Paper No. 73-379.

Effect of Imperfections on the Vibrations of Loaded Structures

I. Elishakoff,[1] V. Birman,[1] and J. Singer[1]

Introduction

Since the classic dissertation [1] by Koiter in 1945, numerous studies have been devoted to the influence of initial imperfections on the buckling load of different structures, whose load-carrying capacity is often reduced by tens of percent. These studies were extended to vibration problems by Rosen and Singer [2, 3], Lipovski and Tokarenko [4], and Nash [5] in isotropic cylindrical shells, while stiffened shells were treated by Singer and Prucz [6]. An interesting conclusion of these papers was that the natural frequency is also significantly lowered or raised due to initial imperfections.

In this study a simple model structure is used to demonstrate imperfection sensitivity in vibrations. Closed formulas are derived for the natural frequency of axially compressed symmetric, asymmetric, and nonsymmetric structures.

Consider the simple model suggested by Budiansky and Hutchinson [7], a three-hinge rigid rod system constrained laterally by a nonlinear spring, shown in Fig. 1. We suppose that the restoring force F is related to the additional displacement x by

$$F=k_1\xi+k_2\xi^2+k_3\xi^3 \tag{1}$$

where $\xi=x/L$. Denoting the nondimensional initial imperfection by $\bar{\xi}=\bar{x}/L$, the equilibrium requirement yields

$$\lambda(\xi+\bar{\xi})=0.5F\sqrt{1-(\xi+\bar{\xi})^2}=0.5(k_1\xi+k_2\xi^2 +k_3\xi^3)\sqrt{1-(\xi+\bar{\xi})^2} \tag{2}$$

and for small values of ξ, the following result is obtained:

$$\lambda(\xi+\bar{\xi})=\lambda_c[\xi+a\xi^2+b\xi^3+\ \ldots\ ]+0(\xi^2\bar{\xi}) \tag{3}$$

$$\lambda_c=k_1/2,\quad a=k_2/k_1,\quad b=(k_3/k_1)-0.5 \tag{4}$$

Structures with $a=0$, $b\neq 0$ are designated as symmetric, those with $a\neq 0$, $b=0$ as asymmetric, and those with $a\neq 0$, $b\neq 0$ as nonsymmetric. Let us first recapitulate how initial imperfections influence the buckling load, i.e., the maximum load the imperfect structure can sustain. As was shown in reference [7], a symmetric structure is imperfection-sensitive (in the sense that the presence of imperfections reduces the buckling load) both at $\bar{\xi}>0$ and $\bar{\xi}<0$ for $b<0$, and imperfection-insensitive for $b>0$. For an imperfection-sensitive structure with respect to buckling the following formula holds, relating the static buckling load λ to the initial imperfection parameter $\bar{\xi}$:

$$(1-\lambda_s/\lambda_c)^{3/2}-(3\sqrt{3}/2)\,|\bar{\xi}|\sqrt{-b}\lambda_s/\lambda_c=0 \tag{5}$$

An asymmetric structure is imperfection-sensitive with respect to buckling at $a\bar{\xi}<0$ and insensitive otherwise, the expression for λ_s being

$$(1-\lambda_s/\lambda_c)^2+4a\bar{\xi}\lambda_s/\lambda_c=0 \tag{6}$$

The nonsymmetric structure ($ab\neq 0$) was considered by Elishakoff [8]. The structure turned out to be imperfection-sensitive for $b<0$ irrespective of the sign of a and $\bar{\xi}$, and insensitive for $b>0$ and $a\bar{\xi}>0$. For $b>0$ and $a\bar{\xi}<0$ there are two subcases: for $a^2\geq 3b$ the structure is imperfection-sensitive; for $a^2<3b$ sensitivity is attained if $\bar{\xi}$ is less than some critical initial imperfection, defined by equation (20) of reference [8].

In what follows, formulas analogous to equations (5), (6), and equation (20) of reference [8] are derived for the natural frequency.

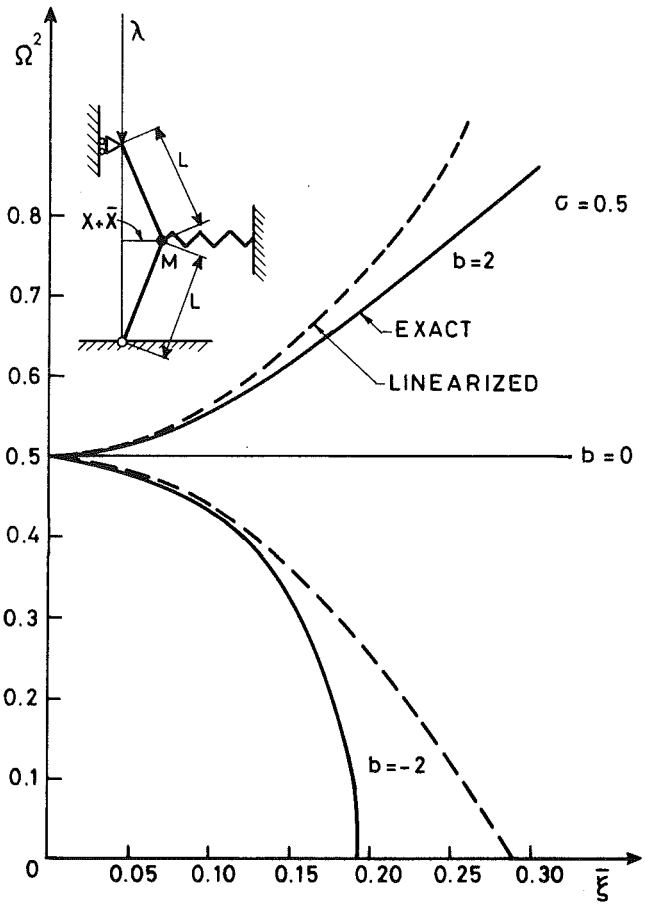

Fig. 1 Mode structure and relative natural frequency versus initial imperfection parameter for symmetric structure ($\sigma=0.5$)

Symmetric Structure

The static state described by equation (3) will be hereinafter referred to as basic and indicated by a circumflex, namely

$$\lambda(\hat{\xi}+\bar{\xi})=\lambda_c(\hat{\xi}+b\hat{\xi}^3+\ \ldots\ ) \tag{7}$$

Then, following references [2–4], small vibrations are superimposed on the basic state, so that now

$$\chi(t)=\hat{\xi}+w(t) \tag{8}$$

The corresponding dynamic equation is obtained from equation (30) of reference [9]:

$$(ML/k_1)d^2\chi/dt^2+(1-\lambda/\lambda_c)\chi+b\chi^3=(\lambda/\lambda_c)\bar{\xi} \tag{9}$$

Substituting equation (8) into equation (9), omitting nonlinear terms with respect to $w(t)$, and using equation (7), one obtains

$$(1/\omega_1^2)d^2w/dt^2+(1-\sigma)w+3b\hat{\xi}^2w=0,$$

$$\omega_1=(k_1/ML)^{1/2},\quad \sigma=\lambda/\lambda_c \tag{10}$$

where ω_1 is the natural frequency of the corresponding linear structural model, and σ is the nondimensional axial load. For free vibrations we have $w(t)=We^{i\omega t}$, which upon substituting into equation (10) yields

[1] Department of Aeronautical Engineering, Technion-Israel Institute of Technology, 32000 Haifa, Israel.

Manuscript received by ASME Applied Mechanics Division, August, 1982; final revision, May, 1983.

Copyright © 1984 by ASME
Downloaded 02 May 2010 to 171.66.16.25. Redistribution subject to ASME license or copyright; see http://www.asme.org/terms/Terms_Use.cfm

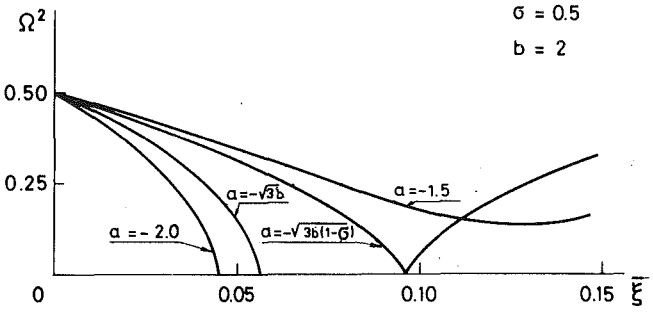

Fig. 2 Nonsymmetric structure may be imperfection-sensitive or not, for different amplitudes of initial imperfection

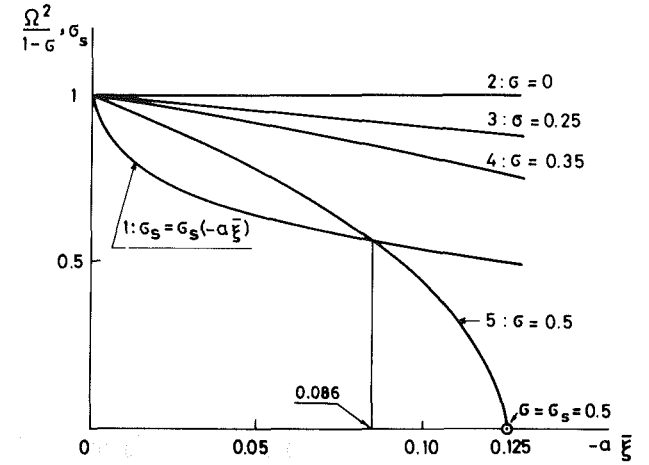

Fig. 3 Comparison of the magnitude of initial imperfection-sensitivity in buckling and in vibrations

$$[-(\omega/\omega_1)^2+(1-\sigma)+3b\hat{\xi}^2]W=0 \tag{11}$$

where ω is the natural frequency. Equation (11) must be solved in conjunction with equation (7).

The final expression for the nondimensional natural frequency $\Omega=\omega/\omega_1$ related to initial imperfections is

$$\left(1-\sigma+\frac{\Omega^2}{2}\right)\left[\frac{\Omega^2-(1-\sigma)}{3b}\right]^{1/2}=\frac{3}{2}\sigma|\bar{\xi}| \tag{12}$$

Equation (12) implies that for the structure to be vibrationally imperfection-sensitive, b must be negative, as in the case of static buckling. For $b>0$, the natural frequency increases with $\bar{\xi}$. The relationship (12) is represented by the solid curves in Fig. 1.

It is of interest to investigate how the final result is influenced by linearization of the basic state equation (7). In that case $\hat{\xi}$ satisfies the equation $\hat{\xi}(1-\sigma)=\sigma\bar{\xi}$ which, substituted in equation (11), yields

$$\Omega^2=1-\sigma+3b\bar{\xi}^2\sigma^2(1-\sigma)^{-2} \tag{13}$$

which is represented by the dashed curves in Fig. 1. For a perfect structure both the "exact" (equation (12)) and approximate (equation (13)) formulas yield $\Omega^2=1-\sigma$, i.e., the natural frequency squared varies linearly with the axial load.

Asymmetric Structure

Following the preceding steps we obtain the nondimensional frequency squared for the asymmetric structure:

$$\Omega^2=(1-\sigma)[1+4a\bar{\xi}\sigma(1-\sigma)^{-2}]^{1/2} \tag{14}$$

A structure that is imperfection-sensitive for buckling turns out to be imperfection-sensitive for vibrations as well: for $a\bar{\xi}<0$, $\Omega^2<1-\sigma$. For an imperfection-insensitive structure the natural frequency increases with the magnitude of initial imperfection, compared with that of a perfect structure.

The solution based on linearization of the basic state is in this case

$$\Omega^2=1-\sigma+2a\bar{\xi}\sigma(1-\sigma)^{-1}$$

Note that this expression is identical to the first two terms of a Taylor series expansion of the exact relationship (14).

Nonsymmetric Case

In this case the two following equations have to be solved simultaneously:

$$-\Omega^2+1-\sigma+2a\hat{\xi}+3b\hat{\xi}^2=0, \tag{15}$$

$$\hat{\xi}(1-\sigma)+a\hat{\xi}^2+b\hat{\xi}^3=\sigma\bar{\xi} \tag{16}$$

yielding the following natural frequency-initial imperfection relationship:

$$\frac{2}{27}\frac{a^3}{b^2}-\frac{1-\sigma}{3b}a\pm\sqrt{a^2-3b(1-\sigma-\Omega^2)}\left(-\frac{2}{27}\frac{a^2}{b^2}+\frac{2}{9}\frac{1-\sigma}{b}+\frac{\Omega^2}{9b}\right)=\sigma\bar{\xi} \tag{17}$$

which is analogous to equation (22) for the static buckling load in reference [8]. Note that for $\Omega=0$, equation (15) represents a linear combination of equation (16) and the expression

$$d\sigma/d\hat{\xi}=0, \quad \sigma=\sigma_s \tag{18}$$

which determines the static buckling (limit) load. This implies that also for the nonsymmetric case, $\Omega=0$ at $\sigma=\sigma_s$. Moreover, after some algebra equation (17) can be written in the following form:

$$\left(1-\sigma-\frac{a^2}{3b}-\Omega^2\right)^3=-27b\left(\sigma\bar{\xi}-\frac{2}{27}\frac{a^3}{b^2}+\frac{1-\sigma}{3b}a\right)^2\times\left(1-\frac{3}{2}\left[1+\frac{\Omega^2/6}{(1-\sigma)/3b-a^2/9b^2}\right]^{-1}\right)^2 \tag{19}$$

which by substituting $\Omega=0$, $\sigma=\sigma_s$ reduces to Elishakoff's result (equation (22) in reference [8]) for the static buckling load.

For buckling the following results were established analytically in reference [8] and numerically in reference [9]: (1) imperfection-sensitivity in terms of buckling for $b>0$ and $a\bar{\xi}<0$ when $a^2\geq 3b$ for any $\bar{\xi}$, and when $a^2<3b$ in a certain interval $(0, \bar{\xi}_{cr})$; (2) imperfection-insensitivity outside this interval. If one now inquires whether this transition from imperfection-sensitivity to insensitivity is preserved also in the case of vibrations one observes in Fig. 2 that for $a^2<3b$ the structure may be imperfection-sensitive or not, depending on the value of $\bar{\xi}$.

Comparison of equation (5) for the buckling (limit) load of a symmetric structure and the corresponding expression (12) for the natural frequency shows that at the limit load $\sigma=\sigma_s$ the natural frequency vanishes (an analogous result for an arch was demonstrated by Johnson et al. [10]). Formula (12) can be rewritten as

$$(1-\sigma+\Omega^2/2)(1-\sigma-\Omega^2)^{1/2}=(\sigma/\sigma_s)(1-\sigma_s)^{3/2} \tag{20}$$

with the initial imperfection parameter appearing only implicitly through σ_s.

The analogous relationship for an asymmetric structure reads

$$\Omega^2=(1-\sigma)[1-(\sigma/\sigma_s)(1-\sigma_s)^2(1-\sigma)^{-2}] \tag{21}$$

It is also of interest to compare the magnitude of initial imperfection-sensitivity in buckling and in vibrations. Consider for example an asymmetric structure. Then for

Downloaded 02 May 2010 to 171.66.16.25. Redistribution subject to ASME license or copyright; see http://www.asme.org/terms/Terms_Use.cfm

$a\xi<0$, and $\xi\to 0$

$$d\sigma_s/d\xi\to-\infty, \quad d\Omega^2/d\xi\to 0. \tag{22}$$

For small imperfections, the structure is, therefore, more imperfection-sensitive in buckling than in vibrations. This is also apparent in Fig. 3, where curve 1 shows the nondimensional buckling load σ_s versus initial imperfection, and curves 2-5 show the nondimensional natural frequency squared of the loaded structure for various values of σ. For $\sigma=0.5$ curves 1 and 5 intersect at $-a\xi=0.086$. This implies that for $-a\xi>0.086$ the structure is more imperfection-sensitive in vibrations. At $-a\xi=0.125$ the natural frequency vanishes, as $\sigma=0.5$ is then the static buckling load σ_s of the structure.

References

1 Koiter, W. T., "On the Stability of Elastic Equilibrium," Ph.D. Thesis, Delft University of Technology, H. J. Paris, Amsterdam; (in Dutch) English translations: (*a*) NASA TTF-10, 833, 1967; (*b*) AFFDL-TR-70-25, 1970.

2 Rosen, A., and Singer, J., "Effect of Axisymmetric Imperfections on the Vibrations of Cylindrical Shells under Axial Compression," *AIAA Journal*, Vol. 12, No. 7, 1974, pp. 995-997.

3 Rosen, A., and Singer, J., "Influence of Asymmetric Imperfections on the Vibrations of Axially Compressed Cylindrical Shells," *Israel Journal of Technology*, Vol. 14, 1976, pp. 23-36.

4 Lipovskii, D. E., and Tokarenko, V. M., "Effect of Initial Imperfections on Free Oscillation Frequencies of Cylindrical Shells," *6th All-Union Conference on the Theory of Shells and Plates*, Nauka, 1966, pp. 542-547 (in Russian).

5 Nash, W. A., "Free Vibrations of Initially Imperfect Cylindrical Shells," *Proceedings of the Eighth Canadian Congress of Applied Mechanics*, Moncton, June 1981, pp. 365-366.

6 Singer, J., and Prucz, J., "Influence of Initial Geometrical Imperfections on Vibrations of Axially Compressed Stiffened Cylindrical Shells," *Journal of Sound and Vibration*, Vol. 80, No. 1, 1982, pp. 117-143.

7 Budiansky, B., and Hutchinson, J. W., "Dynamic Buckling of Imperfection-Sensitive Structures," *Proceedings of the Eleventh International Congress of Applied Mechanics*, Goertler, H., ed., Munich, 1964, pp. 636-651.

8 Elishakoff, I., "Remarks on the Static and Dynamic Imperfection-Sensitivity of Nonsymmetric Structures," ASME JOURNAL OF APPLIED MECHANICS, Vol. 47, 1980, pp. 111-115.

9 Budiansky, B., "Dynamic Buckling of Elastic Structures: Criteria and Estimates," in *Dynamic Stability of Structures*, Herrmann, G., ed., Pergamon, 1967, pp. 83-106.

10 Johnson, E. R., Plaut, R. H., and Deel, II, C. C., "Load-Frequency Relationships for Shallow Elastic Structures," in *Recent Advances in Structural Dynamics*, Petyt, M., ed., Institute of Sound and Vibration Research, University of Southampton Press, 1980, pp. 611-620.

On the Nature of Eigenvalues of General Nonconservative Systems

M. Ahmadian[1] and D. J. Inman[1]

Introduction

The dynamic behavior of a general lumped-parameter system can be described by the vector differential equation

$$M\ddot{x}(t)+C\dot{x}(t)+Kx(t)=0 \tag{1}$$

where M, C, and K are referred to as mass, damping, and stiffness matrices, and $x(t)$ represents the displacement vector. For passive systems of the conventional type, the matrices M, C, and K are symmetric positive-definite or semidefinite and a number of well-known theories have been developed for such systems. One such theory is that developed by Inman and Andry on the oscillatory behavior of a symmetric system [1]. It has been shown that similar to a single degree-of-freedom system the oscillatory nature of a symmetric multidegree-of-freedom system can be predicted by forming a critical damping matrix (i.e., $C_{cr}=2(M^{-1/2}KM^{-1/2})^{1/2}$) and studying the definiteness of the matrix $M^{-1/2}CM^{-1/2}-C_{cr}$. Here the superscript $-1/2$ refers to the inverse of the positive-definite square root, a positive-definite matrix.

For a general nonconservative system, the symmetry restrictions are not met by M, C, and K. These matrices are then merely square arrays of real numbers (i.e., asymmetric matrices). Problems of this type arise in vehicle dynamics as well as in the study of a circulatory and gyroscopic systems [2-5]. In this work it is shown that the results developed in [1] can be stated for a certain class of asymmetric systems. The systems considered are those with nonsingular mass matrix and that are transferable into a symmetric form.

These systems are commonly known as symmetrizable systems and have the form

$$I\ddot{x}(t)+\tilde{C}\dot{x}(t)+\tilde{K}x(t)=0, \tag{2}$$

where $\tilde{C}=M^{-1}C$, and $\tilde{K}=M^{-1}K$ are assumed to have positive eigenvalues and a full set of eigenvectors [6].

Symmetrizable systems are defined in [2] as systems that have symmetrizable coefficients $\tilde{C}$ and $\tilde{K}$, i.e., such that $\tilde{C}$ and $\tilde{K}$ can be factored as

$$\tilde{C}=S_1S_2, \quad S_1=S_1^T>0, \quad S_2=S_2^T \tag{3}$$

$$\tilde{K}=T_1T_2, \quad T_1=T_1^T>0, \quad T_2=T_2^T \tag{4}$$

and such that the coefficients $\tilde{C}$ and $\tilde{K}$ have at least one factor in common, i.e., $S_1=T_1$. Here, the superscript T indicates the matrix transpose and the inequality denotes positive-definiteness.

Results

Substituting (3) and (4) into (2) and considering the symmetrizability property of the system results in a system of the form

$$\ddot{x}(t)+S_1S_2\dot{x}(t)+S_1T_2x(t)=0 \tag{5}$$

Note that since $\tilde{C}$ and $\tilde{K}$ are assumed to have positive eigenvalues, S_1, S_2, and T_2 are all symmetric positive-definite matrices and the system described by (2) is asymptotically stable [2].

Letting $x(t)=S_1^{1/2}y(t)$ and premultiplying (5) by $S_1^{-1/2}$ results in:

$$\ddot{y}(t)+S_1^{1/2}S_2S_1^{1/2}\dot{y}(t)+S_1^{1/2}T_2S_1^{1/2}y(t)=0. \tag{6}$$

Hence, via a similarity transformation the asymmetric system described by (2) has been reduced to a symmetric form, and the definitions and results developed in [1], mentioned in the foregoing can be applied to equation (6). This implies that:

(*i*) If $S_1^{1/2}S_2S_1^{1/2}-2(S_1^{1/2}T_2S_1^{1/2})^{1/2}>0$, then the system is overdamped.

(*ii*) If $2(S_1^{1/2}T_2S_1^{1/2})^{1/2}-S_1^{1/2}S_2S_1^{1/2}>0$, then the system is underdamped.

(*iii*) If $S_1^{1/2}S_2S_1^{1/2}-2(S_1^{1/2}T_2S_1^{1/2})^{1/2}=0$, then the system is critically damped.

(*iv*) If $S_1^{1/2}S_2S_1^{1/2}-2(S_1^{1/2}T_2S_1^{1/2})^{1/2}$ is indefinite and $S_2S_1T_2=T_2S_1S_2$, then the system is mixed damped.

In an attempt to present the preceding relations directly in terms of the coefficient matrices of (1), recall equations (3) and (4), and note that

$$S_2=S_1^{-1}\tilde{C}, \tag{7}$$

$$T_2=S_1^{-1}\tilde{K}. \tag{8}$$

[1]Graduate Research Assistant, Student Mem. ASME, and Assistant Professor, Assoc. Mem. ASME, respectively, Department of Mechanical and Aerospace Engineering, State University of New York at Buffalo, Buffalo, New York 14260.

Manuscript received by ASME Applied Mechanics Division, September, 1982; final revision, August, 1983.

Downloaded 02 May 2010 to 171.66.16.25. Redistribution subject to ASME license or copyright; see http://www.asme.org/terms/Terms_Use.cfm

$a\xi<0$, and $\xi\to 0$

$$d\sigma_s/d\xi\to-\infty, \quad d\Omega^2/d\xi\to 0. \tag{22}$$

For small imperfections, the structure is, therefore, more imperfection-sensitive in buckling than in vibrations. This is also apparent in Fig. 3, where curve 1 shows the nondimensional buckling load σ_s versus initial imperfection, and curves 2-5 show the nondimensional natural frequency squared of the loaded structure for various values of σ. For $\sigma=0.5$ curves 1 and 5 intersect at $-a\xi=0.086$. This implies that for $-a\xi>0.086$ the structure is more imperfection-sensitive in vibrations. At $-a\xi=0.125$ the natural frequency vanishes, as $\sigma=0.5$ is then the static buckling load σ_s of the structure.

References

1 Koiter, W. T., "On the Stability of Elastic Equilibrium," Ph.D. Thesis, Delft University of Technology, H. J. Paris, Amsterdam; (in Dutch) English translations: (*a*) NASA TTF-10, 833, 1967; (*b*) AFFDL-TR-70-25, 1970.

2 Rosen, A., and Singer, J., "Effect of Axisymmetric Imperfections on the Vibrations of Cylindrical Shells under Axial Compression," *AIAA Journal*, Vol. 12, No. 7, 1974, pp. 995-997.

3 Rosen, A., and Singer, J., "Influence of Asymmetric Imperfections on the Vibrations of Axially Compressed Cylindrical Shells," *Israel Journal of Technology*, Vol. 14, 1976, pp. 23-36.

4 Lipovskii, D. E., and Tokarenko, V. M., "Effect of Initial Imperfections on Free Oscillation Frequencies of Cylindrical Shells," *6th All-Union Conference on the Theory of Shells and Plates*, Nauka, 1966, pp. 542-547 (in Russian).

5 Nash, W. A., "Free Vibrations of Initially Imperfect Cylindrical Shells," *Proceedings of the Eighth Canadian Congress of Applied Mechanics*, Moncton, June 1981, pp. 365-366.

6 Singer, J., and Prucz, J., "Influence of Initial Geometrical Imperfections on Vibrations of Axially Compressed Stiffened Cylindrical Shells," *Journal of Sound and Vibration*, Vol. 80, No. 1, 1982, pp. 117-143.

7 Budiansky, B., and Hutchinson, J. W., "Dynamic Buckling of Imperfection-Sensitive Structures," *Proceedings of the Eleventh International Congress of Applied Mechanics*, Goertler, H., ed., Munich, 1964, pp. 636-651.

8 Elishakoff, I., "Remarks on the Static and Dynamic Imperfection-Sensitivity of Nonsymmetric Structures," ASME JOURNAL OF APPLIED MECHANICS, Vol. 47, 1980, pp. 111-115.

9 Budiansky, B., "Dynamic Buckling of Elastic Structures: Criteria and Estimates," in *Dynamic Stability of Structures*, Herrmann, G., ed., Pergamon, 1967, pp. 83-106.

10 Johnson, E. R., Plaut, R. H., and Deel, II, C. C., "Load-Frequency Relationships for Shallow Elastic Structures," in *Recent Advances in Structural Dynamics*, Petyt, M., ed., Institute of Sound and Vibration Research, University of Southampton Press, 1980, pp. 611-620.

On the Nature of Eigenvalues of General Nonconservative Systems

M. Ahmadian[1] and D. J. Inman[1]

Introduction

The dynamic behavior of a general lumped-parameter system can be described by the vector differential equation

$$M\ddot{x}(t)+C\dot{x}(t)+Kx(t)=0 \tag{1}$$

where M, C, and K are referred to as mass, damping, and stiffness matrices, and $x(t)$ represents the displacement vector. For passive systems of the conventional type, the matrices M, C, and K are symmetric positive-definite or semidefinite and a number of well-known theories have been developed for such systems. One such theory is that developed by Inman and Andry on the oscillatory behavior of a symmetric system [1]. It has been shown that similar to a single degree-of-freedom system the oscillatory nature of a symmetric multidegree-of-freedom system can be predicted by forming a critical damping matrix (i.e., $C_{cr}=2(M^{-1/2}KM^{-1/2})^{1/2}$) and studying the definiteness of the matrix $M^{-1/2}CM^{-1/2}-C_{cr}$. Here the superscript $-1/2$ refers to the inverse of the positive-definite square root, a positive-definite matrix.

For a general nonconservative system, the symmetry restrictions are not met by M, C, and K. These matrices are then merely square arrays of real numbers (i.e., asymmetric matrices). Problems of this type arise in vehicle dynamics as well as in the study of a circulatory and gyroscopic systems [2-5]. In this work it is shown that the results developed in [1] can be stated for a certain class of asymmetric systems. The systems considered are those with nonsingular mass matrix and that are transferable into a symmetric form.

These systems are commonly known as symmetrizable systems and have the form

$$I\ddot{x}(t)+\tilde{C}\dot{x}(t)+\tilde{K}x(t)=0, \tag{2}$$

where $\tilde{C}=M^{-1}C$, and $\tilde{K}=M^{-1}K$ are assumed to have positive eigenvalues and a full set of eigenvectors [6].

Symmetrizable systems are defined in [2] as systems that have symmetrizable coefficients $\tilde{C}$ and $\tilde{K}$, i.e., such that $\tilde{C}$ and $\tilde{K}$ can be factored as

$$\tilde{C}=S_1S_2, \quad S_1=S_1^T>0, \quad S_2=S_2^T \tag{3}$$

$$\tilde{K}=T_1T_2, \quad T_1=T_1^T>0, \quad T_2=T_2^T \tag{4}$$

and such that the coefficients $\tilde{C}$ and $\tilde{K}$ have at least one factor in common, i.e., $S_1=T_1$. Here, the superscript T indicates the matrix transpose and the inequality denotes positive-definiteness.

Results

Substituting (3) and (4) into (2) and considering the symmetrizability property of the system results in a system of the form

$$\ddot{x}(t)+S_1S_2\dot{x}(t)+S_1T_2x(t)=0 \tag{5}$$

Note that since $\tilde{C}$ and $\tilde{K}$ are assumed to have positive eigenvalues, S_1, S_2, and T_2 are all symmetric positive-definite matrices and the system described by (2) is asymptotically stable [2].

Letting $x(t)=S_1^{1/2}y(t)$ and premultiplying (5) by $S_1^{-1/2}$ results in:

$$\ddot{y}(t)+S_1^{1/2}S_2S_1^{1/2}\dot{y}(t)+S_1^{1/2}T_2S_1^{1/2}y(t)=0. \tag{6}$$

Hence, via a similarity transformation the asymmetric system described by (2) has been reduced to a symmetric form, and the definitions and results developed in [1], mentioned in the foregoing can be applied to equation (6). This implies that:

(*i*) If $S_1^{1/2}S_2S_1^{1/2}-2(S_1^{1/2}T_2S_1^{1/2})^{1/2}>0$, then the system is overdamped.

(*ii*) If $2(S_1^{1/2}T_2S_1^{1/2})^{1/2}-S_1^{1/2}S_2S_1^{1/2}>0$, then the system is underdamped.

(*iii*) If $S_1^{1/2}S_2S_1^{1/2}-2(S_1^{1/2}T_2S_1^{1/2})^{1/2}=0$, then the system is critically damped.

(*iv*) If $S_1^{1/2}S_2S_1^{1/2}-2(S_1^{1/2}T_2S_1^{1/2})^{1/2}$ is indefinite and $S_2S_1T_2=T_2S_1S_2$, then the system is mixed damped.

In an attempt to present the preceding relations directly in terms of the coefficient matrices of (1), recall equations (3) and (4), and note that

$$S_2=S_1^{-1}\tilde{C}, \tag{7}$$

$$T_2=S_1^{-1}\tilde{K}. \tag{8}$$

[1]Graduate Research Assistant, Student Mem. ASME, and Assistant Professor, Assoc. Mem. ASME, respectively, Department of Mechanical and Aerospace Engineering, State University of New York at Buffalo, Buffalo, New York 14260.

Manuscript received by ASME Applied Mechanics Division, September, 1982; final revision, August, 1983.

Copyright © 1984 by ASME

Downloaded 02 May 2010 to 171.66.16.25. Redistribution subject to ASME license or copyright; see http://www.asme.org/terms/Terms_Use.cfm

Substituting (7) and (8) into

$$S_1^{1/2} S_2 S_1^{1/2} - 2(S_1^{1/2} T_2 S_1^{1/2})^{1/2} \tag{9}$$

results in:

$$S_1^{-1/2} \tilde{C} S_1^{1/2} - 2S_1^{-1/2} \tilde{K}^{1/2} S_1^{1/2}. \tag{10}$$

Considering the fact that a similarity transformation preserves eigenvalues, the foregoing can be written in the following form which necessarily has the same eigenvalues as (10):

$$\tilde{C} - 2\tilde{K}^{1/2}$$

or

$$M^{-1}C - 2(M^{-1}K)^{1/2} \tag{11}$$

Because all the performed transformations preserve eigenvalues, the same concepts developed for the nature of the latent roots of a symmetric system holds true for the asymmetric case described by (1). Thus, using equation (11) (*i*)-(*iv*) can be presented in terms of $M^{-1}C$ and $M^{-1}K$ as follows:

1 If $M^{-1}C - 2(M^{-1}K)^{1/2}$ has all positive eigenvalues, then the system is overdamped in each mode which results in negative real latent roots and real latent vectors.

2 If $M^{-1}C - 2(M^{-1}K)^{1/2}$ has all negative eigenvalues, then the system is underdamped in each mode. In this case all the latent roots are complex numbers, with negative real parts, along with complex latent vectors.

3 If $M^{-1}C - 2(M^{-1}K)^{1/2} = 0$, then each mode is critically damped. Latent roots are pairs of negative real numbers in this case, latent vectors are also real.

4 If $M^{-1}C - 2(M^{-1}K)^{1/2}$ has both positive and negative eigenvalues and $CM^{-1}K = KM^{-1}C$, then the system possesses mixed damping. In this case at least one of the modes is overdamped, which results in negative real latent root, and at least one is underdamped resulting in complex latent root with negative real part.

It is noted that the preceding conditions are only sufficient. However, if the damping and stiffness matrices commute (i.e., $M^{-1}KM^{-1}C = M^{-1}CM^{-1}K$ or $KM^{-1}C = CM^{-1}K$), then they become necessary, too. To illustrate this, let $y = P^{-1}x$ and premultiply (2) by P, then

$$\ddot{y}(t) + P^{-1}\tilde{C}P\dot{y}(t) + P^{-1}\tilde{K}Py(t) = 0 \tag{12}$$

Assuming P to be the modal matrix of $\tilde{C}$ or $\tilde{K}$ (i.e., a matrix that is composed of eigenvectors of $\tilde{C}$ or $\tilde{K}$), then the foregoing can be written as

$$\ddot{y}(t) + \Lambda_{\tilde{C}}\dot{y}(t) + \Lambda_{\tilde{K}}y(t) = 0, \tag{13}$$

where $\Lambda_{\tilde{C}}$ and $\Lambda_{\tilde{K}}$ are diagonal matrices containing the eigenvalues of $\tilde{C}$ and $\tilde{K}$ as their diagonal entries. The eigenvalue problem associated with (13) is:

$$\lambda^2 + \Lambda_{\tilde{C}}\lambda + \Lambda_{\tilde{K}} = 0, \tag{14}$$

which is in diagonal form. The *i*th equation of (14) is:

$$\lambda^2{}_i + (\Lambda_{\tilde{C}})_{ii}\lambda_i + (\Lambda_{\tilde{K}})_{ii} = 0, \tag{15}$$

and its roots are found as:

$$(\lambda_i)_{1,2} = \frac{-(\Lambda_{\tilde{C}})_{ii} \mp ((\Lambda_{\tilde{C}})_{ii}^2 - 4(\Lambda_{\tilde{K}})_{ii})^{1/2}}{2}. \tag{16}$$

Now consider the overdamped case, if $M^{-1}C - 2(M^{-1}K)^{1/2}$ has all positive eigenvalues, then

$$(\Lambda_{\tilde{C}})_{ii} - 2(\Lambda_{\tilde{K}})_{ii}^{1/2} > 0. \tag{17}$$

Since both $(\Lambda_{\tilde{C}})_{ii}$ and $(\Lambda_K)_{ii}^{1/2}$ are positive, the foregoing also implies that

$$(\Lambda_{\tilde{C}})_{ii}^2 - 4(\Lambda_{\tilde{K}})_{ii} > 0, \tag{18}$$

which results in negative real latent roots (i.e., $(\lambda_i)_{1,2}$). It also can be easily seen that if (18) is valid, then (17) holds true and as a result the matrix $M^{-1}C - 2(M^{-1}K)^{1/2}$ has positive eigenvalues, which completes the necessity and sufficiency conditions. The proof for the underdamped, critically damped, and mixed damped cases are very similar to the foregoing and are not presented here.

Further note that since M is assumed to be a nonsingular matrix, then the matrices

$$M^{-1}C - 2(M^{-1}K)^{1/2}$$

and

$$C - 2M(M^{-1}K)^{1/2} \tag{19}$$

have the same eigenvalues and if M and K commute (i.e., $MK = KM$), then (19) can be reduced to:

$$C - 2(MK)^{1/2}. \tag{20}$$

Thus for the special case when the mass and stiffness matrices commute, it is possible to present the matrix $M^{-1}C - 2(M^{-1}K)^{1/2}$ in a computationally more efficient form as given in (20). Additional computational savings are presented in [7].

Concluding Remarks

The previously developed results on the oscillatory behavior of the conventional passive systems described by

$$M\ddot{x}(t) + C\dot{x}(t) + Kx(t) = 0,$$

where M, C, and K are symmetric positive-definite or semidefinite, were briefly mentioned. It was shown that the preceding results can be extended to include nonconservative systems where the matrices M, C, and K are symmetrizable square arrays of real numbers. In particular the concept of a critical damping matrix has been extended to a certain class of asymmetric systems. Similar to a single degree-of-freedom system, the oscillation behavior of an asymmetric system can be predicted by forming the critical damping matrix $2(M^{-1}K)^{1/2}$ and studying the nature of eigenvalues of the matrix $M^{-1}C - 2(M^{-1}K)^{1/2}$. It was further shown that under certain conditions when the damping and stiffness matrices commute (i.e., $CM^{-1}K = KM^{-1}C$) the developed results become both necessary and sufficient.

Acknowledgment

This work was supported in part by NSF grant #MEA8112826 and in part by AFOSR grant #AFOSR820242.

References

1 Inman, D. J., and A. N., Jr. Andry, "Some Results on the Nature of Eigenvalues of Discrete Damped Linear Systems," ASME JOURNAL OF APPLIED MECHANICS, Vol. 47, 1980, pp. 927-930.

2 Inman, D. J., "Dynamics of Asymmetric Non-Conservative Systems," ASME JOURNAL OF APPLIED MECHANICS, Vol. 50, 1983, pp. 199-203.

3 Fawzy, I., and Bishop, R.E.D., "On the Dynamics of Linear Non-Conservative Systems," *Proceedings of the Royal Society*, London, Series, *A*, Vol. 352, 1976, pp. 25-40.

4 Washed, I. F. A., and Bishop, R. E. D., "On the Equations Governing the Free and Forced Vibrations of a General Non-Conservative System," *Journal of Mechanical Engineering Science*, Vol. 18, 1976, pp. 6-10.

5 Shieh, R. C., and Masur, E. F., "Some General Principle of Dynamic Instability of Solid Bodies," *ZAMP*, Vol. 19, 1968, pp. 927-941.

6 Tausskey, O., and Zassenhaus, H., "On the Similarity Transformation Between a Matrix and its Transpose," *Pacific Journal of Mathematics*, Vol. 9, 1959, pp. 893-896.

7 Inman, D. J., and Orabi, I, "An Efficient Method for Computing the Critical Damping Condition," ASME JOURNAL OF APPLIED MECHANICS, Vol. 50, 1983, pp. 679-682.

Downloaded 02 May 2010 to 171.66.16.25. Redistribution subject to ASME license or copyright; see http://www.asme.org/terms/Terms_Use.cfm

A Higher Order Theory for Free Vibration of Orthotropic, Homogeneous, and Laminated Rectangular Plates

A. Bhimaraddi[1] and L. K. Stevens[1]

1 Introduction

The thick homogeneous and laminated plates are basically the three-dimensional problems. The advantages of being able to treat them as two-dimensional problems attracted research workers to develop two-dimensional models for the analysis of such structures. Also, as the use of composites for high-performance design applications increases, the need for more realistic prediction of the response characteristics of composite material structures becomes increasingly important. Recent developments in the analysis of plates and shells laminated of fiber-reinforced materials indicate that thickness has more pronounced effects on the behavior of composite plates than on isotropic laminates. Also, due to the low transverse shear moduli relative to the in-plane Young's moduli, transverse shear deformation effects are even more pronounced in composite laminates. Reliable prediction of the response characteristics of high modulus composite plates, therefore, require the use of shear deformation theories.

Srinivas, et. al [1, 2] have carried out extensive studies of thickness effects on vibration and buckling of homogeneous and laminated plates using three-dimensional elasticity theory. A generalization of Reissner-Mindlin plate theory, for homogeneous isotropic plates, to arbitrarily laminated anisotropic plates including the shear deformation and rotary inertia effects has been carried out by Yang, Norris, and Stavsky [3]. The review of various other theories can be found in [4].

In two-dimensional plate theories displacement components have been considered as power series expressions in normal coordinate (z). Thus, depending on the number of terms considered in the power series the accuracy and the complexity of the problem varies [5, 6]. In this Note an attempt is made to propose a two-dimensional theory for the analysis of thick homogeneous and laminated plates by considering the total of five unknowns, which are the middle surface displacement quantities, and still maintaining the higher order (cubic) polynomial form for in-plane displacement expressions and at the same time the more realistic parabolic variation (with zero values at the top and bottom surfaces of the plate) for transverse shear strains is achieved. The shear deformation theory and thin plate theory have been evaluated using present solution.

2 Derivation of Governing Equations of Motions

Let us select a Cartesian coordinate system such that the x-y plane coincides with the midplane of the plate of sides a, b and of total thickness h (also h_1, h_2, h_3 are the thicknesses of individual layers in the case of layered plate). The components of displacements are assumed as follows

$$u = u_0 + \xi u_1 - z w_{,x}; \quad v = v_0 + \xi v_1 - z w_{,y}; \quad w = w \tag{1}$$

where $\xi = z(1 - 4z^2/3h^2)$, the comma indicates the differentiation with respect to the letter(s) followed by it, and u, v, w are the displacements in x, y, z directions, respectively. It may be noted that the preceding form of expressions for displacement components results in the parabolic variation of transverse shear strains as is evident from equation (2). To limit the complexity of the problem to a reasonable degree, the expression for w is chosen to be a constant and at the same time this allows us to have zero transverse shear strains at the top and bottom surfaces of the plate. The strain displacement relations of the three-dimensional elasticity [7] become

$$\epsilon_x = u_{0,x} + \xi u_{1,x} - z w_{,xx}; \quad \epsilon_y = v_{0,y} + \xi v_{1,y} - z w_{,yy}; \quad \epsilon_z = 0$$
$$\gamma_{xz} = \xi_1 u_1; \quad \gamma_{yz} = \xi_1 v_1; \quad \gamma_{xy} = u_{0,y} + \xi u_{1,y} + v_{0,x} + \xi v_{1,x} - 2z w_{,xy} \tag{2}$$

where

$$\xi_1 = \left(1 - \frac{4z^2}{h^2}\right)$$

Assuming $\sigma_z = 0$, the constitutive relations for any layer of the laminate are of the form

$$\sigma_x = C_{11}\epsilon_x + C_{12}\epsilon_y; \quad \sigma_y = C_{12}\epsilon_x + C_{22}\epsilon_y$$
$$\tau_{xz} = C_{44}\gamma_{xz}; \quad \tau_{yz} = C_{55}\gamma_{yz}; \quad \tau_{xy} = C_{66}\gamma_{xy} \tag{3}$$

We have the following definitions for stress resultants appropriate to this theory

$$\begin{bmatrix} N_x & N_{xy} & N_y \\ M_x & M_{xy} & M_y \\ M'_x & M'_{xy} & M'_y \end{bmatrix} = \int_{-h/2}^{+h/2} \begin{bmatrix} 1 \\ -z \\ \xi \end{bmatrix} (\sigma_x, \tau_{xy}, \sigma_y)\, dz \tag{4}$$

The strain energy of the plate under consideration is given as

$$U = \frac{1}{2}\int_y \int_x \int_z (C_{11}\epsilon_x^2 + 2C_{12}\epsilon_x\epsilon_y + C_{22}\epsilon_y^2 + C_{44}\gamma_{xz}^2 + C_{55}\gamma_{yz}^2 + C_{66}\gamma_{xy}^2)\, dz dx dy \tag{5}$$

The kinetic energy of the plate is

$$K = \frac{1}{2}\int_y \int_x \int_z \rho(u_{,t}^2 + v_{,t}^2 + w_{,t}^2)\, dz dx dy \tag{6}$$

Here, ρ is the mass density (also ρ_1, ρ_2, ρ_3 are the mass densities of each layer in the case of layered plate), and t is the time coordinate. The work done by the applied surface forces, considering applied forces in the z-direction only, may be written as

$$W = \frac{1}{2}\int_y \int_x 2(q_{zo} + q_{zi})\, w\, dx dy \tag{7}$$

where, q_{zo} and q_{zi} are the applied forces in z-direction on outer and inner surfaces of the plate, respectively. Thus, the total potential energy of the plate is written as

$$\Pi = K + W - U \tag{8}$$

Using Hamilton's principle [8] to equation (8) the following equations of dynamic equilibrium can be obtained

Table 1 Orthotropic properties considered in examples

		Mat.-1	Mat.-2	Mat.-3	Mat.-4
E_x	(GPa)	55.8979	36.0885	35.2059	17.5539
E_y	"	13.7293	26.2818	28.7335	12.8467
E_z	"	13.7293	10.7873	17.9462	4.2169
μ_{xy}		0.277	0.105	0.177	0.150
μ_{zx}		0.068	0.405	0.157	0.080
μ_{yz}		0.400	0.431	0.371	0.310
G_{xy}	"	5.5898	4.9033	7.4531	2.7459
G_{xz}	"	5.5898	4.4130	6.4724	2.3536
G_{yz}	"	4.9033	4.0208	6.1782	2.3536

The properties of orthotropic materials refer to four kinds of glass-fiber reinforced plastics [9].

[1]Research Scholar and Professor, respectively, Department of Civil Engineering, University of Melbourne, Parkville, Victoria 3052, Australia.

Manuscript received by ASME Applied Mechanics Division, June, 1983; final revision, August, 1983.

Copyright © 1984 by ASME
Downloaded 02 May 2010 to 171.66.16.25. Redistribution subject to ASME license or copyright; see http://www.asme.org/terms/Terms_Use.cfm

Table 2 Comparison of lowest natural frequency values (Ω/Ω_0) for orthotropic homogeneous square ($a/b=1$) plates

α		Material 1		Material 2		Material 3		Material 4	
		Value	Percent Dif.	Value	Percent Dif.	Value	Percent Dif.	Value	Percent Dif.
0.1	P	0.03617	–	0.04135	–	0.04707	–	0.04362	–
	S	0.03615	0.07	0.04133	0.06	0.04705	0.05	0.04359	0.06
	T	0.03800	5.10	0.04330	4.71	0.04891	4.00	0.04562	4.60
0.2	P	0.12628	–	0.14531	–	0.16800	–	0.15362	–
	S	0.12596	0.25	0.14496	0.24	0.16767	0.20	0.15328	0.23
	T	0.14844	18.0	0.16914	16.4	0.19107	14.0	0.17818	16.0
0.3	P	0.24226	–	0.28005	–	0.32861	–	0.29678	–
	S	0.24098	0.50	0.27866	0.50	0.32727	0.40	0.29536	0.50
	T	0.32181	33.0	0.36668	31.0	0.41421	26.0	0.38628	30.0
0.4	P	0.36885	–	0.42714	–	0.50697	–	0.45354	–
	S	0.36561	0.88	0.42354	0.85	0.50347	0.70	0.44984	0.82
	T	0.54541	48.0	0.62145	46.0	0.70200	39.0	0.65468	44.0
0.5	P	0.50021	–	0.57898	–	0.69285	–	0.61566	–
	S	0.49366	1.30	0.57160	1.30	0.68567	1.00	0.60807	1.23
	T	0.80626	61.0	0.91867	59.0	1.03975	50.0	0.96780	57.0

$\Omega_0=\sqrt{E_\lambda/\rho h^2}$, P-present, S-shear deformation [3], T-thin plate theory

Table 3 Comparison of lowest natural frequency values (Ω/Ω_0) for two-ply (0/90) laminated square ($a/b=1$) plates

α		$h_2/h_1=\beta$				
		1	5	10	15	20
0.1	P	0.06572	0.07061	0.07221	0.07265	0.07282
	S	0.06534	0.07057	0.07218	0.07262	0.07279
	T	0.06766	0.07358	0.07550	0.07606	0.07630
0.2	P	0.23791	0.24995	0.25426	0.25527	0.25556
	S	0.23362	0.24951	0.25390	0.25486	0.25511
	T	0.26205	0.28628	0.29440	0.29684	0.29788
0.3	P	0.47275	0.48536	0.49141	0.49249	0.49255
	S	0.45803	0.48348	0.48961	0.49047	0.49039
	T	0.56005	0.61601	0.63597	0.64221	0.64492
0.4	P	0.74005	0.74507	0.75184	0.75271	0.75235
	S	0.70809	0.73997	0.74659	0.74688	0.74621
	T	0.93079	1.03140	1.07071	1.08398	1.09001
0.5	P	1.02430	1.01518	1.02224	1.02294	1.02219
	S	0.96894	1.00439	1.01076	1.01033	1.00903
	T	1.34366	1.49655	1.56250	1.58762	1.60022

$\Omega_0=\sqrt{E_{x2}/\rho_2 h^2}$, orthotropic properties confirm to material 1 of Table 1

Table 4 Comparison of lowest natural frequency values (Ω/Ω_0) for three-ply (0/90/0) laminated square ($a/b=1$) plates

α		$h_2/h_1=h_2/h_3=\beta$				
		1	5	10	15	20
0.1	P	0.07304	0.07424	0.07458	0.07467	0.07471
	S	0.07290	0.07319	0.07321	0.07315	0.07310
	T	0.07667	0.07659	0.07654	0.07652	0.07650
0.2	P	0.25552	0.26907	0.27348	0.27476	0.27529
	S	0.25396	0.25744	0.25792	0.25751	0.25705
	T	0.29949	0.29919	0.29899	0.29889	0.29883
0.3	P	0.49119	0.53438	0.55000	0.55470	0.55665
	S	0.48588	0.49631	0.49778	0.49669	0.49541
	T	0.64927	0.64861	0.64819	0.64797	0.64784
0.4	P	0.74906	0.83448	0.86850	0.87932	0.88340
	S	0.73740	0.75632	0.75891	0.75729	0.75484
	T	1.10039	1.09928	1.09856	1.09862	1.09797
0.5	P	1.01692	1.15056	1.20875	1.22738	1.23501
	S	0.99607	1.02294	1.02647	1.02395	1.02092
	T	1.62667	1.62504	1.62397	1.62342	1.62310

$\Omega_0=\sqrt{E_{x2}/\rho_2 h^2}$, orthotropic properties confirm to material 1 of Table 1

Downloaded 02 May 2010 to 171.66.16.25. Redistribution subject to ASME license or copyright; see http://www.asme.org/terms/Terms_Use.cfm

$$[L_{ij}]\begin{Bmatrix} u_0 \\ v_0 \\ u_1 \\ v_1 \\ w \end{Bmatrix} = \begin{Bmatrix} 0 \\ 0 \\ 0 \\ 0 \\ -(q_{zo}+q_{zi}) \end{Bmatrix} \tag{9}$$

where the operators L_{ij} are symmetric and have the following forms:

$$\begin{Bmatrix} L_{11} \\ L_{13} \\ L_{22} \\ L_{24} \end{Bmatrix} = \begin{Bmatrix} A_{11} \\ \bar{B}_{11} \\ A_{66} \\ \bar{B}_{66} \end{Bmatrix} ( )_{,xx} + \begin{Bmatrix} A_{66} \\ \bar{B}_{66} \\ A_{22} \\ \bar{B}_{22} \end{Bmatrix} ( )_{,yy} + \begin{Bmatrix} \pounds \\ N \\ \pounds \\ N \end{Bmatrix} ( )_{,tt}$$

$$\begin{Bmatrix} L_{12} \\ L_{14} \\ L_{23} \\ L_{34} \end{Bmatrix} = \begin{Bmatrix} A_{66}+A_{12} \\ \bar{B}_{66}+\bar{B}_{12} \\ \bar{B}_{66}+\bar{B}_{12} \\ \bar{D}_{66}+\bar{D}_{12} \end{Bmatrix} ( )_{,xy}$$

$$\begin{Bmatrix} L_{15} \\ L_{35} \end{Bmatrix} = -\begin{Bmatrix} B_{11} \\ \bar{D}_{11} \end{Bmatrix} ( )_{,xxx} - \begin{Bmatrix} 2B_{66}+B_{12} \\ 2\bar{D}_{66}+\bar{D}_{12} \end{Bmatrix} ( )_{,xyy} - \begin{Bmatrix} M \\ Q \end{Bmatrix} ( )_{,xtt}$$

$$\begin{Bmatrix} L_{25} \\ L_{45} \end{Bmatrix} = -\begin{Bmatrix} 2B_{66}+B_{12} \\ 2\bar{D}_{66}+\bar{D}_{12} \end{Bmatrix} ( )_{,xxy} - \begin{Bmatrix} B_{22} \\ \bar{D}_{22} \end{Bmatrix} ( )_{,yyy} - \begin{Bmatrix} M \\ Q \end{Bmatrix} ( )_{,ytt}$$

$$\begin{Bmatrix} L_{33} \\ L_{44} \end{Bmatrix} = \begin{Bmatrix} \bar{\bar{D}}_{11} \\ \bar{\bar{D}}_{66} \end{Bmatrix} ( )_{,xx} + \begin{Bmatrix} \bar{\bar{D}}_{66} \\ \bar{\bar{D}}_{22} \end{Bmatrix} ( )_{,yy} + \begin{Bmatrix} R \\ R \end{Bmatrix} ( )_{,tt} - \begin{Bmatrix} \bar{\bar{A}}_{44} \\ \bar{\bar{A}}_{55} \end{Bmatrix}$$

$$L_{55} = D_{11}( )_{,xxxx} + 2(2D_{66}+D_{12})( )_{,xxyy} + D_{22}( )_{,yyyy} - \pounds( )_{,tt} + P( )_{,xxtt} + P( )_{,yytt}$$

where $( )_{,xx}$, etc., refers to derivatives of the column matrix of generalized displacements shown in (9) and

$$\begin{Bmatrix} A_{ij} & \bar{\bar{A}}_{ij} \\ B_{ij} & \bar{\bar{B}}_{ij} \\ D_{ij} & \bar{\bar{D}}_{ij} \end{Bmatrix} = \int_{-h/2}^{+h/2} C_{ij} \begin{Bmatrix} 1 & \xi_1^2 \\ z & \xi \\ z^2 & \xi^2 \end{Bmatrix} dz; \quad \bar{D}_{ij} = \int_{-h/2}^{+h/2} C_{ij} z\xi \, dz;$$

$$\begin{Bmatrix} \pounds & M & N \\ P & Q & R \end{Bmatrix} = \int_{-h/2}^{+h/2} \rho \begin{Bmatrix} 1 & z & \xi \\ z^2 & z\xi & \xi^2 \end{Bmatrix} dz$$

Finally, the boundary conditions along the edge of the plate require that one member of each of the following six pairs must be prescribed:

$N_x u_o$; $N_{xy} v_o$; $M'_x u_1$; $M'_{xy} v_1$; $Q_x w$; $M_x w_{,x}$ (along $x = \text{const}$)

$N_{xy} u_0$; $N_y v_0$; $M'_{xy} u_1$; $M'_y v_1$; $Q_y w$; $M_y w_{,y}$ (along $y = \text{const}$)

where

$$Q_x = M_{x,x} + 2M_{xy,y} \quad \text{and} \quad Q_y = M_{y,y} + 2M_{xy,x}$$

It may be observed that thin plate theory equations of motions can be obtained from equations (9) by deleting the rows and columns (third and fourth) corresponding to u_1 and v_1 displacements from L_{ij} matrix and corresponding rows on the right-hand side load vector.

3 Results and Discussions

Free vibration of simply supported square, homogeneous, and laminated plates is analyzed using equations (9). The solution to these equations is assumed in the following modal form,

$$u_0 = K_1 \Phi_1(x,y,t); \quad v_0 = K_2 \Phi_2(x,y,t); \quad u_1 = K_3 \Phi_1(x,y,t)$$
$$v_1 = K_4 \Phi_2(x,y,t); \quad w = K_5 \Phi_3(x,y,t) \tag{10}$$

where

$$\Phi_1(x,y,t) = \text{Cos}(m\pi x/a)\text{Sin}(n\pi y/b)\text{Sin}\Omega t$$

$$\Phi_2(x,y,t) = \text{Sin}(m\pi x/a)\,\text{Cos}(n\pi y/b)\text{Sin}\Omega t$$

$$\Phi_3(x,y,t) = \text{Sin}(m\pi x/a)\text{Sin}(n\pi y/b)\text{Sin}\Omega t$$

and Ω is the angular frequency. Substitution of equations (10) in equations (9), in the absence of applied forces, the problem reduces to finding the eigenvalues and eigenvectors of the following equation

$$X p = \Omega^2 Y p \tag{11}$$

where X and Y are 5×5 matrices and $p^T = (K_1, K_2, K_3, K_4, K_5)$

The results for square ($a/b = 1$) plate are presented in the tabular form for different geometric and material parameters considered, along with the other plate theories. The following geometric parameters have been considered

$$\beta_1 = \beta_3 = \beta = 1,5,10,15,20$$

$$\alpha_1 = \alpha_2 = \alpha = 0.1,0.2,0.3,0.4,0.5$$

where $\beta_1 = h_2/h_1$, $\beta_3 = h_2/h_3$, $\alpha_1 = mh/a$, and $\alpha_2 = nh/b$. The orthotropic material properties considered in the examples have been tabulated in Table 1 and are taken from reference [9].

3.1 Homogeneous Plates. It is observed that the frequencies predicted by shear deformation theory [3], here after referred as SDT, and the present analysis are in very good agreement with exact values [1, 2], even for $\alpha = 0.5$, for isotropic and orthotropic plates (results are not given for brevity). Also, it is observed that the frequencies predicted by the present analysis are closer to exact values than those predicted by SDT. Though, thin plate theory (TPT) predicts the frequencies, corresponding to symmetric modes of vibration about the midplane, correctly there is considerable difference in the frequencies corresponding to flexural mode of vibration and this difference becomes more and more predominant for higher values of α.

In subsequent discussions, for which exact values are not available, the comparison is made taking present solution as the standard, for lowest natural frequencies only. Table 2 shows the frequencies for four kinds of orthotropic plates

Downloaded 02 May 2010 to 171.66.16.25. Redistribution subject to ASME license or copyright; see http://www.asme.org/terms/Terms_Use.cfm

whose material properties are given in Table 1. In general, it may be said that the difference in the present analysis and SDT, as well as TPT, increases as E_x/E_y, E_x/G_{xz}, E_x/G_{yz} values increase. The maximum difference in the present analysis and SDT is about 1.3 percent ($\alpha=0.5$).

3.2 Layered Plates. From Tables 3 and 4 it may be noted that SDT underestimates the frequencies whereas TPT overestimates the same, as compared to the present analysis. The influence of β value is significant, in the case of two-layered plates, for smaller values of α and the same may be said, for larger values of α, in the case of three-layered plates.

Considering two-layered plates SDT underestimates frequencies by about 5.5 percent (for $\beta=1$, $\alpha=0.5$) and this difference decreases as β value increases and appears to remain almost constant for $\beta>20$. But in the case of three-layered plates SDT underestimates the frequencies by about 20 percent for larger values of $\beta\geq 20$ ($\alpha=0.5$). In such cases one has to resort to higher order theories in order to get accurate response characteristics of plate. The difference in the frequencies predicted by present analysis and TPT is very much larger for composite plates.

4 Conclusions

A higher order theory for undamped dynamic response of orthotropic homogeneous and composite laminated plates is developed. The theory accounts for in-plane inertia, rotary inertia, and shear deformation effects. The proposed method assumes parabolic variations across the thickness of plate for transverse shear strains. From the results obtained it may be concluded that thickness has a more pronounced effects on the behavior of composite plates than on the behavior of isotropic plates and transverse shear deformation effects are more pronounced even in thin composite laminated plates. For some of the geometric parameters of the plate it is found that the shear deformation theory is inadequate to predict the response of composite laminates and this necessitates the use of higher order theories like the one presented here.

Acknowledgment

The authors thank Mr. R. Kohoutek for his suggestions and discussions during the course of this work.

References

1 Srinivas, S., Jogarao, C. V., and Rao, A. K., "An Exact Analysis for Vibration of Simply-Supported Homogeneous and Laminated Thick Rectangular Plates," *Journal of Sound and Vibration*, Vol. 12, 1970, pp. 187–199.

2 Srinivas, S., and Rao, A. K., "Bending, Vibration and Buckling of Simply-Supported Thick Orthotropic Rectangular Plates and Laminates," *International Journal of Solids and Structures*, Vol. 6, 1970, pp. 1463–1481.

3 Yang, P. C., Norris, C. H., and Stavsky, Y., "Elastic Wave Propagation in Heterogeneous Plates," *International Journal of Solids and Structures*, Vol. 2, 1966, pp. 665–684.

4 Bert, C. W., "Analysis of Plates," *Structural Design and Analysis*, Part I, Chamis, C. C., ed., Academic Press, New York, 1974.

5 Lo, K. H., Christensen, R. M., and Wu, E. M., "A High-Order Theory for Plate Deformations Part 1: Homogeneous Plates," ASME JOURNAL OF APPLIED MECHANICS, Vol. 44, 1977, pp. 663–668.

6 Lo, K. H., Christensen, R. M., and Wu, E. M., "A High-Order Theory for Plate Deformations Part 2: Laminated Plates," ASME JOURNAL OF APPLIED MECHANICS, Vol. 44, 1977, pp. 669–676.

7 Timoshenko, S., and Goodier, J. N., *Theory of Elasticity*, McGraw-Hill, New York, 1951.

8 Magrab, E. B., *Vibrations of Elastic Structural Members*, Sijthoff and Noordhoff, 1979.

9 Lekhnitskii, S. G., *Theory of Elasticity of an Anisotropic Body*, Mir Publishers, Moscow, 1981, pp. 65–66.

The Stability of Motion of a Rigid Body About a Fixed Point in the Case of Euler With Damping Torque

Z.-M. Ge[1] and X.-X. Wu[2]

When a viscous damping torque $\mathbf{M} = -l\mathbf{K}$ is applied to a rigid body, where l is the damping coefficient, the given solution of the differential equations of motion, of which the stability will be studied, is

$$\left.\begin{aligned} p &= \omega_0 e^{-\frac{l}{A}t}, \quad q = 0, \quad r = 0 \\ \gamma_1 &= 1, \quad \gamma_2 = 0, \quad \gamma_3 = 0 \end{aligned}\right\}$$

where p_0 is the initial value of p. We denote $\omega_0 e^{-l/A\,t}$ by ω. Let

$$\left.\begin{aligned} p &= \omega+\xi, \quad q = 0+\eta, \quad r = 0+\zeta \\ \gamma_1 &= 1+\alpha, \quad \gamma_2 = 0+\beta, \quad \gamma_3 = 0+\delta \end{aligned}\right\}$$

where ξ, η, ζ, α, β, δ are disturbances; then the variational equations become

$$\left.\begin{aligned} A\dot{\xi}+(C-B)\eta\zeta+l\xi&=0,\\ B\dot{\eta}+(A-C)\zeta(\omega+\xi)+l\eta&=0,\\ C\dot{\zeta}+(B-A)\eta(\omega+\xi)+l\zeta&=0, \end{aligned}\right\} \quad \left.\begin{aligned} \dot{\alpha}&=\zeta\beta-\eta\delta\\ \dot{\beta}&=\omega\delta-\zeta+\xi\delta-\zeta\alpha\\ \dot{\delta}&=\eta-\omega\beta+\eta\alpha-\xi\beta \end{aligned}\right\}$$

Since ω is a given function of time t, the system is a nonautonomous one.

We choose a Liapunov function

$$V=\frac{1}{2}(Aa_{11}\xi^2+Ba_{22}\eta^2+CA_{33}\zeta^2)+\frac{1}{2}(\alpha^2+\beta^2+\delta^2)$$

$$-\frac{C}{l}\beta\zeta+\frac{B}{l}\delta\eta+\frac{1}{2}\omega^2(\alpha^2+\beta^2+\delta^2)$$

where a_{11}, a_{22}, a_{33} are positive constants. Then we have

$$-\frac{dV}{dt}=S_2+S_3$$

where

$$S_2=la_{11}\xi^2+\left(la_{22}-\frac{B}{l}\right)\eta^2+\left(la_{33}-\frac{C}{l}\right)\zeta^2$$

$$+[a_{22}(A-C)+a_{33}(B-A)]\omega\eta\zeta+\frac{A}{l}\omega\eta\beta+\frac{A}{l}\omega\zeta\delta$$

$$+\frac{l}{A}\omega^2(\alpha^2+\beta^2+\delta^2)-\omega^2(\delta\eta-\beta\zeta)$$

$$S_3=[a_{11}(C-B)+a_{22}(A-C)+a_{33}(B-A)]\xi\eta\zeta+\frac{A}{l}\xi\eta\beta$$

$$+\frac{A}{l}\xi\zeta\delta-\frac{B}{l}\eta^2\alpha-\frac{C}{l}\zeta^2\alpha$$

We can prove that when

$$l^2>\omega_0^2(A-C)(B-A)$$

a_{11}, a_{22}, a_{33} can be chosen so that $-dV/dt$ is positive

[1] National Committee of Science, Administrative Yuan, Taipei, China.

[2] Senior Student, Engineering Mechanics Department, Shanghai Jiaotong University, Shanghai, China.

Manuscript received by ASME Applied Mechanics Division, August, 1982; final revision, September, 1983.

Downloaded 02 May 2010 to 171.66.16.25. Redistribution subject to ASME license or copyright; see http://www.asme.org/terms/Terms_Use.cfm

whose material properties are given in Table 1. In general, it may be said that the difference in the present analysis and SDT, as well as TPT, increases as E_x/E_y, E_x/G_{xz}, E_x/G_{yz} values increase. The maximum difference in the present analysis and SDT is about 1.3 percent ($\alpha=0.5$).

3.2 Layered Plates. From Tables 3 and 4 it may be noted that SDT underestimates the frequencies whereas TPT overestimates the same, as compared to the present analysis. The influence of β value is significant, in the case of two-layered plates, for smaller values of α and the same may be said, for larger values of α, in the case of three-layered plates.

Considering two-layered plates SDT underestimates frequencies by about 5.5 percent (for $\beta=1$, $\alpha=0.5$) and this difference decreases as β value increases and appears to remain almost constant for $\beta>20$. But in the case of three-layered plates SDT underestimates the frequencies by about 20 percent for larger values of $\beta\geq 20$ ($\alpha=0.5$). In such cases one has to resort to higher order theories in order to get accurate response characteristics of plate. The difference in the frequencies predicted by present analysis and TPT is very much larger for composite plates.

4 Conclusions

A higher order theory for undamped dynamic response of orthotropic homogeneous and composite laminated plates is developed. The theory accounts for in-plane inertia, rotary inertia, and shear deformation effects. The proposed method assumes parabolic variations across the thickness of plate for transverse shear strains. From the results obtained it may be concluded that thickness has a more pronounced effects on the behavior of composite plates than on the behavior of isotropic plates and transverse shear deformation effects are more pronounced even in thin composite laminated plates. For some of the geometric parameters of the plate it is found that the shear deformation theory is inadequate to predict the response of composite laminates and this necessitates the use of higher order theories like the one presented here.

Acknowledgment

The authors thank Mr. R. Kohoutek for his suggestions and discussions during the course of this work.

References

1 Srinivas, S., Jogarao, C. V., and Rao, A. K., "An Exact Analysis for Vibration of Simply-Supported Homogeneous and Laminated Thick Rectangular Plates," *Journal of Sound and Vibration*, Vol. 12, 1970, pp. 187–199.

2 Srinivas, S., and Rao, A. K., "Bending, Vibration and Buckling of Simply-Supported Thick Orthotropic Rectangular Plates and Laminates," *International Journal of Solids and Structures*, Vol. 6, 1970, pp. 1463–1481.

3 Yang, P. C., Norris, C. H., and Stavsky, Y., "Elastic Wave Propagation in Heterogeneous Plates," *International Journal of Solids and Structures*, Vol. 2, 1966, pp. 665–684.

4 Bert, C. W., "Analysis of Plates," *Structural Design and Analysis*, Part I, Chamis, C. C., ed., Academic Press, New York, 1974.

5 Lo, K. H., Christensen, R. M., and Wu, E. M., "A High-Order Theory for Plate Deformations Part 1: Homogeneous Plates," ASME JOURNAL OF APPLIED MECHANICS, Vol. 44, 1977, pp. 663–668.

6 Lo, K. H., Christensen, R. M., and Wu, E. M., "A High-Order Theory for Plate Deformations Part 2: Laminated Plates," ASME JOURNAL OF APPLIED MECHANICS, Vol. 44, 1977, pp. 669–676.

7 Timoshenko, S., and Goodier, J. N., *Theory of Elasticity*, McGraw-Hill, New York, 1951.

8 Magrab, E. B., *Vibrations of Elastic Structural Members*, Sijthoff and Noordhoff, 1979.

9 Lekhnitskii, S. G., *Theory of Elasticity of an Anisotropic Body*, Mir Publishers, Moscow, 1981, pp. 65–66.

The Stability of Motion of a Rigid Body About a Fixed Point in the Case of Euler With Damping Torque

Z.-M. Ge[1] and X.-X. Wu[2]

When a viscous damping torque $\mathbf{M} = -l\mathbf{K}$ is applied to a rigid body, where l is the damping coefficient, the given solution of the differential equations of motion, of which the stability will be studied, is

$$\left.\begin{aligned} p &= \omega_0 e^{-\frac{l}{A}t}, \quad q = 0, \quad r = 0 \\ \gamma_1 &= 1, \quad \gamma_2 = 0, \quad \gamma_3 = 0 \end{aligned}\right\}$$

where p_0 is the initial value of p. We denote $\omega_0 e^{-l/A\,t}$ by ω. Let

$$\left.\begin{aligned} p &= \omega+\xi, \; q = 0+\eta, \; r = 0+\zeta \\ \gamma_1 &= 1+\alpha, \; \gamma_2 = 0+\beta, \; \gamma_3 = 0+\delta \end{aligned}\right\}$$

where ξ, η, ζ, α, β, δ are disturbances; then the variational equations become

$$\left.\begin{aligned} A\dot{\xi}+(C-B)\eta\zeta+l\xi&=0, \\ B\dot{\eta}+(A-C)\zeta(\omega+\xi)+l\eta&=0, \\ C\dot{\zeta}+(B-A)\eta(\omega+\xi)+l\zeta&=0, \end{aligned}\right\} \quad \left.\begin{aligned} \dot{\alpha}&=\zeta\beta-\eta\delta \\ \dot{\beta}&=\omega\delta-\zeta+\xi\delta-\zeta\alpha \\ \dot{\delta}&=\eta-\omega\beta+\eta\alpha-\xi\beta \end{aligned}\right\}$$

Since ω is a given function of time t, the system is a nonautonomous one.

We choose a Liapunov function

$$V=\frac{1}{2}(Aa_{11}\xi^2+Ba_{22}\eta^2+CA_{33}\zeta^2)+\frac{1}{2}(\alpha^2+\beta^2+\delta^2)$$

$$-\frac{C}{l}\beta\zeta+\frac{B}{l}\delta\eta+\frac{1}{2}\omega^2(\alpha^2+\beta^2+\delta^2)$$

where a_{11}, a_{22}, a_{33} are positive constants. Then we have

$$-\frac{dV}{dt}=S_2+S_3$$

where

$$S_2=la_{11}\xi^2+\left(la_{22}-\frac{B}{l}\right)\eta^2+\left(la_{33}-\frac{C}{l}\right)\zeta^2$$

$$+[a_{22}(A-C)+a_{33}(B-A)]\omega\eta\zeta+\frac{A}{l}\omega\eta\beta+\frac{A}{l}\omega\zeta\delta$$

$$+\frac{l}{A}\omega^2(\alpha^2+\beta^2+\delta^2)-\omega^2(\delta\eta-\beta\zeta)$$

$$S_3=[a_{11}(C-B)+a_{22}(A-C)+a_{33}(B-A)]\xi\eta\zeta+\frac{A}{l}\xi\eta\beta$$

$$+\frac{A}{l}\xi\zeta\delta-\frac{B}{l}\eta^2\alpha-\frac{C}{l}\zeta^2\alpha$$

We can prove that when

$$l^2>\omega_0^2(A-C)(B-A)$$

a_{11}, a_{22}, a_{33} can be chosen so that $-dV/dt$ is positive

[1] National Committee of Science, Administrative Yuan, Taipei, China.

[2] Senior Student, Engineering Mechanics Department, Shanghai Jiaotong University, Shanghai, China.

Manuscript received by ASME Applied Mechanics Division, August, 1982; final revision, September, 1983.

Copyright © 1984 by ASME
Downloaded 02 May 2010 to 171.66.16.25. Redistribution subject to ASME license or copyright; see http://www.asme.org/terms/Terms_Use.cfm

semidefinite and V is positive definite on the interval $[t_0, \infty)$. Thus, by Liapunov's theorem of stability, the undisturbed motion is stable on $[t_0, \infty)$ [1] in the sense that the allowable range for the initial disturbances can be found for the given range for disturbances.

The sufficient condition of stability $l^2 > \omega_0^2(A-C)(B-A)$ has clear physical significance. When the rotating axis is the long or short principal axis of inertia, $\omega_0^2(A-C)(B-A)<0$, the condition is always satisfied. When the rotating axis is the middle principal axis of inertia, the condition can be satisfied provided that the damping is sufficiently large. The greater the initial angular velocity ω_0 or the product $(A-C)(B-A)$, the greater the damping coefficient l to guarantee the stability of the rotation. When $A=C$ (also $A=B$, $A=B=C$), it is very interesting to point out that provided there exists a viscous damping torque, however small it may be, the rotations about all principal axes of inertia are all stable.

For the given range for disturbances ϵ, we can find the allowable range for the initial disturbances Ω by the Liapunov function.

We take

$$V_0 = \frac{1}{2}(Aa_{11}\xi^2 + Ba_{22}\eta^2 + Ca_{33}\zeta^2) - \frac{C}{l}\beta\zeta + \frac{B}{l}\delta\eta + \frac{1}{2}(\alpha^2+\beta^2+\delta^2) + \frac{1}{2}\omega_0^2(\alpha^2+\beta^2+\delta^2)$$

$$W = \frac{1}{2}(Aa_{11}\xi^2 + Ba_{22}\eta^2 + Ca_{33}\zeta^2) - \frac{C}{l}\beta\zeta + \frac{B}{l}\delta\eta + \frac{1}{2}(\alpha^2+\beta^2+\delta^2)$$

Since $W < V < V_0$, the moving enclosed hypersurface $V=c$ varies with time within the enclosed hypersurface $W=c$ and outside the enclosed hypersurface $V_0=c$, where c is selected to ensure that the hypersurfaces are all enclosed. Let

$$d^2 = \xi^2+\eta^2+\zeta^2+\alpha^2+\beta^2+\delta^2$$

We find the farthest point on $W=c$ from the origin. Using the method of Lagrange's multiplier, we form the Lagrange's function $L=d^2+\lambda W$. From

$$\frac{\partial L}{\partial \xi}=0, \frac{\partial L}{\partial \eta}=0, \frac{\partial L}{\partial \zeta}=0, \frac{\partial L}{\partial \alpha}=0, \frac{\partial L}{\partial \beta}=0, \frac{\partial L}{\partial \delta}=0$$

we have

$$\lambda_1 = -\frac{2}{Aa_{11}}, \lambda_2 = -2,$$

$$\lambda_{3,4} = \frac{-(Ba_{22}+1) \pm \sqrt{(Ba_{22}+1)^2 - 4\left(Ba_{22} - \frac{B^2}{l^2}\right)}}{Ba_{22} - \frac{B^2}{l^2}}$$

$$\lambda_{5,6} = \frac{-(Ca_{33}+1) \pm \sqrt{(Ca_{33}+1)^2 - 4\left(Ca_{33} - \frac{C^2}{l^2}\right)}}{Ca_{33} - \frac{C^2}{l^2}}$$

When $\lambda=\lambda_1$, we have

$$\xi=\xi, \eta=\zeta=\alpha=\beta=\delta=0$$

Putting these in $W=c$, we have $\xi=\xi(c)=\pm\sqrt{c/(1/2)Aa_{11}}$. Similarly, for λ_2, $\lambda_{3,4}$, $\lambda_{5,6}$ we have

$$\xi=\xi(c), \eta=\eta(c), \zeta=\zeta(c), \alpha=\alpha(c), \beta=\beta(c), \delta=\delta(c).$$

Putting all these solutions in d^2, we obtain $d_1^2(c)$, $d_2^2(c), \cdots, d_6^2(c)$, of which the maximum is

$$d_{\max}^2(c) = \max\{d_1^2(c), \cdots, d_6^2(c)\}$$

Taking $\epsilon = d_{\max}^2(c)$, we have the inverse function $c = d_{\max}^{2\,-1}(\epsilon)$

According to this c, we can find the nearest point on $V_0 = c$ from the origin. Similarly we form a Lagrange's function $L' = d^2 + \lambda V_0$ to find

$$d_{\min}'^2 = \min\{d_1'^2(c), \cdots, d_6'^2(c)\}.$$

Let $\Omega = d'_{\min}/\sqrt{6}$, then $V_0 = c$ is outside of the hypersurface $\max\{\xi, \eta, \zeta, \alpha, \beta, \delta\} = \Omega$. So we have, for given ϵ,

$$\Omega(\epsilon) = \frac{d'_{\min}(c)}{\sqrt{6}} = \frac{d'_{\min}[(d_{\max}^2)^{-1}(\epsilon)]}{\sqrt{6}}$$

Reference

1 Rouche, N., Nobets, P., and Laloy, M., *Stability Theory by Liapunov's Direct Method*, Springer, Berlin, 1977.

Scattering of an Elastic Wave by a Subsurface Elastic Fiber

R. L. Ryan[1] and S. Mall[1]

Introduction

Recent studies [1, 2] on the interaction of elastic waves with a subsurface crack reveal that the stress intensities around the crack are strongly influenced by the proximity of the free surface of the medium. Here we deduce similar results for an elastic fiber. The interaction of elastic waves with a fiber is, of course, more complicated than for a crack on account of the extensional, flexural, and inertia properties of the fiber. For simplicity we consider a problem in which flexural interaction is absent. Moreover, we assume the inertia of the fiber is negligible. Our results, therefore, include the effect of fiber depth and fiber extensional properties only.

The geometry is shown in the insert of Fig. 1, wherein $h << 1-\epsilon$. The input excitation is a standing longitudinal wave oriented parallel to the fiber, i.e., the sum of normal incident and reflected longitudinal waves. A scattered field arises, of course, from the interaction of the input wave with the fiber. To obtain the scattered field we treat the fiber as a singular surface across which the displacements and normal stress are continuous and the tangential stress is discontinuous.

Formulation

Let $(u,v)e^{-i\omega t}$ denote the displacement components of the scattered field and, omitting the time factor, let $(\tau_x, \tau_y, \tau_{xy}) = \mu^{-1}(\sigma_x, \sigma_y, \sigma_{xy})$ denote the associated normalized stress components, where μ is the shear modulus of the medium. On account of symmetry it is sufficient to determine the scattered field in the region $y \geq 0$. The requirements on the planes $x = 0$ and $y = 0$ are, respectively,

$$\tau_x = \tau_{xy} = 0, \quad y > 0, \qquad (1a,b)$$

and

$$v = 0, x \geq 0; \quad \tau_{xy} = 0, 0 < x < \epsilon, x > 1;$$
$$u = u^* - u_0, \epsilon \leq x \leq 1. \qquad (2a,b,c)$$

[1]Department of Mechanical Engineering, University of Maine, Orono, Me. 04469

Manuscript received by ASME Applied Mechanics Division, April, 1983; final revision, September, 1983.

Downloaded 02 May 2010 to 171.66.16.25. Redistribution subject to ASME license or copyright; see http://www.asme.org/terms/Terms_Use.cfm

semidefinite and V is positive definite on the interval $[t_0, \infty)$. Thus, by Liapunov's theorem of stability, the undisturbed motion is stable on $[t_0, \infty)$ [1] in the sense that the allowable range for the initial disturbances can be found for the given range for disturbances.

The sufficient condition of stability $l^2 > \omega_0^2(A-C)(B-A)$ has clear physical significance. When the rotating axis is the long or short principal axis of inertia, $\omega_0^2(A-C)(B-A)<0$, the condition is always satisfied. When the rotating axis is the middle principal axis of inertia, the condition can be satisfied provided that the damping is sufficiently large. The greater the initial angular velocity ω_0 or the product $(A-C)(B-A)$, the greater the damping coefficient l to guarantee the stability of the rotation. When $A=C$ (also $A=B$, $A=B=C$), it is very interesting to point out that provided there exists a viscous damping torque, however small it may be, the rotations about all principal axes of inertia are all stable.

For the given range for disturbances ϵ, we can find the allowable range for the initial disturbances Ω by the Liapunov function.

We take

$$V_0 = \frac{1}{2}(Aa_{11}\xi^2 + Ba_{22}\eta^2 + Ca_{33}\zeta^2) - \frac{C}{l}\beta\zeta + \frac{B}{l}\delta\eta + \frac{1}{2}(\alpha^2+\beta^2+\delta^2) + \frac{1}{2}\omega_0^2(\alpha^2+\beta^2+\delta^2)$$

$$W = \frac{1}{2}(Aa_{11}\xi^2 + Ba_{22}\eta^2 + Ca_{33}\zeta^2) - \frac{C}{l}\beta\zeta + \frac{B}{l}\delta\eta + \frac{1}{2}(\alpha^2+\beta^2+\delta^2)$$

Since $W < V < V_0$, the moving enclosed hypersurface $V=c$ varies with time within the enclosed hypersurface $W=c$ and outside the enclosed hypersurface $V_0=c$, where c is selected to ensure that the hypersurfaces are all enclosed. Let

$$d^2 = \xi^2+\eta^2+\zeta^2+\alpha^2+\beta^2+\delta^2$$

We find the farthest point on $W=c$ from the origin. Using the method of Lagrange's multiplier, we form the Lagrange's function $L=d^2+\lambda W$. From

$$\frac{\partial L}{\partial \xi}=0, \frac{\partial L}{\partial \eta}=0, \frac{\partial L}{\partial \zeta}=0, \frac{\partial L}{\partial \alpha}=0, \frac{\partial L}{\partial \beta}=0, \frac{\partial L}{\partial \delta}=0$$

we have

$$\lambda_1 = -\frac{2}{Aa_{11}}, \lambda_2 = -2,$$

$$\lambda_{3,4} = \frac{-(Ba_{22}+1) \pm \sqrt{(Ba_{22}+1)^2 - 4\left(Ba_{22} - \frac{B^2}{l^2}\right)}}{Ba_{22} - \frac{B^2}{l^2}}$$

$$\lambda_{5,6} = \frac{-(Ca_{33}+1) \pm \sqrt{(Ca_{33}+1)^2 - 4\left(Ca_{33} - \frac{C^2}{l^2}\right)}}{Ca_{33} - \frac{C^2}{l^2}}$$

When $\lambda=\lambda_1$, we have

$$\xi=\xi, \eta=\zeta=\alpha=\beta=\delta=0$$

Putting these in $W=c$, we have $\xi=\xi(c)=\pm\sqrt{c/(1/2)Aa_{11}}$. Similarly, for λ_2, $\lambda_{3,4}$, $\lambda_{5,6}$ we have

$$\xi=\xi(c), \eta=\eta(c), \zeta=\zeta(c), \alpha=\alpha(c), \beta=\beta(c), \delta=\delta(c).$$

Putting all these solutions in d^2, we obtain $d_1^2(c)$, $d_2^2(c), \cdots, d_6^2(c)$, of which the maximum is

$$d_{\max}^2(c) = \max\{d_1^2(c), \cdots, d_6^2(c)\}$$

Taking $\epsilon = d_{\max}^2(c)$, we have the inverse function $c = d_{\max}^{2\,-1}(\epsilon)$

According to this c, we can find the nearest point on $V_0 = c$ from the origin. Similarly we form a Lagrange's function $L' = d^2 + \lambda V_0$ to find

$$d_{\min}'^2 = \min\{d_1'^2(c), \cdots, d_6'^2(c)\}.$$

Let $\Omega = d'_{\min}/\sqrt{6}$, then $V_0 = c$ is outside of the hypersurface $\max\{\xi, \eta, \zeta, \alpha, \beta, \delta\} = \Omega$. So we have, for given ϵ,

$$\Omega(\epsilon) = \frac{d'_{\min}(c)}{\sqrt{6}} = \frac{d'_{\min}[(d_{\max}^2)^{-1}(\epsilon)]}{\sqrt{6}}$$

Reference

1 Rouche, N., Nobets, P., and Laloy, M., *Stability Theory by Liapunov's Direct Method*, Springer, Berlin, 1977.

Scattering of an Elastic Wave by a Subsurface Elastic Fiber

R. L. Ryan[1] and S. Mall[1]

Introduction

Recent studies [1, 2] on the interaction of elastic waves with a subsurface crack reveal that the stress intensities around the crack are strongly influenced by the proximity of the free surface of the medium. Here we deduce similar results for an elastic fiber. The interaction of elastic waves with a fiber is, of course, more complicated than for a crack on account of the extensional, flexural, and inertia properties of the fiber. For simplicity we consider a problem in which flexural interaction is absent. Moreover, we assume the inertia of the fiber is negligible. Our results, therefore, include the effect of fiber depth and fiber extensional properties only.

The geometry is shown in the insert of Fig. 1, wherein $h << 1-\epsilon$. The input excitation is a standing longitudinal wave oriented parallel to the fiber, i.e., the sum of normal incident and reflected longitudinal waves. A scattered field arises, of course, from the interaction of the input wave with the fiber. To obtain the scattered field we treat the fiber as a singular surface across which the displacements and normal stress are continuous and the tangential stress is discontinuous.

Formulation

Let $(u,v)e^{-i\omega t}$ denote the displacement components of the scattered field and, omitting the time factor, let $(\tau_x, \tau_y, \tau_{xy}) = \mu^{-1}(\sigma_x, \sigma_y, \sigma_{xy})$ denote the associated normalized stress components, where μ is the shear modulus of the medium. On account of symmetry it is sufficient to determine the scattered field in the region $y \geq 0$. The requirements on the planes $x = 0$ and $y = 0$ are, respectively,

$$\tau_x = \tau_{xy} = 0, \quad y > 0, \qquad (1a,b)$$

and

$$v = 0, x \geq 0; \quad \tau_{xy} = 0, 0 < x < \epsilon, x > 1;$$
$$u = u^* - u_0, \epsilon \leq x \leq 1. \qquad (2a,b,c)$$

[1]Department of Mechanical Engineering, University of Maine, Orono, Me. 04469

Manuscript received by ASME Applied Mechanics Division, April, 1983; final revision, September, 1983.

Copyright © 1984 by ASME
Downloaded 02 May 2010 to 171.66.16.25. Redistribution subject to ASME license or copyright; see http://www.asme.org/terms/Terms_Use.cfm

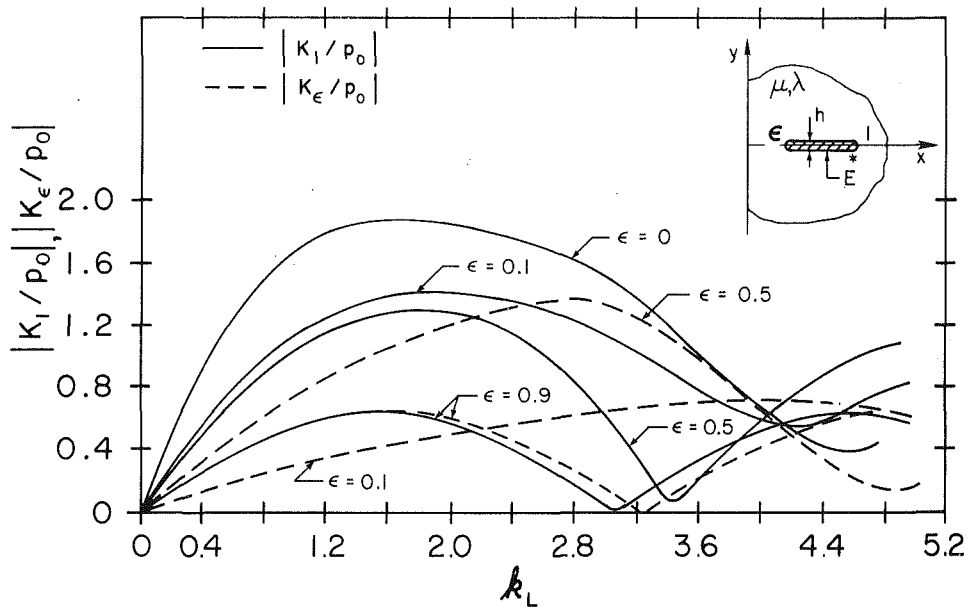

Fig. 1 Stress intensities at $x = 1$ and $x = \epsilon$ versus wave number, $\kappa = \sqrt{3}, \beta = 0.2, p_0 = \mu k_L{}^2 \phi_0$

In (2) u^* and u_0 are the horizontal displacements of the fiber and of the input wave, respectively. For the input wave considered here

$$u_0 = 2ik_L \phi_0 \cos k_L x, \quad v_0 = 0, \tag{3}$$

where ϕ_0 is a constant and k_L is the longitudinal wave number. Further, for equilibrium we have

$$u^*{}_{,x} = -\beta \int_\epsilon^x \tau(s)\, ds, \quad \epsilon < x < 1, \tag{4}$$

where $\tau(s) = \tau_{xy}(s,0)$, $\beta = 2\mu/E^* h$, and E^* is the elastic modulus of the fiber.

The problem as formulated can be reduced to a singular integral equation by an approach similar to that employed in [1]. For the present problem, this approach produces the following integral equation

$$\left(\frac{\partial u}{\partial x}\right)_{y=0} = \frac{2}{\pi} \int\!\!\!\!\!\!- _\epsilon^1 \tau(s)\,[P_1(s,x;k_L) + P_2(s,x;k_L)]ds, \quad \epsilon < x < 1. \tag{5}$$

In (5) the stroke indicates principal value, and the left side is defined by condition (2*c*). In addition,

$$\begin{aligned} 4\kappa^2/i\pi\, P_1(s,x;k_L) &= (s-x)^{-1} H_2{}^{(1)}[k_L|s-x|] \\ &\quad - k_L H_1{}^{(1)}[k_L|s-x|]\,\mathrm{sgn}(s-x) \\ &\quad - k_L H_1{}^{(1)}[k_L(s+x)] + (s+x)^{-1} H_2{}^{(1)}[k_L(s+x)] \\ &\quad - \kappa^2 (s-x)^{-1} H_2{}^{(1)}[\kappa k_L|s-x|] \\ &\quad - \kappa^2 (s+x)^{-1} H_2{}^{(1)}[\kappa k_L(s+x)] \end{aligned} \tag{6}$$

and P_2 is the indented integral

$$k_T^2 P_2(s,x;k_L) = \int\!\!\!\!\!\!- _0^\infty \frac{\beta_L}{R(\eta)} G(s,\eta) H(x,\eta)\, d\eta, \tag{7}$$

where $k_T = \kappa k_L$ is the transverse wave number and

$$G(s,\eta) = (\eta^2 + \beta_T{}^2) e^{-\beta_L s} - 2\eta^2 e^{-\beta_T s}, \tag{8}$$

$$H(x,\eta) = \beta_L (\eta^2 + \beta_T{}^2) e^{-\beta_L x} - 2\beta_T \eta^2 e^{-\beta_T x}, \tag{9}$$

$$R(\eta) = 4\eta^2 \beta_T \beta_L - (\eta^2 + \beta_T{}^2)^2, \tag{10}$$

$$\beta_T = (\eta^2 - k_T{}^2)^{1/2}, \quad \beta_L = (\eta^2 - k_L{}^2)^{1/2}. \tag{11}$$

Aside from equation (5) the solution is also constrained by the equilibrium condition

$$\int_\epsilon^1 \tau(s)\, ds = 0. \tag{12}$$

Equations (5) and (12) may be solved numerically by the Lobatto-Chebyshev technique [3]. For purposes of numerical treatment we recast (5) in terms of the new variables $g(t) = \tau(s)$, $w(z) = u_{,x}(x)$, and $(s,x) = (1-\epsilon)/2\ (t,z) + (1+\epsilon)/2$. Also, defining $k_L{}^* = (1-\epsilon)/2\ k_L$, $\nu = 2(1+\epsilon)/(1-\epsilon)$, and $\beta^* = (1-\epsilon)/2\beta$, and incorporating formulas (3) and (4) gives

$$-w_0(z) = \int\!\!\!\!\!\!- _{-1}^1 g(t)\,[Q_1(t,z;k_L{}^*) + Q_2(t,z;k_L{}^*) + \beta^* H(t-z)]dt, \quad |z| < 1, \tag{13}$$

where $H(\cdot)$ denotes the unit step function, $Q_i(t,z;k_L{}^*) = P_i(s,x;k_L)$, $i = 1, 2$, and $w_0(z) = 2ik_L{}^2 \phi_0 \sin k_L{}^*(z + \nu/2)$. Likewise, equation (12) becomes

$$\int_{-1}^1 g(t)\, dt = 0. \tag{14}$$

It should be noted that (14) is not valid if $\epsilon = 0$, since if the fiber touches the free surface the shear stress at the point of contact must vanish. Hence if $\epsilon = 0$ condition (14) must be replaced by the condition $g(-1) = 0$. The shear stress is expected to exhibit the same type of singularity as in related static problems (e.g., [4]). Accordingly, we set

$$g(t) = -2\pi i\, k_L{}^2 \phi_0 h(t)\,(1-t^2)^{-1/2} \tag{15}$$

and assume $h(t)$ is bounded.

By means of the Lobatto-Chebyshev technique, equations (13)–(15) are replaced by the algebraic system

$$\sum_1^N B_p h_p K_{pq} = \sin k_L{}^*(z_q + \nu/2);$$

$$\sum_1^N B_p h_p = 0, \quad q = 1, 2, N-1 \tag{16a,b}$$

where $h_p = h(t_p)$, $K_{pq} = K(t_p, z_q)$ is the kernel of (13), and the interpolation points t_p, collocation points z_q, and the weights B_p are given in [3]. For the reason stated in the foregoing (16*b*) is replaced by $h_N = 0$ when $\epsilon = 0$.

Downloaded 02 May 2010 to 171.66.16.25. Redistribution subject to ASME license or copyright; see http://www.asme.org/terms/Terms_Use.cfm

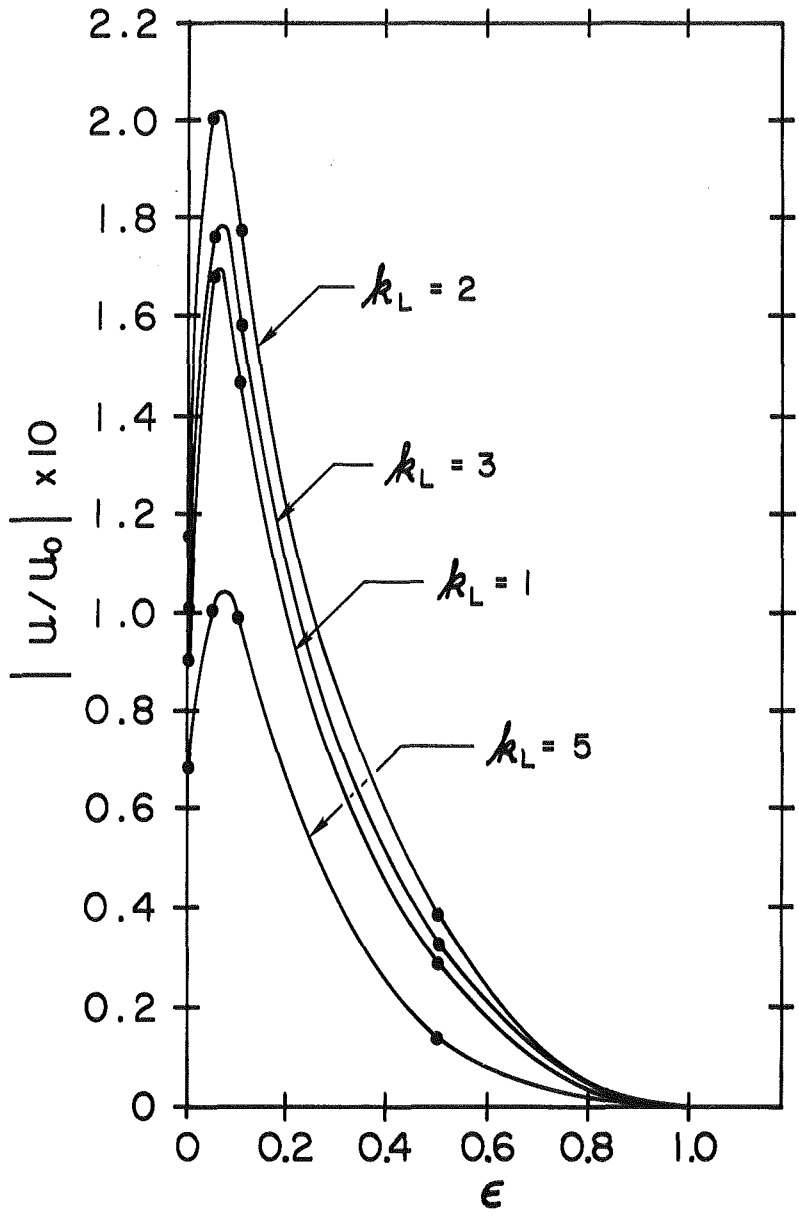

Fig. 2 Peak surface response versus fiber depth, $\kappa = \sqrt{3}$, $\beta = 0.2$, $u_0 = k_L^2 \phi_0$

Numerical Results

Equations (16) were solved by digital computer using $N = 20$. The solution, in turn, was used to compute the peak response of the free surface and the stress intensities at the ends of the fiber. The formula for the peak surface response can be shown to be

$$u(0,0) = 2i\, k_L^2 \phi_0 (1-\epsilon)\pi \sum_1^N B_p h_p I_p, \tag{17}$$

where I_p is the indented integral

$$I_p = \fint_0^\infty \frac{\bar{\beta}_L(\xi)}{\bar{R}(\xi)} G(t_p,\xi)\, d\xi, \tag{18}$$

where $\bar{R}(\xi) = k_L^{-4} R(\eta)$, etc., as previously defined. Moreover, the stress intensities, defined as usual, turn out to be

$$(K_\epsilon, K_1) = \pm\sqrt{2(1-\epsilon)}\, i\, \mu\, k_L^2 \phi_0 h(\mp 1). \tag{19}$$

Figure 1 illustrates the results for the stress intensities for a modulus ratio $\beta = 0.2$. The curves corresponding to $\epsilon = 0.9$ should predict fairly closely the results for an infinite medium. The remaining curves therefore show the relative effect of the proximity of the free surface.

The results for the peak surface response are illustrated in Fig. 2. To obtain the data for Fig. 2 an excessive amount of computation is required. Thus, only a few points (shown by the heavy marks) were obtained. On the basis of the limited data it appears that the peak response occurs at a moderate wave number ($k_L = 2$), when $\epsilon \cong 0.05$. Similar results (not shown) were obtained for the case $\beta = 1.0$; as might be expected, the peak values were substantially less than those given. It is conjectured that the high peaks in the surface response curve are due to a resonance condition in the parent material between the free surface and the head of fiber.

References

1 Achenbach, J. D., and Brind, R. J., "Scattering of Surface Waves by a Subsurface Crack," *Journal of Sound and Vibration*, Vol. 76, 1981, pp. 43-56.

2 Brind, R. J., and Achenbach, J. D., "Scattering of Longitudinal and

Downloaded 02 May 2010 to 171.66.16.25. Redistribution subject to ASME license or copyright; see http://www.asme.org/terms/Terms_Use.cfm

Transverse Waves by a Sub-Surface Crack," *Journal of Sound and Vibration*, Vol. 78, 1981, pp. 555–563.

3 Theocaris, P. S., and Ioakimidis, N. I., "Stress Intensity Factors at Crack Tips Near Boundaries or Other Geometrical Discontinuities," *International Journal of Fracture*, Vol. 15, 1979, pp. 419–428.

4 Erdogan, F., and Gupta, G. D., "Stresses Near a Flat Inclusion in Bonded Dissimilar Metals," *International Journal of Solids and Structures*, Vol. 8, 1972, pp. 533–547.

The Use of Manganin Stress Transducers in Impulsively Loaded Long Rod Experiments

Z. Rosenberg,[1] M. Mayseless,[1] and Y. Partom[1]

The purpose of this Brief Note is to demonstrate the feasibility of using commercial manganin stress gauges in dynamic uniaxial stress experiments. This was demonstrated by measuring the stress-time histories inside long aluminum rods that were impacted by rigid wall impactors. The experimental records are compared with a two-dimensional Lagrangian calculation using a recently developed constitutive model (the Phases Model) to describe material behavior.

Introduction

The transient response of impulsively loaded cylindrical bars has been the subject of numerous investigations for over a century. Most of the experimental work in this field is based on strain measurements, made with either bonded strain gauges or diffraction gratings, at various locations along the impacted bar. Relatively few works have been done, with thin quartz transducers, in which stress was measured directly. Reference [1] summarizes some of the limitations of these gauges which include: mechanical mismatch between gauge and bar and the limit to time resolution because of gauge thickness.

The purpose of the present paper is to demonstrate the feasibility of using commercial manganin stress gauges to measure stress-time histories inside impulsively loaded rods. These gauges (together with their package) are very thin so they do not suffer from the limitations mentioned in the foregoing.

Experimental Techniques

Planar impact experiments were conducted in our 64 mm gas gun described in [2]. A detailed description of the measurement techniques involved in planar impacts can be found in [3]. The impactors which we used were 35 mm thick 4340 steel disks carried by 150 mm plastic sabots. These heavy impactors can be considered as rigid walls as compared to the long aluminum rods that served as targets. These were 2024-T351 aluminum rods, 12.7 mm in diameter, in which we inserted commercial manganin gauges (Micro Measurements type LM-55-125CH-048) at a distance of 127 mm from the impacted end. This distance of 10 diameters was chosen because it is generally accepted (see [4] for example) that at these distances the stress pulse in the rod has *uniaxial-stress* features. This is very important in our case because in the process of data reduction we use the calibration curve, for the gauge, which was determined under *uniaxial strain* conditions [5]. We have shown recently [6] that under *static uniaxial stress* conditions the gauge has the same response as that under *dynamic uniaxial strain* conditions.

The gauges were isolated from the aluminum surfaces with two 19 μm Mylar sheets thus obtaining a total thickness of 0.09 mm for the gauge package. The gauges, with Mylar sheets, were bonded in the middle of the rod with Hysol 0151 - clear epoxy resin. The whole assembly was fastened with a special clamp which ensured axiality of the two parts of the rod. Figure 1 shows the experimental assembly in these experiments just prior to impact.

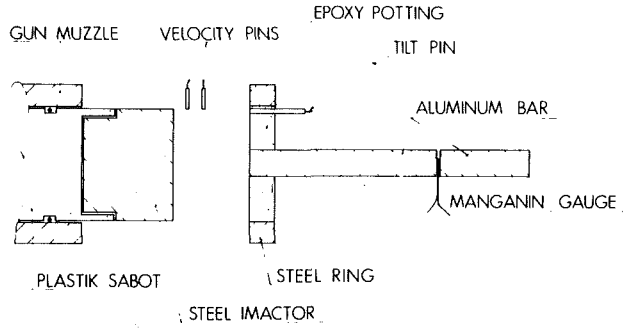

Fig. 1 Schematic representation of the rigid wall impacting the long rod

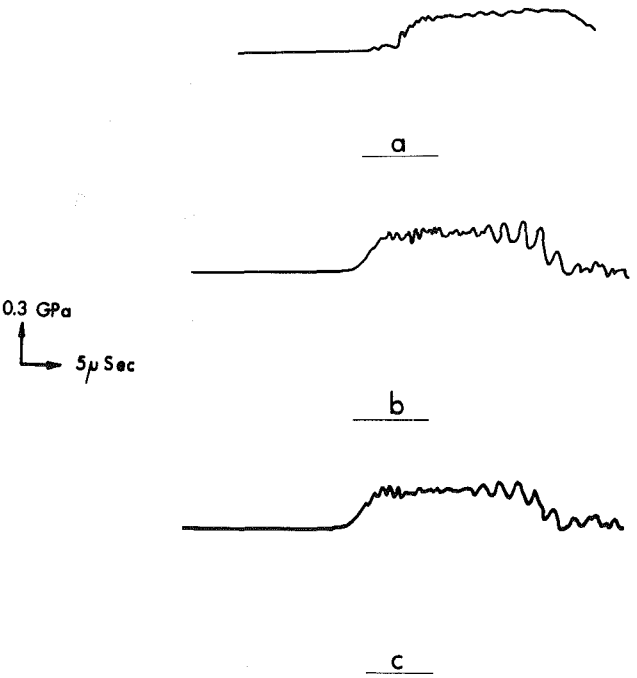

Fig. 2 Experimental and calculated stress time histories in experiment no. 228. (*a*) Experimental gauge record; (*b*) computed with von Mises yield criterion; and (*c*) with the Phases Model.

Calculated Scheme

In order to follow the stress time histories at the gauge's location we used a two-dimensional Lagrangian elasto-plastic code—Disco—which was described in [7]. This code is very similar to the well-known HEMP code. In the calculations the aluminum rods were "impacted" by an undeformable rigid wall allowing for full sliding across the interface. We used the same conditions as in the experiments (rigid wall velocity, rod geometry, and material characterization) and monitored the axial stress-time histories at a distance of 10 diameters from the impact end. We used two constitutive models to describe the behavior of the aluminum bars. The first is based on an isotropic elastic Hooke law with a von-Mises yield criterion. We denote this model as VM. The material parameters used for the VM model were taken from previous experimental studies in our laboratory on 2024 Al [8, 9]. The second

[1] Armament Development Authority, P.O. Box 2250, Haifa, Israel.

Manuscript received by ASME Applied Mechanics Division, March, 1983; final revision, May, 1983.

Downloaded 02 May 2010 to 171.66.16.25. Redistribution subject to ASME license or copyright; see http://www.asme.org/terms/Terms_Use.cfm

Transverse Waves by a Sub-Surface Crack," *Journal of Sound and Vibration*, Vol. 78, 1981, pp. 555–563.

3 Theocaris, P. S., and Ioakimidis, N. I., "Stress Intensity Factors at Crack Tips Near Boundaries or Other Geometrical Discontinuities," *International Journal of Fracture*, Vol. 15, 1979, pp. 419–428.

4 Erdogan, F., and Gupta, G. D., "Stresses Near a Flat Inclusion in Bonded Dissimilar Metals," *International Journal of Solids and Structures*, Vol. 8, 1972, pp. 533–547.

The Use of Manganin Stress Transducers in Impulsively Loaded Long Rod Experiments

Z. Rosenberg,[1] M. Mayseless,[1] and Y. Partom[1]

The purpose of this Brief Note is to demonstrate the feasibility of using commercial manganin stress gauges in dynamic uniaxial stress experiments. This was demonstrated by measuring the stress-time histories inside long aluminum rods that were impacted by rigid wall impactors. The experimental records are compared with a two-dimensional Lagrangian calculation using a recently developed constitutive model (the Phases Model) to describe material behavior.

Introduction

The transient response of impulsively loaded cylindrical bars has been the subject of numerous investigations for over a century. Most of the experimental work in this field is based on strain measurements, made with either bonded strain gauges or diffraction gratings, at various locations along the impacted bar. Relatively few works have been done, with thin quartz transducers, in which stress was measured directly. Reference [1] summarizes some of the limitations of these gauges which include: mechanical mismatch between gauge and bar and the limit to time resolution because of gauge thickness.

The purpose of the present paper is to demonstrate the feasibility of using commercial manganin stress gauges to measure stress-time histories inside impulsively loaded rods. These gauges (together with their package) are very thin so they do not suffer from the limitations mentioned in the foregoing.

Experimental Techniques

Planar impact experiments were conducted in our 64 mm gas gun described in [2]. A detailed description of the measurement techniques involved in planar impacts can be found in [3]. The impactors which we used were 35 mm thick 4340 steel disks carried by 150 mm plastic sabots. These heavy impactors can be considered as rigid walls as compared to the long aluminum rods that served as targets. These were 2024-T351 aluminum rods, 12.7 mm in diameter, in which we inserted commercial manganin gauges (Micro Measurements type LM-55-125CH-048) at a distance of 127 mm from the impacted end. This distance of 10 diameters was chosen because it is generally accepted (see [4] for example) that at these distances the stress pulse in the rod has *uniaxial-stress* features. This is very important in our case because in the process of data reduction we use the calibration curve, for the gauge, which was determined under *uniaxial strain* conditions [5]. We have shown recently [6] that under *static uniaxial stress* conditions the gauge has the same response as that under *dynamic uniaxial strain* conditions.

The gauges were isolated from the aluminum surfaces with two 19 μm Mylar sheets thus obtaining a total thickness of 0.09 mm for the gauge package. The gauges, with Mylar sheets, were bonded in the middle of the rod with Hysol 0151 - clear epoxy resin. The whole assembly was fastened with a special clamp which ensured axiality of the two parts of the rod. Figure 1 shows the experimental assembly in these experiments just prior to impact.

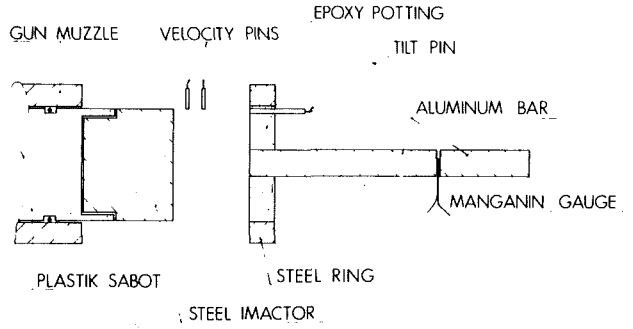

Fig. 1 Schematic representation of the rigid wall impacting the long rod

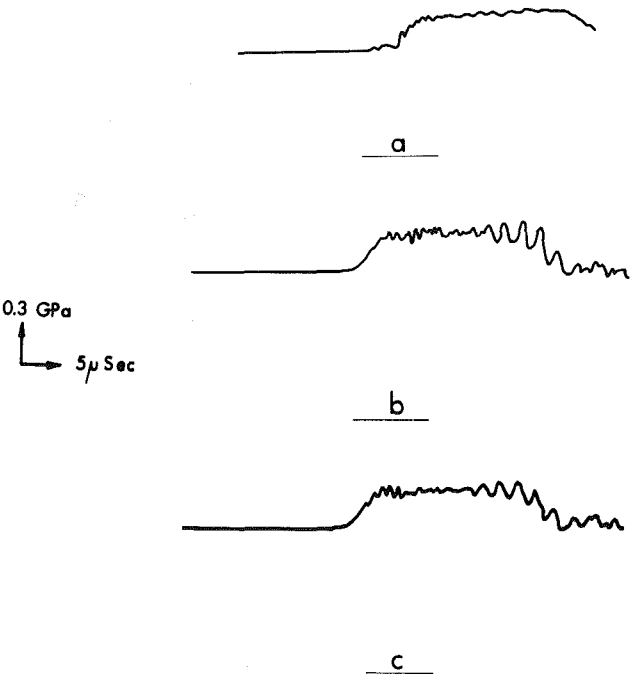

Fig. 2 Experimental and calculated stress time histories in experiment no. 228. (*a*) Experimental gauge record; (*b*) computed with von Mises yield criterion; and (*c*) with the Phases Model.

Calculated Scheme

In order to follow the stress time histories at the gauge's location we used a two-dimensional Lagrangian elasto-plastic code—Disco—which was described in [7]. This code is very similar to the well-known HEMP code. In the calculations the aluminum rods were "impacted" by an undeformable rigid wall allowing for full sliding across the interface. We used the same conditions as in the experiments (rigid wall velocity, rod geometry, and material characterization) and monitored the axial stress-time histories at a distance of 10 diameters from the impact end. We used two constitutive models to describe the behavior of the aluminum bars. The first is based on an isotropic elastic Hooke law with a von-Mises yield criterion. We denote this model as VM. The material parameters used for the VM model were taken from previous experimental studies in our laboratory on 2024 Al [8, 9]. The second

[1] Armament Development Authority, P.O. Box 2250, Haifa, Israel.

Manuscript received by ASME Applied Mechanics Division, March, 1983; final revision, May, 1983.

Copyright © 1984 by ASME
Downloaded 02 May 2010 to 171.66.16.25. Redistribution subject to ASME license or copyright; see http://www.asme.org/terms/Terms_Use.cfm

Table 1 The relevant data for the four experiments

Experiment no.	Impact velocity [m/sec]	Type and length of backing rod
205	135	Al 25.4 mm
228	140	Al 63.5 mm
275	138	Al 40 mm + Cu 29.6 mm
278	135	Al 40 mm + PMMA 28.7 mm

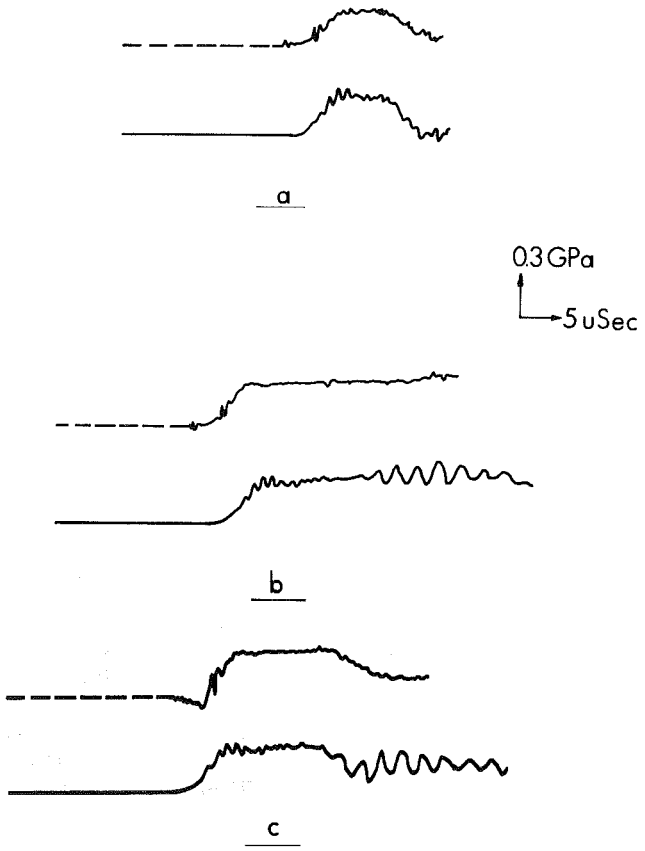

Fig. 3 Experimental (dotted) and calculated (continuous) histories for: (*a*) shot no. 205, short aluminum backing rod; (*b*) shot no. 275, Al + Cu backing; and (*c*) shot no. 278, Al + PMMA backing

constitutive model, which we call the "Phases Model" (PM) was developed by one of us and described in [10, 11].

Results and Discussion

We present experimental and calculated stress-time histories of four different experiments. In all four the gauge was situated in the middle section of a long aluminum rod 10 diameters away from the impacted end. As shown in Table 1, the four experiments differed by the length and structure of the backing rod. These were varied in order to check the gauge's response to different reflected waves. The calculated stress histories were monitored at the central cell of the rod mesh. This cell has a diameter of 1.5 mm which is very close to the dimensions of the manganin gauge (of 3 × 3 mm). Time steps in the calculations were equal to $\Delta x/4 \cdot C$ where Δx is cell size and C is sound velocity.

Figure 2 shows the experimental gauge record and the two calculated stress histories, one with each constitutive model, for experiment no. 228 (the one with the long aluminum backing rod). We first note the similarity of the various features in the three histories. The arrival time of the first disturbance to gauge location is about 20 μsec and this gives a value of 6.35 $\pm$0.1 mm/μsec (considering all experiments) to the velocity of this disturbance. This is in very good agreement with the 6.4 mm/μsec value for the longitudinal elastic velocity in 2024 Al. This small-amplitude disturbance is followed by a slowly rising stress signal (with a rise time of about 5 μs). This kind of dispersion of a step impulse, after long traveling distances were observed by others experimentally and theoretically. The gauge records this wave after a time that corresponds to a velocity of 5.3 mm/μsec which is in very good agreement with the bar velocity of 2024 Al (5.25 mm/μsec). The appearance of very fast oscillations (0.5 μsec from peak to peak at the rise of the stress pulse is also important. Similar fast oscillations were observed also in [1] using very short axial strain gauges. These oscillations are damped after about 5 μs and the gauge (and computational histories) show a nearly constant stress level for about 10 μs after which more stress oscillations appear. The frequency of these corresponds to the lateral dimension of the rod. These oscillations are followed by stress relief from the free end of the bar.

Although the two calculations give similar stress histories we see that the one with the Phases Model follows the measured history more closely. This led us to choose the PM in the rest of the calculations which are presented in Fig. 3 together with the measured histories.

We see that the agreement between measured and calculated histories is good and the only significant difference between them is the amplitude of the lateral oscillations. We attribute these to the amount of friction between rod and impactor at the impact interface. We also note that the manganin records give a constant level stress amplitude of 0.33 GPa which is very close to the value of 0.34 $\pm$0.1 GPa which we found for the static yield stress of 2024-T351 Al [9].

Conclusions

We have demonstrated the feasibility of using very thin piezoresistance stress gauges (manganin in the present study) for direct measurement of stress-time history in long rod experiments. Such measurements can be used for example in split Hopkinson bar experiments. The main point of the present study was to show that the one-dimensional calibration curve for manganin gauges (under uniaxial strain conditions) also applies to the dynamic uniaxial stress conditions. This enabled us to monitor the stress wave histories in various configurations of long aluminum rods impacted by a rigid wall. The amplitude of the transmitted elastic wave is equal to the static yield strength of the rod and is almost constant for relatively long times. After that, lateral oscillations reach the gauge location and raise the average stress level read by the gauge.

We think that these oscillations are the result of lateral reverberations of the impact face of the rod and their amplitude depends on the amount of friction between gauge and wall. This point will be further pursued in the future.

Acknowledgments

The authors wish to thank Mr. R. Kreif and Mr. D. Mazar for invaluable help in performing the experiments.

Downloaded 02 May 2010 to 171.66.16.25. Redistribution subject to ASME license or copyright; see http://www.asme.org/terms/Terms_Use.cfm

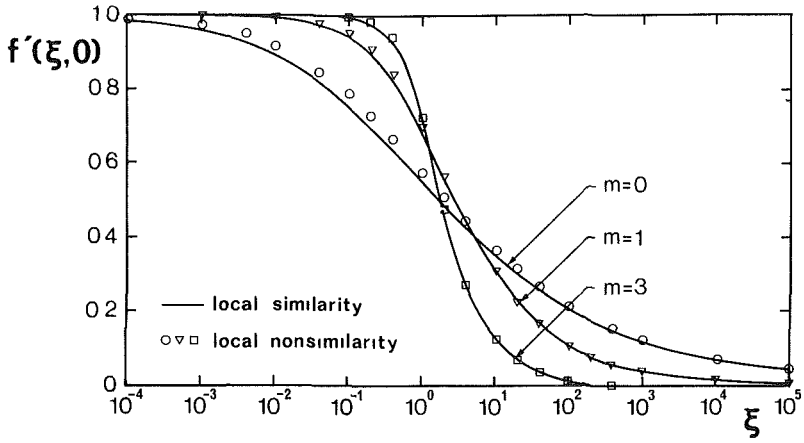

Fig. 1 Variation of dimensionless slip-velocity $f'(\xi,0)$ for various values of m

References

1 Miklowitz, J , and Nisewanger, C R , "The Propagation of Compressional Waves in a Dispersive Elastic Rod," ASME JOURNAL OF APPLIED MECHANICS, Vol 24, 1967, pp 240-244

2 Porat, Y , and Gvishi, M , "The Performance of a Short Barrelled Gas Gun," *Journal of Physics E Sci Inst* , Vol 13, 1980, pp 504-505

3 Davison, L , and Graham, R. A , "Shock Compression of Solids," *Physics Reports*, Vol 55, No 4, 1979, pp 255-379

4 Habberstad, J L , Hoge, K G , and Foster, J. E , "An Experimental and Numerical Study of Elastic Strain Waves on the Center Line of a 6061-T6 Aluminum Bar," ASME JOURNAL OF APPLIED MECHANICS, Vol 39, 1972, pp 367-371

5 Rosenberg, Z., Yaziv, D , and Partom, Y , "Calibration of Foil-Like Manganin Gauges in Planar Shock Wave Experiments," *Journal of Applied Physics*, Vol 51, No 7, 1980, pp 3702-3705

6 Rosenberg, Z , Partom, Y , and Keren, B , "Calibration of Commercial Manganin Stress Gauges Under Static Uniaxial Strain Conditions," *Journal of Applied Physics*, Vol 54, No 5, 1983, pp. 2824-2826

7 Kivity, Y , and Tsur, D , "Study of Projectile Formation in Lined Shallow Cavity Charges," *Proceedings of the 4th International Symposium on Ballistics*, Monterey, Calif , Oct 17-19, 1978

8 Yaziv, D , Rosenberg, Z , and Partom, Y , "Variation of the Elastic Constants of 2024-T351 Al Under Dynamic Pressures," *Journal of Applied Physics*, Vol 53, No 1, 1982, pp 353-355

9 Rosenberg, Z , Partom, Y , and Yeshurun, Y , "Determination of the Hugoniot Elastic Limits of Differently Treated 2024 Al Specimens," *Journal of Physics D App Phys* , Vol 15, 1982, pp 1137-1142

10 Partom, Y , and Schanin, J , "Calculation of Nonlinear Viscoelastic Response," M Sc Thesis of J Schanin, Technion - Israel Institute of Technology, 1979

11 Partom, Y , "Calculation of Viscoplastic Response," in *Physical Nonlinearities in Structural Analysis*, Hult, J , and Lemaitre, J , eds , Senlis, 1980, pp 207-211

Local Nonsimilarity Solutions for Boundary Layers at Lubricated Walls

H. I. Andersson[1]

The effect of the lubricating film is accounted for by a slip flow boundary condition, and the nonsimilar boundary layer problem is solved by a local nonsimilarity solution method.

Introduction

In a recent paper Joseph [1] suggests that, for boundary layer flow along a lubricated surface, the effects of the thin lubrication layer may be accommodated by the boundary condition

$$\frac{\partial u(x,0)}{\partial y} = \frac{\mu_1 u^2(x,0)}{2\mu_2 Q} \tag{1}$$

i.e., the only effect on the boundary layer in the bulk fluid above the lubricating film is that the traditional no-slip condition $u(x,0) = 0$ is replaced with the slip-flow condition (1). Here, μ_1/μ_2 is the ratio of the viscosity of the lubricating fluid to the viscosity of the bulk fluid and y is the coordinate perpendicular to the boundary. Q is the constant volumetric flow rate per unit width of the thin film.

As pointed out by Joseph, most of the similarity solutions of classical boundary layer theory do not carry over to the lubricated wall problem subject to the condition (1). However, as we demonstrate in the present Note, a method for obtaining locally nonsimilar boundary-layer solutions suggested by Sparrow et al. [2], applies to the present problem if the potential flow external to the lubricated layer belongs to the classical Falkner-Skan type [3].

Theory

Consider a freestream of the form $U(x) = cx^m$, where x is the streamwise coordinate and c and m are constants. In terms of the variables

$$\xi = \frac{x}{L}; \quad \eta = \left(\frac{m+1}{2}\frac{U(x)}{\nu_2 x}\right)^{1/2} y \tag{2a}$$

$$\psi = \left(\frac{2}{m+1}U(x)\nu_2 x\right)^{1/2} f(\xi,\eta) \tag{2b}$$

where

$$L = [2c\nu_2\Lambda^2/(m+1)]^{-\frac{1}{m+1}}, \quad \Lambda = \mu_1/(2\mu_2 Q) \tag{3}$$

the incompressible boundary layer momentum equation may be written

$$f''' + ff'' + \frac{2m}{m+1}(1-f'^2) = \frac{2\xi}{m+1}\left(f'\frac{\partial f'}{\partial \xi} - f''\frac{\partial f}{\partial \xi}\right) \tag{4}$$

The primes denote differentiation with respect to η. Then the lubricated wall condition (1) and the usual boundary conditions $v(x,0) = 0$ and $u(x,y) = U(x)$ at $y \to \infty$ become

$$f''(\xi,0) = s, \quad f'(\xi,0) = s^{1/2}\xi^{-(m+1)/4} \tag{5a}$$

$$f(\xi,0) = 0, \quad f'(\xi,\eta) \to 1 \quad \text{as } \eta \to \infty \tag{5b}$$

[1] Institutt for Mekanikk, Norwegian Institute of Technology, N-7034 Trondheim-NTH, Norway

Manuscript received by ASME Applied Mechanics Division, May, 1983, final revision, September, 1983

Downloaded 02 May 2010 to 171.66.16.25. Redistribution subject to ASME license or copyright; see http://www.asme.org/terms/Terms_Use.cfm

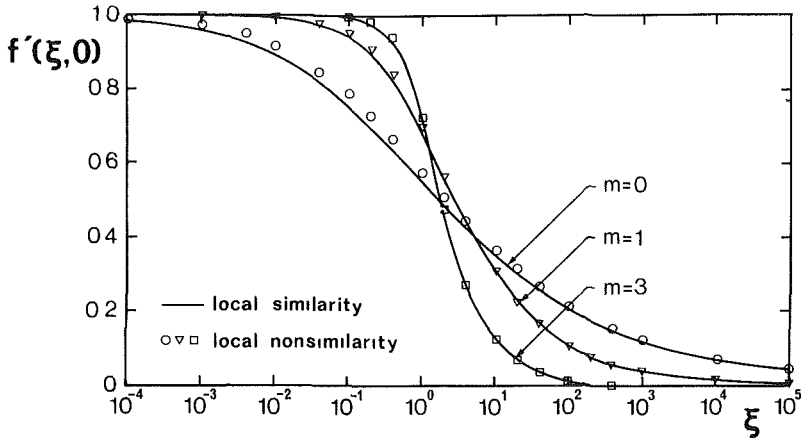

Fig. 1 Variation of dimensionless slip-velocity $f'(\xi,0)$ for various values of m

References

1 Miklowitz, J , and Nisewanger, C R , "The Propagation of Compressional Waves in a Dispersive Elastic Rod," ASME JOURNAL OF APPLIED MECHANICS, Vol 24, 1967, pp 240-244

2 Porat, Y , and Gvishi, M , "The Performance of a Short Barrelled Gas Gun," *Journal of Physics E Sci Inst* , Vol 13, 1980, pp 504-505

3 Davison, L , and Graham, R. A , "Shock Compression of Solids," *Physics Reports*, Vol 55, No 4, 1979, pp 255-379

4 Habberstad, J L , Hoge, K G , and Foster, J. E , "An Experimental and Numerical Study of Elastic Strain Waves on the Center Line of a 6061-T6 Aluminum Bar," ASME JOURNAL OF APPLIED MECHANICS, Vol 39, 1972, pp 367-371

5 Rosenberg, Z., Yaziv, D , and Partom, Y , "Calibration of Foil-Like Manganin Gauges in Planar Shock Wave Experiments," *Journal of Applied Physics*, Vol 51, No 7, 1980, pp 3702-3705

6 Rosenberg, Z , Partom, Y , and Keren, B , "Calibration of Commercial Manganin Stress Gauges Under Static Uniaxial Strain Conditions," *Journal of Applied Physics*, Vol 54, No 5, 1983, pp. 2824-2826

7 Kivity, Y , and Tsur, D , "Study of Projectile Formation in Lined Shallow Cavity Charges," *Proceedings of the 4th International Symposium on Ballistics*, Monterey, Calif , Oct 17-19, 1978

8 Yaziv, D , Rosenberg, Z , and Partom, Y , "Variation of the Elastic Constants of 2024-T351 Al Under Dynamic Pressures," *Journal of Applied Physics*, Vol 53, No 1, 1982, pp 353-355

9 Rosenberg, Z , Partom, Y , and Yeshurun, Y , "Determination of the Hugoniot Elastic Limits of Differently Treated 2024 Al Specimens," *Journal of Physics D App Phys* , Vol 15, 1982, pp 1137-1142

10 Partom, Y , and Schanin, J , "Calculation of Nonlinear Viscoelastic Response," M Sc Thesis of J Schanin, Technion - Israel Institute of Technology, 1979

11 Partom, Y , "Calculation of Viscoplastic Response," in *Physical Nonlinearities in Structural Analysis*, Hult, J , and Lemaitre, J , eds , Senlis, 1980, pp 207-211

Local Nonsimilarity Solutions for Boundary Layers at Lubricated Walls

H. I. Andersson[1]

The effect of the lubricating film is accounted for by a slip flow boundary condition, and the nonsimilar boundary layer problem is solved by a local nonsimilarity solution method.

Introduction

In a recent paper Joseph [1] suggests that, for boundary layer flow along a lubricated surface, the effects of the thin lubrication layer may be accommodated by the boundary condition

$$\frac{\partial u(x,0)}{\partial y} = \frac{\mu_1 u^2(x,0)}{2\mu_2 Q} \tag{1}$$

i.e., the only effect on the boundary layer in the bulk fluid above the lubricating film is that the traditional no-slip condition $u(x,0) = 0$ is replaced with the slip-flow condition (1). Here, μ_1/μ_2 is the ratio of the viscosity of the lubricating fluid to the viscosity of the bulk fluid and y is the coordinate perpendicular to the boundary. Q is the constant volumetric flow rate per unit width of the thin film.

As pointed out by Joseph, most of the similarity solutions of classical boundary layer theory do not carry over to the lubricated wall problem subject to the condition (1). However, as we demonstrate in the present Note, a method for obtaining locally nonsimilar boundary-layer solutions suggested by Sparrow et al. [2], applies to the present problem if the potential flow external to the lubricated layer belongs to the classical Falkner-Skan type [3].

Theory

Consider a freestream of the form $U(x) = cx^m$, where x is the streamwise coordinate and c and m are constants. In terms of the variables

$$\xi = \frac{x}{L}; \quad \eta = \left(\frac{m+1}{2}\frac{U(x)}{\nu_2 x}\right)^{1/2} y \tag{2a}$$

$$\psi = \left(\frac{2}{m+1} U(x)\nu_2 x\right)^{1/2} f(\xi,\eta) \tag{2b}$$

where

$$L = [2c\nu_2\Lambda^2/(m+1)]^{-\frac{1}{m+1}}, \quad \Lambda = \mu_1/(2\mu_2 Q) \tag{3}$$

the incompressible boundary layer momentum equation may be written

$$f''' + ff'' + \frac{2m}{m+1}(1-f'^2) = \frac{2\xi}{m+1}\left(f'\frac{\partial f'}{\partial \xi} - f''\frac{\partial f}{\partial \xi}\right) \tag{4}$$

The primes denote differentiation with respect to η. Then the lubricated wall condition (1) and the usual boundary conditions $v(x,0) = 0$ and $u(x,y) = U(x)$ at $y \to \infty$ become

$$f''(\xi,0) = s, \quad f'(\xi,0) = s^{1/2}\xi^{-(m+1)/4} \tag{5a}$$

$$f(\xi,0) = 0, \quad f'(\xi,\eta) \to 1 \quad \text{as } \eta \to \infty \tag{5b}$$

[1] Institutt for Mekanikk, Norwegian Institute of Technology, N-7034 Trondheim-NTH, Norway

Manuscript received by ASME Applied Mechanics Division, May, 1983, final revision, September, 1983

Copyright © 1984 by ASME
Downloaded 02 May 2010 to 171.66.16.25. Redistribution subject to ASME license or copyright; see http://www.asme.org/terms/Terms_Use.cfm

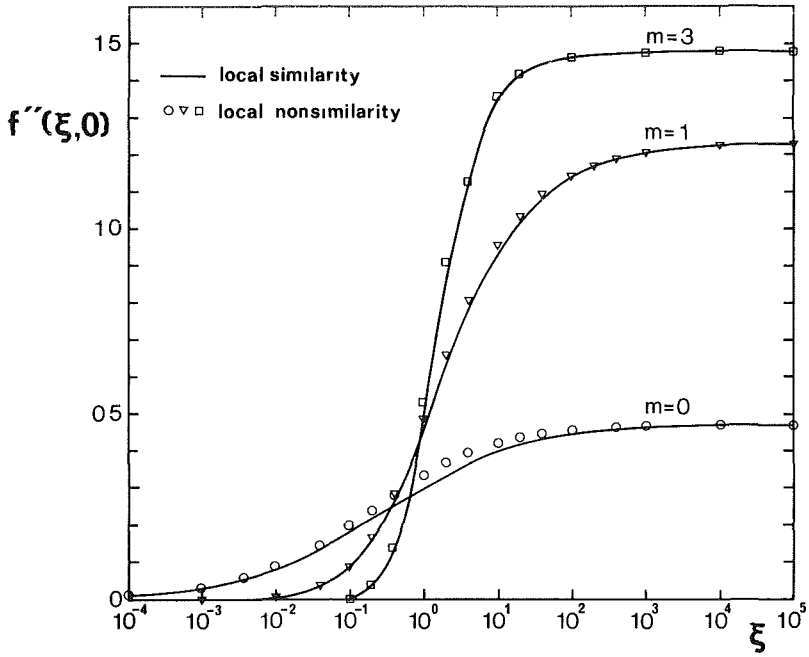

Fig. 2 Variation of dimensionless wall shear stress $f''(\xi,0)$ for various values of m

where s is the unknown wall shear stress, which is obtained with the solution of the problem.

It is well known from classical boundary layer theory that the Falkner-Skan similarity solutions [3] are obtained for potential velocity fields of the form $U(x) \sim x^m$. In the lubricated wall problem, however, the no-slip condition $f'(\xi,0) = 0$ has been replaced with the surface conditions (5*a*). The nonsimilarity introduced through these boundary conditions prohibits similarity solutions to be obtained, except in the singular case $m = -1$ recently considered by Joseph [1].

For $m \neq -1$ the local similarity concept may be applied as a first approximation to the nonsimilar problems. According to this approach [2], the right-hand side of equation (4) is neglected and ξ is regarded as a known constant at any streamwise position. Thus solutions can be obtained locally by some well-established and efficient numerical technique appropriate to similarity problems.

In the local similarity scheme, a part of the momentum equation itself is neglected. Sparrow et al. [2], however, have described a more accurate method for nonsimilar boundary layers, in which the approximation is introduced in a subsidary equation, so that the momentum equation (4) remains intact. Following [2] the local nonsimilarity model is derived by introducing $g(\xi,\eta) = \partial f/\partial\xi$, so that the momentum equation (4) becomes

$$f''' + ff'' + \frac{2m}{m+1}(1-f'^2) = \frac{2\xi}{m+1}(f'g' - f''g) \tag{6}$$

Next, equation (6) and the boundary conditions (5) are differentiated with respect to ξ, terms involving $(\partial/\partial\xi)$ are dropped, and the set of subsidary equations becomes

$$g''' + fg'' + \frac{m+3}{m+1}gf'' - \frac{4m+2}{m+1}f'g' = 0 \tag{7}$$

$$g''(\xi,0) = t, \quad g'(\xi,0) = \frac{1}{2}s^{1/2}\xi^{-(m+1)/4}\cdot\left[\frac{t}{s} - \frac{m+1}{2}\xi^{-1}\right] \tag{8a}$$

$$g(\xi,0) = 0, \quad g'(\xi,\eta) \to 0 \quad \text{as} \quad \eta \to \infty \tag{8b}$$

Thus, the two-equation local nonsimilarity model defined by the nonlinear third-order ordinary differential equations (6 and 7) subject to the boundary conditions (5) and (8), is a two-point boundary value problem. To solve this problem, we employed a shooting method developed by Keller [4]. A basic feature of this method is that a Newton iteration procedure can be used to determine successively improved values for the two unknowns s and t.

Results and Comments

Numerical results were obtained locally for different values of ξ and m. The variation of $f'(\xi,0)$ and $f''(\xi,0)$ with ξ are shown in Fig. 1 and Fig. 2, respectively. The dimensionless slip velocity $f'(\xi,0)$ is a monotonic decreasing function of ξ, and a corresponding increase in the dimensionless wall shear stress $f''(\xi,0)$ is observed.

It should be noted that a small value of ξ, for a given position x, is achieved by a reduction of the lubrication constant Λ, which corresponds to a lower viscosity μ_l of the lubrication fluid, or an increased amount Q of lubricant. In the limiting case $\xi = 0$, $f''(\xi,0) = 0$, and $f'(\xi,0) = 1$. The boundary layer velocity is thus equal to the freestream velocity; i.e., the inviscid region extends to the boundary.

A large value of ξ, however, is obtained for large Λ, which corresponds to using a small amount of high viscosity lubricant. As ξ tends to infinity the usual no-slip condition $f'(\xi,0) = 0$ applies, and the Falkner-Skan similarity results are recovered, see e.g. Evans [5].

On the basis of the displayed results, it can be concluded that the local similarity solutions (lines) are in close agreement with the more accurate two-equation local nonsimilarity model (symbols) for the lubricated wall problem.

References

1 Joseph, D. D, "Boundary Conditions for Thin Lubrication Layers," *Phys Fluids*, Vol 23, 1980, pp 2356-2358

2 Sparrow, E M, Quack, H, and Boerner, C J, "Local Nonsimilarity Boundary-Layer Solutions," *AIAA J*, Vol 8, 1970, pp 1936-1942

3 Falkner, V M, and Skan, S. W, "Some Approximate Solutions of the Boundary-Layer Equations," *Phil Mag.*, Vol 12, 1931, pp. 865-896.

4 Keller, H B, *Numerical Methods for Two-Point Boundary Value Problems*, Ginn-Blaisdell, Waltham, Mass, 1968

5 Evans, H L., *Laminar Boundary-Layer Theory*, Addison-Wesley, Reading, Mass, 1968.

Downloaded 02 May 2010 to 171.66.16.25. Redistribution subject to ASME license or copyright; see http://www.asme.org/terms/Terms_Use.cfm

On the Torsion of the Slit Circular Cylindrical Shell

E. H. Mansfield[1]

The complexity of shell analysis stems from the fact that loads are resisted, in general, by both membrane and flexural action. There is a need to develop a suitable shell finite element, but many of those proposed at the present time fail in the context of the "sensitive solutions" coupled with rigid body movements. These "sensitive solutions" refer to known solutions (within the framework of shell theory) of problem in which it is kinematically possible for the shell to deform with no straining of the midsurface. (Purely inextensional solutions were first considered by Lord Rayleigh [1].) In two cases, namely the torsion of a slit cylinder and the application of uniformly distributed moments M_θ and $M_x = \nu M_\theta$ to a slit cylinder, the contribution of the membrane forces is identically zero. The second of these two cases is too trivial to be used for comparison with finite element solutions, but the first case exhibits many of the features that current finite elements have difficulty in reproducing. An exact solution within the context of shell theory is not necessarily, of course, an exact three-dimensional solution. However, the torsion of a slit cylinder has also been solved three-dimensionally (Love [2]) and the present Note focuses attention on the exact variation of shear stress through the wall of the shell and on how this compares with shell theory

Shear Stresses in the Slit Cylinder Under Torsion

Although the rigorous solution for the slit cylinder is known, what concerns us here is the variation of shear stress through the wall of the shell away from the immediate neighborhood of the slit. This variation is more readily determined from first principles. Note that for a thin-walled shell the soap bubble analogy shows us that the stress distribution is effectively independent of the coordinate θ apart from over hoop lengths of about $2h$ from the slit, where h is the shell thickness.

The shear stresses $\tau_{\theta z}$ are given in terms of a stress function Φ such that

$$\left.\begin{aligned} &\tau_{\theta z} = \frac{d\Phi}{dr}, \\ &\nabla^2\Phi = k, \quad \text{a constant} \end{aligned}\right\} \tag{1}$$

and

$$[\Phi]_{r=r_1 r_2} = 0,$$

where r_1, r_2, are the inner and outer radii of the shell.

When the stresses are independent of θ

$$\nabla^2\Phi \equiv \left(\frac{d^2}{dr^2} + \frac{1}{r}\frac{d}{dr}\right)\Phi$$

and equation (1) can be expressed in the form

$$\left.\begin{aligned} &\frac{d\tau_{\theta z}}{dr} + \frac{\tau_{\theta z}}{r} = k, \\ &\text{and} \\ &\int_{r_1}^{r_2} \tau_{\theta z}\, dr = 0, \end{aligned}\right\} \tag{1a}$$

whence

$$\tau_{\theta z} = \frac{k}{4}\left\{2r - \frac{(r_2^2 - r_1^2)}{r\ln(r_2/r_1)}\right\}. \tag{2}$$

It may be shown that these stresses vary approximately linearly through the thickness with

$$\tau_{\theta z} \approx k\xi,$$

where ξ is measured from the midthickness.

The constant k can be related to the applied torque T by taking moments about the axis of the cylinder:

$$T = 2\pi\int_{r_1}^{r_2} r^2\tau_{\theta z}\, dr$$

$$= \pi k(r_2^2 - r_1^2)\left\{r_2^2 + r_1^2 - \left(\frac{r_2^2 - r_2^2}{\ln(r_2/r_1)}\right)\right\}. \tag{3}$$

If now we write

$$r_1 = R - \frac{1}{2}h,$$

$$r_2 = R + \frac{1}{2}h,$$

and expand the logarithmic term in equation (3) in powers of h/R, we find

$$k = \frac{3T}{\pi R h^3}(1 + 0(h^2/R^2)) \tag{4}$$

and the maximum (surface) values of $\tau_{\theta z}$ are given by

$$|\tau_{\theta z}|_{\max} \approx \frac{3T}{2\pi R h^2}. \tag{5}$$

The Resultant of the Shear Stresses $\tau_{\theta z}$ Across the Thickness

The shear stresses $\tau_{\theta z}$, given by equations (2) and (4) may be resolved into a twisting moment (about $r = R$) per unit length of arc, $M_{\theta z}$ and a shear force per unit length of arc, $N_{\theta z}$.

Thus,

$$\left.\begin{aligned} M_{\theta z} &= \frac{1}{R}\int_{r_1}^{r_2} r(r-R)\tau_{\theta z}\, dr \approx \frac{T}{4\pi R} \\ N_{\theta z} &= \frac{1}{R}\int_{r_1}^{r_2} r\tau_{\theta z}\, dr \approx \frac{T}{4\pi R^2}. \end{aligned}\right\} \tag{6}$$

These results clearly show that in the slit cylinder the torque is carried in equal proportions by the $M_{\theta z}$ and $N_{\theta z}$ components. This, in turn, can be regarded as a "distributed" version of the fact that in a flat strip under torque, the torque is carried in equal proportions by the twisting moments and the edge shears.

Comparison With First Approximation Shell Theory

According to first approximation shell theory (e.g., Morley [3])

[1]Royal Aircraft Establishment, Farnborough, Hampshire, GU 146 TD, England.

Manuscript received by ASME Applied Mechanics Division, May, 1983.

Copyright © 1984 by ASME
Downloaded 02 May 2010 to 171.66.16.25. Redistribution subject to ASME license or copyright; see http://www.asme.org/terms/Terms_Use.cfm

$$M_{\theta z} = \frac{T}{4\pi R} \tag{7}$$

in accordance with equation (6), while

$$RN_{\theta z} = 0(M_{\theta z}) \quad ,$$

but is otherwise indeterminate as it produces stresses at most of order h/R times those due to $M_{\theta z}$.

Finally we note that the assumption that the shear stresses vary *precisely* linearly through the thickness, vanishing at the midthickness, yields the correct value for $N_{\theta z}$ from simple considerations of equilibrium. Thus if $M_{\theta z}$ is given by equation (7) the shear stresses are given by

$$\tau_{\theta z} = \left(\frac{3T}{\pi R h^3}\right)\xi$$

so that

$$\begin{aligned} N_{\theta z} &= \frac{1}{R}\int_{r_1}^{r_2} r\tau_{\theta z}\,dr \\ &= \frac{3T}{\pi R^2 h^3}\int_{-h/2}^{+h/2}(R+\xi)\xi\,d\xi \\ &= \frac{T}{4\pi R^2} \quad , \end{aligned}$$

which agrees with equation (6).

References

1 Rayleigh, Lord, "Infinitesimal Bending of Surfaces of Revolution," *Proc. London Math. Soc.*, Vol. 13, 1881, pp. 4–16.

2 Love, A. E. H., *The Mathematical Theory of Elasticity*, 4th Ed., Cambridge Univ. Press, 1927, p. 319.

3 Morley, L. S. D., "Polynomial Stress States in First Approximation Theory of Circular Cylindrical Shells," *Quart. J. Mech. and Appl. Math.*, Vol. 25, 1972, pp. 13–43.

Large Amplitude Vibrations of Clamped Circular Plate of Variable Thickness

S. K. Chaudhuri[1]

In this paper nonlinear oscillations of a clamped circular plate of linearly varying thickness have been investigated using von Karman equations expressed in terms of displacement components. Numerical results obtained have been compared and discussed.

Nomenclature

λ = Thickness-variation parameter
V = Potential energy
D = Flexural rigidity given by

$$D = \frac{E h^3}{12(1-\nu^2)}$$

E = Modulus of elasticity
h = Thickness of the plate
ν = Poisson's ratio
W = Deflection normal to the middle plane

$$e_1 = \frac{du}{dr} + \frac{1}{2}\left(\frac{dW}{dr}\right)^2 + \frac{u}{r}$$

$$e_2 = \frac{u}{r}\frac{du}{dr} + \frac{1}{2}\frac{u}{r}\left(\frac{dW}{dr}\right)^2$$

u = Displacement
T = Kinetic Energy
ρ = Density of the material
F = Lagrangian function
$W_0(t)$ = Time function
h_0 = Constant thickness
$\frac{\sigma_{rr} \cdot a^2}{E h_0^2}$ = Membrane stress at the center of the plate
a = Radius of the circular plate

Introduction

Nonlinear vibrations are frequently encountered in practice, particularly with thin elastic plates, the deformational response of which is sensitive to the direction of small dimension associated with the thickness. Numerous authors [1, 2] have dealt with linear analysis of oscillations of elastic plates of various shapes. Nonlinear vibrations of circular and rectangular plates have also been investigated by Chu and Hermann [3], Nash and Modeer [4], Bauer [5], Nowinski [6], and many others by reason of relatively simpler mathematical work. Regarding other shapes, two interesting papers which need special mention are due to Nowinski and Ismail [7], and Vendhan and Das [8]. All these investigations are confined to plates of uniform thickness only.

Plates of nonuniform thickness are sometimes used in the design of machine parts such as diaphragms of steam turbines and pistons of reciprocating engines.

Investigations of vibrations of plates of nonuniform thickness based on linear theory have been done by many workers among which the works of Appl and Byers [9] and Ashton [10] are noteworthy.

Nonlinear analysis on Vibrations of thin plates of variable thickness are few in literature. J. Ramachandran [11] and M. Sathyamoorthy and K. A. V. Pandalai [12] quite elegantly carried out some interesting works in this field and achieved satisfactory results.

In this paper the large amplitude vibrations of a clamped tapered circular plate have been investigated following von Karman's equations expressed in terms of displacement components. Numerical results obtained both for immovable and movable edge conditions for different values of the thickness-variation parameter λ have been compared and discussed.

Formulation of Governing Differential Equations

The well-known expression for the potential energy of the plate in polar coordinates is

$$V = \frac{1}{2}\int D\left[\left(\frac{d^2W}{dr^2}\right)^2 + 2\frac{\nu}{r}\cdot\frac{dW}{dr}\cdot\frac{d^2W}{dr^2} + \left(\frac{1}{r}\cdot\frac{dW}{dr}\right)^2 + \frac{12}{h^2}\{e_1^2 + 2(\nu-1)e_2\}\right] r\,dr$$

[1] Department of Mathematics, Acharya B. N. Seal College, Cooch-Behar, West Bengal, India.

Manuscript received by ASME Applied Mechanics Division, January, 1982; final revision, August, 1983.

Downloaded 02 May 2010 to 171.66.16.25. Redistribution subject to ASME license or copyright; see http://www.asme.org/terms/Terms_Use.cfm

$$M_{\theta z} = \frac{T}{4\pi R} \tag{7}$$

in accordance with equation (6), while

$$RN_{\theta z} = 0(M_{\theta z}) \quad ,$$

but is otherwise indeterminate as it produces stresses at most of order h/R times those due to $M_{\theta z}$.

Finally we note that the assumption that the shear stresses vary *precisely* linearly through the thickness, vanishing at the midthickness, yields the correct value for $N_{\theta z}$ from simple considerations of equilibrium. Thus if $M_{\theta z}$ is given by equation (7) the shear stresses are given by

$$\tau_{\theta z} = \left(\frac{3T}{\pi R h^3}\right)\xi$$

so that

$$\begin{aligned} N_{\theta z} &= \frac{1}{R}\int_{r_1}^{r_2} r\tau_{\theta z}\,dr \\ &= \frac{3T}{\pi R^2 h^3}\int_{-h/2}^{+h/2}(R+\xi)\xi\,d\xi \\ &= \frac{T}{4\pi R^2} \quad , \end{aligned}$$

which agrees with equation (6).

References

1 Rayleigh, Lord, "Infinitesimal Bending of Surfaces of Revolution," *Proc. London Math. Soc.*, Vol. 13, 1881, pp. 4–16.

2 Love, A. E. H., *The Mathematical Theory of Elasticity*, 4th Ed., Cambridge Univ. Press, 1927, p. 319.

3 Morley, L. S. D., "Polynomial Stress States in First Approximation Theory of Circular Cylindrical Shells," *Quart. J. Mech. and Appl. Math.*, Vol. 25, 1972, pp. 13–43.

Large Amplitude Vibrations of Clamped Circular Plate of Variable Thickness

S. K. Chaudhuri[1]

In this paper nonlinear oscillations of a clamped circular plate of linearly varying thickness have been investigated using von Karman equations expressed in terms of displacement components. Numerical results obtained have been compared and discussed.

Nomenclature

λ = Thickness-variation parameter
V = Potential energy
D = Flexural rigidity given by

$$D = \frac{E h^3}{12(1-\nu^2)}$$

E = Modulus of elasticity
h = Thickness of the plate
ν = Poisson's ratio
W = Deflection normal to the middle plane

$$e_1 = \frac{du}{dr} + \frac{1}{2}\left(\frac{dW}{dr}\right)^2 + \frac{u}{r}$$

$$e_2 = \frac{u}{r}\frac{du}{dr} + \frac{1}{2}\frac{u}{r}\left(\frac{dW}{dr}\right)^2$$

u = Displacement
T = Kinetic Energy
ρ = Density of the material
F = Lagrangian function
$W_0(t)$ = Time function
h_0 = Constant thickness
$\frac{\sigma_{rr} \cdot a^2}{E h_0^2}$ = Membrane stress at the center of the plate
a = Radius of the circular plate

Introduction

Nonlinear vibrations are frequently encountered in practice, particularly with thin elastic plates, the deformational response of which is sensitive to the direction of small dimension associated with the thickness. Numerous authors [1, 2] have dealt with linear analysis of oscillations of elastic plates of various shapes. Nonlinear vibrations of circular and rectangular plates have also been investigated by Chu and Hermann [3], Nash and Modeer [4], Bauer [5], Nowinski [6], and many others by reason of relatively simpler mathematical work. Regarding other shapes, two interesting papers which need special mention are due to Nowinski and Ismail [7], and Vendhan and Das [8]. All these investigations are confined to plates of uniform thickness only.

Plates of nonuniform thickness are sometimes used in the design of machine parts such as diaphragms of steam turbines and pistons of reciprocating engines.

Investigations of vibrations of plates of nonuniform thickness based on linear theory have been done by many workers among which the works of Appl and Byers [9] and Ashton [10] are noteworthy.

Nonlinear analysis on Vibrations of thin plates of variable thickness are few in literature. J. Ramachandran [11] and M. Sathyamoorthy and K. A. V. Pandalai [12] quite elegantly carried out some interesting works in this field and achieved satisfactory results.

In this paper the large amplitude vibrations of a clamped tapered circular plate have been investigated following von Karman's equations expressed in terms of displacement components. Numerical results obtained both for immovable and movable edge conditions for different values of the thickness-variation parameter λ have been compared and discussed.

Formulation of Governing Differential Equations

The well-known expression for the potential energy of the plate in polar coordinates is

$$V = \frac{1}{2}\int D\left[\left(\frac{d^2W}{dr^2}\right)^2 + 2\frac{\nu}{r}\cdot\frac{dW}{dr}\cdot\frac{d^2W}{dr^2} + \left(\frac{1}{r}\cdot\frac{dW}{dr}\right)^2 + \frac{12}{h^2}\{e_1^2 + 2(\nu-1)e_2\}\right] r\,dr$$

[1] Department of Mathematics, Acharya B. N. Seal College, Cooch-Behar, West Bengal, India.

Manuscript received by ASME Applied Mechanics Division, January, 1982; final revision, August, 1983.

Copyright © 1984 by ASME
Downloaded 02 May 2010 to 171.66.16.25. Redistribution subject to ASME license or copyright; see http://www.asme.org/terms/Terms_Use.cfm

where

$$e_1 = \frac{du}{dr} + \frac{1}{2}\left(\frac{dW}{dr}\right)^2 + \frac{u}{r},$$

$$e_2 = \frac{u}{r}\frac{du}{dr} + \frac{1}{2}\frac{u}{r}\left(\frac{dW}{dr}\right)^2.$$

The kinematic energy of the plate is

$$T = \frac{\rho}{2}\int\int h(\dot{u}^2 + \dot{w}^2) r\, dr\, d\theta$$

Let us form the Lagrangian function

$$F = T - V$$

Now applying Hamilton's principles, Euler's variational equations and remembering that the plate thickness h is a variable quantity one gets the following two differential equations governing the vibrations of the plate.

$$h\frac{d^2u}{dr^2} + \frac{1}{r}\frac{du}{dr}\left(h + r\frac{dh}{dr}\right) + u\left(-\frac{h}{r^2} + \frac{\nu}{r}\frac{dh}{dr}\right)$$
$$= -\frac{h(1-\nu)}{2r}\cdot\left(\frac{dW}{dr}\right)^2 - h\frac{dW}{dr}\cdot\frac{d^2W}{dr^2} - \frac{1}{2}\frac{dh}{dr}\left(\frac{dW}{dr}\right)^2 \quad (1)$$

$$\frac{\rho h}{D}\cdot\frac{\partial^2 W}{\partial t^2} + \left[\frac{d^4W}{dr^4} + \left(\frac{2}{r} + \frac{6}{h}\cdot\frac{dh}{dr}\right)\frac{d^3W}{dr^3}\right.$$
$$+ \frac{1}{r}\left\{6(1+\nu)\cdot\frac{1}{h}\frac{dh}{dr} - \frac{1}{r} + \frac{6r}{h^2}\cdot\left(\frac{dh}{dr}\right)^2 - \frac{3\nu}{h}\frac{dh}{dr}\right\}\frac{d^2W}{dr^2}$$
$$\left. + \frac{1}{r^2}\left\{\frac{1}{r} - \frac{3}{h}\cdot\frac{dh}{dr}\right\}\frac{dW}{dr}\right] - \frac{12}{h^3}\left[h\frac{dW}{dr}\cdot\frac{d^2u}{dr^2}\right.$$
$$+ \frac{1}{r}\left\{r\frac{dh}{dr}\cdot\frac{dW}{dr} + hr\frac{d^2W}{dr^2} + h\frac{dW}{dr} + \nu h\frac{dW}{dr}\right\}\frac{du}{dr}$$
$$+ \frac{1}{r}\left(\nu\frac{dh}{dr}\frac{dW}{dr} + \nu h\frac{d^2W}{dr^2}\right)u + \frac{1}{2}\frac{dh}{dr}\left(\frac{dW}{dr}\right)^3$$
$$\left. + \frac{3}{2}h\left(\frac{dW}{dr}\right)^2\cdot\frac{d^2W}{dr^2} + \frac{1}{2}\frac{h}{r}\left(\frac{dW}{dr}\right)^3\right] = 0 \quad (2)$$

In which u = the displacement along the radius; W = the deflection normal to the middle plane; h = the plate thickness; D = the flexural rigidity given by $D = Eh^3/12(1-\nu^2)$, E and ν being the modulus of elasticity and the Poisson's ratio, respectively; ρ = the density of the material.

Method of Solution

Let us take a clamped circular plate of radius a, the center of the plate being the origin.

Let

$$W = W_0(t)\left[1 - \frac{r^2}{a^2}\right]^2 \quad (3)$$

be the deflection function satisfying the clamped edge conditions.

Let

$$h = h_0\left(1 + \lambda\frac{r}{a}\right) \quad (4)$$

be the thickness variation for the tapered plate where $\lambda(>0)$ is small and h_0 is a constant.

Substituting (3) and (4) in (1) one gets the following differential equation for u

$$\left(r^2 + \lambda\frac{r^3}{a}\right)\frac{d^2u}{dr^2} + \left(r + \frac{2\lambda}{a}r^2\right)\frac{du}{dr} - \left[1 + (1-\nu)\frac{r\lambda}{a}\right]u$$
$$= -\frac{8W_0^2(t)}{a^8}\left[(3-\nu)a^4r^3 + (4-\nu)\lambda a^3r^4 - (10-2\nu)a^2r^5\right.$$
$$\left. - (12-2\nu)\lambda a r^6 + (7-\nu)r^7 + (8-\nu)\frac{\lambda r^8}{a}\right] \quad (5)$$

The solution of (5) takes the following form

$$u = Ar\left[1 - \frac{1+\nu}{3}\cdot\lambda\cdot\left(\frac{r}{a}\right) + \frac{(1+\nu)(5+\nu)}{3\times 8}\cdot\lambda^2\cdot\left(\frac{r}{a}\right)^2\right.$$
$$\left. - \frac{(1+\nu)(5+\nu)(11+\nu)}{3\times 8\times 15}\cdot\lambda^3\cdot\left(\frac{r}{a}\right)^3 + \ldots\ldots\ldots\right]$$
$$- \frac{8W_0^2(t)}{a}\left[a_3\left(\frac{r}{a}\right)^3 + a_4\left(\frac{r}{a}\right)^4 + a_5\left(\frac{r}{a}\right)^5 + a_6\left(\frac{r}{a}\right)^6\right.$$
$$\left. + a_7\left(\frac{r}{a}\right)^7 + a_8\left(\frac{r}{a}\right)^8 + \ldots\ldots\ldots\right] \quad (6)$$

where

$$a_3 = \frac{3-\nu}{8}, \quad a_4 = -\frac{1-\nu^2}{8\times 15}\lambda,$$

$$a_5 = -\frac{5-\nu}{12} + \frac{(19+\nu)(1-\nu^2)\lambda^2}{8\times 15\times 24},$$

$$a_6 = \frac{1-\nu^2}{12\times 35}\lambda - \frac{(19+\nu)(29+\nu)(1-\nu^2)\lambda^3}{8\times 15\times 24\times 35},$$

$$a_7 = \frac{7-\nu}{48} - \frac{(41+\nu)(1-\nu^2)\lambda^2}{12\times 35\times 48},$$

$$a_8 = \left[\frac{8-\nu}{63} - \frac{(7-\nu)(55+\nu)}{48\times 63}\right]\cdot\lambda; \text{ etc.}$$

From (6) we get

$$u = Ar\left[1 - \frac{1.3}{3}\cdot\lambda\cdot\left(\frac{r}{a}\right) + \frac{(1.3)(5.3)}{3\times 8}\lambda^2\left(\frac{r}{a}\right)^2\right.$$
$$\left. - \frac{(1.3)(5.3)(11.3)}{3\times 8\times 15}\cdot\lambda^3\left(\frac{r}{a}\right)^3 + \ldots\ldots\right] - \frac{8W_0^2(t)}{a}\left[b_3\left(\frac{r}{a}\right)^3\right.$$
$$+ b_4\left(\frac{r}{a}\right)^4 + b_5\left(\frac{r}{a}\right)^5 + b_6\left(\frac{r}{a}\right)^6 + b_7\left(\frac{r}{a}\right)^7$$
$$\left. + b_8\left(\frac{r}{a}\right)^8 + \ldots\ldots\ldots\right] \quad (7)$$

where

$\nu = 0.3,$

$b_3 = 0.3375, \quad b_4 = -\lambda(0.00758),$

$b_5 = \lambda^2(0.006) - (0.39166), \quad b_6 = (0.002)\lambda,$

$b_7 = 0.139583,$

$b_8 = -(0.0003)\lambda,$ etc.

(higher powers of λ being neglected since λ is small)

and the constant A is to be determined by the boundary condition imposed on u. Clearly the infinite series given by (6) is convergent for $\lambda < 1$.

The boundary condition for immovable edge is $u = 0$ when

$$r = a \quad (8)$$

and the boundary condition for movable edge is

$$\frac{du}{dr} + \frac{1}{2}\left(\frac{dW}{dr}\right)^2 + \nu\cdot\frac{u}{r} = 0 \quad \text{when} \quad r = a \quad (9)$$

Downloaded 02 May 2010 to 171.66.16.25. Redistribution subject to ASME license or copyright; see http://www.asme.org/terms/Terms_Use.cfm

From (8)

$$A = \frac{8W_0^2(t)}{a^2} \cdot \frac{(0.0854167) - \lambda(0.0058) + \lambda^2(0.006) - \ldots\ldots}{1 - \lambda(0.4333333) + \lambda^2(0.2870833) - \lambda^3(0.2162694) + \ldots\ldots}$$

From (9)

$$A = \frac{8W_0^2(t)}{a^2} \cdot \frac{(0.0568751) - \lambda(0.022507) + \lambda^2(0.0318) - \ldots\ldots\ldots}{(1.3) - \lambda(0.9966666) + \lambda^2(0.947375) - \lambda^3(0.9299586) + \ldots\ldots}$$

Substituting (3), (4), and (7) in (2) and finally applying Galerkin's procedure one gets the following second-order differential equation for the unknown time function $W_0(t)$

$$\frac{d^2W_0(t)}{dt^2} + \frac{1}{a^2} \cdot \frac{L_1}{L_0} W_0(t) + \frac{1}{a^2 h_0^2} \cdot \frac{L_2}{L_0} W_0^3(t) = 0 \quad (10)$$

where

$$L_0 = \frac{12\rho(1-\nu^2)a^2}{E h_0^2} \cdot [(0.1666666) - \lambda(0.1523809) + \lambda^2(0.125) - \lambda^3(0.1015873) + \ldots\ldots]$$

$$L_1 = 10.666666 + \lambda(8.0456984) - \lambda^2(7.3499852) + \lambda^3(4.2666624) - \ldots\ldots\ldots$$

$$L_2 = 12 \times 32[B\{(0.2166665) - \lambda(0.1672803) + \lambda^2(0.0887969) - \lambda^3(0.020831) + \ldots\ldots\} - (0.005417) + \lambda(0.0048563) - \lambda^2(0.003425) + \lambda^3(0.0012474) - \ldots\ldots]$$

For immovable edge

$$B = \frac{(0.0854167) - \lambda(0.0058) + \lambda^2(0.006) - \ldots\ldots\ldots}{1 - \lambda(0.4333333) + \lambda^2(0.2870833) - \lambda^3(0.2162694) + \ldots\ldots}$$

and for immovable edge

$$B = \frac{(0.0568751) - \lambda(0.022507) + \lambda^2(0.0318) - \ldots\ldots\ldots\ldots}{(1.3) - \lambda(0.9966666) + \lambda^2(0.947375) - \lambda^3(0.9299586) + \ldots\ldots}$$

The solution to the equation (10) is well known and can be obtained in terms of Jacobian elliptic function. The ratio of the nonlinear and linear time periods can be now easily evaluated since L_2/L_1 is known.

Numerical Results and Discussions

Table 1 shows different values of L_2/L_1 for different λ. The membrane stress has been calculated at the center of the plate and this is given by

$$\frac{\sigma_{rr} \cdot a^2}{E h_0^2} = \alpha \cdot \left[\frac{W_0(t)}{h_0}\right]^2$$

Table 2 shows different values of α for different λ.

Table 1

Immovable edge $\frac{L_2}{L_1}$	λ	Movable edge $\frac{L_2}{L_1}$
0.4712	0	0.1462
0.4313	0.1	0.1402
0.3997	0.2	0.1370
0.3744	0.3	0.1363

Table 2

Immovable edge α	λ	Movable edge α
0.9768	0	0.4999
1.0114	0.1	0.5194
1.0461	0.2	0.5420
1.0814	0.3	0.5706

From the tables the following observations can be made:

1 When $\lambda = 0$ the results obtained from the present study are in exact agreement with those obtained by Timoshenko [13] for immovable edge and Nowinski [6] for movable edge for constant thickness problem.

2 When λ increases through small values the frequency ratio which depends on L_2/L_1 decreases both in the cases of immovable and movable edges.

3 Since L_2/L_1 decreases as λ increases the ratio of the nonlinear and linear time periods increases. This is expected because the thickness is minimum at the center and maximum at the edge of the tapered plate.

4 It is also observed that for $\lambda = 0$ the values of α both for immovable and movable edges are in excellent agreement with those in [13] and [6].

As λ increases the values of α increase in both cases. This is also expected for a tapered plate.

Acknowledgment

The author wishes to thank Dr. B. Banerjee, Head, Department of Mathematics, Jalpaiguri Govt. Engineering College, West Bengal for his guidance in the preparation of this paper.

Downloaded 02 May 2010 to 171.66.16.25. Redistribution subject to ASME license or copyright; see http://www.asme.org/terms/Terms_Use.cfm

References

1 Gontkevich, V. S., "Free Vibration of Plates and Shells," *Hand book* (in Russian), Kiev, Nenkova Dumka, 1964.

2 Leissa, "Vibration of Plates," Monogram, NASA, Sp 160, 1962.

3 Chu, H., and Hermann, G., "Influence of Large Amplitudes on Free Flexural Vibrations of Rectangular Elastic Plates," ASME JOURNAL OF APPLIED MECHANICS, Vol. 23, 1956, pp. 532-540.

4 Nash, W. A., and Modeer, J. R., "Certain Approximate Analysis of the Non-linear Behaviour of Plates and Shallow Shells," Engineering Progress at the University of Florida, Tech. Paper No. 193, Vol. XIV, No. 10, 1960.

5 Bauer, H. F., "Nonlinear Response of Elastic Plates to Pulse Excitations," ASME JOURNAL OF APPLIED MECHANICS, Vol. 35, 1968, pp. 47-52.

6 Nowinski, J. L., "Non-linear Vibrations of Elastic Circular Plate Exhibiting Rectilinear Orthotropy," *ZAMP*, Vol. 14, 1963, pp. 112-124.

7 Nowinski, J. L., and Ismail, I. A., "Large Oscillations of an Anisotropic Triangular Plate," *Journal of the Franklin Institute*, Vol. 280, No. 5, 1965, pp. 417-424.

8 Vendhan, C. P., and Das, Y. C., "Application of Rayleigh-Ritz and Galerkin Methods to Non-linear Vibration of Plates," *J. Sound Vib.*, Vol. 39, No. 2, 1975, pp. 147-157.

9 Appl, F. C., and Byers, N. R., "Fundamental Frequency of a Simply Supported Rectangular Plate With Linearly Varying Thickness," ASME JOURNAL OF APPLIED MECHANICS, Vol. 31, 1965, pp. 163-168.

10 Ashton, J. E., "Natural Modes of Vibration of Tapered Plates," *Journal of the Structural Division, ASCE*, Vol. 95, No. ST4, Proc. Paper 6489, 1969, pp. 787-790.

11 Ramachandran, J., "Vibration of Variable Thickness Plates at Large Amplitudes," *Journal of the Franklin Institute*, Vol. 299, 1975, pp. 359-362.

12 Sathyamoorthy, M., and Pandalai, K. A. V., "Large Amplitude Vibration of Variable Thickness Skew Plates," *Proceedings of Noise, Shock and Vibration Conference*, Monash University, Australia, 1974, pp. 99-106.

13 Timoshenko, S., and Woinowsky-Krieger, S., *Theory of Plates and Shells*, 2nd Ed., McGraw-Hill, New York, 1959, p. 402.

A Note on the Incompressible Flow Past a Semi-Infinite Flat Plate in a Stream With Uniform Shear

J. Dey[1] and G. Nath[2]

Introduction

The problem of flow over a semi-infinite plate with a shear flow has been studied by a few investigators [1-3]. Such a situation occurs behind a bow shock, where the fluid is compressible. However, in order to understand the role of a shear flow, Li [1], Glauert [2], and Murray [3] studied the problem of incompressible fluid using the boundary-layer approximation, vaild for large Reynolds number. In the boundary-layer approximation, the effect of free-stream vorticity is taken into account by the higher order boundary-layer effect [4]. A review on this by Van-Dyke [4] is very informative. The importance of the streamwise pressure gradient due to interaction between the displacement thickness and the external vorticity, though disputed for a long time, was found by Murray [3] by matched asymptotic expansion. Such a problem arises because of the boundary-layer approximation. In the present analysis, we obtain a perturbed solution of the vorticity equation whereby a direct encounter with the pressure gradient terms is avoided. In the following, it will be evident that for large Reynolds number we obtain the boundary-layer equation of Murray [3], thereby incorporating the pressure gradient effect in the present analysis. In this Note we present some results for moderate to a large Reynolds numbers flow over a semi-infinite plate, when the free stream has a uniform shear.

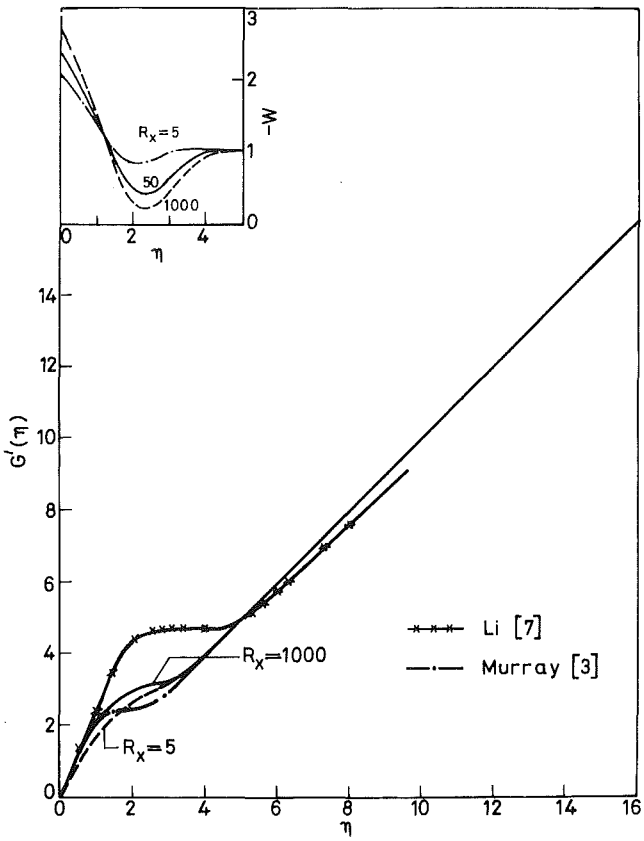

Fig. 1 Velocity and vorticity profiles

Theoretical Analysis

We consider the steady incompressible laminar flow over a semi-infinite flat plate. Let u and v denote the two velocity components in x and y directions, respectively. The free-stream velocity is given by $U = u_0 + W_0 Y$.

We define the nondimensional parabolic coordinate (σ,η) such that

$$x+iy=\nu(\sigma+i\eta)^2/2u_0 \tag{1}$$

where ν is the kinematic viscosity. The vorticity equation in σ and η is

$$P_{\sigma\sigma}+P_{\eta\eta}+\varphi_\sigma P_\eta-\varphi_\eta P_\sigma=0 \tag{2}$$

where suffixes σ and η denote partial derivative with respect to σ and η, respectively. $P=(\varphi_{\sigma\sigma}+\varphi_{\eta\eta})/(\sigma^2+\eta^2)$ and φ is the nondimensional stream function. The boundary conditions are

$$\varphi=\varphi_\eta=0 \quad \text{at} \quad \eta=0$$
$$\varphi\sim\sigma\eta+N\sigma^2\eta^2/2 \quad \text{as} \quad \eta\to\infty \tag{3}$$

where the nondimensional vorticity number N is $N=W_0\nu/u_0^2$.

Since for parallel free stream, equation (2) can be solved assuming local similarity [5], we seek perturbation solution of (2) about the nondimensional vorticity number $N<<1$ as

$$\varphi=f(\sigma,\eta)+N\ g(\sigma,\eta). \tag{4}$$

Then from (2) and (4) we obtain the vorticity equation by equating the coefficients of N

$$T_{\sigma\sigma}+T_{\eta\eta}+f_\sigma T_\eta-f_\eta T_\sigma=0 \tag{5}$$
$$S_{\sigma\sigma}+S_{\eta\eta}+f_\sigma S_\eta-f_\eta S_\sigma+g_\sigma T_\eta-g_\eta T_\sigma=0 \tag{6}$$

where

$$T=(f_{\sigma\sigma}+f_{\eta\eta})/(\sigma^2+\eta^2)$$

[1] Research Scholar, Department of Mechanical Engineering, Indian Institute of Science, Bangalore-560012, India.

[2] Professor, Department of Applied Mathematics, Indian Institute of Science, Bangalore-560012, India.

Manuscript received by ASME Applied Mechanics Division, November, 1982; final revision, June, 1983.

Downloaded 02 May 2010 to 171.66.16.25. Redistribution subject to ASME license or copyright; see http://www.asme.org/terms/Terms_Use.cfm

References

1 Gontkevich, V. S., "Free Vibration of Plates and Shells," *Hand book* (in Russian), Kiev, Nenkova Dumka, 1964.

2 Leissa, "Vibration of Plates," Monogram, NASA, Sp 160, 1962.

3 Chu, H., and Hermann, G., "Influence of Large Amplitudes on Free Flexural Vibrations of Rectangular Elastic Plates," ASME JOURNAL OF APPLIED MECHANICS, Vol. 23, 1956, pp. 532-540.

4 Nash, W. A., and Modeer, J. R., "Certain Approximate Analysis of the Non-linear Behaviour of Plates and Shallow Shells," Engineering Progress at the University of Florida, Tech. Paper No. 193, Vol. XIV, No. 10, 1960.

5 Bauer, H. F., "Nonlinear Response of Elastic Plates to Pulse Excitations," ASME JOURNAL OF APPLIED MECHANICS, Vol. 35, 1968, pp. 47-52.

6 Nowinski, J. L., "Non-linear Vibrations of Elastic Circular Plate Exhibiting Rectilinear Orthotropy," *ZAMP*, Vol. 14, 1963, pp. 112-124.

7 Nowinski, J. L., and Ismail, I. A., "Large Oscillations of an Anisotropic Triangular Plate," *Journal of the Franklin Institute*, Vol. 280, No. 5, 1965, pp. 417-424.

8 Vendhan, C. P., and Das, Y. C., "Application of Rayleigh-Ritz and Galerkin Methods to Non-linear Vibration of Plates," *J. Sound Vib.*, Vol. 39, No. 2, 1975, pp. 147-157.

9 Appl, F. C., and Byers, N. R., "Fundamental Frequency of a Simply Supported Rectangular Plate With Linearly Varying Thickness," ASME JOURNAL OF APPLIED MECHANICS, Vol. 31, 1965, pp. 163-168.

10 Ashton, J. E., "Natural Modes of Vibration of Tapered Plates," *Journal of the Structural Division, ASCE*, Vol. 95, No. ST4, Proc. Paper 6489, 1969, pp. 787-790.

11 Ramachandran, J., "Vibration of Variable Thickness Plates at Large Amplitudes," *Journal of the Franklin Institute*, Vol. 299, 1975, pp. 359-362.

12 Sathyamoorthy, M., and Pandalai, K. A. V., "Large Amplitude Vibration of Variable Thickness Skew Plates," *Proceedings of Noise, Shock and Vibration Conference*, Monash University, Australia, 1974, pp. 99-106.

13 Timoshenko, S., and Woinowsky-Krieger, S., *Theory of Plates and Shells*, 2nd Ed., McGraw-Hill, New York, 1959, p. 402.

A Note on the Incompressible Flow Past a Semi-Infinite Flat Plate in a Stream With Uniform Shear

J. Dey[1] and G. Nath[2]

Introduction

The problem of flow over a semi-infinite plate with a shear flow has been studied by a few investigators [1-3]. Such a situation occurs behind a bow shock, where the fluid is compressible. However, in order to understand the role of a shear flow, Li [1], Glauert [2], and Murray [3] studied the problem of incompressible fluid using the boundary-layer approximation, vaild for large Reynolds number. In the boundary-layer approximation, the effect of free-stream vorticity is taken into account by the higher order boundary-layer effect [4]. A review on this by Van-Dyke [4] is very informative. The importance of the streamwise pressure gradient due to interaction between the displacement thickness and the external vorticity, though disputed for a long time, was found by Murray [3] by matched asymptotic expansion. Such a problem arises because of the boundary-layer approximation. In the present analysis, we obtain a perturbed solution of the vorticity equation whereby a direct encounter with the pressure gradient terms is avoided. In the following, it will be evident that for large Reynolds number we obtain the boundary-layer equation of Murray [3], thereby incorporating the pressure gradient effect in the present analysis. In this Note we present some results for moderate to a large Reynolds numbers flow over a semi-infinite plate, when the free stream has a uniform shear.

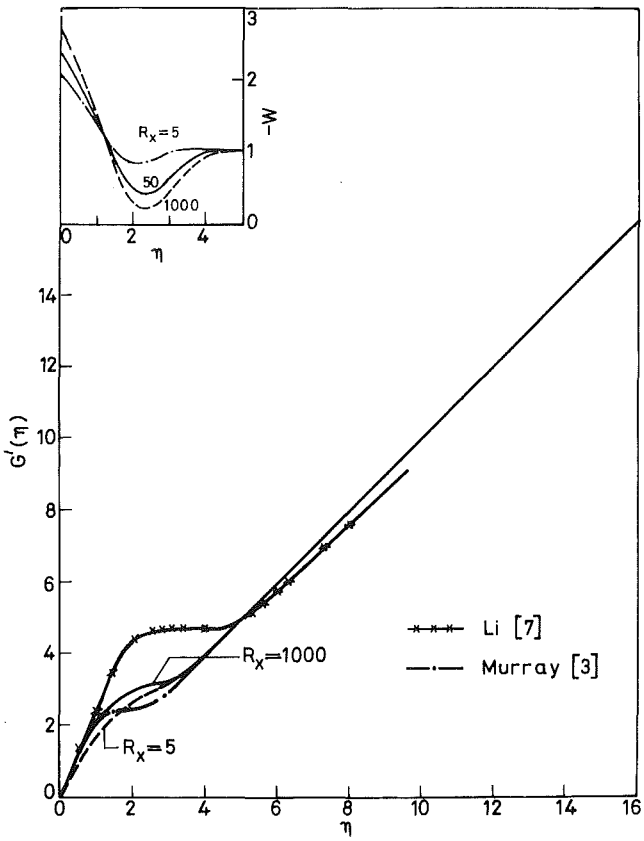

Fig. 1 Velocity and vorticity profiles

Theoretical Analysis

We consider the steady incompressible laminar flow over a semi-infinite flat plate. Let u and v denote the two velocity components in x and y directions, respectively. The free-stream velocity is given by $U = u_0 + W_0 Y$.

We define the nondimensional parabolic coordinate (σ,η) such that

$$x+iy=\nu(\sigma+i\eta)^2/2u_0 \tag{1}$$

where ν is the kinematic viscosity. The vorticity equation in σ and η is

$$P_{\sigma\sigma}+P_{\eta\eta}+\varphi_\sigma P_\eta-\varphi_\eta P_\sigma=0 \tag{2}$$

where suffixes σ and η denote partial derivative with respect to σ and η, respectively. $P=(\varphi_{\sigma\sigma}+\varphi_{\eta\eta})/(\sigma^2+\eta^2)$ and φ is the nondimensional stream function. The boundary conditions are

$$\varphi=\varphi_\eta=0 \quad \text{at} \quad \eta=0$$
$$\varphi\sim\sigma\eta+N\sigma^2\eta^2/2 \quad \text{as} \quad \eta\to\infty \tag{3}$$

where the nondimensional vorticity number N is $N=W_0\nu/u_0^2$.

Since for parallel free stream, equation (2) can be solved assuming local similarity [5], we seek perturbation solution of (2) about the nondimensional vorticity number $N<<1$ as

$$\varphi=f(\sigma,\eta)+N\ g(\sigma,\eta). \tag{4}$$

Then from (2) and (4) we obtain the vorticity equation by equating the coefficients of N

$$T_{\sigma\sigma}+T_{\eta\eta}+f_\sigma T_\eta-f_\eta T_\sigma=0 \tag{5}$$
$$S_{\sigma\sigma}+S_{\eta\eta}+f_\sigma S_\eta-f_\eta S_\sigma+g_\sigma T_\eta-g_\eta T_\sigma=0 \tag{6}$$

where

$$T=(f_{\sigma\sigma}+f_{\eta\eta})/(\sigma^2+\eta^2)$$

[1] Research Scholar, Department of Mechanical Engineering, Indian Institute of Science, Bangalore-560012, India.

[2] Professor, Department of Applied Mathematics, Indian Institute of Science, Bangalore-560012, India.

Manuscript received by ASME Applied Mechanics Division, November, 1982; final revision, June, 1983.

Copyright © 1984 by ASME

Downloaded 02 May 2010 to 171.66.16.25. Redistribution subject to ASME license or copyright; see http://www.asme.org/terms/Terms_Use.cfm

and

$$S=(g_{\sigma\sigma}+g_{\eta\eta})/(\sigma^2+\eta^2).$$

The boundary conditions are

$$f(0)=f_\eta(0)=g(0)=g_\eta(0)=0;$$
$$f(\eta)\sim\sigma\eta;\quad g(\eta)\sim\sigma^2\eta^2/2\quad\text{as}\quad\eta\to\infty \tag{7}$$

These dictate that the local similar form of f and g, about an arbitrary point on the surface $\sigma_0=(2u_0x/\nu)^{1/2}$, is

$$f=\sigma[F(\eta)+(\sigma-\sigma_0)F_1(\eta)\ \ldots]$$
$$g=\sigma^2[G(\eta)+(\sigma-\sigma_0)G_1(\eta)\ \ldots] \tag{8}$$

From (5) and (6) and (8) we obtain, after retaining only the first-order terms,

$$F''''+F'''[F-4\eta(\sigma_0^2+\eta^2)^{-1}]+(\sigma_0^2+\eta^2)^{-1}[(\sigma_0^2-\eta^2)F'-2\eta F]F''=0. \tag{9}$$

$$G''''\sigma_0^2(\sigma_0^2+\eta^2)+G'''[F-4\eta(\sigma_0^2+\eta^2)^{-1}]\sigma_0^2(\sigma_0^2+\eta^2)+G''[4\eta^2-2\eta\sigma_0^2F-2\eta^2\sigma_0^2F']+G'[2F(\sigma_0^2+\eta^2)-8\eta+\sigma_0^2(\sigma_0^2-\eta^2)F'']+G[8-4\eta F+4\sigma_0^2F'-4\eta\sigma_0^2F''+2\sigma_0^2(\sigma_0^2+\eta^2)F''']=0, \tag{10}$$

where prime denotes derivative with respect to η.

The corresponding boundary conditions are

$$F=F'=G=G'=0\quad\text{at}\quad\eta=0,$$
$$F\sim\eta,\ G\sim\eta^2/2\quad\text{as}\quad\eta\to\infty \tag{11}$$

Equation (9) is that obtained by Davis [5] for flat plate with parallel free stream. It can be easily shown that as $\sigma_0\to\infty$, equation (10) reduces to the boundary-layer equation of Murray [3], as:

$$G''''+FG'''+G'F''+2GF'''=0. \tag{12}$$

Results and Conclusions

Equations (9) and (10) were solved for $Rx(=\sigma_0^2/2)=5-1000$ using quasi-linearization and iteration technique for (9) and the principle of superposition for (10). For equation (10), it was found convenient to satisfy $G'(\infty)$ and $G''(\infty)$ conditions rather than $G(\infty)$ and $G'(\infty)$ conditions. The initial value problems were integrated using Hamming's predictor corrector method on a Dec-10 computer. Results, shown in Fig. 1, show that over large η, $G'(\eta)$ is linear while in the region $1.5\le\eta\le3.0$ there is a change of curvature. Results of [6] show that the boundary-layer solution can be obtained from (9) for $Rx=1000$. Hence, we solved (9) and (10) for $Rx=1000$. The velocity profile $G'(\eta)$ for $Rx=1000$ has been compared with that of Murray [3] and Li [7] for boundary-layer equations (Fig. 1). It is found to be in very good agreement except in the range $1\le\eta\le4$. This difference is due to different scaling used in [3, 7]. For example, Li [7] has solved the boundary-layer equation which differs from that of Murray [3] by a factor of 2 in the highest order derivative and the present scaling of σ and η differs from that of Murray [3] by a factor of $(2)^{1/2}$. Also, the skin friction on the surface $G''(0)$ is found to be almost same as that of Murray [3] if we multiply our result by $2^{1/2}$ (i.e., $G''(0)=0.314$ as compared to 0.311 obtained by Murray [3]). The change in the curvature of the G' profiles is associated with the perturbed non-dimensional vorticity $(W=-(2G+\sigma_0^2G'')/(\sigma_0^2+\eta^2))$ minimum, shown on the inset of Fig. 1. Expected vorticity distribution is maximum at $\eta=0$ and unity in the free stream. The vorticity distribution shows that over large η, the vorticity is less than unity. This possibly suggest that the fluid in this region is slightly accelerated, of course relatively. In other words, the free-stream vorticity causes an accelerating fluid to surmount a retarding fluid near the wall. Due to the increase in the boundary-layer thickness with increasing Reynolds number, the region of this acceleration fluid also increases. To summarize, the vorticity distribution for flow over a semi-infinite plate in a stream with uniform shear depends on the local Reynolds number.

References

1 Li, T. V., "Simple Shear Flow Past a Flat Plate in an Incompressible Fluid of Small Viscosity," *Journal of Aeronautical Sciences*, Vol. 22, 1955, pp. 651-652.

2 Glauert, M. B., "The Boundary Layer in Simple Shear Flow Past a Flat Plate," *Journal of Aeronautical Sciences*, Vol. 24, 1957, pp. 848-849.

3 Murray, J. D., "The Boundary Layer on a Flat Plate in a Stream With Uniform Shear," *Journal of Fluid Mechanics*, Vol. 11, 1961, pp. 309-316.

4 Van Dyke, M., "Higher Order Boundary-Layer Theory," *Annual Review of Fluid Mechanics*, Sears, W. R., ed., 1969, pp. 265-292.

5 Davis, R. T., "Laminar Incompressible Flow Past a Semi-Infinite Flat Plate," *Journal of Fluid Mechanics*, Vol. 27, 1967, pp. 691-704.

6 Afzal, N., and Banthiya, N. K., "Mixed Convection Over a Semi-infinite Vertical Flat Plate," *Journal of Applied Mathematics and Physics (ZAMP)*, Vol. 28, 1977, pp. 993-1004.

7 Li, T. V., "Effects of Free-Stream Vorticity on the Behavior of a Viscous Boundary Layer," *Journal of the Aeronautical Sciences*, Vol. 23, 1956, pp. 1128-1129, also Vol. 24, 1957, pp. 849-850.

Large-Amplitude Vibrations of Polygonal Plates – A New Approach

B. Banerjee[1]

Introduction

For nonlinear analysis of thin elastic plates, Banerjee and Datta [1] suggested a modified energy expression by bringing directly the expression for σ_{rr} in the total potential energy of the system and a new set of differential equations has been obtained in a decoupled form. The accuracy of these equations has been tested for a circular and a square plate with immovable as well as movable edge conditions under uniform loading. Results obtained are in excellent agreement with other known results both for movable and immovable edges.

The present study investigates nonlinear vibrations of clamped polygonal plates using complex variable theory. A new set of differential equations has been obtained in a decoupled form following the line of thought as given in [1]. Numerical results obtained have been given in tables and compared with other known results.

Formulation of Differential Equations

We consider the modified energy expression V_1 as suggested in [1]. Kinetic energy of the plate is

$$T=\frac{\rho h}{2}\int\int(\dot u^2+\dot v^2+\dot w^2)dxdy. \tag{1}$$

Forming the Lagrangian function $L=T-V_1$, applying Hamilton's principle, and Euler's variational equations, a set of differential equations in rectangular cartesian coordinates is obtained for vibrations of thin elastic plates. In a complex coordinate system $Z=z+iy$, $\bar Z=x-iy$ the preceding equation changes.

[1]This Note was written when the author was Head, Department of Mathematics, Jalpaiguri Government Engineering College, West Bengal India. Current affiliation: Department of Mathematics, Hooghly-Mohsin College, West Bengal, India.

Manuscript received by ASME Applied Mechanics Division, November, 1982; final revision, August, 1983.

Downloaded 02 May 2010 to 171.66.16.25. Redistribution subject to ASME license or copyright; see http://www.asme.org/terms/Terms_Use.cfm

and

$$S=(g_{\sigma\sigma}+g_{\eta\eta})/(\sigma^2+\eta^2).$$

The boundary conditions are

$$f(0)=f_\eta(0)=g(0)=g_\eta(0)=0;$$

$$f(\eta)\sim\sigma\eta;\quad g(\eta)\sim\sigma^2\eta^2/2\quad\text{as}\quad\eta\to\infty \tag{7}$$

These dictate that the local similar form of f and g, about an arbitrary point on the surface $\sigma_0=(2u_0x/\nu)^{1/2}$, is

$$f=\sigma[F(\eta)+(\sigma-\sigma_0)F_1(\eta)\ \ldots]$$
$$g=\sigma^2[G(\eta)+(\sigma-\sigma_0)G_1(\eta)\ \ldots] \tag{8}$$

From (5) and (6) and (8) we obtain, after retaining only the first-order terms,

$$F''''+F'''[F-4\eta(\sigma_0^2+\eta^2)^{-1}]+(\sigma_0^2+\eta^2)^{-1}[(\sigma_0^2-\eta^2)F'-2\eta F]F''=0. \tag{9}$$

$$G''''\sigma_0^2(\sigma_0^2+\eta^2)+G'''[F-4\eta(\sigma_0^2+\eta^2)^{-1}]\sigma_0^2(\sigma_0^2+\eta^2)+G''[4\eta^2-2\eta\sigma_0^2F-2\eta^2\sigma_0^2F']+G'[2F(\sigma_0^2+\eta^2)-8\eta+\sigma_0^2(\sigma_0^2-\eta^2)F'']+G[8-4\eta F+4\sigma_0^2F'-4\eta\sigma_0^2F''+2\sigma_0^2(\sigma_0^2+\eta^2)F''']=0, \tag{10}$$

where prime denotes derivative with respect to η.

The corresponding boundary conditions are

$$F=F'=G=G'=0\quad\text{at}\quad\eta=0,$$

$$F\sim\eta,\ G\sim\eta^2/2\quad\text{as}\quad\eta\to\infty \tag{11}$$

Equation (9) is that obtained by Davis [5] for flat plate with parallel free stream. It can be easily shown that as $\sigma_0\to\infty$, equation (10) reduces to the boundary-layer equation of Murray [3], as:

$$G''''+FG'''+G'F''+2GF'''=0. \tag{12}$$

Results and Conclusions

Equations (9) and (10) were solved for $Rx(=\sigma_0^2/2)=5-1000$ using quasi-linearization and iteration technique for (9) and the principle of superposition for (10). For equation (10), it was found convenient to satisfy $G'(\infty)$ and $G''(\infty)$ conditions rather than $G(\infty)$ and $G'(\infty)$ conditions. The initial value problems were integrated using Hamming's predictor corrector method on a Dec-10 computer. Results, shown in Fig. 1, show that over large η, $G'(\eta)$ is linear while in the region $1.5\le\eta\le3.0$ there is a change of curvature. Results of [6] show that the boundary-layer solution can be obtained from (9) for $Rx=1000$. Hence, we solved (9) and (10) for $Rx=1000$. The velocity profile $G'(\eta)$ for $Rx=1000$ has been compared with that of Murray [3] and Li [7] for boundary-layer equations (Fig. 1). It is found to be in very good agreement except in the range $1\le\eta\le4$. This difference is due to different scaling used in [3, 7]. For example, Li [7] has solved the boundary-layer equation which differs from that of Murray [3] by a factor of 2 in the highest order derivative and the present scaling of σ and η differs from that of Murray [3] by a factor of $(2)^{1/2}$. Also, the skin friction on the surface $G''(0)$ is found to be almost same as that of Murray [3] if we multiply our result by $2^{1/2}$ (i.e., $G''(0)=0.314$ as compared to 0.311 obtained by Murray [3]). The change in the curvature of the G' profiles is associated with the perturbed non-dimensional vorticity $(W=-(2G+\sigma_0^2G'')/(\sigma_0^2+\eta^2))$ minimum, shown on the inset of Fig. 1. Expected vorticity distribution is maximum at $\eta=0$ and unity in the free stream. The vorticity distribution shows that over large η, the vorticity is less than unity. This possibly suggest that the fluid in this region is slightly accelerated, of course relatively. In other words, the free-stream vorticity causes an accelerating fluid to surmount a retarding fluid near the wall. Due to the increase in the boundary-layer thickness with increasing Reynolds number, the region of this acceleration fluid also increases. To summarize, the vorticity distribution for flow over a semi-infinite plate in a stream with uniform shear depends on the local Reynolds number.

References

1 Li, T. V., "Simple Shear Flow Past a Flat Plate in an Incompressible Fluid of Small Viscosity," *Journal of Aeronautical Sciences*, Vol. 22, 1955, pp. 651-652.

2 Glauert, M. B., "The Boundary Layer in Simple Shear Flow Past a Flat Plate," *Journal of Aeronautical Sciences*, Vol. 24, 1957, pp. 848-849.

3 Murray, J. D., "The Boundary Layer on a Flat Plate in a Stream With Uniform Shear," *Journal of Fluid Mechanics*, Vol. 11, 1961, pp. 309-316.

4 Van Dyke, M., "Higher Order Boundary-Layer Theory," *Annual Review of Fluid Mechanics*, Sears, W. R., ed., 1969, pp. 265-292.

5 Davis, R. T., "Laminar Incompressible Flow Past a Semi-Infinite Flat Plate," *Journal of Fluid Mechanics*, Vol. 27, 1967, pp. 691-704.

6 Afzal, N., and Banthiya, N. K., "Mixed Convection Over a Semi-infinite Vertical Flat Plate," *Journal of Applied Mathematics and Physics (ZAMP)*, Vol. 28, 1977, pp. 993-1004.

7 Li, T. V., "Effects of Free-Stream Vorticity on the Behavior of a Viscous Boundary Layer," *Journal of the Aeronautical Sciences*, Vol. 23, 1956, pp. 1128-1129, also Vol. 24, 1957, pp. 849-850.

Large-Amplitude Vibrations of Polygonal Plates – A New Approach

B. Banerjee[1]

Introduction

For nonlinear analysis of thin elastic plates, Banerjee and Datta [1] suggested a modified energy expression by bringing directly the expression for σ_{rr} in the total potential energy of the system and a new set of differential equations has been obtained in a decoupled form. The accuracy of these equations has been tested for a circular and a square plate with immovable as well as movable edge conditions under uniform loading. Results obtained are in excellent agreement with other known results both for movable and immovable edges.

The present study investigates nonlinear vibrations of clamped polygonal plates using complex variable theory. A new set of differential equations has been obtained in a decoupled form following the line of thought as given in [1]. Numerical results obtained have been given in tables and compared with other known results.

Formulation of Differential Equations

We consider the modified energy expression V_1 as suggested in [1]. Kinetic energy of the plate is

$$T=\frac{\rho h}{2}\int\int(\dot u^2+\dot v^2+\dot w^2)dxdy. \tag{1}$$

Forming the Lagrangian function $L=T-V_1$, applying Hamilton's principle, and Euler's variational equations, a set of differential equations in rectangular cartesian coordinates is obtained for vibrations of thin elastic plates. In a complex coordinate system $Z=z+iy$, $\bar Z=x-iy$ the preceding equation changes.

[1]This Note was written when the author was Head, Department of Mathematics, Jalpaiguri Government Engineering College, West Bengal India. Current affiliation: Department of Mathematics, Hooghly-Mohsin College, West Bengal, India.

Manuscript received by ASME Applied Mechanics Division, November, 1982; final revision, August, 1983.

Copyright © 1984 by ASME
Downloaded 02 May 2010 to 171.66.16.25. Redistribution subject to ASME license or copyright; see http://www.asme.org/terms/Terms_Use.cfm

Let $z=f(\xi)$ . . (1) be the analytic function which maps the given shape in the z-plane on to a unit circle in the ξ-plane. Substituting relation (1) into the transformed equations in (Z, $\bar{Z}$) one gets the following set of differential equations in (ξ, $\bar{\xi}$) coordinates.

$$16\Big[\frac{\partial^4 w}{\partial\xi^2\partial\bar{\xi}^2}\frac{dz}{d\xi}\frac{d\bar{z}}{d\bar{\xi}}-\frac{\partial^3 w}{\partial\xi^2\partial\bar{\xi}}\frac{d^2z}{d\xi^2}\frac{d\bar{z}}{d\bar{\xi}}-\frac{\partial^3 w}{\partial\xi^2\partial\bar{\xi}}\frac{d^2\bar{z}}{d\bar{\xi}^2}\frac{dz}{d\xi}+\frac{\partial^2 w}{\partial\xi\partial\bar{\xi}}\frac{d^2z}{d\xi^2}\frac{d^2\bar{z}}{d\bar{\xi}^2}\Big]-\frac{12Af(t)}{h^2}\Big[(\nu-1)\Big\{\frac{\partial W}{\partial\xi}\cdot\frac{d^2z}{d\xi^2}\Big(\frac{d\bar{z}}{d\bar{\xi}}\Big)^3+\frac{\partial w}{\partial\bar{\xi}}\frac{d^2\bar{z}}{d\bar{\xi}^2}\Big(\frac{dz}{d\xi}\Big)^3\Big\}+2(1+\nu)\frac{\partial^2 w}{\partial\xi\partial\bar{\xi}}\Big(\frac{dz}{d\xi}\Big)^2\Big(\frac{d\bar{z}}{d\bar{\xi}}\Big)^2+(1-\nu)\Big\{\frac{\partial^2 w}{\partial\xi^2}\Big(\frac{dz}{d\xi}\Big)\Big(\frac{d\bar{z}}{d\bar{\xi}}\Big)^3+\frac{\partial^2 w}{\partial\bar{\xi}^2}\Big(\frac{d\bar{z}}{d\bar{\xi}}\Big)\Big(\frac{dz}{d\xi}\Big)^3\Big\}\Big]-\frac{48\lambda_1}{h^2}\Big[\Big(\frac{\partial w}{\partial\xi}\Big)^2\frac{\partial^2 w}{\partial\bar{\xi}^2}\frac{dz}{d\xi}\frac{d\bar{z}}{d\bar{\xi}}+\Big(\frac{\partial w}{\partial\bar{\xi}}\Big)^2\frac{\partial^2 w}{\partial\xi^2}\frac{dz}{d\xi}\frac{d\bar{z}}{d\bar{\xi}}-\Big(\frac{\partial W}{\partial\xi}\Big)^2\frac{\partial W}{\partial\bar{\xi}}\frac{d^2\bar{z}}{d\bar{\xi}^2}\frac{dz}{d\xi}-\Big(\frac{\partial w}{\partial\bar{\xi}}\Big)^2\frac{\partial w}{\partial\xi}\frac{d^2z}{d\xi^2}\frac{d\bar{z}}{d\bar{\xi}}+4\frac{\partial^2 w}{\partial\xi\partial\bar{\xi}}\frac{dz}{d\xi}\frac{d\bar{z}}{d\bar{\xi}}\frac{\partial w}{\partial\xi}\frac{\partial w}{\partial\bar{\xi}}\Big]+\frac{\rho h}{D}\frac{\partial^2 w}{\partial t^2}\Big(\frac{dz}{d\xi}\cdot\frac{d\bar{z}}{d\bar{\xi}}\Big)^3=\frac{q}{D}\Big(\frac{dz}{d\xi}\cdot\frac{d\bar{z}}{d\bar{\xi}}\Big)^3 \tag{2}$$

$$\Big(\frac{dz}{d\xi}\cdot\frac{d\bar{z}}{d\bar{\xi}}\Big)^2 Af(t)=\frac{1}{2}(1-\nu)\Big(\frac{\partial w}{\partial\xi}\Big)^2\Big(\frac{d\bar{z}}{d\bar{\xi}}\Big)^2+\frac{1}{2}(1-\nu)\Big(\frac{dw}{\partial\bar{\xi}}\Big)^2\Big(\frac{dz}{d\xi}\Big)^2+\frac{\partial u}{\partial\xi}\cdot\frac{dz}{d\xi}\Big(\frac{d\bar{z}}{d\bar{\xi}}\Big)^2+\frac{\partial u}{\partial\bar{\xi}}\Big(\frac{dz}{d\xi}\Big)^2\frac{d\bar{z}}{d\bar{\xi}}+\nu i\Big\{\frac{\partial v}{\partial\xi}\cdot\Big(\frac{d\bar{z}}{d\bar{\xi}}\Big)^2\frac{dz}{d\xi}-\frac{\partial v}{\partial\bar{\xi}}\Big(\frac{dz}{d\xi}\Big)^2\frac{d\bar{z}}{d\bar{\xi}}\Big\}+(1+\nu)\frac{\partial w}{\partial\xi}\frac{\partial w}{\partial\bar{\xi}}\frac{dz}{d\xi}\frac{d\bar{z}}{d\bar{\xi}} \tag{3}$$

where $\xi=re^{i\theta}$, $\bar{\xi}=re^{-i\theta}$, r being the radius of the circle. λ_1 has been defined in [1]. Values of λ_1 have been obtained from the conditions $\partial V_1/\partial\lambda_1=0$ for minimum potential energy.

For regular polygons of side a, the mapping function is

$$Z=L\xi+\lambda\xi^5 \tag{4}$$

Let us choose the deflection in the following form

$$W=W_0(t)[1-(\xi\cdot\bar{\xi})]^2\Big[1+\frac{1}{2}(\xi^2+\bar{\xi}^2)\Big] \tag{5}$$

Table 1

Polygons	L	λ
Square	$0.54\,a$	$-0.055a$
Pentagon	$0.5265a$	$-0.035a$
Hexagon	$0.519a$	$-0.025a$
Heptagon	$0.5145a$	$-0.018a$
Octagon	$0.511a$	$-0.014a$

Table 2, $\nu=0.3$, $\lambda_1=2\nu^2$

Polygons	Present study		Other known results		Present study	Other known results
	Movable edge	Immovable edge	Movable edge	Immovable edge		
	ψ_1	ψ_1	ψ_1	ψ_1	ψ_2	ψ_2
Square	0.1719	0.444	0.20 [4]	0.51 [4]	0.045	0.045 [4]
Pentagon	0.0641	0.187	Absurd by Berger method [3]	0.20 [3]	0.0248	0.0249 [3]
Hexagon	0.0522	0.17	Absurd by Berger method [3]	0.19 [3]	0.0207	0.0209 [3]
Heptagon	0.0452	0.165	Absurd by Berger method [3]	0.18 [3]	0.0196	0.0193 [3]
Octagon	0.0401	0.153	Absurd by Berger method [3]	0.16 [3]	0.0162	0.0165 [3]

Table 3, $\nu=0.3$, $\lambda_1=2\nu^2$

	Square		Pentagon		Hexagon		Heptagon		Octagon	
	B/h	T^*/T	B/h	T^*/T	B/h	T^*/T	B/h	T^*/T	B/h	T^*/T
Movable edge	0.5	.97 .96 [2]	0.5	0.99	0.5	1.01	0.5	1.03	0.5	1.04
	0.75	.94 .932 [2]	0.75	0.96	0.75	0.98	0.75	0.99	0.75	0.998
	1	.92 .91 [2]	1	0.95	1	0.99	1	1.01	1	1.02
Immovable edge	0.5	.95 .94 [2]	0.5	0.969	0.5	1	0.5	1.02	0.5	1.03
	0.75	.86 .854 [2]	0.75	0.898	0.75	0.908	0.75	0.929	0.75	0.967
	1	.83 .821 [2]	1	0.86	1	0.902	1	0.920	1	0.962

Downloaded 02 May 2010 to 171.66.16.25. Redistribution subject to ASME license or copyright; see http://www.asme.org/terms/Terms_Use.cfm

where $W_0(t)$ is a function of time. Clearly W is θ-dependent and satisfies the clamped edge boundary conditions. Substituting (4) and (5) in (2) the error function $\epsilon(\xi,\bar{\xi},t)$ is obtained. Galerkin's procedure requires that

$$\int_{\theta=0}^{2\pi}\int_{r=0}^{1}\epsilon(\xi,\bar{\xi},t)W(\xi,\bar{\xi},t)r\,dr\,d\theta=0 \tag{6}$$

After evaluating the integrals one gets the cubic equation determining $W_0(t)$.

The constant A is determined by integrating (3) over the area of the unit circle. The in-plane displacements u and v have been eliminated by choosing suitable expressions for u and v and integrating over the area of the plate.

Numerical Results

Nonlinear Static Case. Rejecting the inertia term in the cubic equation for $W_0(t)$ and considering the value of A one gets the following equation determining the central deflection W_0.

$$\frac{W_0}{h}+\psi_1\left(\frac{W_0}{h}\right)^3=\frac{\psi_2 qa^4}{Eh^4} \tag{7}$$

where a is the side of each polygon.

Table 1 shows the mapping function coefficient and Table 2 shows different values of ψ_1 and ψ_2 for different polygons.

Free Nonlinear Vibrations. Rejecting the loading term, considering the value of A and putting $W_0(t)=B\tau(t)$ the cubic equation for W_0 takes the following form

$$\frac{d^2\tau}{dt^2}+K_1\tau+K_2\left(\frac{B}{h}\right)^2\tau^3=0 \tag{8}$$

The initial conditions are $\tau(0)=1$, $\dot{\tau}(0)=0$.

The solution of the preceding is well known and is obtained in terms of Jacobi's elliptic function. The ratio of the linear and nonlinear time periods is given by

$$\frac{T^*}{T}=\frac{\frac{2K}{\Pi}}{\left[1+\frac{K_2}{K_1}\left(\frac{B}{h}\right)^2\right]^{1/2}}$$

where K is the complete elliptic integral of first kind. Table 3 shows different values of T^*/T of different polygons for different values of B/h.

Discussions

(1) The Tables show that the new approach given in [1] can be extended to study the dynamic behavior of different regular polygonal plates and the results obtained are sufficiently accurate both for movable and immovable edge conditions.

(2) The results for both movable and immovable edge conditions have been obtained from the same cubic equation. This is an additional advantage.

References

1 Banerjee, B., and Dutta, S., "A New Approach to an Analysis of Large Deflections of Elastic Plates," *International Journal of Non-linear Mechanics*, Vol. 16, No. 1, 1981, pp. 47-52.

2 Bauer, B. F., "Non-linear Response of Elastic Plates to Pulse Excitations," ASME JOURNAL OF APPLIED MECHANICS, 1968, pp. 47-52.

3 Banerjee, B., and Dutta, S., "Large Deflections of Polygonal Plates by the Method of Conformal Transformation," *Mechanics Research Communication*, Vol. 8, No. 6, 1981.

4 Timoshenko, S., and Woinowksy-Krieger, S., *Theory of Plates and Shells*, McGraw-Hill, New York, 1962.

On Transverse Membrane Vibration of Conical Shells

C. H. Chang[1]

Because of mathematical difficulty, the vibrations of conical shells have been approached by approximate numerical methods [1]. Exact solutions are available only for two simple cases of axisymmetrical membrane vibrations in meridional [2, 3] and circumferential directions [4, 5]. One may wonder whether an exact solution for the simple case of axisymmetrical membrane vibration in the normal direction is possible. The present note addresses this question.

It is found that a theoretically exact solution may be formulated. The solution, however, containing hypergeometric functions, and undue effort would be involved to obtain numerical results.

Formulation

The three equations of motion expressed in terms of membrane stresses for axisymmetrical transverse membrane vibration of a conical shell are [6]

$$\begin{aligned}(s\bar{N}_s)_{,s}-\bar{N}_\theta&=0\\(s\bar{N}_{s\theta})_{,s}+\bar{N}_{s\theta}&=0\\\bar{N}_\theta\cot\alpha&=-s\rho h\ddot{\bar{w}}\end{aligned}\qquad(1a\text{-}c)$$

where $\bar{N}_s$ and $\bar{N}_\theta$ are membrane normal stresses in s (meridional) and θ (circumferential) directions, respectively, and $\bar{N}_{s\theta}$ is shearing stress, ρ is the mass density, h is the shell thickness, $\bar{w}$ is the displacement in the direction normal to the shell surface, α is the semivertex angle of the cone, and t is time. A comma followed by a subscript indicates derivative with respect to that subscript.

The solution to equation (1b) is

$$\bar{N}_{s\theta}=c/s^2 \tag{2}$$

where c is a constant. Because $\bar{N}_{s\theta}$ is not involved in other two equations, it may be dropped from further discussion.

Let

$$\begin{aligned}\bar{N}_s&=Eh\,N_s(\eta)\exp(iqt)\\\bar{N}_\theta&=Eh\,N_\theta(\eta)\exp(iqt)\end{aligned}\qquad(3a,b)$$

$$\begin{aligned}\bar{w}&=h\,w(\eta)\exp(iqt)\\\bar{v}&=h\,v(\eta)\exp(iqt)\end{aligned}\qquad(4a,b)$$

where E is the modulus of elasticity, q is the circular frequency, $\eta=s/L$, L is the distance measured from the apex to the larger end of the cone, and $\bar{v}$ is the displacement in the s-direction.

Introducing $k^2=h/L$ and $\tau^2=\rho L^2q^2/E$ $\qquad(5a,b)$

equations (1a,c) becomes, respectively,

$$\begin{aligned}(\eta N_s)_{,\eta}-N_\theta&=0\\N_\theta&=k^2\tau^2\eta w\tan\alpha\end{aligned}\qquad(6a,b)$$

The stress-displacement relations [6], by use of the Hooke's law, are

$$\begin{aligned}N_s&=\frac{k^2}{1-\nu^2}\left[v_{,\eta}+\frac{\nu}{\eta}(v+w\cot\alpha)\right]\\N_\theta&=\frac{k^2}{1-\nu^2}\left[\frac{1}{\eta}(v+w\cot\alpha)+\nu v_{,\eta}\right]\end{aligned}\qquad(7a,b)$$

[1]Professor of Engineering Mechanics, The University of Alabama, University, Ala. 35486. Mem. ASME.

Manuscript received by ASME Applied Mechanics Division, June, 1983; final revision, October, 1983.

Downloaded 02 May 2010 to 171.66.16.25. Redistribution subject to ASME license or copyright; see http://www.asme.org/terms/Terms_Use.cfm

where $W_0(t)$ is a function of time. Clearly W is θ-dependent and satisfies the clamped edge boundary conditions. Substituting (4) and (5) in (2) the error function $\epsilon(\xi,\bar{\xi},t)$ is obtained. Galerkin's procedure requires that

$$\int_{\theta=0}^{2\pi}\int_{r=0}^{1}\epsilon(\xi,\bar{\xi},t)W(\xi,\bar{\xi},t)r\,dr\,d\theta=0 \tag{6}$$

After evaluating the integrals one gets the cubic equation determining $W_0(t)$.

The constant A is determined by integrating (3) over the area of the unit circle. The in-plane displacements u and v have been eliminated by choosing suitable expressions for u and v and integrating over the area of the plate.

Numerical Results

Nonlinear Static Case. Rejecting the inertia term in the cubic equation for $W_0(t)$ and considering the value of A one gets the following equation determining the central deflection W_0.

$$\frac{W_0}{h}+\psi_1\left(\frac{W_0}{h}\right)^3=\frac{\psi_2 qa^4}{Eh^4} \tag{7}$$

where a is the side of each polygon.

Table 1 shows the mapping function coefficient and Table 2 shows different values of ψ_1 and ψ_2 for different polygons.

Free Nonlinear Vibrations. Rejecting the loading term, considering the value of A and putting $W_0(t)=B\tau(t)$ the cubic equation for W_0 takes the following form

$$\frac{d^2\tau}{dt^2}+K_1\tau+K_2\left(\frac{B}{h}\right)^2\tau^3=0 \tag{8}$$

The initial conditions are $\tau(0)=1$, $\dot{\tau}(0)=0$.

The solution of the preceding is well known and is obtained in terms of Jacobi's elliptic function. The ratio of the linear and nonlinear time periods is given by

$$\frac{T^*}{T}=\frac{\frac{2K}{\Pi}}{\left[1+\frac{K_2}{K_1}\left(\frac{B}{h}\right)^2\right]^{1/2}}$$

where K is the complete elliptic integral of first kind. Table 3 shows different values of T^*/T of different polygons for different values of B/h.

Discussions

(1) The Tables show that the new approach given in [1] can be extended to study the dynamic behavior of different regular polygonal plates and the results obtained are sufficiently accurate both for movable and immovable edge conditions.

(2) The results for both movable and immovable edge conditions have been obtained from the same cubic equation. This is an additional advantage.

References

1 Banerjee, B., and Dutta, S., "A New Approach to an Analysis of Large Deflections of Elastic Plates," *International Journal of Non-linear Mechanics*, Vol. 16, No. 1, 1981, pp. 47-52.

2 Bauer, B. F., "Non-linear Response of Elastic Plates to Pulse Excitations," ASME JOURNAL OF APPLIED MECHANICS, 1968, pp. 47-52.

3 Banerjee, B., and Dutta, S., "Large Deflections of Polygonal Plates by the Method of Conformal Transformation," *Mechanics Research Communication*, Vol. 8, No. 6, 1981.

4 Timoshenko, S., and Woinowksy-Krieger, S., *Theory of Plates and Shells*, McGraw-Hill, New York, 1962.

On Transverse Membrane Vibration of Conical Shells

C. H. Chang[1]

Because of mathematical difficulty, the vibrations of conical shells have been approached by approximate numerical methods [1]. Exact solutions are available only for two simple cases of axisymmetrical membrane vibrations in meridional [2, 3] and circumferential directions [4, 5]. One may wonder whether an exact solution for the simple case of axisymmetrical membrane vibration in the normal direction is possible. The present note addresses this question.

It is found that a theoretically exact solution may be formulated. The solution, however, containing hypergeometric functions, and undue effort would be involved to obtain numerical results.

Formulation

The three equations of motion expressed in terms of membrane stresses for axisymmetrical transverse membrane vibration of a conical shell are [6]

$$\begin{aligned}(s\bar{N}_s)_{,s}-\bar{N}_\theta&=0\\(s\bar{N}_{s\theta})_{,s}+\bar{N}_{s\theta}&=0\\\bar{N}_\theta\cot\alpha&=-s\rho h\ddot{\bar{w}}\end{aligned}\qquad(1a\text{-}c)$$

where $\bar{N}_s$ and $\bar{N}_\theta$ are membrane normal stresses in s (meridional) and θ (circumferential) directions, respectively, and $\bar{N}_{s\theta}$ is shearing stress, ρ is the mass density, h is the shell thickness, $\bar{w}$ is the displacement in the direction normal to the shell surface, α is the semivertex angle of the cone, and t is time. A comma followed by a subscript indicates derivative with respect to that subscript.

The solution to equation (1b) is

$$\bar{N}_{s\theta}=c/s^2 \tag{2}$$

where c is a constant. Because $\bar{N}_{s\theta}$ is not involved in other two equations, it may be dropped from further discussion.

Let

$$\begin{aligned}\bar{N}_s&=Eh\,N_s(\eta)\exp(iqt)\\\bar{N}_\theta&=Eh\,N_\theta(\eta)\exp(iqt)\end{aligned}\qquad(3a,b)$$

$$\begin{aligned}\bar{w}&=h\,w(\eta)\exp(iqt)\\\bar{v}&=h\,v(\eta)\exp(iqt)\end{aligned}\qquad(4a,b)$$

where E is the modulus of elasticity, q is the circular frequency, $\eta=s/L$, L is the distance measured from the apex to the larger end of the cone, and $\bar{v}$ is the displacement in the s-direction.

Introducing $k^2=h/L$ and $\tau^2=\rho L^2q^2/E$ $\qquad(5a,b)$

equations (1a,c) becomes, respectively,

$$\begin{aligned}(\eta N_s)_{,\eta}-N_\theta&=0\\N_\theta&=k^2\tau^2\eta w\tan\alpha\end{aligned}\qquad(6a,b)$$

The stress-displacement relations [6], by use of the Hooke's law, are

$$\begin{aligned}N_s&=\frac{k^2}{1-\nu^2}\left[v_{,\eta}+\frac{\nu}{\eta}(v+w\cot\alpha)\right]\\N_\theta&=\frac{k^2}{1-\nu^2}\left[\frac{1}{\eta}(v+w\cot\alpha)+\nu v_{,\eta}\right]\end{aligned}\qquad(7a,b)$$

[1]Professor of Engineering Mechanics, The University of Alabama, University, Ala. 35486. Mem. ASME.

Manuscript received by ASME Applied Mechanics Division, June, 1983; final revision, October, 1983.

Copyright © 1984 by ASME
Downloaded 02 May 2010 to 171.66.16.25. Redistribution subject to ASME license or copyright; see http://www.asme.org/terms/Terms_Use.cfm

Solving for v from the preceding four equations results in

$$v=\tau^2\tan\alpha[\eta^2 w-\nu\int\eta w d\eta]-w\cot\alpha \tag{8}$$

Then through a lengthy manipulation of equations (6)–(8), the following equation for w is obtained:

$$\tau^2\tan^2\alpha(\eta^2 w_{,\eta\eta}+5\eta^2 w_{,\eta}+3\eta w)-\eta w_{,\eta\eta}-w_{,\eta}=0 \tag{9}$$

Solution

Letting $x=\tau^2\tan^2\eta^2$ (10)

equation (9) becomes

$$x(x-1)w''+(3x-1)w'+\frac{3}{4}w=0 \tag{11}$$

where a prime indicates derivative with respect to x.

Equation (11) is in the form of the Gauss hypergeometric equation [7, 8]:

$$x(x-1)w''-[\gamma-(\alpha+\beta+1)x]+\alpha\beta w=0 \tag{12}$$

whose first solution is

$$w_1(x)=1+\sum_{n=1}^{\infty}\frac{\Gamma(\alpha+\eta)\Gamma(\beta+1)\Gamma(\gamma)}{\Gamma(\alpha)\Gamma(\beta)(\alpha+\eta)}\frac{x^2}{\eta!}=1+F(\alpha,\beta,\gamma,x) \tag{13}$$

For the present case:

$$\alpha=\frac{1}{2},\ \beta=\frac{3}{2}\ \text{and}\ \gamma=1 \tag{14}$$

No confusion should arise between the semiapex angle α, and the present constant α. Since $\gamma=1$, the other solution is in logarithmic form:

$$w_2(x)=F(\alpha,\beta,1,x)\ln x+\frac{1}{\Gamma(\alpha)\Gamma(\beta)}\sum_{n=1}^{\infty}\frac{\Gamma(\alpha+n)\Gamma(\beta+n)}{(n!)^2}x^n[\psi(\alpha+n)-\psi(\alpha)+\psi(\beta+n)-\psi(\beta)-2\psi(n+1)+2\psi(1)] \tag{15}$$

where $\psi(k)=\Gamma'(k)/\Gamma(k)$ (16)

The general solution is

$$w(x)=Aw_1(x)+Bw_2(x) \tag{17}$$

where A and B are constants. The solution has one boundary condition at each end: For a fixed end $w=0$ and for a free end $N_s=0$ at $x=\tau^2\tan^2\alpha$ for the larger end, and $x=\tau^2\tan^2\alpha(L_1/L)^2$ at the smaller end, where L_1 is the length measured from the apex to the smaller end.

Equation (9) may be converted to the Sturm-Liousville type

$$[\eta(1-\lambda\eta^2)^2 w_{,\eta}]_{,\eta}-(1-\lambda\eta^2)3\lambda\eta w=0 \tag{18}$$

where

$$\lambda=\tau^2\tan^2\alpha \tag{19}$$

In turn equation (18) or equation (9) may be obtained from the vanishing of the variation of a functional such as

$$\delta\int[\eta(1-\lambda\eta^2)^2 w'^2+(1-\lambda\eta^2)3\lambda\eta w^2]d\eta=0 \tag{20}$$

which may be used for approximate eigenvalues λ, by assuming a geometrically acceptable function of w if so desired.

Neither tabulated values nor programmed subroutines of equations (13) and (15) are available. Thus, even for the present most simple case of the transverse vibrations of a conical shell, exact numerical results are almost impossible to obtain. Furthermore the hypergeometric series converges only for $|x|=|\tau^2\tan^2\alpha\,\eta^2|<1$. Therefore, the solution to equation (17) could only be used for a few basic frequencies, if the difficulty involved could be overcome. Thus, the approximate numerical methods would prevail for the transverse vibrations of conical shells.

References

1 Chang, C. H., "Vibration of Conical Shells," *The Shock and Vibration Digest*, Vol. 13, No. 6, June 1981, pp. 9–17.

2 Keefle, R. E., "Natural Frequencies of Meridional Vibration in Thin Conical Shelis," *AIAA J.*, Vol. 2, No. 10, 1964, pp. 1825–1927.

3 Chang, C. H., "Membrane Vibrations of Conical Shells," *Journal of Sound and Vibration*, Vol. 60, No. 3, Oct. 1978, pp. 331–343.

4 Garnet, H., Goldberg, M. A., and Salerno, V. L., "Torsional Vibrations of Shells of Revolution," ASME JOURNAL OF APPLIED MECHANICS, Vol. 28, No. 4, 1961, pp. 511–573.

5 Chang, C. H., "Axisymmetrical Torsional Vibration of Conical Shells," ASME JOURNAL OF APPLIED MECHANICS, Vol. 46, No. 3, 1979, pp. 699–701.

6 Flugge, W., *Stresses in Shells*, 3rd printing, Springer-Verlag, 1966, Chapter 6.

7 Rainville, E. D., *Intermediate Differential Equations*, Wiley, 1957, Chapter 6.

8 Abramowitz, M., and Stegun, I. A., *Handbook of Mathematical Functions*, Dover, 1965.

Plane Thermostatic Problems for Inhomogeneous Anisotropic Materials

D. L. Clements[1] and D. L. Hill[1]

Introduction

Referred to Cartesian coordinates x_1, x_2, and x_3 the equation governing the static plane temperature field $T(x_1, x_2)$ in an anisotropic inhomogeneous material may be written in the form (see Carslaw and Jaeger [1])

$$\frac{\partial}{\partial x_i}\left[\lambda_{ij}\frac{\partial T}{\partial x_j}\right]=0, \tag{1}$$

where $\lambda_{ij}=\lambda_{ji}$ are the coefficients of heat conduction and the repeated suffix summation convection (summing from 1 to 2) has been used. In the case of a homogeneous material with the λ_{ij} constants this equation admits the general solution (see Clements [2])

$$T(x_1,x_2)=\chi(z)+\bar{\chi}(\bar{z}) \tag{2}$$

where χ is an arbitrary analytic function, $z=x_1+cx_2$, where τ is the root with positive imaginary part of the quadratic equation

$$\lambda_{11}+2\lambda_{12}\tau+\lambda_{22}\tau^2=0. \tag{3}$$

The general solution (2) may be effectively used to solve a large number of thermostatic boundary value problems for homogeneous materials (see Clements [2]). Hence it is reasonable to enquire as to whether the governing equation for the static temperature field in an inhomogeneous anisotropic material admits a simple general solution which is similar to (1.2). In this Note it is shown that in the inhomogeneous case the governing equation does have a simple general solution provided the coefficients of heat conduction adopt certain multiparametric forms. As in the homogeneous case, this general solution may be used to solve a number of boundary value problems and as an example a particular problem is solved for an inhomogeneous halfspace.

A Matrix Form for the Basic Equation

The λ_{ij} will be assumed to depend only on the Cartesian coordinate x_2 and hence equation (1) may be written in the form

$$\frac{\lambda_{11}}{\lambda_{22}}\frac{\partial^2 T}{\partial x_1^2}+\frac{2\lambda_{12}}{\lambda_{22}}\frac{\partial^2 T}{\partial x_1\partial x_2}+\frac{\partial^2 T}{\partial x_2^2}+\frac{\lambda_{22}'}{\lambda_{22}}\frac{\partial T}{\partial x_2}+\frac{\lambda_{12}'}{\lambda_{22}}\frac{\partial T}{\partial x_1}=0, \tag{4}$$

[1]Department of Applied Mathematics, University of Adelaide, Australia.
Manuscript received by ASME Applied Mechanics Division, February, 1983.

Downloaded 02 May 2010 to 171.66.16.25. Redistribution subject to ASME license or copyright; see http://www.asme.org/terms/Terms_Use.cfm

Solving for v from the preceding four equations results in

$$v=\tau^2\tan\alpha[\eta^2 w-\nu\int\eta w d\eta]-w\cot\alpha \tag{8}$$

Then through a lengthy manipulation of equations (6)–(8), the following equation for w is obtained:

$$\tau^2\tan^2\alpha(\eta^2 w_{,\eta\eta}+5\eta^2 w_{,\eta}+3\eta w)-\eta w_{,\eta\eta}-w_{,\eta}=0 \tag{9}$$

Solution

Letting $x=\tau^2\tan^2\eta^2$ (10)

equation (9) becomes

$$x(x-1)w''+(3x-1)w'+\frac{3}{4}w=0 \tag{11}$$

where a prime indicates derivative with respect to x.

Equation (11) is in the form of the Gauss hypergeometric equation [7, 8]:

$$x(x-1)w''-[\gamma-(\alpha+\beta+1)x]+\alpha\beta w=0 \tag{12}$$

whose first solution is

$$w_1(x)=1+\sum_{n=1}^{\infty}\frac{\Gamma(\alpha+\eta)\Gamma(\beta+1)\Gamma(\gamma)}{\Gamma(\alpha)\Gamma(\beta)(\alpha+\eta)}\frac{x^2}{\eta!}=1+F(\alpha,\beta,\gamma,x) \tag{13}$$

For the present case:

$$\alpha=\frac{1}{2},\ \beta=\frac{3}{2}\ \text{and}\ \gamma=1 \tag{14}$$

No confusion should arise between the semiapex angle α, and the present constant α. Since $\gamma=1$, the other solution is in logarithmic form:

$$w_2(x)=F(\alpha,\beta,1,x)\ln x+\frac{1}{\Gamma(\alpha)\Gamma(\beta)}\sum_{n=1}^{\infty}\frac{\Gamma(\alpha+n)\Gamma(\beta+n)}{(n!)^2}x^n[\psi(\alpha+n)-\psi(\alpha)+\psi(\beta+n)-\psi(\beta)-2\psi(n+1)+2\psi(1)] \tag{15}$$

where $\psi(k)=\Gamma'(k)/\Gamma(k)$ (16)

The general solution is

$$w(x)=Aw_1(x)+Bw_2(x) \tag{17}$$

where A and B are constants. The solution has one boundary condition at each end: For a fixed end $w=0$ and for a free end $N_s=0$ at $x=\tau^2\tan^2\alpha$ for the larger end, and $x=\tau^2\tan^2\alpha(L_1/L)^2$ at the smaller end, where L_1 is the length measured from the apex to the smaller end.

Equation (9) may be converted to the Sturm-Liousville type

$$[\eta(1-\lambda\eta^2)^2 w_{,\eta}]_{,\eta}-(1-\lambda\eta^2)3\lambda\eta w=0 \tag{18}$$

where

$$\lambda=\tau^2\tan^2\alpha \tag{19}$$

In turn equation (18) or equation (9) may be obtained from the vanishing of the variation of a functional such as

$$\delta\int[\eta(1-\lambda\eta^2)^2 w'^2+(1-\lambda\eta^2)3\lambda\eta w^2]d\eta=0 \tag{20}$$

which may be used for approximate eigenvalues λ, by assuming a geometrically acceptable function of w if so desired.

Neither tabulated values nor programmed subroutines of equations (13) and (15) are available. Thus, even for the present most simple case of the transverse vibrations of a conical shell, exact numerical results are almost impossible to obtain. Furthermore the hypergeometric series converges only for $|x|=|\tau^2\tan^2\alpha\,\eta^2|<1$. Therefore, the solution to equation (17) could only be used for a few basic frequencies, if the difficulty involved could be overcome. Thus, the approximate numerical methods would prevail for the transverse vibrations of conical shells.

References

1 Chang, C. H., "Vibration of Conical Shells," *The Shock and Vibration Digest*, Vol. 13, No. 6, June 1981, pp. 9–17.

2 Keefle, R. E., "Natural Frequencies of Meridional Vibration in Thin Conical Shelis," *AIAA J.*, Vol. 2, No. 10, 1964, pp. 1825–1927.

3 Chang, C. H., "Membrane Vibrations of Conical Shells," *Journal of Sound and Vibration*, Vol. 60, No. 3, Oct. 1978, pp. 331–343.

4 Garnet, H., Goldberg, M. A., and Salerno, V. L., "Torsional Vibrations of Shells of Revolution," ASME JOURNAL OF APPLIED MECHANICS, Vol. 28, No. 4, 1961, pp. 511–573.

5 Chang, C. H., "Axisymmetrical Torsional Vibration of Conical Shells," ASME JOURNAL OF APPLIED MECHANICS, Vol. 46, No. 3, 1979, pp. 699–701.

6 Flugge, W., *Stresses in Shells*, 3rd printing, Springer-Verlag, 1966, Chapter 6.

7 Rainville, E. D., *Intermediate Differential Equations*, Wiley, 1957, Chapter 6.

8 Abramowitz, M., and Stegun, I. A., *Handbook of Mathematical Functions*, Dover, 1965.

Plane Thermostatic Problems for Inhomogeneous Anisotropic Materials

D. L. Clements[1] and D. L. Hill[1]

Introduction

Referred to Cartesian coordinates x_1, x_2, and x_3 the equation governing the static plane temperature field $T(x_1, x_2)$ in an anisotropic inhomogeneous material may be written in the form (see Carslaw and Jaeger [1])

$$\frac{\partial}{\partial x_i}\left[\lambda_{ij}\frac{\partial T}{\partial x_j}\right]=0, \tag{1}$$

where $\lambda_{ij}=\lambda_{ji}$ are the coefficients of heat conduction and the repeated suffix summation convection (summing from 1 to 2) has been used. In the case of a homogeneous material with the λ_{ij} constants this equation admits the general solution (see Clements [2])

$$T(x_1,x_2)=\chi(z)+\bar{\chi}(\bar{z}) \tag{2}$$

where χ is an arbitrary analytic function, $z=x_1+cx_2$, where τ is the root with positive imaginary part of the quadratic equation

$$\lambda_{11}+2\lambda_{12}\tau+\lambda_{22}\tau^2=0. \tag{3}$$

The general solution (2) may be effectively used to solve a large number of thermostatic boundary value problems for homogeneous materials (see Clements [2]). Hence it is reasonable to enquire as to whether the governing equation for the static temperature field in an inhomogeneous anisotropic material admits a simple general solution which is similar to (1.2). In this Note it is shown that in the inhomogeneous case the governing equation does have a simple general solution provided the coefficients of heat conduction adopt certain multiparametric forms. As in the homogeneous case, this general solution may be used to solve a number of boundary value problems and as an example a particular problem is solved for an inhomogeneous halfspace.

A Matrix Form for the Basic Equation

The λ_{ij} will be assumed to depend only on the Cartesian coordinate x_2 and hence equation (1) may be written in the form

$$\frac{\lambda_{11}}{\lambda_{22}}\frac{\partial^2 T}{\partial x_1^2}+\frac{2\lambda_{12}}{\lambda_{22}}\frac{\partial^2 T}{\partial x_1\partial x_2}+\frac{\partial^2 T}{\partial x_2^2}+\frac{\lambda_{22}'}{\lambda_{22}}\frac{\partial T}{\partial x_2}+\frac{\lambda_{12}'}{\lambda_{22}}\frac{\partial T}{\partial x_1}=0, \tag{4}$$

[1]Department of Applied Mathematics, University of Adelaide, Australia.
Manuscript received by ASME Applied Mechanics Division, February, 1983.

Copyright © 1984 by ASME
Downloaded 02 May 2010 to 171.66.16.25. Redistribution subject to ASME license or copyright; see http://www.asme.org/terms/Terms_Use.cfm

where primes denote differentiation with respect to x_2. For the present purposes it is advantageous to consider the more general equation

$$\frac{\lambda_{11}}{\lambda_{22}}\frac{\partial^2 T}{\partial x_1^2}+\frac{2\lambda_{12}}{\lambda_{22}}\frac{\partial^2 T}{\partial x_1 \partial x_2}+\frac{\partial^2 T}{\partial x_2^2}+\frac{\lambda_{22}'}{\lambda_{22}}\frac{\partial T}{\partial x_2}+\frac{\lambda_{12}'}{\lambda_{22}}\frac{\partial T}{\partial x_1}+\lambda T=0 \tag{5}$$

so that (4) may be obtained from (5) by setting $\lambda=0$. It is now convenient to introudce a new function $U(x_1, x_2)$ so that equation (5) emerges as a consequence of the matrix system

$$\Omega_{x_2}=M\Omega_{x_1}+N\Omega \tag{6}$$

where the subscripts denote partial derivatives with respect to the variable in question and

$$\Omega=\begin{pmatrix}T\\U\end{pmatrix},\quad M=\begin{pmatrix}m_{11} & m_{12}\\ m_{21} & 0\end{pmatrix},\quad N=\begin{pmatrix}n_{11} & 0\\ 0 & 0\end{pmatrix}, \tag{7}$$

with the entries in the matrices M and N being functions of x_2 which are related to the λ_{ij} by the equations

$$m_{11}=-2\lambda_{12}/\lambda_{22}, \tag{8}$$

$$\frac{m_{12}'}{m_{12}}+n_{11}=-\lambda_{22}'/\lambda_{22}, \tag{9}$$

$$m_{12}\frac{d}{dx_2}\left(\frac{m_{11}}{m_{12}}\right)=-\lambda_{12}'/\lambda_{22}, \tag{10}$$

$$m_{12}\frac{d}{dx_2}\left(\frac{n_{11}}{m_{12}}\right)=\lambda, \tag{11}$$

$$m_{12}m_{21}=-\lambda_{11}/\lambda_{22}. \tag{12}$$

Now equation (9) yields, upon integration,

$$m_{12}=\Phi/\lambda_{22}, \tag{13}$$

where

$$\Phi=\exp[-\int n_{11}dx_2]$$

or

$$n_{11}=-\frac{1}{\Phi}\frac{d\Phi}{dx_2} \tag{14}$$

so (11) yields

$$\frac{\Phi}{\lambda_{22}}\frac{d}{dx_2}\left[\frac{\lambda_{22}}{\Phi^2}\frac{d\Phi}{dx_2}\right]=\lambda. \tag{15}$$

Now (12) and (13) provide

$$m_{21}=-\lambda_{11}/\Phi. \tag{16}$$

Also use of (8) and (13) in (10) yields

$$\alpha\Phi^2=\lambda_{12} \tag{17}$$

where α is an arbitrary constant.

General Solution of the Basic Equation

In this section solutions of the governing equation (1) are sought for some particular multiparameter variations in the λ_{ij}. The new variables

$$T^*=\Phi T,\quad U^*=U \tag{18),(19}$$

reduce the system (6) to the form (using (8), (13), and (16))

$$\begin{pmatrix}T^*\\U^*\end{pmatrix}_{x_2}=\begin{pmatrix}-\dfrac{2\lambda_{12}}{\lambda_{22}} & \Phi^2/\lambda_{22}\\ -\lambda_{11}/\Phi^2 & 0\end{pmatrix}\begin{pmatrix}T^*\\U^*\end{pmatrix}_{x_1} \tag{20}$$

The change in independent variables

$$y=\int_0^{x_2}k(s)ds,\quad x=x_1 \tag{21),(22}$$

with $k(x_2)$ arbitrary now yields

$$\begin{pmatrix}T^*\\U^*\end{pmatrix}_y=\begin{pmatrix}\dfrac{-2\lambda_{12}}{k\lambda_{22}} & \dfrac{\Phi^2}{k\lambda_{22}}\\ \dfrac{-\lambda_{11}}{k\Phi^2} & 0\end{pmatrix}\begin{pmatrix}T^*\\U^*\end{pmatrix}_x \tag{23}$$

Now if the entries in the 2×2 matrix in (23) are constants then this system yields a simple general solution of the type (2). Hence, through (18) and (21) it will be possible to find a general analytical solution to (5) or (4). In particular, if solutions to (4) are required then $\lambda=0$ so (17) and (15) provide

$$\lambda_{12}=\alpha\Phi^2, \tag{24}$$

$$\lambda_{22}=\frac{K\Phi^2}{\Phi'} \tag{25}$$

where K is an arbitrary constant. Now if the entry $2\lambda_{12}/\lambda_{22}$ in the 2×2 matrix in (23) is to be constant then it is necessary that

$$\alpha\Phi^2/[K\Phi^2/\Phi']k(x_2)=G\quad\text{(constant)}$$

so that

$$\Phi'=\frac{d\Phi}{dx_2}=Ck(x_2)\quad(C=\alpha^{-1}KG) \tag{26}$$

and hence, using (21)

$$\Phi=Cy+D \tag{27}$$

where D is a constant. Hence, from (24) and (25)

$$\lambda_{12}=\alpha(Cy+D)^2,\quad \lambda_{22}=\frac{K(Cy+D)^2}{Ck(x_2)} \tag{28),(29}$$

where α, K, C, and D are constants. Now if the entries in the 2×2 matrix in (23) are to be constants then in addition to (28) and (29) it is necessary that

$$\lambda_{11}=\beta k(x_2)(Cy+D)^2 \tag{30}$$

where β is a constant. With (28)–(30) the system (23) now yields

$$\begin{pmatrix}T^*\\U^*\end{pmatrix}_y=\begin{pmatrix}-\dfrac{2\alpha C}{K} & \dfrac{C}{K}\\ -\beta & 0\end{pmatrix}\begin{pmatrix}T^*\\U^*\end{pmatrix}_x \tag{31}$$

Elimination of U^* from (31) provides

$$K\frac{\partial^2 T^*}{\partial y^2}+2\alpha C\frac{\partial^2 T^*}{\partial x\partial y}+C\beta\frac{\partial^2 T^*}{\partial x^2}=0. \tag{32}$$

This equation has the general solution

$$T^*=\Re\psi(z), \tag{33}$$

where ψ is an arbitrary analytic function, $\Re$ denotes the real part of a complex number, and

$$z=x+py, \tag{34}$$

where

Downloaded 02 May 2010 to 171.66.16.25. Redistribution subject to ASME license or copyright; see http://www.asme.org/terms/Terms_Use.cfm

$$p = -\frac{\alpha C}{K} \pm \frac{i}{K}(KC\beta - \alpha^2 C^2)^{1/2}. \tag{35}$$

Note that in (35) the ellipticity condition $\lambda_{11}\lambda_{22} > \lambda_{12}^2$ ensures that $KC\beta - \alpha^2 C^2 > 0$.

Hence from (33), (18), and (27) it follows that if λ_{12}, λ_{11} and λ_{22} are given by (28)–(30) then the solution to (4) may be written in the form

$$T = (Cy + D)^{-1}\Re[\psi(z)] \tag{36}$$

where ψ is an arbitrary analytic function, $z = x + py$, with x, y, and p defined, respectively, by (22), (21), and (35).

A Specific Boundary Value Problem

Complex function theory may be used in conjunction with the solution (36) to provide the solution to a number of thermostatic boundary value problems for inhomogeneous materials. As an illustration a particular boundary value problem will be examined in this section.

Consider the anisotropic half space occupying the region $x_2 > 0$ and let the temperature distribution on the boundary $x_2 = 0$ of the half space be given by

$$T(x_1, 0) = \begin{cases} T_0(x_1) & \text{for} \quad |x_1| < a \\ 0 & \text{for} \quad |x_1| > a \end{cases} \tag{37}$$

where $T_0(x_1)$ is a given function of x_1. Suppose further that the half space is inhomogeneous and is of a form that, for suitable values of the constants, the coefficients λ_{11}, λ_{12}, and λ_{22} are given by (28)–(30). It is required to find the temperature throughout the half space.

The temperature in the half space may be represented by the form (36) with the analytic function $\psi(z)$ satisfying the boundary condition

$$D^{-1}\Re[\psi(x)] = \begin{cases} T_0(x) & \text{for} \quad |x_1| < a \\ 0 & \text{for} \quad |x_1| > a \end{cases} \tag{38}$$

Thus it is required to find function $\psi(z)$ which is analytic in the upper half space $x_2 > 0$, vanishes at infinity and satisfies the boundary condition (38). This is a standard problem (see for example Clements [2]) and the solution is

$$\psi(z) = \frac{1}{2\pi i}\int_{-a}^{a} \frac{DT_0(t)}{t - z}. \tag{39}$$

Hence, from (36), the temperature in the half space is given by

$$T = (Cy + D)^{-1}\Re\left\{\frac{1}{2\pi i}\int_{-a}^{a} \frac{DT_0(t)}{t - z}\right\}. \tag{40}$$

In the particular case when $T_0(t) = t_0$ (constant) equation (40) provides

$$T = (Cy + D)^{-1} Dt_0 \Re\left\{\frac{1}{2\pi i} ln\left[\frac{z - a}{z + a}\right]\right\}. \tag{41}$$

Consider now some particular cases for the function $k(x_2)$ occurring in (21)

(*i*) $k(x_2) = 1$. In this case $y = x_2$ and hence (40) and (28)–(30) yield

$$T = (Cx_2 + D)^{-1} Dt_0 \Re\left\{\frac{1}{2\pi i} ln\left[\frac{z - a}{z + a}\right]\right\} \tag{42}$$

with $z = x + py = x_1 + px_2$ and

$$\lambda_{12} = \alpha(Cx_2 + D)^2, \quad \lambda_{22} = KC^{-1}(Cx_2 + D)^2,$$
$$\lambda_{11} = \beta(Cx_2 + D)^2. \tag{43}$$

Thus if the conductivities λ_{ij} increase with x_2 as prescribed by (43) then the temperature as given by (42) decreases with x_2 more rapidly than would be the case with constant conductivities ($C = 0$).

(*ii*) $k(x_2) = ae^{bx_2}$ $(b > 0)$. Here $y = a/b(e^{bx_2} - 1)$ so that

$$T = (Cab^{-1}e^{bx_2} - Cab^{-1} + D)^{-1} Dt_0 \Re\left\{\frac{1}{2\pi i} ln\left[\frac{z - a}{z + a}\right]\right\}$$

with $z = x_1 + pab^{-1}(e^{bx_2} - 1)$ and

$$\lambda_{12} = \alpha[Cab^{-1}(e^{bx_2} - 1) + D]^2, \quad \lambda_{22} = K[Cab^{-1}(e^{bx_2} - 1) + D]^2/Cae^{bx_2},$$
$$\lambda_{11} = \beta ae^{bx_2}[Cab^{-1}(e^{bx_2} - 1) + D]^2.$$

(*iii*) $k(x_2) = a(1 + \cos bx_2)$. In this case $y = a(x_2 + b^{-1}\sin bx_2)$

$$T = [Ca(x_2 + b^{-1}\sin bx_2) + D]^{-1} Dt_0 \Re\left\{\frac{1}{2\pi i} ln\left[\frac{z - a}{z + a}\right]\right\}$$

with $z = x_1 + pa(x_2 + b^{-1}\sin bx_2)$ and

$$\lambda_{12} = \alpha[Ca(x_2 + b^{-1}\sin bx_2) + D]^2,$$
$$\lambda_{22} = K[Ca(x_2 + b^{-1}\sin bx_2) + D]^2/Ca(1 + \cos bx_2),$$
$$\lambda_{11} = \beta a(1 + \cos bx_2)[Ca(x_2 + b^{-1}\sin bx_2) + D]^2.$$

These three examples give some indication of the possible types of variations in the λ_{ij} for which an elementary general solution of (2.1) exists. In general the aim would be to choose a suitable multiparameter form for $k(x_2)$ so that the λ_{ij} could be fitted to given numerical values.

References

1 Carslaw, H. S., and Jaeger, J. C., *Conduction of Heat in Solids*, Clarendon Press, Oxford, 1959.

2 Clements, D. L., *Boundary Value Problems Governed by Second Order Elliptic Systems*, Pitman, London, 1981.

Effects of Geometric Imperfections on Large-Amplitude Vibrations of Rectangular Plates With Hysteresis Damping

David Hui[1]

The present paper deals with the effects of initial geometric imperfections on large-amplitude vibrations of simply supported rectangular plates. The vibration mode, the geometric imperfection, and the forcing function are taken to be of the same spatial shape. It is found that geometric imperfections of the order of a fraction of the plate thickness may significantly raise the free linear vibration frequencies. Furthermore, contrary to the commonly accepted theory that large-amplitude vibrations of plates are of the hardening type, the presence of small geometric imperfections may cause the plate to exhibit a soft-spring behavior. The effects of hysteresis (structural) damping on the vibration amplitude are also examined.

[1] Assistant Professor, Department of Engineering Mechanics, The Ohio State University, Columbus, Ohio 43210. Mem. ASME.

Manuscript received by ASME Applied Mechanics Division, September, 1982; final revision, July, 1983.

Downloaded 02 May 2010 to 171.66.16.25. Redistribution subject to ASME license or copyright; see http://www.asme.org/terms/Terms_Use.cfm

$$p = -\frac{\alpha C}{K} \pm \frac{i}{K}(KC\beta - \alpha^2 C^2)^{1/2}. \tag{35}$$

Note that in (35) the ellipticity condition $\lambda_{11}\lambda_{22} > \lambda_{12}^2$ ensures that $KC\beta - \alpha^2 C^2 > 0$.

Hence from (33), (18), and (27) it follows that if λ_{12}, λ_{11} and λ_{22} are given by (28)–(30) then the solution to (4) may be written in the form

$$T = (Cy + D)^{-1}\Re[\psi(z)] \tag{36}$$

where ψ is an arbitrary analytic function, $z = x + py$, with x, y, and p defined, respectively, by (22), (21), and (35).

A Specific Boundary Value Problem

Complex function theory may be used in conjunction with the solution (36) to provide the solution to a number of thermostatic boundary value problems for inhomogeneous materials. As an illustration a particular boundary value problem will be examined in this section.

Consider the anisotropic half space occupying the region $x_2 > 0$ and let the temperature distribution on the boundary $x_2 = 0$ of the half space be given by

$$T(x_1, 0) = \begin{cases} T_0(x_1) & \text{for} \quad |x_1| < a \\ 0 & \text{for} \quad |x_1| > a \end{cases} \tag{37}$$

where $T_0(x_1)$ is a given function of x_1. Suppose further that the half space is inhomogeneous and is of a form that, for suitable values of the constants, the coefficients λ_{11}, λ_{12}, and λ_{22} are given by (28)–(30). It is required to find the temperature throughout the half space.

The temperature in the half space may be represented by the form (36) with the analytic function $\psi(z)$ satisfying the boundary condition

$$D^{-1}\Re[\psi(x)] = \begin{cases} T_0(x) & \text{for} \quad |x_1| < a \\ 0 & \text{for} \quad |x_1| > a \end{cases} \tag{38}$$

Thus it is required to find function $\psi(z)$ which is analytic in the upper half space $x_2 > 0$, vanishes at infinity and satisfies the boundary condition (38). This is a standard problem (see for example Clements [2]) and the solution is

$$\psi(z) = \frac{1}{2\pi i}\int_{-a}^{a} \frac{DT_0(t)}{t - z}. \tag{39}$$

Hence, from (36), the temperature in the half space is given by

$$T = (Cy + D)^{-1}\Re\left\{\frac{1}{2\pi i}\int_{-a}^{a} \frac{DT_0(t)}{t - z}\right\}. \tag{40}$$

In the particular case when $T_0(t) = t_0$ (constant) equation (40) provides

$$T = (Cy + D)^{-1} Dt_0 \Re\left\{\frac{1}{2\pi i} \ln\left[\frac{z - a}{z + a}\right]\right\}. \tag{41}$$

Consider now some particular cases for the function $k(x_2)$ occurring in (21)

(*i*) $k(x_2) = 1$. In this case $y = x_2$ and hence (40) and (28)–(30) yield

$$T = (Cx_2 + D)^{-1} Dt_0 \Re\left\{\frac{1}{2\pi i} \ln\left[\frac{z - a}{z + a}\right]\right\} \tag{42}$$

with $z = x + py = x_1 + px_2$ and

$$\lambda_{12} = \alpha(Cx_2 + D)^2, \quad \lambda_{22} = KC^{-1}(Cx_2 + D)^2,$$
$$\lambda_{11} = \beta(Cx_2 + D)^2. \tag{43}$$

Thus if the conductivities λ_{ij} increase with x_2 as prescribed by (43) then the temperature as given by (42) decreases with x_2 more rapidly than would be the case with constant conductivities ($C = 0$).

(*ii*) $k(x_2) = ae^{bx_2}$ $(b > 0)$. Here $y = a/b(e^{bx_2} - 1)$ so that

$$T = (Cab^{-1}e^{bx_2} - Cab^{-1} + D)^{-1} Dt_0 \Re\left\{\frac{1}{2\pi i} \ln\left[\frac{z - a}{z + a}\right]\right\}$$

with $z = x_1 + pab^{-1}(e^{bx_2} - 1)$ and

$$\lambda_{12} = \alpha[Cab^{-1}(e^{bx_2} - 1) + D]^2, \quad \lambda_{22} = K[Cab^{-1}(e^{bx_2} - 1) + D]^2 / Cae^{bx_2},$$
$$\lambda_{11} = \beta ae^{bx_2}[Cab^{-1}(e^{bx_2} - 1) + D]^2.$$

(*iii*) $k(x_2) = a(1 + \cos bx_2)$. In this case $y = a(x_2 + b^{-1}\sin bx_2)$

$$T = [Ca(x_2 + b^{-1}\sin bx_2) + D]^{-1} Dt_0 \Re\left\{\frac{1}{2\pi i} \ln\left[\frac{z - a}{z + a}\right]\right\}$$

with $z = x_1 + pa(x_2 + b^{-1}\sin bx_2)$ and

$$\lambda_{12} = \alpha[Ca(x_2 + b^{-1}\sin bx_2) + D]^2,$$
$$\lambda_{22} = K[Ca(x_2 + b^{-1}\sin bx_2) + D]^2 / Ca(1 + \cos bx_2),$$
$$\lambda_{11} = \beta a(1 + \cos bx_2)[Ca(x_2 + b^{-1}\sin bx_2) + D]^2.$$

These three examples give some indication of the possible types of variations in the λ_{ij} for which an elementary general solution of (2.1) exists. In general the aim would be to choose a suitable multiparameter form for $k(x_2)$ so that the λ_{ij} could be fitted to given numerical values.

References

1 Carslaw, H. S., and Jaeger, J. C., *Conduction of Heat in Solids*, Clarendon Press, Oxford, 1959.

2 Clements, D. L., *Boundary Value Problems Governed by Second Order Elliptic Systems*, Pitman, London, 1981.

Effects of Geometric Imperfections on Large-Amplitude Vibrations of Rectangular Plates With Hysteresis Damping

David Hui[1]

The present paper deals with the effects of initial geometric imperfections on large-amplitude vibrations of simply supported rectangular plates. The vibration mode, the geometric imperfection, and the forcing function are taken to be of the same spatial shape. It is found that geometric imperfections of the order of a fraction of the plate thickness may significantly raise the free linear vibration frequencies. Furthermore, contrary to the commonly accepted theory that large-amplitude vibrations of plates are of the hardening type, the presence of small geometric imperfections may cause the plate to exhibit a soft-spring behavior. The effects of hysteresis (structural) damping on the vibration amplitude are also examined.

[1] Assistant Professor, Department of Engineering Mechanics, The Ohio State University, Columbus, Ohio 43210. Mem. ASME.

Manuscript received by ASME Applied Mechanics Division, September, 1982; final revision, July, 1983.

Copyright © 1984 by ASME
Downloaded 02 May 2010 to 171.66.16.25. Redistribution subject to ASME license or copyright; see http://www.asme.org/terms/Terms_Use.cfm

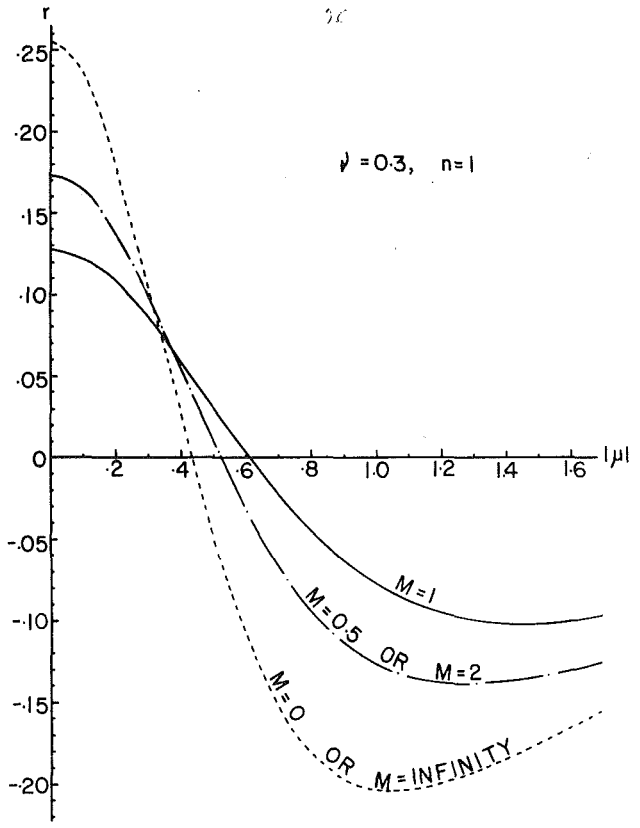

Fig. 1(*a*) Nonlinearity parameter versus imperfection amplitude for simply supported rectangular plates with $\nu = 0.3$ and $n = 1$

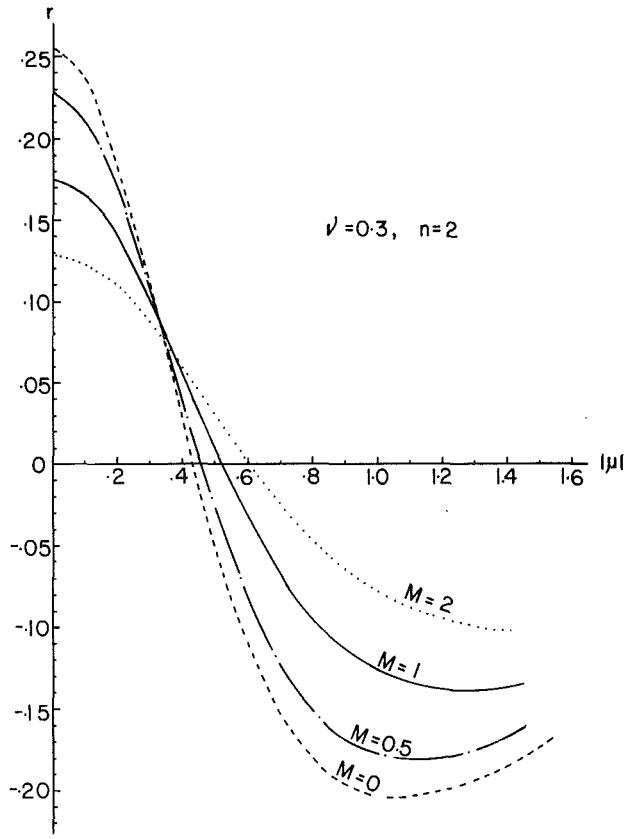

Fig. 1(*b*) Nonlinearity parameter versus imperfection amplitude for simply supported rectangular plates with $\nu = 0.3$ and $n = 2$

Fig. 1

1 Introduction

Large-amplitude vibration of isotropic homogeneous plates is an important subject which has been investigated by many authors in the past decades [1–4] and an excellent introduction to this topic can be found in a book by Chia [5]. Many other relevant papers are cited by the foregoing references. It was found that the large amplitude vibrations of plates were always of the hardening type for various types of boundary conditions and shapes of the plates.

Much less is known about the effects of initial geometric imperfections on linear or nonlinear vibrations of plates. Hui and Leissa [6] examined the effects of geometric imperfections on linear free vibrations of simply supported rectangular plates with two in-plane biaxial preloaded forces. They found that initial geometric imperfections of the order of the plate thickness may significantly raise the vibration frequencies, especially in the region of large in-plane preload. Large-amplitude vibrations of clamped circular plates with initial geometric imperfections and initial in-plane edge displacements was investigated by Yamaki et al. [4]; however, the results are restricted to only one value of the geometric imperfection amplitude being 10 percent of the plate thickness and only hard-spring behavior was found. A reexamination of the large-amplitude vibrations of circular plates shows that the geometric imperfections of the order of half the plate thickness may significantly raise the free linear vibration frequencies and cause the circular plates to exhibit soft-spring behavior [7]. The large-amplitude vibration behavior of imperfect plates was examined earlier [8]; but the results are confined to square plates with only one half-wave in both directions and the imperfection amplitudes are too large to be considered practically unavoidable. In passing, the effects of geometric imperfections on linear vibration of shallow spherical shells with pressurized preload [9] and nonlinear vibrations of shallow spherical shells [10] have been examined. The important related work on the cylindrical panels [11] and cylindrical shells is in progress.

The present paper aims to examine the effects of geometric imperfections on large-amplitude vibrations of simply supported rectangular plates. The vibration mode, the initial geometric imperfection, and the forcing function are all of the same spatial shape. The effects of structural damping are studied using the complex-modulus model [12]. The analysis is based on a solution of the nonlinear von Kármán differential equations for plates. The nonlinear compatibility equation is satisfied exactly by a suitable choice of the stress function, and the nonlinear dynamic equilibrium equation is satisfied approximately using a Galerkin procedure. The resulting second-order nonlinear ordinary differential equation in time can be written in the form of Duffing's equation with an additional quadratic-spring term.

It is found that the presence of geometric imperfection may significantly raise the free vibration frequency. Contrary to the well-established and widely accepted theory that the nonlinear vibration of flat plates is of the hardening type, the present analysis shows that the presence of unavoidable geometric imperfection amplitudes of the order of only half the plate thickness may change the nonlinear hard-spring character of the plate to one with a soft-spring behavior. Appropriate backbone curves are plotted. Structural damping is shown to reduce significantly the forced linear vibration amplitude of the plate near resonance.

2 Analysis

The dynamic analogue of von Karman equilibrium and compatibility differential equations for moderately large-amplitude vibrations of plates, written in terms of the out-of-plane displacement w and the Airy stress function f, in-

Downloaded 02 May 2010 to 171.66.16.25. Redistribution subject to ASME license or copyright; see http://www.asme.org/terms/Terms_Use.cfm

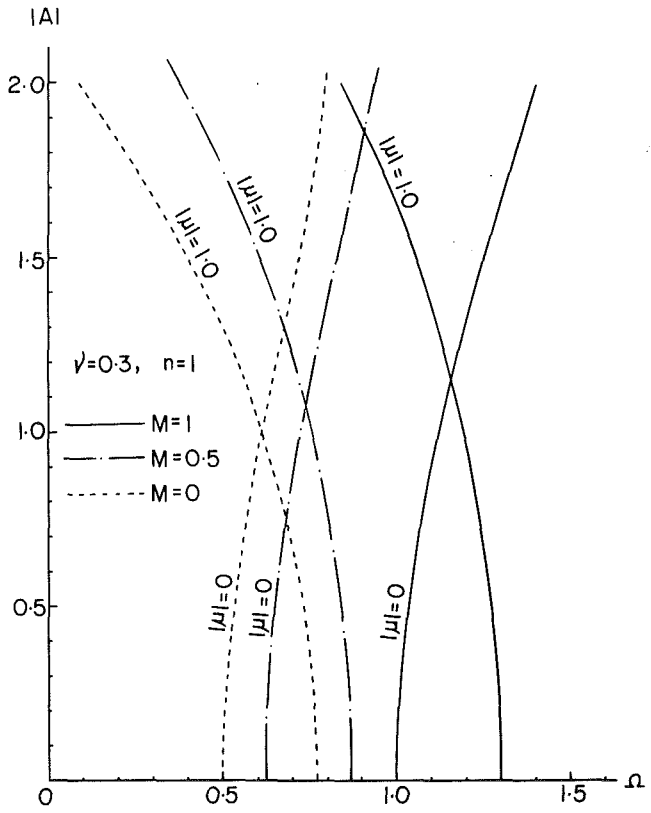

Fig. 2(a) Backbone curves for free nonlinear vibration of simply supported imperfect rectangular plates with no damping ($|\mu| = 0$, 1.0, $\nu = 0.3$, and $n = 1$)

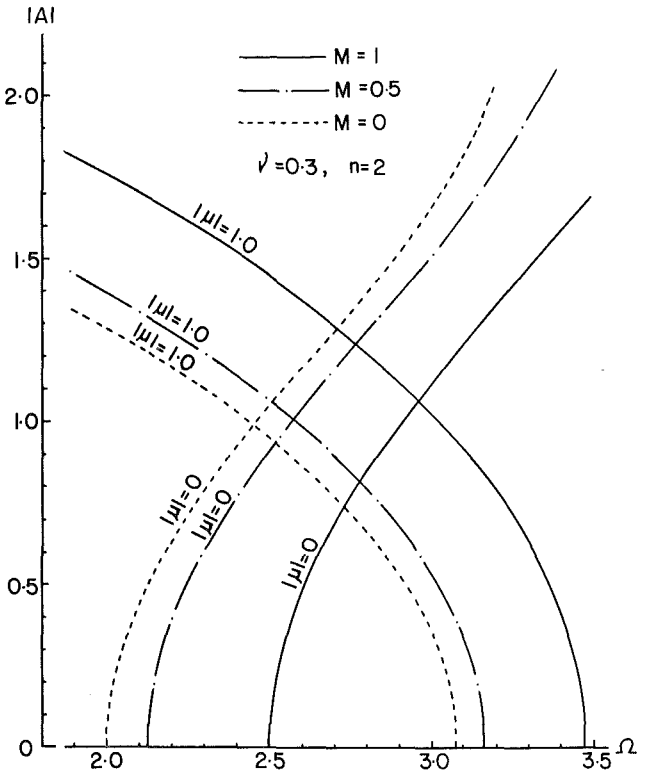

Fig. 2(b) Backbone curves for free nonlinear vibration of simply supported imperfect rectangular plates with no damping ($|\mu| = 0$, 1.0, $\nu = 0.3$, and $n = 2$)

Fig. 2

corporating the possibility of a geometric imperfection w_0 are, respectively, in nondimensional form [5, 11, 13],

$$(1+i\eta)(w_{,xxxx}+w_{,yyyy}+2w_{,xxyy}) = 4\pi^4 q(x,y,t) - 4\pi^4 w_{,tt} + (2c)[f_{,xx}(w+w_0)_{,yy} + f_{,yy}(w+w_0)_{,xx} - 2f_{,xy}(w+w_0)_{,xy}] \quad (1)$$

$$[1/(1+i\eta)](f_{,xxxx}+f_{,yyyy}+2f_{,xxyy}) = (2c)[(w_{,xy})^2 + 2w_{0,xy}w_{,xy} - (w+w_0)_{,xx}w_{,yy} - w_{0,yy}w_{,xx}] \quad (2)$$

where,

$$(w,w_0) = (W,W_0)/h, \quad f = 2cF/(Eh^3), \quad (x,y) = (X,Y)/b, \quad t = \bar{t}\omega_r, \quad q(x,y,t) = [c^2b^4/(Eh^4\pi^4)]Q(X,Y,\bar{t})$$
$$(\omega_r)^2 = 4\pi^4 D/(\rho b^4) = \pi^4 Eh^3/(\rho c^2 b^4) \quad (3)$$

In the foregoing, E is Young's modulus, η is the loss factor associated with the complex-modulus model for structural damping, $i = (-1)^{1/2}$, h is the plate thickness, W_o is the initial geometric imperfection, X and Y are the in-plane coordinates, $Q(X,Y,\bar{t})$ is the forcing function, ρ is the plate mass per unit area, $\bar{t}$ is the time, $c = [3(1-\nu^2)]^{1/2}$, ν is Poisson's ratio, b is the width of the plate, and ω_r is the reference frequency.

The boundary conditions are taken to be simply supported of the form (a is the length of the plate)

$$w(x=0 \text{ or } a/b) = 0$$
$$w_{,xx}(x=0 \text{ or } a/b) = 0$$
$$w(y=0 \text{ or } 1) = 0$$
$$w_{,yy}(y=0 \text{ or } 1) = 0 \quad (4)$$

Further, the in-plane displacements normal to the edges are constant and there is no in-plane shear along all the edges, that is, $f_{,xy}(x=0 \text{ or } x=a/b) = 0$ and $f_{,xy}(y=0 \text{ or } y=1) = 0$.

For a rectangular plate, the fundamental vibration mode corresponds to half sine-waves in both the x and y directions. From a physical point of view, it is realistic to assume that the shape of the geometric imperfection (unavoidable deviation from flatness) is the same as that of the fundamental mode. This will serve as an example problem to demonstrate that the large-amplitude vibration of imperfect plates is not necessarily of the hardening type. The influence of geometric imperfections (of shapes other than the vibration mode) on small-amplitude vibrations of plates was examined [6]. However, their influence on large-amplitude vibrations of plates will not be presented here. The shape of the forcing pressure distribution is taken to be of the same shape as the vibration mode; the specification of this type of pressure distribution will not affect the problem since the present paper deals primarily with free vibrations of plates. Accordingly, the vibration mode, the initial geometric imperfection, and the forcing pressure distributions are taken to be the same spatial shape,

$$[w(x,y,t), w_0(x,y), q(x,y,t)] = [w(t), \mu, q_1\cos(\omega t/\omega_r)]\sin(M\pi x)\sin(n\pi y) \quad (5)$$

where μ is the amplitude of the geometric imperfection normalized with respect to the plate thickness, $M = mb/a$, and m and n are the number of half-waves in the x and y directions, respectively. Substituting $w(x,y,t)$ and $w_0(x,y)$ into equation (2), the stress function that satisfies the boundary conditions and the nonlinear compatibility equation exactly is,

$$f(x,y,t) = (1+i\eta)[w(t)^2 + 2\mu w(t)](c/16)[(n/M)^2\cos(2M\pi x) + (M/n)^2\cos(2n\pi y)] \quad (6)$$

Downloaded 02 May 2010 to 171.66.16.25. Redistribution subject to ASME license or copyright; see http://www.asme.org/terms/Terms_Use.cfm

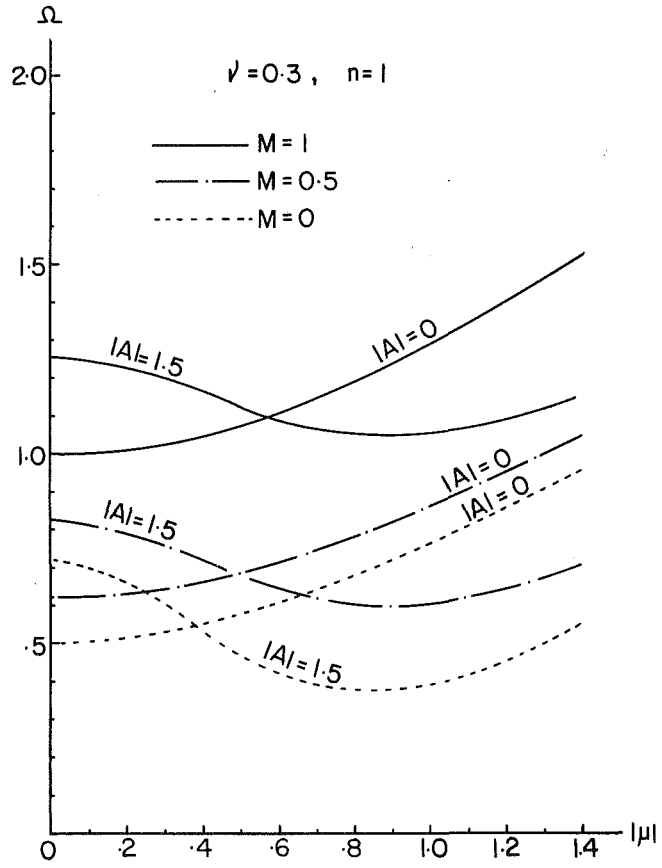

Fig. 3 Free vibration frequency versus imperfection amplitude for simply supported rectangular plates with $|A| = 0, 1.5$, $\nu = 0.3$, and $n = 1$

Finally, substituting $w(x,y,t)$, $w_0(x,y)$ and $f(x,y,t)$ into the nonlinear dynamic equilibrium equation and applying the Galerkin procedure (i.e., multiplication of both sides by $\sin(M\pi x)\sin(n\pi y)$ followed by integration over the plate surface) yields a second-order nonlinear ordinary differential equation in time which can be written in the form of Duffing's equation with the additional quadratic term,

$$w(t)_{,tt} + [kw(t) + (\epsilon k a_2)w(t)^2 + (\epsilon k)w(t)^3](1 + i\eta) = q_1 \cos(\omega t/\omega_r) \tag{7}$$

where k, ϵ, and a_2 are found to be,

$$k = [(M^2+n^2)^2 + (M^4+n^4)(\mu^2 c^2/2)](1/4)$$
$$\epsilon = (M^4+n^4)[c^2/(16k)] \tag{8}$$
$$a_2 = 3\mu$$

Thus, the solution of the linearized differential equation is,

$$w(t) = A\cos(\omega t/\omega_r) \tag{9}$$

where the absolute value of the complex quantity A is,

$$|A| = \frac{(q_1/k)}{\{[1-(\Omega^2/k)]^2 + \eta^2\}^{1/2}} \tag{10}$$

Further, using Linstedt's perturbation technique (see the Appendix of [7]), the ratio of the nonlinear to the linear vibration frequency Ω/Ω_0 is related to the vibration amplitude A in the form (assuming no damping, $\eta = 0$),

$$\Omega/\Omega_0 = 1 + rA^2 - (15\epsilon^2 A^4/256) \tag{11}$$

where

$$r = (3\epsilon/8) - (5a_2{}^2\epsilon^2/12) \tag{12}$$

Thus, the sign of the nonlinearity parameter r determines whether the plate behaves (at least for small values of the amplitude A) as a hard-spring or a soft-spring. Clearly, a sign change in the imperfection amplitude will not affect the problem. Setting r to zero, the transition imperfection amplitude is,

$$\mu_t = \frac{M^2+n^2}{[(2c)^2(M^4+n^4)]^{1/2}} \tag{13}$$

so that for the amplitude of the geometric imperfection greater than μ_t, the nonlinear vibrations of simply supported rectangular plates is of the softening type.

3 Results and Discussion

The influence of structural damping on the linear forced vibration response (for practical values of the loss factor [12] η being 0.1, 0.01, and 0.001) is summarized in Table 1. The amplitude is normalized with respect to its static value ($|Ak/q_1|$) while the forcing frequency is normalized ($\Omega = \omega/\omega_r$) with respect to the linear vibration frequency ($\Omega/\sqrt{k}$). It can be seen that the peaks of the response curves remains unshifted at $\Omega/\sqrt{k} = 1$. Also, the peak value is equal to $1/\eta$.

Figure 1(*a*) shows a graph of the nondimensional nonlinearity parameter r versus the amplitude of the geometric imperfection for simply supported rectangular plates with Poisson's ratio $\nu = 0.3$ and wave numbers $n = 1$ and $M = mb/a = 0$, 0.5, 1, 2, and infinity. Since the influence of the quartic term A^4 in equation (11) is generally small (it is negligible compared with the A^2 term for small A), the large-amplitude vibration problem can be classified as a hard-spring or a soft-spring type depending on whether r is positive or negative, respectively. These curves show that the nonlinearity parameter r decreases and then increases slightly with increasing imperfection amplitude. A similar plot for the wave number $n = 2$ is presented in Fig. 1(*b*). The transitional values of the imperfection amplitude at which the nonlinearity parameter r changes sign can be computed using equation (13); for $n = 1$ or $n = 2$, $|\mu_t|$ lies between 0.42 and 0.60 for all possible values of M. Finally, the aspect ratio of the plate affects the problem via the wave number M.

The backbone curves (magnitude of the vibration amplitude $|A|$ versus free nonlinear vibration frequency Ω) for simply supported rectangular plates with no damping are shown in Fig. 2(*a*). Again, Poisson's ratio ν is taken to be 0.3 and the wave numbers are $n = 1$ and $M = mb/a = 0$, 0.5, and 1.0. It can be seen that for perfect plates ($\mu = 0$), the nonlinear vibration is of the hardening type. Note that although the geometric imperfection raises the free linear vibration frequency (at $|A| = 0$), the nonlinear frequency may be signficantly reduced as a result of the nonlinear softening character of the imperfect plate. A similar plot for the wave number $n = 2$ is depicted in Fig. 2(*b*). Note that in order to show the preceding effects, the nonlinearity frequency Ω is not normalized with respect to its linear value.

Figure 3 shows the nonlinear frequency versus the imperfection amplitude for simply supported rectangular plates with $\nu = 0.3$, $n = 1$, and $M = 0$, 0.5, and 1.0 for fixed values of the magnitude of the vibration amplitude $|A| = 0$ and 1.5. Again, the nondimensional frequency Ω, defined to be ω/ω_r, is not to be confused with ω(nonlinear)/ω(linear). Whereas the effect of geometric imperfection is to raise free vibration frequency as seen in the $|A| = 0$ curves, the effect of imperfection may actually lower the nonlinear frequency for a fixed value of the magnitude of the vibration amplitude, say $|A| = 1.5$. It should be noted that the eventual rise of the nonlinear frequency for $|A| = 1.5$ is attributed to two factors: the nonlinearity parameter r becomes slightly less negative as seen in Fig. 1(*a*) and the linear vibration frequency continues to rise with increasing magnitude of the geometric im-

Downloaded 02 May 2010 to 171.66.16.25. Redistribution subject to ASME license or copyright; see http://www.asme.org/terms/Terms_Use.cfm

Table 1 Normalized amplitude ($|Ak/q_1|$) versus normalized frequency ($\Omega/\sqrt{k}$) for a given loss factor

$\Omega/(k^{1/2})$	$\lvert Ak/q_1 \rvert$ (at $\eta=0.1$)	$\lvert Ak/q_1 \rvert$ (at $\eta=0.01$)	$\lvert Ak/q_1 \rvert$ (at $\eta=0.001$)
0.00	0.995037	0.999950	0.999999
0.20	1.036060	1.041610	1.041660
0.40	1.182130	1.190390	1.190470
0.60	1.543770	1.562310	1.562480
0.80	2.676440	2.776710	2.777670
0.85	3.390200	3.601270	3.603370
0.90	4.657460	5.255880	5.262430
0.95	7.160000	10.202900	10.251000
0.975	8.966580	19.850100	20.211800
1.00	10.000000	100.000000	1000.000000
1.025	8.921860	19.378600	19.714700
1.05	6.983240	9.710000	9.751460
1.10	4.299340	4.756510	4.761370
1.15	2.961660	3.099290	3.100630
1.20	2.216210	2.272140	2.272670
1.40	1.036060	1.041610	1.041660
1.60	0.639713	0.641013	0.641024
1.80	0.445984	0.446424	0.446428
2.00	0.333148	0.333332	0.333333
2.50	0.190442	0.190476	0.190476
3.00	0.124990	0.125000	0.125000
4.00	0.0666652	0.0666667	0.0666667
5.00	0.0416663	0.0416667	0.0416667
7.50	0.0180995	0.0180995	0.0180995
10.00	0.0101010	0.0101010	0.0101010

perfection. For brevity, a similar plot for the $n=2$ case will not be presented here.

4 Concluding Remarks

The effects of geometric imperfections on the linear and nonlinear vibrations of simply supported rectangular plates were examined. It was found that the presence of geometric imperfections of the order of a fraction of the plate thickness may significantly raise the free linear vibration frequencies. Furthermore, small geometric imperfections may drastically change the nonlinear character of the vibration problem from the well-accepted hard-spring behavior to one with a soft-spring behavior. The soft-spring behavior of nonlinear axisymmetric vibrations of clamped shallow spherical caps with circular edges [14] supports qualitatively the soft-spring findings of the present paper for the special case when $M=m=n=a/b=1$.

Finally, it should be mentioned that the geometric imperfection is taken to be of the same shape as the vibration mode. Analogous to the buckling and initial postbuckling problems [15], it is quite possible that this type of geometric imperfection is the most influential one. That is, if the effects of this type of imperfection are not significant, then it is probably not worthwhile to consider other types of imperfection. The severe effects of geometric imperfections in the present analysis show that the influence of unavoidable random imperfections cannot be "safely" neglected in practical designs. While it is highly desirable to obtain more accurate hard-spring curves (using the amplitude incremental method [16] and including the effects of shear and rotatory inertia [17]), it is equally important to investigate whether practical imperfect plates behave as hard-spring or soft-spring in large-amplitude vibrations. Further work on the effects of geometric imperfections on large-amplitude vibrations of angle and cross-ply composite plates will be presented in separate papers.

5 Acknowledgment

The work was started while the author was a graduate student at the Department of Ocean Engineering, Massachusetts Institute of Technology, Cambridge, Mass. 02139.

References

1 Chu, H. N., and Herrmann, G., "Influence of Large Amplitudes on Free Flexural Vibrations of Rectangular Elastic Plates," ASME JOURNAL OF APPLIED MECHANICS, Vol. 23, 1956, pp. 532–540.

2 Yamaki, N., "Influence of Large Amplitudes on Flexural Vibrations of Elastic Plates," *Zeitschrift fur Angewandte Mathematik und Mechanik (ZAMM)*, Dec. 1961, pp. 501–510.

3 Prathap, G., and Varadan, T. K., "On the Non-Linear Vibrations of Rectangular Plates," *J. of Sound and Vibration*, Vol. 56, No. 4, 1978, pp. 521–530. Also, letter to the editor, *J. of Sound and Vibration*, Vol. 61, No. 2, pp. 311–314.

4 Yamaki, N., Otomo, K., and Chiba, M., "Non-Linear Vibrations of a Clamped Circular Plate With Initial Deflection and Initial Edge Displacement, Part 1: Theory," *J. of Sound and Vibration*, Vol. 79, No. 1, 1981, pp. 23–42.

5 Chia, C. Y., *Nonlinear Analysis of Plates*," McGraw-Hill, New York, 1980.

6 Hui, D., and Leissa, A. W., "Effects of Geometric Imperfections on Vibrations of Biaxially Compressed Rectangular Flat Plates," ASME JOURNAL OF APPLIED MECHANICS, Vol. 51, 1984, pp. 00–00.

7 Hui, D., "Large Amplitude Axisymmetric Vibrations of Geometrically Imperfect Circular Plates," *J. of Sound and Vibration*, Vol. 91, No. 3, Dec. 1983, pp. 750–756.

8 Celep, Z., "Free Flexural Vibration of Initially Imperfect Thin Plates," *Zeitschrift fur Angewandte Mathematik und Mechanik (ZAMM)*, Vol. 56, Sept. 1976, pp. 423–428.

9 Hui, D., and Leissa, A. W., "Effects of Uni-Directional Geometric Imperfections on Vibrations of Pressurized Shallow Spherical Shells," *Int. J. of Nonlinear Mechanics*, Vol. 18, 1983, pp. 279–285.

10 Hui, D., "Large Amplitude Vibrations of Geometrically Imperfect Shallow Spherical Shells with Structural Damping," *AIAA Journal*, Vol. 21, 1983, pp. 1736–1741.

11 Hui, D., "Influence of Geometric Imperfections and In-Plane Constraints on Nonlinear Vibrations of Simply Supported Cylindrical Panels," ASME JOURNAL OF APPLIED MECHANICS, Vol. 51, 1984, in press.

12 Bert, C. W., "Material Damping: An Introductory Review of Mathematical Models, Measures and Experimental Techniques," *J. of Sound and Vibration*, Vol. 29, No. 2, 1973, pp. 129–153.

13 Tvergaard, V., "Influence of Post-Buckling Behaviour on Optimum Design of Stiffened Panels," *Int. J. of Solids and Structures*, Vol. 9, 1973, pp. 1519–1534.

14 Grossman, P. L., Koplik, B., and Yu, Y. Y., "Nonlinear Vibrations of Shallow Spherical Shells," ASME JOURNAL OF APPLIED MECHANICS, 1969, pp. 451–458.

15 Koiter, W. T., "On the Stability of Elastic Equilibrium," Doctoral Thesis, Delft, Amsterdam, 1945, English Translations: NASA TT-F10, 833, 1967 and AFFDL-TR-70-25, 1970.

16 Lau, S. L., and Cheung, Y. K., "Amplitude Incremental Variational Principle for Nonlinear Vibration of Elastic Systems," ASME JOURNAL OF APPLIED MECHANICS, Vol. 48, Dec. 1981, pp. 959–964.

17 Sathyamoorthy, M., "Effects of Large Amplitude, Shear and Rotatory Inertia on Vibration of Rectangular Plates," *J. of Sound and Vibration*, Vol. 63, 1979, pp. 161–167.

Downloaded 02 May 2010 to 171.66.16.25. Redistribution subject to ASME license or copyright; see http://www.asme.org/terms/Terms_Use.cfm

Journal of Applied Mechanics

Discussion

Stress Distributions for a Quarter Plane Containing an Arbitrarily Oriented Crack[1]

B. Durai-Swamy.[2] The authors should be congratulated for their excellent article on the stress distributions in an isotropic elastic quarter plane containing an arbitrarily oriented crack. However, the following comments are in order.

To get the solution for the quarter plane with a crack, first the solution for a quarter plane with a single edge dislocation is obtained. For this, the Mellin integral transform is used to obtain the stress field and Green's functions. Then the fundamental solutions are superposed such that the boundary conditions are satisfied for the desired quarter plane. This procedure leads to a system of integral equations which is solved numerically.

Almost an identical but more thorough and rigorous procedure was used in references [1] and [2] to obtain a solution for a more general orthotropic elastic quarter plane subjected to arbitrary surface loadings. In [1] and [2] Fourier-Plancherel integral transform was used to solve the boundary value problems of half planes. Then by superpositioning two half plane solutions, the stress field and Green's functions for the quarter plane were obtained. This procedure leads to a system of integral equations which was solved analytically and numerically.

It is unfortunate that such a closely related work [2] went unnoticed and unreferenced.

References

1 Durai-Swamy, B., Dvorak, J., and Godfrey, G. E., "Theoretical Investigations of Stresses in an Orthotropic Elastic Quarter Plane," UTME-TP7002, Department of Mechanical Engineering, University of Toronto, Toronto, Aug. 1970.

2 Durai-Swamy, B., "A Theoretical Investigation of Stresses Near the Corner of an Orthotropic Elastic Orthogonal Wedge," *International Journal of Solids and Structures*, Vol. 17, 1981, pp. 499-514.

[1] By L. M. Keer, J. C. Lee, and T. Mura and published in the March issue of the ASME JOURNAL OF APPLIED MECHANICS, Vol. 50, pp. 43-49.

[2] Design Engineer, Nuclear Systems Department, Ontario Hydro, Toronto, Canada.

Authors' Closure

Our result, giving the stress field for the loaded quarter plane, was solved explicitly in terms of infinite integrals; the crack problem based on this solution required numerical solution of a system of integral equations. The quarter plane technique used was essentially that given in our reference [2]* for an isotropic material. We regret not having cited his extension to the orthotropic case.

References

*Sneddon, I. N., "Fourier Transform Solution of the Quarter Plane Problem in Elasticity," File No. PSR-99/6, Applied Mathematics Research Group, North Carolina State University, May 1971.

Analysis of the Weibull Distribution Function[1]

P. Kittl.[2] In Chang's article [1] about the Weibull distribution function a criticism is made on the lack of a theoretical justification for this distribution. This paper is on the probabilistic deduction given by Weibull [2], perhaps in a primitive but exact way, and in a more elaborated way by other authors like Freudenthal [3] or Kittl [4].

In Weibull's original paper [2], the basic hypothesis is that

$$S_{12} = S_1 \cdot S_2 \tag{1}$$

where S_{12} is the probability of survival of a chain composed of two identical rods placed beside each other, and S_1 and S_2 are the probabilities of survival of the first and second rods. If in equation (1) we put as argument the length of the rods, we get:

$$S_{12}(\ell_1 + \ell_2) = S_1(\ell_1) S_2(\ell_2) \tag{2}$$

The chain is subjected to a uniaxial uniform traction stress. The functional equations (2) has the boundary conditions

$$S_{12}(0) = S_1(0) = S_2(0) = 1$$
$$S_{12}(\infty) = S_1(\infty) = S_2(\infty) = 0 \tag{3}$$

[1] By K. T. Chang and published in the June, 1982 issue of the ASME JOURNAL OF APPLIED MECHANICS, Vol. 49, pp. 450-451.

[2] Instituto de Investigaciones y Ensayes de Materials (IDIEM), Facultad de Ciencas Fisicas y Matemáticas, Universidad de Chile, Casilla 1420, Santiago, Chile.

Copyright © 1984 by ASME
Downloaded 02 May 2010 to 171.66.16.25. Redistribution subject to ASME license or copyright; see http://www.asme.org/terms/Terms_Use.cfm

Journal of Applied Mechanics

Book Reviews

Mechanics of Solids—The Rodney Hill 60th Anniversary Volume. Edited by H. G. Hopkins and M. J. Sewell. Pergamon Press, England, 1982. 693 Pages. Price $100.00.

REVIEWED BY E. H. LEE[1]

As stated in the Editor's Preface, this volume was planned to have "some balanced structure, in the hope that it might achieve a degree of permanence in the literature of the (title) subject." It consists of "a restricted number of substantial articles" which provide an indepth introduction to selected subject areas in solid mechanics. The topics are ones to which Rodney Hill has made contributions or "certain topics immediately adjacent thereto in either physical or mathematical or engineering terms." The book begins with a general biographical sketch which illuminates the career and achievements of this unusually talented and dedicated person. There follows a complete bibliography of Rodney Hill's publications up to 1981. The volume is elegantly produced and bound for lasting use.

The contributors and their topics are: J. F. W. Bishop, Distortions and Interactions in a Fast Reactor Core; B. Budiansky, J. W. Hutchinson, and S. Slutsky, Void Growth and Collapse in Viscous Solids; P. Chadwick and G. D. Smith, Surface Waves in Cubic Elastic Materials; D. R. J. Chillingworth, Universal Bifurcation Problems; I. F. Collins, Boundary Value Problems in Plane Strain Plasticity; J. D. Eshelby, Aspects of the Theory of Dislocations; J. H. Gittus, Superplasticity; K. S. Havner, The Theory of Finite Plastic Deformation of Crystalline Solids; W. Johnson, The Mechanics of Some Industrial Pressing, Rolling, and Forging Processes; R. J. Knops, Instability and the Ill-posed Cauchy Problem in Elasticity; P. B. Mellor, Experimental Studies of Plastic Anisotropy in Sheet Metal; F. Milstein, Crystal Elasticity; A. Needleman and V. Tvergaard, Aspects of Plastic Postbuckling Behavior; R. W. Ogden, Elastic Deformations of Rubberlike Solids; J. R. Rice, Elastic-Plastic Crack Growth; M. J. Sewell, Legendre Transformations and Extremum Principles; A. J. M. Spencer, Deformation of Ideal Granular Materials; and J. R. Willis, Elasticity Theory of Composites.

I have read a number of the articles and I have indeed found them to be thorough, up-to-date presentations of their topics. I judge that the volume does offer the promise of achieving the goal stated in the Preface of becoming a contribution of lasting value to the literature of solid mechanics. It stands as a tribute to the editors' concept of a volume of this nature and it is sad that Geoffrey Hopkins did not live to see the idea come to fruition.

[1]Professor, Department of Mechanical Engineering, Aeronautical Engineering and Mechanics, Rensselaer Polytechnic Institute, Troy, N.Y. 12181. Life Fellow ASME.

Soil Mechanics – Transient and Cyclic Loads, Constitutive Relations and Numerical Treatment. Edited by G. N. Pande and O. C. Zienkiewicz. Wiley, New York, 1982. 627 Pages. Price $78.95.

REVIEWED BY S. C. COWIN[2]

This volume is a collection of 22 contributions by 37 authors. It is an attractively printed hardbound volume. The collection represents the state of the art in the understanding of the behavior of soils under transient and cyclic loads at the beginning of the 1980s. The titles of the contributions and their authors are as follows:

(1) Soils and Other Saturated Media under Transient, Dynamic Conditions; General Formulation and the Validity of Various Simplifying Assumptions (O. C. Zienkiewicz and P. Bettess).

(2) Boundary Layer Theory of Waves in Poro-elastic Sea Bed (C. C. Mei and M. A. Foda).

(3) Approximations of Cyclic Pore Pressures Caused by Sea Waves in a Poro-elastic Half-Plane (A. Verruijt).

(4) On the Importance of Dissipation Effects in Evaluating Pore Pressure Changes Due to Cyclic Loading (H. B. Seed and I. M. Idriss).

(5) Liquefaction and Permanent Deformation under Dynamic Conditions – Numerical Solution and Constitutive Relations (O. C. Zienkiewicz, K. H. Leung, E. Hinton, and C. T. Chang).

(6) Dynamic Response Analyses of Saturated Sands (W. D. L. Finn).

(7) Dynamic Response Analysis of Level Ground Based on the Effective Stress Method (K. Ishihara and I. Towhata).

(8) Elastoplastic and Viscoplastic Constitutive Models for Soils With Application to Cyclic Loading (Z. Mroz and V. A. Norris).

(9) A Critical State Soil Model for Cyclic Loading (J. P. Carter, J. R. Booker, and C. P. Wroth).

(10) Bounding Surface Formulation of Soil Plasticity (Y. F. Dafalias and L. R. Herrmann).

(11) A Model for the Cyclic Loading of Overconsolidated Soil (M. J. Pender).

(12) Modelling and Analysis of Cyclic Behaviour of Sands (J. Ghaboussi and H. Momen).

(13) A Constitutive Model for Soil under Monotonic and Cyclic Loading (R. Nova).

(14) A New Endochronic Plasticity Model for Soils (K. C. Valanis and H. E. Read).

(15) Endochronic Models for Soils (Z. P. Bazant, A. M. Ansal, and R. J. Krizek).

[2]Professor, Department of Biomedical Engineering, Tulane University, New Orleans, La. 70118. Fellow ASME.

Copyright © 1984 by ASME
Downloaded 02 May 2010 to 171.66.16.25. Redistribution subject to ASME license or copyright; see http://www.asme.org/terms/Terms_Use.cfm

(16) On Dynamic and Static Behavior of Granular Materials (S. Nemat-Nasser).

(17) Fatigue Models for Cyclic Degradation of Soils (H. A. M. van Eekelen).

(18) Shakedown of Foundations Subjected to Cyclic Loads (G. N. Pande).

(19) Comments on the Use of Physical and Analytical Models (P. W. Rowe and I. M. Smith).

(20) Laboratory Investigations of the Behavior of Soils under Cyclic Loading: a Review (D. M. Wood).

(21) The Cyclic Simple Shear Test (W. D. L. Finn, S. K. Bhatia, and D. J. Pickering).

(22) Soil Liquefaction Studies in the People's Republic of China (W. D. L. Finn).

The primary concern of many of the contributions is the constitutive modeling of the soil matrix under cyclic loading. Under cyclic loading the structure of the soil changes progressively with permanent changes occurring in the volume occupied by the soil grains. These permanent changes are referred to by various authors as material degradation or fatigue. If the soil is saturated with water, the reduction in the volume occupied by the soil grains induces an increase in the pore water pressure within the soil structure. If the pore water pressure increases to a value equal to the intergranular pressure, the soil loses its shear strength and the soil mass is said to be liquefied.

Roughly, the contributions contained in this volume can be divided into those that are experimental in nature, those that are theoretical or computational in nature, and those that deal with the practical problem of the evaluation of liquefaction potential at a site. In the following paragraphs some of the contributions in each of these three divisions will be discussed. The relatively few papers concerned with experiments and engineering practice were generally more interesting than the more numerous papers concerned with theory or numerical methods.

The practical engineering problem of site liquefaction analysis has undergone a major change in methodology in the last decade. The "total stress method" of site liquefaction analysis was employed in the late sixties and early seventies. This method assumed that the soil was undrained, that is to say, there was no dissipation of pore water pressure due to water diffusion to other parts of the soil structure. The newer method of site liquefaction analysis is called the "effective stress method" and it accounts for the mitigation of the induced pore water pressure due to water movement. The effective stress method employs the effective stress concept in conjunction with the Biot theory for porous, deforming continua. Contribution (4) gives three excellent and convincing illustrations of the necessity of considering pore water pressure dissipation due to water movement. Contribution (6) describes the evolution of the effective stress method, and assesses its ability to meet the demands of practice. Contribution (7) describes a version of the effective stress method in detail. These contributions illustrate the development of an engineering methodology based on experience, laboratory testing, and theory.

The contributions of theoretical or computational nature are applications or special developments of continuum theories for the mechanical behavior of saturated or partially saturated soils. The Biot theory of flow through porous elastic media is the subject of contributions (1), (2), (3), and (5). Contributions (2) and (3) contain interesting sea bed applications of the Biot theory. Contribution (1) presents an incremental form of the Biot theory that is recast in a format appropriate for the finite element method in (5). Contributions (8), (9), (10), (11), (12), (13), and (16) concern plasticity or viscoplasticity models for soil behavior. The models assume strain hardening and, generally, nonassociated flow rules are employed. The endochronic theory is applied to soils in contributions (14) and (15). The application of shakedown theories to the soil liquefaction problem is suggested in contribution (18). The analogy between metal fatigue and soil degradation by irreversible soil volume changes is discussed in contribution (17).

There are only two contributions that deal directly with experimental methods, contributions (20) and (21). The question of prime importance in experimental soil mechanics and, in particular, in the experimental soil mechanics associated with liquefaction, is discussed in both of these papers. That is the question of uniformity or homogeneity of the strain field within the test domain of a test sample. Contribution (20) reviews the experimental literature on soil liquefaction research and shows that the basic test procedures of cyclic triaxial testing and cyclic simple shear testing induce inhomogeneities in the strain field during the course of the test. The seriousness of these inhomogeneities leads to the suggestion in contribution (20) that liquefaction testing could be a phenomenological study of imperfection sensitivity. This lack of homogeneity in the test sample poses a fundamental problem for soil mechanics because continuum theories for the mechanical behavior of materials are usually based on data obtained from homogeneous test situations. This is the case, for example, in the theories of elasticity and of viscous fluids. There are two approaches to the solution of this fundamental problem. The first, which is the approach described in contribution (21) for simple shear testing, is to try to achieve cyclic test procedures that are always characterized by uniform or homogeneous strain. The other approach is to consider the test itself as a boundary value problem from which the soil constitutive relation must be deduced by analytical or computational methods. This problem amply demonstrates the degree to which experimental procedures lag behind computational and theoretical developments.

This volume does communicate a consensus of the present status of soil liquefaction research. The consensus, which appears to be shared by practitioner, theoretician and experimentalist alike, is that appropriate effective stress-strain-volume change laws for soils under cyclic loading have not been established. Thus, in spite of developments in multiphase continuum mechanics (Biot theory) and computational continuum mechanics (the finite element method), the immediate future development of liquefaction research is blocked by the nonexistence of a widely accepted constitutive equation for saturated soils. The prime deterrent to development of an accepted constitutive equation is the lack of convincing experimental data and, in particular, the lack of an experimental situation in which the strain remains homogeneous throughout the course of the test.

Mechanics of Composite Materials: Recent Advances. Edited by Z. Hashin and C. T. Herakovich. Pergamon Press, New York, 1983. 499 Pages, Price $75.00.

REVIEWED BY Y. WEITSMAN[3]

The subject of Composite Materials covers a wide category of responses and configurations. It provides for an abundance of research topics and practical applications. Several, but

[3]Professor, Mechanics and Materials Center, Civil Engineering Department, Texas A&M University, College Station, Texas 77843.

Copyright © 1984 by ASME
Downloaded 02 May 2010 to 171.66.16.25. Redistribution subject to ASME license or copyright; see http://www.asme.org/terms/Terms_Use.cfm

clearly not all, of those subjects are represented in this book, which forms the proceedings of an IUTAM symposium held at Blacksburg, Va. during Aug. 16–19, 1982.

The proceedings contain 30 papers divided into several groupings which can be roughly delineated as follows:

1 Basic models. This group includes papers on micromechanics, effective properties, statistics of random media, and certain aspects of inelastic behavior.

2 Strength, failure, and damage. This group contains a variety of papers which propose statistical, deterministic, and semiempirical approches to what is probably the most difficult and urgent problem area in composites.

3 Fracture. Several papers deal with the application of fracture mechanics to composites. The methods vary between numerical, finite-element techniques, and analytical solutions in anisotropic elasticity.

4 Laminate and structural analyses and behavior. This category contains works on higher order laminated-plate theory as well as applications-oriented papers which discuss the response of specific structural components under special loads.

5 Additional papers cover a variety of subjects like structural optimization, dynamic behavior, and experimental techniques.

The papers contain extensive lists of references and provide an up-to-date information on several areas of current concern in composites. This makes the Proceedings a worthwhile book for readers who specialize in the area, especially to those interested in fundamental aspects of the subject.

Ultrasonic Testing of Materials. By J. Krautkrämer and H. Krautkrämer. Springer-Verlag, New York, 1983. 667 Pages. Price $79.50.

REVIEWED BY W. SACHSE[4]

This book is the latest edition of the Krautkrämers' standard reference monograph on ultrasonic materials testing. There are only minor differences between this new third edition and the previous second edition. These include the correction of several misprints, replacement of a few figures in one section, and a minor change in the list of ultrasonic nondestructive testing standards. The copy of the book available for review appeared to be of somewhat lower quality than the earlier edition, principally in the half-tone photographs appearing in the text and the paper stock.

For those not familiar with this reference text it is worth reviewing some of its features. The book is a comprehensive text covering all aspects of ultrasonic testing, including the fundamental principles of such testing, the methods and instruments used, a review of general test procedures and applications with an extended summary of approaches to special inspection situations.

The first quarter of the book contains an elementary overview of acoustics, including wave propagation, scattering and attenuation effects, and the operation of piezoelectric and other transducers. This is followed by a slightly shorter section dealing with various ultrasonic measurement techniques used for flaw identification and materials characterization. This section also contains specific examples of instruments, transducer configurations and calibration test blocks. In the next, shorter section, aspects of the transducer used in an ultrasonic test are reviewed. The emphasis is on piezoelectric transducers and various means for coupling them to flat or more complex specimen geometries. Also treated by example are the effects of boundaries and the use of specific wave modes in testing situations and procedures for characterizing flaw signals. This section even includes some ideas for organizing an inspection station. The final section of the book is also its longest, being nearly 250 pages long. It is a compendium of results obtained with ultrasonic measurements in specific testing situations. Included are examples of inspecting forgings, railway components, finished and semifinished metal stock (plates, strips, wires, etc.), pipes and cylinders, castings, joints (welded and other), metals and nonmetals, and more.

From the foregoing it should be clear that this book is very comprehensive. Nevertheless, it has several limitations. Principal among them is that while some of the European work and particularly that of Germany is well summarized, much work done elsewhere, in England and the United States and especially in Japan, is missing. The list of references at the end of the book includes few more recent than 1973 and clearly the ultrasonic testing field has advanced most rapidly since then. It is unfortunate that the new edition made no improvements in this regard over the 1977 edition.

As a reference to the science base of ultrasonic materials testing, the book is not especially strong. Mentioned briefly, but not to the extent deserving, are the results of research in acoustic emission, acoustoelasticity and stress measurements, scattering and ultrasonic spectroscopy, imaging, and electromagnetic-acoustic transducers (EMAT's), and laser generation and detection of ultrasound. Absolute ultrasonic measurements including transducer characterization procedures are not considered in detail. The book's focus is more to the existing technology of the field. The examples and figures shown pertain to specific ultrasonic inspection situations. Thus the book is a useful compilation of existing ultrasonic materials measurement techniques which are used in the field and which are of interest to an inspector and which may not be familiar to the ultrasonic researcher but which he should be aware of if his research is to be applicable. As such, this book is a valuable reference text to both groups and it should be familiar and readily available to all who are active in this field.

Contact Mechanics and Wear of Rail/Wheel Systems. Edited by J. Kalousek, R. V. Dukkipati, and G. M. L. Gladwell. Proceedings, International Symposium, University of British Columbia, July 1982. 600 pages. Price $48.00.

REVIEWED BY L. M. KEER[5]

The International Symposium, from which this volume is the proceedings, was held at the University of British Columbia, July 6–9, 1982. The objectives, as stated in the Introduction, were threefold: (1) To celebrate the 100th anniversary of the work of Heinrich Hertz in the field of contact mechanics. (2) To provide a forum whereby theoreticians and applied scientists could meet and discuss problems of mutual interest. (3) To focus attention on the importance of contact mechanics and wear mechanisms in

[4]Professor, Department of Theoretical and Applied Mechanics, Cornell University, Ithaca, N. Y. 14853.

[5]Professor, Department of Civil Engineering, Northwestern University, Evanston, Ill. 60201. Mem. ASME

Downloaded 02 May 2010 to 171.66.16.25. Redistribution subject to ASME license or copyright; see http://www.asme.org/terms/Terms_Use.cfm

clearly not all, of those subjects are represented in this book, which forms the proceedings of an IUTAM symposium held at Blacksburg, Va. during Aug. 16–19, 1982.

The proceedings contain 30 papers divided into several groupings which can be roughly delineated as follows:

1 Basic models. This group includes papers on micromechanics, effective properties, statistics of random media, and certain aspects of inelastic behavior.

2 Strength, failure, and damage. This group contains a variety of papers which propose statistical, deterministic, and semiempirical approches to what is probably the most difficult and urgent problem area in composites.

3 Fracture. Several papers deal with the application of fracture mechanics to composites. The methods vary between numerical, finite-element techniques, and analytical solutions in anisotropic elasticity.

4 Laminate and structural analyses and behavior. This category contains works on higher order laminated-plate theory as well as applications-oriented papers which discuss the response of specific structural components under special loads.

5 Additional papers cover a variety of subjects like structural optimization, dynamic behavior, and experimental techniques.

The papers contain extensive lists of references and provide an up-to-date information on several areas of current concern in composites. This makes the Proceedings a worthwhile book for readers who specialize in the area, especially to those interested in fundamental aspects of the subject.

Ultrasonic Testing of Materials. By J. Krautkrämer and H. Krautkrämer. Springer-Verlag, New York, 1983. 667 Pages. Price $79.50.

REVIEWED BY W. SACHSE[4]

This book is the latest edition of the Krautkrämers' standard reference monograph on ultrasonic materials testing. There are only minor differences between this new third edition and the previous second edition. These include the correction of several misprints, replacement of a few figures in one section, and a minor change in the list of ultrasonic nondestructive testing standards. The copy of the book available for review appeared to be of somewhat lower quality than the earlier edition, principally in the half-tone photographs appearing in the text and the paper stock.

For those not familiar with this reference text it is worth reviewing some of its features. The book is a comprehensive text covering all aspects of ultrasonic testing, including the fundamental principles of such testing, the methods and instruments used, a review of general test procedures and applications with an extended summary of approaches to special inspection situations.

The first quarter of the book contains an elementary overview of acoustics, including wave propagation, scattering and attenuation effects, and the operation of piezoelectric and other transducers. This is followed by a slightly shorter section dealing with various ultrasonic measurement techniques used for flaw identification and materials characterization. This section also contains specific examples of instruments, transducer configurations and calibration test blocks. In the next, shorter section, aspects of the transducer used in an ultrasonic test are reviewed. The emphasis is on piezoelectric transducers and various means for coupling them to flat or more complex specimen geometries. Also treated by example are the effects of boundaries and the use of specific wave modes in testing situations and procedures for characterizing flaw signals. This section even includes some ideas for organizing an inspection station. The final section of the book is also its longest, being nearly 250 pages long. It is a compendium of results obtained with ultrasonic measurements in specific testing situations. Included are examples of inspecting forgings, railway components, finished and semifinished metal stock (plates, strips, wires, etc.), pipes and cylinders, castings, joints (welded and other), metals and nonmetals, and more.

From the foregoing it should be clear that this book is very comprehensive. Nevertheless, it has several limitations. Principal among them is that while some of the European work and particularly that of Germany is well summarized, much work done elsewhere, in England and the United States and especially in Japan, is missing. The list of references at the end of the book includes few more recent than 1973 and clearly the ultrasonic testing field has advanced most rapidly since then. It is unfortunate that the new edition made no improvements in this regard over the 1977 edition.

As a reference to the science base of ultrasonic materials testing, the book is not especially strong. Mentioned briefly, but not to the extent deserving, are the results of research in acoustic emission, acoustoelasticity and stress measurements, scattering and ultrasonic spectroscopy, imaging, and electromagnetic-acoustic transducers (EMAT's), and laser generation and detection of ultrasound. Absolute ultrasonic measurements including transducer characterization procedures are not considered in detail. The book's focus is more to the existing technology of the field. The examples and figures shown pertain to specific ultrasonic inspection situations. Thus the book is a useful compilation of existing ultrasonic materials measurement techniques which are used in the field and which are of interest to an inspector and which may not be familiar to the ultrasonic researcher but which he should be aware of if his research is to be applicable. As such, this book is a valuable reference text to both groups and it should be familiar and readily available to all who are active in this field.

Contact Mechanics and Wear of Rail/Wheel Systems. Edited by J. Kalousek, R. V. Dukkipati, and G. M. L. Gladwell. Proceedings, International Symposium, University of British Columbia, July 1982. 600 pages. Price $48.00.

REVIEWED BY L. M. KEER[5]

The International Symposium, from which this volume is the proceedings, was held at the University of British Columbia, July 6–9, 1982. The objectives, as stated in the Introduction, were threefold: (1) To celebrate the 100th anniversary of the work of Heinrich Hertz in the field of contact mechanics. (2) To provide a forum whereby theoreticians and applied scientists could meet and discuss problems of mutual interest. (3) To focus attention on the importance of contact mechanics and wear mechanisms in

[4]Professor, Department of Theoretical and Applied Mechanics, Cornell University, Ithaca, N. Y. 14853.

[5]Professor, Department of Civil Engineering, Northwestern University, Evanston, Ill. 60201. Mem. ASME

Copyright © 1984 by ASME
Downloaded 02 May 2010 to 171.66.16.25. Redistribution subject to ASME license or copyright; see http://www.asme.org/terms/Terms_Use.cfm

relation to the economics of maintenance of modern railroads.

As one reads through this book, one realizes that the contents represent a good example of the philosophy that if the goals are ambitious, they may sometimes be successful. In the reviewer's opinion, this volume contains one of the best summaries of the field of contact mechanics applied to rail/wheel systems and must be read if one wishes to familiarize oneself with the current research.

The book consists of six parts covering research that includes the mathematical, experimental and design aspects. The flavor and scope of the book can be best deduced by a listing of the contents, which are as follows:

(Part I) "Elastic Contact Analysis"—This part has an introductory paper by Goodman, analytical papers by Gladwell and Greenwood, and an analytical-numerical paper by Kikuchi.

(Part II) "Developments in Contact Mechanics"—Fremond discusses adhesion in the contact; Johnson, inelastic contact; Tevaarwerk, traction in lubricated contacts; and Lawn and Wiederhorn, brittle fracture. Kalker relates two numerical algorithms for contact elastostatics and Süsskind ends the chapter with a tribute to H. Hertz.

(Part III) "Wheel/Rail Mechanics: Applied Theory"—The reality of the wheel/rail applications aspects begin to appear at this point. The wheel/rail contact geometry is detailed by Duffek; its consequences for the surface and subsurface stresses are given by Paul; tangential force-creepage in theory and practice is discussed by Pearce and Rose. Dynamic loading of rails at corrugation frequencies is mentioned by Grassie, et al., and the estimation of creep coefficients by testing is made by ul-Haque and Law.

(Part IV) "Rail/Wheel Wear and its Reduction"—Papers in this section are concerned with the wear and fatigue of the rail/wheel tribosystem. Ghonem, et al. relate observations of rail wear for heavy haul systems, while Steele and Devine discuss gage face wear resistance. Caldwell discusses the contribution of self-steering trucks to rail and wheel wear reduction and Gilmore, the use of conformal wheel profiles to develop a light steerable transit truck. Roney discusses rail wear from the economic viewpoint.

(Part V) "Laboratory Studies of Rail/Wheel Tribosystems"—This section is devoted to experiments performed at various laboratories throughout the world. Some of the experimental studies are as follows: Krause and Poll on the influence of real material and system properties on the traction/creep rolling contact relationships; Kalousek, et al. on the effects of lateral creepage on wear; Ohyama and Maruyama on traction and slip at higher speeds; Clayton, et al. on the results of their studies of surface damage phenomena; and Bugarcic and Lipinsky on their research on two newly developed rolling friction test rigs.

(Part VI) "Design Aspects of Rail/Wheel Contact Mechanics"—The end product of the research of the previous sections is the practical design, which is discussed in papers by Lyon and Weeks on the design of bogies for low wear, by El Maraghy on the design of a power braking railway coach, by Barwell on wheel to rail adhesion, by Elkins on the effect of modifying suspension and wheel profile, by Mufti and Dukkipati on the dynamics associated with a certain simulator, and by Kumar, et al. on the IIT-GMEMD Wheel Rail Simulation Facility to study dynamic effects.

A seventh part summarizes the symposium through panel discussions on the following topics: Contact Mechanics Fundamentals, Rail/Wheel Wear and Wear Reduction, Laboratory Studies of Rail/Wheel Tribosystems, and Design Aspects of Rail/Wheel Contact Mechanics.

Although one has to have a relatively high level of sophistication in mathematics, mechanics, and metallurgy to appreciate all aspects of this book, it represents an invaluable source for the investigator wishing to do useful research in this area. It serves as a good introduction to the mechanics problems specific to the railroad industry and to the terminology used there.

Theory of Viscoelasticity, An Introduction, 2nd Edition. By R. M. Christensen. Academic Press, New York, 1982. 364 Pages. Price $45.00.

REVIEWED BY L. B. FREUND[6]

This is a significantly revised and updated version of the first edition of Dr. Christensen's book which was published in 1971. The material which appeared in the chapters of the first edition has been revised and expanded to account for developments in the field during the intervening decade. The overall treatment of the mechanics of viscoelastic materials has been expanded to include discussion of recent progress in three principal areas, namely (*i*) mathematical approximations which have been found useful in practical applications of the theory, (*ii*) solution of boundary value problems in linear viscoelasticity for which integral transform methods do not apply (e.g., transient contact and crack growth problems), and (*iii*) the theory of viscoelastic materials with nonlinear mechanical response.

The book is intended mainly as a text for a graduate level course for students with some background in the theory of elasticity and the methods of mathematical physics. It could be used effectively in this way because the coverage is broad, many literature references are included, and each chapter is followed by a set of exercises to guide further development of the text material. Because numerous references to the recent literature are given, and because some of the material included in the current edition is still receiving attention from the research community the book should also have value as a research reference volume.

[6] Professor, Division of Engineering, Brown University, Providence, R.I. 02912. Fellow ASME.

Copyright © 1984 by ASME
Downloaded 02 May 2010 to 171.66.16.25. Redistribution subject to ASME license or copyright; see http://www.asme.org/terms/Terms_Use.cfm

ERRATA

Erratum on "A Treatment of Rigid Body Dynamics," by J. Casey, and published in the December, 1983 issue of the ASME JOURNAL OF APPLIED MECHANICS, Vol. 50, pp. 905-907.

Editor's note: This Note was inadvertently published before the author was given the opportunity to correct the proof. This accounts for the large number of errors in the following list.

Page 905:

Three lines above equation (2): $\overline{\mathbf{X}}$ should read $\overline{X}$.

Equation (2):

$$\int_{\mathcal{R}} \rho\, \pi\, dv = \mathbf{0}$$

One line after equation (4):

$$\text{grad}\, \mathbf{v} = \boldsymbol{\Omega},\ \text{curl}\, \mathbf{v} = 2\boldsymbol{\omega},\ \text{div}\, \mathbf{v} = 0$$

Two lines after equation (4): the linear momentum

Two lines after (9): Replace Q^{T} by $\mathbf{Q}^{\mathrm{T}}$.

Equation (10):

$$\mathbf{F} = \int_{\mathcal{R}} \rho \mathbf{b}\, dv + \int_{\partial\mathcal{R}} \mathbf{t}\, da,$$

$$\mathbf{M} = \int_{\mathcal{R}} \rho \boldsymbol{\pi} \times \mathbf{b}\, dv + \int_{\partial\mathcal{R}} \boldsymbol{\pi} \times \mathbf{t}\, da$$

Equation $(11)_2$:

$$\mathbf{M} = \dot{\mathbf{H}} = \dot{\mathbf{J}}\boldsymbol{\omega} + \mathbf{J}\dot{\boldsymbol{\omega}}$$

Equation (12): Replace final comma by period.

Three lines after equation (13): *corotational*

Footnote 3: [6, Sections 10 and 13]

Page 906:

One line after equation (16):

$$\mathring{\mathring{\boldsymbol{\beta}}} = \ddot{\beta}_i \mathbf{e}_i$$

Equation (17):

$$\ddot{\boldsymbol{\beta}} = \mathring{\mathring{\boldsymbol{\beta}}} + 2\boldsymbol{\omega} \times \mathring{\boldsymbol{\beta}} + \dot{\boldsymbol{\omega}} \times \boldsymbol{\beta} + \boldsymbol{\omega} \times (\boldsymbol{\omega} \times \boldsymbol{\beta})$$

Equation (21):

$$\mathbf{M} = (\boldsymbol{\Omega}\mathbf{J} - \mathbf{J}\boldsymbol{\Omega})\boldsymbol{\omega} + \mathbf{J}\mathring{\boldsymbol{\omega}} = \boldsymbol{\omega} \times (\mathbf{J}\boldsymbol{\omega}) + \mathbf{J}\mathring{\boldsymbol{\omega}}$$

One line after equation (22): Replace second period by comma.

Two lines after equation (23): equations

Four lines after equation (23):

$$M_1 = \lambda_1 \dot{\omega}_1 + (\lambda_3 - \lambda_2)\omega_3 \omega_2$$

One line after equation (24): $\bar{\mathbf{v}} = \dot{\bar{\mathbf{x}}}$

Equation (25):

$$\mathbf{F} = m\{\mathring{\mathring{\bar{\mathbf{x}}}} + 2\boldsymbol{\omega} \times \mathring{\bar{\mathbf{x}}} + \mathring{\boldsymbol{\omega}} \times \bar{\mathbf{x}} + \boldsymbol{\omega} \times (\boldsymbol{\omega} \times \bar{\mathbf{x}})\}$$

Two lines after equation (25): as well as a similar . . .

Three lines after equation (25):

$$\mathring{\bar{\mathbf{x}}} = \mathring{\mathbf{x}} = \mathring{\mathbf{a}}, \quad \mathring{\mathring{\bar{\mathbf{x}}}} = \mathring{\mathring{\mathbf{x}}} = \mathring{\mathring{\mathbf{a}}}$$

Five lines after equation (25):

$$\mathbf{F} = m\{\mathring{\mathring{\mathbf{a}}} + 2\boldsymbol{\omega} \times \mathring{\mathbf{a}} + \mathring{\boldsymbol{\omega}} \times \bar{\mathbf{x}} + \boldsymbol{\omega} \times (\boldsymbol{\omega} \times \bar{\mathbf{x}})\}$$

Two lines before equation (27): period is missing

Equation (29):

$$R = \int_{\mathcal{R}} \rho \mathbf{b} \cdot \mathbf{v}\, dv + \int_{\partial\mathcal{R}} \mathbf{t} \cdot \mathbf{v}\, da$$

One line before equation (31): should read (27), (28), (11), and (30).

Reference [9]: Vol. III/1

I should also like to take this opportunity to mention that while the Note was in press I received from Professor P. M. Naghdi of the University of California at Berkeley, some material on Rigid Body Dynamics which is also based on the concepts of the continuum mechanics. Specifically, the approach adopted by Naghdi is substantially the same as in the sections of the Note which are entitled "Basic Equations" and "Work-Energy Theorem." Naghdi's material, which was prepared a number of years ago, will be included in his forthcoming book (coauthored by A. E. Green) on continuum mechanics.

Copyright © 1984 by ASME
Downloaded 02 May 2010 to 171.66.16.25. Redistribution subject to ASME license or copyright; see http://www.asme.org/terms/Terms_Use.cfm